Biomacromolecular Therapeutics for Oncotherapy via Active Targeting and Dynamic Covalent Drug Conjugation

Dissertation

zur Erlangung des Grades

„Doktor der Naturwissenschaften“ (Dr. rer. nat.)

im Promotionsfach Chemie

Am Fachbereich 09

Chemie, Pharmazie, Geographie und Geowissenschaften

der Johannes Gutenberg-Universität Mainz

Bellinda Lantzberg

geb. in Mosbach

Mainz, Januar 2026

MAX-PLANCK-INSTITUT FÜR POLYMERFORSCHUNG

JOHANNES GUTENBERG UNIVERSITÄT MAINZ

First Reviewer: [redacted]

Second Reviewer: [redacted]

Date of defense:

Acknowledgement

[redacted]

"Gratitude is the fairest blossom which springs from the soul."

~Henry Ward Beecher

Abstract

Nanocarriers have entered the oncological treatment landscape with the aim of improving the safety, delivery, and efficacy of chemotherapeutic agents. However, they still suffer from insufficient targeting capability across organ, tissue, and cell-type levels. In parallel, conventional drug conjugation chemistries often lack sufficient systemic stability. Together, these limitations contribute to suboptimal therapeutic efficacy and systemic toxicity. Meanwhile, the growing understanding of tumor biology, particularly the pivotal role of the immune system in both disease progression and eradication, has shifted the focus from solely cytostatic interventions toward immunomodulatory strategies. They are designed to alleviate the immunosuppressive tumor microenvironment and potentiate anti-tumor immune responses, for which precise tissue- and cell-type selectivity is even more critical, explaining why nanocarriers are increasingly considered for immuno-oncology applications.

This thesis addresses two fundamental challenges in drug delivery systems: selective nanocarrier targeting and drug conjugation stability. Specifically, (a) a nanocarrier was designed, synthesized, and evaluated for improved tissue and cell selectivity in the context of immunomodulation, and (b) a linker system was developed that combines two different dynamic covalent linkages that act cooperatively, and thereby overcomes the limitations of individual linkage chemistries. In the first part of this thesis (Chapter 3), a monomolecular human serum albumin-based nanocarrier forming a protective core-shell structure below 40 nm was established. The carrier was decorated with trimannose, a targeting ligand for CD209/CD206 receptors that are highly expressed on certain immune cells, and was dynamically covalently loaded with an immunomodulatory drug, enabling reductant-responsive, traceless release. Cell-selective delivery accompanied by potent immune activation was demonstrated *in vitro* and *ex vivo*. Rapid and efficient organ- and cell-type selectivity was further achieved *in vivo* in healthy mice, positioning this nanocarrier for targeted immunotherapy of liver diseases such as hepatocellular carcinoma. Subsequent studies investigated comparatively mannose-based targeting structures with varying epitope structure and ligand valency (Chapter 4), revealing ligand density on the carrier and epitope structure as key determinants of uptake efficiency and cell selectivity. The second part of the thesis (Chapter 5) introduces a peptide-based linker system comprising two complementary peptide strands, both bearing a cysteine and each either phenylboronic acid- or catechol-containing non-canonical amino acids. Fast and selective heterodimerization via boronate ester formation pre-organized the thiols for formation of a stabilizing disulfide bridge. The resulting dynamic covalent bioconjugate exhibited enhanced stability under tumor microenvironment-like conditions, resisting acid- and dilution-induced dissociation while maintaining dual-responsiveness under intracellular conditions.

Collectively, the results presented in this thesis confront foundational challenges in drug delivery systems related to selective targeting and conjugate stability. The findings introduce modular design strategies, relevant beyond oncotherapy, that contribute to the development of translatable and innovative delivery platforms with efficient *in vivo* performance.

Zusammenfassung

Nanotransporter wurden im onkologischen Behandlungsspektrum etabliert, mit dem Ziel, die Sicherheit, Transport und Freisetzung sowie die Wirksamkeit von Chemotherapeutika zu verbessern. Allerdings weisen sie nach wie vor eine unzureichende Targeting-Fähigkeit auf, was sich in einer schlechten Anreicherung am Zielort auf Organ-, Gewebe- und Zellebene widerspiegelt. Gleichzeitig mangelt es herkömmlichen chemischen Wirkstoffkonjugationen oft an ausreichender systemischer Stabilität. Zusammen tragen diese Einschränkungen zu einer suboptimalen therapeutischen Wirksamkeit und zu systemischer Toxizität bei. Unterdessen hat das wachsende Verständnis der Tumorbiologie, insbesondere der entscheidenden Rolle des Immunsystems sowohl für das Fortschreiten als auch für die Bekämpfung der Krankheit, den Fokus von rein zytostatischen Interventionen auf immunmodulatorische Strategien verlagert. Diese sind darauf ausgelegt, die immunsuppressive Tumormikroumgebung abzuschwächen und die Anti-Tumor-Immunantworten zu verstärken, wobei eine präzise Gewebe- und Zelltypspezifität besonders entscheidend ist, was erklärt, warum Nanoträgern zunehmend für immunonkologische Anwendungen in Betracht gezogen werden.
Diese Arbeit befasst sich mit zwei grundlegenden Herausforderungen bei Wirkstofftransportsystemen: das selektive Targeting von Nanoträgern und die Stabilität der Wirkstoffkonjugation. Konkret wurden (a) ein Nanoträger für eine verbesserte Gewebe- und Zellselektivität im Kontext der Immunmodulation entworfen, synthetisiert und evaluiert und (b) ein Linkersystem entwickelt, welches zwei verschiedene dynamische kovalente Bindungen kombiniert, die kooperativ wirken und dadurch die individuellen Nachteile der einzelnen Bindungen kompensieren.

Im ersten Teil dieser Arbeit (Kapitel 3) wurde ein monomolekularer Nanoträger auf Basis von Humanalbumin entwickelt, der eine schützende Core-Shell-Struktur von weniger als 40 nm aufweist. Der Träger wurde mit Trimannose, einem Targeting-Liganden für CD209/CD206, welche auf bestimmten Immunzellen stark exprimiert werden, dekoriert und dynamisch kovalent mit einem immunmodulatorischen Wirkstoff beladen, was eine reduktionsresponsive, spurlose Freisetzung ermöglicht. Eine zellselektive Aufnahme, begleitet von einer starken Immunaktivierung, wurde *in vitro* und *ex vivo* nachgewiesen. Eine schnelle und effiziente Organ- und Zelltyp-Selektivität wurde darüber hinaus *in vivo* bei gesunden Mäusen erreicht, wodurch dieser Nanoträger für die gezielte Immuntherapie von Lebererkrankungen wie dem hepatozellulären Karzinom Potential aufweist. In nachfolgenden, vergleichenden Studien wurden Mannose-basierte Targeting-Strukturen mit unterschiedlicher Epitopstruktur und Ligandvalenz untersucht (Kapitel 4), wobei sich die Ligandendichte auf dem Träger und die Epitopstruktur als entscheidende Faktoren für die Aufnahmeeffizienz und Zellselektivität herausstellten.
Der zweite Teil der Arbeit (Kapitel 5) beschreibt ein peptidbasiertes Linkersystem, das aus zwei komplementären Peptidsträngen besteht, die beide ein Cystein und jeweils entweder Phenylboronsäure- oder Catechol-haltige nicht-kanonische Aminosäuren enthalten. Die schnelle und selektive Heterodimerisierung über die Bildung von Boronsäureestern

vororganisierte die Thiole für die Bildung einer stabilisierenden Disulfidbrücke. Das resultierende dynamisch kovalente Biokonjugat zeigte unter tumorähnlichen Mikroumgebungsbedingungen eine verbesserte Stabilität, widerstand einer durch Säure und Verdünnung induzierten Dissoziation und behielt gleichzeitig seine duale Responsivität unter intrazellulären Bedingungen bei.

Zusammenfassend gehen die in dieser Dissertation dargestellten Ergebnisse auf grundlegende Herausforderungen von Wirkstoffträgersystemen in Bezug auf selektives Targeting und Konjugatstabilität ein. Die gewonnenen Erkenntnisse stellen modulare Designprinzipien vor, die über die Onkotherapie hinaus relevant sind und zur Entwicklung translationaler und innovativer Plattformen mit effizienter *in-vivo*-Wirksamkeit beitragen.

Contents

List of Abbreviations

Aβ	amyloid β
ADC	antibody-drug conjugate
APC	antigen presenting cell
API	active pharmaceutical ingredient
ApoE	apolipoprotein E
BA	boronic acid
BSA	bovine serum albumin
CA	catechol
CAR	chimeric antigen receptor
CD4	cluster of differentiation 4
CD36	cluster of differentiation 36
CD80	cluster of differentiation 80
CD86	cluster of differentiation 86
CD206	cluster of differentiation 206
CD209	cluster of differentiation 209
CLL	chronic lymphocytic leukemia
CLR	C-type lectin receptor
CMT	critical micelle temperature
CMC	critical micelle concentration
CMPF	carboxy-4-methyl-5-propyl-2-furanpropionic acid
CRD	carbohydrate recognition domain
CRS	cytokine release syndrome
CTLA-4	cytotoxic T-lymphocyte associated protein 4
Cys, C	cysteine
DAMP	damage-associated molecular pattern
DC	dendritic cell
DC-SIGN	dendritic cell-specific intercellular adhesion molecule-3-grabbing non-integrin
DCvC	dynamic covalent chemistry
DDS	drug delivery system
D_h	hydrodynamic diameter
DLS	dynamic light scattering
ECM	extracellular matrix
EMA	European Medicines Agency
EPR	enhanced permeability and retention
EWG	electron withdrawing group
FDA	Food and Drug Administration
F_HAB	fully human albumin binding domain
GalNAc	*N*-acetylgalactosamin

GILT	gamma-interferon-inducible lysosomal thiol reductase
GlcNAc	*N*-acetylglucosamin
GnRH	gonadotropin-releasing hormone
gp18	18-kDa glycoprotein
gp30	30-kDa glycoprotein
gp60	60-kDa glycoprotein
Grb2	growth factor receptor-bound protein 2
GSH	glutathione
GSSG	glutathione disulfide
HCC	hepatocellular carcinoma
H_2O_2	hydrogen peroxide
HPMA	*N*-(2-Hydroxypropyl)methacrylamide
HSA	human serum albumin
ICB	immune checkpoint blockade
ICD	immunogenic cell death
ICG	indocyanine green.
ICI	immune checkpoint inhibitors
IEP	isoelectric point
IgG	immunoglobulin G
IgM	immunoglobulin M
IL	interleukine
ITAM	immunoreceptor tyrosine-based activation motif
ITIM	immunoreceptor tyrosine-based inhibitory motif
IV	intravenous
K_D	dissociation constant
LacNAc	*N*-acetyllactosamine
LAG-3	lymphocyte activation gene-3
LNP	lipid nanoparticle
LSEC	liver sinusoidal endothelial cell
Lys	lysine
M	mannose
MBL	mannose-binding lectin
MDSC	myeloid-derived suppressor cells
MFDS	Ministry of Food and Drug Safety
MGL	macrophage galactose-specific lectin
MHC	major histocompatibility complex
MMR	macrophage mannose receptor
MR	mannose receptor
mRNA	messenger ribonucleic acid
MSA	mouse serum albumin
MTD	maximum tolerated dose
nab	nanoparticle albumin bound

NK	natural killer cell
NLC	nanostructured lipid carriers
NO	nitric oxide
NSCLC	non-small cell lung cancer
PAMP	pathogen-associated molecular pattern
PBA	phenylboronic acid
PD-1	programmed cell death protein 1
PD-L1	programmed cell death ligand 1
PDLLA	poly(D,L-lactide)
PEG	polyethylene glycol
PFS	progression free survival
pK_a	negative logarithm of the acid dissociation constant
PLGA	poly(DL-lactide-co-glycolide)
PLN	polymer-lipid hybrid nanoparticles
PRR	pattern recognition receptor
RES	reticuloendothelial system
RNA	ribonucleic acid
SHP1/2	Src homology region 2 domain-containing phosphatase-1/2
Siglec	sialic acid-binding immunoglobulin-like lectins
siRNA	small interfering ribonucleic acid
SLN	solid lipid nanoparticle
SPARC	secreted protein acidic and rich in cysteine
SPPS	solid phase peptide synthesis
$t_{1/2}$	circulation half-life
TAM	tumor-associated macrophages
TLR7/8a	toll-like receptor 7/8 agonist
TM	trimannose
TME	tumor microenvironment
Treg	regulatory T cell

1. Introduction

Drug delivery as an independent and distinct field of research was coined in the early 1950s with the introduction of Spansule®, the first sustained drug release capsule. A drug delivery system (DDS) is defined as a formulation or a device that enables the introduction of a therapeutic substance into the body. They are often classified by route of administration—oral, rectal, ocular, nasal, pulmonary, transdermal, or injectable—and include forms such as tablets, capsules, powders, suspensions, or gels. The definition also encompasses advanced technologies that simplify delivery, like microneedle patches, hydrogels, or osmotic pumps. The field of drug delivery focuses on the development and optimization of strategies to improve the efficiency and safety of drugs by controlling location, time and/or rate of drug release.[1] To achieve this, the following approaches or combinations thereof are exploited: (a) modifications of the drug, (b) modifications of the environment in which the drug should accumulate and be active, or (c) exploitation of inherent environmental characteristics by tailored DDS design.[2] Drug modifications usually include chemical alterations, such as introduction, masking or replacement of functional groups or amino acids, and the conjugation to targeting units like carbohydrates or antibodies to form antibody-drug conjugates (ADC), or to polyethylene glycol (PEG) for improved circulation times and low immunogenicity. These small molecule modifications are often supported by high-throughput screenings and serve to tune their pharmacokinetics and -dynamics. Modifications of the environment comprise the co-administration of either pharmaceutical or physical interventions to influence the pharmacokinetics of the drug, specifically bioavailability and distribution. Pharmaceutical microenvironment modifiers can include pH modifiers, dispersion enhancers, permeation enhancers, immunomodulators, endosomal pH modifiers or release agents, and inhibitors of drug clearance or metabolism. The physical interventions include for example ultrasound, which can cause vasodilation, enhance tissue perfusion and cell membrane permeability thereby promoting greater drug accumulation at the target site.[3,4] The last strategic drug delivery approach focuses on tailoring delivery systems to address specific environments. These systems often combine several of the above-mentioned strategies, (a) and (b), by chemical, physical and biological design. It was also this approach that led to the development of nanomedicines, which continue to drive innovation in drug delivery and remain a central focus of current research efforts to overcome delivery-related

challenges. To provide a structured understanding of this field, the following Chapter 1.1 will define nanomedicines and nanocarriers, followed by a brief overview of the historical development of nanocarriers as DDSs and a summary of the most important nanocarrier materials that have emerged to date.

1.1. Nanocarriers as drug delivery systems

Nanomedicines are purposefully engineered in nanoscale dimensions to leverage the unique advantages that emerge at this size, which is also the predominant feature for their definition. Nanoparticles have three – according to ISO – or two to three – according to ASTM – dimensions in a size range of 1 – 100 nm.[5,6] Nanocarriers, specifically, can have a size range of 1 – 1000 nm though materials <200 nm are more common in therapeutic approaches due to the microcapillary width and the associated vortex-like flow between red blood cells.[7–10] They are additionally defined by their function, namely to transport and deliver another substance, such as drugs, nucleic acids or enzymes.[11] This definition excludes nanomedicines in which the carrier itself is, directly or indirectly, the active agent, for example PEGylated therapeutic proteins, such as the PEGylated IFN-α-2A pegIntron®, metallic nanoparticles, e.g., iron oxide particles Nanotherm®, or in which the drug is delivered carrier-free in the form of nanocrystals. Importantly, this definition does not strictly exclude ADCs. However, ADCs follow different established antibody regulatory pathways as they are precise three-component protein conjugates in which the antibody function, rather than the nano size and carrier function, is the primary focus, which is why ADCs are considered a distinct class of nanomedicines.[12,13] Noteworthy, these definitions, which were introduced considerably after the implementation of the respective systems both in research and clinical settings, overlap and thus designations are often used interchangeably, albeit within the scope of this thesis in the context of drug delivery systems, the focus is on nanocarrier systems as defined in the beginning of this section.

The development of nanocarriers started with a polymer-drug conjugate which was first reported in 1955 by Von Horst Jatzkewitz. This marked not only the introduction of macromolecules to modify the pharmacokinetics of a small molecule drug but also the importance of cleavable linker chemistry in this context.[14] Shortly afterwards, in 1961, the hematologist Alec Bangham and his colleague Robert Horne, a virologist and expert in

electron microscopy, observed liposomes for the first time. They published the resulting work in 1964 and 1965, and the term liposome was introduced thereafter, leading to the development of this field.[15–18] In 1972, Gregoriadis and Ryman suggested the use of liposomes as drug delivery systems and specifically for enzyme replacement therapy in lysosomal storage disease. They encapsulated the enzyme β-Fructofuranosidase into liposomes and delivered it functional into lysosomes of hepatic cells *in vivo* in rats.[19] They were the first to conceptualize and showcase that liposomal nanocarriers can be applied to protect a biological, active cargo and deliver it to a specific tissue and even subcellular region. To this day, this has had a lasting impact on our understanding of classic nanocarriers. Since then, the research of nano-sized drug delivery systems started to thrive. Liposomal approaches have been further developed which led to the clinical introduction of the first FDA-approved therapeutic nanocarrier Doxil® in 1995, a PEGylated liposome encapsulating doxorubicin. This breakthrough was followed by an era of expansion and diversification of different nanomedicines. As of 2025, over 60 nanomedicines are FDA-approved including over 20 nanocarriers.[20–23] They are used for pain management, hormone therapy and for treating infectious diseases, anemia, enzyme or immune deficiencies, and neoplasms. Despite this variety, cancer remains the dominant application: cancer constitutes the primary indication for about 53% of all nanomedicines marketed or in clinical trials and roughly half of all nanocarriers are approved for oncology.[20,21,24] Despite intense innovation at the bench and a rich literature on nanocarriers, many are mainly preclinical, *i.e.* systems that have not progressed beyond *in vitro* testing. Most clinically tested nanocarriers follow the classical chemotherapeutic cancer treatment regimen, while the use of nanocarriers for cancer immunotherapy, especially beyond formulated cancer vaccination, is a promising emerging approach (see Figure 1),[25–27] but still requires more advancement into clinical research due to the bench-to-bedside gap.[28] However, since most challenges arise from the interaction between nanocarriers and the body, the insights gained from clinically tested nanocarriers are equally valuable for systems that target other tissues or immune cells. Therefore, the introduction centers on nanocarriers that have reached the market or entered clinical trials, where practical benefits, shortcomings, and lessons learned can inform next-generation designs for both traditional chemotherapeutic and immunomodulatory DDSs. Relevant cutting-edge preclinical systems are discussed selectively when they provide additional

insight or exemplify successful approaches to overcome limitations observed in marketed nanocarriers.

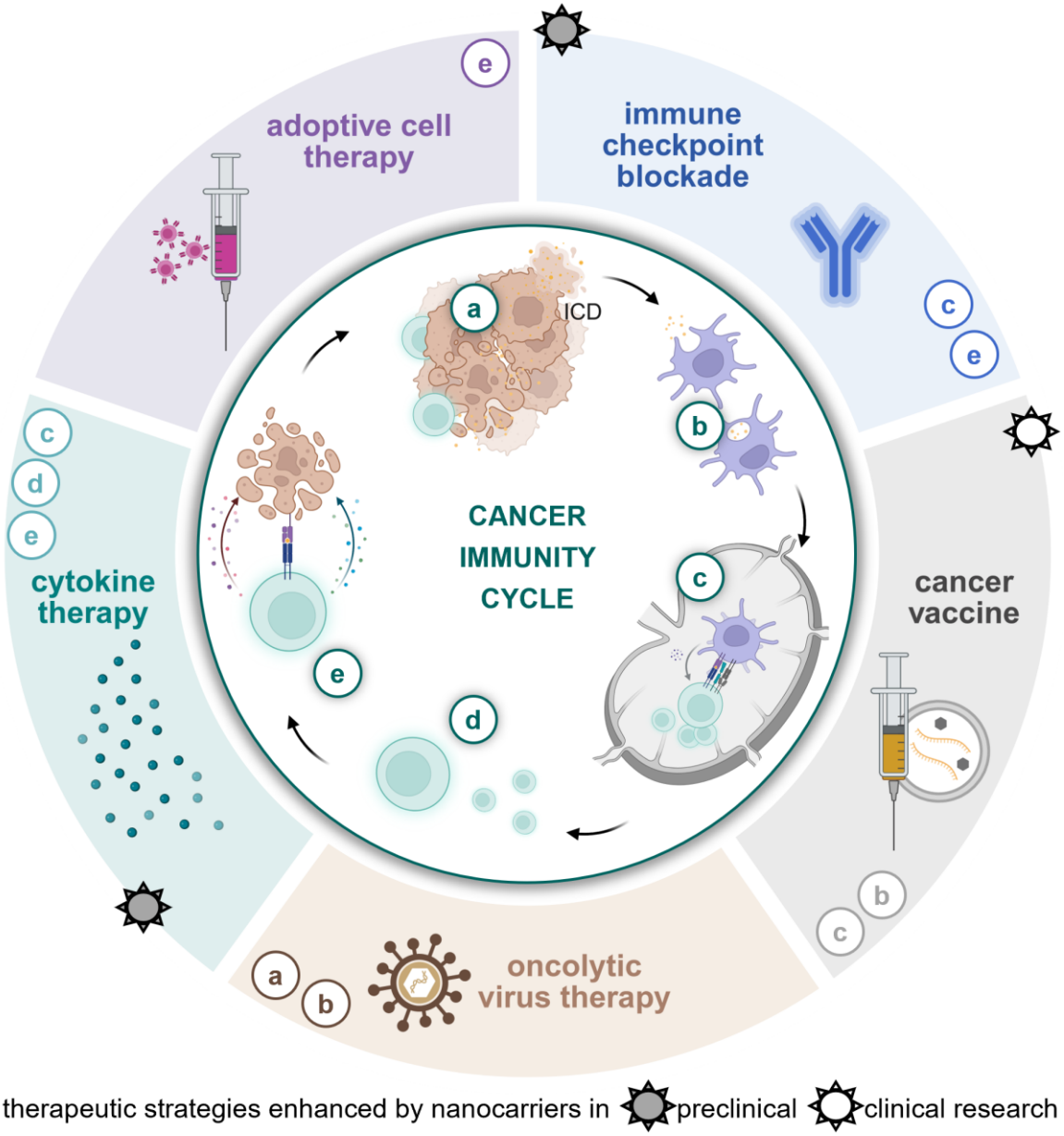

Figure 1: Current immunotherapeutic strategies and which part of the cancer immunity cycle they modulate. Within the natural cancer immunity cycle, dying cancer cells release antigens (a) which are taken up and presented by antigen-presenting cells such as dendritic cells (b). These dendritic cells activate and prime T cells in the lymph nodes (c) after which the T cells migrate into the tumor tissue (d) where they recognize and attack cancer cells (e). The steps (a – e) at which current immunotherapeutics enhance the anti-tumor immune response, as well as the therapy strategies that could benefit from nanocarrier technology and are being investigated in this context, are indicated. Created with BioRender.com.

Reflecting on the successes and shortcomings of clinically tested nanocarriers, researchers are pursuing a variety of new materials to advance next-generation designs. An increasing number of potential carrier materials are under development to improve existing systems and address some of the shortcomings that arose with them. The most important material classes approved by regulatory authorities (see Table 1) are discussed below, with a focus on the nanocarrier types, *i.e.* the developed architectures – highlighting their advantages and disadvantages, and examining research trends that they have prompted. Further materials are also extensively studied but either do not meet the specific definition of nanocarriers or currently lack clinical relevance in oncotherapy and are excluded from discussion. These materials include, but are not limited to, carbon-based materials,[29] metal-based nanoparticles,[30] silica nanoparticles,[31,32] polysaccharide-based nanoparticles,[33,34] and composite or hybrid systems.[35–37] The overall diversity of nanocarrier materials, spanning lipids, polymers, and proteins, is not redundant but rather essential to address the complexity of challenges associated with drug delivery. Several research trends can be identified across all material classes: (a) the development of hybrid systems that combine the strengths of individual carrier materials while mitigating their respective limitations,[38,39] (b) incorporation of stimuli responsiveness for spatiotemporally controlled release,[40] (c) the implementation of multidrug loading strategies to achieve synergistic therapeutic effects and enhanced efficacy,[41,42] and (d) an increasing focus on manufacturing processes and quality control to improve clinical translatability.[43] In general, nanocarriers – regardless of material class – are evolving toward more sophisticated, biomimetic systems through rational design approaches aimed at developing next-generation platforms with translatable potential beyond proof-of-concept. These overarching trends (a–d) will become apparent in the detailed discussion of individual material classes, including lipids, polymers, and proteins, that follows.

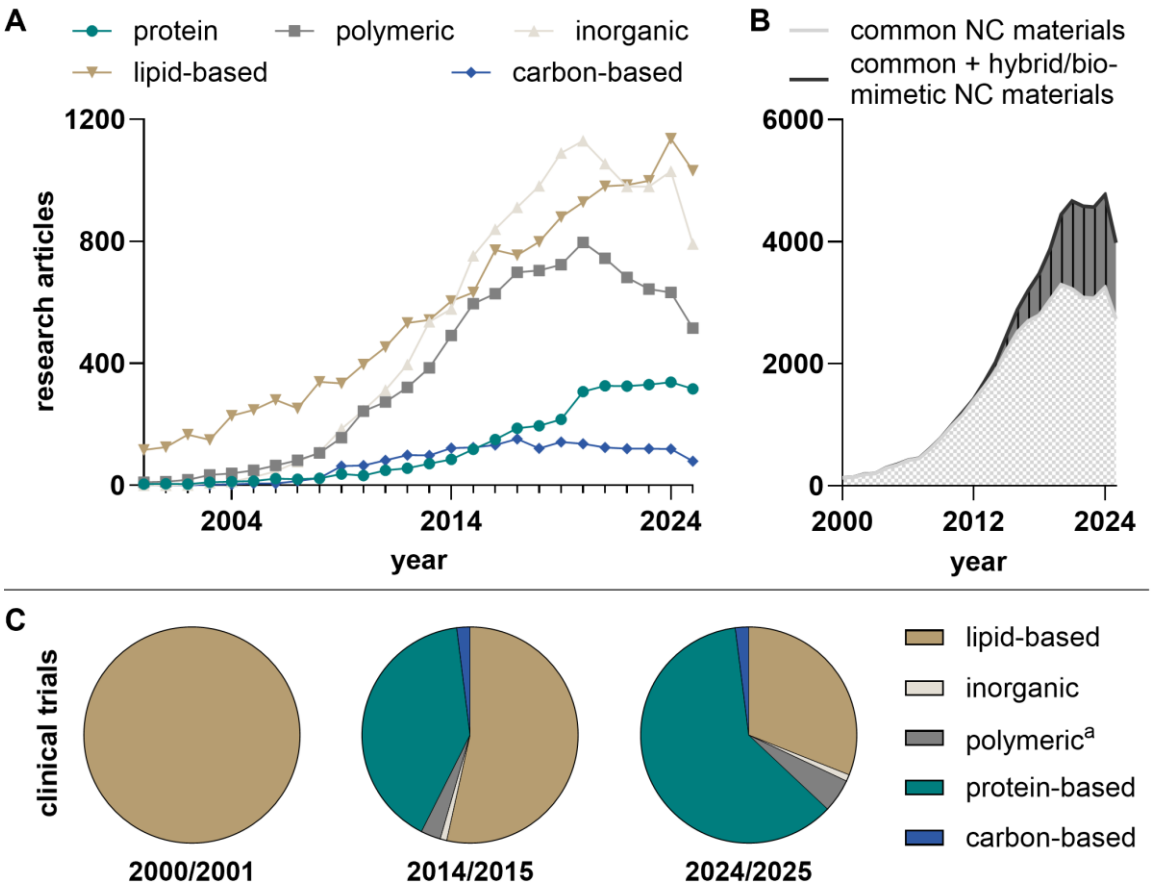

Figure 2: PubMed analysis of the development of nanocarrier materials in preclinical and clinical research from 2000 to September 28, 2025. Search terms are provided in the appendix. A) Annual number of research articles reporting common nanocarrier materials. B) Increasing diversification of nanocarrier platforms, illustrated by the annual ratio of research articles on the sum of common nanocarrier materials relative to all common nanocarrier materials including hybrid and biomimetic systems. C) Percentile distribution of nanocarrier material classes used in all clinical trials evaluating oncotherapeutic nanocarriers across selected time periods. [a] refers to synthetic polymers. NC, nanocarriers.

Lipid-based carrier systems are undoubtedly the most extensively studied class of materials. This is partly due to historical reasons, as they were among the first nanocarriers, and partly due to their excellent biocompatibility, as they were made exclusively from natural components at the beginning of their development. Nanocarrier types of this material class include micelles, liposomes, lipid nanoparticles (LNP), solid lipid nanoparticles (SLN) and nanostructured lipid carriers (NLC). Liposomes are vesicular structures (typically 50 – 450 nm) mainly consisting of amphiphilic (phospho)lipids that naturally form one or more lipid bilayers, which enclose an aqueous core, enabling simultaneous loading of both hydrophobic and hydrophilic drugs, including sensitive payloads such as mRNA or proteins.[44] Their widespread, long-standing use has led to a considerable library of

compositions that can be used to control physicochemical and functional properties such as size, size distribution, surface charge, fluidity, drug encapsulation efficiency and stability.[45–49] Functionalized lipids that already contain stealth-coating PEG or reactive groups for surface modification are also established and even readily available commercially, which vastly increases the versatility of this nanocarrier type and, not least, enables the introduction of targeted and stimuli-responsive approaches.[50] While their biomembrane properties can be beneficial for intracellular delivery, they are also a drawback when it comes to the stability of liposomes, as they can fuse or aggregate during storage.[51] In addition, lipid oxidation and cargo leakage are observed.[51,52] To date, liposomes comprise the largest class among oncotherapeutic nanocarriers with four being currently approved and on the market, including Doxil®, the first approved classical nanocarrier (see Table 1). Liposomes continue to evolve into increasingly complex and 'smart' platforms, following the general trend in drug delivery. Significant efforts are still being made to further enhance their stability and thereby significantly increase clinical translatability.[46,47,50,53,54] This is evidenced, for example, by the U.S. Patent US10456360B2, issued in 2019 to Ipsen Biopharm Ltd. (Slough, UK), for a more stable liposomal formulation of irinotecan during storage.[53] In addition, hybrid materials are being explored to address ongoing challenges such as polymer-lipid hybrids for stability,[36,55] biopolymer-liposome hybrids for increased targeting efficiency[56] or liposome-metal nanoparticle hybrids for multi-functionality.[57,58] The development of LNPs emerged as a key advancement in the effort to optimize nucleic acid encapsulation though they are also explored for other cargo types. LNPs share several similarities with liposomes, including many of their constituent components and inherent biocompatibility; however, they are structurally distinct. LNPs comprise a lipid monolayer that encloses multiple reverse micelles, which encapsulate the negatively charged nucleic acid cargo. Through the incorporation of ionizable lipids that become charged under acidic conditions and careful optimization of LNP composition, they have demonstrated higher encapsulation efficiency,[59] reduced payload leakage,[60] and, notably, enhanced endosomal escape of oligonucleotides.[61] Owing to their optimized retention–release properties and overall modularity, LNPs have become the leading nanocarriers for ribonucleic acid (RNA) delivery.[62–64] This progress has been propelled by the FDA approval of the first-in-class small interfering RNA (siRNA) nanotherapeutic, Onpattro® (2018), as well as the messenger RNA (mRNA)-based COVID-19 vaccines Comirnaty® (Pfizer-BioNTech) and Spikevax® (Moderna). Together with rapid

advancements in RNA therapeutics, these milestones have driven the exponential development of LNP-based cancer vaccines. Although no LNP-based oncotherapeutics, including cancer vaccines, have received FDA approval to date, several have shown promising results in clinical trials. Nonetheless, fast and high uptake of LNPs by the reticuloendothelial system (RES) *in vivo* makes tumor or organ accumulation beyond the liver a major challenge in research.[65–67] Current research trends focus on enhancing targeting through various strategies – ranging from active targeting to lipid structure optimization[67,68] – and on improving downstream parameters related to translational efficiency such as endosomal escape.[69,70] Both approaches are increasingly supported by high-throughput screening and machine learning techniques.[71,72] Lipid-based micelles, the third major lipid-based nanocarrier type, contain a lipid monolayer forming a hydrophilic shell and a hydrophobic core, and are commonly used to solubilize and transport lipophilic drugs. They are comparably easy to synthesize, as they can form spontaneously at their critical micelle concentration (CMC, typically $< 10^{-3}$ mM) and temperature (CMT), making them attractive for large-scale manufacture.[73] Due to their small sizes ranging from 5 – 100 nm, they offer favorable tissue penetration and the ability to cross biological barriers, but their limited hydrophobic core volume constrains their drug loading capacity. Their major disadvantage, however, is their poor stability. Upon dilution, as it is the case during intravenous (i.v.) injection, they rapidly disintegrate and leak cargo.[74] Moreover, their inherent dynamic nature contributes to short shelf life and premature drug release, while interactions with blood proteins can further destabilize the micellar structure. Currently, two micellar oncotherapeutic formulations are FDA-approved: Taxol® and Taxotere®. These formulations use Cremophor® EL and Polysorbate 80 as micelle forming, solubilizing excipients, respectively, which not only form unstable nanocarriers but are also associated with severe adverse reactions that significantly limit the maximum tolerated dose (MTD).[75] To address the inherent limitations of lipid-based micelles in systemic delivery, cross-linking strategies and next-generation micelles, which are mainly based on polymers, were developed.

Table 1: Representative list of oncotherapeutic nanocarriers approved by FDA, EMA, and other regulatory authorities. Illustrated vial images and corresponding particle structures were adapted from Pallares et al. (2025),[76] used under CC BY 4.0. Rearranged. https://creativecommons.org/licenses/by/4.0/. Mepact particle structure was adapted from Wang et al. (2025),[77] used under CC BY-NC-ND 4.0. https://creativecommons.org/licenses/by-nc-nd/4.0/. NSCLC, non-small cell lung cancer, API, active pharmaceutical ingredient, D_h, hydrodynamic diameter, $t_{1/2}$, circulation half-life.

Cat.	Product	Indication	Approval Year
Micellar	**Taxol** *API*: Paclitaxel D_h: 20 – 80 nm	ovarian cancer, breast cancer, Kaposi´s sarcoma, NSCLC	1992 [US] 1994 [US] 1997 [US] 1998 [US]
	Taxotere *API*: Docetaxel D_h: 20 – 80 nm	breast cancer NSCLC prostate cancer gastric cancer head and neck cancer	1996 [US] - 1995 [EU] 1999 [US] - 1995 [EU] 2004 [US] - 1995 [EU] 2006 [US] - 1995 [EU] 2006 [US] - 1995 [EU]
Liposomal	**Doxil / Caelyx** PEG liposome *API:* Doxorubicin HCl D_h: 80 – 100 nm $t_{1/2}$: > 2 days 	Kaposi´s sarcoma, breast cancer ovarian cancer myeloma	1995 [US] - 1996 [EU] 1996 [EU] 2005 [US] - 1996 [EU] 2008 [US] - 1996 [EU]
	Myocet Non-PEG liposome *API:* Doxorubicin D_h: 180 nm $t_{1/2}$: – 	metastatic breast cancer	2000 [EU]
	Onivyde PEG liposome *API:* Irinotecan D_h: ~ 110 nm $t_{1/2}$: ~ 2 days 	pancreatic cancer	2015 [US] - 2016 [EU]
	Vyxeos Non-PEG liposome *API:* Daunorubicin and cytarabine (1:5 molar ratio) D_h: ~ 100 nm $t_{1/2}$: ~ 32 / 40 h 	acute myeloid leukemia	2017 [US] - 2018 [EU]

	Mepact Non-PEG liposome *API:* Mifamurtide D_h: 2 – 3.5 µm $t_{1/2}$: ~ 2 h 	osteosarcoma	2009 [EU]
Polymeric	**Genexol-PM** PEG–PDLLA copolymer *API:* Paclitaxel D_h: 20 – 50 nm $t_{1/2}$: 2.5 – 5 h 	breast cancer NSCLC	2006 [KR] - 2009 [VN/PH] [IN]
	Nanoxel-M PEG–PDLLA copolyme *API:* Docetaxel D_h: 10 – 50 nm $t_{1/2}$: 2 – 3 h 	breast cancer NSCLC prostate cancer ovarian cancer gastric cancer head and neck cancer esophageal cancer	2012 [KR]
Protein-based	**Abraxane** Albumin-bound particle *API:* Paclitaxel D_h: 130 nm $t_{1/2}$: ~ 8 – 10 h 	breast cancer, NSCLC pancreatic cancer	2005 [US] - 2008 [EU] 2012 [US] - 2005 [EU] 2013 [US] - 2008 [EU]
	Fyarro Albumin-bound particle *API:* Sirolimus D_h: ~ 100 nm $t_{1/2}$: > 2 days 	perivascular epithelioid cell tumor	2021 [US]

The use of synthetic block copolymers comprising solvophilic and –phobic blocks for micellar nanocarrier systems, instead of lipids, provides several advantages: lower CMCs that improve stability upon dilution, and enhanced tunability *via* control over polymer chain length and monomer composition, that enables increased drug loading and reduces dynamicity.[73] The synthetic possibility of incorporation of reactive functionalities enables stimuli-responsive behavior or surface modifications. which aim to prolong circulation time, enhance cellular internalization and selectivity, and reduce carrier-associated toxicity and immunogenicity.[78] The advantages achieved as a result are reflected in the Korean Ministry

of Food and Drug Safety (MFDS)-approval of two micellar methoxy poly(ethylene glycol)-*b*-poly(D,L-lactide) (mPEG-*b*-PDLLA)-based chemotherapeutic nanocarriers: Genexol® PM and Nanoxel® M, while several more are in clinical trial phases.[79,80] Polymer-based nanocarrier development has brought forth several more nanocarrier types: nanocapsules, nanospheres, polymersomes, and dendrimers.[81] Although polymeric micelles have overcome some of the previous limitations, no other polymeric architecture types or synthetic polymer types have yet been approved for systemic use in oncotherapy, despite several clinical trials, for example with *N*-(2-Hydroxypropyl)methacrylamide (HPMA)-based nanocarriers.[82] Main concerns include toxicity and immune- and biocompatibility.[79,83,84] As a result, biocompatible and biodegradable polymers such as poly(DL-lactide-co-glycolide) (PLGA) are increasingly being investigated, especially because their non-systemic administration is already approved, for example in Eligard®, a formulation for advanced prostate cancer in which PLGA serves as polymeric matrix with depot function for subcutaneous release of leuprolide acetate, a synthetic gonadotropin-releasing hormone (GnRH) analogue.[79,85] Moreover, hybrid materials are strategically designed to combine complementary strengths, e.g., the versatility of polymers with the biomimetic properties of a lipid shell in polymer-lipid hybrid nanoparticles (PLN) such as in Bevetex®, a paclitaxel-loaded self-assembling polymer lipid nanocarrier approved for metastatic breast cancer in India.[86]

The third major class of materials used for oncotherapeutic nanocarriers comprises proteins. Both natural and engineered proteins offer inherent advantages, including biocompatibility, biodegradability, and substantial structural and functional diversity.[87,88] Endogenous proteins, in particular, are generally non-cytotoxic and elicit only weak, transient immunogenic responses, if any.[89] They are readily recognized by respective receptor proteins and can be enzymatically degraded into natural amino acids, with tunable degradation rates determined by their metabolic stability.[90–92]

The structural and consequent functional diversity of proteins provides a natural library of building blocks with broad physicochemical properties and intrinsic biological activities. With respect to payload encapsulation, the presence of both hydrophilic and hydrophobic domains supports encapsulation of a wide range of therapeutic payloads. In addition to this inherent versatility, their sequence-defined nature allows for further tailoring of nanocarrier properties when needed, for example to optimize drug interactions or incorporate specialized

payloads. At the primary-structure level, proteins can be modified through variation of the natural amino acid sequence,[93,94] site-selective functionalization,[95] or incorporation of unnatural amino acids bearing certain functional groups.[96] These modifications can introduce additional responsiveness or impart new physicochemical characteristics.[97–100] Beyond the primary sequence, secondary to quaternary structures, intrinsic biological activities, and overall nanoarchitecture can likewise be tuned to meet application-specific requirements.

Among the many protein candidates, virus-like particles (VLPs), gelatin, and zein as exogenous proteins, as well as endogenous human proteins such as ferritin and albumin, have been widely investigated as nanocarriers.[101,102] Nanoarchitectures developed from these proteins as oncotherapeutic nanocarriers can be roughly divided into the following types: nanospheres/capsules, nanocages, and monomolecular globular nanocarriers. Of these architectures, nanospheres are currently the only ones approved and marketed. They consist of a biopolymeric matrix made from several protein chains that encapsulate their payload. They were initially developed as microspheres mainly for depot release applications during the controlled release revolution in the 1970s and 1980s. However, in the following years, synthetic polymers quickly became the preferred choice due to their greater controllability, easier characterization and lower regulatory hurdles, and therefore surpassed proteins as the material of choice.[103,104] Until today, only two protein-based nanospheric carriers for cancer treatment have been FDA-approved both utilizing the nanoparticle albumin bound™ (nab™) technology: Abraxane® (ABI-007) in 2005 and Fyarro® (ABI-009) in 2021. Abraxane® was directly inspired by the need to replace Cremophor EL in Taxol® due to vehicle-related toxicity.[105] A human serum albumin (HSA)-based carrier for paclitaxel was selected due to the exceptional affinity of human serum albumin for paclitaxel, the great solubilizing effect without additional excipients (5 mg/mL vs. 0.03 mg/mL),[106,107] and the opportunity to simultaneously exploit natural albumin transport pathways and the enhanced permeation and retention (EPR) effect (for detailed explanation, see Chapter1.2.1).[108–111] The success of Abraxane® led to a revived interest in research in developing proteinaceous nanocarriers which is reflected, albeit to a limited extend, in recent clinical trials. Three of those trials are testing nab™ technology-based therapeutics: nab-docetaxel (ABI-008, NCT00477529), nab-17-AAG (ABI-010, NCT00820768), nab-5404 (ABI-011, NCT01163071). However, no further protein nanocarriers as specified in Chapter 1.1 for cancer treatment have reached clinical stages. From a scientific perspective, this can be attributed to complex, costly

production with high batch-to-batch variability and scale-up difficulties,[112] and aggregation tendency during production and storage.[113] Recognition of these translation-limiting disadvantages has led to an increased focus on new and standardized manufacturing processes, such as continuous manufacturing or microfluidics,[114–117] and stabilizing methods, for example cryoprotectants.[118] Additionally, hybrid materials – especially protein-polymer hybrids – are increasingly explored as the protein component confers additional advantages when combined with polymer nanocarriers in terms of stability, protein corona formation and *in vitro*/*in vivo* performance.[119–123] Within this landscape, albumin has emerged as the most thoroughly investigated protein, a topic that is examined in greater detail in the following chapter.

1.1.1. Albumin

One of the most successful translational protein carriers consists of HSA. It is the most abundant plasma protein with a 60 % (w/w) share and serum concentrations of 3.5 – 5.5 g/dL (53 – 83 uM). It is produced in hepatocytes at a rate of 9 – 12 g/day and released into the intravascular space.[124] From there, it extravasates *via* 60 kDa-glycoprotein (gp60, albondin) receptor-mediated transcytosis through vascular endothelial cells into the interstitial space,[125] leading to a circulatory half-life of approximately 13 hours.[126] The cellular internalization of native albumin is followed either by lysosomal degradation in the case of damaged albumin or by recycling into the extracellular space via neonatal Fc receptors (FcRn) in the case of intact albumin.[127] Albumin is then returned to the blood stream mainly *via* lymphatic drainage.[128] FcRn-mediated recycling is the main contributor for the total half-life of 19 days.[129–131] 60 % of total HSA content are found in the tissue and 40 % in the blood. HSA is a globular, heart-shaped protein with a hydrodynamic radius (R_h) of 3.5 nm,[132] a molecular weight of 66.5 kDa and an isoelectric point (IEP) of 4.7 – 5.1.[133] It consists of 585 amino acids that are organized into three homologous regions I-III each with two subdomains A and B. The tertiary protein structure is substantially stabilized by 17 disulfide bridges between 34 out of 35 cysteines. HSA's primary functions include regulation of osmotic pressure and transport of endogenous ligands. For that, HSA has various ligand binding sites: three primary drug binding sites (Sudlow's site I, II and drug binding site III) and fatty acid binding sites 1-9. Endogenous ligands include hormones,[134,135] peptides,[136] metal ions,[137,138] heme and fatty

acids,[139–141] and often exhibit dissociation constants (K_D) in low micromolar to medium-nanomolar range. Noteworthy, a few ligands stand out with exceptional low K_Ds: Cu^{2+} ions (K_D = 0.9 – 0.35 pM),[137] hemin (K_D = 10 nM)[140] and testosterone (K_D = 17.8 nM).[142] Many drugs such as analgesics, anticoagulants and chemotherapeutics are exogenous ligands and compete with endogenous ligands, usually exhibiting K_Ds in low to medium-micromolar range.[141] Ligand binding and dissociation is controlled by concentration gradients and allosteric modulation.[143–146]

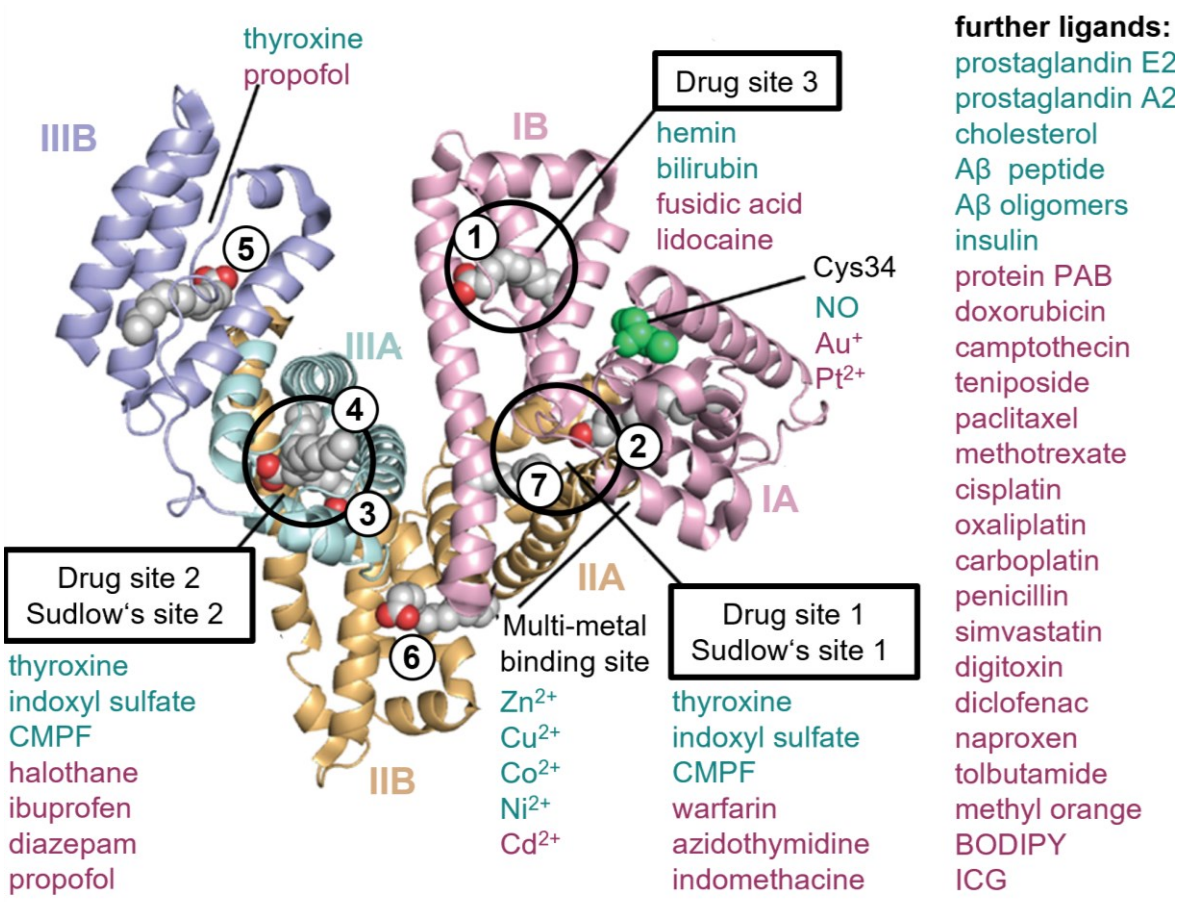

Figure 3: Crystal structure of human serum albumin in the presence of palmitic acid. The three domains (I–III), each divided into subdomains (A/B), contain drug sites (1–3) and fatty acid sites (1–7). Examples of endogenous and exogenous ligands are listed in green and red, respectively. Adapted from Knudsen Sand et al. (2015),[147] used under CC BY 4.0, redrawn with expanded list of ligands.[136,141,148] https://creativecommons.org/licenses/by/4.0/. Aβ, amyloid β; CMPF, carboxy-4-methyl-5-propyl-2-furanpropionic acid; NO, nitric oxide; ICG, indocyanine green.

The structural features of HSA and the resulting binding capacity of various ligands are one primary reason for the special position of many albumin-based DDSs compared to other protein-based systems. The second reason that sets the naturally nano-sized albumin apart as

a carrier is its pharmacokinetics, specifically its biodistribution in the context of cancer. It shows interactions with various receptors, including gp60/18/30, cluster of differentiation 36 (CD36), secreted protein acidic and rich in cysteine (SPARC), and FcRn, that can be harnessed for oncotherapy.[127,149]

Gp60 only binds native, intact albumin, whereas gp18 and gp30 bind damaged or modified albumin, such as ischemia-modified albumin, followed by cellular internalization.[150] Many tumors are reported to overexpress both CD36 and SPARC. The transmembrane receptor CD36 is essential for uptake of long-chain fatty acids and lipoproteins, and it also binds to modified albumins. SPARC is anti-adhesive, involved in several cancer-progression pathways, and promotes extracellular matrix (ECM) degradation and angiogenesis. SPARC is particularly high concentrated in the tumor-stroma interface where it can bind intact and modified albumin (K_D = 19 μM) effectively under physiological conditions and facilitates α5β1 integrin-mediated cellular uptake into tumor cells.[111,151,152] Due to these interactions, in combination with the enhanced vascular permeability, an increased albumin accumulation occurs.[153] Understanding the physiological trafficking of intact and modified albumin is essential to assess different albumin-based nanocarrier approaches.

After Abraxane®'s success, albumin-based systems experienced an exponential growth illustrated by albumin-nanoparticle-related publications from 2001 to 2023 (see Figure 5). The variety of albumin-based nanocarriers that are being developed, can be roughly divided into nanoparticulate albumin (nanospheres), hybrid systems with albumin as building block or coating, albumin as single-chain scaffold and albumin as template (see Figure 5).

In research, HSA, bovine serum albumin (BSA), and mouse serum albumin (MSA) are most commonly used. HSA is typically employed for direct translational relevance, BSA for cost-effectiveness, and MSA for greater compatibility in mouse models. Although albumins from different species share a high degree of homology,[124,154] the pharmacokinetics of an albumin derived from one species can differ when administered to another organism.[129] However, from the perspective of nanocarrier design and manufacture, the systems are generally transferable to other albumins as building blocks, which is why the following examples that highlight research trends regarding the different albumin-based nanocarrier types are not limited to HSA.

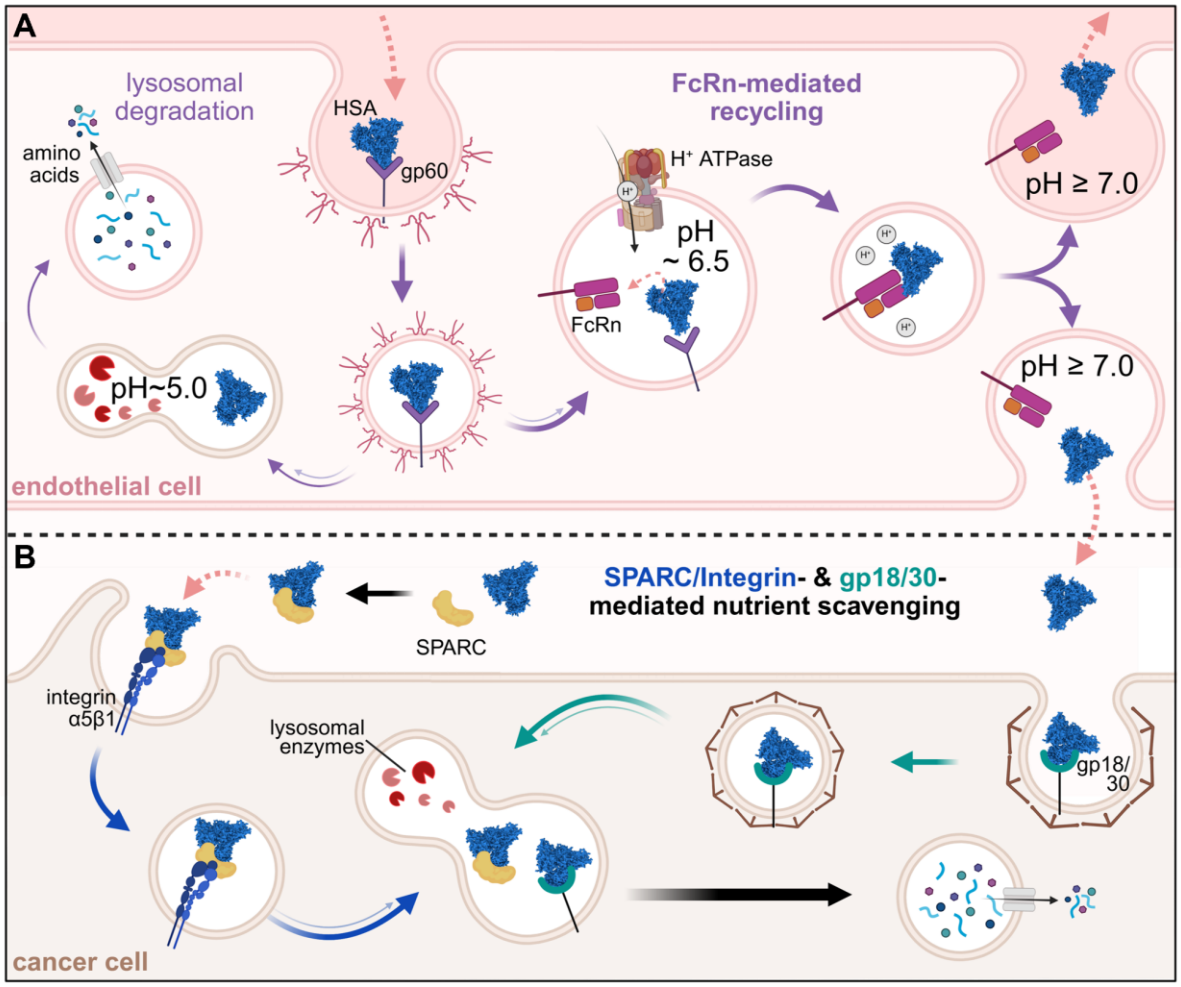

Figure 4: Receptor-mediated trafficking of albumin. A) Native albumin enters the tumor interstitium via gp60/caveolin-1/FcRn-mediated transcytosis. Only small amounts are redirected toward lysosomal degradation. B) SPARC binds albumin and albumin-based nanocarriers in the tumor interstitium and is subsequently recognized by the α5β1 integrin complex on cancer cells and internalized via micropinocytosis followed by lysosomal degradation; Gp18/30 bind and internalize non-native albumin and albumin-based nanocarriers followed by lysosomal degradation. Adapted in concept from Stukan et al. (2024),[127] used under CC BY-NC 3.0, redrawn, rearranged. https://creativecommons.org/licenses/by-nc/3.0/. SPARC, secreted protein acidic and rich in cysteine, FcRn, neonatal Fc receptor. Created with BioRender.com.

When it comes to nanospheric albumin carriers, which are exemplified by Abraxane®, research focused on further development of preparation methods. Established preparation methods such as desolvation are being improved with respect to reproducibility by standardized set ups and quality by design approaches.[155–157] Additionally, new methods that are self-assembly driven are being developed to preserve albumin's native structure and biological functions upon nanocarrier formation.[158–162] In addition to the stabilizing effects

that albumin can have, it is also these biological functions that inspired albumin coatings.[163–167] Albumin coatings display a protective effect within circulation against degradation and uncontrolled protein corona formation, enhancing nanocarrier stability *in vivo*. It can also serve as targeting ligand, increasing tumor accumulation, penetration and cellular internalization.[165,168] In that regard, native albumin coatings are often superior to those formed from denatured albumin.[165] Nanocarriers which exploit albumin as a single-chain biopolymer scaffold often exploit both covalent conjugation, e.g. *via* single cysteine residue (Cys34) or lysine (Lys) residues, and noncovalent interaction to integrate active targeting or responsive drug release.[169–176] However, examples of resulting conjugates exhibiting a combination of active targeting, high drug to albumin ratios and responsive release mechanism on a single protein level remain sparse.[169–171] Albumin can be used not only as a bioconjugation scaffold but also as a biological scaffold to exploit its discussed physiological trafficking for pharmacokinetic improvements. In albumin fusion proteins a protein cargo is genetically fused to albumin hitchhiking it to achieve longer half-lives and tumor accumulation. Some albumin fusion proteins are already in clinical trials for example for solid tumors or chemotherapy-induced neutropenia (NCT01642342, NCT02465801).[177,178] A current, clinically advanced fusion protein, SON-1010, takes advantage of albumin as template.[179] It is an albumin-binding fusion protein made of the cytokine Interleukin (IL)-12 and a fully human albumin binding domain (F_HAB). Upon i.v. injection it binds to its biological template, HSA, by which half-life, tumor accumulation and, consequently, the local immune response are increased. This template strategy has also been employed for optimized small molecules, to load the cargo *in situ* non-covalently onto circulating endogenous albumin as supramolecular template,[175,180–184] or to pre-assemble the complex *ex vivo* before administration.[185] Additionally, by targeting the single Cys34, albumin can serve as chemical template for thiol-reactive cargoes such as maleimides or phenyloxadiazolyl methyl sulfones achieving fast and efficient drug loading *in vivo,*[186–192] as HSA provides about 80 % (~0.4 – 0.5 mM) of the thiol content in human blood.[193]The depicted examples of albumin nanocarriers illustrate the various targeting strategies currently employed to achieve *in vivo* delivery: passive, active and endogenous targeting. The underlying principles and molecular mechanisms of these approaches will be briefly discussed in the following chapter.

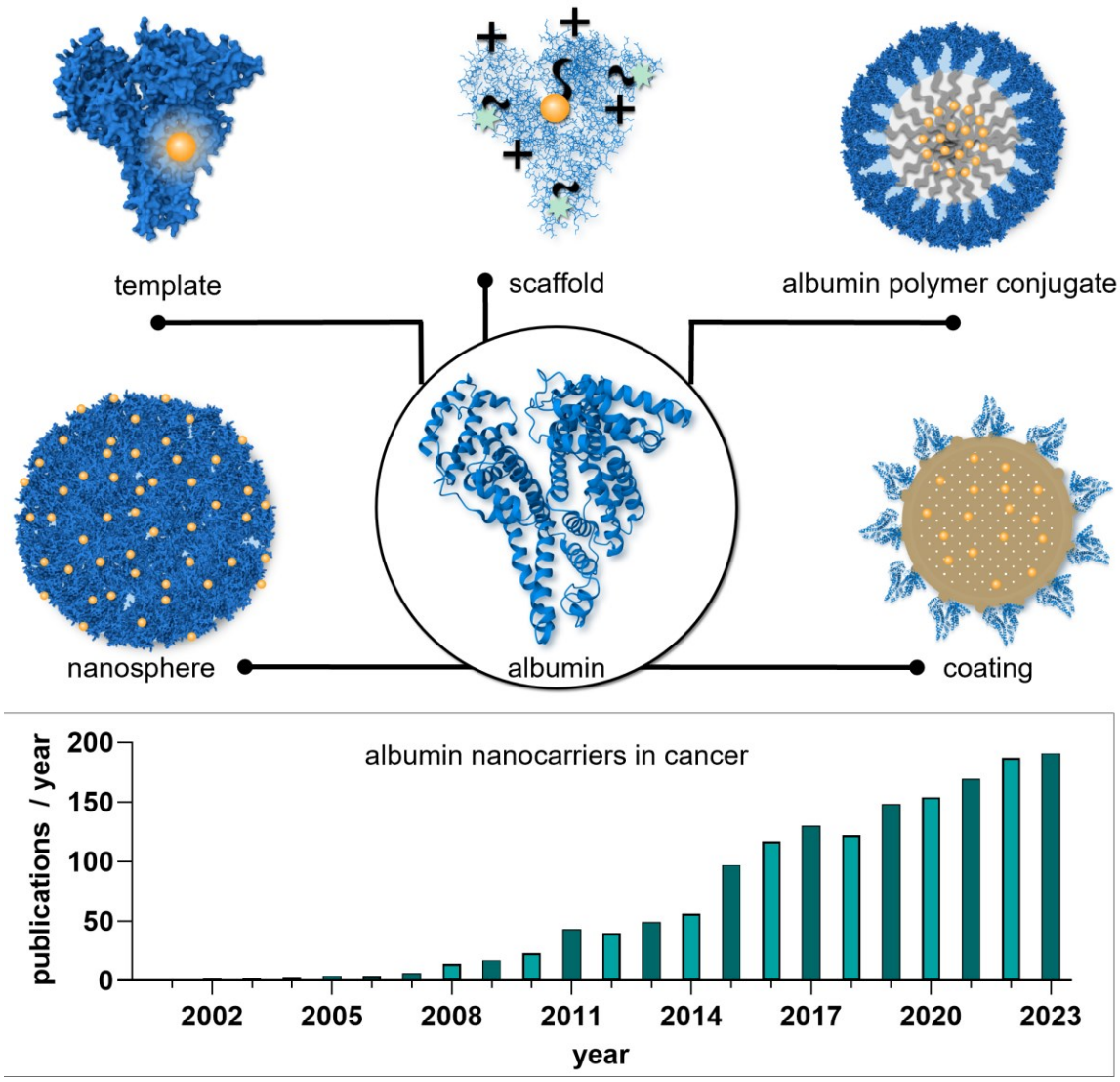

Figure 5: Albumin-based nanocarriers. Scheme of different types of albumin-based nanocarriers (top). Illustrations are representative examples and may vary depending on specific design. Adapted in concept from An et al. (2017),[194] *used under CC BY-NC 4.0, redrawn and modified. https://creativecommons.org/licenses/by-nc/4.0/. Trends in the annual number of publications on albumin nanocarriers in cancer from 2001 to 2023 (below). Replotted and adapted from Liu et al. (2024),*[195] *used under CC BY 4.0, simplified by omission of non-relevant information. https://creativecommons.org/licenses/by/4.0/. Albumin structure was adapted from RCSB PDB: 1AO6.*[196,197]

1.2. Targeting strategies for nanocarriers

Naturally, targeting strategies have developed simultaneously with, or slightly offset from, nanocarrier development. In 1986, Matsumura and Maeda observed the preferential accumulation of high-molecular-weight proteins and polymer conjugates within tumor tissue,

thereby formally establishing the principles of passive targeting.[198] Key milestones for active targeting had already been achieved earlier, with the development of the first monoclonal antibody against tumor antigens in 1975.[199] However, the concept of ligand-mediated targeting in cancer therapy was mainly advanced during the 1980s and 1990s. Building on the growing understanding of nanocarrier behavior *in vivo*, organ-targeting strategies that exploit endogenous transport mechanisms are being systematically developed since the early 2010s.[200,201] These three concepts are grouped under static targeting and are complemented by dynamic targeting and controlled drug release to further improve biodistribution and to reduce off-target toxicity. Dynamic targeting refers to an intrinsically or extrinsically triggered change in the nanocarrier that increases target site accumulation, retention or cellular internalization.[202] The nanocarrier adapts in a dynamic way to environmental cues within the target site thereby influencing its biodistribution. On the other hand, stimuli-responsive controlled release deals with the release kinetics and spatiotemporal control over the release of an active drug substance from a carrier. As targeting fundamentally determines the spatial fate of nanocarriers prior to drug release, static and dynamic targeting strategies are discussed first. Controlled drug release through responsiveness, in particular, which has received considerable attention in recent years, represents a distinct yet complementary design layer and is therefore addressed separately in Chapter 1.3.

1.2.1. Static and dynamic targeting

Passive targeting refers to the accumulation of therapeutics based on inherent, specific characteristics of the target tissue due to anatomical differences that can be both physiological and pathological.[203] For instance, the glomerular filtration barrier within kidneys efficiently filters macromolecules < 6 nm, while liver sinusoids show natural fenestration of 50 – 100 nm and inter-endothelial slits in spleen range from 200 – 500 nm.[204] In addition, the latter two examples in particular contain large parts of the reticuloendothelial system (RES). The RES consists of specialized phagocytic cells, for example Kupffer cells (liver macrophages), involved in the breakdown of foreign materials, such as bacteria or nanocarriers, enabling targeting of the organs in which they reside.[203] Many oncotherapeutic nanocarriers try to leverage the pathophysiological vascular fenestrations that can be found in the tumor tissue. The typically poor and aberrant neovasculature is also characterized by

wide fenestrations, further augmented by elevated levels of vascular permeability factors, allowing nano-sized carriers and plasma proteins (10 – 200 nm) to extravasate paracellularly into the tissue. In addition, transcellular extravasation *via* transendothelial pores has been observed.[205] Because of presumed reduced lymphatic drainage in tumor tissue, nanocarriers are less efficiently cleared and are instead retained. Taken together, this phenomenon is referred to as the enhanced permeability and retention (EPR) effect.[206] Notably, the universality of impaired lymphatic drainage within tumors has recently been disproved for at least two tumor mouse models and requires further investigations.[207] Endogenous targeting exploits host molecules that are recruited by the therapeutic *in vivo* to guide it toward specific tissues. Notably, many nanocarriers acquire a corona of serum proteins upon intravenous administration. The composition of this protein corona depends on the physicochemical properties of the nanocarrier surface. Some strategies employ anti-opsonization agents, such as PEG, to reduce opsonin adsorption and thereby circumvent clearance by the RES and liver tropism. Others focus on fine-tuning these nanocarrier surface characteristics to preferentially adsorb particular serum proteins. This intended, tailored, endogenous protein corona can then facilitate tissue-specific nanocarrier uptake, when complementary receptors are overexpressed in the target site.[208] In 2018, the first nanocarrier using this strategy, Onpattro®, was approved for a non-oncological indication, employing *in vivo* apolipoprotein E (ApoE) recruitment followed by receptor-mediated hepatocyte uptake to deliver therapeutic siRNA for treating polyneuropathy caused by hereditary transthyretin amyloidosis.[209] In addition to binding of an endogenous protein as trafficking agent non-covalently *via* molecular recognition, nanocarriers can be designed to covalently attach to a specific endogenous protein such as HSA in a monomolecular manner *via in vivo* chemistry, as discussed in detail in Chapter 1.1.1. The latter approach bridges endogenous and active targeting, as endogenous albumin is conjugated to the therapeutic and serves, among other functions, as an active targeting ligand for albumin-binding receptors. In general, active targeting refers to the modification of nanocarrier surfaces with targeting ligands that bind to receptors or antigens specifically expressed or overexpressed on cells within the target site, thereby seeking to promote homing, retention and often cellular uptake.[203] The concept of active targeting does not contradict passive targeting; rather, it complements it. The presence of a targeting ligand alone is not sufficient to achieve the desired organ distribution,[210–212] though it has been shown to influence the whole-body distribution in certain cases and it does

increase cellular uptake once a nanocarrier is in close proximity to the target cells.[213,214] Typical targeting ligands include antibodies or fragments thereof, aptamers, peptides, vitamins and carbohydrates.[215]

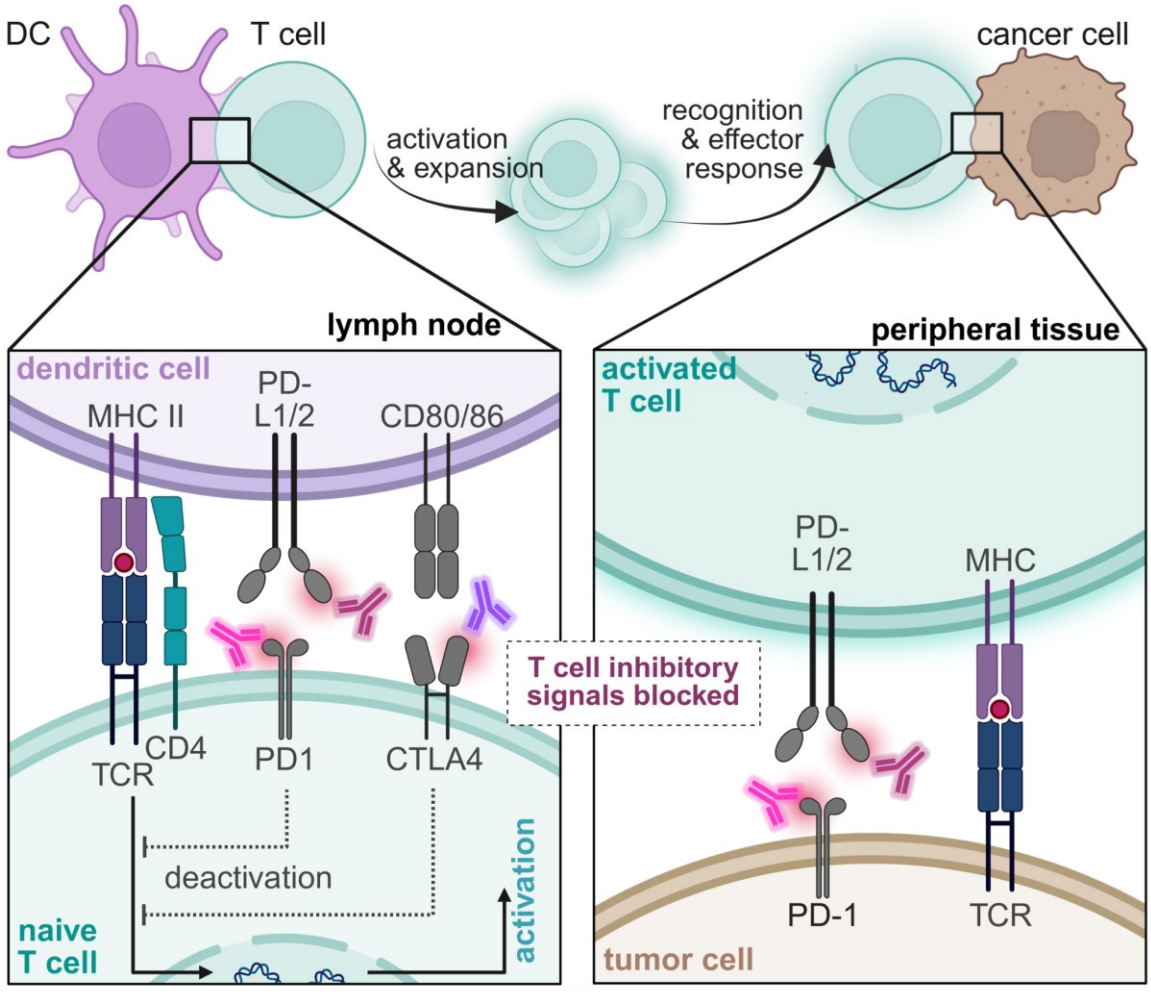

Figure 6: Immune checkpoint blockade using monoclonal antibodies. Anti-PD-L, Anti-PD-1 and Anti-CTLA-4 inhibit the suppressive signaling between DCs and T cells during T-cell priming. Anti-PD-L1 and Anti-PD-1 antibodies also block inhibitory interactions between activated T cells and cancer cells, thereby facilitating tumor cell recognition and promoting an anti-tumor immune response. DC, dendritic cell; MHC, major histocompatibility complex; PD-L1/2, programmed death ligand 1/2; PD-1, programmed cell death protein 1; CD4/80/86, cluster of differentiation 4/80/86; TCR, T-cell receptor; CTLA4, cytotoxic T-lymphocyte-associated protein 4. Created with BioRender.com.

The recognition of tumors as complex ecosystems, rather than merely malignant monoclonal cell masses, led to the establishment of cancer immunotherapy. In this context, antibodies and carbohydrates play key roles. Antibodies are used for immune checkpoint blockade (ICB) as immune checkpoint inhibitors (ICI), which bind to the immune checkpoint molecules

programmed cell death protein 1 (PD-1), programmed cell death ligand 1 (PD-L1), cytotoxic T-lymphocyte-associated protein 4 (CTLA-4), or lymphocyte activation gene-3 (LAG-3), thereby inhibiting major pathways of immune evasion in cancer cells (see Figure 6).[216,217] Carbohydrate-recognizing proteins, known as lectins, also play an important role in immunity. Certain subsets of lectins are highly expressed on professional antigen-presenting cells (APC), such as dendritic cells (DC) and macrophages. As these cells are key players in regulating immunity and immune homeostasis,[218–220] carbohydrates are promising targeting ligands for actively targeted nanocarriers for onco-immunotherapy that aim to modulate immune responses, as explained in more detail in the following Chapter 1.2.1.1.

The different static targeting approaches – active, passive and endogenous – can also be extended in form of dual or hybrid targeting. Dual targeting refers to the active targeting of two distinct entities, such as different receptors, whereas hybrid targeting will be used within this thesis to denote the combination of intended different targeting strategies, such as endogenous plus active targeting.[221,222] The designated static targeting strategy of a nanocarrier provides information about the design and intended routing mechanism of distribution rather than about the actual routing mechanisms *in vivo*. This is best depicted by the emergence of endogenous targeting *via* the protein corona. It arose from the understanding of interactions between passively targeted nanoparticles and the body, resulting in an unanticipated, endogenously directed biodistribution *in vivo*.[208]

Another extension of targeting strategies comprises dynamic targeting approaches, often also termed hierarchical targeting, as introduced earlier. Dynamic targeting aims to improve the nanocarriers localization or retention on tissue and cell level and must therefore be distinguished from stimuli-responsive drug-release, though both increase specificity. The stimuli and the chemistry utilized are similar to those employed for responsive drug release, which are detailed in Chapter 1.3. For dynamic targeting, stimuli-responsive behavior is incorporated on the nanocarrier level to change characteristics such as surface properties, size or ligand presentation. These properties influence the distribution of the nanocarrier during circulation and at the tissue level in different ways, which is why their adaptive modification depending on the environment can improve the delivery result. Change in surface charge is one of the most utilized strategies either to promote cellular uptake within the tumor microenvironment (TME) or to facilitate endosomal escape. Sun et al. created a dual-enzyme

responsive polymeric nanocarrier which exposes cationizable groups upon enzymatic decapping by overexpressed enzymes of cancer-associated fibroblasts or cancer cells, thereby enabling transcytotic transport throughout dense orthotopic pancreatic tumors and deep tumor penetration.[223] Liu et al. employed a hybrid targeting strategy by designing a nanocarrier with charge/size dual-conversion capacity for tumor cell engineering to reverse the immune escape.[224] They coloaded cationic liposomes with immunogenic cell death (ICD)-inducer doxorubicin and a dual-gene plasmid which encodes for expression of a T cell recognition surface complex and for silencing RNA that downregulates an immunosuppressive surface protein. Through electrostatic interactions, multiple liposomes were wrapped with an NGR peptidic ligand-modified chitosan layer to actively target tumor endothelial cells forming negatively charged carriers approximately 160 nm in diameter. Protonation of chitosan within the acidic TME triggers layer shedding and releases positively charged liposomes of about 42 nm, enabling superior tumor penetration and adsorption-mediated cellular uptake.

While most dynamic targeting examples demonstrate benefits regarding tissue penetration, retention and cellular internalization at the target site, only small effects have been observed in increasing target-site accumulation in the first place. Those benefits usually arise from a stealth layer that helps to avoid the RES while also decreasing cellular uptake by target cells. Niu et al. demonstrated that an acid-sensitive PEG layer on mannose-modified PLGA nanocarriers reduces their accumulation in macrophages of typical RES organs during circulation *in vivo*.[225] Upon PEG shedding in the acidic TME, mannose is exposed as an active targeting ligand for CD206 (macrophage mannose receptor, MMR), a lectin receptor highly expressed on protumoral M2-polarized tumor-associated macrophages (TAM).

Overall, these approaches illustrate how environmentally triggered modulation of nanocarrier properties can substantially improve delivery within the tumor tissue and partially mitigate RES uptake. However, they offer only limited benefit regarding initial site-specific accumulation.

Within the broad spectrum of static and dynamic targeting strategies, carbohydrates constitute a particularly promising class of ligands for active targeting as briefly mentioned above. Their interactions with lectins are central to immune regulation and cell–cell communication. For this reason, carbohydrates are discussed in detail in the following Chapter 1.2.1.1 as a

mechanistically relevant targeting ligand for immunomodulating nanocarrier systems, as envisaged in this thesis.

Building on the conceptual framework of targeting strategies, the subsequent Chapter 1.2.2 will critically assess the *in vivo* performance of marketed oncotherapeutic nanocarriers, highlighting which design principles have been translated successfully and elucidating the key challenges that have limited the progression of many targeting strategies from *in vitro* concepts to *in vivo* application and ultimately to clinical implementation.

1.2.1.1. Carbohydrates as targeting ligands

In general, lectins are ubiquitously expressed in nucleated cells with at least 215 identified in humans.[226] Intracellular lectins are involved in intracellular glycoprotein quality control, trafficking, and other processes.[227,228] Extracellular lectins, which are secreted or membrane-localized, play a role in cell adhesion, signaling, glycoprotein clearance and pathogen recognition.[229] While all cells express lectins, differences in their expression profiles enable specialization. Immune cells express a variety of extracellular lectins in high abundance and with high plasticity from different lectin families including C-type lectin receptors (CLR), sialic acid-binding immunoglobulin-like lectins (Siglecs), and galectins as the major families (see Figure 7) each of which serves distinct roles. Notably, downstream effects of carbohydrate-lectin interactions are highly dependent on cell type, the specific receptor–ligand pair, and the potential co-activation of other receptors, which together allow flexible downstream signaling. Dendritic cell-specific intercellular adhesion molecule-3-grabbing non-integrin (DC-SIGN, CD209), for example, can trigger both activating and inhibitory immune effects depending on whether mannose or fucose is the ligand.[219] The large number of lectins indicates their diversity in function, but nevertheless, some shared roles within the major lectin families can be identified.

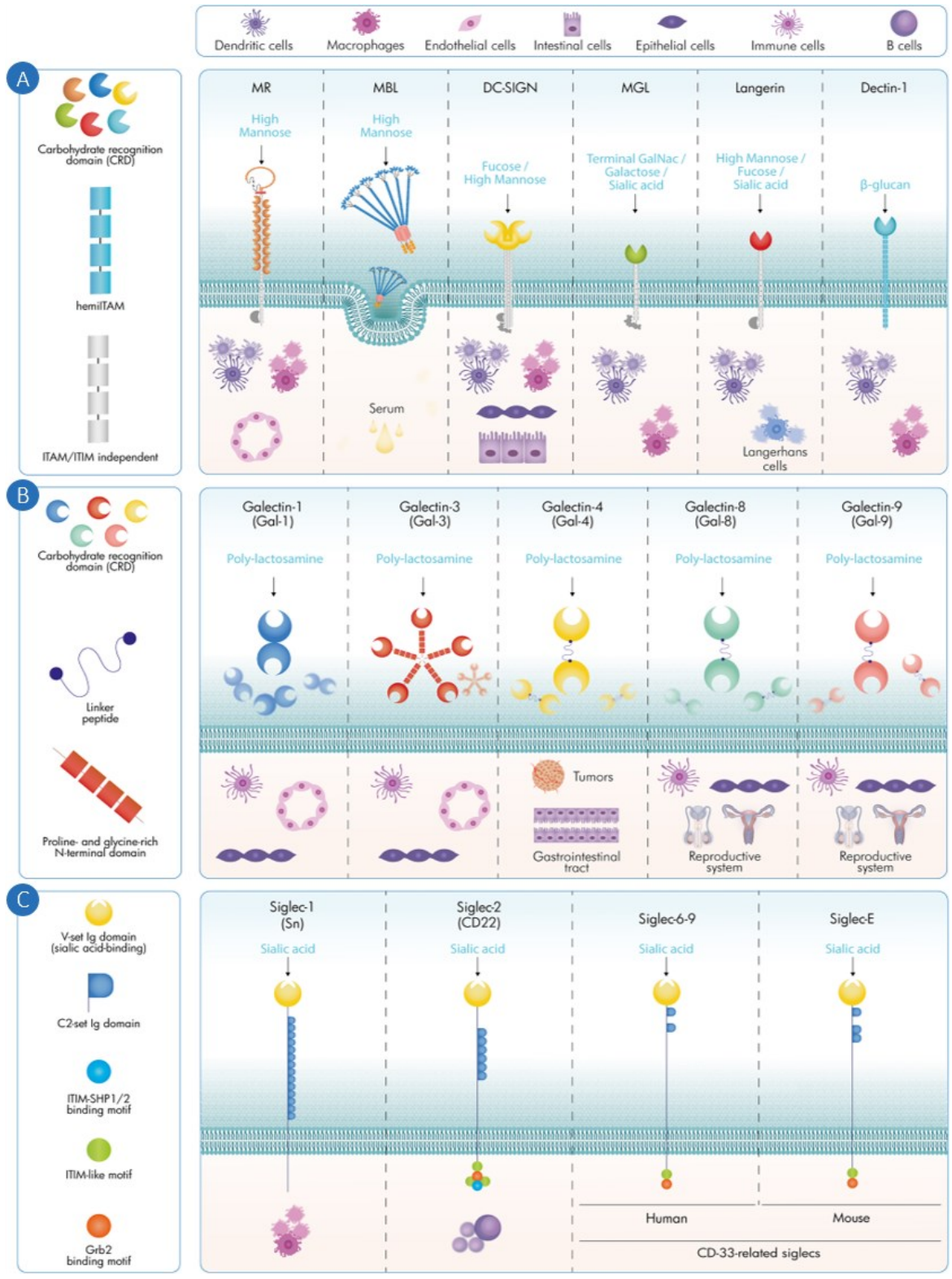

*Figure 7: Carbohydrate binding receptors: main localization, structure and glycan recognition by the lectin families: (**A**) C-type lectins (CLRs), (**B**) galectins, and (**C**) siglecs. Adapted from Pinho et al. (2023),*[230] *used under CC BY 4.0. Rearranged, no other changes. https://creativecommons.org/licenses/by/4.0/. ITAM, immunoreceptor tyrosine-based activation motif, ITIM, immunoreceptor tyrosine-based inhibitory motif, SHP1/2, Src homology region 2 domain-containing phosphatase-1/2, Grb2, growth factor receptor-bound*

protein 2, MR, mannose receptor, MBL, mannose-binding lectin, DC-SIGN, Dendritic cell-specific intercellular adhesion molecule-3-grabbing nonintegrin, MGL, macrophage galactose-specific lectin, siglec, sialic acid–binding immunoglobulin-like lectin.

Galectins are predominantly soluble lectins expressed by all immune cells and are upregulated by activated B and T cells, M1-polarized Macrophages, decidual natural killer cells (NK) and regulatory T cells (Treg).[231,232] They preferentially bind *N*-acetyllactosamine (LacNAc) repeats usually in low- to medium-micromolar range[233] and are involved in mediating immune tolerance *via* (a) induction of tolerogenic DCs and M2-polarized Macrophages, (b) promoting expansion of myeloid-derived suppressor cells (MDSC) and (c) stabilizing immune checkpoints such as CTLA-4, PD-1 or LAG-3.[230] They also control the signaling threshold of glycosylated receptors such as the T-cell receptor activation threshold.[234] The relative expression of different galectins changes during both tumor progression and fibrotic diseases, some galectins have been investigated as therapeutic targets for cancer, liver and lung fibrosis.[234–236] Candidate agents include mainly natural or synthetic polysaccharides and small molecule inhibitors which entered mostly phase I/II trials in the late 2010s and early 2020s.[234]

Siglecs are transmembrane lectins expressed by most immune cells except T cells. They preferentially bind to sialylated glycans, with low- to medium-micromolar affinity,[237] self and non-self, recognizing them as self-associated molecular patterns and mediating immune regulation mainly through inhibitory signaling, thereby acting as immune checkpoints to induce self-tolerance.[230,238] This is exploited by many tumors to evade the immune system: Upregulation of sialyltransferases results in hypersialylation of cancer cell surfaces which leads to the suppression of anti-tumor immune responses. This Siglec-sialic acid axis is therapeutically addressed in clinical trials or preclinically using Siglec blocking antibodies (e.g., NC318; anti-Siglec-15 mAB), sialidase-antibody fusion proteins for enzymatic cleavage of sialylated glycans (e.g., E-602; bi-salidase fused to IgG1 Fc region), and Siglec-Fc fusion proteins to trap sialic acid residues (e.g., AL009; Siglec-9 extracellular domain fused to Fc region).[239,240]

CLRs are predominantly transmembrane receptors mainly expressed by DCs and Macrophages. They preferentially bind mannose, fucose, *N*-acetylgalactosamin (GalNAc) and *N*-Acetylglucosamin (GlcNAc) in low-millimolar range and often in a Ca^{2+}-dependent manner. They primarily function as pattern recognition receptors (PRR) recognizing

pathogen-associated molecular patterns (PAMP), though recognition of damage-associated molecular patterns (DAMP), self and altered-self molecules such as tumor-associated carbohydrate antigens (TACA) is also reported.[219,241] After binding and internalizing PAMPs, antigens are processed and presented *via* major histocompatibility complex (MHC) molecules, leading to T cell activation with the help of co-stimulatory receptors. In the context of cancer, tumors hijack the glycan/CLR axis through TACA binding to CLRs on immune cells, to dampen anti-tumoral responses and to promote a pro-tumoral, tolerogenic TME.[218,242–247] Additionally, intrinsic CLR expression, e.g. of CD206, in cancer cells induces cell-autonomous oncogenic signaling, drives metabolic reprogramming, and mediates paracrine immune suppression, thereby fostering tumor progression in multiple ways, though the precise underlying mechanisms have not yet been fully elucidated.[243,244,248,249] Currently, CLRs on cancer cells are not regularly targeted. Noteworthy, a subset of CLRs, group XIV, which is preferentially expressed by mesoderm-derived cells, has emerged as target for anti-angiogenic therapy concepts.[250] Contrary, CLRs on immune cells are heavily exploited mainly for repolarization[251–254] or depletion[255,256] of TAMs and for cancer vaccine approaches.[244,257–259] In the latter, tumor antigens are targeted toward DCs, usually together with adjuvants, to initiate a strong tumor-specific immune response. Commonly utilized carbohydrate-based targeting ligands are high mannan oligosaccharides (e.g., mannan, $Man_9GlcNAc_2$) or single mannose presented in a multivalent manner.[260,261]

Co-expression of different lectins allows for recognition of diverse carbohydrate patterns, self and non-self, and differentiated, appropriate immune responses. Importantly, most lectins exhibit low binding affinities in millimolar range for their preferential monomeric carbohydrate ligand. Efficient binding is achieved by properly spaced, multivalent ligand presentation, as is the case, for example, with the glycocalix of pathogens, which leads to high functional affinities (micro- to picomolar).[262–264] This tunable affinity is only one of the several unique advantages that carbohydrates offer as targeting ligands on nanocarrier systems. Depending on their complexity, carbohydrates are easily accessible, modular in structure, and inexpensive, especially when compared to antibodies, although most are inferior to them in terms of specificity, which necessitates well-considered receptor selection. Similar to PEG, glycans can also have shielding effects against plasma protein-mediated inhibition of active targeting.[265–267] The evolutionary adaptation of the immune system to

recognize these biomolecules as self and non-self not only enables efficient receptor targeting, but also, under certain circumstances, a simultaneous adjuvant effect by activating downstream signaling, further enhanced through subsequent natural intracellular routing and processing.[268,269]

In summary, both the advantages and the currently emerging understanding of lectins as immune checkpoints make carbohydrates a promising targeting structure for immuno-oncological interventions, potentially improving targeting at a cellular level *in vivo*. However, despite their potential, no carbohydrate-ligand-based nanocarriers have yet reached the clinic. To guide the design of improved nanocarriers, including the potential incorporation of carbohydrate ligands, it is therefore necessary to examine those concepts that have been successfully translated into marketed oncotherapeutic nanocarrier systems and to analyze their limitations in the context of *in vivo* targeting.

1.2.2. Targeting *in vivo*

Currently, besides chemoresistance, low accumulation and retention of anticancer drugs in tumors is considered one of the main reasons for the failure of chemotherapy.[270,271] Despite the advances in drug delivery achieved by oncotherapeutic nanocarriers in clinics, it is undisputed that significant challenges still remain. Attempts are being made to address these, and some preclinically tested systems appear promising. Analyses indicate a targeting efficiency *in vivo* of nanocarriers of below 1 %[205] or, at best, 2 – 3 %,[272] however, a general quantitative and systematic analysis is extremely difficult for several reasons. First, the lack of uniformity in preclinical testing prevents systematic comparison.[273] Relative measures, such as the percentage of intravenously injected dose per gram of tissue (%ID/g), are typically reported; however, significant differences in experimental design such as tumor model,[273] tumor cell line,[273] tumor size,[273,274] administration route,[275,276] injected dose,[273] and labeling strategy[277–279] have all been shown to influence tumor accumulation outcomes. Furthermore, macroscopic tumor accumulation does not necessarily correlate with microscopic delivery to cancer cells.[280,281] A comparative analysis is further complicated by recent trends in immuno-oncology, arising from advances in the understanding of the TME. The classical nanocarrier approach aimed to maximize tumor accumulation in order to achieve high intratumoral

concentrations of small-molecule chemotherapeutics, which were expected to result in high concentrations inside cancer cells. Contrary, it has been demonstrated that significant proportions of delivered nanotherapeutics end up in tumor-associated immune cells changing the immunological milieu und thereby influencing the tumor progression.[282] More recent immuno-oncological approaches target non-cancer cells in the first place – both within a tumor, such as TAMs, or in close proximity, like DCs in tumor-draining lymph nodes.[283–285] The resulting diversity in the oncological landscape of target cells, payloads and intracellular targets further complicates a general, evaluative comparison of targeting strategies in a quantitative manner. However, case by case analysis of both clinically established and preclinical nanocarriers allows for a generalized assessment of the achievements of nanocarriers in the context of targeting *in vivo*, the limitations that have been addressed successfully and the challenges that still remain. Despite primarily being designed for cancer cell-targeted chemotherapy, clinically established nanocarriers included in the following assessment continue to provide valuable insights into *in vivo* targeting mechanisms that are applicable to other target sites, including immunological organs and immune cells, which are important targets in the TME.

The first generation nanocarriers, Doxil® and Abraxane®, successfully reduced side effects stemming from dose-limiting cardiotoxicity and toxic excipients like Cremophor EL, respectively, without forfeiting efficacy compared to the small molecule formulations.[286] Studies in the 2000s focused on reduction of systemic toxicities due to improved pharmacokinetics, such as prolonged retention in the vascular compartment. This enabled significantly higher MTDs and often proved non-inferiority to small molecule treatment, but new side effects or an enhanced relative risk for certain side effects also occurred that can be attributed to nanocarrier formulation and distribution.[86,287,288] Clinical imaging trials are sparse but have confirmed tumor accumulation of nanocarriers to varying degrees, though these studies mainly use passively targeted liposomal formulations and often lack determination of intratumoral drug concentrations and even more so intracellular drug concentrations inside cancer cells.[289] Many examples in preclinical animal experiments exist with intratumoral drug concentration increases ranging from 1.3-fold increase for Abraxane® over 4 – 16-fold increases for Doxil® to 90-fold increase for T-cell hitchhiking SN-38-carrying nanocarriers compared to the respective small molecule formulations.[290–292] But recent investigations in several cancer mouse models revealed that up to 80 % of tumor-

delivered drugs remain trapped extracellularly.[281] In terms of efficacy, nanocarrier formulations have achieved significant but modest improvements in overall survival (OS) and progression free survival (PFS).[293] To improve therapy outcomes and address tumor complexity, nanocarriers are currently extensively investigated for the co-delivery of, ideally, synergistic drugs at the cellular level. In clinics, a prominent example is Vyxeos®, a liposomal nanocarrier for subtypes of acute myeloid leukemia that encapsulates cytarabine and daunorubicin in an optimized, synergistic molar ratio of 5:1 while exhibiting reduced systemic toxicity and therapy-related mortality in older adults.[294] Importantly, this 5:1 ratio is maintained in blood circulation and intracellularly for at least 24 h,[295] whereas free-drug cocktails can lead to suboptimal or even antagonistic drug ratios, undermining the therapy response.[294] In the preclinical setting, nanocarrier-mediated co-delivery has been exploited to overcome drug resistance by delivery of cytostatics in combination with silencing RNAs that suppress the expression of proteins important for chemoresistance. Also, nanocarriers enable optimized chemoimmunotherapy, in which chemotherapeutics that induce a strong ICD are locally and temporally co-delivered with, for example, stimulating immunomodulators that amplify the subsequent adaptive immune response, or therapeutic nucleic acids that interfere with immune evasion pathways. Multi-drug combination therapy regimes with small molecule drugs are already a cornerstone of oncological intervention, but the nanocarrier-mediated co-delivery of drugs at the same time and site enhances tumor growth inhibition further by 29 % in preclinical mouse models according to a meta-analysis performed by Benderski et al.[296] It also achieved the highest overall survival with 56 % of studies showing full or partial survival of the cohort compared to 37 % in the small molecule combination therapy control group and 28 % in the single-drug nanocarrier control group.

Despite encouraging preclinical results from state-of-the-art approaches, these findings are largely based on animal models that fail to capture the complexity and heterogeneity of human tumors. Such heterogeneity occurs not only between tumor types and patients but also between lesions within a single patient, affecting multiple characteristics relevant to nanocarrier targeting efficiency.[280,297] Reduced vascular perfusion and permeability, for example, limit delivery *via* the vascular compartment for both small molecules and nanocarriers. This is also influenced by the stromal architecture of the tumor exerting pressure on blood vessels. Stromal density also influences, among other things, the interstitial pressure within tumor tissue which restricts the penetration depth particularly for large nanocarriers

(> 50 nm).[298] This can hinder intratumoral delivery despite apparent macroscopic accumulation. Consequently, most nanocarriers in clinical use or development (80 – 150 nm) heavily depend on vascular status and tissue density of the tumor.[280] This reliance may explain their limited efficacy in very dense, poorly perfused tumors such as pancreatic cancer, where smaller nanocarriers (10 – 35 nm) perform significantly better in preclinical studies.[202] Noteworthy, it appears that targeting metastases follows the same rules and that nanocarriers are a valid strategy here, even though further elucidation is necessary, since most studies focus on treating primary tumors.[280,299]

A tumor-unrelated factor contributing to high interpatient variability in targeting efficiency is opsonization by anti-PEG antibodies, followed by RES clearance, since many approved nanocarriers are PEGylated. In *ex vivo* blood samples of chronic lymphocytic leukemia (CLL) patients, PEGylated doxorubicin-loaded liposomes showed a 234-fold difference in target cell uptake between patients and a 65 – 112-fold difference in off-target uptake.[300] Target uptake negatively correlated with immunoglobulin M (IgM) anti-PEG antibodies, while the variance in off-target association positively correlated with IgG anti-PEG antibodies. Although not in a solid tumor setting, this study already highlights the before mentioned challenge of achieving cellular-level targeting. In solid tumors it has been demonstrated for some nanocarriers that tumor accumulation correlates with uptake by TAMs rather than uptake by cancer cells.[301–304]

In this context, high expectations have been placed on targeting ligands. Preclinical models and clinical *ex vivo* studies have indeed demonstrated that actively-targeted nanocarriers enhance internalization into cancer cells and reduce off-target uptake.[211,300,305] Yet, translation remains hampered by a number of factors. Significant variability in the protein expression profile of patient tumors is impeding the identification of an universal targeting ligand with sufficient selectivity over healthy cells.[300] More critically, many targeting ligands increase RES recognition accelerating clearance and shortening blood circulation times, which can ultimately reduce overall long-term intracellular accumulation compared with passively targeted systems.[302,306] This outcome conflicts with the classical nanocarrier paradigm for delivery of cytostatics, which relies on prolonged circulation to maximize tumor accumulation over several days. It should be noted, however, that this concept does not necessarily apply to immunotherapeutic strategies, in which rapid clearance may be desirable due to strongly immune-activating payloads, provided that the anti-tumor effect is sufficiently

potent, i.e. that the targeting occurs rapidly enough.[307] Studies have shown that ligand density on nanocarriers and the resulting avidity of the system strongly affects internalization *in vitro* and biodistribution *in vivo*.[306,308,309] Moreover, high avidity systems that do accumulate at the target tissue might be hampered *via* the binding-site barrier, resulting in poor deep tissue penetration due to fast and strong binding in the outer tissue layers. However, systematic comparisons *in vivo* of identical nanocarriers with varying ligand densities are rare.[310] Nanocarrier properties and biological interactions influence targeting efficiency and ligands themselves often alter carrier characteristics.[300] These interdependencies complicate experimental design and hinder generalized conclusions across nanocarriers. The mismatch between *in vitro*–optimized designs and their *in vivo* performance further hinders the advancement of actively targeted nanocarriers.[311]

In summary, nanocarrier-mediated drug delivery has successfully reduced formulation-induced side effects and systemic toxicities, while achieving modest improvements in therapeutic outcomes. It enables spatial and temporal co-delivery, thereby improving multi-drug chemotherapy and supporting the development of new synergistic treatment strategies that address drug resistance and/or engage the patient's immune system. Remarkably, nanocarriers were expected to overcome *in vivo* challenges that had already been identified for ADCs in 1988, but many remain unresolved to this day.[312] These include suboptimal tumor localization and inadequate or unknown intratumoral distribution. Additional challenges are RES recognition and clearance, as consequence or independent of opsonization by plasma proteins, and, despite important insights gained, an incomplete understanding of the *in vivo* fate of nanocarriers. While the individual limitations in *in vivo* targeting are being addressed and steadily improved, complementary strategies have been developed in parallel to reduce the reduction of active substances in healthy tissue and release them in diseased cells. These strategies include (a) priming the target site for subsequent nanocarrier delivery by changing the physiological environment, as outlined in Chapter 0, and (b) triggering drug release in a controlled manner to ensure presence of the active compound only at the desired site. Such stimuli-responsive release systems, serving as a complementary design layer, are discussed in detail in the following Chapter 1.3.

1.3. Stimuli-responsive drug release through dynamic covalent chemistry

Controlled drug release in nanocarrier systems aims to enable precise control over the rate of active agent release. Ideally, optimized release kinetics prevent burst release and depletion of the nanocarrier reservoir while maintaining therapeutic drug concentrations. Unlike sustained release, which solely focuses on the release period, controlled release regulates the release rate, thereby maintaining the active drug concentration within the therapeutic window for an extended period. Taken together, and in combination with the pharmacokinetic advantages of nanocarriers, this strategy enhances therapeutic efficacy and reduces toxicity.[313] Additionally, these formulations allow for a reduced dosing frequency and reduced infusion times, which supports patient compliance and adherence to medication regimens. Classical mechanisms include the physical release processes, such as swelling, diffusion, and degradation-controlled release, which often occur in combination and are determined by the nanocarrier material and architecture.[314] Depending on the exact nanocarrier, pre-programmed release profiles can be tuned, for example, by increasing non-covalent interactions between the drug and carrier *via* chemical modifications in the material, or by adding an outer diffusion barrier through a nanocapsule architecture. These strategies are suitable to tune systems for long-term therapy, as is the case, for example, for androgen suppression in prostate cancer where Eligard®, a PLGA matrix releasing a GnRH agonist over several weeks, is indicated.[315] The release is driven by thermodynamic forces seeking equilibrium but increasing stability at off-target sites always comes at the cost of insufficient release at target sites. Nanocarriers designed for systemic circulation and accumulation at specific target sites introduced an adaptive release via stimuli-responsiveness, which allows release quantitatively within a specific environment where the stimulus is present, thereby adding spatiotemporal control to the release. External stimuli are physical triggers including ultrasound, irradiation, and magnetic/electric field.[316–320] As intended, drug release by systems exploiting external stimuli is limited to the site where this stimulus is applied excluding other uncertain diseased sites, such as micrometastases, or deeper regions if the stimulus has tissue penetration limitations, as is the case, for example, for near-infrared radiation. Endogenous stimuli include pH, redox potential and enzymes, among others, each of which can exhibit a characteristic equilibrium in pathophysiological sites distinct from healthy regions, depending on the disease, its stage and the affected site.

A prominent example of such a pathophysiological site is the TME, which exhibits an aberrant physicochemical and metabolic environment (see Figure 8) that is not only a consequence of the pathology but also actively drives tumor progression through multiple pathways.[321–324] Notably, different equilibrium states can also occur based on cell type or subcellular compartment.[325,326] Methodologically, the chemical design of enzyme-responsive systems is based on recognition sites of natural substrates and therefore enzyme-dependent. Physicochemical stimuli responsiveness has been introduced using both non-covalent interactions, such as host-guest interactions, hydrogen bonding and π-stacking, and covalent linkages *via* dynamic covalent chemistry (DCvC), which denotes chemical reactions that proceed reversibly under equilibrium-controlled conditions.[327–329] Both approaches are employed in state-of-the-art responsive systems. However, DCvC, which occupies an intermediate position between non-covalent and covalent chemistry, combines advantages of both and offers superior robustness, reliability, and controllability. Consequently, it has emerged as an essential tool in the design of stimuli-responsive drug release.

Both the carrier matrix enclosing a drug and the linkage between drug and carrier matrix (so-called prodrug nanocarriers) can be stimuli-responsive, whereby the types of chemistry used do not differ in principle. For prodrug nanocarriers, the advantage lies in the higher stability conferred by the covalent nature of drug binding, which counteracts premature leakage into the bloodstream while preserving drug activity through the dynamic nature of binding leading to release at target sites and improved treatment efficacy.[330–335] Among the broad range of dynamic covalent reactions, those that are responsive to biologically occurring gradients in relevant equilibrium states have become predominant for prodrug nanocarrier conjugation.[336] The linkage additionally should exhibit reliable formation and stability in biocompatible conditions (i.e. aqueous media, ambient temperature, no or non-toxic byproducts/catalysts) and in reasonable time-scales (< days). Based on these requirements Schiff bases, boronate esters and disulfides have emerged as preferred choices among dynamic covalent linkages both for direct drug carrier conjugation or within linkers connecting the two entities.[337]

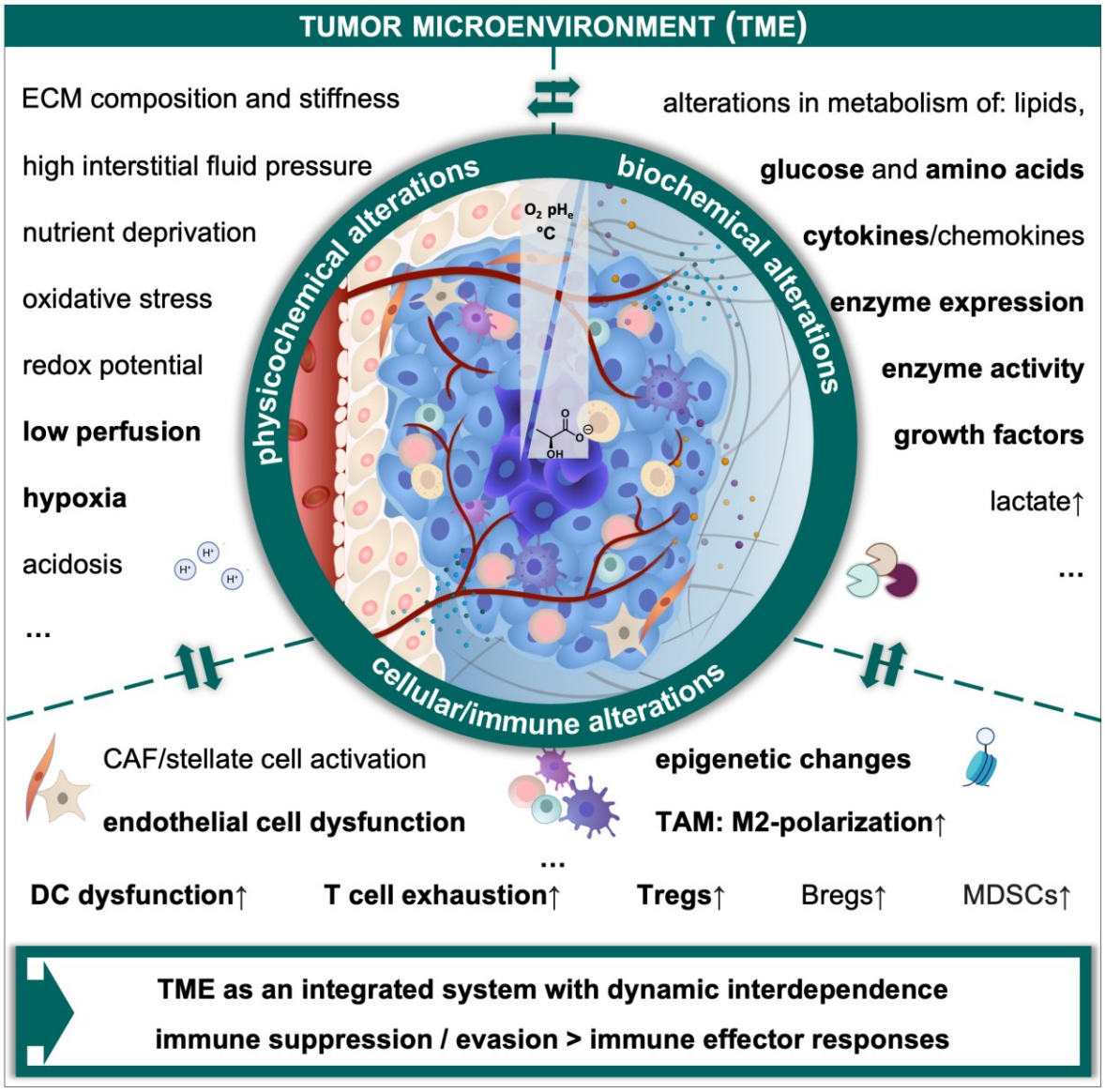

Figure 8: Schematic representation of the physicochemical, biochemical and cellular/immune alterations that shape the immunosuppressive tumor microenvironment. Bolded phrases denote TME alterations addressed in clinical research. ECM, extracellular matrix; CAF, cancer-associated fibroblast; TAM, tumor-associated macrophage; DC, dendritic cell; T/Breg, regulatory T/B cell; MDSC, myeloid-derived suppressor cell. Created with BioRender.com.

Imines, (acyl)hydrazones and oximes are dynamic covalent linkages formed through condensation reactions of aldehydes or ketones with primary amines, (acyl)hydrazides or *O*-substituted hydroxylamines, respectively. The chemical products, which in a broader sense can be referred to as Schiff bases, are reversible under neutral to acidic conditions.[338] Uncatalyzed, Schiff bases are slow in formation (10^{-4} – 10^{-3} $M^{-1}s^{-1}$)[339–341] and exhibit low

stability which increases in the order imines < hydrazones < acylhydrazones < oximes.[342] Their susceptibility to hydrolysis can be further reduced by introducing electron withdrawing groups (EWG) in adjacent positions because the protonation of the imine nitrogen becomes less favorable which impedes the subsequent rate-limiting nucleophilic attack at the imine carbon by water. Provided that the release is efficient under target site pH, hydrolytic stability in neutral conditions is often too low with half-times of just minutes to a few hours.[343] Acylhydrazones exhibit the most favorable ratio of stability in neutral pH and reversibility in lysosomal pH 5, and have therefore been investigated extensively as drug linkage, mainly in ADCs such as gemtuzumab ozogamicin (Mylotarg®), but also in nanocarrier systems.[344–346] Noteworthy, there are a few nanocarrier systems in which imines have also been successfully incorporated as drug linkage when combined with additional stabilizing forces, for example, within self-assembling micellar structures or within conjugated systems such as benzoic-imines.[347,348] Despite some successful exceptions, broad applicability is often restricted by the chemical structure of the drug scaffold. For example, only 0.7 % of anticancer drugs contain an aldehyde function, which could potentially participate in Schiff base formation;[349] their rarity is due to high reactivity and rapid metabolism. Primary amines are more common with 17.6 %, but Schiff base stability can only be tuned from the nanocarrier's side, which – depending on the carrier material – can also be limited, and is otherwise dictated by the drug scaffold. Additionally, emerging cationizable functional groups on the carrier material such as hydrazides or primary amines upon drug release can cause unwanted nanocarrier toxicity.[350]

Another pH-sensitive dynamic covalent linkage in a pH range of 5 – 8 are boronate esters. They are formed by reversible esterification of boronic acids (BA) with diols. In general, formation is fast ($10 – 10^3$ $M^{-1}s^{-1}$)[351,352] but boronate esters exhibit moderate to weak binding affinities (K_D = 0.8 mM – 220 mM),[353] depending on the exact binding partners. Saccharides, offering vicinal cis-diols, are prominent binding partners. The dynamicity of boronate esters has been exploited for sensing applications, particularly glucose monitoring in diabetes type 1 and 2, which led to the FDA and EMA approval of a long-term implantable bidentate anthracene diboronic acid-based sensor chip in 2022.[354,355] Additionally, macromolecules, for example albumin, decorated with multiple phenylboronic acids (PBA) are being explored as simple lectin mimetics offering multiple carbohydrate binding domains similar to CRDs.[356] But these conjugates lack the selectivity of lectins usually provided by secondary interactions

with the protein structure. In general, BAs act as lewis acids and exist, just like boronate esters, in their trigonal planar form or in tetrahedral anionic form. Boronate ester stability can be tuned by several factors.[357] The pK_a of the boronate ester is intrinsically linked to the pK_a of the corresponding boronic acid. It can be lowered through substituent effects, which enhances hydrolytic stability of the boronate ester by shifting the equilibrium under neutral conditions toward the tetrahedral anionic form. In this form, the boron *p*-orbital is occupied, which impedes a nucleophilic attack by water. The dihedral angle between the hydroxyl groups within the diol determines the ring strain within the boronate ester, which is why rigid, coplanar arranged diols such as catechols (CA) or nopoldiol show much higher binding affinities compared to flexible, non-coplanar diols.[357] High steric demand additionally increases ester stability, exemplified by pinacol or pinanediol regularly used as protecting groups.[358] Finally, stabilization of the boronate center within the tetrahedral form further increases stability. This can be achieved by coordination with tridentate nucleophiles as is the case in Wulff-type complexes, iminoboronates or the saccharide sorbitol.[359–362] Particularly B–N stabilization can enhance stability tremendously, exemplified by salicylhydroxamic acid (SHA) boronate complexes (K_D = 8 – 60 µM),[363–366] even resulting in the loss of reversibility in drug delivery relevant timeframes under physiological conditions for some diazaborines and oxime-boronates (K_D = 10 – 1000 nM).[367] Beyond single binding-site systems, boronate ester stability can be further enhanced through multivalent interactions, as demonstrated by Hebel et al.[368] They incorporated BA and CA residues onto a peptide backbone, enabling selective hybridization of peptide strands due to the high dynamicity of this linkage and the resulting sequence-programmable recognition. Notably, boronate ester binding affinities increased 10-fold and 63-fold for di- and trivalent dynamic covalent interactions, respectively, rendering the divalent BA–CA peptides as stable as a single BA–SHA interaction.

One of the very few cytostatics that naturally contain a boronic acid group is the proteasome inhibitor Bortezomib. Ma et al. synthesized L-DOPA-containing, RGD- plus fluorescein-modified peptide amphiphiles and conjugated the aliphatic BA of Bortezomib *via* the tetravalent CA groups of DOPA before self-assembled, micellar-like nanocarrier formation.[369] They were able to increase drug retention within the vascular compartment compared to free drug, and increased therapeutic efficacy with no impaired body weight increases. Intermolecular B–N stabilization was impressively utilized by Xiao et al. within

dextran-based nanocarrier systems using established cytostatics such as antimetabolites or topoisomerase inhibitors that were PBA modified using a *p*-borono benzyl carbonate/carbamate spacer.[370] Boronate esters linking the prodrugs to the dextran backbone were stabilized by the addition of dodecanamine introducing a "dual lock" with protonation as master key. These nanocarriers showed not only improved stability at pH 7.4 but also increased drug release at endolysosomal pH 5.5 as well as improved efficacy *in vivo* compared to single lock boronate ester nanocarriers. Notably, the used PBA moiety can be oxidatively deborylated selectively by hydrogen peroxide (H_2O_2), which is elevated in cancer cells, to the phenolic derivative triggering self-immolation and traceless release restoring full activity of the cytostatics.[371]

As with all condensation-based linkages, including Schiff bases, boronate esters intrinsically suffer from dilution-induced dissociation, which can occur after administration and during biodistribution. This behavior arises because water is participating as nucleophile in the equilibrium; upon dilution, its effectively infinite concentration shifts the equilibrium toward hydrolysis according to the law of mass action (Le Chatelier's principle), representing a major drawback for their translatability from *in vitro* to *in vivo* models.

In this regard, disulfides are a robust alternative linkage. Thiol groups can form covalent disulfide bridges under oxidative conditions. Disulfides play a key role in protein folding and stabilization of the tertiary structure of extracellular proteins, particularly those requiring high stability due to long half-lives or localization in harsh environments (e.g. extreme pH or temperature).[372,373] These bonds are reversible under reducing conditions such as those found intracellularly, which explains the low abundancy of permanent disulfides in intracellular proteins. Glutathione (GSH), a cysteine-containing tripeptide, is a major contributor to cellular redox homeostasis. Alongside iron, cysteine, and thiol-reducing enzymes, it maintains redox balance by undergoing reversible oxidation to glutathione disulfide (GSSG) and mitigating oxidative stress.[374] GSH cleaves disulfides through thiol–disulfide exchange: the first reaction liberates one thiol partner while forming a mixed disulfide with GSH; a second exchange with another GSH molecule generates GSSG and fully releases the other thiol partner. Its intracellular concentration ranges on average from 1 – 10 mM, far exceeding those of most other redox buffers, whereas extracellular concentrations are much lower with 2 – 20 µM.[374,375] Notably, total intracellular GSH concentrations (GSH_{tot}) vary among

different cells based on type, state and function, and also among cellular organelles. For instance, for cancer cells and hepatocytes GSH_{tot} of about 10 mM are reported.[376,377] Among immune cells, B-cells contain the lowest levels of GSH_{tot}, T cells intermediate and monocytes the highest.[378] Subcellularly, most of GSH is localized in cytosol, mitochondria and the endoplasmic reticulum, whereas the latter stands out by an over 7000-fold lower GSH:GSSG ratio due to the oxidizing environment.[379] Given GSH´s high abundance and the steep gradient between intra and extracellular space, incorporation of GSH(reductant)-responsive disulfide linkages within prodrug nanocarriers is a feasible strategy.

Disulfide formation and exchange are relatively slow but can be accelerated up to 100,000-fold by enzymatic catalysis[380]. Disulfide cleavage *in vivo* can further occur by other thiol containing compounds and by additional reaction mechanisms including radical cleavage or enzymatic cleavage, for example by gamma-interferon-inducible lysosomal thiol reductase (GILT) which is highly expressed in antigen-processing cells and localized within the lysosome.[374] However, it has been demonstrated repeatedly that drug release from disulfide linked prodrug nanocarriers is rapid and quantitative under intracellular GSH concentrations with negligible payload release under extracellular concentrations. Nonetheless, increased stability might be necessary for more surface exposed linkages as GSH is not the only free thiol within extracellular compartments. Introducing steric hindrance *via* adjacently positioned methyl groups can slow down drug release in plasma by up to four orders of magnitude.[381] One main limitation for disulfide-based prodrug nanocarriers can be the absolute necessity of cellular internalization to induce drug release as well as limitations regarding the type of functional groups on payload or carrier. With the development of amine-/hydroxyl- and thiol-reactive, self-immolative small linkers, payload/carrier combination possibilities have been broadened immensely.[382,383] Wang et al. conjugated the topoisomerase I inhibitor camptothecin (CPT) to lipids utilizing different linkages, including self-immolative disulfide linkages, and assembled them into liposomes with bilayer-anchored payloads.[272] Their camptothesome exhibited excellent stability during circulation and high, controlled intracellular release within tumors, with around 20 % of present drug molecules being released at the 2.5 h timepoint and 50 % at timepoints 24 h and 72 h.

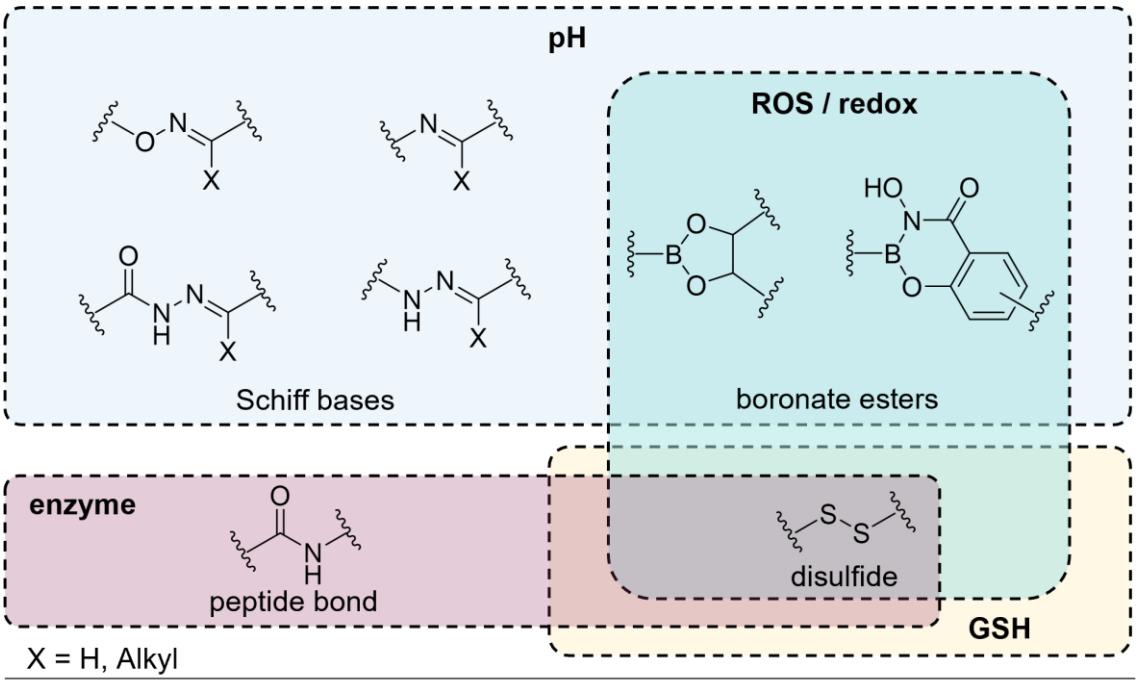

Figure 9: Representative depiction of the most commonly exploited endogenous stimuli-responsive linkages used in in vivo prodrug nanocarriers, ordered by stimuli type. Schiff bases: oximes, imines, (acyl)hydrazones; boronate esters: boronate ester, salicylhydroxamic acid boronate complex.

Despite the successful application of single-stimuli-responsive prodrug nanocarriers, the overall low accumulation at the target site, and consequently high presence at off-target sites, together with individual heterogeneity in stimuli equilibria, prompted researchers to develop dual-/multi-stimuli-responsive systems. These systems aim to further increase target site-specific release while decreasing undesired release.[384] The simultaneous presence of multiple triggers enhances drug release reliably, thereby improving spatial control and maximizing disease specificity.[385–387] In 2024 Schauenburg et al. combined redox-responsive disulfide and pH-responsive boronic acid–salicylhydroxamic acid linkages to macro-cyclize a BA-prodrug CPT, keeping the drug "locked" until exposure to acidic pH, glutathione and H_2O_2 triggered traceless release.[388] By this specific combination of DCvC linkages they enabled fast macrocyclization, prevented dilution-induced disassembly, and used the incorporated BA as H_2O_2-responsive masking group which is converted intracellularly from the less active prodrug to the fully active CPT. Some nanocarriers systems incorporate the different responsiveness not only on the drug site but also within the carrier matrix.[389] Their sophisticated designs show promising preclinical results, but also pose challenges that currently hinder their translation.

Although the concept of stimuli-responsive oncotherapeutic nanocarriers (mainly external stimuli) emerged in the 1980s, none has yet received full FDA approval, despite several advanced clinical trials, for example thermosensitive liposomal doxorubicin ThermoDox® for breast, liver and pediatric refractory solid tumors.[390] This large translational gap underscores the need for delivery systems that are functionally sophisticated and simple, safe, and scalable in their design.

The introduction of this thesis has outlined the fundamental concepts of nanocarrier-based drug delivery, including nanocarrier definitions and terminology, clinically relevant materials and architectures, and strategies to improve biodistribution through static and dynamic targeting. While substantial progress has been made in understanding how nanocarrier composition, size, and surface properties influence *in vivo* fate, the translation of nanocarriers with significantly improved target-site accumulation remains limited. Insights from marketed oncotherapeutic nanocarriers highlight the complexity of *in vivo* targeting, especially on a cellular level, and show that delivery performance is governed by multiple, interdependent factors that are difficult to predict, making precise control over drug accumulation through targeting alone challenging. Stimuli-responsive drug release systems therefore represent a complementary design approach to decouple biodistribution from site-specific drug release and improve therapeutic selectivity. Together, these considerations demonstrate both the opportunities and persistent gaps in current nanocarrier design and provide the conceptual basis for the research objectives addressed in this thesis.

2. Motivation

Nanocarriers have emerged as one of the most versatile and intensely studied DDSs, aiming to overcome long-standing barriers that limit the success of cancer therapies. Despite major advances in oncology over the last decades, including immunotherapy breakthroughs such as antibody-mediated ICB and chimeric antigen receptor (CAR) T cell therapy, treatments are either limited to small subsets of patients and cancer types, or hampered by insufficient tumor exposure and specificity, leading to suboptimal efficacy accompanied by systemic toxicity and significant damage to healthy tissue.

Although some nanocarrier formulations are associated with unique adverse events, they have generally improved safety profiles of chemotherapeutics, increased MTDs, and translated into modest gains in quality of life and overall survival.[85,391] However, their ability to enhance drug accumulation at the tissue and cellular level, remains limited, while premature drug release before reaching the intended target cells continues to pose a major challenge.

In an effort to address limitations in stability, targeting, and delivery, preclinical research focused on incorporation of responsive drug release to increase therapeutic indices and, concurrently, on the development of novel nanocarrier materials and architectures. But many of these sophisticated designs raise concerns about translatability and biological safety and, if at all, are only slowly progressing beyond the *in vitro* stage.

Spurred by the growing recognition of cancer's biological complexity and the pivotal role of the immune system, there has been a marked shift in nanocarrier research emphasis toward immuno-oncology applications over recent years. Besides enabling cancer vaccination, nanocarriers offer the potential to target potent immunomodulators to specific immune compartments or cell populations, enabling localized modulation while reducing systemic immune-related toxicities. Depending on targeting and payload, they can amplify natural anti-tumor responses or alleviate immune evasion, e.g. by repolarizing immunosuppressive M2-polarized macrophages. As many pathologies involve dysregulated immune responses that could be modulated through targeted delivery of immunomodulators, the potential of nanocarriers extends beyond cancer therapy. Yet, translating these concepts into effective therapies is still hindered by the fundamental challenge of achieving precise tissue- and, more importantly, cell-type-specific targeting.

To address the need for smart, clinically translatable DDSs that incorporate lessons learned from preclinical to real-world applications, and that align with ongoing developments in immune-oncology, this thesis pursues two main objectives (see Figure 10): (1) the design, optimization and systematic evaluation of a nanocarrier for its ability to selectively target defined immune cell types and deliver immunomodulators intracellularly, utilizing static targeting and responsive drug release, and (2) the development of a dynamic covalent linker system with improved extracellular stability and stimuli-responsive intracellular release, designed to overcome the intrinsic chemical limitations of established DCvCs by harnessing cooperative effects.

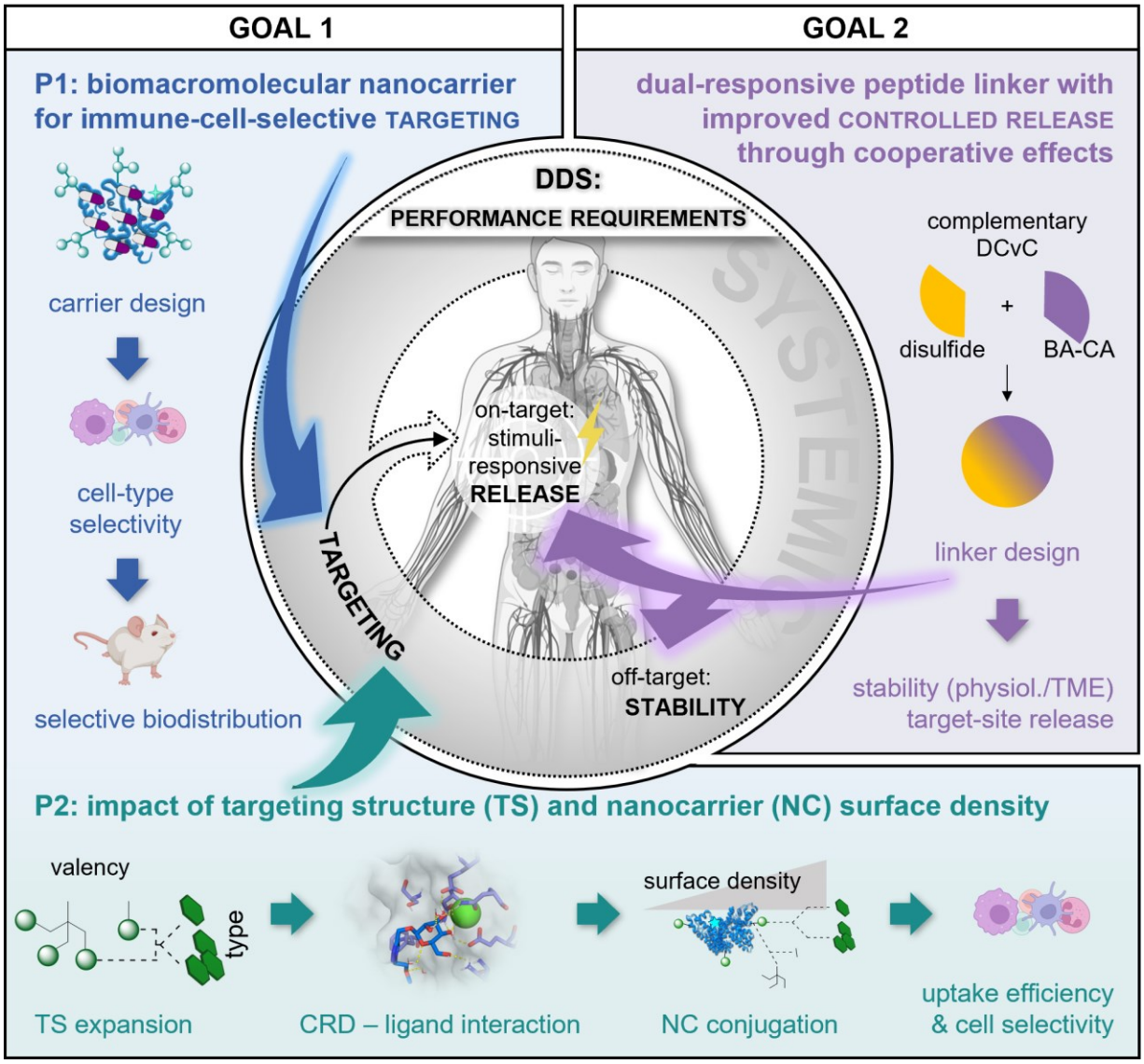

Figure 10: Schematic illustration of the performance requirements of drug delivery systems and the research framework of this thesis, which addresses two central performance criteria of DDSs. Goal 1 focuses on targeting efficiency of nanocarriers and comprises two projects:

P1 entails the design and evaluation of immune-cell-type-selective nanocarriers for targeted immunomodulation, while P2 investigates expanded targeting structures to elucidate ligand-receptor interactions and the effects on cellular internalization and specificity of correspondingly modified nanocarrier systems. Goal 2 addresses the stability of DDSs for systemic administration by developing a dynamic covalent linker system with improved extracellular stability and stimuli-responsive intracellular release through the combination of complementary DCvC linkages that exhibit cooperative effects. DDS, drug delivery system; DCvC, dynamic covalent chemistry; TME, tumor microenvironment; CRD, carbohydrate recognition domain; P1/2, project 1/2; TS, targeting structure; NC, nanocarrier. Created with BioRender.com.

To achieve the first objective, HSA was selected as carrier material for the nanocarrier design due to its established medical use, monomolecular single-chain structure and associated versatile bioconjugation sites as decisive factors. The single-chain structure was chosen over a classical nanoparticulate formulation (e.g. nab™ technology), as it allows for a more precise analytical characterization of chemical modifications in a quantitative manner. Additionally, the small carrier size (< 50 nm) is preferable, as it is generally associated with enhanced tissue penetration and reduced protein corona formation during circulation.[298,392]

Capitalizing on the abundance of amino acid residues and their chemical reactivity, a dye label for tracking and multiple clickable mannose-based targeting ligands were attached to the surface. The depicted incorporation of the bifunctional linker endowed the system with a platform character enabling straightforward modulation of targeting structure density and variety throughout the project, while maintaining an overall negative surface charge, which is associated with biocompatibility and reduced unspecific uptake *in vivo*.[393,394] The selected mannose-based targeting ligands bind the lectins MMR and DC-SIGN, which are highly expressed on M2-polarized Macrophages, liver sinusoidal endothelial cells (LSEC), and DCs, all of which play pivotal roles in shaping their immune microenvironment (see Chapter 1.2.1.1). Notably, LSECs occupy a central role in maintaining the tolerogenic hepatic immune environment.[395]

In the first project, increasing numbers of α-(1→6)-α-(1→3)-branched trimannose (TM) as mannose-based targeting ligand were attached to the carrier surface. The multivalent carriers were systematically evaluated for uptake efficiency *in vitro* in, among others, an immortalized receptor-transduced cell line. The most effective high-valency construct was loaded with multiple copies of immunomodulatory toll-like receptor 7/8 agonist (TLR7/8a) *via* reductant-responsive, self-immolative disulfide chemistry exploiting the thiols of HSA's 34 disulfide

bridges. This carrier was extensively investigated for cell-selectivity, serum and plasma compatibility, and *in vitro* efficacy, as well as for its biodistribution *in vivo* (Chapter 3).
The targeting ligand itself and its mode of presentation critically influence carrier selectivity and avidity. In turn, both parameters affect *in vivo* biodistribution, although the relationship remains incompletely understood due to the lack of systematic studies.[310,396] Therefore, in the second project, the ligand repertoire was expanded; and both low- and high-valency ligand regimes were compared by exploiting the platform character of the HSA nanocarrier. To elucidate correlations between uptake efficiency, cell type selectivity and ligand density/avidity, two different mannose-based targeting ligands were studied, mannose (M) and TM, given literature evidence suggesting preferential recognition of terminal M by MMR and TM by DC-SIGN.[397,398] To further assess the contribution of avidity effects, M and TM were also presented on a dendron-like scaffold enabling multivalent presentation within a single ligand (Chapter 4). The uptake behavior was analyzed in primary cells, which exhibit a more authentic endocytotic behavior than immortalized cell lines,[399] to provide deeper insights into the effects of nanocarrier avidity (Chapter 4).

Payload conjugation *via* DCvC, whether for small-molecule drug conjugates (SMDC), ADCs, prodrug nanocarriers or other DDSs, recurrently suffers from premature cleavage *in vivo* or under *in vivo*-mimicking conditions. As discussed in detail in Chapter 1.3, most strategies to stabilize dynamic covalent linkages rely on proximal chemical modifications that shift the equilibrium of a single bond toward greater stability under physiological conditions, often at the expense of rapid reversibility or ease of synthesis. Therefore, the second objective of this thesis is the development of a linker system with improved stability by combining two complementary DCvC linkages to overcome the intrinsic limitations of single-mode linkers. To this end, boronic acid–catechol (BA–CA) interactions were integrated with disulfide bond formation within short peptide scaffolds, using commercially available amino acids and established solid-phase peptide synthesis. The system was designed to exploit the rapid formation and dissociation of boronate esters between divalent peptide tags, providing both fast association and selective self-sorting into heterodimers. The templated peptide tags were stabilized *via* disulfide formation between the precoordinated cysteine thiols, yielding a dual-locked system. Ultimately, this project aimed to establish a peptide-based, intelligent linker architecture that remains stable under extracellular tumor-like conditions while retaining

responsiveness to intracellular reductive environments through cooperative design (Chapter 5).

In summary, this thesis addresses two central challenges that continue to limit the therapeutic success of DDSs: the lack of precise cell type selectivity and the insufficient stability of drug conjugation chemistries. Through a dual focus on targeted nanocarrier development and dynamic covalent linker concept, this work aims to contribute to the evolution of next-generation DDSs with improved translational potential in (immuno)oncology.

3. Glycogen-inspired trimannosylated serum albumin nanocarriers for targeted delivery of toll-like receptor 7/8 agonists to immune cells and liver

The first research project addresses the currently insufficient targeting efficiency of nanocarriers through the development of a biomacromolecular, immune cell type-selective targeted nanocarrier. Extensive physicochemical characterization and systematic evaluation of cell selectivity, immunomodulatory efficacy *in vitro*/*ex vivo*, and biodistribution *in vivo* were performed to assess its therapeutic potential.

Authors

B. Lantzberg‡, Y. Zeyn‡, R. Forster‡, L. Jian, D. Schauenburg, C. Hieber, L. Nuhn, T. Zhou, M. J.S.A. Silva, K. Koynov, H. Jiang, S. L. Kuan*, M. Bros*, T. Opatz*, and T. Weil*

‡ Authors contributed equally to this work.

* Corresponding author

Published in Journal of Controlled Release 2025, 382, 113705

DOI: 10.1016/j.jconrel.2025.113705

Date of Publication: 7th of April 2025

Contributions

As co-first author, **Bellinda Lantzberg** conceptualized the chemical design of the nanocarrier and conducted the synthetic and analytical experiments regarding small molecule cargoes, including HR-ESI-MS, MALDI-ToF-MS and NMR analyses. She conducted the synthetic and analytical experiments regarding the HSA conjugates and nanocarriers, including MALDI-ToF-MS, DLS, zeta potential, SDS-PAGE and agarose gel electrophoresis analyses. She planned and carried out the *in vitro* experiments in $MMR^{+/-}$ CHO cell lines, analyzed the data, and performed the formal analysis. She performed drug release experiments from the

nanocarriers and assisted Maria J. S. A. Silva in LC-HRMS measurements and data analysis. Furthermore, she planned the *in vitro* experiments in primary cell lines as well as the *ex vivo* and *in vivo* experiments together with Yanira Zeyn and analyzed the data. She drafted and edited the manuscript.

Yanira Zeyn, as co-first author, conducted all *in vitro* and *ex vivo* experiments in primary cell lines as well as *in vivo* experiments, processed data, and performed formal analysis. She prepared the respective data plots and drafted the respective parts of the manuscript and assisted with manuscript corrections. As co-first author, Robert Forster conducted all synthetic and experimental work related to the trimannose structure, analyzed and processed the data. He prepared the respective figures and drafted the respective parts of the manuscript as well as the supplementary information and assisted with manuscript corrections. Lin Jian and Kaloian Koynov planned the FCS experiments for characterization of nanocarriers and in vivo monitoring in plasma. Lin Jian conducted the FCS experiments, analyzed and processed the data, and assisted with manuscript corrections. Dominik Schauenburg conducted synthetic and analytical work related to the benzyl (2-(pyridin-2-yldisulfanyl)ethyl)carbamate structure (linker) for cargo modification and contributed to discussion of results. Christoph Hieber conducted parts of the *in vivo* experiments and assisted with data processing. Lutz Nuhn provided the MMR transduced CHO cell line and flow cytometer, trained Bellinda Lantzberg in handling, data processing and analysis, and contributed to discussion of results. Tianjiao Zhou prepared the concept figure and reviewed and edited the manuscript and assisted with manuscript corrections. Maria J. S. A. Silva optimized the LC-HRMS method, performed data analysis of cargo release experiments, processed and plotted respective graphs. from nanocarriers Kaloian Koynov reviewed and edited the manuscript, assisted with discussion of results, and supervised Lin Jian. Seah Ling Kuan managed administrative tasks for the project, contributed to discussion of experiments and results, and drafted and edited the manuscript. Matthias Bros supervised Yanira Zeyn, reviewed and edited the manuscript, and assisted with manuscript corrections. Till Opatz and Tanja Weil were involved in the inception, design concept and chemical design as well as project administration and contributed to discussion of the concept and design. They corrected the manuscript and acquired funding for the project. Furthermore, Till Opatz supervised Robert Forster and Tanja Weil supervised Tianjiao Zhou and Bellinda Lantzberg.

Journal of Controlled Release 382 (2025) 113705

Contents lists available at ScienceDirect

Journal of Controlled Release

journal homepage: www.elsevier.com/locate/jconrel

Glycogen-inspired trimannosylated serum albumin nanocarriers for targeted delivery of toll-like receptor 7/8 agonists to immune cells and liver☆

Bellinda Lantzberg [a,1], Yanira Zeyn [b,1], Robert Forster [c,1], Lin Jian [a], Dominik Schauenburg [a], Christoph Hieber [b], Lutz Nuhn [d], Tianjiao Zhou [a,e], Maria J.S.A. Silva [a], Kaloian Koynov [a], Hu-Lin Jiang [e], Seah Ling Kuan [a,*], Matthias Bros [b,*], Till Opatz [c,*], Tanja Weil [a,*]

[a] Max Planck Institute for Polymer Research, Ackermannweg 10, 55128 Mainz, Germany
[b] Department of Dermatology, University Medical Center of Johannes Gutenberg-University Mainz, Obere Zahlbacher Straße 63, 55131 Mainz, Germany
[c] Department of Chemistry, Johannes Gutenberg University Mainz, Duesbergweg 10–14, 55128 Mainz, Germany
[d] Faculty for Chemistry and Pharmaceutics, Julius-Maximilians-University Würzburg, Röntgenring 11, 97070 Würzburg, Germany
[e] State Key Laboratory of Natural Medicines, China Pharmaceutical University, 210009, PR China

ARTICLE INFO

Keywords:
Immunotherapy
Nanomedicine
Nano-immunotherapy
Biomacromolecular therapeutics
Albumin-carrier
Trimannose targeting

ABSTRACT

Nanocarriers can improve the therapeutic efficiency of small molecule immunomodulators or inhibitors, which is important for immunotherapy of liver diseases or cancer. Macromolecular protein carriers, such as human serum albumin (HSA), could provide better penetration compared to large nanoparticles (>50 nm) but are hampered by systemic biodistribution. To overcome these limitations, inspired by the natural glycogen structure, we have designed the HSA nanocarrier (<40 nm) consisting of multiple trimannose (TM) ligands attached to the protein surface, to target mannose or dendritic cell-specific intercellular adhesion molecule-3-grabbing non-integrin (DC-SIGN) receptors in immune cells or immunological organs such as the liver. Capitalizing on the chemical reactivity of different amino acids present in HSA, we have incorporated multiple copies of a cargo relevant for immunotherapy, *i.e.* the toll-like receptor (TLR) 7/8 agonist. The resulting TM-HSA conjugates exhibit excellent and specific uptake *ex vivo* in various immune cells and liver-specific uptake *in vivo*, opening access to protein nanocarriers with rapid and efficient *in vivo* targeting with great potential for immune-related diseases.

1. Introduction

Immunotherapy plays a critical role in the modern strategy for treating fatal diseases such as cancer and liver diseases and is experiencing rapid growth to address these global health threats (9.7 million cancer-related deaths in 2022 [1], two million deaths annually due to liver diseases) [2]. It has become state of the art to formulate immunotherapeutics in nanosized delivery systems to enhance their therapeutic efficacy and to improve their pharmacokinetic and –dynamic profile. To improve delivery, different targeting strategies, divided into passive and active targeting, are used for better biodistribution. At the same time, long circulation times are sought to increase delivery efficiency. However, in the case of cancer, for example, the median delivery efficiency of most nanocarriers remains critically low at 0.7 % [3]. Some possible reasons could be limited tissue penetration of large nanoparticles (≥ 50 nm) to reach deeper targets [4–7], particle instability and off-target release of the drug payloads, and their passive accumulation in other organs such as the liver, lung, and spleen [8]. Although the toxicity profiles of nanoparticle formulations have improved compared to their free drug counterparts, their therapeutic index remains a limiting factor [3,9]. Therefore, to overcome the existing limitations of prolonged systemic exposure and associated off-target or even on-target/off-site accumulation, alternative delivery strategies for immunotherapy have emerged: *i.e.* from designs emphasizing maximum tolerable concentrations with long circulation times for effective accumulation to those characterized by rapid, cell-type or tissue-specific uptake with limited

☆ This article is part of a Special issue entitled: 'SI Feijen' published in Journal of Controlled Release.

* Corresponding authors.
E-mail addresses: kuan@mpip-mainz.mpg.de (S.L. Kuan), mbros@uni-mainz.de (M. Bros), opatz@uni-mainz.de (T. Opatz), weil@mpip-mainz.mpg.de (T. Weil).

[1] authors contributed equally

https://doi.org/10.1016/j.jconrel.2025.113705
Received 20 September 2024; Received in revised form 20 March 2025; Accepted 4 April 2025
Available online 7 April 2025

systemic exposure [10]. For example, receptors on the surface of hepatic stellate cells or Kupffer cells (liver macrophages) have been targeted to achieve cell-type specific delivery of small molecule drugs for more effective treatment of liver fibrosis [11,12].

Thus, attaching ligands to the surface of low nanometer-sized carriers that target receptors present in high density may be attractive to achieve higher immune cell or immunological organ specificity *in vivo* and to enable fast uptake [13–18]. C-type lectin receptors (CLRs), such as the macrophage mannose receptor (MMR, CD206) or the dendritic cell-specific ICAM-3 grabbing nonintegrin receptor (DC-SIGN, CD209), are ideal candidates [19,20]. They are a class of pattern recognition receptors (PRRs) highly expressed on the surface of professional antigen-presenting cells (APCs) such as macrophages and dendritic cells, as well as on Kupffer and liver sinusoidal endothelial cells (LSEC) [21,22]. Moreover, they enable the recognition of pathogen-associated molecular patterns (PAMPs) containing saccharide moieties, especially branched mannopyranosides that are found in high mannose glycopeptides [23,24]. MMR recognizes end-standing single mannose branched structures or di-mannose clusters, like α-(1 → 2)-mannobiose [25], while DC-SIGN recognizes both internal branched mannose structures with a minimum of three mannoses, like α-(1 → 3), α-(1 → 6)-mannotriose [20,21,26] and end-standing di-mannoses [21,27–29]. Thus, mannose-based targeting moieties are highly relevant for efficient drug delivery to immune cells [30,31]. It has been reported that a branched, highly mannosylated structure binds 130 times more strongly to DC-SIGN than single mannose [20]. However, progress has been limited because the chemical synthesis of hyperbranched polymannosides is challenging. Therefore, multiple smaller mannose-based oligosaccharide targeting structures attached to a single carrier are more attractive for practical implementation and widespread application. The trimannose (TM) group [19,32,33] is an excellent candidate as it meets the required binding features [34] and the synthesis is easily upscaled.

For widespread application, nanocarriers with exceptional biocompatibility and biodegradability are of particular interest. Proteins have been applied as versatile macromolecular drug delivery systems with smaller dimensions (<50 nm) than many of the conventional nanoparticle formulations. Human serum albumin (HSA), the most abundant human plasma protein, has endogenous transport functions in the bloodstream, is non-immunogenic [35,36] and has a hydrodynamic diameter of less than 10 nm making it an attractive nanocarrier for drug

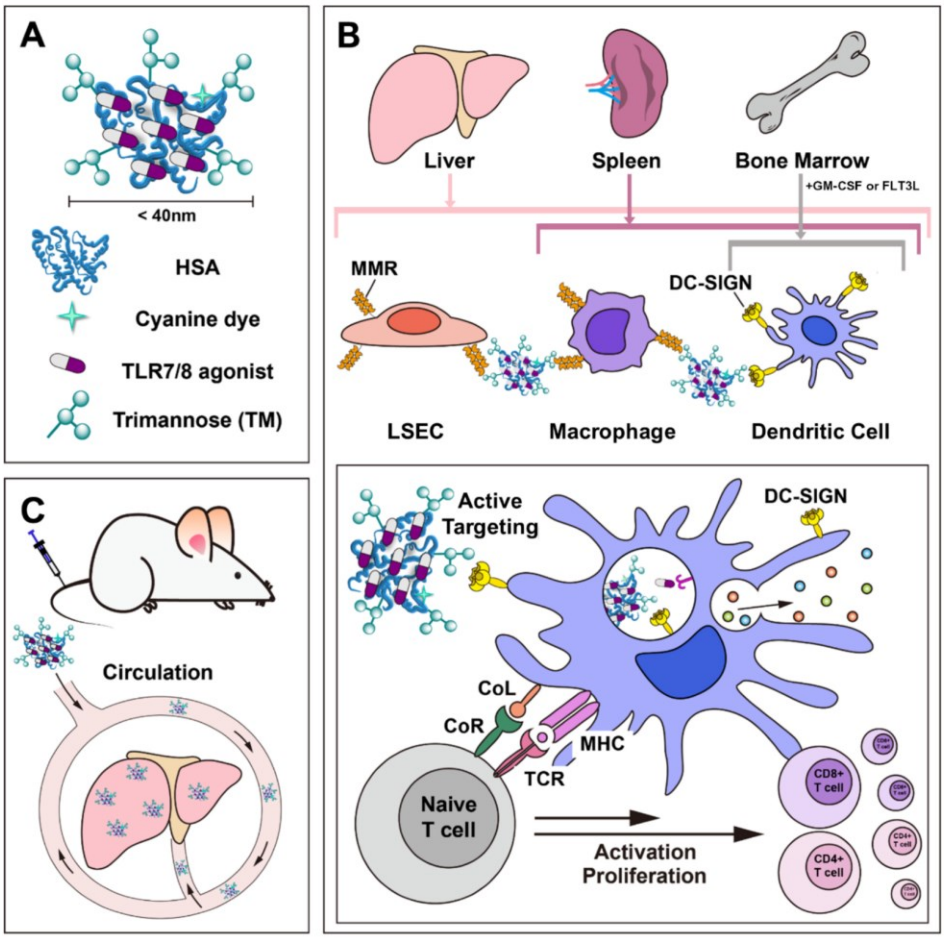

Fig. 1. Illustration of A) trimannosylated human serum albumin carrier with TLR 7/8 agonist and B) main target cell populations derived from murine liver (LSECs, macrophages (Kupffer cells), dendritic cells), spleen (macrophages, dendritic cells) and bone marrow (dendritic cells) that were investigated in *ex vivo* experiments regarding carrier uptake (top) and carrier effects on dendritic cells (bottom). C) Biodistribution of trimannosylated HSA nanocarrier *in vivo* in healthy mice. HSA = human serum albumin, CoL = co-stimulatory ligand, CoR = co-stimulatory receptor, TCR = T-cell receptor, MHC = major histocompatibility complex, LSEC = liver sinusoidal endothelial cells.

delivery applications [37]. HSA also offers various functional groups on its surface, such as amines, carboxylic acids or a thiol that can be easily modified to accommodate multiple copies of targeting groups or drug molecules.

Inspired by glycogen, in which branches of glucose units surround a core protein, we propose to attach TM in a multivalent manner to the HSA surface (Fig. 1A) to enable high cell-type specificity *ex vivo* through active cell targeting and rapid accumulation *in vivo* (Fig. 1B, C). The glycogen-inspired design allows the number of TM per HSA to be varied to systematically investigate the influence of ligand density on their selective binding to cell lines expressing MMR/DC-SIGN and on uptake efficiency [38,39], which has been limited to date [19]. We also incorporated multiple copies of molecular cargoes, such as toll-like receptors 7/8 agonist (TLR7/8a), into the highly saturated $TM_{38–41}$-HSA (henceforth TM-HSA), using a disulfide linker. Cell-type selective activation *ex vivo* was observed in dendritic cells and macrophages through controlled receptor targeting and activation of synergistic immune pathways was achieved using TM-HSA-TLR7/8a. Fast and specific accumulation of the TM-HSA conjugates was observed only in the liver *in vivo*. The TM-HSA nanocarrier, which combines TM and HSA in a core-shell architecture, provides access to a biodegradable, organ-selective, and safe drug delivery system with high drug loading capacity (independent of the drug polarity) and long-term stability to provide new avenues for immunotherapy through cell-type specific or/and liver targeting.

2. Results and discussion

2.1. Synthesis and characterization of TM_n-HSA

To prepare HSA carriers with varying numbers of TM targeting moieties, a mannotrioside containing an azide-functionalized linker was prepared following an optimized synthesis route based on literature methods [33]. The nine-step synthesis sequence involved two telescoped reaction procedures to reduce the amount of necessary intermediate chromatographic purification steps and to improve the overall yield compared to non-telescoped synthesis procedures [33]. The TM unit was obtained with an overall yield of 42 %, over six linear steps starting from commercially available D-mannose and triethylene glycol (Scheme S1 in supporting information (SI)). The yield was significantly improved, compared to the 20 % over seven linear steps previously reported [33]. Inclusion of a two-step propargylation and Zemplén deacylation sequence, based on the work of *Krabicová* et al. [40], afforded the propargyl mannoside (**1**). A three-step silylation, benzoylation, and desilylation sequence, based on the work of *Ramos-Soriano* et al. [41], efficiently delivered the 2,4-protected mannoside (**2**). Both methods allowed the preparation of the building blocks efficiently in multigram scale reactions for further transformations to yield the trimannose targeting unit (TM, Fig. 2A, for abbreviations, see SI). Furthermore, employing the selective silylation strategy, proved to be superior to the formerly used method [33]. The clickable TM and all involved intermediates were characterized by ^{1}H-, ^{13}C-, and 2D-NMR, as well as high-resolution mass spectrometry (see SI). The TM unit was used for subsequent conjugation with dibenzocyclooctyne (DBCO)-modified HSA.

Next, we proceeded to functionalize HSA with varying numbers of TM. To facilitate subsequent characterization, a sulfo-cyanine 5 (Cy5) dye was first incorporated into native HSA *via* the single unpaired cysteine (Cys 34, Fig. 2B) yielding Cy5-labeled HSA. All HSA and chemically modified HSA analogs used in subsequent studies are fluorescently labeled unless otherwise stated. Ring-opening of the succinimide thioether was promoted by incubation in borate buffer at pH 9.2 and 37 °C for 24 h [42] to prevent displacement of the Cy5 *via* exchange with thiols, which has been reported [43]. Next, varying equivalents of NHS-PEG_4-DBCO (5, 10, 20, 2 × 25, 4 × 25 equiv.) were added to HSA and different $DBCO_m$-HSA conjugates were isolated with varying average numbers of DBCO groups (Fig. 2B). The increasing amount of DBCO groups bound to HSA was confirmed in agarose gel electrophoresis (Figure S1), in which proteins smaller than 600 kDa are separated predominantly by charge [44]. By attaching NHS-PEG_4-DBCO, lysine residues in the protein are converted to amides, leading to a more negative overall charge and further migration towards the positive electrode. The average number of DBCO per HSA was calculated to be 3, 6, 15, 30, and 50, respectively, as determined by the average molecular weight of the statistical modification from MALDI-ToF analysis (Table S1). The molecular mass (M) of these DBCO-HSA conjugates was calculated as the *m/z* value of the center of the peak of the singly charged species, with the variation of the respective mass range (Δm) given as the full width at half maximum (FWHM, see SI for calculation method). Thereafter, TM (5–12 equiv. per DBCO) was added to the $DBCO_m$-HSA conjugates, followed by purification *via* spin filtration (molecular weight cutoff = 10 kDa) to remove excess reagent. Upon lyophilization, the TM_n-HSA conjugates, TM_1-HSA, TM_3-HSA TM_9-HSA, TM_{20}-HSA, and TM_{38}-HSA, were isolated with a 78–95 % recovery rate. Successful click reactions were confirmed by agarose gel electrophoresis (Figure S2). The interaction between TM and agarose leads to a reduced migration of TM-HSA conjugates through the gel with an increasing number of TM attached and when compared to the corresponding DBCO-HSA precursors (Figure S1). The average number of TM groups attached as well as FWHMs (Δm) were determined by MALDI-ToF-MS (Table S2, Fig. 2C). Based on the Δm values, we obtained the number variation in the degree of modification for each TM_n-HSA conjugate (Fig. 2C). The sizes of the TM_n-HSA bioconjugates were determined using fluorescence correlation spectroscopy (FCS) [45]. The size ranges from 4.7 ± 0.5 to 7.0 ± 0.7 nm, with the greatest increase in size in TM_{38}-HSA (Fig. 2C). The trend is consistent with observation in dynamic light scattering (DLS) measurements (Figure S3). The PDI increases with an increasing number of TM (up to 1), presumably due to hydrogen bonding and carrier-carrier interaction increase (Figure S3). Notably, no precipitation for trimannosylated conjugates was observed even after long storage in solution, suggesting that there is no uncontrolled aggregation. Zeta potential measurements (Fig. 4B) also indicated that there is not a large difference in charge between the negatively charged HSA (−7.7 ± 1.9 mV) and the $TM_{38–41}$-HSA (−9.0 ± 1.9 mV).

Next, we investigated the influence of the number of TM present on the HSA surface on the uptake of cells expressing MMR/DC-SIGN. Chinese hamster ovary (CHO) cells or CHO transductants expressing murine MMR (CHO-MMR^+) were used and 100 nM of the TM_n-HSA carriers were applied and incubated for 24 h before fluorescence-activated cell sorting (FACS) analysis (Fig. 3C). HSA (n(TM) = 0) was used as negative control. We already observed significant differences in cellular uptake of TM_1-HSA carrying an average of one TM group. The uptake increased even further with higher number of TM attached in the MMR-positive CHO cells. Confocal studies of TM_{38}-HSA *versus* HSA further corroborated the TM-mediated internalization into CHO-MMR^+ cells and low non-specific uptake of the HSA control (Fig. 3A).

As dendritic cells play a crucial role in shaping adaptive immunity and naturally express the target receptor DC-SIGN, we studied the uptake using a commonly used culture of murine bone marrow (BM) cells treated with granulocyte-macrophage colony-stimulating factor (GM-CSF) to generate BM-derived dendritic cells (BMDCs). Similarly, we observed a significant uptake of the TM_n-HSA carriers into the GM-CSF differentiated BMDC after overnight incubation (Fig. 3D). The corresponding DC-SIGN expression upon treatment was determined, proving consistent receptor availability and showing no increase in expression levels regardless of the amount of TM attached to the carrier in contrast to lipopolysaccharides (LPS) treatment, which serves as a positive PAMP control. The results demonstrate that TM-HSA conjugates exhibit selectivity towards cell lines expressing MMR in first *in vitro* studies. For n(TM) = 38, the highest cellular uptake was obtained indicating that this bioconjugate could potentially serve as nanocarrier for cell-type selective delivery into MMR/DC-SIGN positive cells. For all further studies, we prepared carriers that are saturated with TM (n(TM) = 38–41 ± 12)

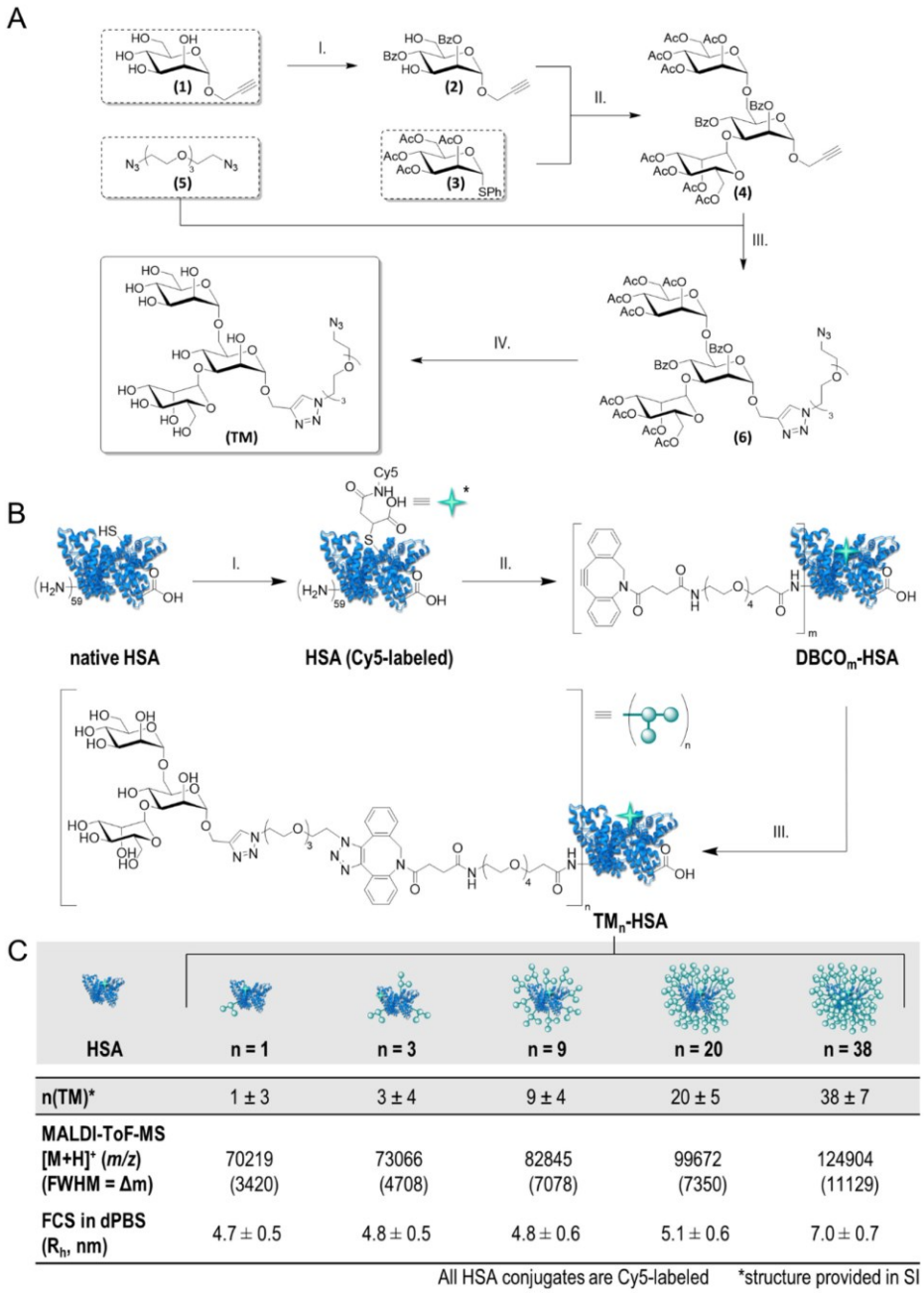

Fig. 2. A) Synthesis scheme of TM: I.) i.) TBDMSCl, imidazole, DMF, Ar-atm., MS 3 Å, 0 °C, 4 h; ii.) BzCl, Pyr., DMAP, DCM, Ar-atm., MS 3 Å, 0 °C to RT, 42 h; iii.) $(HF)_X \times$ Pyr., Pyr., THF, 0 °C to RT, 24 h, 62 %*; II.) NIS, AgOTf, DCM, Ar-atm., −40 °C to −20 °C, 4 h, 70 %; III.) CuBr, PMDETA, DMF, Ar-atm., 45 °C, 3 h, 97 %; IV.) NaOMe, NaOH, MeOH, 45 °C, 4 h, quant. (* telescoped yield, *i.e.* yield for a sequential one-pot synthesis with reagents added one at a time and without work-up) for further details see Scheme S1). B) Synthesis scheme of trimannosylated HSA conjugate: I.) Sulfo-Cy5-maleimide, 50 mM PB pH 7.4, RT, 4 h; 50 mM Na-borate buffer pH 9.2, 37 °C, o.n., 93 % recovery rate; II.) NHS-PEG_4-DBCO, 50 mM PB pH 7.4, RT, 4–6 h, 95–100 % recovery rate; III.) TM, 50 mM PB (8 M urea, 2 mM EDTA) pH 8, RT, 4–16 h, 78–95 % recovery rate. C) MALDI-ToF-MS and FCS characterization of HSA conjugates carrying varying numbers of TM. Variation in the degree of modification was calculated from FWHM, see SI for calculation method; see SI Fig. S4 for FCS correlation curves. HSA structure was adapted from RCSB PDB: 1AO6. [74–76]

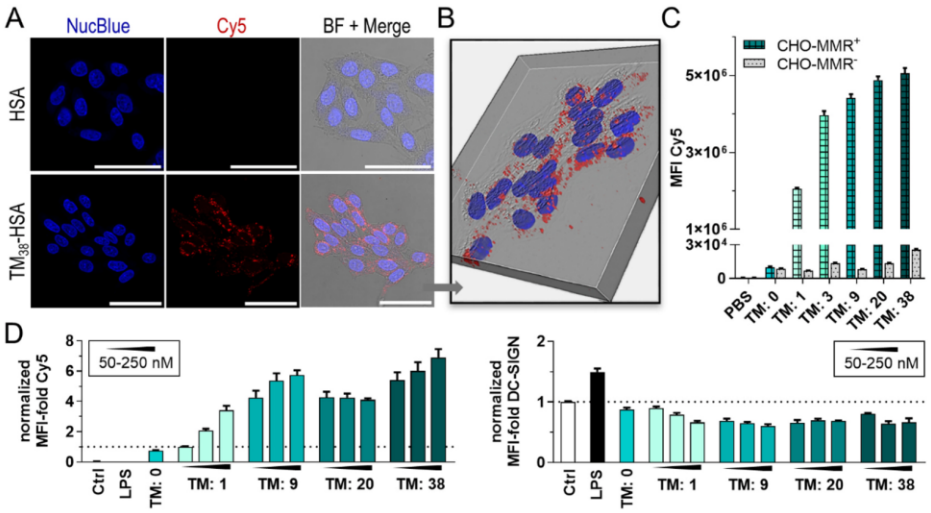

Fig. 3. A) Confocal microscopy of MMR-positive CHO cells incubated with trimannosylated TM_{38}-HSA or HSA (1 μM, 20 h) (Scale bar: 50 μm, Channels: Nuc Blue (Nuclei), Cy5 (HSA conjugates)) and B) corresponding z-stack of internalized TM_{38}-HSA conjugate. C) FACS analysis of Cy5-labeled HSA conjugates (HSA or TM_n-HSA, 100 nM) with varying numbers of TM groups into MMR-positive and MMR-negative CHO cells after 24 h incubation. D) FACS analysis of concentration-dependent cellular uptake (left) of Cy5-labeled TM_n-HSA conjugates (50, 100, 250 nM) with varying numbers of TM into GM-CSF differentiated BMDC after overnight incubation normalized to 50 nM TM_1-HSA and the corresponding DC-SIGN expression (right) upon treatment normalized to the untreated control. LPS = Lipopolysaccharides (100 ng/mL). Data are presented as mean ± SEM, $n = 9$ (C), $n = 5$ (D). All HSA and HSA conjugates are Cy5-labeled. (For interpretation of the references to colour in this figure legend, the reader is referred to the web version of this article.)

to minimize the influence of smaller variations on our experiments, *e.g.* changes in receptor densities of the different cells used in this study.

2.2. Synthesis and characterization of TM-HSA drug conjugates

Having determined the optimum range of TM groups for the HSA carrier, we proceeded to prepare various TM_{38-41}-HSA conjugates (with average n(TM) = 38–41 ± 12, henceforth referred always as TM-HSA) consisting of different cargoes for further studies. All HSA and HSA conjugates are fluorescently labeled with Cy5 or Cy7.5 unless otherwise stated. For cargo loading, we adopted and modified a HSA denaturation and refolding method previously reported by our group [46]. Specifically, TM-HSA was first denatured and reduced to allow the conjugation of multiple cargoes to the 34 cysteine groups originating from the 17 disulfide groups of HSA (Fig. 4A). **1-(4-(Aminomethyl)benzyl)-2-butyl-1*H*-imidazo[4,5-*c*]quinolin-4-amine,** an imiquimod derivative as representative TLR 7/8 agonist was selected as a weakly basic cargo after functionalization, while benzylamine was chosen as a neutral, non-active model cargo that has no immunostimulatory effects. At the same time, it serves as a negative control for subsequent investigations, to consider effects of loaded cargoes on the cellular uptake properties of the nanocarrier. Both cargoes were modified with a pyridinyldisulfanyl-ethyl-carbonate linker to form a carbamate bond, which can undergo thiol exchange and thereby attach to the thiol groups of the reduced cysteines of the denatured TM-HSA backbone [47–51]. In addition, *N*-ethylmaleimide was added to cap unreacted thiols to enhance the stability of the bioconjugate as reported previously [52,53]. Afterwards, excess reactants were removed *via* spin filtration ((molecular weight cutoff = 10 kDa) with the denaturing buffer. By rapid dilution with MilliQ water (MQ), the conjugates were backfolded based on hydrophobic and hydrophilic interactions as reported before [46,54]. After purification *via* spin filtration with MQ and lyophilization, the TM-HSA drug conjugates, TM-HSA-TLR7/8a and TM-HSA-Benzyl, were isolated with a 34 % and 46 % recovery rate, respectively.

SDS-PAGE analysis showed differences between the migration behavior of the final protein-drug conjugates (TM-HSA-Benzyl and TM-HSA-TLR7/8a) under reducing and non-reducing conditions in comparison to the precursor conjugates, TM-HSA (Figure S6), suggesting successful loading of the cargoes. For further confirmation, the cargo-to-carrier loading was determined, using MALDI-ToF-MS, to consist of an average number of 25 (benzylamine) or 20 (TLR 7/8 agonist). Agarose gel electrophoresis of the final TM-HSA-cargo conjugates indicates absence of large aggregates and no major charge differences to the precursor TM-HSA (Figure S5), which is corroborated by Zeta Potential (ZP) measurements (Fig. 4B). Circular dichroism (CD) measurements were performed for TM-HSA-Benzyl, TM-HSA-TLR7/8a, and native HSA, showing slight changes in intensity in HSA's signature peaks at 208 and 222 nm but an overall retained curve indicating that the α-helix-rich secondary structures are preserved even after denaturation and modifications (Figure S7) [55].

Sizes and size distribution profiles of TM-HSA-cargo conjugates were determined using FCS (Fig. 4C and Figure S9) and DLS (Fig. 4D and Figure S8), respectively. From FCS, the hydrodynamic radii in *Dulbecco's Phosphate-Buffered Saline* (dPBS) were determined as follows: HSA (4.1 ± 0.4 nm), TM-HSA (7.1 ± 0.7 nm), TM-HSA-Benzyl (11.0 ± 2.8 nm) and TM-HSA-TLR7/8a (12.0 ± 1.2 nm). The determined hydrodynamic radius of HSA is consistent with previously reported literature [37] and the increase in size after denaturing and cargo loading is consistent with previous reports [56]. DLS shows similarly an increase in size in the TM-HSA drug conjugates compared to TM-HSA after cargo loading. Furthermore, the conjugate sizes were determined after long-term storage (after 1 year) in solution (Figure S9–11), showing that they are stable and no uncontrolled aggregation of the TM-HSA conjugates was observed. As many nanocarriers are known to degrade, aggregate or interact with components in biological media, *e.g.* to form a protein corona, the hydrodynamic radii of the TM-HSA conjugates in human plasma were also determined using FCS. Here, a higher value of the plasma viscosity (1.5 times higher than that of water) was used according to earlier studies [45,57]. There was no significant size increase observed for TM-HSA (8.3 ± 0.8 nm) and only a slight increase for both, TM-HSA-Benzyl (15.0 ± 1.5 nm) and TM-HSA-TLR7/8a (16.5 ± 1.7 nm) suggesting no protein corona formation. Additionally, preincubation of

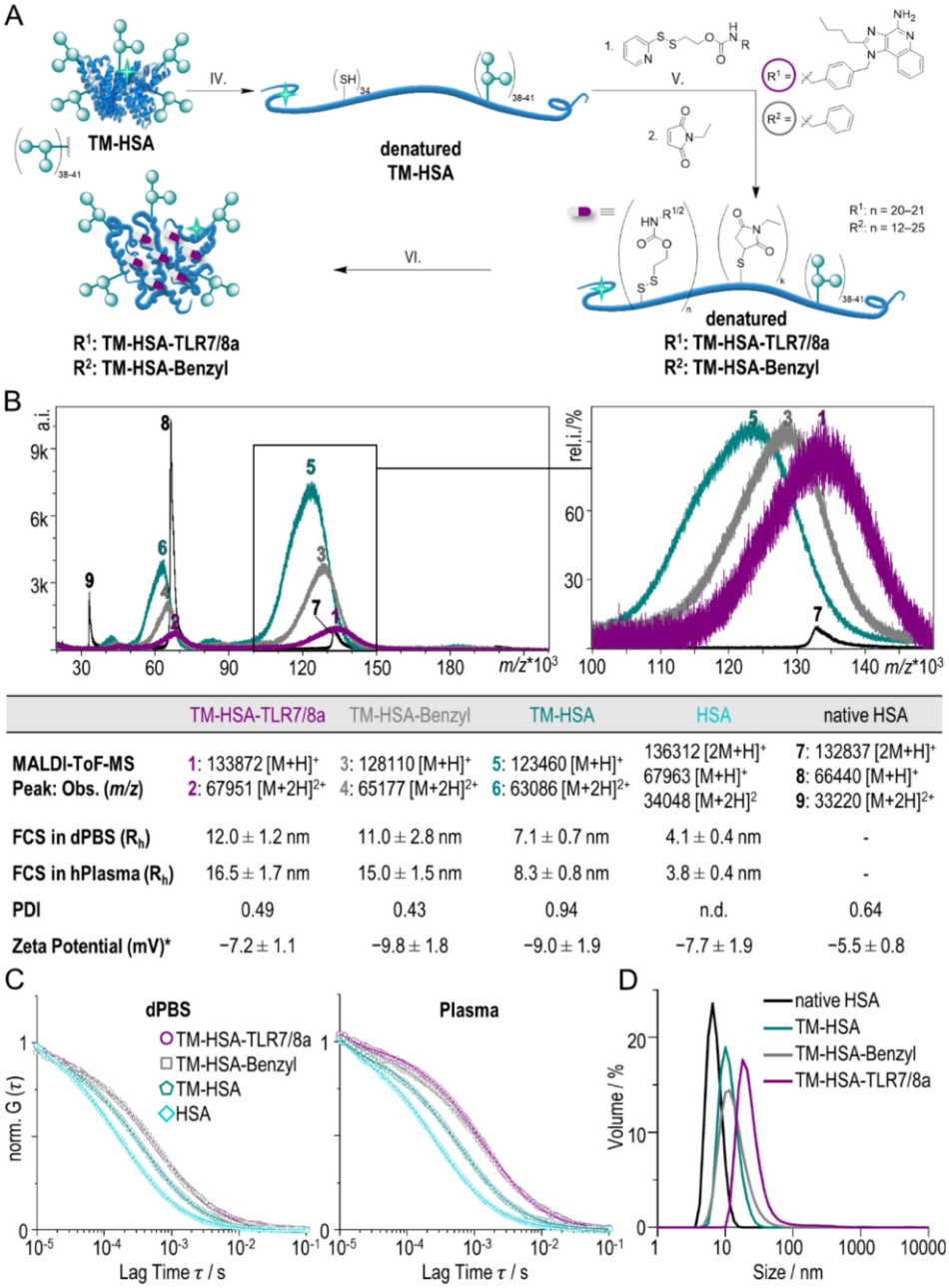

	TM-HSA-TLR7/8a	TM-HSA-Benzyl	TM-HSA	HSA	native HSA
MALDI-ToF-MS Peak: Obs. (*m/z*)	**1**: 133872 $[M+H]^+$ **2**: 67951 $[M+2H]^{2+}$	**3**: 128110 $[M+H]^+$ **4**: 65177 $[M+2H]^{2+}$	**5**: 123460 $[M+H]^+$ **6**: 63086 $[M+2H]^{2+}$	136312 $[2M+H]^+$ 67963 $[M+H]^+$ 34048 $[M+2H]^2$	**7**: 132837 $[2M+H]^+$ **8**: 66440 $[M+H]^+$ **9**: 33220 $[M+2H]^{2+}$
FCS in dPBS (R_h)	12.0 ± 1.2 nm	11.0 ± 2.8 nm	7.1 ± 0.7 nm	4.1 ± 0.4 nm	-
FCS in hPlasma (R_h)	16.5 ± 1.7 nm	15.0 ± 1.5 nm	8.3 ± 0.8 nm	3.8 ± 0.4 nm	-
PDI	0.49	0.43	0.94	n.d.	0.64
Zeta Potential (mV)*	−7.2 ± 1.1	−9.8 ± 1.8	−9.0 ± 1.9	−7.7 ± 1.9	−5.5 ± 0.8

Fig. 4. A) Synthesis scheme of drug loading procedure onto trimannosylated HSA to obtain final nanocarrier conjugates; IV.) TCEP, 50 mM PB (8 M Urea, 2 mM EDTA) pH 8 V.) 1. Pyr-S-S-R, 2. N-ethylmaleimide, 50 mM PB (8 M Urea, 2 mM EDTA) pH 8 (if R = TLR7/8 agonist, readjust buffer to pH 6.3 for washing steps) VI.) rapid dilution 1:10, MQ, recovery rate 34–46 % B) MALDI-ToF-spectra of TLR7/8a- / benzyl-loaded nanocarriers as well as precursors, FWHM values are given in the SI (top) and summary of nanocarrier characterization (below). C) Normalized FCS autocorrelation curves measured for TLR7/8a- / benzyl-loaded nanocarriers as well as precursors in dPBS and human plasma. The solid lines correspond to fits with eq. S1. D) Size distribution of final, loaded nanocarriers compared to native HSA and trimannosylated precursor conjugate (1 mg/mL in dPBS) showing sizes of d.nm. = 7.02 ± 1.77 for native HSA, d.nm = 11.81 ± 0.67 for TM-HSA, d.nm = 14.28 ± 1.34 for TM-HSA-Benzyl and d.nm = 25.89 ± 0.84 for TM-HSA-TLR7/8a determined by DLS. Measurements were performed in quadruplicates, errors are given as standard deviation. *ZP measurements were performed with Cy7.5-labeled conjugates (see SI, section 6.4). (For interpretation of the references to colour in this figure legend, the reader is referred to the web version of this article.)

TM-HSA-Benzyl and TM-HSA-TLR7/8a with native or heat-inactivated mouse plasma did not reduce or prevent cellular uptake into BMDC (Figure S15). Next, we tested the release profile of the TLR7/8a cargo with the disulfide linker. As the endolysosomal compartments in immune cells are reductive and denaturing [58], we have performed the investigation under (1) reductive (+ glutathione, GSH) and (2) denaturing + reductive (8 M urea + GSH) conditions (Figure S12–14). These show that under reductive and denaturing conditions we have fast drug release from the carrier. In comparison, under reductive and non-denaturing conditions, the nanocarrier shows a slower drug release, indicating that the drug is folded into the inner parts of the HSA conjugate.

2.3. Ex vivo evaluation

Next, we studied the uptake and activation of immune cells of the TM-HSA drug conjugates *ex vivo* (Fig. 5 and S17). As APCs are key targets for cancer immunotherapy due to their role in boosting pathogen-specific adaptive immune responses [59,60] and the liver is an immunological organ, we first investigated the uptake of TM-HSA-Benzyl and TM-HSA-TLR7/8a into BMDC, splenic and liver cells (Fig. 5A). Cells that were not treated with HSA derivatives or only treated with HSA were used as controls for comparison. While HSA showed no significant uptake in all cells tested, we observed an exceptional uptake for TM-HSA drug conjugates in differentiated BMDC, in splenic macrophages and DC, and in LSEC, Kupffer cells, and liver DC both after 3 h incubation and overnight incubation time and at low dosage (50 nM Figure S17). This further corroborates the *in vitro* results of TM-mediated and enhanced uptake in cell lines expressing MMR/DC-SIGN. We also observed that TM-HSA-Benzyl has a higher uptake than TM-HSA-TLR7/8a in some of the tested cell types, which could be due to the influence of hydrophobicity of the cargoes [61,62]. To confirm that the uptake is enhanced by the fast association of the TM to the cell surface, we incubated BMDC with TM-HSA-Benzyl and HSA at 0 °C to slow down energy-dependent endocytosis and analyzed the percentage of Cy5-positive cells after 30, 60 and 180 min (Figure S18). TM-HSA-Benzyl reaches a plateau of Cy5 positive cells already after 30 min, which further supports the high avidity and fast association of the protein conjugate [63]. TLR7/8 agonists are applied in cancer immunotherapy for activation of DC and induce a change in receptor expression levels and cytokine production such as TNFα and interleukins (ILs) [64]. Additionally, TLR7 activation has been proposed for the treatment of alcoholic hepatitis, which is a form of alcohol-associated liver disease [65], and autoimmune diseases such as systemic lupus erythematodes [66]. Analysis of the cytokine levels in BMDC, spleen, and liver NPC cultures show that the TM-HSA-TLR7/8a conjugate offers superior performance in cytokine production, in comparison to the untreated or decoy-loaded carrier TM-HSA-Benzyl controls, even at low concentration of 50 nM (Fig. 5E and S20). The TM-HSA-TLR7/8a conjugate even outperforms small molecule TLR7/8 agonist at the same applied concentration in inducing interleukin production, *e.g.* in GM-CSF differentiated BMDC IL-10, 12 and -1β concentrations were found 3–4-times and IL-6 concentrations 34-times higher. These results are in accordance with previous findings demonstrating a higher immunostimulatory activity of adjuvants when applied at equimolar amounts in a particulate *versus* soluble form, which may be due to higher cellular uptake [67]. FACS analysis shows that CD86 and MHC II expression levels in GM-CSF- and FLT3L-differentiated BMDC after overnight incubation with TM-HSA-TLR7/8a (50 nM) were comparable to incubation with small molecule TLR7/8 agonist at the corresponding equimolar drug concentration (1.025 μM, 0.371 μg/mL) (Fig. 5B and C), whereas TM-HSA-Benzyl induced no upregulation of these activation markers, nor did unloaded TM-HSA (Figure S16). In addition, we tested the ability of TM-HSA-TLR7/8a to induce T-cell responses by preincubating GM-CSF BMDC with Ovalbumin (OVA) and subsequently with the different HSA conjugates before co-culturing with $CD8^+$ (OT-I) or $CD4^+$ (OT-II) T cells. Out of all the TM-HSA-TLR7/8a concentrations (1–50 nM) tested (Figure S19), 10 nM was optimal in inducing OVA peptide-specific OT-I and OT-II T cell proliferation and exhibited similar effects as five-times higher concentrations of the free drug (Fig. 5D). This observation corresponds to the stronger state of activation evoked by the delivery of particulate adjuvant. It is noteworthy that HSA or TM-HSA-Benzyl did not lead to an increase in the activation markers (CD86, MHC II, OT-I/-II proliferation) compared to untreated controls, which could support that the nanocarrier is immunocompatible. Our results suggest that TM-HSA serves as an efficient and receptor-selective macromolecular nanocarrier for the delivery of TLR 7/8 agonist *ex vivo*.

2.4. Rapid liver selective uptake of TM-HSA conjugates in vivo

To evaluate the uptake and targeting specificity of TM-HSA derivatives *in vivo*, we performed a biodistribution experiment in B6 albino mice. These experiments aimed to identify potential organ-specific accumulation and immunogenic effects of the TM-HSA bioconjugates compared to no TM (HSA) as well as the influence of the drug cargo on carrier biodistribution. For *in vivo* imaging, all HSA and modified HSA used are labeled with Cy7.5 dye (see SI, section 6.4), which is compatible with the instrument settings. We used HSA as control, as well as different TM-HSA conjugates, either with TLR7/8a (TM-HSA-TLR7/8a), benzylamine (TM-HSA-Benzyl), or without cargo (TM-HSA). Next, 100 μL of a 2.94 μM solution of these conjugates were injected intravenously (i.v.) into healthy mice (mouse body weight dosage in case of TM-HSA-TLR7/8a: 2 mg/kg mouse corresponding to 0.14 mg/kg TLR7/8 cargo). Biodistribution was assessed through surface fluorescence imaging *via* an *in vivo* imaging system (IVIS), blood sampling followed by plasma analysis, and *ex vivo* analysis of harvested organs. Mice that received complete intravenous tail vein injection were used for quantification and statistical analysis, mice that did not receive the full dose *via* tail vein injection intravenously (Figure S22) were excluded.

In order to monitor the TM-HSA conjugates in the bloodstream, small blood samples (50 μL) were obtained from the studied mice shortly after injection (0.1 h) and 24 h later, and the generated plasma was analyzed. As a control, plasma samples of mouse blood incubated with TM-HSA-TLR7/8a at a concentration (140 nM) similar to the injected ones (estimated initial blood concentration = 230 nM) [68] were also studied. The size and the concentration of the TM-HSA conjugates in plasma obtained from all blood samples were measured by FCS. Slight size increases in hydrodynamic radii of 9.1 ± 1.7 nm, 6.2 ± 1.8 nm and 4.9 ± 3.8 nm were observed for trimannosylated conjugates TM-HSA, TM-HSA-Benzyl and TM-HSA-TLR7/8a, respectively, as compared to the measurements in PBS (Figure S9B). Furthermore, the results showed that immediately after injection, HSA exhibited high concentrations of 238 ± 8 nM in the bloodstream, with detectable levels (40 ± 6 nM) persisting up to 24 h post injection (Fig. 6B, all correlation curves: Figure S26). In contrast, TM-HSA conjugates showed rapid clearance from the bloodstream, independent of any cargo. For TM-HSA, TM-HSA-Benzyl and TM-HSA-TLR7/8a, we observed concentrations ranging from 1 ± 1 nM to 4 ± 2 nM shortly after injection to non-detectable levels at 24 h post injection of these conjugates. The plasma control sample, TM-HSA-TLR7/8a incubated *ex vivo* in whole blood, showed no such decrease in concentration, ruling out a reduction in sample concentration due to adsorptive interaction with whole blood components during plasma generation. This was verified by IVIS imaging, showing that HSA distributed throughout the body, with a trend for higher accumulation in the liver, which is a known phenomenon for i.v. administered fluorescently labeled albumin (Fig. 6A) [69,70]. Trimannosylation, however, leads to direct accumulation mainly in the liver post injection, which has been shown for some glycosylated systems [71,72]. *Ex vivo* fluorescence analysis of organs highlighted significant differences in organ enrichment of HSA and the TM-HSA conjugates (Fig. 6D and E). Notably, HSA showed enrichment in the heart 24 h post injection, confirming its prolonged presence in the bloodstream. It also

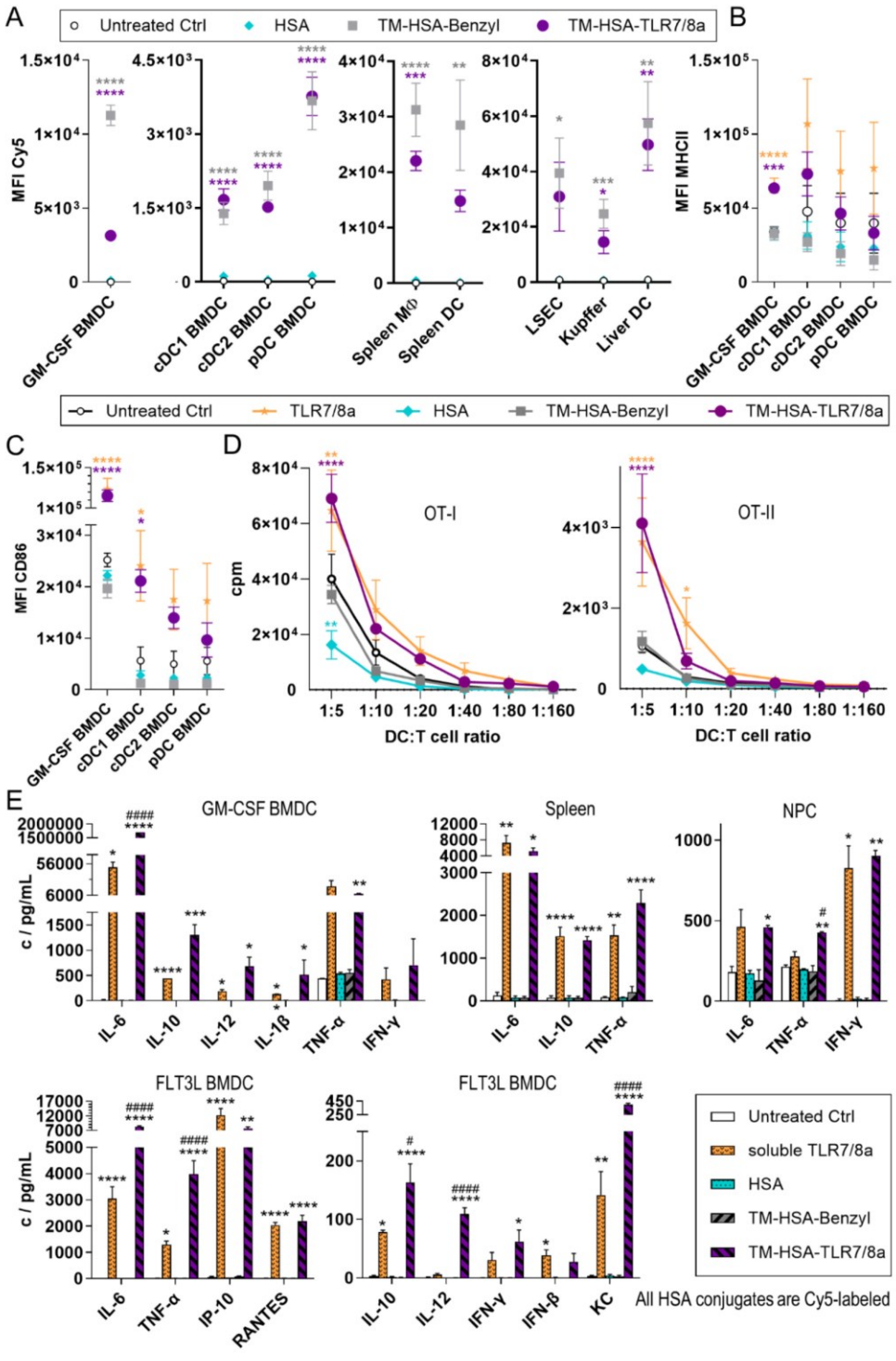

(caption on next page)

Fig. 5. A) FACS analysis of uptake in GM-CSF differentiated BMDC, in FLT3L differentiated BMDC, in splenic macrophages and DC, and in LSEC, Kupffer cells, and liver DC after 3 h incubation with different HSA conjugates (50 nM). FACS analysis of B) MHC II expression levels and C) CD86 expression levels in GM-CSF- and FLT3L-differentiated BMDC after overnight incubation with different HSA conjugates (50 nM) or small molecule TLR7/8 agonist at the corresponding concentration (1.025 μM, 0.371 μg/mL). D) T-cell proliferation (cpm) of OVA peptide-specific $CD8^+$ (OT-I) or $CD4^+$ (OT-II) after co-culture with GM-CSF-differentiated BMDC which were preincubated with OVA (5 μg/mL) and subsequently with different HSA conjugates (10 nM, corresponds to 205 nM TLR7/8-cargo) or small molecule TLR7/8 agonist (1.025 μM, 0.371 μg/mL). E) Production of cytokines in response to overnight incubation with different HSA conjugates (50 nM) or small molecule TLR7/8 agonist (1.025 μM, 0.371 μg/mL) of GM-CSF differentiated BMDC, in FLT3L differentiated BMDC, in splenic macrophages and DC, and in LSEC, Kupffer cells and liver DC. Data are presented as mean ± SEM, $n = 4$–6 (A–D), $n = 2$–3 (E); Statistical differences are indicated: *vs.* # soluble TLR7/8 agonist and * Untreated Ctrl (one-way ANOVA, Tukey test or *t*-test for samples where n = 2). *,# $p < 0.05$, **,## $p < 0.01$, ***,### $p < 0.001$, ****,#### $p < 0.0001$. All HSA and HSA conjugates are Cy5-labeled.

demonstrated higher accumulation in the lungs compared to TM-HSA conjugates as well as in the kidneys, indicating renal clearance of the HSA [73]. Conversely, TM-HSA conjugates did not or only to a much lower extent accumulate in these organs, again verifying enhanced selective liver targeting *in vivo*. TM-HSA conjugates were also observed in the spleen, however, the difference to HSA uptake in the spleen was not statistically significant. The ratio of liver fluorescence intensity to total body intensity revealed that liver-specific targeting was significantly enhanced for TM-HSA bioconjugates, also indicating enhanced organ specificity when using TM as targeting units (Fig. 6C and S24). Taken together, the results show that the TM moieties enabled fast organ-specific uptake and the type of cargo did not affect the biodistribution profiles. *Ex vivo* FACS analysis of isolated liver NPC and spleen cells revealed that the TM-HSA conjugates were uptaken by target cells (LSEC, Kupffer cells and liver DC) but there is no statistical significance due to variability (Figure S25). Low uptake observed in spleen immune cells is in agreement with the *ex vivo* organ analysis (Fig. 6E).

In addition to imaging analysis, we evaluated the potential immunogenic responses towards our protein nanocarriers by measuring plasma cytokine levels 24 h post injection. A significant increase in IP-10 (CXCL10) and RANTES (CCL5) was observed in the plasma when TLR7/8 ligands were coupled to TM-HSA (TM-HSA-TLR7/8a) indicating immune cell activation possibly mediated by T-cellular or T cell-induced immune activation (Figure S27). No statistically significant increase in plasma MCP-1 and IFN-α levels was observed, which is not unexpected due to the low dosage of TLR 7/8 used for the *in vivo* biodistribution study. Furthermore, no other cytokines were detectable in the sera, in particular IL1β, TNFα, IFNα and IFNγ (Figure S27). In conjunction with the fact that the rate of apoptotic leukocytes was not increased in *ex vivo* samples from treated animals (data not shown), these observations suggest that the TM-HSA-TLR7/8a did not induce systemic inflammation.

In summary, we could demonstrate that trimannosylation of HSA significantly enhanced liver-specific targeting *in vivo* as well as activation, which was shown for the TLR7/8a loaded bioconjugate TM-HSA-TLR7/8a. The TM moieties enabled fast organ-specific uptake and cargo loading and the type of cargo did not affect the biodistribution profiles.

3. Conclusion

Inspired by the polysaccharide-core-shell protein glycogen, we have reported TM-HSA bioconjugates consisting of an HSA core with a dense trimannose shell. The small-sized (< 40 nm) protein nanocarriers were rapidly and highly selectively uptaken into immune cells as well as the liver. The number of TM groups present on the surface of HSA was varied to tune the uptake efficiency of the nanocarriers. Furthermore, TM-HSA was denatured to incorporate multiple copies of a TLR 7/8 agonist with a redox-sensitive linker for the first time, which allows controlled drug delivery and traceless release under denaturing and reducing conditions, often found in immune cells.

In comparison to HSA, TM-HSA serves as an efficient transporter of cargo molecules as exemplified by the delivery of TLR 7/8 agonist *ex vivo*. Moreover, specific and selective uptake into cell lines expressing MMR/DC-SIGN, such as MMR transductants, BMDC, splenic and liver cells was demonstrated and the resulting TM-HSA-TLR7/8a conjugate even outperformed TLR7/8 in stimulating interleukin production at similar concentrations. The resultant TM-HSA conjugates, through tailored surface modifications, not only revealed enhanced specificity for and binding affinity to immune cells *ex vivo* but also selective uptake into the liver over other organs, *in vivo* in healthy mice. Furthermore, TM-HSA nanocarriers were rapidly cleared from the bloodstream, independent of the cargo attached (none, Benzyl and TLR7/8a tested), which could serve as a first indication of the potential of TM-HSA conjugates as versatile nanocarriers for targeting liver diseases.

The application of TM-HSA nanocarriers providing rapid clearance *via* uptake by the target organ offers the potential to reach immune cells in diseased liver tissue, to minimize off-target as well as on-target/off-site effects, to avoid prolonged organ deposition, and could in the future be employed as a carrier to maximize therapeutic efficacy in immunotherapy of liver cancer or liver diseases. Therefore, the TM-HSA nanocarriers reported herein could offer new possibilities for the treatment of liver fibrosis or cancer. Potentially, this could be further extended in the future to look into diseases that are related to the immune system such as infections, immunodeficiencies or autoimmune disorders.

4. Methods

Nuclear magnetic resonance spectroscopy (NMR): NMR spectra were measured on Avance-III 700 or 400 Neo (*Bruker Corporation*, Ettlingen, BW, Germany) NMR spectrometers. For carbohydrate structures NMR-spectra were recorded utilizing an AC300 (*Bruker Corporation*, Ettlingen, BW, Germany) with 5 mm Dual-^{13}C-head and B-ACS 60 sample changer for 300 MHz ^{1}H NMR-, 75.5 MHz ^{13}C NMR- as well as 2D-NMR-experiments, an Avance-II 400 (*Bruker Corporation*, Ettlingen, BW, Germany) with 5 mm BBFO-head with z-gradient and ATM as well as SampleXPress 60 sample changer for 400 MHz ^{1}H NMR-, 100.6 MHz ^{13}C NMR- and 2D-NMR experiments and an Avance-III 600 (*Bruker Corporation*, Ettlingen, BW, Germany) with 5 mm TCI-Cryoprobe with z-Gradient and ATM as well as SampleXPress Lite 16 sample changer for 600 MHz ^{1}H NMR-, 151.0 MHz ^{13}C NMR- and 2D-NMR experiments. Samples were dissolved in an appropriate deuterated solvent ($CDCl_3$, CD_3OD, D_2O). Spectra were processed using the MestReNova software (*Mestrelab Research*, Santiago de Compostela, Spain) for baseline correction (Whittaker smoother) and automated phase correction. Spectra were referenced to the signal of the respective deuterated solvent ($CDCl_3$: ^{1}H: $\delta = 7.26$ ppm, CD_3OD: ^{1}H: $\delta = 3.31$ ppm, D_2O: ^{1}H: $\delta = 4.79$ ppm) and using the absolute reference function of the analysis software. Observed signals are described using their chemical shifts (δ) in ppm, multiplicity (s-singlet, d-doublet, t-triplet, dd-double of doublet, *etc.* and m-multiplet; app-apparent and br-broad), integral and locator of ^{1}H- and ^{13}C-position in the molecule. Signal assignment was supported utilizing 2D-NMR spectra: COSY, HSQC, HSQC-NoDec, HMBC, TOCSY, NOESY (data not shown).

Matrix assisted laser desorption ionization-time of flight mass spectrometry (MALDI-ToF-MS): Mass spectra for nanocarrier structures were acquired using sinapinic acid matrix on a ToF MS rapifleX (*Bruker Corporation*, Ettlingen, BW, Germany).

Dynamic light scattering (DLS): DLS measurements of the HSA based

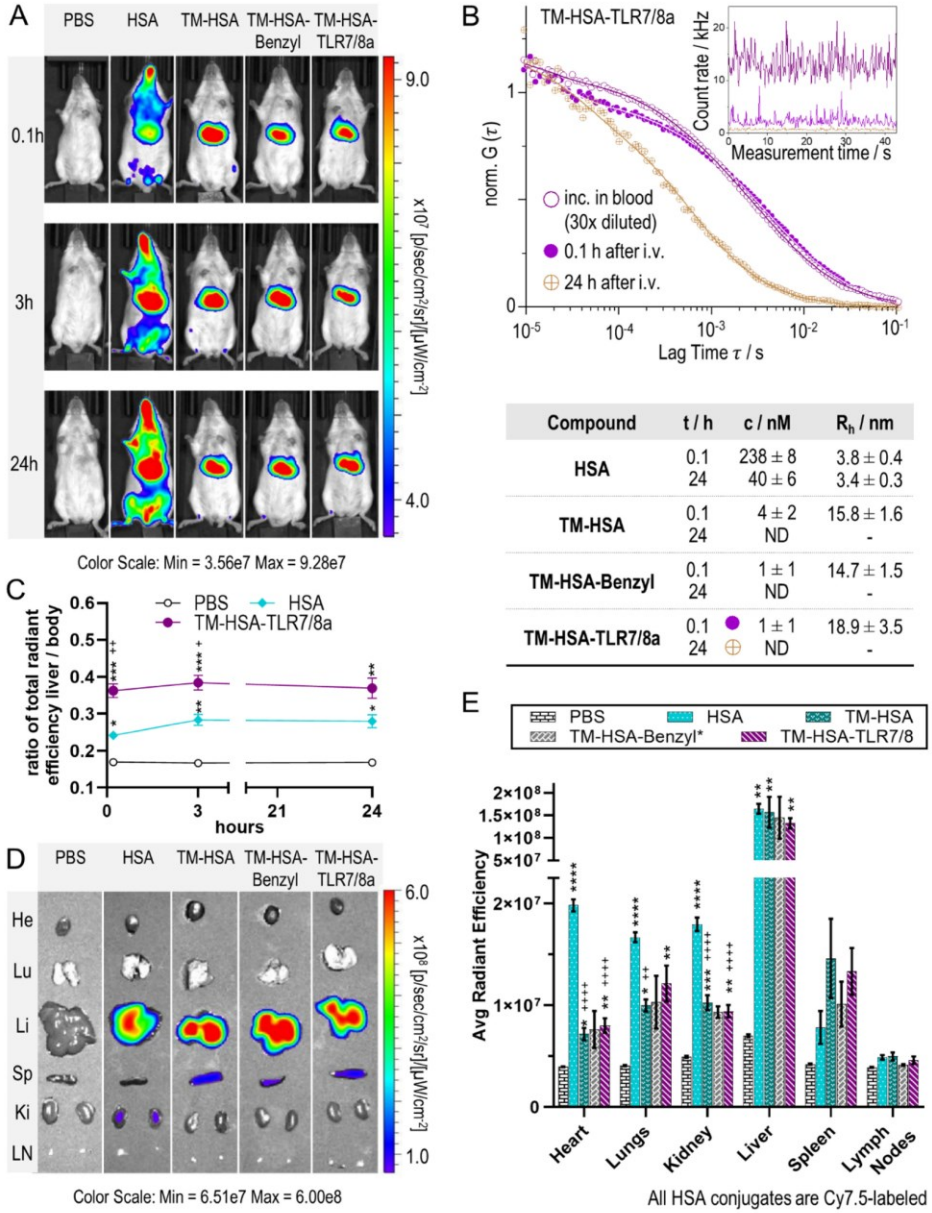

Compound	t / h	c / nM	R_h / nm
HSA	0.1	238 ± 8	3.8 ± 0.4
	24	40 ± 6	3.4 ± 0.3
TM-HSA	0.1	4 ± 2	15.8 ± 1.6
	24	ND	-
TM-HSA-Benzyl	0.1	1 ± 1	14.7 ± 1.5
	24	ND	-
TM-HSA-TLR7/8a	0.1	1 ± 1	18.9 ± 3.5
	24	ND	-

Fig. 6. Evaluation of *in vivo* biodistribution experiment. A) *In vivo* imaging of Cy7.5 dye-labeled HSA and TM-HSA conjugates using IVIS after 0.1, 3, and 24 h post intravenous injection. B) (top) Exemplary normalized FCS correlation curves of TM-HSA-TLR7/8a during biodistribution and incubated in whole blood *ex vivo*. The inset shows the corresponding intensity time traces (note that the curves for the sample taken 24 h after i.v. injection originated from a very small amount of initially non-covalently bound Cy7.5 attaching to endogenous mouse blood proteins); (bottom) FCS results for the concentrations (c) and the hydrodynamic radii (R_h) of HSA conjugates in mouse plasma 0.1 h and 24 h after injection. Data are presented as mean ± SD, $n = 3$ (PBS), $n = 2$ (TM-HSA-Benzyl), $n = 4$ (HSA, TM-HSA) and $n = 5$ (TM-HSA-TLR7/8a). C) Ratio of total radiant efficiency of liver to whole body 0.1, 3, 24 h post injection based on IVIS images. D) IVIS images of Cy7.5 dye on organ level 24 h post injection. E) Quantification of organ-specific fluorescence 24 h post injection. Data denote average radiant efficiency ± SEM, n = 3 (PBS), n = 2 (TM-HSA-Benzyl), n = 4 (HSA, TM-HSA) and n = 5 (TM-HSA-TLR7/8a) B6 albino mice. C) + E) Statistical differences are indicated: *vs.* + HSA and * PBS Ctrl ((C) two-way, (E) one-way ANOVA, Tukey test). *,+ $p < 0.05$, **,++ $p < 0.01$, ***,+++ $p < 0.001$, ****,++++ $p < 0.0001$; *TM-HSA-Benzyl group was excluded from statistical analysis (n = 2).

compounds (1 mg/mL in dPBS or MQ unless otherwise noted) were performed at 25 °C using a Zetasizer Nano S (*Malvern Instruments*, Malvern, England) equipped with a He/Ne Laser (λ = 633 nm) and a narrow band filter at a fixed scattering angle of 173°. Volume distribution of DLS measurements of nanocarriers in dPBS was used to determine their size range.

Fluorescence correlation spectroscopy (FCS): FCS experiments were performed using a commercial confocal LSM 880 microscope (*Carl Zeiss*,

Jena, TH, Germany) equipped with a C-Apochromat 40×/1.2 W (*Carl, Zeiss*, Jena, TH, Germany) water immersion objective. A HeNe laser (λ = 633 nm) fiber coupled to the LSM 880 was used for the excitation of the Sulfo-Cyanine5 dye. The emission light in the spectral range 655–699 nm (Cy5) was detected using a Quasar spectral detection unit (*Carl Zeiss*, Jena, TH, Germany) that comprises a diffraction grating and a 32 channel GaAsP photomultiplier array operating in the photon counting mode. Sulfo-Cyanine7.5 dye was excited at 780 nm by a strongly attenuated Mai Tai Ti:Sa laser (*Newport Spectra Physics*, Milpitas, CA, USA) coupled to the LSM 880. The emission light passed through a band-pass filter EM835/70 (*Chroma Technology*, Bellows Falls, Vermont, USA) and was directed to a PDM SPAD detector (*Micro Photon Devices*, Bolzano, Italy) connected to a TimeHarp 260 TCSPC board (*PicoQuant*, Berlin, B, Germany). For each sample, 30 μL of solution (PBS, human palsma or mouse blood serum) was added to a 15 wells chamber (*ibidi*, Munich, BY, Germany). The confocal detection volume was placed ~ 30 μm above the glass coverslip and series of 20 measurements, 10 s each, were performed at room temperature (23 °C). For experiments with human plasma, the nanocarriers were incubated with plasma for 1 h at 23 °C before the measurement. The obtained experimental autocorrelation curves were fitted with the following analytical model function:

$$G(\tau) = 1 + \left[1 + \frac{f_T}{1-f_T} e^{-\tau/\tau_T}\right] \frac{1}{N} \sum_{i=1}^{m} \frac{f_i}{\left(1+\frac{\tau}{\tau_{Di}}\right) \bullet \sqrt{1+\frac{\tau}{S^2 \bullet \tau_{Di}}}} \quad \text{(S1)}$$

whereby N is the average number of diffusing fluorescence species in the observation volume, f_T and τ_T are the fraction and the decay time of the triplet state, τ_{Di} is the diffusion time of the i-th type of species, f_i is the fraction of the component i ($1 \le i \le m$), and S is the structure parameter, $S = z_0/r_0$, where z_0 and r_0 represent the axial and radial dimensions of the observation volume. The fit yielded the values of τ_{Di} and N. The diffusion coefficients of the species D_i are related to the respective diffusion times τ_{Di} and the radial dimension r_0 of V_{obs} by $D_i = r_0^2/(4\tau_{Di})$. By inserting D_i into the Stokes-Einstein equation, the hydrodynamic radius can be calculated as $R_h = \frac{k_B \bullet T}{6 \bullet \pi \bullet \eta \bullet D}$, here, k_B is the Boltzmann constant, T is the temperature, and η is the viscosity of the solvent. For the viscosity of water and plasma at 23 °C values of 0.93 mPas and 1.4 mPas, respectively were used. Errors are given as standard deviation but rounded up to 10 % of absolute values of hydrodynamic radii (R_h) if SD < 10 % of R_h to account for systematic errors based on temperature, viscosity, diffusion coefficient value of reference sample and later individual variations in plasma samples. Furthermore, the concentration of the fluorescent species was calculated as $c = N/V_{obs}$. For calibration of the confocal volume V_{obs}, dyes with known diffusion coefficients in water, *i.e.* Alexa 647 and IRDye®800CW were used.

Fluorescence activated cell sorting (FACS): For FACS analysis the $CHO^{MMR+/-}$ cells (200,000 cells/well, 24-well plates, 24 h seeding, 24 h treatment, 0.1 μM of TM_n-HSA, HSA, or PBS) were washed with dPBS and harvested using cell dissociation buffer for 15 min at 37 °C. After centrifugation for 10 min at 350 xg and 5 °C cell pellets were resuspended in dPBS. All samples were kept on ice prior to flow cytometric analysis by a BD Accuri C6 (*BD Biosciences*, Franklin Lakes, NJ, USA). Data were processed with FlowJo software. For *ex vivo* uptake experiments, cells were harvested, washed with staining buffer (PBS, 1 % FBS, 0.5 mM EDTA) and incubated with rat anti-mouse CD16/CD32 antibody (clone 2.4G2; 15 min, 4 °C) to prevent antibody binding to Fcγ receptors. Following this, samples were incubated with fluorescence-labeled antibodies (20 min, 4 °C). Then, samples were washed with PBS and incubated with FVD to identify live/dead cells. Measurements were carried out using an Attune NxT flow cytometer and data were analyzed using Attune NxT software (both *Thermo Fisher*, Waltham, MA, USA).

Cytokine detection: Cytokines were detected using the BD™ Cytometric Bead Array (CBA) Mouse Flex Set (*BD Biosciences*, Franklin Lakes, NJ, USA), which was performed according to the manufacturer's specifications.

Animals: *In vivo* experiments followed an approval by the local ethics committee on animal care (number 23177–07/G 20–1-123, Government of Rhineland Palatinate, Germany). B6N-*Tyr*$^{c\text{-}Brd}$/BrdCrCrl were purchased from Charles River. Female mice were 8 weeks old (body weight ~ 20 g) and kept according to the guidelines of the institute and the local government. To explore the biodistribution of the nanoparticles 100 μL of a solution of the respective Cy7.5 labeled nanoparticles (2.94 μM in dPBS, corresponding to mouse body weight dosages of TM-HSA-TLR7/8a: 2.0 mg/kg, TM-HSA-Benzyl: 1.9 mg/kg, TM-HSA: 1.9 mg/kg, HSA: 1.0 mg/kg) were intravenously administered to B6 albino mice (n = 5, three mice receiving dPBS as controls). Directly after injection and 3 h, the mice were once again anesthetized with isoflurane gas and placed into an IVIS (*in vivo* imaging spectrum) system (*Caliper Life Sciences*, Hopkinton, MA, USA) for *in vivo* NIR fluorescence imaging. The picture integration time of the fluorescence source was set to 10 s. Recording parameters were adjusted for excitation at 745 nm and emission at 820 nm to visualize the Cy7.5 labeled nanoparticles. Additionally, after injection blood was retrieved from *vena facialis*. After 24 h, mice were imaged *in vivo* and afterwards anesthetized with Ketamine/Rompun. After heart puncture, the mice were euthanized, the organs harvested and returned to the imaging chamber for *ex vivo* signal quantification by Live Image software (*Perkin Elmer*, Waltham, MA, USA). Organs were analyzed by region-of-interests (ROIs), and the fluorescence was quantified as the average of area-normalized radiant efficiency. Mice that received complete intravenous tail vein injection were used for quantification and statistical analysis.

Trimannosylation and Nanocarrier Loading: Detailed experimental including all precursor molecule synthesis can be found in the supporting information. For the optimized procedure for the SPAAC reaction to attach TM to HSA, DBCO-HSA (15.0 mg, 166 nmol, 1.00 eq.) was dissolved in 50 mM phosphate buffer with 8 M urea and 2 mM EDTA (pH = 8) to a final protein concentration of 1 mg/mL. The azide functionalized TM (14.1 mg, 17.9 μmol, 115 eq. or 2.5 eq/DBCO) dissolved in MQ (10 mg/mL) was added and the reaction solution was shaken at room temperature overnight. Afterwards, the reaction solution was purified (5 x MQ) and concentrated *via* ultracentrifugation spin filter (Vivaspin, PES, 10 kDa). The product was lyophilized and obtained in form of a blue lyophilizate. For drug loading, *e.g.* TLR7/8a, TM-HSA (1.13 mg, 9.19 nmol, 1 eq.) was dissolved in denaturing buffer (50 mM phosphate buffer +8 M urea +2 mM EDTA, 1.00 mL) and inverted for 20 min before TCEP (263 μg, 919 nmol, 100 eq.) dissolved in MQ (23 μL) was added. The reaction solution was inverted for 1–2 h and the residual TCEP was removed *via* ultracentrifugation spin filter (2 x denaturing buffer, Vivaspin, PES, 10 kDa). To the protein solution (1 mg/mL) Pyr-S-S-TLR7/8a (1.11 mg, 1.38 μmol, 150 eq.) dissolved in DMF (105 μL) was added. The reaction solution was inverted for 1 h and the buffer exchanged *via* ultracentrifugation (denaturing buffer) before reaction control *via* MALDI-ToF-MS to determine drug modification rate. *N*-Ethylmaleimide (173 μg, 1.38 μmol, 150 eq) was added to cap residual free thiols on the HSA for 14 h. The product was washed (5 x denaturing buffer) and backfolded *via* rapid dilution in MQ (1:10). If aggregation during washing steps occurred, the washing solutions were adjusted to pH = 6.3. The product was washed again (5 x MQ) and concentrated *via* ultracentrifugation spin filter (Vivaspin, PES, 10 kDa). The product was lyophilized and obtained in form of a blue lyophilizate with a modification rate of 20.5 TLR7/8a units per HSA.

CRediT authorship contribution statement

Bellinda Lantzberg: Writing – review & editing, Writing – original draft, Visualization, Validation, Methodology, Investigation, Formal analysis, Data curation, Conceptualization. **Yanira Zeyn:** Writing – original draft, Visualization, Investigation, Formal analysis, Data curation. **Robert Forster:** Writing – original draft, Visualization, Methodology, Investigation, Formal analysis, Data curation. **Lin Jian:** Methodology, Investigation, Formal analysis. **Dominik Schauenburg:**

Visualization, Investigation. **Christoph Hieber:** Investigation. **Lutz Nuhn:** Supervision, Resources. **Tianjiao Zhou:** Writing – review & editing, Visualization, Formal analysis. **Maria J.S.A. Silva:** Visualization, Methodology, Investigation. **Kaloian Koynov:** Writing – review & editing, Supervision, Resources, Methodology. **Hu-Lin Jiang:** Writing – review & editing, Supervision, Resources. **Seah Ling Kuan:** Writing – review & editing, Writing – original draft, Supervision, Resources, Project administration. **Matthias Bros:** Supervision, Resources, Methodology, Funding acquisition. **Till Opatz:** Writing – review & editing, Supervision, Resources, Project administration, Funding acquisition, Conceptualization. **Tanja Weil:** Writing – review & editing, Supervision, Resources, Project administration, Funding acquisition, Conceptualization.

Declaration of competing interest

The authors declare the following financial interests/personal relationships which may be considered as potential competing interests: BL, YZ, RF, SLK, MB, TO and TW are coinventors of a pending patent that claims to use human serum albumin based nanocarriers for targeted immunotherapy.

Acknowledgements

The authors would like to thank the Max Planck Society and the Deutsche Forschungsgemeinschaft (DFG, German Research Foundation) project number 213555243 – SFB 1066 (Q05, B16, B05) for financial support, Prof. Jo A. Van Ginderachter for the MMR-positive CHO cells, Ingrid Tubbe and Nadine Röhrig for technical assistance in the biodistribution experiments and the MPIP mass spectrometry department for measurements.

Appendix A. Supplementary data

Supplementary data to this article can be found online at https://doi.org/10.1016/j.jconrel.2025.113705.

Data availability

Data will be made available on request.

References

[1] Global Cancer Observatory. https://gco.iarc.fr/en. (Accessed 14 February 2025).
[2] H. Devarbhavi, S.K. Asrani, J.P. Arab, Y.A. Nartey, E. Pose, P.S. Kamath, Global burden of liver disease: 2023 update, J. Hepatol. 79 (2) (2023) 516–537, https://doi.org/10.1016/j.jhep.2023.03.017.
[3] S. Wilhelm, A.J. Tavares, Q. Dai, S. Ohta, J. Audet, H.F. Dvorak, W.C.W. Chan, Analysis of nanoparticle delivery to tumours, Nat. Rev. Mater. 1 (5) (2016) 1–12, https://doi.org/10.1038/natrevmats.2016.14.
[4] H. Wang, C.A. Thorling, X. Liang, K.R. Bridle, J.E. Grice, Y. Zhu, D.H.G. Crawford, Z.P. Xu, X. Liu, M.S. Roberts, Diagnostic imaging and therapeutic application of nanoparticles targeting the liver, J. Mater. Chem. B 3 (6) (2015) 939–958, https://doi.org/10.1039/C4TB01611D.
[5] H. Cabral, Y. Matsumoto, K. Mizuno, Q. Chen, M. Murakami, M. Kimura, Y. Terada, M.R. Kano, K. Miyazono, M. Uesaka, N. Nishiyama, K. Kataoka, Accumulation of sub-100 nm polymeric micelles in poorly permeable tumours depends on size, Nat. Nanotechnol. 6 (12) (2011) 815–823, https://doi.org/10.1038/nnano.2011.166.
[6] J. Zhou, T.R. Patel, R.W. Sirianni, G. Strohbehn, M.Q. Zheng, N. Duong, T. Schafbauer, A.J. Huttner, Y. Huang, R.E. Carson, Y. Zhang, D.J. Sullivan, J. M. Piepmeier, W.M. Saltzman, Highly penetrative, drug-loaded nanocarriers improve treatment of glioblastoma, Proc. Natl. Acad. Sci. USA 110 (29) (2013) 11751–11756, https://doi.org/10.1073/pnas.1304504110.
[7] C. Wong, T. Stylianopoulos, J. Cui, J. Martin, V.P. Chauhan, W. Jiang, Z. Popovíc, R.K. Jain, M.G. Bawendi, D. Fukumura, Multistage nanoparticle delivery system for deep penetration into tumor tissue, Proc. Natl. Acad. Sci. USA 108 (6) (2011) 2426–2431, https://doi.org/10.1073/pnas.1018382108.
[8] N. Hoshyar, S. Gray, H. Han, G. Bao, The effect of nanoparticle size on in vivo pharmacokinetics and cellular interaction, Nanomedicine 11 (6) (2016) 673, https://doi.org/10.2217/NNM.16.5.
[9] K. Park, Y.H. Bae, R.J. Mrsny, The missing components today and the new treatments tomorrow, Cancer Target. Drug Deliv. An Elus. Dream (2013) 689–707, https://doi.org/10.1007/978-1-4614-7876-8_26.
[10] D.J. Irvine, E.L. Dane, Enhancing cancer immunotherapy with nanomedicine, Nat. Rev. Immunol. 20 (5) (2020) 321–334, https://doi.org/10.1038/s41577-019-0269-6.
[11] L. Giannitrapani, M. Soresi, M.L. Bondì, G. Montalto, M. Cervello, Nanotechnology applications for the therapy of liver fibrosis, World J. Gastroenterol. 20 (23) (2014) 7242–7251, https://doi.org/10.3748/wjg.v20.i23.7242.
[12] X. Han, N. Gong, L. Xue, M.M. Billingsley, R. El-Mayta, S.J. Shepherd, M. G. Alameh, D. Weissman, M.J. Mitchell, Ligand-tethered lipid nanoparticles for targeted RNA delivery to treat liver fibrosis, Nat. Commun. 14 (1) (2023) 1–12, https://doi.org/10.1038/s41467-022-35637-z.
[13] J. Conniot, A. Scomparin, C. Peres, E. Yeini, S. Pozzi, A.I. Matos, R. Kleiner, L.I. F. Moura, E. Zupančič, A.S. Viana, H. Doron, P.M.P. Gois, N. Erez, S. Jung, R. Satchi-Fainaro, H.F. Florindo, Immunization with mannosylated nanovaccines and inhibition of the immune-suppressing microenvironment sensitizes melanoma to immune checkpoint modulators, Nat. Nanotechnol. 14 (9) (2019) 891–901, https://doi.org/10.1038/s41565-019-0512-0.
[14] M. Glaffig, N. Stergiou, S. Hartmann, E. Schmitt, H. Kunz, A synthetic MUC1 anticancer vaccine containing mannose ligands for targeting macrophages and dendritic cells, ChemMedChem 13 (1) (2018) 25–29, https://doi.org/10.1002/cmdc.201700646.
[15] A. Gabba, R. Attariya, S. Behren, C. Pett, J.C. van der Horst, H. Yurugi, J. Yu, M. Urschbach, J. Sabin, G. Birrane, E. Schmitt, S.J. van Vliet, P. Besenius, U. Westerlind, P.V. Murphy, MUC1 Glycopeptide vaccine modified with a GalNAc glycocluster targets the macrophage galactose C-type lectin on dendritic cells to elicit an improved humoral response, J. Am. Chem. Soc. 145 (24) (2023) 13027–13037, https://doi.org/10.1021/jacs.2c12843.
[16] K. Hirata, M. Otagiri, T. Nakamura, J. Saruwatari, H. Arima, Y. Mizuta, H. Maeda, Y. Ishima, Y. Minayoshi, S. Ichimizu, R. Kinoshita, I. Fujita, T. Kai, K. Hirata, T. Nakamura, J. Saruwatari, H. Arima, H. Watanabe, M. Otagiri, T. Maruyama, Y. Mizuta, H. Maeda, Y. Minayoshi, S. Ichimizu, R. Kinoshita, I. Fujita, T. Kai, H. Watanabe, T. Maruyama, Y. Ishima, A mannosylated, PEGylated albumin as a drug delivery system for the treatment of cancer stroma cells, Adv. Funct. Mater. 31 (43) (2021) 2104136, https://doi.org/10.1002/adfm.202104136.
[17] T. Lammers, F. Kiessling, W.E. Hennink, G. Storm, Drug targeting to tumors: principles, pitfalls and (pre-) clinical progress, J. Control. Release 161 (2) (2012) 175–187, https://doi.org/10.1016/j.jconrel.2011.09.063.
[18] C. Feng, P. Tan, G. Nie, M. Zhu, Biomimetic and bioinspired nano-platforms for cancer vaccine development, Exploration 3 (3) (2023) 20210263, https://doi.org/10.1002/EXP.20210263.
[19] R.J.E. Li, T.P. Hogervorst, S. Achilli, S.C. Bruijns, T. Arnoldus, C. Vivès, C.C. Wong, M. Thépaut, N.J. Meeuwenoord, H. van den Elst, H.S. Overkleeft, G.A. van der Marel, D.V. Filippov, S.J. van Vliet, F. Fieschi, J.D.C. Codée, Y. van Kooyk, Systematic dual targeting of dendritic cell C-type lectin receptor DC-SIGN and TLR7 using a trifunctional mannosylated antigen, Front. Chem. 7 (2019) 479517, https://doi.org/10.3389/fchem.2019.00650.
[20] D.A. Mitchell, A.J. Fadden, K. Drickamer, A novel mechanism of carbohydrate recognition by the C-type lectins DC-SIGN and DC-SIGNR: subunit organization and binding to multivalent ligands, J. Biol. Chem. 276 (31) (2001) 28939–28945, https://doi.org/10.1074/jbc.M104565200.
[21] H. Feinberg, D.A. Mitchell, K. Drickamer, W.I. Weis, Structural basis for selective recognition of oligosaccharides by DC-SIGN and DC-SIGNR, Science (80-.) 294 (5549) (2001) 2163–2166, https://doi.org/10.1126/science.1066371.
[22] Y. Guo, H. Feinberg, E. Conroy, D.A. Mitchell, R. Alvarez, O. Blixt, M.E. Taylor, W. I. Weis, K. Drickamer, Structural basis for distinct ligand-binding and targeting properties of the receptors DC-SIGN and DC-SIGNR, Nat. Struct. Mol. Biol. 11 (7) (2004) 591–598, https://doi.org/10.1038/nsmb784.
[23] A. Varki, S. Kornfeld, Structural studies of phosphorylated high mannose-type oligosaccharides, J. Biol. Chem. 255 (22) (1980) 10847–10858, https://doi.org/10.1016/S0021-9258(19)70385-8.
[24] Y. Van Kooyk, T.B.H. Geijtenbeek, DC-SIGN: Escape mechanism for pathogens, Nat. Rev. Immunol. 3 (9) (2003) 697–709, https://doi.org/10.1038/nri1182.
[25] H. Feinberg, S.A.F. Jégouzo, Y. Lasanajak, D.F. Smith, K. Drickamer, W.I. Weis, M. E. Taylor, Structural analysis of carbohydrate binding by the macrophage mannose receptor CD206, J. Biol. Chem. 296 (2021) 100368–100369, https://doi.org/10.1016/j.jbc.2021.100368.
[26] A. Holla, A. Skerra, Comparative analysis reveals selective recognition of glycans by the dendritic cell receptors DC-SIGN and Langerin, Protein Eng. Des. Sel. 24 (9) (2011) 659–669, https://doi.org/10.1093/protein/gzr016.
[27] T.B.H. Geijtenbeek, R. Torensma, S.J. Van Vliet, G.C.F. Van Duijnhoven, G. J. Adema, Y. Van Kooyk, C.G. Figdor, Identification of DC-SIGN, a novel dendritic cell–specific ICAM-3 receptor that supports primary immune responses, Cell 100 (5) (2000) 575–585, https://doi.org/10.1016/S0092-8674(00)80693-5.
[28] N. Frisont, M.E. Taylor, E. Soilleux, M.T. Bousser, R. Mayer, M. Monsigny, K. Drickamer, A.C. Roche, Oligolysine-based oligosaccharide clusters: selective recognition and endocytosis by the mannose receptor and dendritic cell-specific intercellular adhesion molecule 3 (ICAM-3)-grabbing nonintegrin, J. Biol. Chem. 278 (26) (2003) 23922–23929, https://doi.org/10.1074/jbc.M302483200.
[29] P. Valverde, J.D. Martínez, F.J. Cañada, A. Ardá, J. Jiménez-Barbero, Molecular recognition in C-type lectins: the cases of DC-SIGN, Langerin, MGL, and L-Sectin, ChemBioChem 21 (21) (2020) 2999–3025, https://doi.org/10.1002/cbic.202000238.
[30] J.M. Silva, E. Zupancic, G. Vandermeulen, V.G. Oliveira, A. Salgado, M. Videira, M. Gaspar, L. Graca, V. Préat, H.F. Florindo, In vivo delivery of peptides and toll-like receptor ligands by mannose-functionalized polymeric nanoparticles induces prophylactic and therapeutic anti-tumor immune responses in a melanoma model,

J. Control. Release 198 (2015) 91–103, https://doi.org/10.1016/J.JCONREL.2014.11.033.
[31] H. Chung, J.Y. Park, K. Kim, R.J. Yoo, M. Suh, G.J. Gu, J.S. Kim, T.H. Choi, J. W. Byun, Y.W. Ju, W. Han, H.S. Ryu, G. Chung, D.W. Hwang, Y. Kim, H.R. Kang, Y. R. Na, H. Choi, H.J. Im, Y.S. Lee, S.H. Seok, Circulation time-optimized albumin nanoplatform for quantitative visualization of lung metastasis via targeting of macrophages, ACS Nano 16 (8) (2022) 12262–12275, https://doi.org/10.1021/acsnano.2c03075.
[32] P. Cmoch, Z. Pakulski, J. Swaczynová, M. Strnad, Synthesis of Lupane-type saponins bearing mannosyl and 3,6-branched trimannosyl residues and their evaluation as anticancer agents, Carbohydr. Res. 343 (6) (2008) 995–1003, https://doi.org/10.1016/j.carres.2008.02.011.
[33] S. Kramer, J. Langhanki, M. Krumb, T. Opatz, M. Bros, R. Zentel, S. Kramer, J. Langhanki, M. Krumb, T. Opatz, R. Zentel, M. Bros, HPMA-based nanocarriers for effective immune system stimulation, Macromol. Biosci. 19 (6) (2019) 1800481, https://doi.org/10.1002/mabi.201800481.
[34] A.G. Heck, D. Schwiertz, B. Lantzberg, H.C. Nguyen, R. Forster, M. Scherger, T. Opatz, J.A. Van Ginderachter, L. Nuhn, Introducing targeting units or pH-releasable immunodrugs into core-clickable nanogels, Eur. Polym. J. 214 (2024) 113150, https://doi.org/10.1016/j.eurpolymj.2024.113150.
[35] C. Li, W. Xiang, M. Wu, H. Zhang, J. Cheng, T. Yang, J. Mai, X. Chi, X. Gao, Y. Ding, J. Niu, A randomized dose-escalation study on the safety, tolerability, immunogenicity, pharmacokinetics and pharmacodynamics of a novel recombinant human albumin in healthy subjects, Eur. J. Pharm. Sci. 165 (2021) 105923, https://doi.org/10.1016/j.ejps.2021.105923.
[36] M. Hashimoto, V.T.G. Chuang, Y. Ishima, M. Ikeda, T. Maruyama, K. Yamasaki, K. Taguchi, M. Otagiri, A safety evaluation study in mice revealed that albumin dimer is safe for medical and pharmaceutical applications, BPB Reports 3 (2) (2020) 87–91, https://doi.org/10.1248/bpbreports.3.2_87.
[37] N. Gull, J.M. Khan, Rukhsana; Khan, R. H., Spectroscopic studies on the Gemini surfactant mediated refolding of human serum albumin, Int. J. Biol. Macromol. 102 (2017) 331–335, https://doi.org/10.1016/j.ijbiomac.2017.03.134.
[38] C. Gerke, M.F. Ebbesen, D. Jansen, S. Boden, T. Freichel, L. Hartmann, Sequence-controlled glycopolymers via step-growth polymerization of precision glycomacromolecules for lectin receptor clustering, Biomacromolecules 18 (3) (2017) 787–796, https://doi.org/10.1021/acs.biomac.6b01657.
[39] A.M. Alkilany, L. Zhu, H. Weller, A. Mews, W.J. Parak, M. Barz, N. Feliu, Ligand density on nanoparticles: a parameter with critical impact on nanomedicine, Adv. Drug Deliv. Rev. 143 (2019) 22–36, https://doi.org/10.1016/j.addr.2019.05.010.
[40] I. Krabicová, B. Dolenský, M. Řezanka, Selectivity of 1-O-Propargyl-d-Mannose preparations, Molecules 27 (5) (2022) 1483, https://doi.org/10.3390/molecules27051483.
[41] J. Ramos-Soriano, M.C. De La Fuente, N. De La Cruz, R.C. Figueiredo, J. Rojo, J. J. Reina, Straightforward synthesis of Man9, the relevant epitope of the high-mannose oligosaccharide, Org. Biomol. Chem. 15 (42) (2017) 8877–8882, https://doi.org/10.1039/C7OB02286G.
[42] L.N. Tumey, M. Charati, T. He, E. Sousa, D. Ma, X. Han, T. Clark, J. Casavant, F. Loganzo, F. Barletta, J. Lucas, E.I. Graziani, Mild method for succinimide hydrolysis on ADCs: impact on ADC potency, stability, exposure, and efficacy, Bioconjug. Chem. 25 (10) (2014) 1871–1880, https://doi.org/10.1021/BC500357N.
[43] S.D. Fontaine, R. Reid, L. Robinson, G.W. Ashley, D.V. Santi, Long-term stabilization of maleimide-thiol conjugates, Bioconjug. Chem. 26 (1) (2015) 145–152, https://doi.org/10.1021/BC5005262.
[44] S. Mesapogu, C.M. Jillepalli, D.K. Arora, Agarose Gel Electrophoresis and Polyacrylamide Gel Electrophoresis: Methods and Principles, Springer, Berlin, Heidelberg, 2013, pp. 73–91, https://doi.org/10.1007/978-3-642-34410-7_5.
[45] S. Schmitt, L. Nuhn, M. Barz, H.J. Butt, K. Koynov, Shining light on polymeric drug nanocarriers with fluorescence correlation spectroscopy, Macromol. Rapid Commun. 43 (12) (2022) 2100892, https://doi.org/10.1002/marc.202100892.
[46] Y. Wu, S. Ihme, M. Feuring-Buske, S.L. Kuan, K. Eisele, M. Lamla, Y. Wang, C. Buske, T. Weil, A core-shell albumin copolymer nanotransporter for high capacity loading and two-step release of doxorubicin with enhanced anti-leukemia activity, Adv. Healthc. Mater. 2 (6) (2013) 884–894, https://doi.org/10.1002/ADHM.201200296.
[47] M. Lapeyre, J. Leprince, M. Massonneau, H. Oulyadi, P.Y. Renard, A. Romieu, G. Turcatti, H. Vaudry, Aryldithioethyloxycarbonyl (Ardec): a new family of amine protecting groups removable under mild reducing conditions and their applications to peptide synthesis, Chem. – A Eur. J. 12 (13) (2006) 3655–3671, https://doi.org/10.1002/CHEM.200501538.
[48] L.R. Jones, E.A. Goun, R. Shinde, J.B. Rothbard, C.H. Contag, P.A. Wender, Releasable luciferin-transporter conjugates: tools for the real-time analysis of cellular uptake and release, J. Am. Chem. Soc. 128 (20) (2006) 6526–6527, https://doi.org/10.1021/ja0586283.
[49] A. Latorre, P. Couleaud, A. Aires, A.L. Cortajarena, Á. Somoza, Multifunctionalization of magnetic nanoparticles for controlled drug release: a general approach, Eur. J. Med. Chem. 82 (2014) 355–362, https://doi.org/10.1016/j.ejmech.2014.05.078.
[50] M. Scherger, Y.A. Pilger, J. Stickdorn, P. Komforth, S. Schmitt, K. Koynov, H. J. Räder, L. Nuhn, Efficient self-immolative RAFT end group modification for macromolecular immunodrug delivery, Biomacromolecules 24 (5) (2023) 2380–2391, https://doi.org/10.1021/acs.biomac.3c00239.
[51] M. Scherger, Y.A. Pilger, J. Stickdorn, P. Komforth, S. Schmitt, S.M. Arnouk, E. Lebegge, K. Koynov, H.-J. Räder, J.A. van Ginderachter, L. Nuhn, Self-immolative nanobody-cysteine residue modification for controlled immunodrug delivery, Adv. Ther. (2023) 2300076, https://doi.org/10.1002/ADTP.202300076.
[52] Y. Wu, G. Pramanik, K. Eisele, T. Weil, Convenient approach to polypeptide copolymers derived from native proteins, Biomacromolecules 13 (6) (2012) 1890–1898, https://doi.org/10.1021/BM300418R.
[53] Y. Wu, S. Chakrabortty, R.A. Gropeanu, J. Wilhelmi, Y. Xu, K.S. Er, S.L. Kuan, K. Koynov, Y. Chan, T. Weil, pH-responsive quantum dots via an albumin polymer surface coating, J. Am. Chem. Soc. 132 (14) (2010) 5012–5014, https://doi.org/10.1021/JA909570V.
[54] Y. Wu, T. Wang, D.Y.W. Ng, T. Weil, Multifunctional polypeptide–PEO nanoreactors via the hydrophobic switch, Macromol. Rapid Commun. 33 (17) (2012) 1474–1481, https://doi.org/10.1002/MARC.201200227.
[55] Y.D. Xu, L. Tian, R.Y. Lai, Z. Li, E. Procházková, J. Ho, M.H. Stenzel, Development of an albumin-polymer bioconjugate via covalent conjugation and supramolecular interactions, Bioconjug. Chem. 33 (2) (2022) 321–332, https://doi.org/10.1021/acs.bioconjchem.1c00536.
[56] S. Ling Kuan, B. Sto, R. Reichenwallner, W.D.Y. Ng, Y. Wu, M. Doroshenko, K. Koynov, D. Hinderberger, K. Mu, T. Weil, Dendronized albumin core–shell transporters with high drug loading capacity, 2012, https://doi.org/10.1021/bm301531c.
[57] I. Negwer, A. Best, M. Schinnerer, O. Schäfer, L. Capeloa, M. Wagner, M. Schmidt, V. Mailänder, M. Helm, M. Barz, H.J. Butt, K. Koynov, Monitoring drug Nanocarriers in human blood by near-infrared fluorescence correlation spectroscopy, Nat. Commun. 9 (1) (2018) 1–9, https://doi.org/10.1038/s41467-018-07755-0.
[58] K. Li, X. Hu, X.Y. Tu, M.Y. Xian, L.L. Huang, T. Huang, R. Luo, H. Jin, Z. Liu, Enhancing COVID-19 vaccine efficacy: dual adjuvant strategies with TLR7/8 agonists and glycolipids, J. Med. Chem. (2024) 67, https://doi.org/10.1021/acs.jmedchem.4c01801.
[59] V. Porkolab, M. Lepšík, S. Ordanini, A. St John, A. Le Roy, M. Thépaut, E. Paci, C. Ebel, A. Bernardi, F. Fieschi, Powerful avidity with a limited valency for virus-attachment blockers on DC-SIGN: combining chelation and statistical rebinding with structural plasticity of the receptor, ACS Cent. Sci. 9 (4) (2023) 709–718, https://doi.org/10.1021/acscentsci.2C01136.
[60] J. Banchereau, R.M. Steinman, Dendritic cells and the control of immunity, Nature 392 (6673) (1998) 245–252, https://doi.org/10.1038/32588.
[61] M.V. Baranov, M. Kumar, S. Sacanna, S. Thutupalli, G. van den Bogaart, Modulation of immune responses by particle size and shape, Front. Immunol. 11 (2021) 607945, https://doi.org/10.3389/FIMMU.2020.607945.
[62] S. Futaki, I. Nakase, Cell-surface interactions on arginine-rich cell-penetrating peptides allow for multiplex modes of internalization, Acc. Chem. Res. 50 (10) (2017) 2449–2456, https://doi.org/10.1021/acs.accounts.7b00221.
[63] S. Hong, P.R. Leroueil, I.J. Majoros, B.G. Orr, J.R. Baker, M.M. Banaszak Holl, The binding avidity of a nanoparticle-based multivalent targeted drug delivery platform, Chem. Biol. 14 (1) (2007) 107–115, https://doi.org/10.1016/j.chembiol.2006.11.015.
[64] H. Sun, Y. Li, P. Zhang, H. Xing, S. Zhao, Y. Song, D. Wan, J. Yu, Targeting toll-like receptor 7/8 for immunotherapy: recent advances and prospectives, Biomark. Res. 10 (1) (2022) 1–19, https://doi.org/10.1186/S40364-022-00436-7.
[65] Q. Wang, S.Y. Kim, H. Matsushita, Z. Wang, V. Pandyarajan, M. Matsuda, K. Ohashi, T. Tsuchiya, Y.S. Roh, C. Kiani, Y. Zhao, M. Chan, S. Devkota, S.C. Lu, T. Hayashi, D.A. Carson, E. Seki, Oral administration of PEGylated TLR7 ligand ameliorates alcohol-associated liver disease via the induction of IL-22, Proc. Natl. Acad. Sci. USA 118 (1) (2021) e2020868118, https://doi.org/10.1073/pnas.2020868118.
[66] M. Wang, H. Chen, T. Zhang, Z. Zhang, X. Xiang, M. Gao, Y. Guo, S. Jiang, K. Yin, M. Chen, J. Huang, X. Zhong, U. Ohto, J. Li, T. Shimizu, H. Yin, Targeting toll-like receptor 7 as a therapeutic development strategy for systemic lupus erythematosus, Acta Pharm. Sin. B 14 (11) (2024) 4899–4913, https://doi.org/10.1016/j.apsb.2024.08.016.
[67] S. Shirai, M. Shibuya, A. Kawai, S. Tamiya, L. Munakata, D. Omata, R. Suzuki, T. Aoshi, Y. Yoshioka, Lipid nanoparticles potentiate CpG-oligodeoxynucleotide-based vaccine for influenza virus, Front. Immunol. 10 (2020) 484276, https://doi.org/10.3389/fimmu.2019.03018.
[68] C. Vanhove, J.P. Bankstahl, S.D. Krämer, E. Visser, N. Belcari, S. Vandenberghe, Accurate molecular imaging of small animals taking into account animal models, handling, Anaesthesia, quality control and imaging system performance, EJNMMI Phys. 2 (1) (2015) 1–25, https://doi.org/10.1186/S40658-015-0135-Y.
[69] G. Kijanka, M. Prokopowicz, H. Schellekens, V. Brinks, Influence of aggregation and route of injection on the biodistribution of mouse serum albumin, PLoS One 9 (1) (2014) e85281, https://doi.org/10.1371/journal.pone.0085281.
[70] K.O. Vasquez, C. Casavant, J.D. Peterson, Quantitative whole body biodistribution of fluorescent-labeled agents by non-invasive tomographic imaging, PLoS One 6 (6) (2011) e20594, https://doi.org/10.1371/journal.pone.0020594.
[71] P. Opanasopit, K. Shirashi, M. Nishikawa, F. Yamashita, Y. Takakura, M. Hashida, In vivo recognition of mannosylated proteins by hepatic mannose receptors and mannan-binding protein, Am. J. Physiol. Gastrointest. Liver Physiol. 280 (5) (2001) G879–G889, https://doi.org/10.1152/ajgpi.2001.280.5.G879.
[72] L. Beljaars, K. Poelstra, G. Molema, D.K.F. Meijer, Targeting of sugar- and charge-modified albumins to fibrotic rat livers: the accessibility of hepatic cells after chronic bile duct ligation, J. Hepatol. 29 (4) (1998) 579–588, https://doi.org/10.1016/S0168-8278(98)80153-0.
[73] D.G. Levitt, M.D. Levitt, Human serum albumin homeostasis: a new look at the roles of synthesis, catabolism, renal and gastrointestinal excretion, and the clinical value of serum albumin measurements, Int. J. Gen. Med. 9 (2016) 229–255, https://doi.org/10.2147/IJGM.S102819.

[74] H.M. Berman, J. Westbrook, Z. Feng, G. Gilliland, T.N. Bhat, H. Weissig, I. N. Shindyalov, P.E. Bourne, The Protein Data Bank, Nucleic Acids Res. 28 (1) (2000) 235–242, https://doi.org/10.1093/NAR/28.1.235.
[75] S. Sugio, S. Mochizuki, M. Noda, A. Kashima, Crystal structure of human serum albumin (1997), https://doi.org/10.2210/pdb1AO6/pdb.
[76] S. Sugio, S. Mochizuki, M. Noda, A. Kashima, Crystal structure of human serum albumin at 2.5 Å resolution, Protein Eng. 12 (6) (1999) 439–466, https://doi.org/10.1093/protein/12.6.439.

Supporting Information

Glycogen-Inspired Trimannosylated Serum Albumin Nanocarriers for Targeted Delivery of Toll-like Receptor 7/8 Agonists to Immune Cells and Liver

Bellinda Lantzberg[1,#], Yanira Zeyn[2,#], Robert Forster[3,#], Lin Jian[1], Dominik Schauenburg[1], Christoph Hieber[2], Lutz Nuhn[4], Tianjiao Zhou[1,5], Maria J. S. A. Silva[1], Kaloian Koynov[1], Hu-Lin Jiang[5], Seah Ling Kuan[1,*], Matthias Bros[2,*], Till Opatz[3,*], Tanja Weil[1,*]

[1]Max Planck Institute for Polymer Research, Ackermannweg 10, 55128 Mainz, Germany. *E-mail: kuan@mpip-mainz.mpg.de; weil@mpip-mainz.mpg.de.

[2]Department of Dermatology, University Medical Center of Johannes Gutenberg-University Mainz, Obere Zahlbacher Straße 63, 55131 Mainz, Germany. *E-mail: mbros@uni-mainz.de.

[3]Department of Chemistry, Johannes Gutenberg-University Mainz, Duesbergweg 10–14, 55128 Mainz, Germany. *E-mail: opatz@uni-mainz.de.

[4]Faculty for Chemistry and Pharmaceutics, Julius-Maximilians-University Würzburg, Röntgenring 11, 97070 Würzburg, Germany.

[5]State Key Laboratory of Natural Medicines, China Pharmaceutical University, 210009, PR China.

[#]Authors contributed equally.

Keywords: Immunotherapy, nanomedicine, nano-immunotherapy, biomacromolecular therapeutics, albumin-carrier, trimannose targeting.

Supporting Information

1 Table of Contents

Supporting Information

2 Chemicals and materials

Chemicals: Unless otherwise stated, all chemicals were purchased from *ABCR* (Karlsruhe, BW, Germany), *Acros Organics* (Geel, Belgium), *Alfa Aesar* (Haverhill, MA, USA), *Arctom Scientific* (Westlake Village, CA, USA), *Carbolution* (St. Ingbert, SL, Germany), *Sigma Aldrich* (St. Louis, MO, USA), *TCI* (Tokyo, Japan), *Thermo Fisher Scientific* (Waltham, MA, USA) or *VWR* (Radnor, PA, USA) and used without further purification. Deuterated solvents for NMR experiments were obtained from *Deutero* (Kastellaun, RP, Germany) for $CDCl_3$, CD_3OD and D_2O or from *Sigma Aldrich* (St. Louis, MO, USA) for CD_2Cl_2, and DMF-d_7. Deuterated chloroform was stored over molecular sieves and powdered, basic aluminum oxide (Brockmann activity I, pore size 58 Å) supplied from *Sigma Aldrich* (St. Louis, MO, USA).

Materials: Human blood plasma for FCS measurements was obtained from the Transfusion Center of the University Clinic of Mainz (RP, Germany) from ten healthy donors after physical examination and after obtaining informed consent in accordance with the Declaration of Helsinki. The study was approved by the local ethics committee "Landesärztekammer Rheinland-Pfalz" (837.439.12 (8540-F)). All plasma batches were pooled and stored at -20 °C. Mouse blood plasma was generated from fresh mouse blood *via* centrifugation. NucBlue™ Live ReadyProbes™ reagent was purchased from *Thermo Fisher Scientific* (Waltham, MA, USA). PE- or PE-eFl610-labeled anti-CD11c (clone N418), PE-eFl610-MHCII (M5/114.15.2), PE-Cy7- or FITC-CD86 (GL-1), V500-CD3 (500A2), SB600-CD11b (M1/70), PerCP-Cy5.5-CD19 (1D3), PE-Cy7-NK1.1 (PK136), PE-eFl610-Ly6G (1A8-L6g), AF488-CD209a (MMD3), SB702-CD45 (30-F11), eFl450-F4/80 (BM8), PE-CD32b (AT130-2), BV421-XCR1 (ZET), HorizonV500-CD45R/B220 (RA3-6B2), Pe-Cy7-CD172a/Sirp1α (P84) and eFl780-FVD used for flow cytometric analysis were purchased from *BD Biosciences* (Franklin Lakes, NJ, USA), *Bio Legend* (San Diego, CA, USA) or *Thermo Fisher Scientific* (Waltham, MA, USA).

3 Reaction conditions and purification methods

General experimental conditions: Unless stated otherwise, all reactions were performed without taking precautions to exclude air and moisture. All organic solvents (CH_3CN HPLC grade, CH_2Cl_2 HPLC grade, DMF peptide grade, DMSO >99.7%) were obtained from *Thermo Fisher Scientific* (Waltham, MA, USA) and used without further purification. H_2O (MQ) used for the reactions was obtained from a Millipore purification system. For the synthesis of the carbohydrate structures sensitive and reactive species were protected against humidity or oxidation by conducting the reactions under an atmosphere of Argon-gas in dried glass ware utilizing standard Schlenk-technique. If required dried solvents were used, which were obtained from a SPS 5 solvent drier (*M. Braun Inertgas-Systeme*, Garching, BY, Germany) for toluene and DCM. Further dried solvents were obtained from *Acros Organics* (Geel, Belgium) in AcroSeal™ bottles over molecular sieves for DMF, MeOH and pyridine. Glycosylation reactions were conducted in presence of spherical molecular sieve beads (diameter 1 – 2 mm, pore size 3 Å) supplied from *Alfa Aesar* (Haverhill, MA, USA). The stated temperatures refer to the temperatures measured with a contact thermometer in the used heating mantle or cooling bath. Heated reactions were conducted in an aluminum block placed on the stirring plate. Glycosylation reactions conducted in a temperature range between -40 °C to -20 °C were placed in an acetone bath, which had its temperature adjusted using a FT902 cryostat (*Julabo*, Seelbach, BW, Germany). Zemplén-deacylations were neutralized using the ion exchange resin Amberlite IR 120 (H-Form) supplied from *Merck Millipore* (Burlington, MA, USA). The resin was thoroughly washed with MeOH, H_2O, 1 M HCl and MeOH in that order prior to use utilizing a glass frit. To remove molecular sieves, ion exchange resin and other solids prior to reaction work up, reaction mixtures were filtered through a glass frit using Celite® Hyflo Super Cel® diatomaceous earth, supplied from *Sigma Aldrich* (St. Louis, MO, USA).

Thin layer chromatography (TLC): For carbohydrate synthesis monitoring of reaction progress and chromatographic separation *via* normal phase TLC was conducted using silica gel 60 F_{254} modified aluminum plates and reversed phase TLC on silica gel 60 RP-18 F_{254S} modified aluminum plates (*Merck*

Supporting Information

KGaA, Darmstadt, Germany) containing manganese doted zinc silicate for detection upon UV irradiation. Mobile phases consisted of binary eluent mixtures as described below with the composition stated as volumetric ratio (*v*:*v*). For further substance detection the following staining reagents were applied, and the plates heated with a heat gun: "Potassium permanganate staining reagent": $KMnO_4$ (1.00 g), K_2CO_3 (7.00 g) dissolved in H_2O (100 mL) adding a NaOH-solution (5 %, 2.00 mL) and "Carbohydrate staining reagent": 3-Methoxyphenol (0.20 mL) dissolved in EtOH (100 mL) adding conc. H_2SO_4 (7.00 mL). Ratio of Fronts values (R_f) were stated for each compound.

Analytical high performance liquid chromatography (HPLC-ELS-MS): HPLC-ELS-MS analysis was performed using a LCMS-2020 Single Quadrupole equipped with an electrospray ionization source and a SPD-20A UV-VIS detector (*Shimadzu Corporation*, Kyōto, Japan) on an analytical reversed phase Kinetex EVO C_{18}-column (2.1 mm x 50 mm, 2.6 µm) (*Phenomenex*, Torrance, CA, USA). For carbohydrate synthesis monitoring of reaction progress was accomplished utilizing a 1260 Infinity II HPLC system, consisting of a 1260 Infinity Solvent rack, 1260 Infinity HiP Degasser (G4225A), 1260 Infinity Binary Pump (G1312B) operated at a flow rate of 0.7 mL/min, 1260 Infinity II Vial sampler (G7129A) adjusted to an injection volume of 1.5 µL., 1260 Infinity TCC (G1316A) operated at 40 °C, 1260 Infinity II DAD HS (G7117C) for multiple wavelength detection in combination with an 1290 Infinity II ELSD (G7102A) and an Infinity Lab 6100 Series LCMSD (G6125B) *via* electro spray ionization (ESI) (*Agilent Technologies Deutschland GmbH*, Waldbronn, BW, Germany). Separation was conducted using an analytical reversed phase Ascentis Express C_{18}-column (30 mm x 2.1 mm, 2.7 µm) (*Supelco Deutschland GmbH*, Bad Homburg v. d. Höhe, HE, Germany). The mobile phase was composed of a gradient mixture consisting of A = H_2O with 0.1 % HCOOH and B = MeCN using a gradient profile starting with ratio A:B = 10:90 until t = 0.2 min, followed by a linear increase to ratio A:B = 90:10 until t = 7.5 min followed by an isocratic hold until t = 10 min. Solvents were obtained from commercial suppliers in optima HPLC-MS grade quality: MeCN (*VWR*, Radnor, PA, USA), H_2O (*VWR*, Radnor, PA, USA) and HCOOH (*Thermo Fisher Scientific*, Waltham, MA, USA).

Flash column chromatography (FCC): For carbohydrate synthesis purification of larger amounts of crude products *via* manual normal phase flash column chromatography was accomplished with nitrogen overpressure following the method of *Still et al.*[1] Silica gel (particle size 35–70 µm) obtained from *Acros Organics* (Geel, Belgium) was utilized as stationary phase and binary, isocratic mixtures of cyclohexane (^{c}Hex) and ethyl acetate (EtOAc) as mobile phase. The solvents were obtained with "technical grade" quality and purified *via* distillation prior to use. Purification of small amounts of crude products *via* normal phase flash column chromatography was accomplished utilizing an Isolera Four Flash Purification System (*Biotage,* Uppsala, Sweden) equipped with pumps for variable gradient mixtures at flow rates of 1–200 mL/min, a DAD for detection at wavelengths between 200 – 800 nm and an integrated fraction collector. Normal phase separation was conducted using SNAP KP-SIL cartridges (*Biotage*, Uppsala, Sweden) packed with 10 g, 25 g, 50 g and 100 g of silica gel suitable for the separation of < 0.20 g, 0.20 – 0.50, 0.50 – 1.00 g or > 1.00 g of crude material. Binary eluent mixtures consisting of cyclohexane, ethyl acetate or DCM and MeOH were used. Purification of small amounts of crude products *via* reversed phase flash column chromatography was accomplished utilizing an Isolera One Flash Purification System (*Biotage*, Uppsala, Sweden) equipped with pumps for variable gradient mixtures at flow rates of 1–200 mL/min, a DAD for detection at wavelengths between 200 – 400 nm and an integrated fraction collector. Reversed phase separation used SNAP C18 cartridges (*Biotage*, Uppsala, Sweden) packed with 12 g, 30 g and 60 g of stationary phase suitable for the separation of < 0.20 g, 0.20 – 0.50 or > 1.00 g of crude material. Binary eluent mixtures consisting of MeCN and H_2O were used. Isolation of purified material was accomplished *via* lyophilization utilizing an Alpha 2-4LDPlus freeze dryer (*Martin Christ Gefriertrocknungsanlagen*, Osterode, NI, Germany).

Preparative high performance liquid chromatography (HPLC): HPLC purifications were carried out using a Shimadzu HPLC system equipped with a semi preparative reversed phase Eclipse XBD-C_{18}-column (9.4 mm x 250 mm, 5 µm) (*Agilent Technologies Deutschland GmbH*, Waldbronn, BW, Germany).

Supporting Information

4 Analytical methods

Absorbance spectroscopy measurements: The absorbance was measured using a NANODROP 2000c spectrophotometer (*Thermo Fisher scientific*, Waltham, MA, USA) or Spark 20M microplate reader (*Tecan*, Wiesbaden, HE, Germany).

Infrared spectroscopy (IR): Infrared spectra were measured utilizing a Tensor 27 FT-IR spectrometer with built in Diamant-ATR-unit (*Bruker Corporation*, Ettlingen, BW, Germany). The absorption frequencies of characteristic vibration bands are stated as wave number $\tilde{\nu}$ [cm^{-1}]. Spectra were processed using the Opus software (*Bruker Corporation*, Ettlingen, BW, Germany) for baseline correction and peak detection.

Melting range determination: For carbohydrate compounds obtained as crystalline solid the melting range Θ [°C] was determined using a KSP1N melting point meter (*A. Krüss Optronic*, Hamburg, HH, Germany). Samples were transferred into a capillary tube and heated with a rate of 1 °C/min. The melting process was observed and temperature values for onset and end of melting are given.

Polarimetry: For carbohydrate compound specific optical rotation values $[\alpha]_D^\theta$ of all optical active carbohydrate compounds were determined using an automated 241 MC polarimeter (*PerkinElmer Inc.*, Waltham, MA, USA). Measurements were undertaken utilizing a sodium-vapor lamp at the sodium D-double line (λ_{D1} = 590 nm und λ_{D2} = 589 nm) with an aperture adjustment of 600 nm and a slit width of 2 nm. Optical rotation values α were determined at an integration time of 20 seconds. Measurements were carried out at ambient temperature with the actual value stated for each optical rotation value. Glass cuvettes (l = 10 cm, V = 1.00 mL) were filled with a sample solution (c = 0.01 g/mL) in an appropriate solvent ($CHCl_3$, MeOH, H_2O). The polarimeter was calibrated with the pure solvent prior to the measurement. The unit of the specific optical rotation $[\alpha]_\lambda^\theta$ of [°·cm^2/10·g] is neglected in the following.

Nuclear magnetic resonance spectroscopy (NMR): NMR spectra were measured on Avance-III 700 or 400 Neo (*Bruker Corporation*, Ettlingen, BW, Germany) NMR spectrometers. For carbohydrate structures NMR-spectra were recorded utilizing an AC300 (*Bruker Corporation*, Ettlingen, BW, Germany) with 5 mm Dual-^{13}C-head and B-ACS 60 sample changer for 300 MHz ^{1}H-NMR-, 75.5 MHz ^{13}C-NMR- as well as 2D-NMR-experiments, an Avance-II 400 (*Bruker Corporation*, Ettlingen, BW, Germany) with 5 mm BBFO-head with z-gradient and ATM as well as SampleXPress 60 sample changer for 400 MHz ^{1}H-NMR-, 100.6 MHz ^{13}C-NMR- and 2D-NMR experiments and an Avance-III 600 (*Bruker Corporation*, Ettlingen, BW, Germany) with 5 mm TCI-Cryoprobe with z-Gradient and ATM as well as SampleXPress Lite 16 sample changer for 600 MHz ^{1}H-NMR-, 151.0 MHz ^{13}C-NMR- and 2D-NMR experiments. Samples were dissolved in an appropriate deuterated solvent ($CDCl_3$, CD_3OD, D_2O). Spectra were processed using the MestReNova software (*Mestrelab Research*, Santiago de Compostela, Spain) for baseline correction (Whittaker smoother) and automated phase correction. Spectra were referenced to the signal of the respective deuterated solvent ($CDCl_3$: ^{1}H: δ = 7.26 ppm, CD_3OD: ^{1}H: δ = 3.31 ppm, D_2O: ^{1}H: δ = 4.79 ppm) and using the absolute reference function of the analysis software. Observed signals are described using their chemical shifts (δ) in ppm, multiplicity (s-singlet, d-doublet, t-triplet, dd-doublet of doublet, etc. and m-multiplet; app-apparent and br-broad), integral and locator of ^{1}H- and ^{13}C-position in the molecule. Signal assignment was supported utilizing 2D-NMR spectra: COSY, HSQC, HSQC-NoDec, HMBC, TOCSY, NOESY (data not shown).

Matrix assisted laser desorption ionization-time of flight mass spectrometry (MALDI-ToF-MS): Mass spectra for nanocarrier structures were acquired on a ToF MS rapifleX (*Bruker Corporation*, Ettlingen, BW, Germany) (matrix: sinapinic acid).

Supporting Information

High resolution mass spectrometry (HR-ESI-MS): HR-ESI-MS was recorded using a Synapt G2-Si mass spectrometer (*Waters Corporation*, Eschborn, HE, Germany). High resolution exact mass determination for carbohydrate structures was performed using a G6545A Q-ToF (*Agilent Technologies Deutschland GmbH*, Waldbronn, BW, Germany) *via* electro spray ionization (ESI). Sample injection was achieved using a 1260 Infinity II HPLC-System (*Agilent Technologies Deutschland GmbH*, Waldbronn, BW, Germany) with a G7111B 1260 Quaternary Pump, G7129A 1260 Vialsampler und G7116A 1260 Multicolumn Thermostat. Mass calibration was done on the day of sample measurement utilizing an external standard.

Liquid chromatography and high resolution mass spectrometry (LC-HRMS): LC-HRMS analysis was conducted on the Synapt G2-Si, coupled to an Acquity UPLC system using an Acquity UPLC Protein BEH C4 column (300Å, 1.7 µm, 2.1 × 50 mm) with the column oven at 80 °C. Water with 0.1% formic acid (solvent A) and acetonitrile 0.1% formic acid (solvent B), were used as the mobile phase at a flow rate of 0.2 mL. The gradient was t = 0 min, 0% B; t = 2 min, 0% B; t = 18 min, 90% B; t = 19 min, 90% B; t = 20 min, 0% B, stop, detection UV/Vis detection with Diode Array (200-800 nm). The electrospray source was operated with capillary voltage of 2.0 kV, sampling cone of 40 V and source offset 80 V. Source temperature was 150 °C, desolvation temperature was 500 °C and desolvation gas at a total flow of 800 $L \cdot h^{-1}$.

Agarose gel electrophoresis: For agarose gel electrophoresis an 1 % Agarose gel (0.5 g agarose, 50 mL 1xTAE buffer) was prepared and samples (20 µL: 30.1 pmol + MQ, 10 µL 50 % glycerol solution) were loaded. The gel was run at 150 V for 33 min. The gel was imaged using the Cy5 channel and stained with Coomassie brilliant blue before imaging using a ChemiDoc Imaging system (*Bio-Rad Laboratories*, Hercules, CA, USA) using the Coomassie brilliant blue channel.

Sodium dodecyl sulfate polyacrylamide gel electrophoresis (SDS-PAGE): The SDS-PAGE analysis was conducted using commercially available Mini-PROTEAN Precast Gel (*Bio-Rad Laboratories*, Hercules, CA, USA). Samples (reducing condition: 10 µL: 7.5 µL (30 pmol*) sample, 2.5 µL 4x Laemmli sample buffer + DTT (200 mM); non-reducing condition: 10 µL: 7.5 µL sample, 2.5 µL 4x Laemmli sample buffer) were prepared, heated to 95 °C for 10 min and loaded (*sample amount was decreased to 15 pmol for native HSA and Cy5-labeled HSA). The gel was run for 10 – 15 min at 80 V and then for 120 min at 120 V. The gel was imaged using the Cy5 channel and stained with Coomassie brilliant blue before imaging using a ChemiDoc Imaging system (*Bio-Rad Laboratories*, Hercules, CA, USA) using the Coomassie brilliant blue channel.

Circular dichroism spectroscopy (CD): CD spectra were recorded on a J-1500 spectrometer (*Jasco*, Pfungstadt, HE, Germany) in a 0.1 cm High Precision Cell (*Hellma Analytics*, Müllheim, BW, Germany). The recorded data was processed in Spectra Analysis (*Jasco*, Pfungstadt, HE, Germany). The compounds were dissolved in a 10 mM sodium phosphate buffer with pH 7.4 (800 nM). CD-spectra were recorded at wavelengths from 260 – 180 nm with a bandwidth of 1 nm, data pitch of 0.2 nm and a scanning speed at 20 nm min^{-1} at 37 °C.

Dynamic light scattering (DLS): DLS measurements of the HSA based compounds (1 mg/mL in dPBS unless otherwise noted) were performed at 25 °C using a Zetasizer Nano S (*Malvern Instruments*, Malvern, England) equipped with a He/Ne Laser (λ = 633 nm) and a narrow band filter at a fixed scattering angle of 173 °. Volume distribution of DLS measurements of nanocarriers in dPBS was used to determine their size range.

Zeta Potential (*ζ*): To determine the ζ-potential, 800 uL of conjugate solution (0.3mg/mL conjugate in 50mM NaPB pH 7.4) was measured in a folded capillary (DTS1070) and analyzed using a Zetasizer NanoZ (Malvern).

Fluorescence correlation spectroscopy (FCS): FCS experiments were performed using a commercial confocal LSM 880 microscope (*Carl Zeiss*, Jena, TH, Germany) equipped with a C-Apochromat 40×/1.2

Supporting Information

W (*Carl, Zeiss*, Jena, TH, Germany) water immersion objective. A HeNe laser (λ = 633 nm) fiber coupled to the LSM 880 was used for the excitation of the Sulfo-Cyanine5 dye. The emission light in the spectral range 655 – 699 nm (Cy5) was detected using a Quasar spectral detection unit (*Carl Zeiss*, Jena, TH, Germany) that comprises a diffraction grating and a 32 channel GaAsP photomultiplier array operating in the photon counting mode. Sulfo-Cyanine7.5 dye was excited at 780 nm by a strongly attenuated Mai Tai Ti:Sa laser (*Newport Spectra Physics*, Milpitas, CA, USA) coupled to the LSM 880. The emission light passed through a band-pass filter EM835/70 (*Chroma Technology*, Bellows Falls, Vermont, USA) and was directed to a PDM SPAD detector (*Micro Photon Devices*, Bolzano, Italy) connected to a TimeHarp 260 TCSPC board (*PicoQuant*, Berlin, B, Germany). For each sample, 30 µL of solution (PBS, human palsma or mouse blood serum) was added to a 15 wells chamber (*ibidi*, Munich, BY, Germany). The confocal detection volume was placed ~30 µm above the glass coverslip and series of 20 measurements, 10 s each, were performed at room temperature (23 °C). For experiments with human plasma, the nanocarriers were incubated with plasma for 1 h at 23 °C before the measurement. The obtained experimental autocorrelation curves were fitted with the following analytical model function:

$$G(\tau) = 1 + \left[1 + \frac{f_T}{1-f_T} e^{-\tau/\tau_T}\right] \frac{1}{N} \sum_{i=1}^{m} \frac{f_i}{\left(1+\frac{\tau}{\tau_{D,i}}\right) \cdot \sqrt{1+\frac{\tau}{S^2 \cdot \tau_{D,i}}}} \qquad \text{(eq. S1)}$$

whereby N is the average number of diffusing fluorescence species in the observation volume, f_T and τ_T are the fraction and the decay time of the triplet state, τ_{Di} is the diffusion time of the i-th type of species, f_i is the fraction of the component i ($1 \leq i \leq m$), and S is the structure parameter, $S = z_0/r_0$, where z_0 and r_0 represent the axial and radial dimensions of the observation volume.[2] The fit yielded the values of τ_{Di} and N. The diffusion coefficients of the species D_i are related to the respective diffusion times τ_{Di} and the radial dimension r_0 of V_{obs} by $D_i = r_0^2/(4\tau_{Di})$. By inserting D_i into the Stokes-Einstein equation, the hydrodynamic radius can be calculated as $R_h = \frac{k_B \cdot T}{6 \cdot \pi \cdot \eta \cdot D}$, here, k_B is the Boltzmann constant, T is the temperature, and η is the viscosity of the solvent. For the viscosity of water and plasma at 23 °C values of 0.93 mPas and 1.4 mPas, respectively were used. Errors are given as standard deviation but rounded up to 10 % of absolute values of hydrodynamic radii (R_h) if SD < 10 % of R_h to account for systematic errors based on temperature, viscosity, diffusion coefficient value of reference sample and later individual variations in plasma samples. Furthermore, the concentration of the fluorescent species was calculated as $c = N/V_{obs}$. For calibration of the confocal volume V_{obs}, dyes with known diffusion coefficients in water, i.e. Alexa 647 and IRDye®800CW were used.

Supporting Information

5 *In vitro* and *in vivo* experiments

Cell culture: Immortalized Chinese Hamster Ovary cells (CHO^{MMR-}) (*ATCC*, Molsheim Cedex, France) were cultured in Ham´s F12K (Kaighn´s) Medium or DMEM/F12 (*Sigma Aldrich*, Deisenhofen, BY, Germany) supplemented with 10 % fetal bovine serum (FBS), 1 % penicillin/streptomycin (*Sigma Aldrich*, Deisenhofen, BY, Germany). For transduced Chinese Hamster Ovary cells stably expressing the MMR (CHO^{MMR+})[3] (kindly provided by the lab of Prof. Jo A. Van Ginderachter), their culture medium was supplemented with 0.06 % geneticin (G418). Cells were subcultured every 2 – 3 days. Murine bone marrow cells ($1 \cdot 10^6$/1 mL for FLT3-Ligand supplemented culture, $2 \cdot 10^5$/1 mL for GM-CSF supplemented culture) were seeded in 12-well suspension culture plates (*Greiner Bio-One*, Frickenhausen, BW, Germany) in culture medium (IMDM, 2 mM L-glutamine, 100 U/mL penicillin, 100 µg/mL streptomycin (*Sigma-Aldrich*, Deisenhofen, BY, Germany) and 50 µM β-mercaptoethanol (*Carl Roth*, Karlsruhe, BW, Germany) containing 5 % FBS (*PAN-Biotech*, Aidenbach, BY, Germany)) supplemented with recombinant murine GM-CSF (10 ng/mL) (*Miltenyi Biotec*, Bergisch Gladbach, NRW, Germany) or FLT3-Ligand (250 ng/ml) (*BioLegend*, San Diego, CA, USA). Cells were kept at 37 °C, 95 % relative humidity and 5 % CO_2. Culture media was replenished on days 3 and 6 of culture of GM-CSF supplemented cell culture.

Spleen cell and liver NPC isolation: Murine spleens were mechanically disrupted with a pestle and pressed through a cell strainer with a pore size of 40 µm (*Greiner Bio-One*, Frickenhausen, BW, Germany) to obtain a single-cell suspension. Spleen cells ($2 \cdot 10^6$/500 µL) were cultured in culture medium in FACS tubes. For enrichment of liver NPC, mice were sacrificed by cervical dislocation and the liver was removed. For enzyme-based liver dissociation, a special enzyme mixture (Liver dissociation kit; *Miltenyi Biotec*, Bergisch-Gladbach, NRW, Germany) was prepared as recommended by the manufacturer. The enzyme mixture was preincubated for 15 min in C tubes (*Miltenyi Biotec*, Bergisch-Gladbach, NRW, Germany). Subsequently, livers were cut in pieces and transferred into prepared C tubes and placed into a gentleMACS dissociator (*Miltenyi Biotec*, Bergisch-Gladbach, NRW, Germany). The tissue was minced (program m_liver_03). Following this, the cell suspension was incubated for 30 min at 37 °C under continuous shaking. Then the C tubes were again placed on the gentleMACS dissociator and mixed (program m_liver_04). Samples were filtered using a Cell Strainer (100 µm) (*Sarstedt*, Nümbrecht, NRW, Germany) and the liver NPCs were enriched by density centrifugation. Cells were resuspended using 30 % Histodenz™-HBSS and a HBSS layer was placed on top (*Sigma Aldrich*, St. Louis, MO, USA). Then a gradient centrifugation (1500 x g, 20 min, 4 °C, without break and acceleration) was performed and liver NPC were retrieved from the interphase. Cells were cultured in HEPES buffered RPMI 1640 medium (10 % FBS, 100 U/mL penicillin, 100 µg/mL streptomycin, 1 mM L-glutamine, 1 % essential and non-essential amino acids, 50 µM β-mercaptoethanol) and placed in 96-well plates at a concentration of $4 \cdot 10^5$/200 µL.

Cellular uptake: CHO^{MMR+} cells were detached by TrypLE Select (Gibco by *Thermo Fisher Scientific*, Dreieich, HE, Germany) and centrifuged for 5 min at 1000 rpm. Collected cells were resuspended in culture medium and seeded in Cellview cell culture slides (PS, 75/25 mM) (*Greiner Bio-One*, Frickenhausen, BW, Germany) at a cell density of 6250 cells/well. 24 h after seeding, cells were treated with 1 µM of Cy5 labeled TM_{38}-HSA or HSA or dPBS for 20 h. Cells were washed with dPBS, fixed (4 % PFA, 10 min) and nuclei were stained with NucBlue™ before *confocal laser scanning microscopy* images and z-stacks were acquired on a STELLARIS 8 confocal microscope (NucBlue: Ex = 405 nm, Em = 415 – 569 nm; sulfo-Cy5: Ex = 649 nm, Em = 658 – 834 nm) (*Leica Microsystems*, Wetzlar, HE, Germany).

Fluorescence activated cell sorting: For FACS analysis the $CHO^{MMR+/-}$ cells (200000 cells/well, 24-well plates, 24 h seeding, 24 h treatment, 0.1 µM of TM_n-HSA, HSA, or PBS) were washed with dPBS and harvested using cell dissociation buffer for 15 min at 37 °C. After centrifugation for 10 min at 350 x g and 5 °C cell pellets were resuspended in dPBS. All samples were kept on ice prior to flow cytometric analysis by a BD Accuri C6 (*BD Biosciences*, Franklin Lakes, NJ, USA). Data were

Supporting Information

processed with FlowJo software. For *ex vivo* uptake experiments, cells were harvested, washed with staining buffer (PBS, 1 % FBS, 0.5 mM EDTA) and incubated with rat anti-mouse CD16/CD32 antibody (clone 2.4G2; 15 min, 4 °C) to prevent antibody binding to Fcγ receptors. Following this, samples were incubated with fluorescence-labeled antibodies (20 min, 4 °C). Then, samples were washed with PBS and incubated with FVD to identify live/dead cells. Measurements were carried out using an Attune NxT flow cytometer and data were analyzed using Attune NxT software (both *Thermo Fisher*, Waltham, MA, USA).

Cytokine detection: Cytokines were detected using the BD™ Cytometric Bead Array (CBA) Mouse Flex Set (*BD Biosciences*, Franklin Lakes, NJ, USA), which was performed according to the manufacturer's specifications.

T-cell proliferation assay: GM-CSF differentiated BMDCs were incubated with 5 µg/ml OVA protein. After 3 h, nanocarriers (1-10-50 nM) or TLR7/8 agonist (1 µM) were added. The following day, samples were harvested, washed, and resuspended in culture medium w/o GM-CSF. BMDCs were seeded in wells (2×10^4/200 µL in triplicates) of 96-well plates (*Greiner Bio-One*, Kremsmünster, Austria) and were serially titrated five times (1:2). Splenic OVA peptide-specific CD4+ (OT-II) and CD8+ (OT-I) T cells were immunomagnetically sorted and enriched as recommended by the manufacturer (*Miltenyi Biotec*, Bergisch-Gladbach, Germany) and added to serially diluted BMDCs at a concentration of $5 \cdot 10^4$ cells/100 µL. After 3 – 4 days of co-culture, ^{3}H-thymidine (0.5 µCi/well) was introduced to the co-cultures for 16 – 18 h to assess T-cell proliferation. For measuring, cell lysates were transferred onto Harvester 96 glass fiber filter mats (*TomTec*, Hamden, CT, USA) and the genomically incorporated radioactivity was quantified using a 1450 MicroBeta Trilux microplate β-counter (*Perkin Elmer*, Waltham, MA, USA).

Animals: *In vivo* experiments followed an approval by the local ethics committee on animal care (number 23 177-07/G 20-1-123, Government of Rhineland Palatinate, Germany). B6N-*Tyr*$^{c\text{-}Brd}$/BrdCrCrl were purchased from Charles River. Female mice were 8 weeks old (body weight ~20 g) and kept according to the guidelines of the institute and the local government. To explore the biodistribution of the nanoparticles 100 µL of a solution of the respective Cy7.5 labeled nanoparticles (2.94 µM in dPBS, corresponding to mouse body weight dosages of TM-HSA-TLR7/8a: 2.0 mg/kg, TM-HSA-Benzyl: 1.9 mg/kg, TM-HSA: 1.9 mg/kg, HSA: 1.0 mg/kg) were intravenously administered to B6 albino mice (n = 5, three mice receiving dPBS as controls). Directly after injection and 3 hours, the mice were once again anesthetized with isoflurane gas and placed into an IVIS (*in vivo* imaging spectrum) system (*Caliper Life Sciences*, Hopkinton, MA, USA) for *in vivo* NIR fluorescence imaging. The picture integration time of the fluorescence source was set to 10 s. Recording parameters were adjusted for excitation at 745 nm and emission at 820 nm to visualize the Cy7.5 labeled nanoparticles. Additionally, after injection blood was retrieved from *vena facialis*. After 24 hours, mice were imaged *in vivo* and afterwards anesthetized with Ketamine/Rompun. After heart puncture, the mice were euthanized, the organs harvested and returned to the imaging chamber for *ex vivo* signal quantification by Live Image software (*Perkin Elmer*, Waltham, MA, USA). Organs were analyzed by region-of-interests (ROIs), and the fluorescence was quantified as the average of area-normalized radiant efficiency. Mice that received complete intravenous tail vein injection were used for quantification and statistical analysis.

Supporting Information

6 Synthesis procedures

6.1 Synthesis of the targeting structure TM

The complete synthesis of the targeting structure (**TM**) starting from commercially available D-mannose and triethylene glycol is described in Scheme S1. The synthesis sequence includes a total of nine reaction steps involving two telescoped reaction procedures reducing needed purification steps and improving overall yield. The telescoped procedures involve a two-step propargylation and Zemplén deacylation sequence delivering compound (**1**)[4] as well as a three-step silylation, benzoylation and desilylation sequence delivering compound (**2**).[5] Reaction with mannosyl donor (**3**) accesses trimannose building block (**4**). CuAAC reaction with azide (**5**) delivers the protected molecule (**6**) and global Zemplén deacylation the desired targeting structure (**TM**). Analytically pure samples of the intermediate products (**I1-3**) of the telescoped sequences were also isolated and used for their characterization. The longest linear sequence starting from D-Mannose involving the glycosyl acceptor (**2**) delivers the targeting structure (**TM**) with a yield of 42 % over six steps.

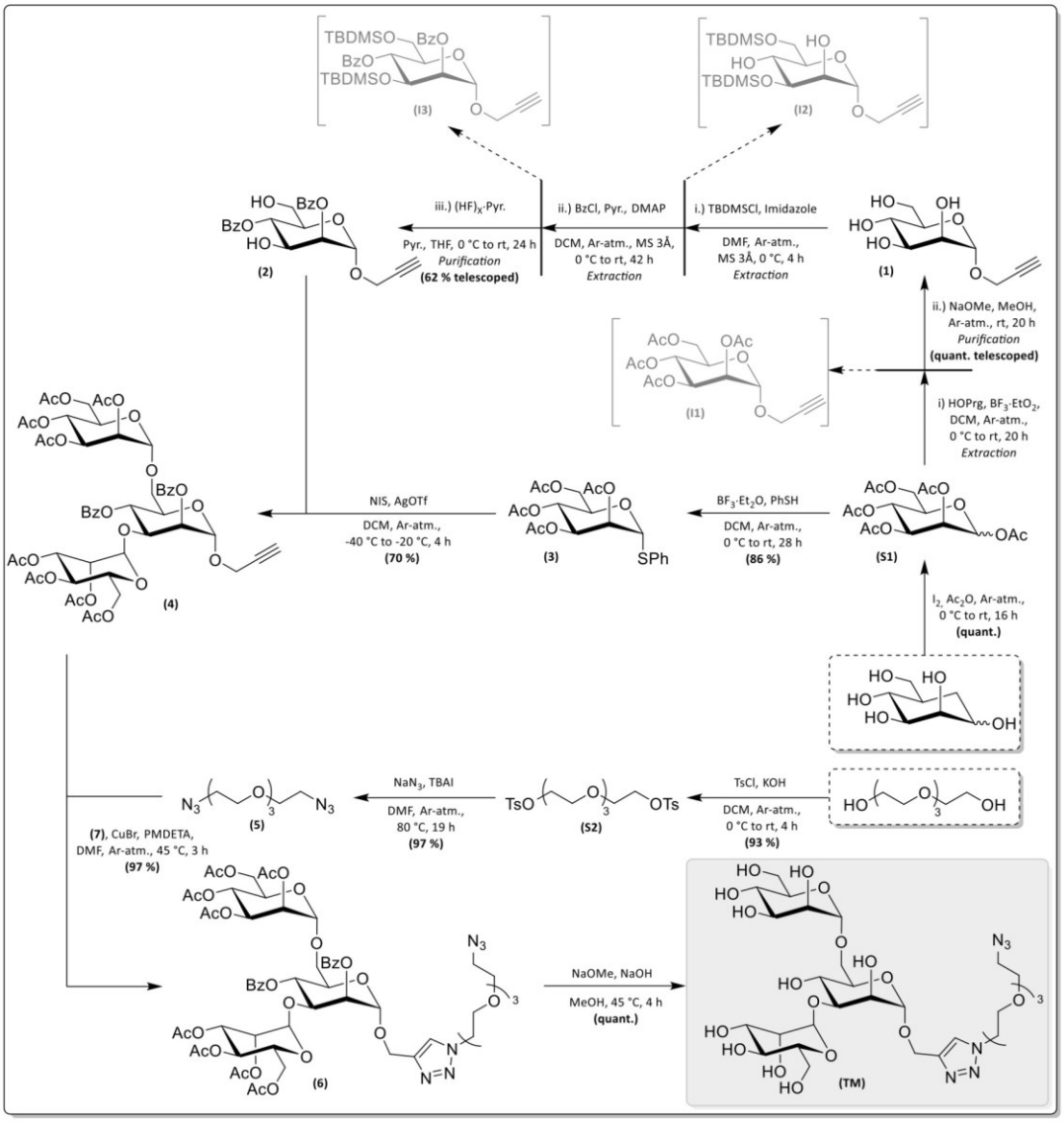

Scheme S1: Overview of the complete nine-step synthesis of the targeting structure (**TM**). The route contains two literature based telescoped synthesis sequences obtaining compounds (**1**) and (**2**). The targeting structure (**TM**) was obtained with a yield of 42 % over six linear steps starting from D-Mannose involving the glycosyl-acceptor (**2**).

Supporting Information

6.1.1 1,2,3,4,6-Penta-*O*-acetyl-α,β-D-mannopyranose (S1)

The compound was synthesized according to Scheme S2 following a synthesis protocol by *Percec et al.*[6]

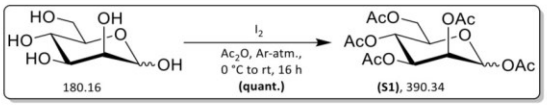

Scheme S2: Synthesis of 1,2,3,4,6-Penta-*O*-acetyl-α,β-D-mannopyranose (**S1**).

The reaction was conducted using an oven dried Schlenk flask equipped with a magnetic stirring bar. I_2 (0.56 g, 2.22 mmol, 0.04 eq.) was dissolved in Ac_2O (50.0 mL) under an atmosphere of Argon. The resulting black solution was cooled to a temperature of 0 °C using an ice bath. D-Mannose (10.0 g, 55.5 mmol, 1.00 eq.) was added portion by portion against a flow of Argon. After removing the ice bath, the reaction mixture was stirred at room temperature for 16 hours until reaction control *via* TLC and HPLC-MS indicated complete consumption of the starting material and product formation. The reaction mixture was diluted with DCM (50.0 mL), then washed with an ice cold saturated aqueous solution of $Na_2S_2O_3$ (2 x100 mL) and a saturated aqueous solution of $NaHCO_3$ (4 x100 mL). The separated organic layer was dried over anhydrous Na_2SO_4, filtered and all volatiles were removed in vacuo to afford the desired product **(S1)** as mixture of anomers (α:β = 4:1) in form of a colorless solid.

Yield: 21.7 g (55.5 mmol, quant.), colorless solid.

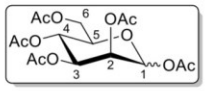

NMR-signals of the α-anomer: ^{1}H-NMR (400 MHz, $CDCl_3$)**:** δ (ppm) = 6.07 (d, ^3J = 2.0 Hz, 1H, H-1), 5.35 – 5.32 (m, 2H, H-2, H-3), 5.26 – 5.23 (m, 1H, H-4), 4.27 (dd, ^2J = 12.4, ^3J = 4.9 Hz, 1H, H-6a), 4.08 (dd, ^2J = 12.4, ^3J = 2.4 Hz, 1H, H-6b), 4.06 – 4.01 (m, 1H, H-5), 2.16 (s, 3H, C-4-O(C=O)CH_3), 2.15 (s, 3H, C-1-O(C=O)CH_3), 2.08 (s, 3H, C-6-O(C=O)CH_3), 2.04 (s, 3H, C-2-O(C=O)CH_3), 1.99 (s, 3H, C-3-O(C=O)CH_3). **^{13}C-NMR** (101 MHz, $CDCl_3$)**:** δ (ppm) = 170.7 (C-6-O(*C*=O)CH_3), 170.1 (C-3-O(*C*=O)CH_3), 169.8 (C-4-O(*C*=O)CH_3), 169.6 (C-2-O(*C*=O)CH_3), 168.2 (C-1-O(*C*=O)CH_3), 90.7 (C-1), 70.7 (C-5), 68.8 (C-3), 68.4 (C-2), 65.6 (C-4), 62.2 (C-6), 21.0 (C-4-O(C=O)*C*H_3), 20.9 (C-1-O(C=O)*C*H_3), 20.8 (C-6-O(C=O)*C*H_3), 20.8 (C-2-O(C=O)*C*H_3), 20.7 (C-3-O(C=O)*C*H_3).

NMR-signals of the β-anomer: ^{1}H-NMR (400 MHz, $CDCl_3$, 25 °C)**:** δ (ppm) = 5.85 (d, ^3J = 1.2 Hz, 1H, H-1), 5.47 (dd, ^3J = 3.3, 1.2 Hz, 1H, H-2), 5.31–5.27 (m, 1H, H-4), 5.12 (dd, ^3J = 10.0, 3.3 Hz, 1H, H-3), 4.29 (dd, ^2J = 12.3 Hz, ^3J = 5.3 Hz, 1H, H-6a), 4.14 (dd, ^2J = 12.3 Hz, ^3J = 2.4 Hz, 1H, H-6b), 3.79 (ddd, ^3J = 9.9, 5.3, 2.4 Hz, 1H, H-5), 2.20 (s, 3H, C-4-O(C=O)CH_3), 2.09 (s, 3H, C-1-O(C=O)CH_3), 2.08 (s, 3H, C-6-O(C=O)CH_3), 2.04 (s, 3H, C-2-O(C=O)CH_3), 1.99 (s, 3H, C-3-O(C=O)CH_3). **^{13}C-NMR** (101 MHz, $CDCl_3$)**:** δ (ppm) = 170.7 (C-6-O(*C*=O)-CH_3), 170.3 (C-3-O(*C*=O)-CH_3), 169.9 (C-4-O(*C*=O)-CH_3), 169.7 (C-2-O(*C*=O)-CH_3), 168.5 (C-1-O(*C*=O)-CH_3), 90.5 (C-1), 73.4 (C-5), 70.7 (C-3), 68.3 (C-2), 65.5 (C-4), 62.2 (C-6), 21.0 (C-4-O(C=O)*C*H_3), 20.9 (C-1-O(C=O)*C*H_3), 20.8 (C-6-O(C=O)*C*H_3), 20.8 (C-2-O(C=O)*C*H_3), 20.6 (C-3-O(C=O)*C*H_3).

Analytical data of obtained anomeric mixture (α:β = 4:1): HR-MS (ESI$^+$)**:** calculated for $C_{16}H_{22}O_{11}$ *m/z* = 413.1054 $[M+Na]^+$, found *m/z* = 413.1058 $[M+Na]^+$. R_f = 0.45 (^{c}Hex/EtOAc 1:1), 0.25 (^{c}Hex/EtOAc 2:1). **Melting range:** Θ (°C = 60.0 – 61.0 (DCM). **Optical rotation:** $[\alpha]_D^{21}$ = +48 ($CHCl_3$). **IR** (ATR)**:** $\tilde{\nu}$ (cm^{-1}) = 2991, 1745, 1434, 1370, 1213, 1148, 1088, 1052, 1026, 974, 912, 786, 732, 686, 601, 562, 500, 467, 449.

The analytical data followed literature data.[6]

Supporting Information

6.1.2 Propargyl α-D-Mannopyranoside (1)

The title compound was synthesized utilizing a telescoped two-step protocol according to Scheme S3 following modified synthesis protocols by *Percec et al.*[6], *Schibilla et al.*[7] and *Kramer et al.*[8]

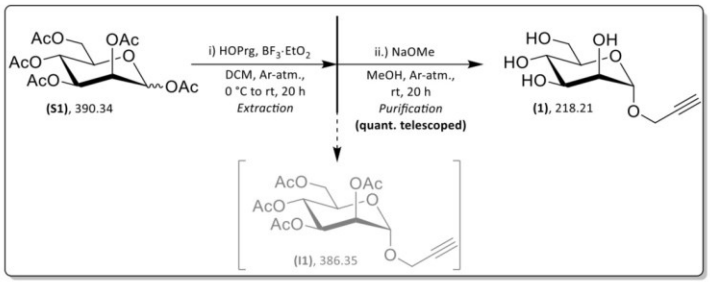

Scheme S3: Telescoped synthesis of Propargyl α-D-Mannopyranoside **(1)**.

Both reaction steps were conducted using oven dried Schlenk flasks equipped with magnetic stirring bars. Compound (**S1**) (1.50 g, 3.84 mmol, 1.00 eq.) was dissolved in dry DCM (20.0 mL) under an atmosphere of Argon. The colorless solution was cooled to a temperature of 0 °C using an ice bath. Propargyl alcohol (1.08 g, 1.14 mL, 19.2 mmol, 5.00 eq.) and $BF_3{\cdot}OEt_2$ (5.45 g, 4.87 mL, 38.4 mmol, 10.0 eq.) were added dropwise one after another. The resulting yellow reaction mixture was stirred for 20 hours, while slowly warming up to room temperature, showing a color change to deep red until reaction control *via* TLC and HPLC-MS indicated complete consumption of the starting material and product formation. The reaction mixture was diluted with DCM (1 50.0 mL), washed with H_2O (3 x 50.0 mL), with a saturated aqueous solution of $NaHCO_3$ (3 x 50.0 mL) and a saturated solution of NaCl (1 x 50.0 mL). The separated organic layer was dried over anhydrous Na_2SO_4, filtered and all volatiles removed in vacuo. The crude intermediate product (**I1**) (1.76 g) was obtained in form of a yellow oil and suspended in dry MeOH (10.0 mL) under an atmosphere of Argon. NaOMe (0.02 g, 0.32 mmol, 0.10 eq.) was added. The reaction mixture was stirred for 20 hours at room temperature with slow dissolution of the substrate until reaction control *via* TLC and HPLC-MS indicated complete consumption of the starting material and product formation. Subsequently, the solution was neutralized using Amberlite IR120 H^+ ion exchange resin (0.10 g) until a neutral solution was obtained. The mixture was filtered over *Celite*, which was washed thoroughly with MeOH (1 x 100 mL). All volatiles were removed in vacuo to afford the crude product in form of a yellow foam, which was dissolved in H_2O (0.1 M), washed twice with the same volume of a mixture of ^{c}Hex and EtOAc (10:1 *v*:*v*). The desired product (**1**) was obtained after lyophilization of the aqueous phase and co-distillation with MeOH in form of a colorless solid.

Yield: 0.84 g (3.99 mmol, quant.), colorless solid.

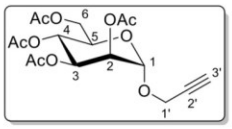

^{1}H-NMR (400 MHz, $CDCl_3$)**:** δ (ppm) = 5.35 (dd, ^3J = 9.5, 3.2 Hz, 1H, H-3), 5.31 (dd, ^3J = 9.5, 9.3 Hz, 1H, H-4), 5.28 (dd, ^3J = 3.2, 1.7 Hz, 1H, H-2), 5.03 (d, ^3J = 1.7 Hz, 1H, H-1), 4.29 (dd, ^2J = 12.3 Hz, ^3J = 5.1 Hz, 1H, H-6a), 4.27 (d, ^2J = 12.6 Hz, ^3J = 2.4 Hz, 2H, H-1‘), 4.11 (dd, ^2J = 12.3, ^3J = 2.5 Hz, 1H, H-6b), 4.02 (ddd, ^3J = 9.3, 5.1, 2.5 Hz, 1H, H-5), 2.47 (t, ^3J = 2.4 Hz, 1H, H-3‘), 2.16 (s, 3H, C-3-O(C=O)CH_3), 2.11 (s, 3H, C-6-O(C=O)CH_3), 2.04 (s, 3H, C-2-O(C=O)CH_3), 1.99 (s, 3H, C-4-O(C=O)CH_3). **^{13}C-NMR** (101 MHz, $CDCl_3$)**:** δ (ppm) = 170.8 (C-6-O(*C*=O)CH_3), 170.1 (C-3-O(*C*=O)CH_3), 170.0 (C-4-O(*C*=O)CH_3), 169.8 (C-2-O(*C*=O)CH_3), 96.4 (C-1), 78.1 (C-2‘), 75.7 (C-3‘), 69.5 (C-2), 69.1 (C-5), 69.1 (C-3), 66.2 (C-4), 62.5 (C-6), 55.1 (C-1‘), 21.0 (C-3-O(C=O)*C*H_3), 20.9 (C-6-O(C=O)*C*H_3), 20.8 (C-2-O(C=O)*C*H_3), 20.8 (C-4-O(C=O)*C*H_3).

Supporting Information

HR-MS (ESI$^+$)**:** calculated for $C_{17}H_{22}O_{10}$ *m/z* = 409.1105 $[M+Na]^+$, found *m/z* = 409.1104 $[M+Na]^+$. R_f = 0.59 (cHex/EtOAc 1:1). **Melting range:** Θ (°C) = 103.0 – 104.5 (EtOAc). **Optical rotation:** $[\alpha]_D^{19}$ = +58.3 ($CHCl_3$). **IR** (ATR)**:** $\tilde{\nu}$ (cm^{-1}) = 3272, 2958, 1747, 1437, 1371, 1224, 1137, 1078, 1050, 982, 919, 797, 691, 601, 450.

The analytical data followed literature data.[7]

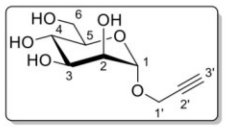

^{1}H-NMR (400 MHz, $CDCl_3$)**:** δ (ppm) = 4.96 (d, ^3J = 1.7 Hz, 1H, H-1), 4.27 (d, ^3J = 2.4 Hz, 2H, H-1'), 3.84 (dd, ^2J = 11.8, ^3J = 2.3 Hz, 1H, H-6a), 3.79 (dd, ^2J = 3.2, 1.7 Hz, 1H, H-2), 3.70 (dd, ^2J = 11.8 Hz, ^3J = 5.9 Hz, 1H, H-6b), 3.67 (dd, ^3J = 9.1, 3.2 Hz, 1H, H-3), 3.62 (t_{app}, ^3J = 9.4 Hz, 1H, H-4), 3.51 (ddd, ^3J = 8.8, 5.9, 2.3 Hz, 1H, H-5), 2.86 (t, ^3J = 2.4 Hz, 1H, H-3'). **^{13}C-NMR** (101 MHz, $CDCl_3$)**:** δ (ppm) = 99.8 (C-1), 80.0 (C-2'), 76.0 (C-3'), 75.1 (C-5), 72.5 (C-3), 72.0 (C-2), 68.5 (C-4), 62.8 (C-6), 54.8 (C-1'). **HR-MS** (ESI$^+$)**:** calculated $C_9H_{14}O_6$ *m/z* = 241.0683 $[M+Na]^+$, found *m/z* = 241.0682 $[M+Na]^+$. R_f = 0.13 (DCM:MeOH 10:1). **Melting range:** Θ (°C) = 119.0 – 120.1 °C (H_2O). **Optical rotation:** $[\alpha]_D^{20}$ = +116.7 ° (MeOH). **IR** (ATR)**:** $\tilde{\nu}$ (cm^{-1}) = 3288, 2929, 2118, 1599, 1351, 1213, 1131, 1058, 1008, 970, 919, 881, 813, 683.

The analytical data followed literature data.[6, 8]

6.1.3 Propargyl 2,4-Di-*O*-benzoyl-α-D-mannopyranoside (2)

The title compound was synthesized utilizing a telescoped two-step protocol according to Scheme S4 following modified synthesis protocols by *Zhang et al.*[9], *Du et al.*[10] and *Ramos-Soriano et al.*[5]

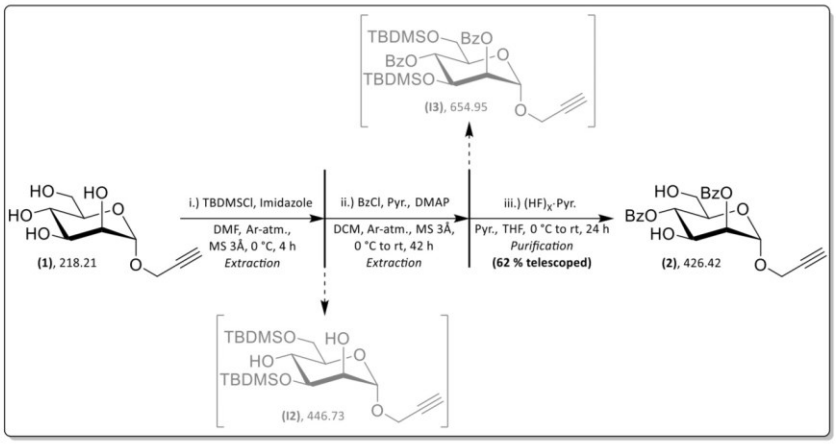

Scheme S4: Telescoped synthesis of Propargyl 2,4-Di-*O*-benzoyl-α-D-mannopyranoside **(2)**.

The first two reaction steps were conducted using oven dried Schlenk flasks equipped with magnetic stirring bars. Compound (**1**) (4.50 g, 20.6 mmol, 1.00 eq.) was dissolved in dry DMF (40.0 mL) under Argon-atmosphere and the solution cooled to a temperature of 0 °C using an ice bath. One after another TBDMSCl (9.43 g, 61.9 mmol, 3.00 eq) and imidazole (8.55 g, 124 mmol, 6.00 eq.) were added. The yellow reaction mixture was stirred for four hours at a temperature of 0 °C until reaction control *via* TLC and HPLC-MS indicated complete consumption of the starting material and product formation. The mixture was diluted with DCM (1 x 500 mL) and washed with a saturated solution of $NaHCO_3$ (1 x 300 mL), with H_2O (2 x 300 mL) and a saturated solution of NaCl (1 x 300 mL). The collected aqueous phases were extracted with DCM (1 x 300 mL). The collected organic phases were dried over anhydrous Na_2SO_4, filtered and all volatiles were removed in vacuo. The first crude intermediate product **(I2)** (8.29 g) was obtained in form of a colorless oil and dissolved in dry pyridine (30.0 mL) under an atmosphere of Argon. Molecular sieves 3 Å (0.50 g) were added and the mixture stirred at

Supporting Information

room temperature for 15 min before DMAP (0.45 g, 4.12 mmol, 0.20 eq.) was added. Subsequently a solution of benzoyl chloride (14.4 g, 11.9 mL, 113 mmol, 5.50 eq.) in dry pyridine (30.0 mL), which had been also stirred for 15 minutes with molecular sieves 3 Å (0.50 g) at room temperature before, was added slowly using a syringe at room temperature under stirring. The colorless reaction mixture was stirred for 24 hours at a temperature of 50 °C under an atmosphere of Argon showing a color change to orange and formation of a colorless precipitation until reaction control *via* TLC and HPLC-MS indicated complete consumption of the starting material. After cooling to room temperature, the mixture was diluted with EtOAc (1 x 500 mL) and washed three times with H_2O (3 x 300 mL). The collected aqueous phases were extracted with EtOAc (1 x 300 mL). The collected organic phases were dried over anhydrous Na_2SO_4, filtered and all volatiles were removed in vacuo. The second crude intermediate product (**I3**) (12.2 g) was obtained as a colorless oil and dissolved in THF (70.0 mL) and AcOH (3.40 mL) was added. The solution was cooled to a temperature of 0°C using an ice bath. Subsequently a 30 % solution of hydrogen fluoride pyridine complex in pyridine (13.0 mL) was added dropwise within 45 minutes at this temperature. After complete addition the reaction mixture was stirred for 24 hours while slowly warming up to room temperature until reaction control *via* TLC and HPLC-MS indicated complete consumption of the starting material. The mixture was diluted with DCM (1 x 100 mL) and washed with a saturated aqueous solution of $NaHCO_3$ (3 x 100 mL). The collected aqueous phases were extracted with DCM (1 x 100 mL). The collected organic phases were dried over anhydrous Na_2SO_4, filtered and all volatiles were removed in vacuo. The final crude product (4.87 g) was obtained in form of a yellow oil. Purification using FCC (^{c}Hex/EtOAc, gradient 0 % to 5 % to 100 % EtOAc) as well as RP-FCC (MeCN/H_2O, gradient 10 % to 100 % MeCN) delivered the desired product (**2**) in form of a colorless foam.

Yield: 5.27 g (12.4 mmol, 60 %), colorless foam.

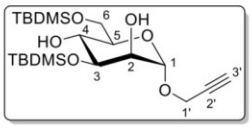

^{1}H-NMR (400 MHz, $CDCl_3$)**:** δ (ppm) = 5.05 (d, ^3J = 1.5 Hz, 1H, H-1), 4.24 (d, ^3J = 2.4 Hz, 2H, H-1‘), 3.91–3.81 (m, 3H, H-3, H-6a, H-6b), 3.79 (ddd, ^3J = 3.7, 1.5, 1.2 Hz, 1H, H-2), 3.73 (td, ^3J = 9.1, 8.6, 2.1 Hz, 1H, H-4), 3.60 (dt, ^3J = 9.1, 5.5 Hz, 1H, H-5), 2.69 (d, ^3J = 2.1 Hz, 1H, C-4-O*H*), 2.60 (d, ^3J = 1.2 Hz, 1H, C-2-O*H*), 2.43 (t, ^4J = 2.4 Hz, 1H, H-3‘), 0.92 (s, 9H, -C-3-O-Si-C(C*H*$_3$)$_3$), 0.90 (s, 9H, -C-6-O-Si-C(C*H*$_3$)$_3$), 0.16 (s, 3H, -C-3-O-Si-C*H*$_3$), 0.14 (s, 3H, -C-3-O-Si-C*H*$_3$), 0.09 (s, 6H, -C-6-O-Si-C*H*$_3$). **^{13}C-NMR** (101 MHz, $CDCl_3$, 25 °C)**:** δ (ppm) = 97.6 (C-1), 79.0 (C-2‘), 74.9 (C-3‘), 73.1 (C-3), 71.2 (C-2), 71.1 (C-5), 70.6 (C-4), 65.0 (C-6), 54.2 (C-1‘), 26.0 (-C-6-O-Si-C(*C*H$_3$)$_3$), 26.0 (-C-3-O-Si-C(*C*H$_3$)$_3$), 18.4 (-C-6-O-Si-*C*(CH$_3$)$_3$), 18.2 (-C-3-O-Si-*C*(CH$_3$)$_3$), - 4.3 (-C-3-O-Si-*C*H$_3$), - 4.7 (-C-3-O-Si-*C*H$_3$), - 5.3 (-C-6-O-Si-*C*H$_3$), - 5.3 (-C-6-O-Si-*C*H$_3$). **HR-MS** (ESI$^+$)**:** calculated for $C_{21}H_{42}O_6Si_2$ *m/z* = 469.2412 [M+Na]$^+$, found *m/z* = 469.2414 [M+Na]$^+$. R_f = 0.41 (^{c}Hex/EtOAc 4:1). **Melting range:** Θ (°C) = 78.5–80.0 (EtOAc). **Optical rotation:** $[\alpha]_D^{20}$ = +58.7 ($CHCl_3$). **IR**(ATR)**:** $\tilde{\nu}$ (cm^{-1}) = 3508, 3312, 2953, 2929, 2858, 1472, 1254, 1215, 1138, 1108, 1048, 1012, 970, 916, 868, 836, 779, 671.

The analytical data followed literature data.[9, 11]

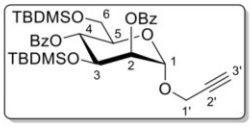

^{1}H-NMR (400 MHz, $CDCl_3$)**:** δ (ppm) = 8.14 – 8.10 (m, 2H, C-2-O(C=O)Ph, H_{ortho}), 8.07 – 8.02 (m, 2H, C-4-O(C=O)Ph, H_{ortho}), 7.61 – 7.54 (m, 2H, H_{para}), 7.50 – 7.41 (m, 4H, H_{meta}), 5.60 (t_{app}, ^3J = 9.8 Hz, 1H, H-4), 5.39 (dd, ^3J = 3.6, 1.8 Hz, 1H, H-2), 5.16 (d, ^3J = 1.8 Hz, 1H, H-1), 4.35 (dd, ^3J = 9.8, 3.6 Hz, 1H, H-3), 4.34 (d, ^3J = 2.4 Hz, -C*H*$_2$-C≡C-H) 3.94 (ddd, ^3J = 9.8, 5.7, 2.8 Hz, 1H, H-5), 3.79 (dd, ^2J = 11.3 Hz, ^3J = 5.7 Hz, 1H, H-6a), 3.75 (dd, ^2J = 11.3 Hz, ^3J = 2.8 Hz, 1H, H-6b), 2.49 (t, ^4J = 2.4 Hz, 1H, H-3’), 0.86 (s, 9H, -C-6-O-Si-C(C*H*$_3$)$_3$), 0.61 (s, 9H, -C-3-O-Si-C(C*H*$_3$)$_3$), 0.04 (s, 3H, -C-3-O-Si-C*H*$_3$), 0.00 (s, 3H, -C-6-O-Si-C*H*$_3$), -0.01 (s, 3H, -C-6-O-Si-C*H*$_3$), -0.15 (s, 3H, -C-3-O-Si-C*H*$_3$). **^{13}C-NMR** (101 MHz, $CDCl_3$)**:** δ (ppm) = 166.0 (C-2-O(*C*=O)Ph), 165.3 (C-4-O(*C*=O)Ph), 133.3 (C-2-O(C=O)Ph, C_{para}), 133.2 (C-4-O(C=O)Ph, C_{para}), 130.1 (C-2-O(C=O)Ph, C_{ortho}), 130.0 (C-2-O(C=O)Ph, C_{ipso}), 129.9 (C-4-O(C=O)Ph, C_{ipso}),

129.9 (C-4-O(C=O)Ph, C_{ortho}), 128.6 (C-2-O(C=O)Ph, C_{meta}), 128.5 (C-4-O(C=O)Ph, C_{meta}), 96.2 (C-1), 78.6 (-CH_2-*C*≡C-H), 75.4 (-CH_2-C≡*C*-H), 72.6 (C-2), 72.3 (C-5), 70.1 (C-4), 69.1 (C-3), 62.9 (C-6), 54.4 (-*C*H_2-C≡C-H), 26.0 (-C-6-O-Si-C(*C*H_3)$_3$), 25.4 (-C-3-O-Si-C(*C*H_3)$_3$), 18.4 (-C-6-O-Si-*C*(CH_3)$_3$), 17.7 (-C-3-O-Si-*C*(CH_3)$_3$), - 4.60 (-C-3-O-Si-*C*H_3), - 4.98 (-C-3-O-Si-*C*H_3), - 5.28 (-C-6-O-Si-*C*H_3), - 5.33 (-C-6-O-Si-*C*H_3). **HR-MS** (ESI$^+$)**:** calculated for $C_{35}H_{50}O_8Si_2$ *m/z* = 677.2936 [M+Na]$^+$, *m/z* = 677.2929 [M+Na]$^+$. R_f = 0.53 (^{c}Hex/EtOAc 10:1). **Optical rotation:** $[\alpha]_D^{20}$ = -10.4 ($CHCl_3$). **IR**(ATR)**:** $\tilde{\nu}$ (cm^{-1}) = 2929, 2857, 1728, 1602, 1452, 1389, 1361, 1323, 1261, 1108, 1062, 1028, 990, 878, 837, 778, 710, 677.

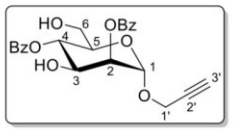

^{1}H-NMR (400 MHz, $CDCl_3$)**:** δ (ppm) = 8.15 – 8.04 (m, 4H, H_{ortho}), 7.65 – 7.56 (m, 2H, H_{para}), 7.52 – 7.42 (m, 4H, H_{meta}), 5.52 (t, ^3J = 10.0 Hz, 1H, H-4), 5.45 (dd, ^3J = 3.5, 1.7 Hz, 1H, H-2), 5.25 (d, ^3J = 1.7 Hz, 1H, H-1), 4.44 (dd, ^3J = 9.9, 3.5 Hz, 1H, H-3), 4.33 (d, ^4J = 2.4 Hz, 2H, H-1'), 4.00 (ddd, ^3J = 10.1, 4.2, 2.3 Hz, 1H, H-5), 3.82 (dd, ^2J = 12.7 Hz, ^3J = 2.3 Hz, 1H, H-6a), 3.74 (d, ^2J = 12.7 Hz, ^3J = 4.2 Hz, 1H), 2.51 (t, ^4J = 2.4 Hz, 1H, H-3'). **^{13}C-NMR** (101 MHz, $CDCl_3$)**:** δ (ppm) = 167.3 (C-4-O(*C*=O)Ph), 166.0 (C-2-O(*C*=O)Ph), 133.8 (C_{para}), 133.6 (C_{para}), 129.9 (C_{ortho}), 129.1 (C_{ipso}), 129.0 (C_{ipso}), 128.6 (C_{meta}), 128.6 (C_{meta}), 96.6 (C-1), 78.3 (C-2'), 75.5 (C-3'), 72.6 (C-2), 71.1 (C-5), 70.2 (C-4), 68.6 (C-3), 61.3 (C-6), 55.3 (C-1'). **HR-MS** (ESI$^+$)**:** calculated for $C_{23}H_{22}O_8$ *m/z* = 449.1207, found *m/z* = 449.1206. **Optical rotation:** $[\alpha]_D^{20}$ = -16.2 ($CHCl_3$). R_f = 0.30 (^{c}Hex/EtOAc 2:1). **IR**(ATR)**:** $\tilde{\nu}$ (cm^{-1}) = 3491, 3297, 2927, 1720, 1602, 1452, 1318, 1265, 1178, 1114, 1069, 1027, 1012, 971, 912, 794, 711, 686.

The analytical data followed literature data.[8]

6.1.4 Phenyl 2,3,4,6-Tetra-*O*-acetyl-1-thio-α-D-mannopyranoside (3)

The compound was synthesized according to Scheme S5 following a synthesis protocol by *Ekholm et al.*[12]

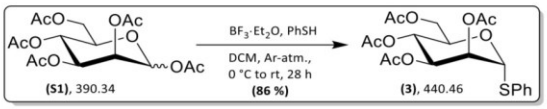

Scheme S5: Synthesis of Phenyl 2,3,4,6-Tetra-*O*-acetyl-1-thio-α-D-Mannopyranoside **(3)**.

The reaction was conducted using an oven dried Schlenk flask equipped with a magnetic stirring bar. Compound (**S1**) (10.8 g, 27.8 mmol, 1.00 eq.) was dissolved in dry DCM (40.0 mL) under an atmosphere of Argon and molecular sieves 3Å (1.00 g) were added. Thiophenol (4.90 g, 4.54 mL, 44.5 mmol, 1.60 eq.) was added using a syringe. The brown mixture was stirred at room temperature for 30 minutes and then cooled to a temperature of 0 °C using an ice bath. $BF_3{\cdot}OEt_2$ (19.7 g, 17.6 mL, 139 mmol, 5.00 eq.) was added dropwise using a syringe. The resulting yellow reaction mixture was stirred for 24 hours, while slowly warming up to room temperature, showing a color change to deep red until reaction control *via* TLC and HPLC-MS indicated complete consumption of the starting material and product formation. The mixture was diluted with DCM (1 x 100 mL) and poured into ice cooled H_2O (1 x 150 mL) with stirring. The separated organic phase was washed with a saturated aqueous solution of $NaHCO_3$ (1 100 mL), separated again and poured into an ice cooled 1M solution of NaOH (1 x 150 mL) with vigorous stirring. After stirring at 0 °C for one hour, the organic phase was separated and washed again with a saturated aqueous solution of $NaHCO_3$ (1 x 150 mL), a 1 M solution of NaOH (1 x 150 mL) and finally a saturated solution of NaCl (1 x 150 mL). The separated organic layer was dried over anhydrous Na_2SO_4, filtered and all volatiles were removed in vacuo to afford the crude product in form of an orange oil. Purification using FCC (^{c}Hex/EtOAc, isocratic with 33 % EtOAc) delivered the desired product (**3**) in form of a colorless solid.

Supporting Information

Yield: 10.5 g (23.8 mmol, 86 %), colorless solid.

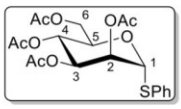

^{1}H-NMR (400 MHz, $CDCl_3$)**:** δ (ppm) = 7.51–7.47 (m, 2H, C-1-S-Ph, H_{ortho}), 7.35 – 7.28 (m, 3H, C-1-S-Ph, H_{meta}, H_{para}), 5.55 (dd, ^3J = 3.1, 1.6 Hz, 1H, H-2), 5.49 (d, ^3J = 1.6 Hz, 1H, H-1), 5.33 (dd, ^3J = 9.9, 9.8 Hz, 1H, H-4), 5.32 (dd, ^3J = 9.8, 3.1 Hz, 1H, H-3), 4.55 (ddd, ^3J = 9.9, 5.9, 2.4 Hz, 1H, H-5), 4.31 (dd, ^2J = 12.2, ^3J = 5.9 Hz, 1H, H-6a), 4.10 (dd, ^2J = 12.2, ^3J = 2.4 Hz, 1H, H-6b), 2.15 (s, 3H, C-4-O(C=O)CH_3), 2.07 (s, 3H, C-6-O(C=O)CH_3), 2.05 (s, 3H, C-3-O(C=O)CH_3), 2.02 (s, 3H, C-2-O(C=O)CH_3). **^{13}C-NMR** (101 MHz, $CDCl_3$)**:** δ (ppm) = 170.5 (C-6-O(*C*=O)CH_3), 169.9 (C-3-O(*C*=O)CH_3), 169.8 (C-4-O(*C*=O)CH_3), 169.7 (C-2-O(*C*=O)CH_3), 132.6 (C-1-S-Ph, C_{ipso}), 132.1 (C-1-S-Ph, C_{ortho}), 129.2 (C-1-S-Ph, C_{meta}), 128.1 (C-1-S-Ph, C_{para}), 85.7 (C-1), 70.9 (C-2), 69.5 (C-5) 69.4 (C-3), 66.4 (C-4), 62.5 (C-6), 20.9 (C-4-O(C=O)*C*H_3), 20.7 (C-6-O(C=O)*C*H_3), 20.7 (C-3-O(C=O)*C*H_3), 20.7 (C-2-O(C=O)*C*H_3). **HR-MS** (ESI$^+$)**:** calculated for $C_{20}H_{24}O_9S$ *m/z* = 463.1033 $[M+Na]^+$, found *m/z* = 463.1031 $[M+Na]^+$. R_f = 0.33 (^{c}Hex/EtOAc 2:1). **Melting range:** Θ (°C) = 79.5 – 81.1 (EtOAc). **Optical rotation:** $[\alpha]_D^{21}$ = +104 ($CHCl_3$). **IR** (ATR)**:** $\tilde{\nu}$ (cm^{-1}) = 1745, 1440, 1369, 1221, 1106, 1050, 976, 915, 749, 692.

The analytical data followed literature data.[8]

6.1.5 Propargyl 2,4-Di-*O*-benzoyl-3,6-di-*O*-(2,3,4,6-tetra-*O*-acetyl-α-D-mannopyranosyl)-α-D-mannopyranoside (4)

The compound was synthesized according to Scheme S6 following a modified synthesis protocol by *Krumb et al.*[13]

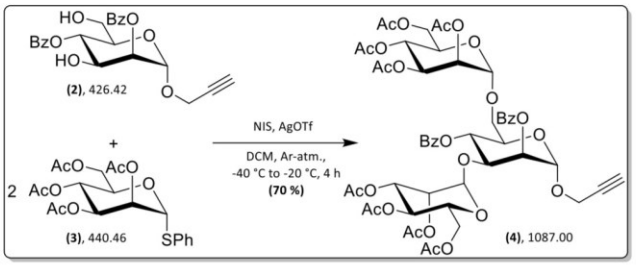

Scheme S6: Synthesis of Propargyl 2,4-Di-*O*-benzoyl-3,6-di-*O*-(2,3,4,6-tetra-*O*-acetyl-α-D-manno¬pyran¬osyl)-α-D-manno¬pyranoside (**4**).

The reaction was conducted using an oven dried Schlenk flask equipped with a magnetic stirring bar. Compound (**2**) (0.10 g, 0.23 mmol, 1.00 eq.) and compound (**3**) (0.31 g, 0.70 mmol, 3.00 eq.) were co-evaporated with dry toluene (3 x 5.00 mL), dried in high vacuum for 30 minutes and then dissolved in dry DCM (2.00 mL) under an atmosphere of Argon. Molecular sieves 3 Å (0.10 g) were added and the solution stirred at room temperature for 30 minutes. Subsequently the reaction mixture was cooled to a temperature of -40°C using a cryostat. Silver triflate (0.03 g, 0.11 mmol, 0.45 eq.) dissolved in dry toluene (0.50 mL) was added followed by the addition of *N*-iodosuccinimide (0.24 g, 1.06 mmol, 4.50 eq.). The solution was slowly warmed up to a temperature of -20°C within two hours showing a color change to deep red and stirred at this temperature for another two hours until reaction control *via* TLC and HPLC-MS indicated complete consumption of glycosyl acceptor (**2**) and product formation. The reaction was quenched by the addition of NEt_3 (0.07 g, 0.10 mL, 0.69 mmol, 3.00 eq.). The mixture was filtered over *Celite*, which was washed thoroughly with DCM (1 x 100 mL). The organic phase was washed with a saturated solution of $Na_2S_2O_3$ (2 x 100 mL), with a saturated solution of $NaHCO_3$ (2 x 100 mL) and with a saturated solution of NaCl (1 x 100 mL). The collected organic phases were dried over anhydrous Na_2SO_4, filtered and all volatiles were removed in vacuo. The crude product (0.53 g) was obtained in form of a brown oil. Purification using FCC (^{c}Hex/EtOAc, gradient 0 % to 5 %

to 100 % EtOAc) as well as RP-FCC (MeCN/H_2O, gradient 10 % to 100 % MeCN) delivered the desired product (**4**) in form of a colorless foam.

Yield: 0.17 g (0.16 mmol, 70 %), colorless foam.

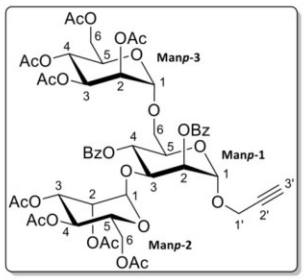

^{1}H-NMR (600 MHz, $CDCl_3$)**:** δ (ppm) = 8.17 – 8.13 (m, 2H, C-2$_{Manp\text{-}1}$-O(C=O)Ph, H_{ortho}), 8.05 – 8.00 (m, 2H, C-4$_{Manp\text{-}1}$-O(C=O)Ph, H_{ortho}), 7.65 – 7.61 (m, 1H, C-2$_{Manp\text{-}1}$-O(C=O)Ph, H_{para}), 7.60 – 7.57 (m, 1H, C-4$_{Manp\text{-}1}$-O(C=O)Ph, H_{para}), 7.56 – 7.52 (m, 2H, C-2$_{Manp\text{-}1}$-O(C=O)Ph, H_{meta}), 7.47 – 7.43 (m, 2H, C-4$_{Manp\text{-}1}$-O(C=O)Ph, H_{meta}), 5.63 (t_{app}, ^3J = 10.0 Hz, 1H, H-4$_{Manp\text{-}1}$), 5.54 (dd, ^3J = 3.5, 1.8 Hz, 1H, H-2$_{Manp\text{-}1}$), 5.33 (dd, ^3J = 10.1, 3.4 Hz, 1H, H-3$_{Manp\text{-}3}$), 5.24 (d, ^3J = 1.8 Hz, 1H, H-1$_{Manp\text{-}1}$), 5.27 – 5.21 (m, 2H, H-2$_{Manp\text{-}3}$, H-4$_{Manp\text{-}3}$), 5.11 – 5.06 (dd, 2H, H-3$_{Manp\text{-}2}$, H-4$_{Manp\text{-}2}$), 4.97 (d, ^3J = 1.9 Hz, 1H, H-1$_{Manp\text{-}2}$), 4.88 – 4.85 (m, 1H, H-2$_{Manp\text{-}2}$), 4.80 (d, ^3J = 1.8 Hz, 1H, H-1$_{Manp\text{-}3}$), 4.49 (dd, ^3J = 9.8, 3.4 Hz, 1H, H-3$_{Manp\text{-}1}$), 4.36 (d, ^4J = 2.4 Hz, 2H, H-1‘), 4.22 – 4.13 (m, 3H, H-5$_{Manp\text{-}1}$, H-6a$_{Manp\text{-}2}$, H-6a$_{Manp\text{-}3}$), 4.11 (ddd, ^3J = 9.4, 5.7, 1.8 Hz, 1H, H-5$_{Manp\text{-}2}$), 4.06 (ddd, ^3J = 10.2, 5.5, 2.1 Hz, 1H, H-5$_{Manp\text{-}3}$), 4.01 (ddd, ^2J = 12.2, ^3J = 5.7, 2.0 Hz, 2H, H-6b$_{Manp\text{-}2}$, H-6b$_{Manp\text{-}3}$), 3.90 (dd, ^2J = 10.8 Hz, ^3J = 6.8 Hz, 1H, H-6a$_{Manp\text{-}1}$), 3.61 (dd, ^2J = 10.8 Hz, ^3J = 2.2 Hz, 1H, H-6b$_{Manp\text{-}1}$), 2.55 (t, ^4J = 2.4 Hz, 1H, H-3‘), 2.14 (s, 3H, C-6$_{Manp\text{-}3}$-O(C=O)CH_3), 2.11 (s, 3H, C-4$_{Manp\text{-}3}$-O(C=O)CH_3), 2.04 (s, 3H, C-3$_{Manp\text{-}3}$-O(C=O)CH_3), 1.98 (s, 3H, C-3$_{Manp\text{-}2}$-O(C=O)CH_3), 1.94 (s, 3H, C-6$_{Manp\text{-}2}$-O(C=O)CH_3), 1.94 (s, 3H, C-4$_{Manp\text{-}2}$-O(C=O)CH_3), 1.84 (s, 3H, C-2$_{Manp\text{-}3}$-O(C=O)CH_3), 1.82 (s, 3H, C-2$_{Manp\text{-}2}$-O(C=O)CH_3). **^{13}C-NMR** (151 MHz, $CDCl_3$)**:** δ (ppm) = 170.8 (C-6$_{Manp\text{-}2}$-O(*C*=O)CH$_3$), 170.6 (C-6$_{Manp\text{-}3}$-O(*C*=O)CH$_3$), 170.0 (C-4$_{Manp\text{-}3}$-O(*C*=O)CH$_3$), 169.8 (C-3$_{Manp\text{-}3}$-O(*C*=O)CH$_3$), 169.8 (C-3$_{Manp\text{-}2}$-O(*C*=O)CH$_3$), 169.7 (C-4$_{Manp\text{-}2}$-O(*C*=O)CH$_3$), 169.1 (C-2$_{Manp\text{-}3}$-O(*C*=O)CH$_3$), 169.1 (C-2$_{Manp\text{-}2}$-O(*C*=O)CH$_3$), 165.9 (C-2$_{Manp\text{-}1}$-O(*C*=O)Ph), 165.2 (C-4$_{Manp\text{-}1}$-O(*C*=O)Ph), 133.7 (C-2$_{Manp\text{-}1}$-O(C=O)Ph, C_{para}), 133.6 (C-4$_{Manp\text{-}1}$-O(C=O)Ph, C_{para}), 130.0 (C-2$_{Manp\text{-}1}$-O(C=O)Ph, C_{ortho}), 129.9 (C-4$_{Manp\text{-}1}$-O(C=O)Ph, C_{ortho}), 129.0 (C-2$_{Manp\text{-}1}$-O(C=O)Ph, C_{ipso}), 128.8 (C-2$_{Manp\text{-}1}$-O(C=O)Ph, C_{meta}), 128.6 (C-4$_{Manp\text{-}1}$-O(C=O)Ph, C_{ipso}), 128.5 (C-4$_{Manp\text{-}1}$-O(C=O)Ph, C_{meta}), 99.4 (C-1$_{Manp\text{-}2}$), 97.2 (C-1$_{Manp\text{-}3}$), 96.1 (C-1$_{Manp\text{-}1}$), 78.0 (C-2‘), 75.7 (C-3‘), 74.9 (C-3$_{Manp\text{-}1}$), 71.5 (C-2$_{Manp\text{-}1}$), 70.0 (C-5$_{Manp\text{-}1}$), 69.3 (C-5$_{Manp\text{-}2}$, C-2$_{Manp\text{-}3}$), 69.2 (C-2$_{Manp\text{-}2}$), 69.0 (C-3$_{Manp\text{-}3}$), 68.7 (C-4$_{Manp\text{-}1}$), 68.6 (C-5$_{Manp\text{-}3}$), 68.2 (C-3$_{Manp\text{-}2}$), 66.7 (C-6$_{Manp\text{-}1}$), 66.0 (C-4$_{Manp\text{-}2}$), 65.8 (C-4$_{Manp\text{-}3}$), 62.4 (C-6$_{Manp\text{-}2}$), 62.3 (C-6$_{Manp\text{-}3}$), 55.0 (C-1‘), 20.9 (C-4$_{Manp\text{-}3}$-O(C=O)*C*H$_3$), 20.8 (C-6$_{Manp\text{-}3}$-O(C=O)*C*H$_3$), 20.8 (C-3$_{Manp\text{-}3}$-O(C=O)*C*H$_3$), 20.7 (C-6$_{Manp\text{-}2}$-O(C=O)*C*H$_3$), 20.7 (C-3$_{Manp\text{-}2}$-O(C=O)*C*H$_3$), 20.6 (C-4$_{Manp\text{-}2}$-O(C=O)*C*H$_3$), 20.5 (C-2$_{Manp\text{-}2}$-O(C=O)*C*H$_3$), 20.5 (C-2$_{Manp\text{-}3}$-O(C=O)*C*H$_3$). **HR-MS** (ESI$^+$)**:** calculated for $C_{51}H_{58}O_{26}$ *m/z* = 1109.3117, found *m/z* = 1109.3117. **Optical rotation:** $[\alpha]_D^{20}$ = + 12.0 ($CHCl_3$). R_f = 0.19 (^{c}Hex/EtOAc 1:1). **IR**(ATR)**:** $\tilde{\nu}$ (cm^{-1}) = 3278, 2948, 1750, 1602, 1452, 1370, 1319, 1225, 1139, 1046, 981, 916, 715, 601, 486, 441.

6.1.6 1,11-Di[(p-toluenesulfonyl)oxy]-3,6,9-trioxaundecane (S2)

The compound was synthesized according to Scheme S7 following syntheses protocols by *Bonger et al.*[14] and *Krumb et al.*[13]

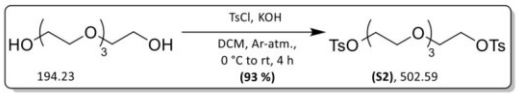

Scheme S7: Synthesis of 1,11-Di[(*p*-toluenesulfonyl)oxy]-3,6,9-trioxaundecane (**S2**).

The reaction was conducted using an oven dried Schlenk flask equipped with a magnetic stirring bar. Tetraethylenglycol (22.5 g, 20.1 mL, 116 mmol, 1.00 eq.) was stirred in high vacuum for 30 minutes and subsequently dissolved in dry DCM (110 mL) under an atmosphere of Argon. The mixture was

cooled to a temperature of 0 °C using an ice bath. Then *p*-TsCl (53.1 g, 279 mmol, 2.40 eq.) was added and the reaction mixture stirred for 15 minutes while warming to room temperature until the reagent was completely dissolved. The mixture was again cooled to a temperature of 0 °C using an ice bath and pulverized KOH (50.8 g, 905 mmol, 7.80 eq.) was added portion wise within 10 minutes so that only mild boiling occurred. Upon complete addition the resulting cloudy solution was stirred for four hours while slowly warming up to room temperature with formation of a colorless precipitation occurring. The reaction mixture was stirred until reaction control *via* TLC and HPLC-MS indicated complete consumption of the substrate and product formation. The reaction mixture was diluted with DCM (1 x 150 mL) and then ice cooled H_2O (1 x 300 mL) was added. The separated aqueous phase was extracted with DCM (3 x 50.0 mL). The collected organic phases were washed with H_2O (1 x 200 mL) and a saturated solution of NaCl (1 x 200 mL), dried over anhydrous Na_2SO_4, filtered and all volatiles were removed in vacuo. The crude product (56.1 g) was obtained in form of a yellow oil. Purification using FCC (ᶜHex/EtOAc, gradient 0 % to 40 % to 100 % EtOAc) delivered the desired product (**S2**) in form of a colorless oil.

Yield: 54.1 g (108 mmol, 93 %), colorless oil.

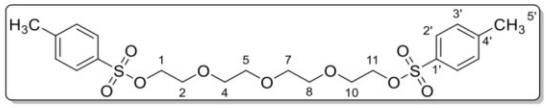

^{1}H-NMR (400 MHz, $CDCl_3$)**:** δ (ppm) = 7.79 – 7.73 (m, 4H, H-2‘), 7.34 – 7.30 (m, 4H, H-3‘), 4.14 – 4.11 (m, 4H, H-1, H-11), 3.66 – 3.64 (m, 4H, H-2, H-10), 3.56 – 3.51 (m, 8H, H-4, H-5, H-7, H-8), 2.42 (s, 6H, H-5‘). **^{13}C-NMR** (101 MHz, $CDCl_3$)**:** δ (ppm) = 144.9 (C-4‘), 133.0 (C-1‘), 129.9 (C-3‘), 128.0 (C-2‘), 70.7 (C-5, C-7), 70.6 (C-4, C-8), 69.3 (C-2, C-10), 68.7 (C-1, C-11), 21.7 (C-5‘). **HR-MS** (ESI^+)**:** calculated for $C_{22}H_{30}O_9S_2$ *m/z* = 525.1223 $[M+Na]^+$, found *m/z* = 525.1221 $[M+Na]^+$. R_f = 0.25 (ᶜHex/EtOAc 1:1). **IR**(ATR)**:** $\tilde{\nu}$ (cm^{-1}) = 2874, 1598, 1452, 1353, 1293, 1248, 1189, 1175, 1097, 1016, 921, 817, 776, 664, 583, 554.

The analytical data followed literature data.[13, 14]

6.1.7 1,11-Diazido-3,6,9-trioxaundecane (5)

The compound was synthesized according to Scheme S8 following syntheses protocols by *Davila et al.*[15] and *Krumb et al.*[13]

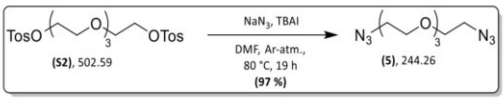

Scheme S8: Synthesis of 1,11-Diazido-3,6,9-trioxaundecane **(5)**.

The reaction was conducted using an oven dried Schlenk flask equipped with a magnetic stirring bar. Compound (**S2**) (54.1 g, 108 mmol, 1.00 eq.) was dissolved in dry DMF (225 mL) under an atmosphere of Argon. NaN_3 (17.5 g, 270 mmol, 2.50 eq.) and TBAI (2.00 g, 5.40 mmol, 0.05 eq.) were added one after the other. The yellow reaction mixture was stirred for 19 hours at a temperature of 80 °C with formation of a colorless precipitate occurring until reaction control *via* TLC and HPLC-MS indicated complete consumption of the substrate and product formation. The mixture was filtered over *Celite* and thoroughly eluted with Et_2O (1 x 150 mL). All volatile components were removed in vacuum and then high vacuum. The obtained residue was co-evaporated for three times with toluene (3 x 50.0 mL), then dissolved in Et_2O (1 x 50 mL) and again filtered over *Celite*, to remove undissolved salts. All volatile components were removed in vacuo and the desired product (**5**) was obtained in form of a yellow oil.

Yield: 25.5 g (104 mmol, 97 %), yellow oil.

Supporting Information

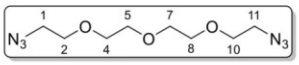

^{1}H-NMR (300 MHz, $CDCl_3$)**:** δ (ppm) = 3.72 – 3.63 (m, 12H, H-2, H-4, H-5, H-7, H-8, H-10), 3.38 (t, ^3J = 5.1 Hz, 4H, H-1, H-11). **^{13}C-NMR** (75.5 MHz, $CDCl_3$)**:** δ (ppm) = 70.8 (C-4, C-5, C-7, C-8), 70.2 (C-2, C-10), 50.8 (C-1, C-11). **HR-MS** (ESI^+)**:** calculated for $C_8H_{16}N_6O_3$ *m/z* = 267.1176, found *m/z* = 267.1175. R_f = 0.37 (cHex/EtOAc 2:1). **IR**(ATR)**:** $\tilde{\nu}$ (cm^{-1}) = 2868, 2097, 1443, 1346, 1285, 1122, 992, 936, 853, 648, 556, 436, 419.

The analytical data followed literature data.[8]

6.1.8 (1-(11-Azido-3,6,9-trioxaundec-1-yl)-1*H*-1,2,3-triazol-4-yl)-methyl 2,4-Di-*O*-benzoyl-3,6-di-*O*-(2,3,4,6-tetra-*O*-acetyl-α-D-mannopyranosyl)-α-D-mannopyranoside (6)

The compound was synthesized according to Scheme S9 following a modified synthesis protocol by *Kramer et al.*[8]

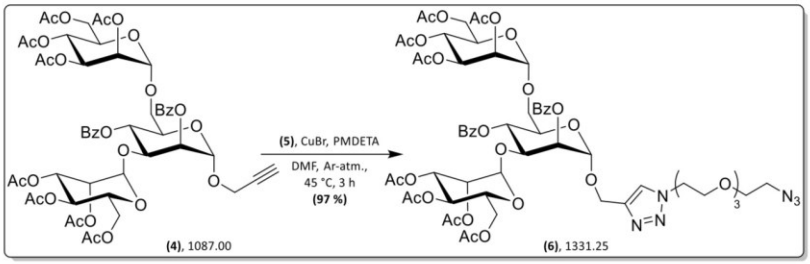

Scheme S9: Synthesis of (1-(11-Azido-3,6,9-trioxaundec-1-yl)-1*H*-1,2,3-triazol-4-yl)-methyl 2,4-Di-*O*-benzoyl-3,6-di-*O*-(2,3,4,6-tetra-*O*-acetyl-α-D-mannopyranosyl)-α-D-mannopyranoside (**6**).

The reaction was conducted using an oven dried Schlenk flask equipped with a magnetic stirring bar. Compound (**4**) (0.50 g, 0.46 mmol, 1.00 eq.) and compound (**5**) (1.69 g, 6.90 mmol, 15.0 eq.) were dissolved in dry DMF (45.0 mL), which was degassed using ultrasonication while introducing a stream of Argon gas. The solution again was degassed by conducting three freeze-pump-thaw-cycles. Subsequently PMDTA (0.07 g, 0.08 mL, 0.39 mmol, 0.85 eq.) was added, and the mixture warmed to a temperature of 45 °C followed by the addition of Cu(I)Br (0.03 g, 0.23 mmol, 0.50 eq.) against a flow of Argon. The resulting turquoise reaction mixture was stirred for three hours at a temperature of 45 °C until reaction control *via* TLC and HPLC-MS indicated complete consumption of compound (**4**) and product formation. The reaction mixture was allowed to cool to room temperature and diluted with EtOAc (1 x 100 mL). The organic layer was washed with a saturated aqueous solution of NH_4Cl (2 x 50.0 mL). The aqueous phase was diluted with H_2O (1 x 50.0 mL) to dissolve the precipitated salts and extracted with EtOAc (1 x 50.0 mL). The combined organic layers were dried over anhydrous Na_2SO_4, filtered and all volatile components were removed in high vacuum. The crude product (2.56 g) was obtained in form of a yellow liquid. Purification using FCC (cHex/EtOAc, gradient 0 % to 100 % EtOAc) delivered the desired product (**6**) in form of a colorless oil. Additional compound (**7**) (1.44 g, 5.90 mmol, 12.8 eq.) was recovered corresponding to a recovery rate of 92 % of the employed linker structure.

Yield: 0.60 g (0.45 mmol, 97 %), colorless oil.

Supporting Information

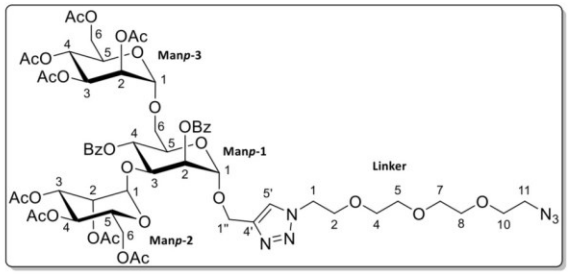

^{1}H-NMR (600 MHz, $CDCl_3$)**:** δ (ppm) = 8.16 – 8.13 (m, 2H, C-2$_{Manp\text{-}1}$-O(C=O)Ph, H$_{ortho}$), 8.04 – 8.01 (m, 2H, C-4$_{Manp\text{-}1}$-O(C=O)Ph, H$_{ortho}$), 7.85 (s, 1H, H-5‘), 7.64 – 7.60 (m, 1H, C-2$_{Manp\text{-}1}$-O(C=O)Ph, H$_{para}$), 7.60 – 7.57 (m, 1H, C-4$_{Manp\text{-}1}$-O(C=O)Ph, H$_{para}$), 7.57 – 7.53 (m, 2H, C-2$_{Manp\text{-}1}$-O(C=O)Ph, H$_{meta}$), 7.46 – 7.42 (m, 2H, C-4$_{Manp\text{-}1}$-O(C=O)Ph, H$_{meta}$), 5.70 (t_{app}, ^3J = 10.0 Hz, 1H, H-4$_{Manp\text{-}1}$), 5.52 (dd, ^3J = 3.4, 1.8 Hz, 1H, H-2$_{Manp\text{-}1}$), 5.34 (dd, ^3J = 10.1, 3.5 Hz, 1H, H-3$_{Manp\text{-}3}$), 5.28 (dd, ^3J = 3.5, 1.7 Hz, 1H, H-2$_{Manp\text{-}3}$), 5.25 (t_{app}, ^3J = 10.1 Hz, 1H, H-4$_{Manp\text{-}3}$), 5.17 (d, ^3J = 1.8 Hz, 1H, H-1$_{Manp\text{-}1}$), 5.10 – 5.04 (m, 2H, H-3$_{Manp\text{-}2}$, H-4$_{Manp\text{-}2}$), 4.94 (d, ^3J = 1.9 Hz, 1H, H-1$_{Manp\text{-}2}$), 4.89 (d, ^2J = 12.1 Hz, 1H, H-1$_a$‘‘), 4.86 (d, ^3J = 1.7 Hz, 1H, H-1$_{Manp\text{-}3}$), 4.85 (dd, ^3J = 3.0, 1.9 Hz, 1H, H-2$_{Manp\text{-}2}$), 4.72 (d, ^2J = 12.1 Hz, 1H, H-1$_b$‘‘), 4.58 (t, ^3J = 5.2 Hz, 2H, H-1), 4.46 (dd, ^3J = 10.0, 3.4 Hz, 1H, H-3$_{Manp\text{-}1}$), 4.25 (ddd, ^3J = 10.0, 6.1, 2.3 Hz, 1H, H-5$_{Manp\text{-}1}$), 4.18 – 4.12 (m, 2H, H-6a$_{Manp\text{-}2}$, H-6a$_{Manp\text{-}3}$), 4.08 – 4.03 (m, 2H, H-5$_{Manp\text{-}2}$, H-5$_{Manp\text{-}3}$), 3.97 (dd, ^2J = 12.2, ^3J = 2.1 Hz, 1H, H-6b$_{Manp\text{-}3}$), 3.96 – 3.93 (m, 2H, H-6a$_{Manp\text{-}1}$, H-6b$_{Manp\text{-}2}$), 3.93 – 3.89 (m, 2H, H-2), 3.69 – 3.59 (m, 11H, H-6b$_{Manp\text{-}1}$, H-4, H-5, H-7, H-8, H-10), 3.38 (t, ^3J = 5.0 Hz, 2H, H-11), 2.11 (s, 3H, C-2$_{Manp\text{-}3}$-O(C=O)CH_3), 2.04 (s, 3H, C-4$_{Manp\text{-}3}$-O(C=O)CH_3), 2.03 (s, 3H, C-6$_{Manp\text{-}3}$-O(C=O)CH_3), 1.96 (s, 3H, C-3$_{Manp\text{-}3}$-O(C=O)CH_3), 1.93 (s, 3H, C-6$_{Manp\text{-}2}$-O(C=O)CH_3), 1.92 (s, 3H, C-4$_{Manp\text{-}2}$-O(C=O)CH_3), 1.84 (s, 3H, C-2$_{Manp\text{-}2}$-O(C=O)CH_3), 1.81 (s, 3H, C-3$_{Manp\text{-}2}$-O(C=O)CH_3). **^{13}C-NMR** (151 MHz, $CDCl_3$)**:** δ (ppm) = 170.7 (C-6$_{Manp\text{-}2}$-O(*C*=O)CH$_3$), 170.6 (C-6$_{Manp\text{-}3}$-O(*C*=O)CH$_3$), 169.9 (C-2$_{Manp\text{-}3}$-O(*C*=O)CH$_3$), 169.9 (C-4$_{Manp\text{-}3}$-O(*C*=O)CH$_3$), 169.8 (C-4$_{Manp\text{-}2}$-O(*C*=O)CH$_3$), 169.6 (C-3$_{Manp\text{-}3}$-O(*C*=O)CH$_3$), 169.1 (C-2$_{Manp\text{-}2}$-O(*C*=O)CH$_3$), 169.1 (C-3$_{Manp\text{-}2}$-O(*C*=O)CH$_3$), 165.9 (C-2$_{Manp\text{-}1}$-O(*C*=O)Ph), 165.2 (C-4$_{Manp\text{-}1}$-O(*C*=O)Ph), 142.9 (C-4‘), 133.6 (C-2$_{Manp\text{-}1}$-O(C=O)Ph, C$_{para}$), 133.6 (C-4$_{Manp\text{-}1}$-O(C=O)Ph, C$_{para}$), 130.0 (C-2$_{Manp\text{-}1}$-O(C=O)Ph, C$_{ortho}$), 129.9 (C-4$_{Manp\text{-}1}$-O(C=O)Ph, C$_{ortho}$), 129.1 (C-4$_{Manp\text{-}1}$-O(C=O)Ph, C$_{ipso}$), 128.8 (C-2$_{Manp\text{-}1}$-O(C=O)Ph, C$_{meta}$), 128.7 (C-2$_{Manp\text{-}1}$-O(C=O)Ph, C$_{ipso}$), 128.5 (C-4$_{Manp\text{-}1}$-O(C=O)Ph, C$_{meta}$), 124.5 (C-5‘), 99.4 (C-1$_{Manp\text{-}2}$), 97.3 (C-1$_{Manp\text{-}3}$), 96.7 (C-1$_{Manp\text{-}1}$), 75.5 (C-3$_{Manp\text{-}1}$), 71.6 (C-2$_{Manp\text{-}1}$), 70.7 (-*C*H$_2$O-), 70.6 (-*C*H$_2$O-), 70.6 (-*C*H$_2$O-), 70.5 (-*C*H$_2$O-), 70.1 (-*C*H$_2$O-), 69.4 (C-5$_{Manp\text{-}1}$), 69.4 (C-2), 69.3 (C-5$_{Manp\text{-}2}$), 69.2 (C-2$_{Manp\text{-}3}$), 69.2 (C-2$_{Manp\text{-}2}$), 69.2 (C-3$_{Manp\text{-}3}$), 68.6 (C-5$_{Manp\text{-}3}$), 68.2 (C-3$_{Manp\text{-}2}$), 66.5 (C-6$_{Manp\text{-}1}$), 65.9 (C-4$_{Manp\text{-}2}$), 65.8 (C-4$_{Manp\text{-}3}$), 62.3 (C-6$_{Manp\text{-}3}$), 62.2 (C-6$_{Manp\text{-}2}$), 60.5 (C-1‘‘), 50.6 (C-11), 50.2 (C-1), 20.9 (C-2$_{Manp\text{-}3}$-O(C=O)*C*H$_3$), 20.8 (C-6$_{Manp\text{-}3}$-O(C=O)*C*H$_3$), 20.7 (C-3$_{Manp\text{-}3}$-O(C=O)*C*H$_3$), 20.7 (C-4$_{Manp\text{-}3}$-O(C=O)*C*H$_3$), 20.6 (C-6$_{Manp\text{-}2}$-O(C=O)*C*H$_3$), 20.5(C-2$_{Manp\text{-}2}$-O(C=O)*C*H$_3$), 20.5 (C-3$_{Manp\text{-}2}$-O(C=O)*C*H$_3$). **HR-MS** (ESI^+)**:** calculated for $C_{59}H_{74}N_6O_{29}$ *m/z* = 1353.4392 $[M+Na]^+$, found *m/z* = 1353.4375 $[M+Na]^+$. R_f = 0.25 (EtOAc). **Optical rotation:** $[\alpha]_D^{20}$ = 10.6 ($CHCl_3$). **IR**(ATR)**:** $\tilde{\nu}$ (cm^{-1}) = 2942, 2103, 1749, 1451, 1370, 1226, 1134, 1087, 1070, 1048, 980, 936, 715, 653, 600, 529, 479, 466, 450.

Supporting Information

6.1.9 (1-(11-Azido-3,6,9-trioxaundec-1-yl)-1*H*-1,2,3-triazol-4-yl)-methyl 3,6-Di-*O*-(α-D-mannopyranosyl)-α-D-mannopyranoside (TM)

The compound was synthesized according to Scheme S10 following a modified synthesis protocol by *Kramer et al.*[8]

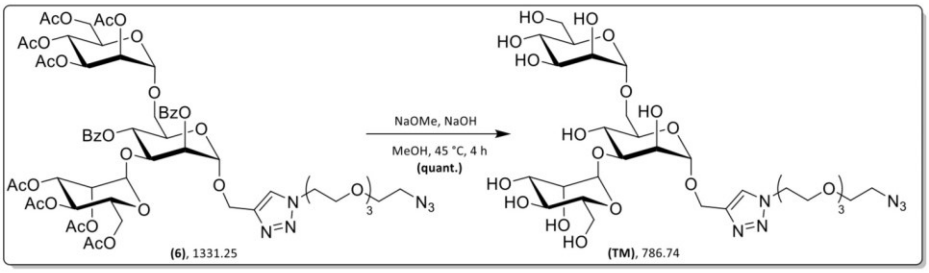

Scheme S10: Synthesis of (1-(11-Azido-3,6,9-trioxaundec-1-yl)-1*H*-1,2,3-triazol-4-yl)-methyl 3,6-Di-*O*-(α-D-mannopyranosyl)-α-D-mannopyranoside (**TM**).

The reaction was conducted using an oven-dried Schlenk flask equipped with a magnetic stirring bar. Compound (**6**) (0.27 g, 0.21 mmol, 1.00 eq.) was dissolved in dry MeOH (5.00 mL) under an atmosphere of Argon. NaOMe (0.01 g, 0.21 mmol, 1.00 eq.) and NaOH (1.00 mg, 0.02 mmol, 0.10 eq.) were added, and the reaction mixture was stirred for 4 hours at a temperature of 35 °C with slow dissolution of the substrate until reaction control *via* TLC and HPLC-MS showed complete conversion of the substrate and product formation. The solution was neutralized using Amberlite IR120 H^+ ion exchange resin (0.10 g) until a neutral solution was obtained. The mixture was filtered over *Celite* and was thoroughly eluted with MeOH (1 x 100 mL). All volatiles were removed in vacuo. The obtained residue was dissolved in H_2O (1 x 20.0 mL) and washed three times with the same volume of Et_2O (3 x 20.0 mL). After lyophilization of the aqueous phase, the crude product was obtained in the form of a light-yellow oil. Purification using RP-FCC (MeCN/H_2O, gradient 10 % to 100 % MeCN) delivered the desired product (**TM**) after lyophilization in form of a colorless lyophilizate.

Yield: 0.17 g (0.21 mmol, quant.), colorless lyophilizate.

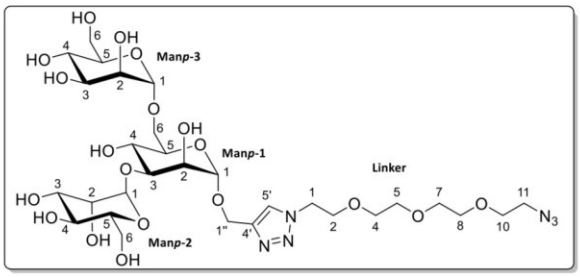

^{1}H-NMR (600 MHz, D_2O)**:** δ (ppm) = 8.07 (s, 1H, H-5‘), 5.03 (s, 1H, H-1$_{Manp-2}$), 4.89 (s, 1H, H-1$_{Manp-1}$), 4.85 (s, 1H, H-1$_{Manp-3}$), 4.78 – 4.77 (m, 1H, H-1a‘‘), 4.68 (d, ^2J = 12.6 Hz, 1H, H-1b‘‘), 4.60 (t, ^3J = 5.0 Hz, 2H, H-1), 4.05 (s, 1H, H-2$_{Manp-1}$), 4.01 (dd, ^3J = 3.5, 1.6 Hz, 1H, H-2$_{Manp-2}$), 3.98 – 3.92 (m, 4H, H-2, H-2$_{Manp-3}$, H-6a$_{Manp-1}$), 3.90 – 3.85 (m, 1H, H-4$_{Manp-1}$), 3.85 – 3.78 (m, 4H, H-3$_{Manp-1}$, H-3$_{Manp-2}$, H-3$_{Manp-3}$, H-6a$_{Manp-3}$), 3.76 – 3.69 (m, 3H, H-5$_{Manp-1}$, H-5$_{Manp-2}$, H-6b$_{Manp-3}$), 3.68 – 3.55 (m, 16H, H-4, H-5, H-7, H-8, H-10, H-6b$_{Manp-1}$, H-4$_{Manp-2}$, H-6$_{Manp-2}$, H-4$_{Manp-3}$, H-5$_{Manp-3}$), 3.43 (t, ^3J = 4.9 Hz, 2H, H-11). **^{13}C-NMR** (151 MHz, D_2O)**:** δ (ppm) = 143.5 (C-4‘), 125.5 (C-5‘), 102.4 (C-1$_{Manp-2}$), 99.7 (C-1$_{Manp-1}$), 99.4 (C-1$_{Manp-3}$), 78.6 (C-3$_{Manp-1}$), 73.3 (C-5$_{Manp-2}$), 72.7 (C-5$_{Manp-3}$), 71.3 (C-5$_{Manp-1}$), 70.6 (C-3$_{Manp-3}$), 70.3 (C-3$_{Manp-2}$), 70.0 (C-2$_{Manp-2}$), 69.9 (C-2$_{Manp-3}$), 69.7 (C-6$_{Manp-2}$), 69.6 (C-4, C-5, C-7, C-8), 69.5 (C-2$_{Manp-1}$), 69.2 (C-10), 68.8 (C-2), 66.7 (C-4$_{Manp-2}$, C-4$_{Manp-3}$), 65.5 (C-4$_{Manp-1}$), 65.0 (C-6$_{Manp-1}$), 60.9 (C-6$_{Manp-3}$), 60.0 (C-1‘‘), 50.1 (C-11), 50.1 (C-1). **HR-MS** (ESI$^+$)**:** calculated for $C_{29}H_{50}N_6O_{19}$ *m/z* = 809.3032 $[M+Na]^+$, found *m/z* = 809.3024 $[M+Na]^+$. R_f = 0.60 (MeCN:H_2O 1:4). **Optical rotation:** $[\alpha]_D^{23}$ = +45.6 (MeOH). **IR**(ATR)**:** $\tilde{\nu}$ (cm^{-1}) = 3327, 2921, 2107, 1592, 1349, 1025, 979, 807, 501.

The analytical data are in correspondence with those from the literature.[8]

Supporting Information

6.2 Synthesis of thiol-exchange linker and modified cargos

The synthesis of the thiol-exchange linker (**S4**), which is subsequently modified to carry cargo molecules, starting from commercially available 1,2-di(pyridin-2-yl)disulfane and 2-mercaptoethan-1-ol is described in Scheme S11. The synthesis sequence includes two linear steps to obtain the thiol-exchange linker (**S4**) followed by two single reaction steps to connect the cargo molecules obtaining the modified cargos (**Pyr-S-S-Benzyl**) and (**Pyr-S-S-TLR7/8a**), which are obtained with yield of 45 % and 61 % over three steps each.

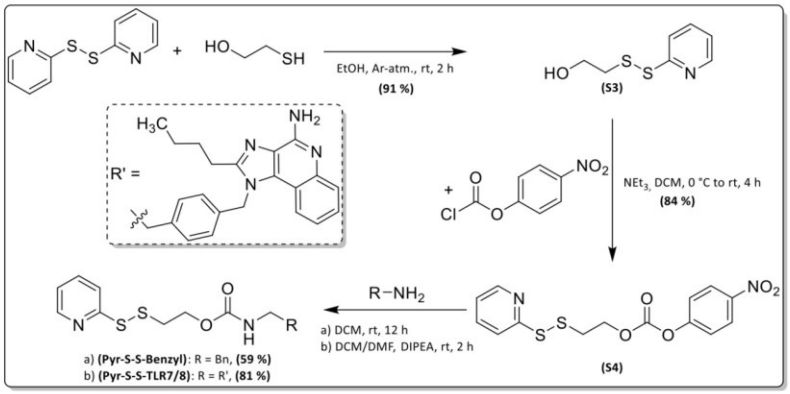

Scheme S11: Overview of the three-step synthesis of the modified cargo molecules (**Pyr-S-S-Benzyl**) and (**Pyr-S-S-TLR7/8a**), which were obtained with a yield of 45 % and 61 % over three linear steps respectively.

6.2.1 2-(Pyridin-2-yldisulfanyl)ethan-1-ol (S3)

The compound was synthesized according to Scheme S12 following a modified synthesis protocol by *Lapeyre et al.*[16]

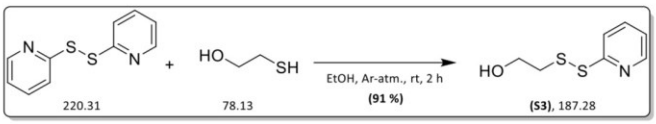

Scheme S12: Synthesis of 2-(pyridin-2-yldisulfanyl)ethan-1-ol (**S3**).

The reaction was conducted using an oven-dried Schlenk flask equipped with a magnetic stirring bar. 1,2-di(pyridin-2-yl)disulfane (4.72 g, 21.4 mmol, 3.00 eq.) was dissolved in dry EtOH (20.0 mL) under an atmosphere of Argon. 2-Mercaptoethan-1-ol (557 mg, 7.13 mmol, 1.00 eq.) was added dropwise and the reaction solution was stirred for 2 h at room temperature. The solvent was removed under reduced pressure. The crude product was purified *via* column chromatography (*n*Hex/EtOAc, isocratic with 20 % EtOAc) yielding the pure product (**S3**) in the form of a colorless solid.

Yield: 1.22 g (6.51 mmol, 91 %), colorless solid.

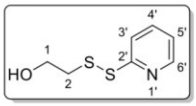

^{1}H-NMR (400 MHz, CD_2Cl_2)**:** δ (ppm) = 8.52 – 8.45 (m, 1H, H-6'), 7.66 – 7.57 (m, 1H, H-4'), 7.47 – 7.40 (m, 1H, H-5'), 7.21 – 7.13 (m, 1H, H-3'), 5.23 (t, ^3J = 7.1 Hz, 1H, -O*H*), 3.79 – 3.70 (m, 2H, H-1), 2.96 – 2.89 (m, 2H, H-2).
^{13}C-NMR (101 MHz, CD_2Cl_2)**:** δ (ppm) = 159.5 (1C, C-2'), 150.2 (1C, C-6'), 137.3 (1C, C-4'), 122.1 (1C, C-3'), 121.9 (1C, C-5'), 58.6 (1C, C-1), 43.3 (1C, C-2).

The analytical data are in correspondence with those from the literature.[16]

Supporting Information

6.2.2 4-Nitrophenyl (2-(pyridin-2-yldisulfanyl)ethyl) carbonate (S4)

The compound was synthesized according to Scheme S13 following a modified synthesis protocol by *Lapeyre et al.*[16]

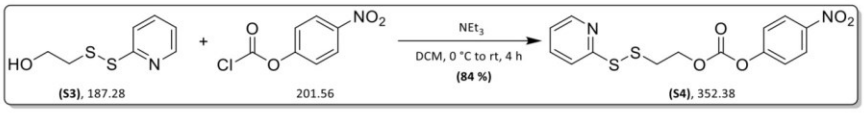

Scheme S13: Synthesis of 4-Nitrophenyl (2-(pyridin-2-yldisulfanyl)ethyl) carbonate **(S4)**.

2-(Pyridin-2-yldisulfanyl)ethan-1-ol (**S3**) (0.63 g, 3.36 mmol, 1.00 eq.) and NEt_3 (0.68 g, 0.94 mL, 6.72 mmol, 2.00 eq.) were dissolved in DCM (13.0 mL) and cooled to 0°C using an ice bath. 4-nitrophenyl chloroformate (0.75 g, 3.72 mmol, 1.10 eq.) was added to the solution. The reaction was allowed to warm to room temperature and was stirred for 4 h. The reaction mixture was washed twice with water, dried over anhydrous Na_2SO_4, filtered and the solvent was removed under reduced pressure. The crude product was purified using column chromatography (*n*Hex/EtOAc, isocratic with 50 % EtOAc) yielding the pure product (**S4**) in the form of a yellow oil.

Yield: 0.99 g (2.81 mmol, 84 %), yellow oil.

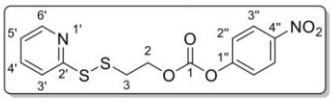

^{1}H-NMR (400 MHz, CDCl3)**:** δ (ppm) = 8.48 – 8.40 (m, 1H, H-6'), 8.27 – 8.18 (m, 2H, H-3''), 7.68 – 7.56 (m, 2H, H-4', H-5'), 7.39 – 7.30 (m, 2H, H-2''), 7.13 – 7.03 (m, 1H, H-3'), 4.53 (t, ^3J = 6.4 Hz, 2H, H-2), 3.13 (t, ^3J = 6.4 Hz, 2H, H-3). **^{13}C-NMR** (101 MHz, $CDCl_3$)**:** δ (ppm) = 159.1 (1C, C-2'), 155.4 (1C, C-1''), 152.2 (1C, C-1), 149.8 (1C, C-6'), 145.4 (1C, C-4''), 137.2 (1C, C-4'), 125.3 (2C, C-3''), 121.8 (1C, C-3'), 121.2 (2C, C-2''), 120.2 (1C, C-5'), 66.7 (1C, C-2), 36.8 (1C, C-3).

The analytical data are in correspondence with those from the literature.[16]

6.2.3 Benzyl (2-(pyridin-2-yldisulfanyl)ethyl)carbamate (Pyr-S-S-Benzyl)

The compound was synthesized according to Scheme S14 following a modified synthesis protocol by *Latorre et al.*[17]

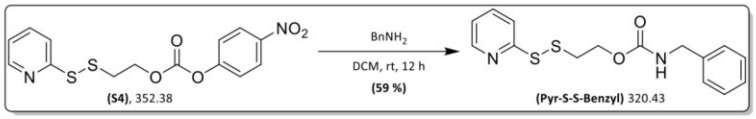

Scheme S14: Synthesis of Benzyl (2-(pyridin-2-yldisulfanyl)ethyl)carbamate **(Pyr-S-S-Benzyl)**.

4-Nitrophenyl (2-(pyridin-2-yldisulfanyl)ethyl) carbonate (**S4**) (39.5 mg, 112 µmol, 1.00 eq.) was dissolved in DCM (40 µL and mixed with benzylamine (12.0 mg, 112 µmol, 1.00 eq.). The reaction was shaken overnight at room temperature. All volatiles were removed under reduced pressure and the crude mixture was purified *via* RP-HPLC. After lyophilization the pure product (**Pyr-S-S-Benzyl**) was obtained as its TFA salt in the form of a colorless solid.

Yield: 28.5 mg (65.6 µmol, 59 %), colorless solid.

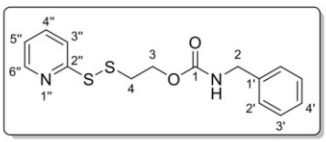

^{1}H-NMR (700 MHz, CD_2Cl_2)**:** δ (ppm) = 8.48 – 8.44 (m, 1H, H-6''), 7.82 – 7.78 (m, 1H, H-5''), 7.73 – 7.68 (m, 1H, H-4''), 7.36 – 7.31 (m, 2H, H-3'), 7.30 – 7.25 (m, 3H, H-2', H-4'), 7.18 – 7.13 (m, 1H, H-3''), 5.20 (t, ^3J = 6.8 Hz, 1H, -N*H*), 4.34 – 4.29 (m, 4H, H-2, H-3), 3.06 (t, ^3J = 6.2 Hz, 2H, H-4).

Supporting Information

^{13}C-NMR (101 MHz, CD_2Cl_2)**:** δ (ppm) = 160.1 (1C, C-2''), 156.4 (1C, C-1), 149.0 (1C, C-6''), 139.1 (1C, C-1'), 138.5 (1C, C-4''), 129.0 (2C, C-3'), 127.8 (3C, C-2', C-4'), 121.6 (1C, C-5''), 120.7 (1C, C-3''), 63.1 (1C, C-3), 45.3 (1C, C-2), 38.6 (1C, C-4). **HPLC-MS** (ESI^+)**:** *m/z* = 321 $[M+H]^+$; t_R = 6.06 min (Figure S28). **MALDI-TOF-MS:** *m/z* = 321.0793 (Figure S30). **HR-MS**) (ESI^+)**:** calculated for $C_{15}H_{16}N_2O2S_2$ *m/z* = 321.0726 $[M+H]^+$, found *m/z* = 321.0728 $[M+H]^+$.

6.2.4 2-(Pyridin-2-yldisulfanyl)ethyl (4-((4-amino-2-butyl-1*H*-imidazo[4,5-*c*]quinolin-1-yl) methyl)benzyl)carbamate (Pyr-S-S-TLR7/8a)

The compound was synthesized according to Scheme S15 following a modified synthesis protocol by *Latorre et al.*[17]

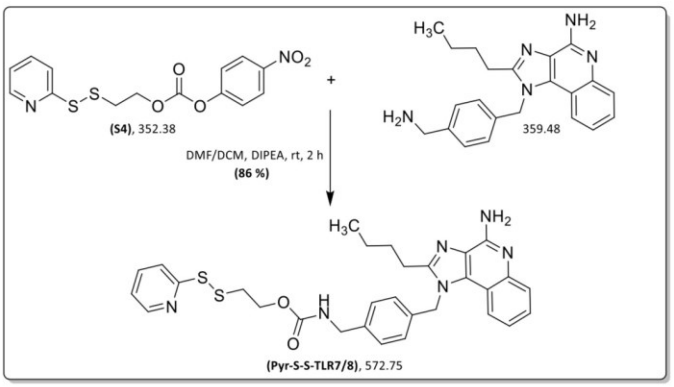

Scheme S15: Synthesis of 2-(Pyridin-2-yldisulfanyl)ethyl (4-((4-amino-2-butyl-1H-imidazo[4,5-c]quinolin-1-yl)methyl)-benzyl)carbamate (**Pyr-S-S-TLR7/8a**).

1-(4-(Aminomethyl)benzyl)-2-butyl-1*H*-imidazo[4,5-*c*]quinolin-4-amine (TLR7/8 agonist) in the form of its TFA salt (0.85 mg, 1.45 µmol, 1.00 eq.) was dissolved in DMF (21.9 µL and diisopropylethylamine (DIPEA) (0.33 µL, 1.88 µmol, 1.30 eq) was added. Subsequently, 4-nitrophenyl (2-(pyridin-2-yldisulfanyl)ethyl) carbonate (**S4**) (0.46 mg, 1.30 µmol, 0.90 eq.) dissolved in DCM (8.1 µL was added. The reaction was shaken for 2 h at room temperature. All volatiles were removed under reduced pressure and the crude product was purified *via* RP-HPLC. After lyophilization the pure product (**Pyr-S-S-TLR7/8a**) was obtained as its TFA salt in the form of a colorless solid.

Yield: 1.00 mg (1.25 µmol, 86 %), colorless solid.

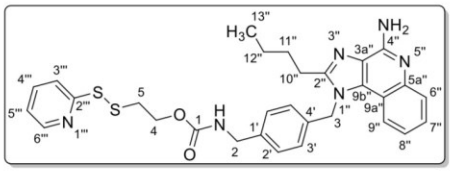

^{1}H NMR (400 MHz, DMF-d_7)**:** δ (ppm) = 14.97 (s, 1H, CF_3-COOH), 8.49 – 8.46 (m, 1H, H-6'''), 8.15 – 8.09 (m, 1H, H-6''), 7.90 – 7.84 (m, 1H, H-9''), 7.84 – 7.78 (m, 2H, H-3''', H-4'''), 7.75 – 7.70 (m, 1H, H-8''), 7.72 (t, 1H, -N*H*-), 7.43 – 7.36 (m, 1H, H-7''), 7.36 – 7.32 (m, 2H, H-3'), 7.27 – 7.22 (m, 1H, H-5'''), 7.20 – 7.15 (m, 2H, H-2'), 6.08 (s, 2H, H-3), 4.28 (d, ^3J = 6.3 Hz, 2H, H-2), 4.26 (t, ^3J = 6.2 Hz, 2H, H-4), 3.13 (t, ^3J = 6.2 Hz, 2H, H-5), 3.04 (t, ^3J = 7.7 Hz, 2H, H-10''), 1.83 (p, ^3J = 7.4 Hz, 2H, H-11''), 1.46 (h, ^3J = 7.4 Hz, 2H, H-12''), 0.92 (t, ^3J = 7.4 Hz, 3H, H-13''). **HPLC-MS** (ESI^+): *m/z* = 573 $[M+H]^+$, t_R = 5.491 min (Figure S29). **MALDI-TOF-MS:** *m/z* = 573.2283 (Figure S31); **HR-MS** (ESI^+)**:** calculated for $C_{30}H_{32}N_6O_2S_2$ *m/z* = 573.2101 $[M+H]^+$, found *m/z* = 573.2118 $[M+H]^+$.

Supporting Information

6.3 Synthesis of cargo-loaded TM-HSA nanocarriers

Prior to use, native HSA was dissolved in MQ-water, subjected to spin-filtration through a 300 kDa ultracentrifugation tube to remove large aggregates, and lyophilized. The mass of all HSA conjugates is expressed as the *m/z* value of the peak of the singly charged species and expressed as M (FWHM), where the variation in mass range is expressed with the full peak width at half maximum (FWHM = Δm), which is expressed and calculated with TM$_9$-HSA used as an example as follows:

MALDI-ToF-MS for TM$_9$-HSA: *m/z* = 82845 $[M+H]^+$ (7078)

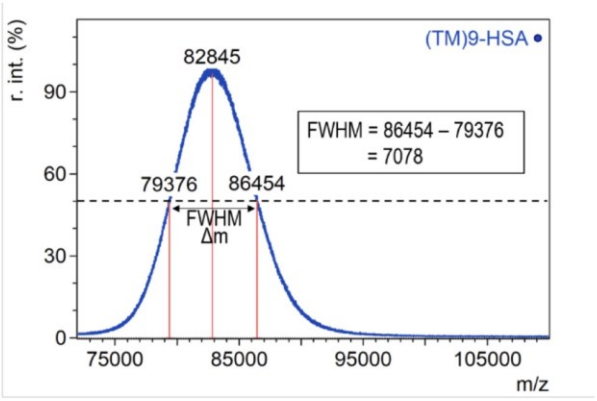

From FWHM (Δm), the variation in the degree of modification (DoM) was calculated, with TM$_9$-HSA used as an example as follows:

$$variation\ for\ DoM = \frac{1}{2}\frac{\Delta m}{M_{TM}} = \frac{1}{2}\frac{7078\ g \cdot mol^{-1}}{786.7 g \cdot mol^{-1}} = \frac{1}{2}\frac{\Delta m}{M_{Mod}} = 4.5 = 5$$

Therefore, for TM$_9$-HSA n(TM) = 9 ± 5. For calculation of DoM refer to chapter 6.3.3. This variation always includes natural peak broadness of native HSA as well as peak broadening of previous statistical modifications.

6.3.1 Preparation of labeled HSA *via* thiol-maleimide Michael addition

Native HSA (27.6 mg, 415 nmol, 1.00 eq.) was dissolved in 50 mM sodium phosphate buffer (pH = 7.4) to obtain a protein concentration of 5 mg/mL. Sulfo-Cy5 maleimide (1.00 mg, 1.25 µmol, 3.00 eq.) (structure provided below) dissolved in MQ (25 mg/mL) was added to the native HSA. The reaction was shaken at room temperature for 16 hours and afterwards purified (5 x MQ) and concentrated *via* ultracentrifugation spin filter (Vivaspin, PES, 10 kDa). The product was lyophilized and obtained in the form of a blue lyophilizate.

Recovery rate: 26.5 mg (390 nmol, 94 %), blue lyophilizate.

MALDI-ToF-MS: *m/z* = 67948 $[M+H]^+$ (2654) (Figure S33).

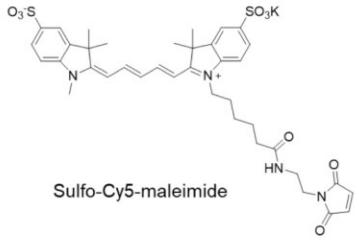

Sulfo-Cy5-maleimide

Supporting Information

6.3.2 Maleimide ring opening of labeled HSA

Labeled HSA (26.5 mg, 390 nmol) was diluted in 50 mM sodium borate buffer (pH = 9.2) to a final protein concentration of 1 mg/mL and shaken at 37 °C for 24 h. Afterwards, it was concentrated *via* ultracentrifugation spin filter (Vivaspin, PES, 10 kDa) and purified *via* SEC (Sephadex G-25, MQ). The product was lyophilized and obtained in the form of a blue powder.

Recovery rate: 26.3 mg (387 nmol, 99 %), blue lyophilizate.

DoL: 0.66, **MALDI-ToF-MS:** *m/z* = 67963 $[M+H]^+$ (2691) (Figure S34).

6.3.3 Preparation of $DBCO_m$-HSA *via* NHS-ester activated DBCO-linker

DBCO-HSA conjugates (Table S1, Entry 1–5) were prepared by the following general procedure: First portion of DBCO-PEG_4-NHS (100mg/mL, DMSO) was diluted in 50 mM PB pH 7.4 and labeled HSA was added to obtain a protein concentration of 6–7 mg/mL. The reaction was shaken at room temperature and monitored *via* Maldi-ToF-MS analysis. DBCO-PEG_4-NHS was added sequentially until desired modification rate was achieved. The products were purified *via* ultracentrifugation spin filter (Vivaspin, PES, 10 kDa). The product was lyophilized and obtained in the form of a blue lyophilizate.

The DBCO-HSA conjugate (Table S1, Entry 6) was synthesized *via* the following, optimized procedure: Labeled HSA (12.0 mg, 177 nmol, 1.00 eq) was diluted in 50mM phosphate buffer (pH = 7.4, 12.0 mL) to a protein concentration of 1 mg/mL. DBCO-PEG_4-NHS (23.0 mg, 35.5 µmol, 200 eq.) dissolved in DMSO (100 mg/mL) was added in six portions over 40 hours. Afterwards, the reaction solution was purified (5 x MQ) and concentrated *via* ultracentrifugation spin filter (Vivaspin, PES, 10 kDa). The product was lyophilized and obtained in the form of a blue lyophilizate.

Recovery rate: 15.0 mg (164 nmol, 93 %), blue lyophilizate.

MALDI-ToF-MS: *m/z* = 91504 $[M+H]^+$ (9751) (Figure S44).

The DBCO-HSA conjugate (Table S1, Entry 7) was synthesized *via* this optimized procedure. DBCO-PEG_4-NHS was added sequentially until desired modification rate was achieved.

MALDI-ToF-MS: *m/z* = 90973 $[M+H]^+$ (10090) (Figure S45)

Degree of lysine modification with the DBCO linker (DoM_{DBCO}) was monitored with MALDI-ToF-MS and calculated exemplary as follows:

$$DoM_{DBCO} = m = \frac{(M_{DBCO_m-HSA} - M_{Cy5HSA})}{(M_{DBCO-PEG_4-NHS} - M_{NHS})} = \frac{(91504 g\cdot mol^{-1} - 67963 g\cdot mol^{-1})}{(649.69 g\cdot mol^{-1} - 115.09 g\cdot mol^{-1})} = \frac{23541 g\cdot mol^{-1}}{534.6 g\cdot mol^{-1}} = 44.03$$

$$DoM_{DBCO} = 44$$

Table S1: Cy5-labeled DBCO-HSA conjugates with different degrees of modification (DoM).

Entry	DBCO-PEG_4-NHS eq.	MALDI-ToF-MS *m/z* $[M+H]^+$	FWHM	DoM_{DBCO} m	MS spectrum
1	5	69564	3000	3 ± 3	Figure S39
2	10	70970	3706	6 ± 4	Figure S40
3	20	75778	4277	15 ± 4	Figure S41
4	50	83714	4901	30 ± 5	Figure S42
5	100	94538	7950	50 ± 7	Figure S43
6	200	91504	9751	44 ± 9	Figure S44
7	150	90973	10090	45 ± 9	Figure S45

Supporting Information

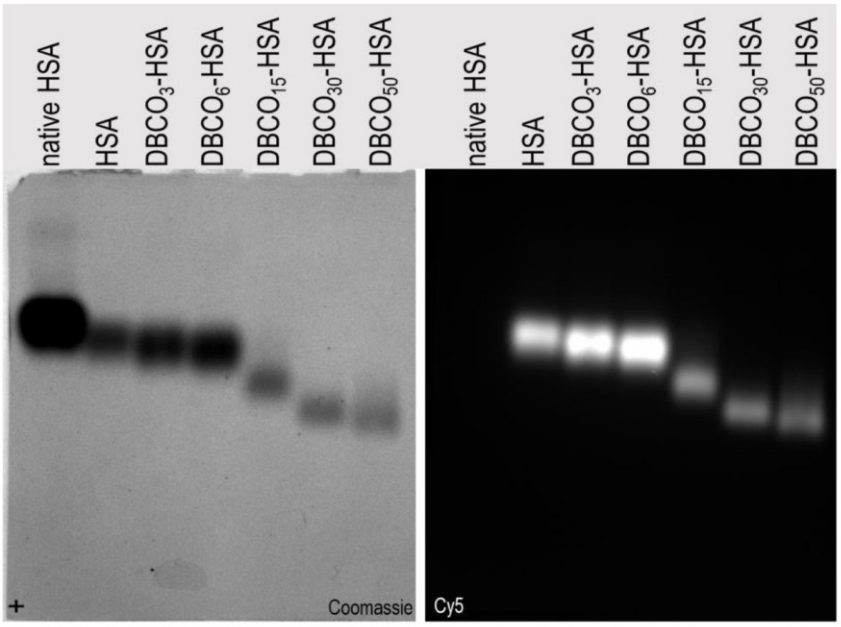

Figure S1: Agarose gel electrophoresis of (from left to right) native HSA, Cy5-labeled HSA and varying DBCO-HSA conjugates (Table S1, Entry 1–5) (left Coomassie brilliant blue staining, right Cy5-channel).

6.3.4 Preparation of TM_n-HSA *via* SPAAC-reaction

TM-HSA conjugates (Table S2, Entry 1–5) were prepared by the following general procedure for the SPAAC reaction: The respective DBCO-HSA conjugate (Table S1) was dissolved in 50 mM PB pH 7.4 before the azide functionalized TM (5–12 eq.) dissolved in MQ (10 mg/mL) was added sequentially and the reaction solution was shaken at a final protein concentration of 5 mg/mL at room temperature overnight. After maximum possible DBCO modification was confirmed by reaction monitoring *via* Maldi-ToF-MS analysis the products were purified *via* ultracentrifugation spin filter (Vivaspin, PES, 10 kDa). The product was lyophilized and obtained in the form of a blue lyophilizate.

The TM-HSA conjugate (Table S2, Entry 6) was synthesized *via* the following, optimized procedure: DBCO-HSA (15.0 mg, 166 nmol, 1.00 eq.) was dissolved in 50 mM phosphate buffer with 8 M urea and 2 mM EDTA (pH = 8) to a final protein concentration of 1 mg/mL. The azide functionalized TM (14.1 mg, 17.9 µmol, 115 eq. or 2.5 eq/DBCO) dissolved in MQ (10 mg/mL) was added and the reaction solution was shaken at room temperature overnight. Afterwards, the reaction solution was purified (5 x MQ) and concentrated *via* ultracentrifugation spin filter (Vivaspin, PES, 10 kDa). The product was lyophilized and obtained in the form of a blue lyophilizate.

Recovery rate: 19.8 mg (160 nmol, 97 %), blue lyophilizate.

MALDI-ToF-MS: *m/z* = 123460 $[M+H]^+$ (18587) (Figure S53).

The TM-HSA conjugate (Table S2, Entry 7) was synthesized *via* this optimized procedure.

MALDI-ToF-MS: *m/z* = 121154 $[M+H]^+$ (21032) (Figure S54)

Degree of DBCO modification with TM (DoM_{TM}) was monitored with MALDI-ToF-MS and calculated exemplary as follows:

$$DoM_{TM} = n = \frac{(M_{TM_n-HSA} - M_{DBCO_m-HSA})}{(M_{TM})} = \frac{(123460 g \cdot mol^{-1} - 91504 g \cdot mol^{-1})}{(786.7 g \cdot mol^{-1})} = \frac{31956 g \cdot mol^{-1}}{786.7 g \cdot mol^{-1}} = 40.62$$

$DoM_{TM} = 41$

Supporting Information

Table S2: Cy5-labeled TM-HSA conjugates with different degrees of modification (DoM).

Entry	MALDI-ToF-MS *m/z* $[M+H]^+$	FWHM	DoM_{TM} n	MS spectrum
1	70219	3420	1 ± 2	Figure S48
2	73066	4708	3 ± 3	Figure S49
3	82845	7078	9 ± 5	Figure S50
4	99672	7350	20 ± 5	Figure S51
5	124904	11129	38 ± 7	Figure S52
6	123460	18587	41 ± 12	Figure S53
7	121154	21032	38 ± 13	Figure S54

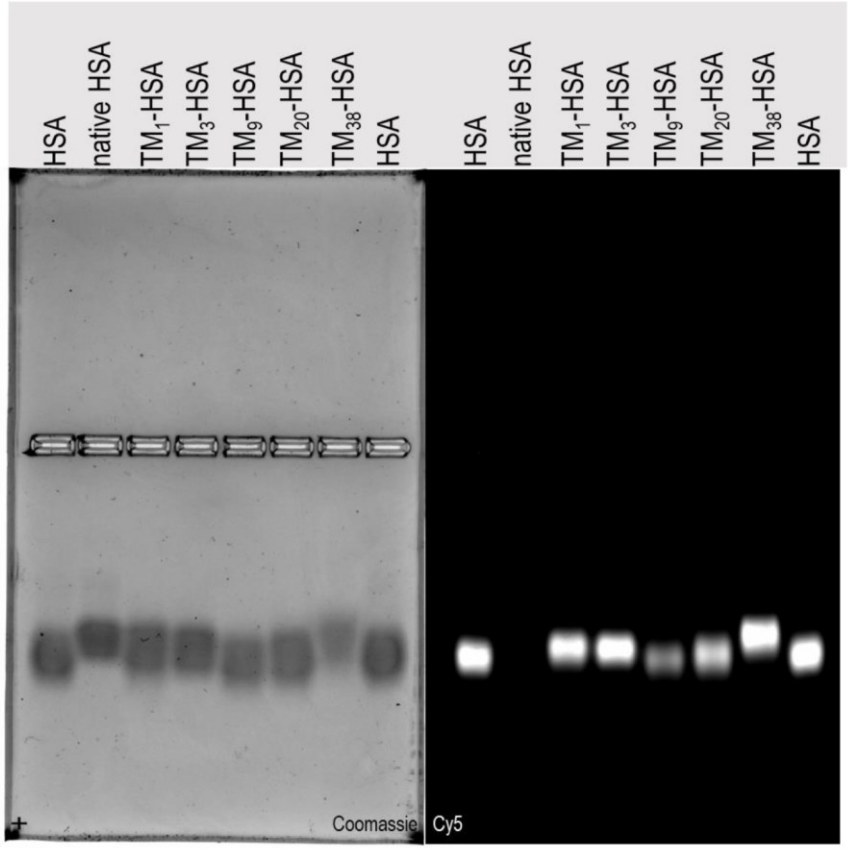

Figure S2: Agarose gel electrophoresis of (from left to right) Cy5-labeled HSA, native HSA, varying TM-HSA conjugates (Table S2, Entry 1–5) and Cy5-labeled HSA (left Coomassie brilliant blue staining, right Cy5-channel).

Supporting Information

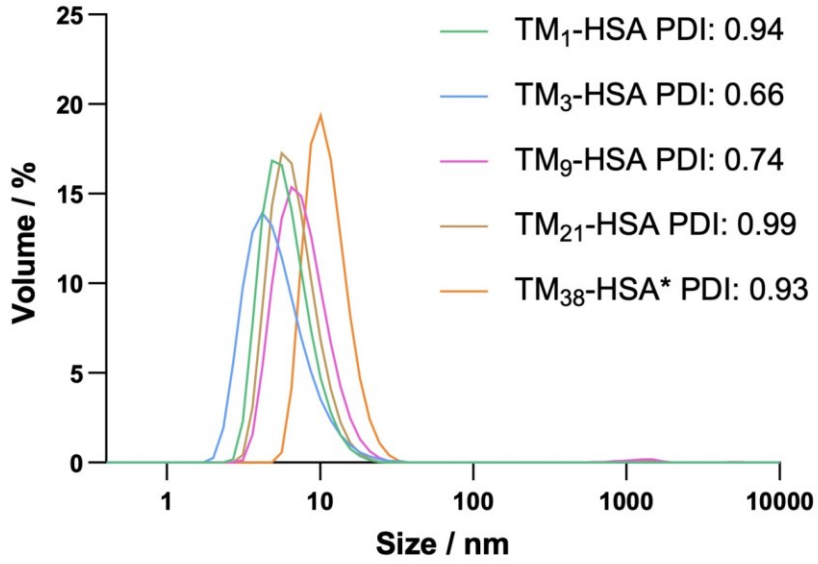

Figure S3: Size distribution and polydispersity indices (PDI) of Cy5-labeled HSA conjugates carrying varying numbers of TM (0.36–1 mg/mL in dPBS) showing sizes of d.nm = 6.28 ± 0.21 for TM_1-HSA, d.nm = 5.70 ± 0.16 for TM_3-HSA, d.nm = 8.05 ± 1.46 for TM_9-HSA, d.nm = 7.00 ± 0.38 for TM_{21}-HSA and d.nm = 11.45 ± 0.34 for TM_{38}-HSA* determined by DLS. Measurements were performed in triplicates, errors are given as standard deviation.*Size distribution was determined using a different batch.

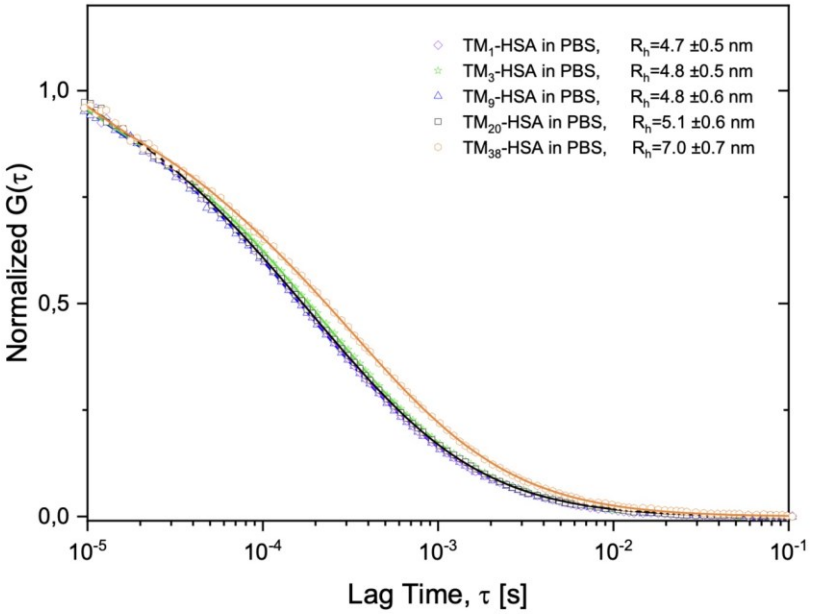

Figure S4: Normalized FCS autocorrelation curves and hydrodynamic radii (Rh) of Cy5-labeled HSA conjugates carrying varying numbers of TM.

Supporting Information

6.3.5 Cargo Loading *via* Disulfide Exchange (TM-HSA-TLR7/8a & TM-HSA-Benzyl)

TM-HSA (1.13 mg, 9.19 nmol, 1 eq.) was dissolved in denaturing buffer (50 mM phosphate buffer + 8 M urea + 2 mM EDTA, 1.00 mL) and inverted for 20 min before TCEP (263 µg, 919 nmol, 100 eq.) dissolved in MQ (23 µL) was added. The reaction solution was inverted for 1–2 hours and the residual TCEP was removed *via* an ultracentrifugation spin filter (2 x denaturing buffer, Vivaspin, PES, 10 kDa). To the protein solution (1 mg/mL) Pyr-S-S-TLR7/8a (1.11 mg, 1.38 µmol, 150 eq.) dissolved in DMF (105 µL) was added. The reaction solution was inverted for 1 h and the buffer was exchanged *via* ultra-centrifugation (denaturing buffer) before reaction control *via* MALDI-ToF-MS to determine the drug modification rate. *N*-Ethylmaleimide (173 µg, 1.38 µmol, 150 eq) was added to cap residual free thiols on the HSA for 14 h. The product was washed (5 x denaturing buffer) and backfolded *via* rapid dilution in MQ (1:10). If aggregation during washing steps occurred, the washing solutions were adjusted to pH = 6.3. The product was washed again (5 x MQ) and concentrated *via* an ultracentrifugation spin filter (Vivaspin, PES, 10 kDa). The product was lyophilized and obtained in the form of a blue lyophilizate with a modification rate of 20.5 TLR7/8a units per HSA.

Recovery rate: 417 µg (3.12 nmol, 34 %), blue lyophilizate.

MALDI-ToF-MS: *m/z* = 133872 $[M+H]^+$ (23495) (Figure S58).

This procedure was also applied in the case of Pyr-S-S-Benzyl as cargo to yield TM-HSA-Benzyl with a modification rate of 25 benzyl groups per HSA.

Recovery rate: 3.36 mg (26.2 nmol, 46 %), blue lyophilizate.

MALDI-ToF-MS: *m/z* = 128110 $[M+H]^+$ (16679) (Figure S57).

This procedure was also applied to further batches of TM-HSA-TLR7/8a and TM-HSA-Benzyl.

MALDI-ToF-MS: *m/z* = 134179 $[M+H]^+$ (19722) (Figure S59)

MALDI-ToF-MS: *m/z* = 126248 $[M+H]^+$ (19559) (Figure S60)

6.4 Synthesis of nanocarriers for *in vivo* experiments

Due to instability of the tested NIR-dyes to maleimide ring opening conditions and a need for higher degree of labeling for *in vivo* experiments, slight modifications of the synthesis route have been made. Thiol capping of the unpaired cysteine (Cys34), followed by dye labeling *via* NHS-ester chemistry has been performed to avoid the need for maleimide hydrolysis and still ensure high degree of labeling and protein-dye stability.

6.4.1 Preparation of $^{N\text{-EtMal}}$HSA *via* thiol-maleimide Michael addition and maleimide ring opening

The single unpaired Cys34 was capped to prevent cross reaction or dimerization over the course of synthesis. To this end, native HSA (36.6 mg, 551 nmol, 1.00 eq) was dissolved in 50 mM PB (pH = 7.4) to a final protein concentration of 2 mg/mL and *N*-ethylmaleimide (0.21 mg, 165 nmol, 3.00 eq.) dissolved in DMSO (25 mg/mL) was added. The reaction was shaken overnight at room temperature and purified (5 x MQ) *via* ultracentrifugation spin filter (Vivaspin, PES, 10 kDa). Cysteine capping was confirmed to be quantitative *via* MALDI-ToF-MS (*m/z* = 66565 $[M+H]^+$, Figure S35). The product was diluted in 50 borate buffer pH = 9.2 in a 100 mL round bottom flask and stirred for 24 h at 37 °C before purifying (5 x MQ) *via* ultracentrifugation spin filter (Vivaspin, PES, 10 kDa).

MALDI-ToF-MS: *m/z* = 66678$[M+H]^+$ (1805) (Figure S36).

Supporting Information

6.4.2 Preparation of labeled HSA *via* NHS-ester activated sulfo-Cy7.5 dye

$^{N\text{-EtMal}}$HSA (33.5 mg, 502 nmol, 1.00 eq) and sulfo-Cy7.5-NHS (1.60 mg, 64.0 µL, 1.36 nmol, 2.70 eq) (structure provided below) dissolved in DMSO (25 mg/mL) were diluted each with 50 mM phosphate buffer pH = 7.9 (15.5 mL). Both solutions were mixed and shaken for 1.5 h at room temperature. The product was purified (5 x MQ) *via* ultracentrifugation spin filter (Vivaspin, PES, 10 kDa)

MALDI-ToF-MS: *m/z* = 69293 $[M+H]^+$ (2830) (Figure S37).

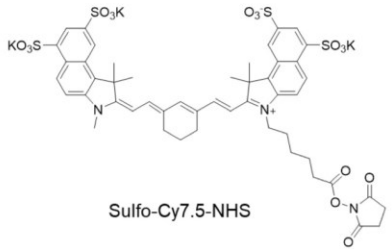

Sulfo-Cy7.5-NHS

A sulfo-Cy5-labeled conjugate has also been synthesized following this procedure.

MALDI-ToF-MS: *m/z* = 68306 $[M+H]^+$ (2352) (Figure S38)

6.4.3 Preparation of DBCO-HSA *via* NHS-ester activated DBCO-linker

Linker attachment was performed as reported for Cy5-labeled HSA (section 6.3.3), except DBCO-PEG_4-NHS equivalents were reduced to 185 eq. as MALDI-ToF-MS showed a modification rate of 51 ± 15 DBCO units per HSA which is similar (51 vs 50 DBCO/HSA) to conjugates prepared for *in vitro* studies.

MALDI-ToF-MS: *m/z* = 96633 $[M+H]^+$ (15946) (Figure S46).

A sulfo-Cy5-labeled conjugate has also been synthesized following this procedure.

MALDI-ToF-MS: *m/z* = 98495 $[M+H]^+$ (7924) (Figure S47Figure S45)

6.4.4 Preparation of TM-HSA *via* SPAAC reaction

SPAAC was performed as reported for Cy5-labeled DBCO-HSA (section 6.3.4), except 1.5 equivalents of TM per DBCO group were used yielding 38 ± 12 TM groups per HSA.

MALDI-ToF-MS: *m/z* = 126396 $[M+H]^+$ (18125) (Figure S55).

A sulfo-Cy5-labeled conjugate has also been synthesized following this procedure.

MALDI-ToF-MS: *m/z* = 132798 $[M+H]^+$ (10017) (Figure S56)

6.4.5 Preparation of TM-HSA-TLR7/8a and TM-HSA-Benzyl *via* disulfide exchange

Cargo loading was performed as reported for Cy5-labeled TM-HSA, except number of equivalents of TCEP was increased to 150 eq and number of equivalents of Pyr-S-S-Benzyl was increased to 2x150 eq. MALDI-ToF-MS showed a modification rate of 21 TLR7/8a per HSA and 12 Benzyl per HSA.

MALDI-ToF-MS: for TM-HSA-Benzyl *m/z* = 128895 $[M+H]^+$ (17189) (Figure S61).

for TM-HSA-TLR7/8a *m/z* = 135987 $[M+H]^+$ (13266) (Figure S62).

A sulfo-Cy5-labeled TM-HSA-TLR7/8a conjugate has also been synthesized following this procedure.

MALDI-ToF-MS: *m/z* = 143311 $[M+H]^+$ (11590) (Figure S63)

Supporting Information

6.5 Additional nanocarrier characterization

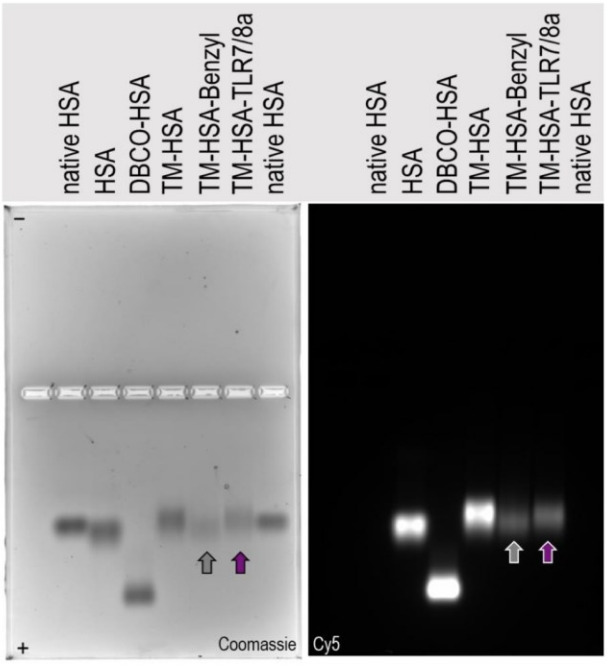

Figure S5: Agarose gel electrophoresis of final, loaded nanocarriers, indicated by arrows, as well as precursor conjugates (left Coomassie brilliant blue staining, right Cy5-channel).

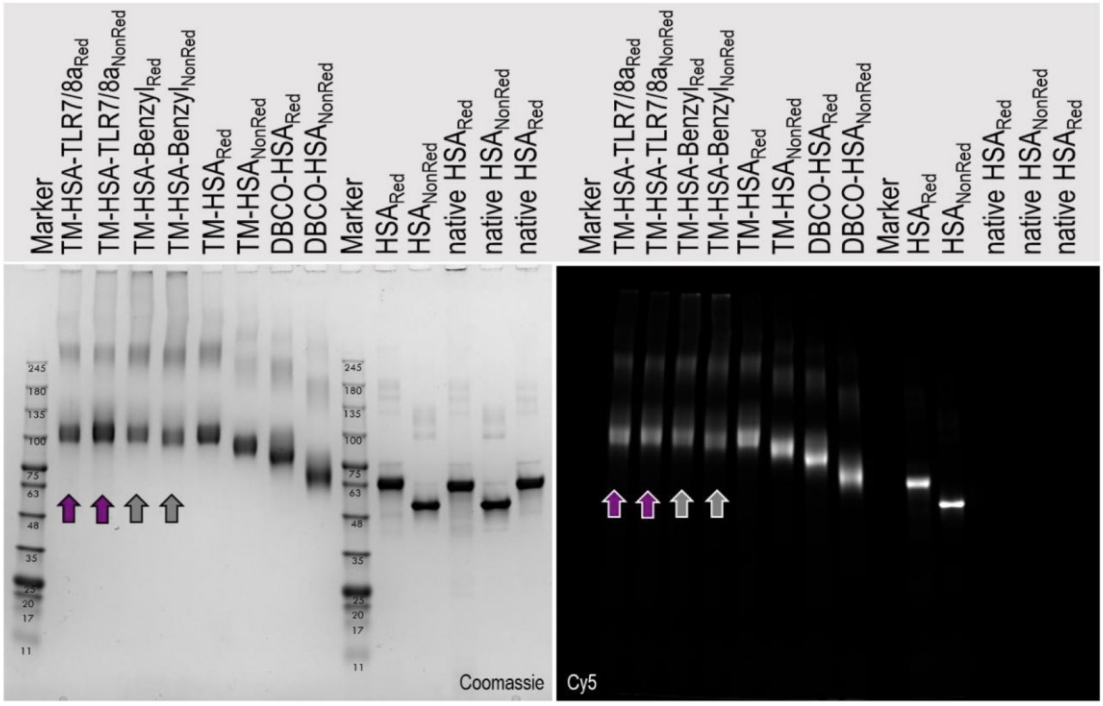

Figure S6: SDS-PAGE of final, loaded nanocarriers, indicated by arrows, as well as precursor conjugates under reducing ("Red", 50 mM DTT) and non-reducing ("NonRed", no DTT) conditions (left Coomassie blue staining, right Cy5-channel).

Supporting Information

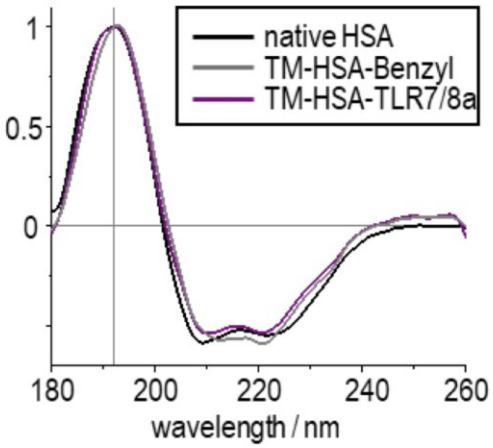

Figure S7: Normalized CD-spectra of Cy5-labeled TLR7/8a- / benzyl-loaded nanocarriers and HSA (0.8 µM, 10 mM PB pH 7.4).

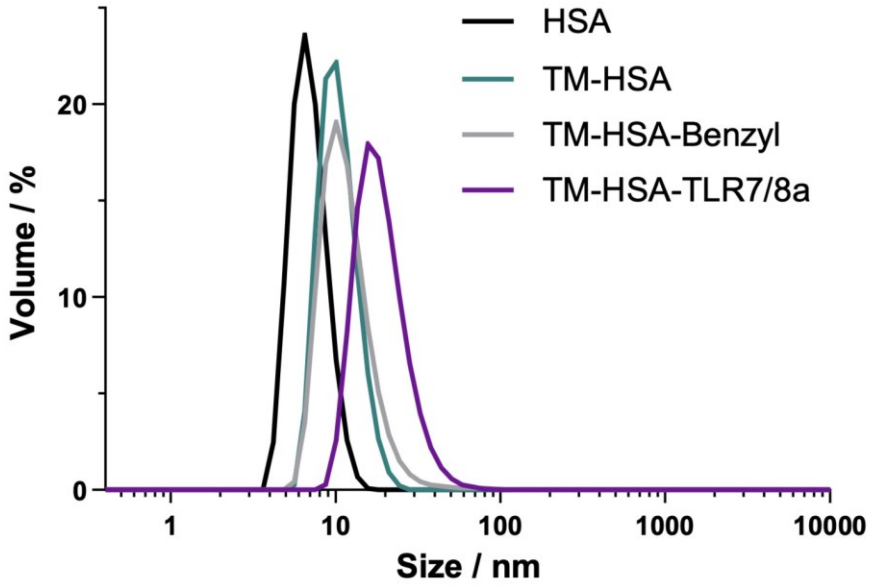

Figure S8: Size distribution of Cy7.5-labeled final, loaded nanocarriers compared to native HSA and trimannosylated precursor conjugate (1 mg/mL in dPBS) showing sizes of d.nm. = 7.02 ± 0.10 for native HSA, d.nm = 10.65 ± 0.13 for TM-HSA, d.nm = 12.61 ± 0.19 for TM-HSA-Benzyl and d.nm = 19.76 ± 0.48 for TM-HSA-TLR7/8a determined by DLS. Measurements were performed in quadruplicates, errors are given as standard deviation.

Supporting Information

6.5.1 Nanocarrier stability

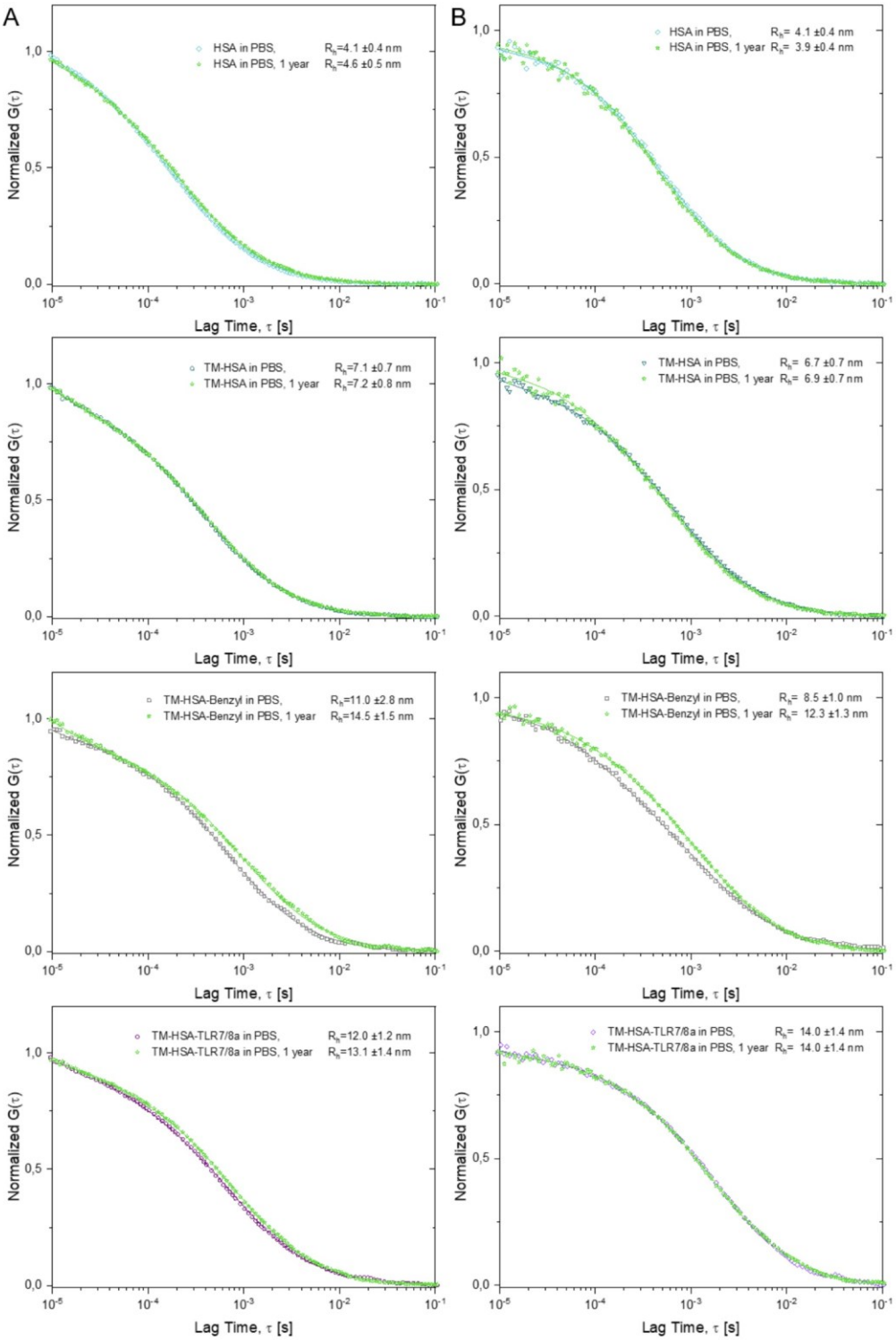

Figure S9: Normalized FCS correlation curves and hydrodynamic radii (Rh) of (A) Cy5-labeled and (B) Cy7.5-labeled HSA, TM-HSA, TM-HSA-Benzyl and TM-HSA-TLR7/8a (from top to bottom) re-analyzed after 1-year storage in solution at 8°C.

Supporting Information

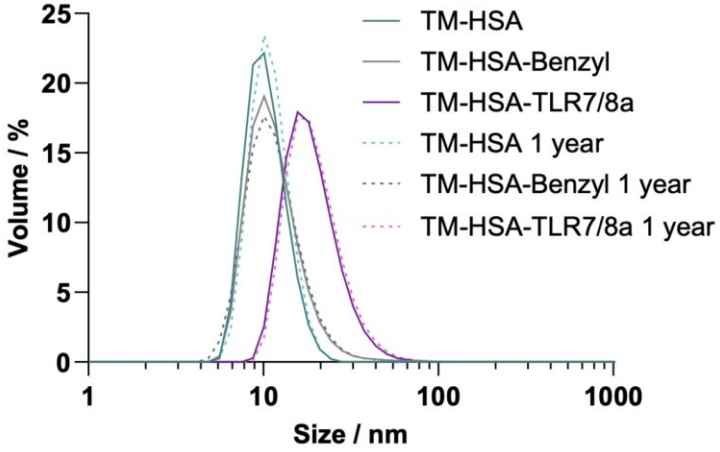

Figure S10: Size distribution profiles of Cy7.5-labeled trimannosylated HSA conjugates (1 mg/mL in dPBS) after 1 year storage in solution at 8°C determined by DLS. Sizes were for TM-HSA d.nm = 10.65 ± 0.13 and 11.13 ± 0.38, for TM-HSA-Benzyl d.nm = 12.61 ± 0.19 and 12.42 ± 0.64, for TM-HSA-TLR7/8a d.nm = 19.76 ± 0.48 and 20.54 ± 0.56. Measurements were performed in quadruplicates, errors are given as standard deviation.

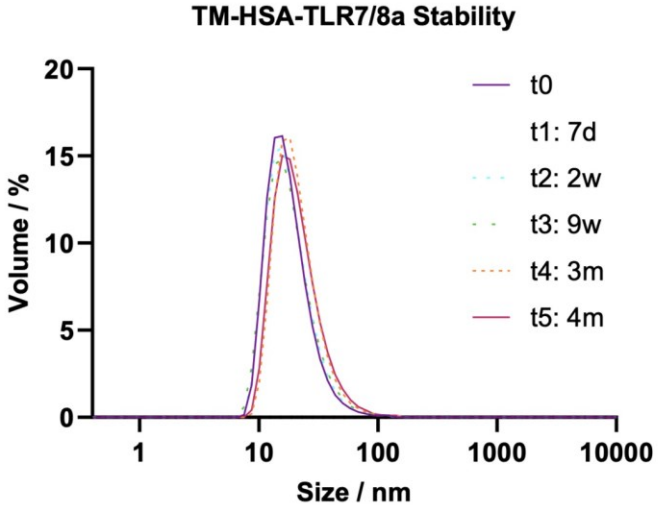

Figure S11: Size distribution profiles of Cy5-labeled TM-HSA-TLR7/8a (1 mg/mL in dPBS) over 4 months determined by DLS. t0: .d.nm. = 20.03 ± 0.29, t1: d.nm = 20.44 ± 0.38, t2: d.nm = 19.54 ± 0.55, t3: d.nm = 19.88 ± 1.09, t4: d.nm = 22.71 ± 0.6, t5: d.nm = 22.56 ± 0.24. Measurements were performed in triplicates, errors are given as standard deviation. d = days, w = weeks, m = months.

Supporting Information

Cargo release from final, loaded nanocarrier TM-HSA-TLR7/8a: For TLR7/8a release studies from TM-HSA-TLR7/8a nanocarrier, the nanocarrier was pre-incubated at a carrier concentration of 10.2 µM at 37 °C in buffer (conditions 1 and 2: 50 mM PB pH 7.4, condition 3: 50 mM PB pH 7.4, 8 M Urea, 2 mM EDTA). For conditions 2 and 3, GSH (50 mM, 50 mM PB pH 7.4) was added to reach a final concentration of 1 mM GSH and 10 µM TM-HSA-TLR7/8a. For sample collection, an aliquot of 10 µL reaction solution was taken at different time intervals and mixed with 2 µL internal standard (IS: Leucine encephalin, 400 ng/µL, MQ) for analysis via LC-HRMS.

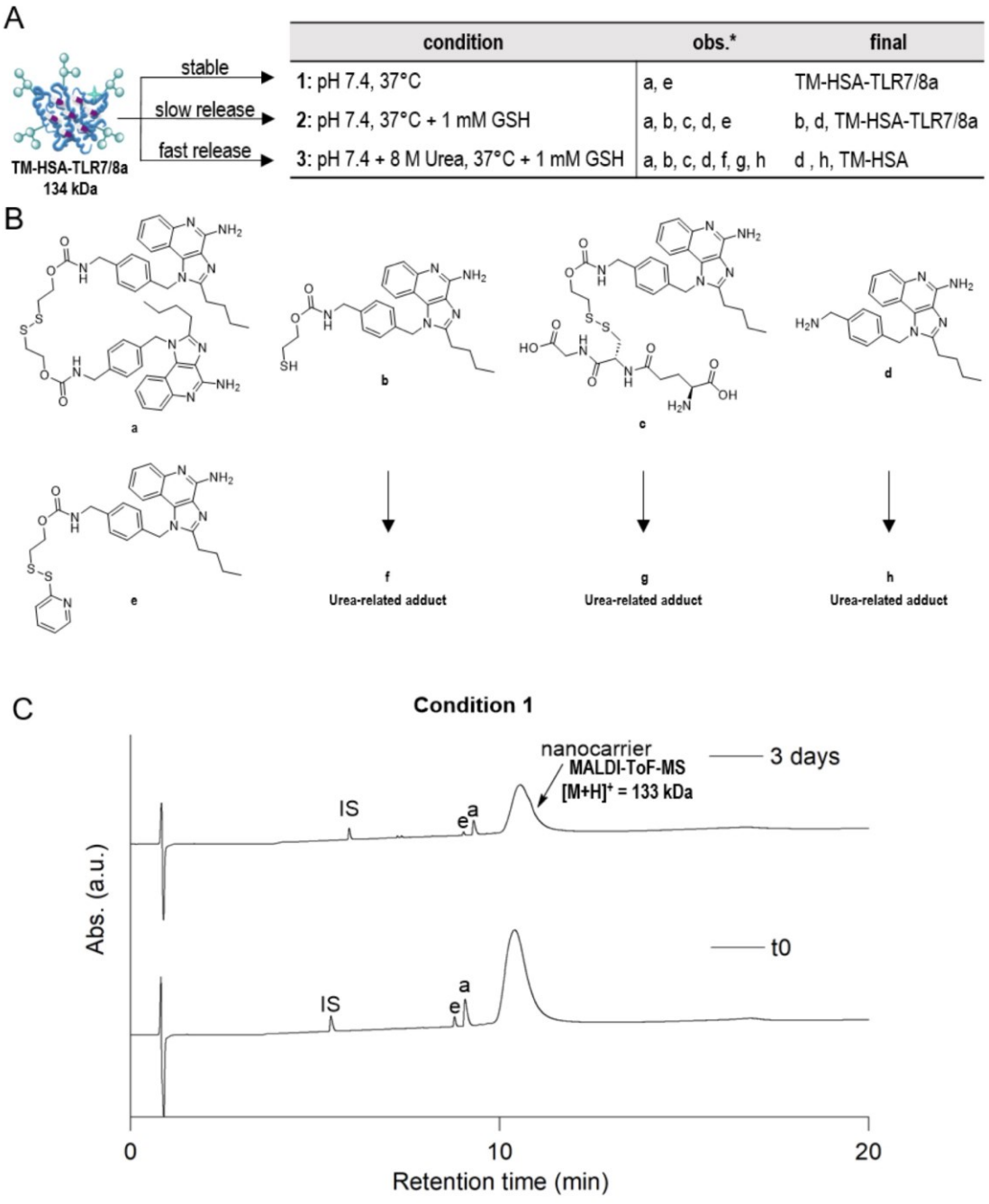

Figure S12: Drug release studies from TM-HSA-TLR7/8a under different incubation conditions 1-3. B) Proposed structures of reaction products and intermediates. *Based on ESI-MS analysis (for spectra, see section 9.6) and observed masses, no full structure elucidation has been performed. C) UV-Chromatograms with detection at 214 nm of drug release from TM-HSA-

Supporting Information

TLR7/8a incubated at 37 °C in 50 mM PB pH 7.4 over time (t0, 3 days). MALDI-ToF-MS spectra for nanocarriers after 3 days are provided in section 9.5.

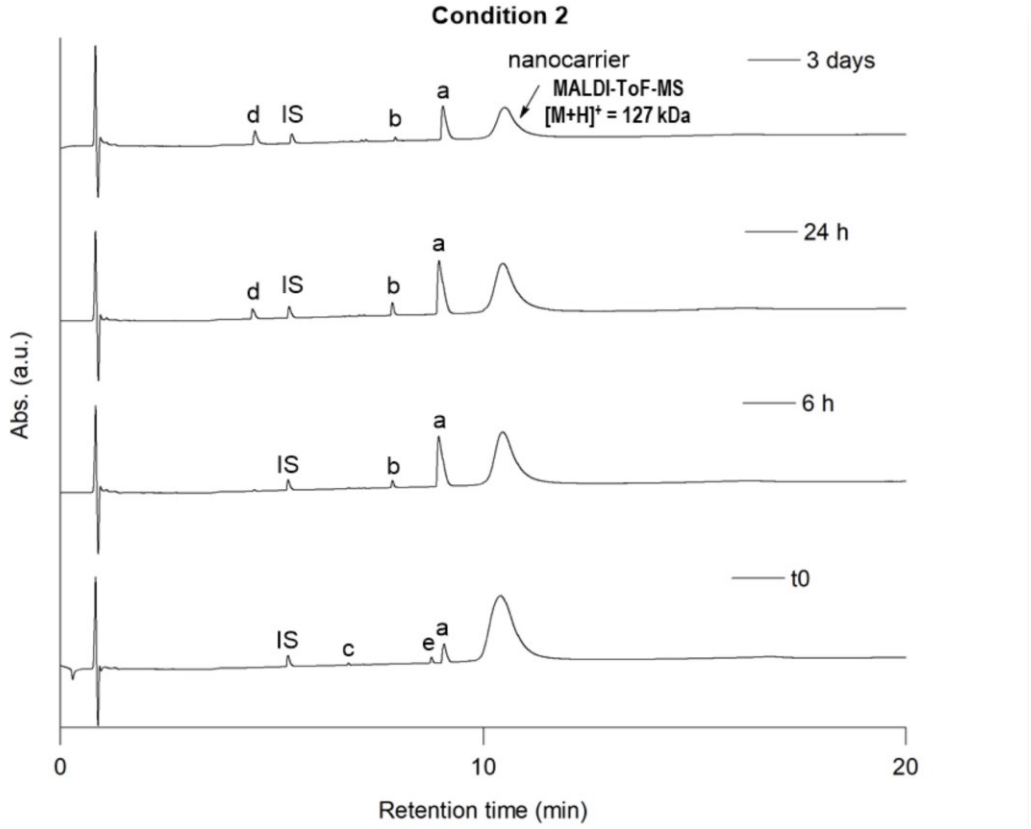

Figure S13: UV-Chromatograms with detection at 214 nm of drug release from TM-HSA-TLR7/8a incubated at 37 °C in 50 mM PB pH 7.4, with 1 mM GSH over time (t0, 6 h, 24 h and 3 days).

Supporting Information

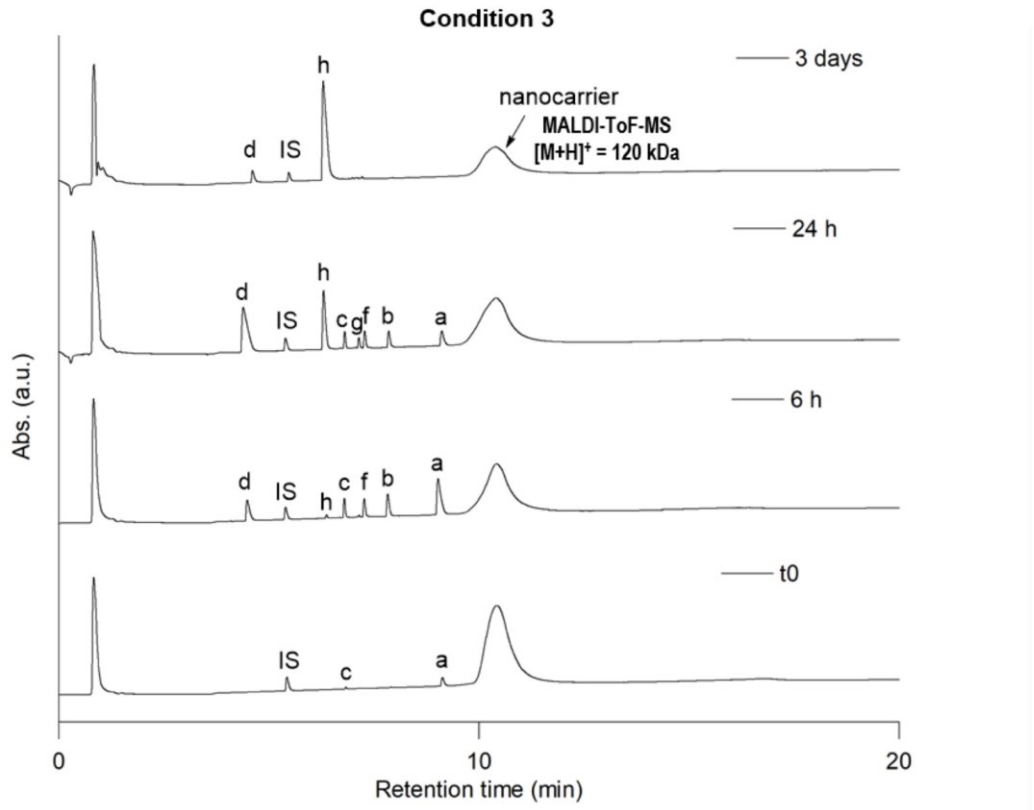

Figure S14: UV-Chromatograms with detection at 214 nm of drug release from TM-HSA-TLR7/8a incubated at 37 °C in 50 mM PB pH 7.4, with 8 M Urea, 2 mM EDTA and 1 mM GSH over time (t0, 6 h, 24 h and 3 days).

Supporting Information

7 *In vitro* and *ex vivo* experiments

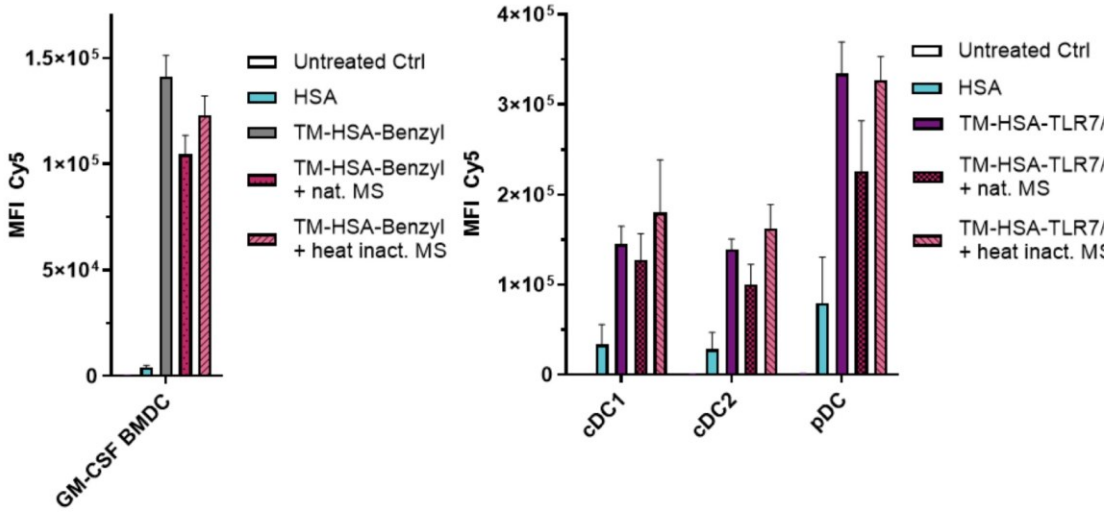

Figure S15: FACS analysis of benzyl loaded nanocarrier uptake in GM-CSF dif. BMDC (left) and TLR7/8a loaded nanocarrier uptake in FLT3L dif. BMDC (right) after preincubation in native mouse plasma and heat inactivated mouse plasma (50 nM). Data are presented as mean ± SEM, n=3–4.

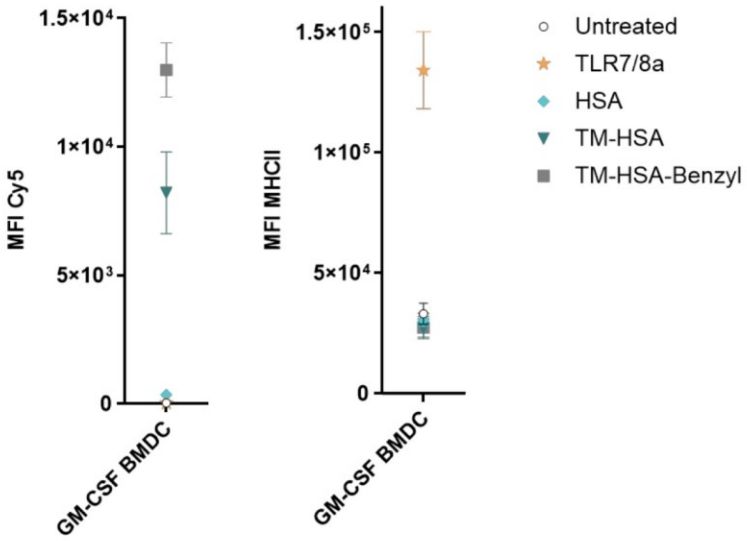

Figure S16: FACS analysis of uptake of unloaded TM-HSA and benzyl loaded nanocarrier uptake in GM-CSF dif. BMDC (left) and corresponding immunostimulation (MHC II expression) after overnight incubation (50 nM). Data are presented as mean ± SEM, n=3.

Supporting Information

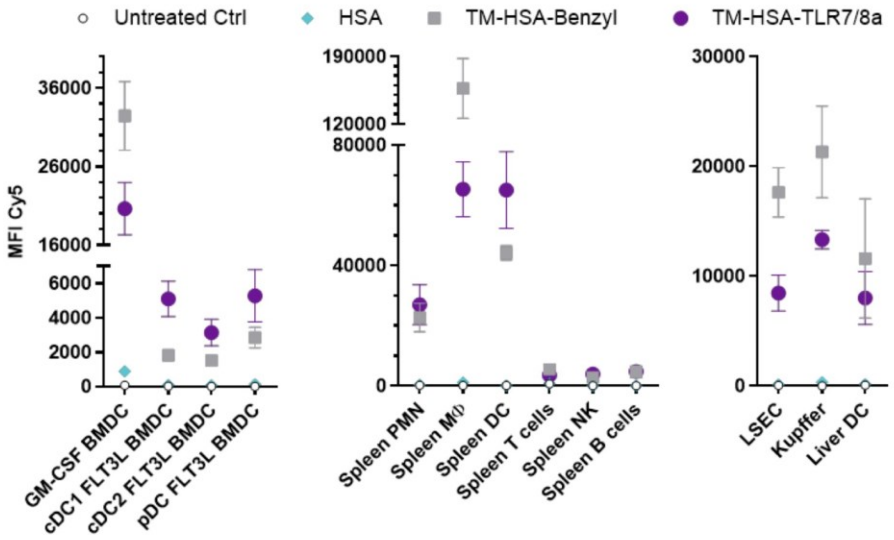

Figure S17: FACS analysis of uptake in GM-CSF differentiated BMDC, in FLT3L differentiated BMDC, in spleenic macrophages and DC, and in LSEC, Kupffer cells and liver DC after overnight incubation with different HSA conjugates (50 nM). Data are presented as mean ± SEM, n=3–6.

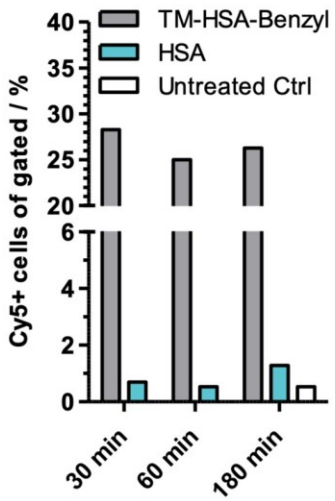

Figure S18: FACS analysis of time dependent benzyl loaded nanocarrier uptake in GM-CSF BMDC after incubation on ice (10 nM, n=1).

Supporting Information

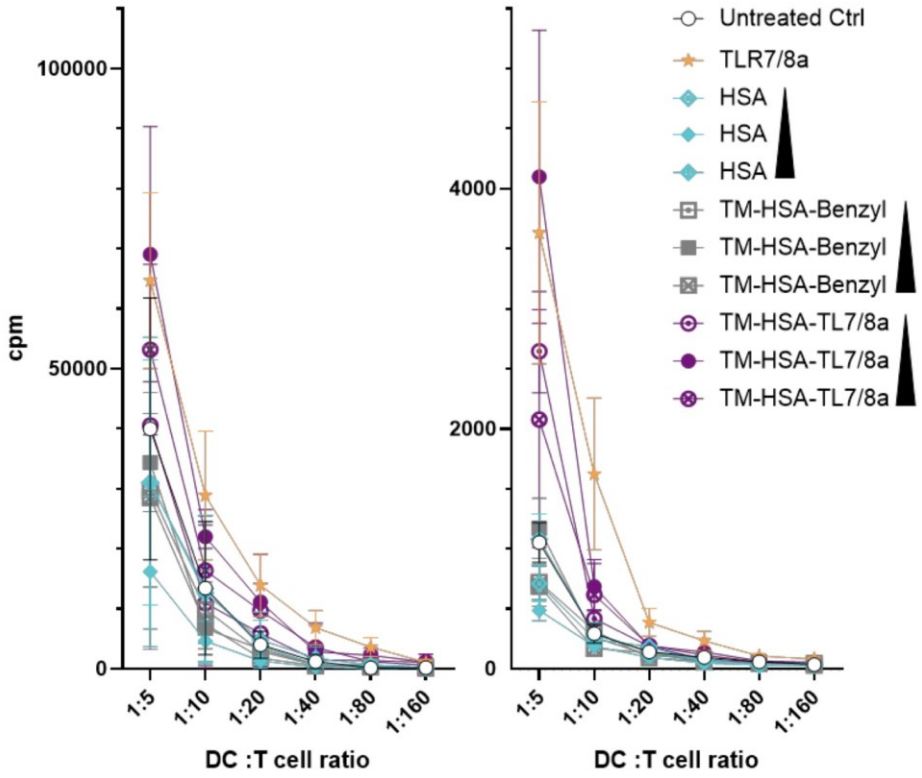

Figure S19: T-cell proliferation (cpm) of OVA peptide-specific $CD8^+$ (OT-I) or $CD4^+$ (OT-II) after co-culture with GM-CSF-differentiated BMDC which were preincubated with OVA (5 µg/mL) and subsequently with different HSA conjugates (1, 10 or 50 nM,corresponding to 20.5, 205 or 1025 nM TLR7/8 agonist) or small molecule TLR7/8 agonist (1.025 µM, 0.371 µg/mL). Data are presented as mean ± SEM, n=6.

Supporting Information

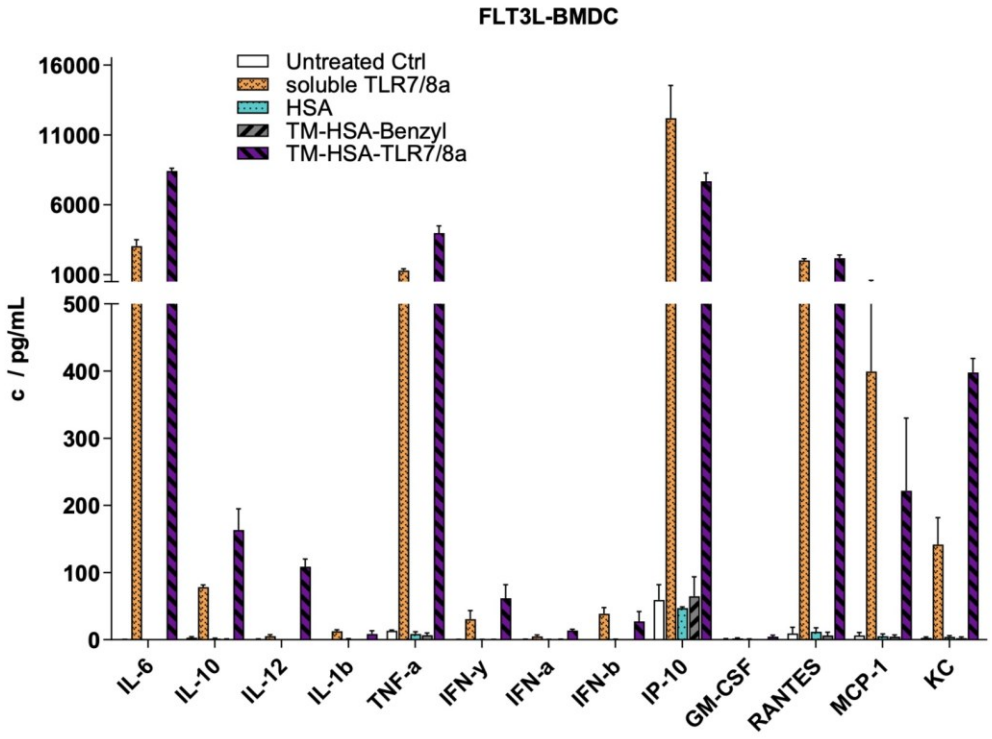

Figure S20: Full CBA of FLT3L-differentiated BMDC after overnight incubation with TLR7/8a-loaded nanocarrier or controls (50 nM, n=2). Data are presented as mean ± SEM, n=3.

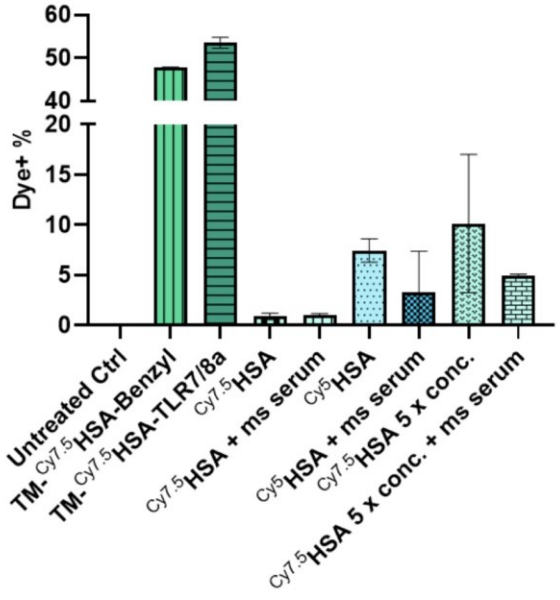

Figure S21: FACS analysis comparison of dye-positive spleen cells incubated overnight with Cy5- or Cy7.5 labeled HSAs and negative (untreated) or positive (TM-HSA-Benzyl, TM-HSA-TLR7/8a) controls (50 nM). Data are presented as mean ± SEM, n=2.

Supporting Information

8 Biodistribution

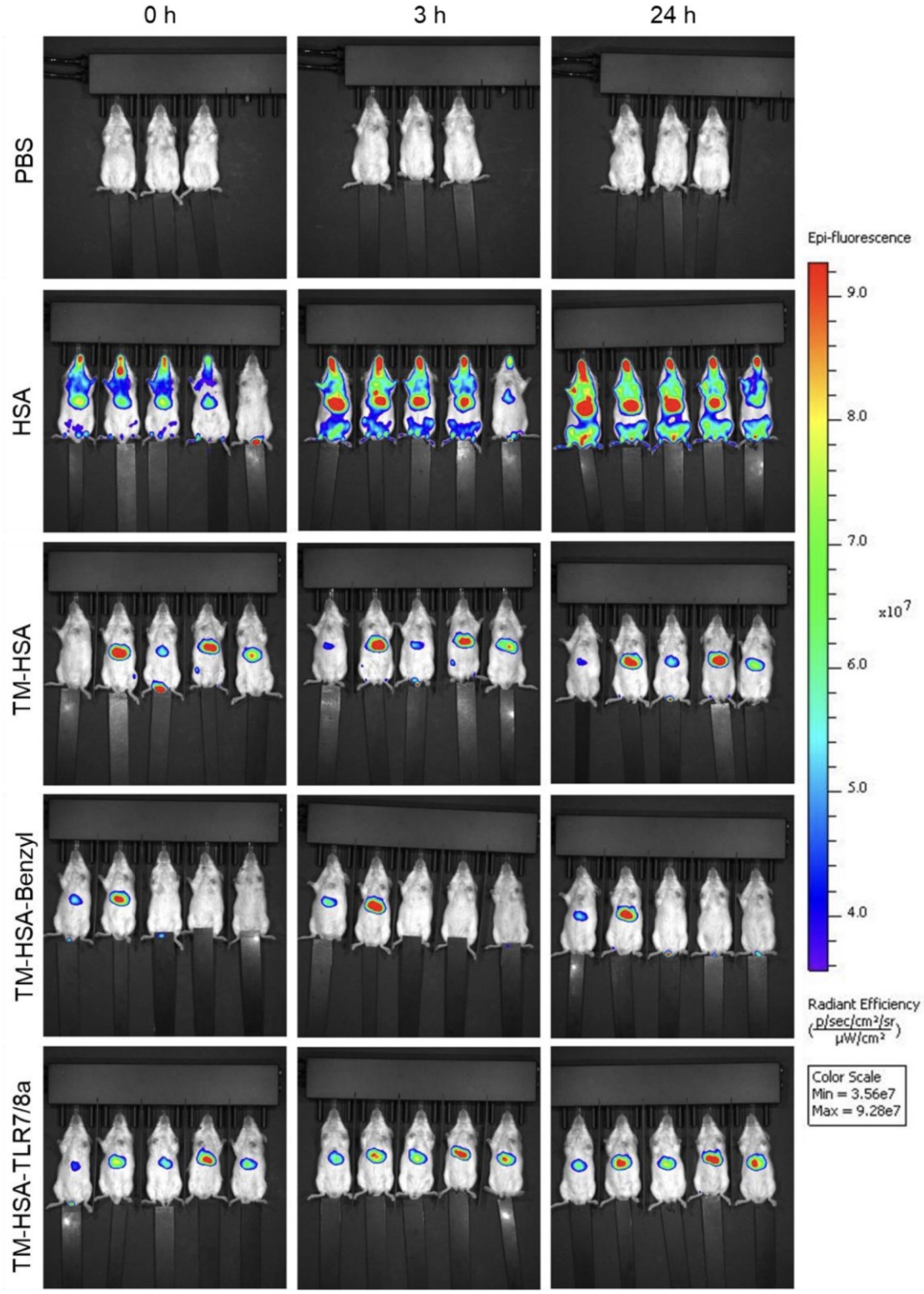

Figure S22: IVIS *in vivo* imaging of biodistribution experiment of Cy7.5 dye labeled HSA and TM-HSA conjugates after 0, 3 and 24 h post-injection. Excitation time = 15 s. n=3 (PBS) or 5 (all other groups). Mouse 5 (HSA group), Mouse 1 (TM-HSA

Supporting Information

group) and Mice 3–5 (TM-HSA-benzyl group) are excluded from quantification and statistical analysis because the injection *via* the tail vein was not complete and therefore they show no or significantly reduced fluorescence signals.

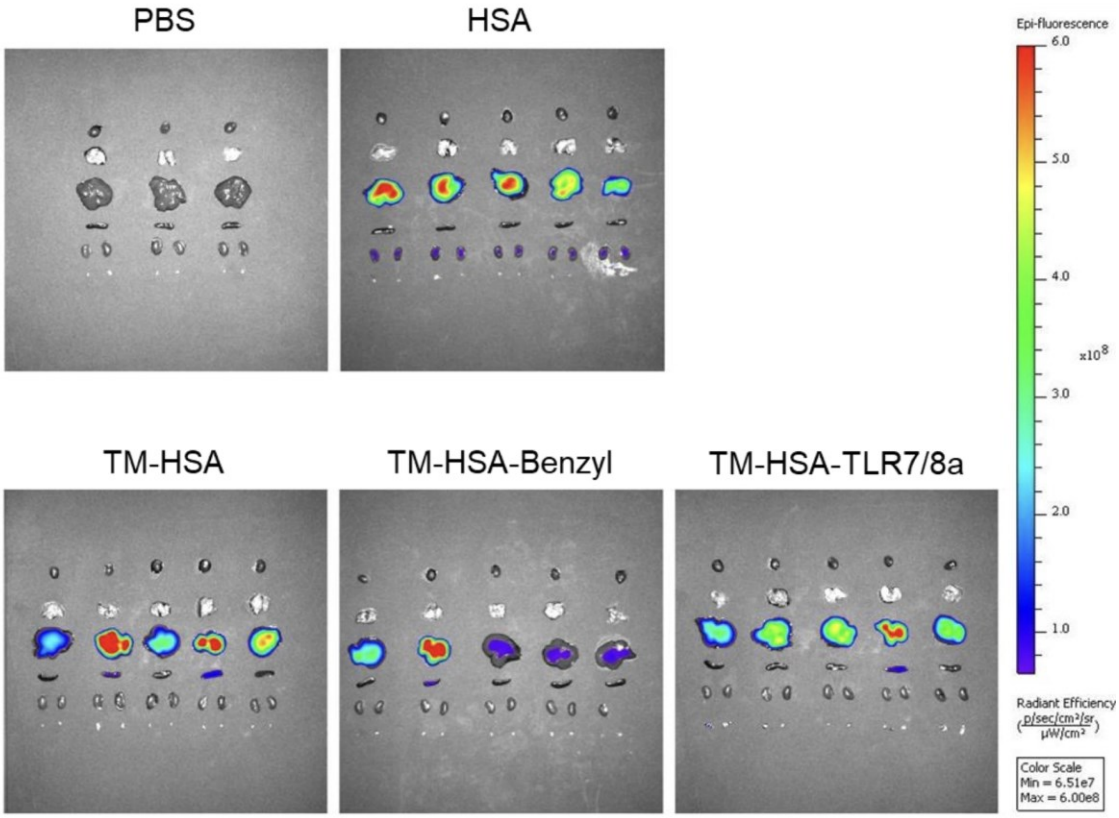

Figure S23: IVIS ex vivo imaging of organs of Cy7.5 dye labeled HSA and TM-HSA conjugates after 24 h post-injection. Excitation time = 15 s. . n=3 (PBS) or 5 (all other groups).

Supporting Information

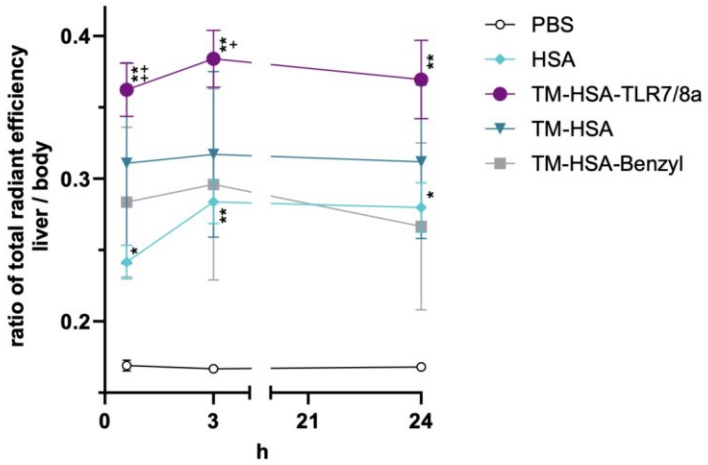

Figure S24: Ratio of total radiant efficiency of liver to whole body 0.1, 3, 24 h post injection based on in vivo IVIS images. Data denote ratio of total radiant efficiency ± SEM , n=3 (PBS), n=2 (TM-HSA-Benzyl), n=4 (HSA, TM-HSA) and n=5 (TM-HSA-TLR7/8a) . Statistical differences are indicated: vs. + HSA and * PBS Ctrl (two-way ANOVA, Tukey test). *,+ $p < 0.05$, **,++ $p < 0.01$, ***,+++ $p < 0.001$, ****,++++ $p < 0.0001$; TM-HSA-Benzyl group was excluded from statistical analysis due to sample size (n=2).

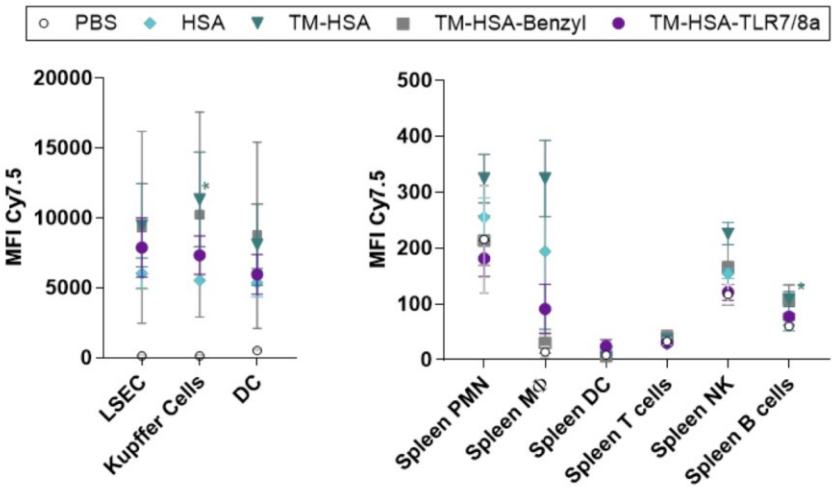

Figure S25: FACS analysis of isolated liver NPC and spleen cells 24 h after injection of HSA conjugates. Graphs denote mean ± SEM of Cy7.5 signal. Statistical differences versus * PBS Ctrl are indicated (one way ANOVA, Tukey test). * $p < 0.05$, **** $p < 0.0001$. TM-HSA-Benzyl group was excluded from statistical analysis due to sample size (n=2).

Supporting Information

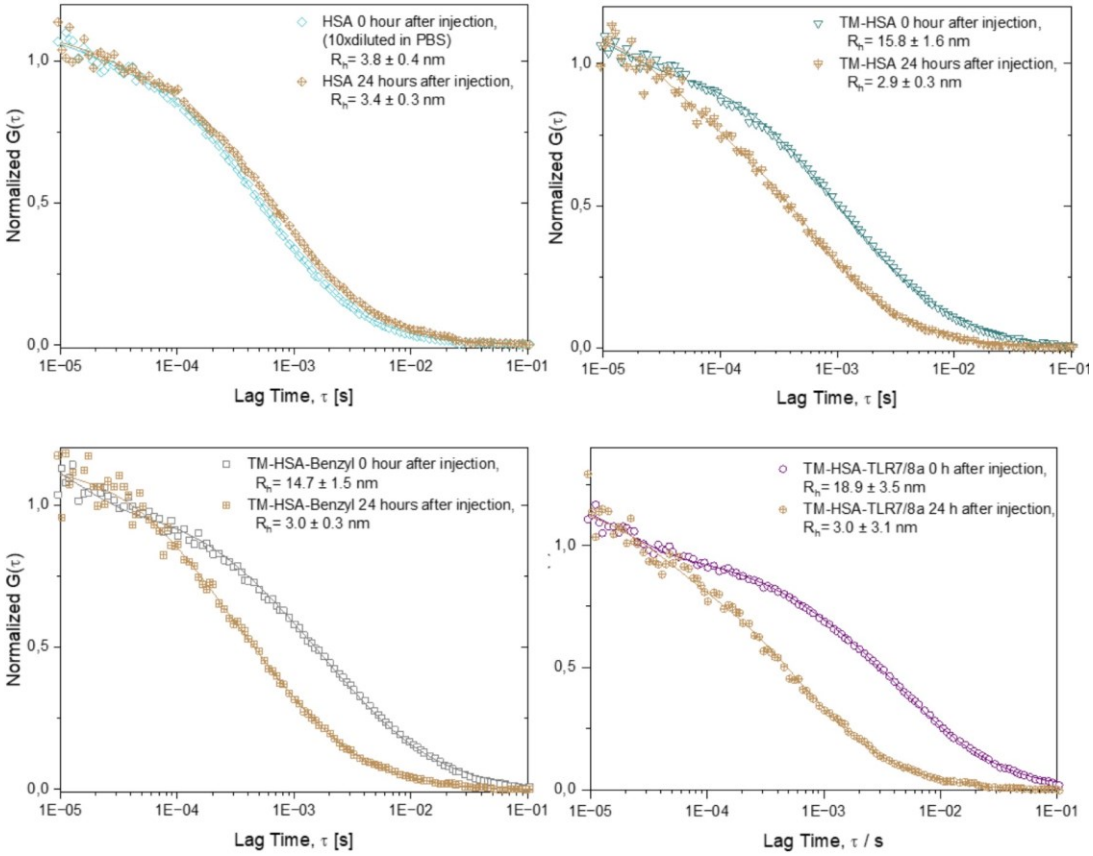

Figure S26: Representative, normalized FCS correlation curves and hydrodynamic radii (Rh) of HSA (top left), TM-HSA (top right), TM-HSA-Benzyl (bottom left) and TM-HSA-TLR7/8a (bottom right) during biodistribution. Note that the curves for the trimannosylated samples 24 h after i.v. injection originate from a very small amount of initially non covalently bound Cy7.5 attaching to endogenous mouse blood proteins. Data are presented as mean ± SD, n=2–5.

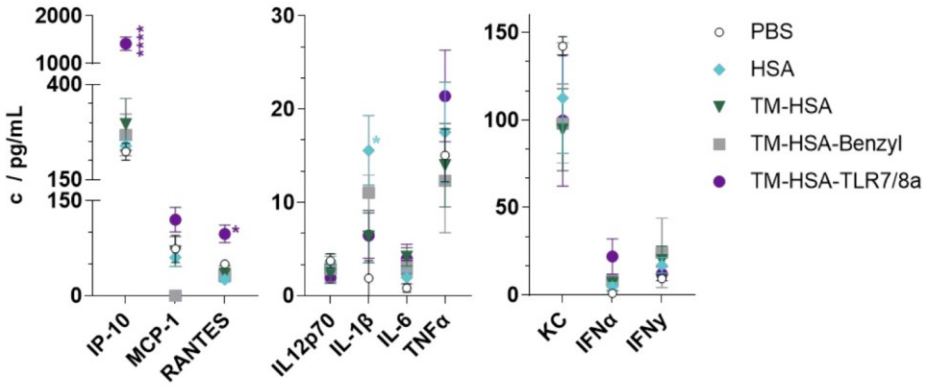

Figure S27: Serum cytokine levels 24 h post-injection assayed by CBA. Data denote mean ± SEM, n=3 (PBS), n=2 (TM-HSA-Benzyl), n=4 (HSA, TM-HSA, TM-HSA-TLR7/8). Statistical differences versus * PBS Ctrl are indicated (one way ANOVA, Tukey test). * $p < 0.05$, **** $p < 0.0001$. TM-HSA-Benzyl group was excluded from statistical analysis due to sample size (n=2).

Supporting Information

9 Appendix

9.1 List of references

(1) Still, W. C.; Kahn, M.; Mitra, A. Rapid chromatographic technique for preparative separations with moderate resolution. *J. Org. Chem.* **1978**, *43* (14), 2923-2925. DOI: 10.1021/jo00408a041.

(2) Rigler, R.; Elson, E. S. *Fluorescence correlation spectroscopy: theory and applications*; Springer Berlin, Heidelberg, 2012.

(3) Martinez-Pomares, L.; Reid, D. M.; Brown, G. D.; Taylor, P. R.; Stillion, R. J.; Linehan, S. A.; Zamze, S.; Gordon, S.; Wong, S. Y. C. Analysis of mannose receptor regulation by IL-4, IL-10, and proteolytic processing using novel monoclonal antibodies. *J. Leukocyte Biol.* **2003**, *73* (5), 604-613. DOI: 10.1189/jlb.0902450.

(4) Krabicová, I.; Dolenský, B.; Řezanka, M. Selectivity of 1-O-Propargyl-d-Mannose Preparations. *Molecules* **2022**, *27* (5), 1483. DOI: 10.3390/molecules27051483.

(5) Ramos-Soriano, J.; de la Fuente, M. C.; de la Cruz, N.; Figueiredo, R. C.; Rojo, J.; Reina, J. J. Straightforward synthesis of Man9, the relevant epitope of the high-mannose oligosaccharide. *Org. Biomol. Chem.* **2017**, *15* (42), 8877-8882, 10.1039/C7OB02286G. DOI: 10.1039/C7OB02286G.

(6) Percec, V.; Leowanawat, P.; Sun, H.-J.; Kulikov, O.; Nusbaum, C. D.; Tran, T. M.; Bertin, A.; Wilson, D. A.; Peterca, M.; Zhang, S. Modular synthesis of amphiphilic Janus glycodendrimers and their self-assembly into glycodendrimersomes and other complex architectures with bioactivity to biomedically relevant lectins. *J. Am. Chem. Soc.* **2013**, *135* (24), 9055-9077. DOI: 10.1021/ja403323y.

(7) Schibilla, F.; Voskuhl, J.; Fokina, N. A.; Dahl, J. E. P.; Schreiner, P. R.; Ravoo, B. J. Host–Guest Complexes of Cyclodextrins and Nanodiamonds as a Strong Non-Covalent Binding Motif for Self-Assembled Nanomaterials. *Chem. Eur. J.* **2017**, *23* (63), 16059-16065. DOI: 10.1002/chem.201703392.

(8) Kramer, S.; Langhanki, J.; Krumb, M.; Opatz, T.; Bros, M.; Zentel, R. HPMA-Based Nanocarriers for Effective Immune System Stimulation. *Macromol. Biosci.* **2019**, *19* (6), 1800481. DOI: 10.1002/mabi.201800481.

(9) Zhang, Y.; Chen, C.; Jin, L.; Tan, H.; Wang, F.; Cao, H. Synthesis of unsymmetrical 3,6-branched Man5 oligosaccharide: a comparison between one-pot sequential glycosylation and stepwise synthesis. *Carbohydr. Res.* **2015**, *401*, 109-114. DOI: 10.1016/j.carres.2014.09.010.

(10) Du, Y.; Zhang, M.; Kong, F. Highly efficient and practical synthesis of 3, 6-branched oligosaccharides. *Org. Lett.* **2000**, *2* (24), 3797-3800. DOI: 10.1021/ol000243w.

(11) Traboni, S.; Bedini, E.; Iadonisi, A. Orthogonal protection of saccharide polyols through solvent-free one-pot sequences based on regioselective silylations. *Beilstein J. Org. Chem.* **2016**, *12* (1), 2748-2756. DOI: 10.3762/bjoc.12.271.

(12) Ekholm, F. S.; Poláková, M.; Pawłowicz, A. J.; Leino, R. Synthesis of divalent 2, 2′-linked mannose derivatives by homodimerization. *Synth.* **2009**, *2009* (4), 567-576. DOI: 10.1055/s-0028-1083283.

(13) Krumb, M.; Frey, M.-L.; Langhanki, J.; Forster, R.; Kowalczyk, D.; Mailänder, V.; Landfester, K.; Opatz, T. Multivalency Beats Complexity: A Study on the Cell Uptake of Carbohydrate Functionalized Nanocarriers to Dendritic Cells. *Cells* **2020**, *9* (9), 2087. DOI: 10.3390/cells9092087.

(14) Bonger, K. M.; van den Berg, R. J. B. H. N.; Heitman, L. H.; Ijzerman, A. P.; Oosterom, J.; Timmers, C. M.; Overkleeft, H. S.; van der Marel, G. A. Synthesis and evaluation of homo-bivalent GnRHR ligands. *Bioorg. Med. Chem.* **2007**, *15* (14), 4841-4856. DOI: 10.1016/j.bmc.2007.04.065.

(15) Davila, J.; Chassepot, A.; Longo, J.; Boulmedais, F.; Reisch, A.; Frisch, B.; Meyer, F.; Voegel, J.-C.; Mésini, P. J.; Senger, B.; et al. Cyto-mechanoresponsive Polyelectrolyte Multilayer Films. *J. Am. Chem. Soc.* **2012**, *134* (1), 83-86. DOI: 10.1021/ja208970b.

(16) Lapeyre, M.; Leprince, J.; Massonneau, M.; Oulyadi, H.; Renard, P.-Y.; Romieu, A.; Turcatti, G.; Vaudry, H. Aryldithioethyloxycarbonyl (Ardec): A New Family of Amine Protecting Groups Removable under Mild Reducing Conditions and Their Applications to Peptide Synthesis. *Chem. Eur. J.* **2006**, *12* (13), 3655-3671. DOI: 10.1002/chem.200501538.

(17) Latorre, A.; Couleaud, P.; Aires, A.; Cortajarena, A. L.; Somoza, Á. Multifunctionalization of magnetic nanoparticles for controlled drug release: A general approach. *Eur. J. Med. Chem.* **2014**, *82*, 355-362. DOI: 10.1016/j.ejmech.2014.05.078.

Supporting Information

9.2 List of abbreviations

$(HF)_X$·Pyr	Hydrogen fluoride pyridine complex	ESI	Electrospray ionization
Ac_2O	Acetic anhydride	Et_2O	Diethylether
AgOTf	Silver triflate	EtOAc	Ethyl acetate
Ar-atm.	Argon atmosphere	EtOH	Ethanol
ATR	Attenuated total reflection	FACS	Florescence assisted cell sorting
BF_3·OEt_2	Boron trifluoride diethyl etherate	FCC	Flash column chromatography
BMDC	Bone marrow derived dendritic cell	FCS	Fluorescence correlation spectroscopy
$BnNH_2$	Benzylamine	H_2O (MQ)	Ultrapure water
BzCl	Benzoyl chloride	H_2SO_4	Sulfuric acid
CD	Circular dichroism	HCl	Hydrochloric acid
CD_2Cl_2	Deuterated DCM	HCOOH	Formic acid
CD_3CN	Deuterated Acetonitrile	HMBC	Heteronuclear multiple bond correlation
CD_3OD	Deuterated methanol	HOPrg	Propargyl alcohol
$CDCl_3$	Deuterated Chloroform	HPLC	High performance liquid chromatography
^{c}Hex	Cyclohexane	HR	High resolution
CHO	Chinese hamster ovary	HSA	Human serum albumin
COSY	Correlated spectroscopy	HSQC	Heteronuclear Single Quantum Coherence
Crtl	Control	HSQC-NoDec	HSQC without decoupling
CuBr	Copper(I)bromide	I_2	Molecular iodine
Cy5	Cyanine 5 dye	IR	Infra-red
D	Diffusion coefficient	$KMnO_4$	Potassium permanganate
D_2O	Deuterium oxide	KOH	Potassium hydroxide
DAD	Diode array detector	MALDI-ToF-MS	Matrix assisted laser desorption ionization with time-of-flight mass spectrometry
DBCO	Dibenzocyclooctyne	MeOH	Methanol
DCM	Dichloromethane	MMR	Macrophage mannose receptor
DC-SIGN	Dendritic cell specific icam-3 grabbing non integrin	MS	Mass spectrometry
DIPEA	*N,N*-Diisopropylethylamine	MS 3 Å	Molecular sieves (Pore size 3 Å)
DLS	Dynamic light scattering	$Na_2S_2O_3$	Sodium thiosulfate
DMAP	*N,N*-Dimethylpyridin-4-amine	Na_2SO_4	Sodium sulfate
DMF	Dimethylformamide	NaCl	Sodium chloride
DMF-d_7	Deuterated DMF	$NaHCO_3$	Sodium bicarbonate
DMSO	Dimethyl sulfoxide	NaN_3	Sodium azide
DoL	Degree of labeling	NaOH	Sodium hydroxide
DoM	Degree of modification	NaOMe	Sodium methoxide
dPBS	Dulbecco´s phosphate-buffered solution	NEt_3	Triethylamine
DTT	Dithiothreitol	NHS	*N*-Hydroxysuccinimide
EDTA	Ethylenediaminetetraacetic acid	NIR	Near-infrared
ELS	Evaporative light scattering	NIS	*N*-Iodosuccinimide
Eq.	Equivalent	NMR	Nuclear magnetic resonance

Supporting Information

NOESY	Nuclear Overhauser enhancement spectroscopy
NPC	non-parenchymal cell
OVA	Ovalbumin
PBS	Phosphate-buffered solution
PEG	Polyethylene glycol
pH	Potentia hydrogenii
PhSH	Thiophenol
PMDTA	N^1-[2-(Dimethylamino)ethyl]-N^1,N^2,N^2-trimethylethane-1,2-diamine
Pyr	Pyridine
R_f	Ratio of fronts
R_h	Hydrodynamic radius
RP	Reversed phase
SDS PAGE	Sodium dodecyl sulfate polyacrylamide gel electrophoresis
TBAI	Tetrabutylammonium iodide
TBDMS	*tert*-Butyldimethylsilyl
TCEP	Tris(2-carboxyethyl)phosphine
TFA	Trifluoromethanesulfonic acid
THF	Tetrahydrofuran
TLC	Thin layer chromatography
TLR7/8a	Toll-like receptor 7/8 agonist 1
TM	Trimannose
TOCSY	Total correlation spectroscopy
t_R	Retention time
TsCl	Tosyl chloride

Supporting Information

9.3 NMR spectra

^{1}H-NMR, (300 MHz, $CDCl_3$): **(S1)**

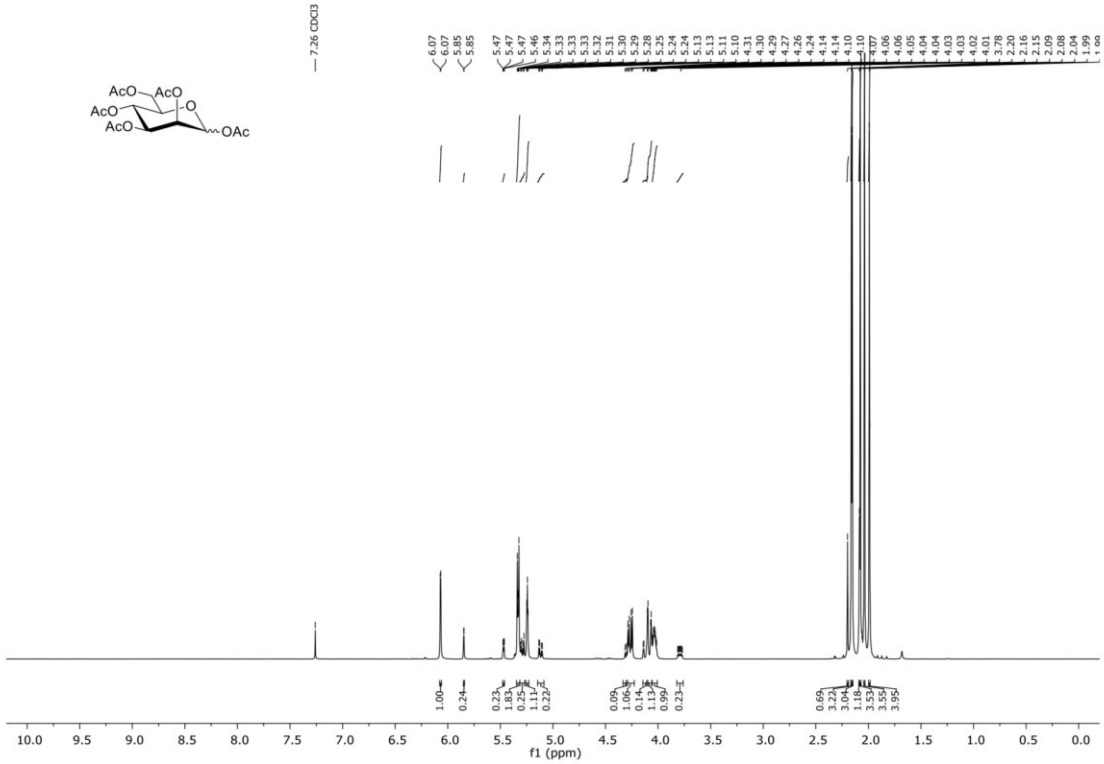

^{1}H-NMR Zoom, (300 MHz, $CDCl_3$): **(S1)**

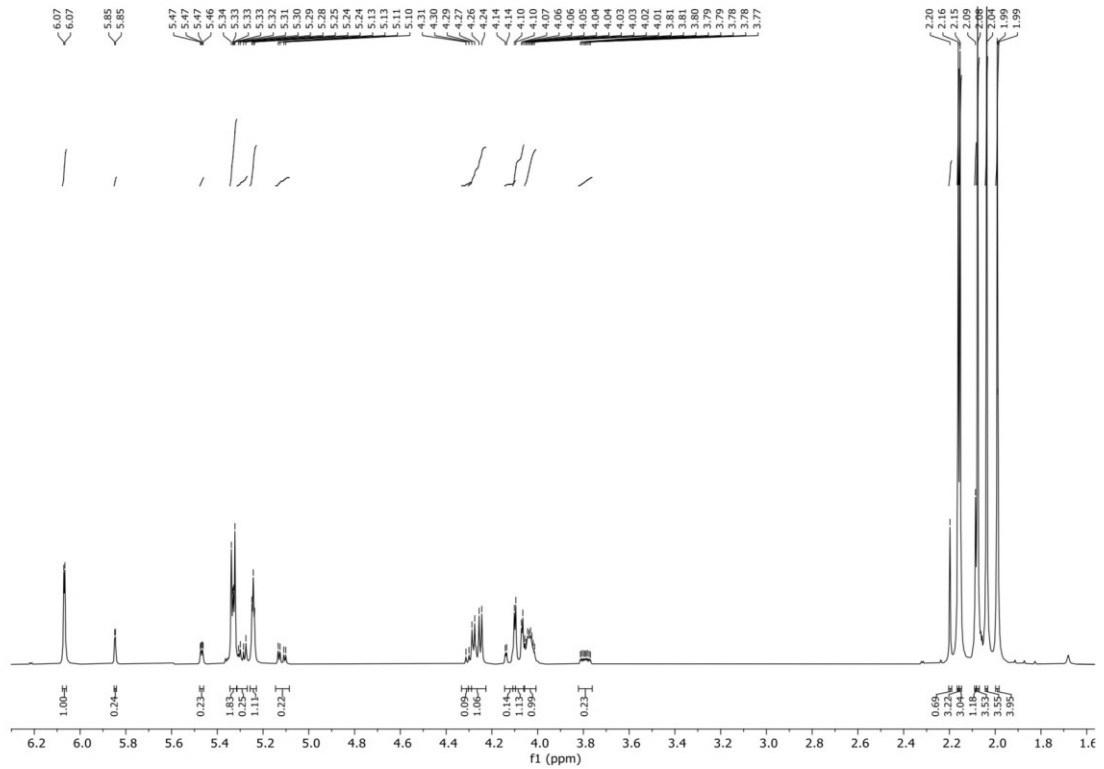

Supporting Information

^{13}C-NMR, (75.5 MHz, $CDCl_3$): **(S1)**

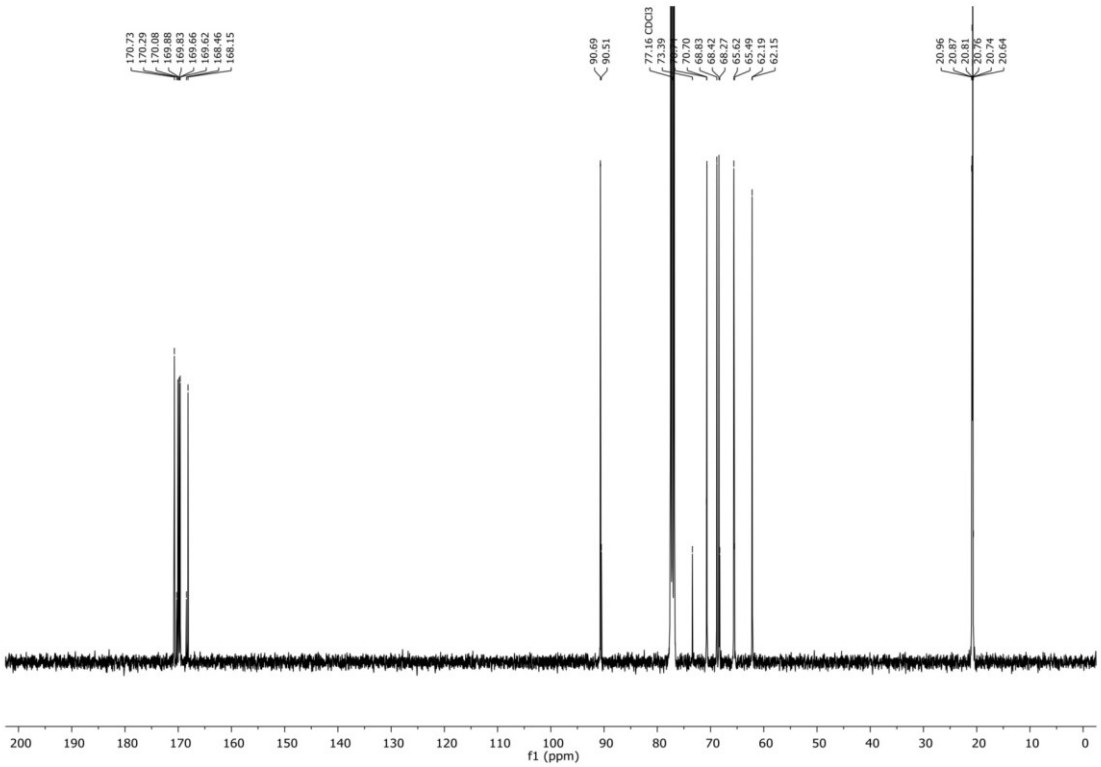

^{1}H-NMR, (400 MHz, $CDCl_3$): **(I1)**

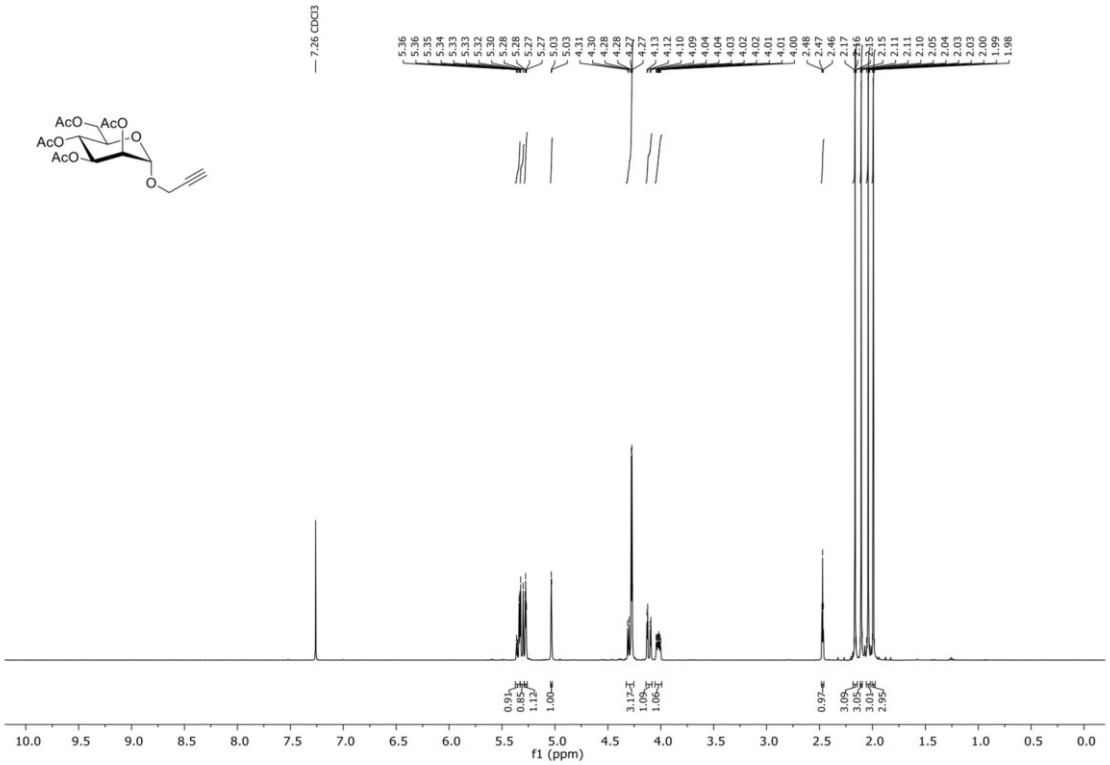

Supporting Information

^{1}H-NMR Zoom, (400 MHz, $CDCl_3$): **(I1)**

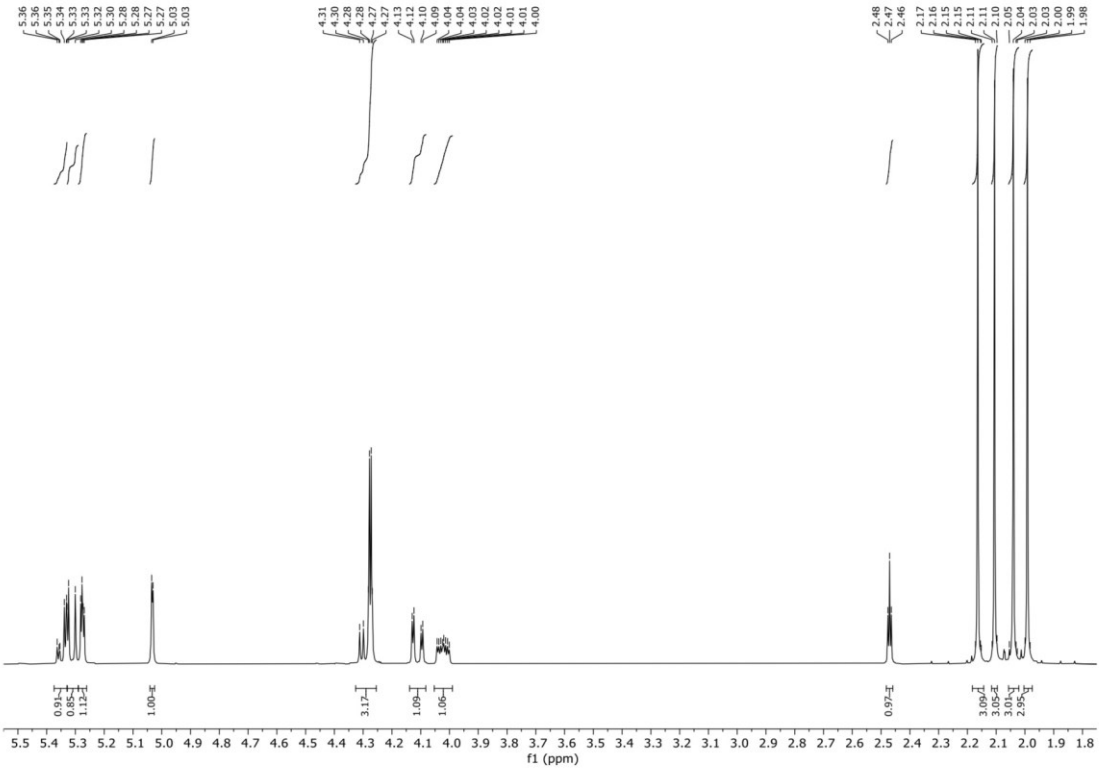

^{13}C-NMR, (100.6 MHz, $CDCl_3$): **(I1)**

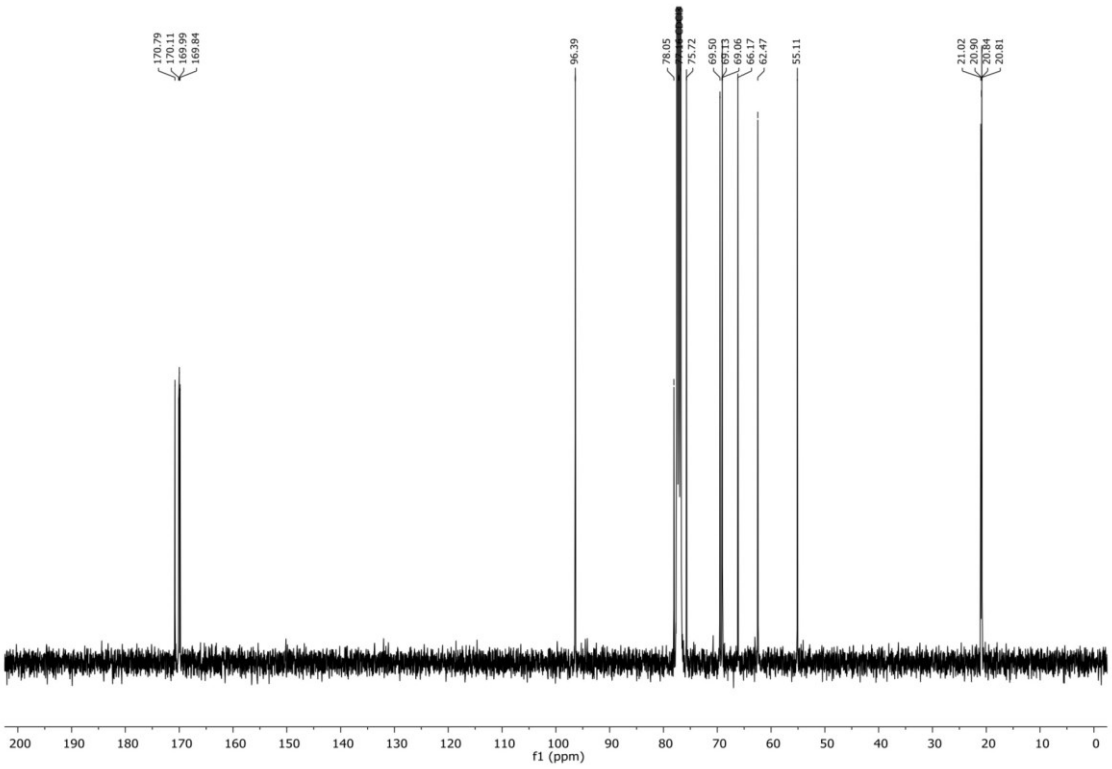

Supporting Information

^{1}H-NMR, (400 MHz, CD_3OD): **(1)**

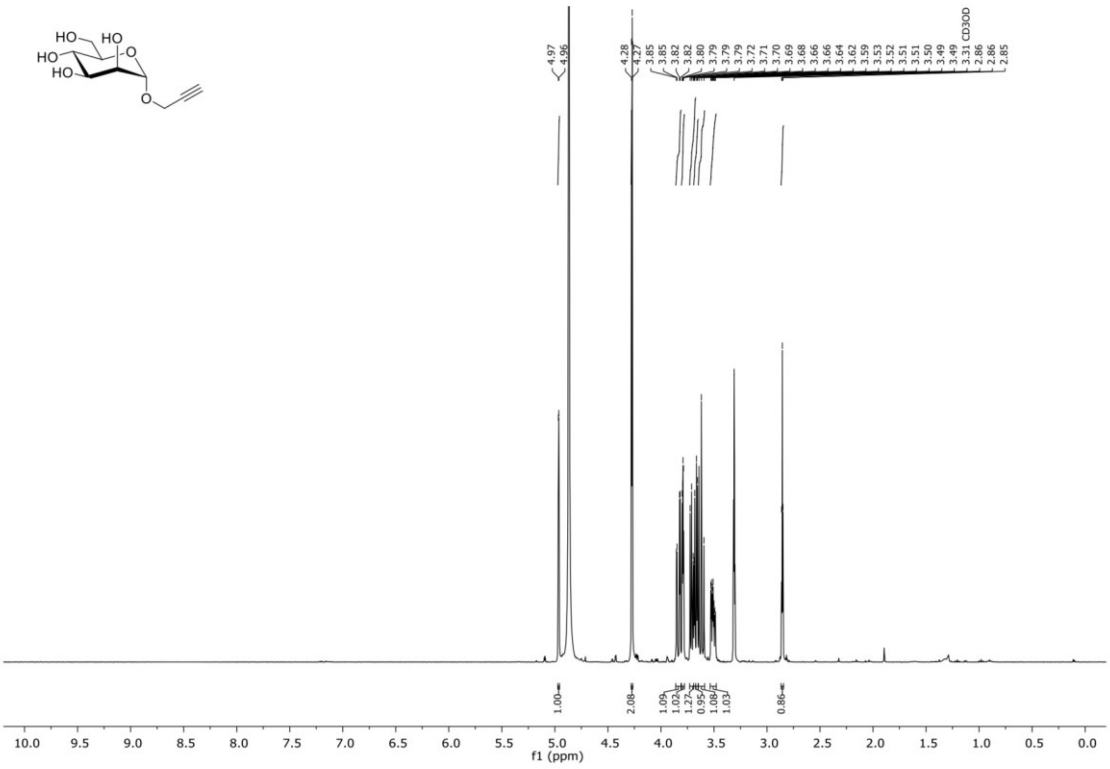

^{1}H-NMR Zoom, (400 MHz, CD_3OD): **(1)**

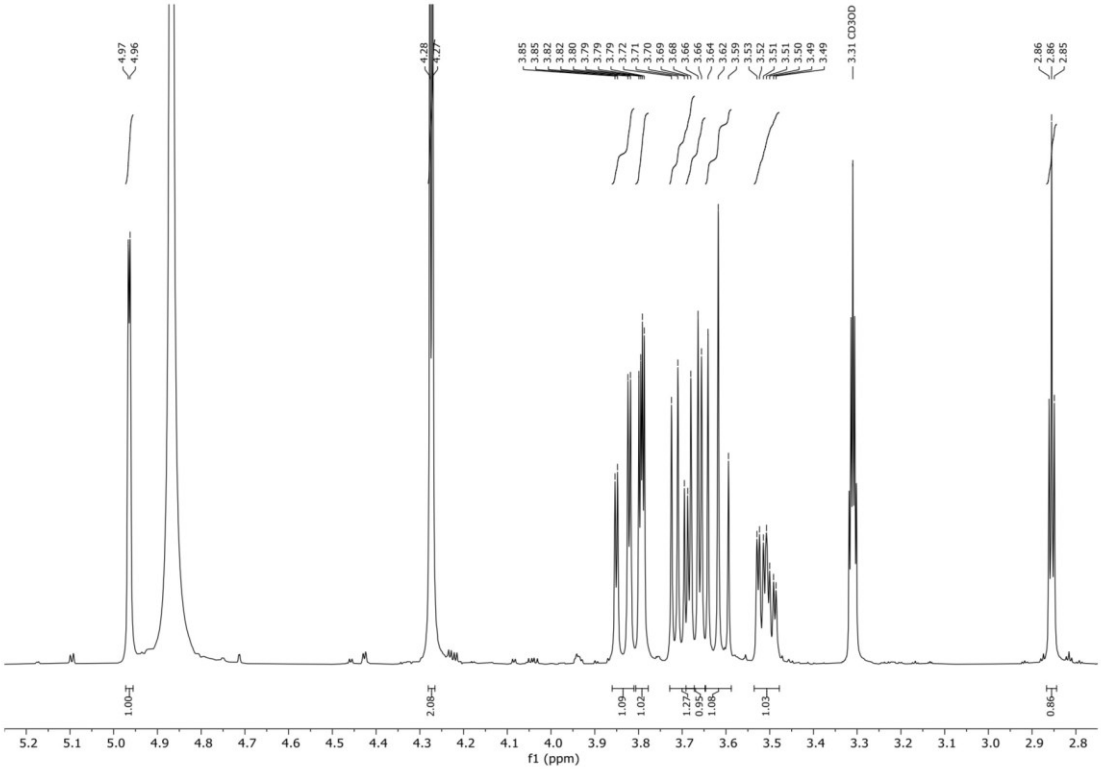

Supporting Information

^{13}C-NMR, (100.6 MHz, CD_3OD): **(1)**

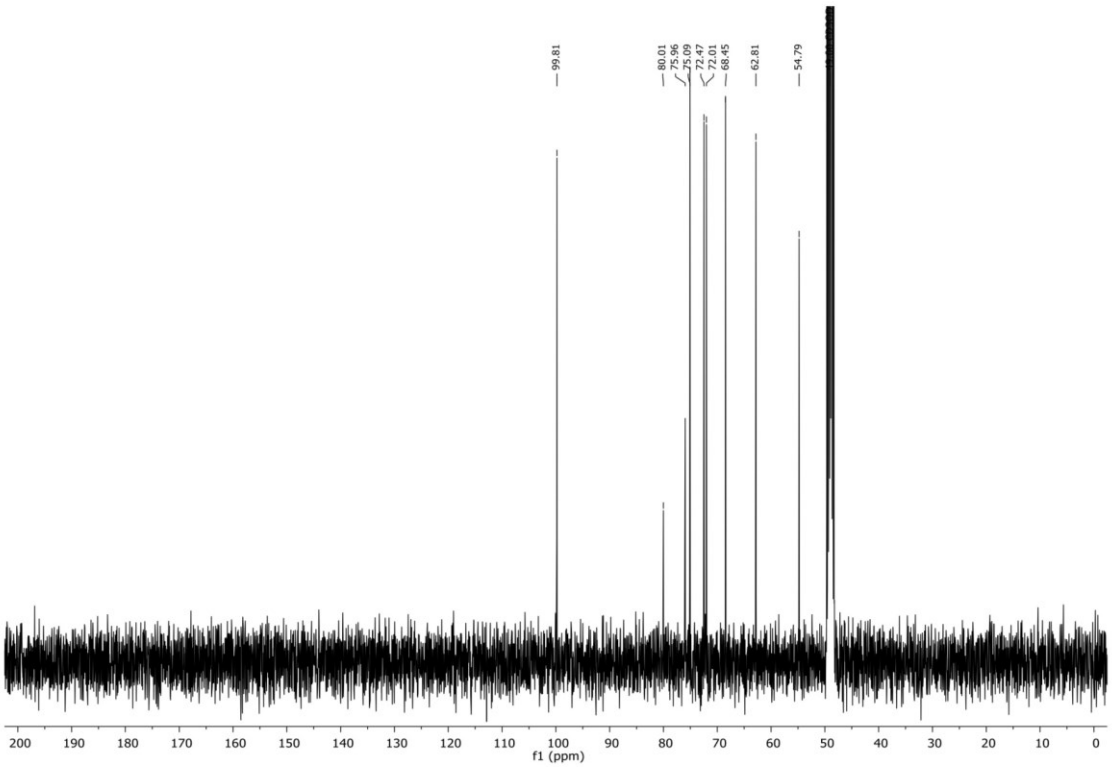

^{1}H-NMR, (400 MHz, $CDCl_3$): **(I2)**

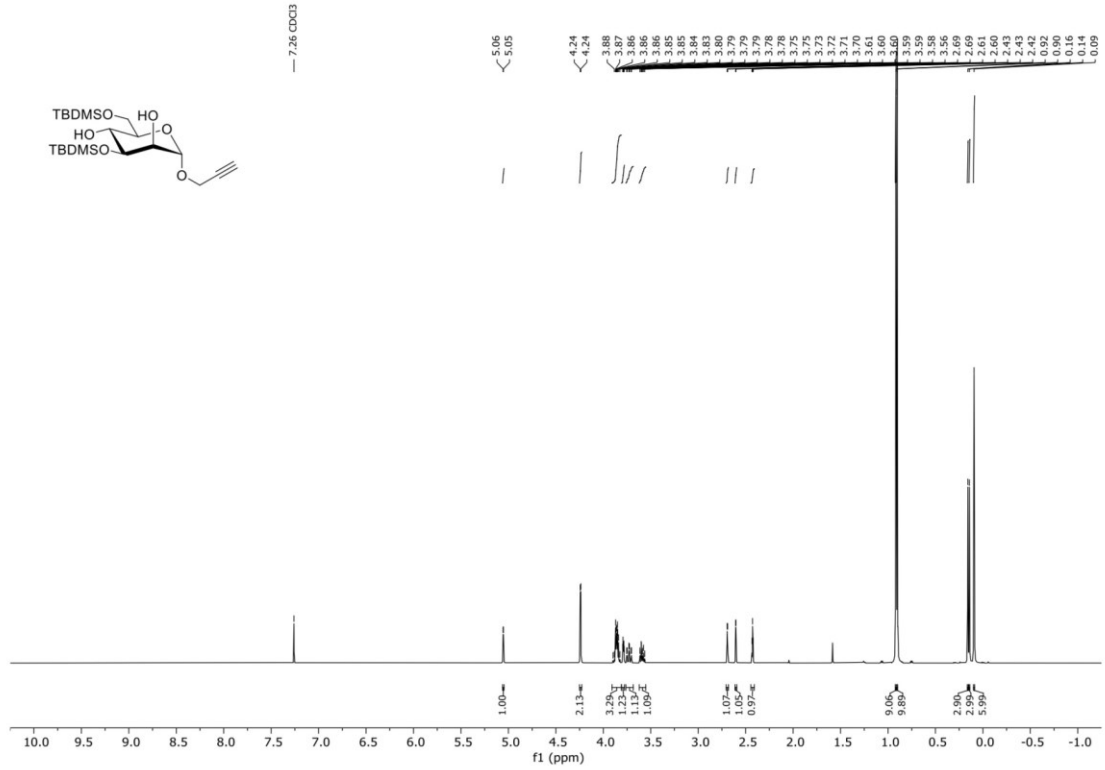

Supporting Information

^{1}H-NMR Zoom, (400 MHz, $CDCl_3$): **(I2)**

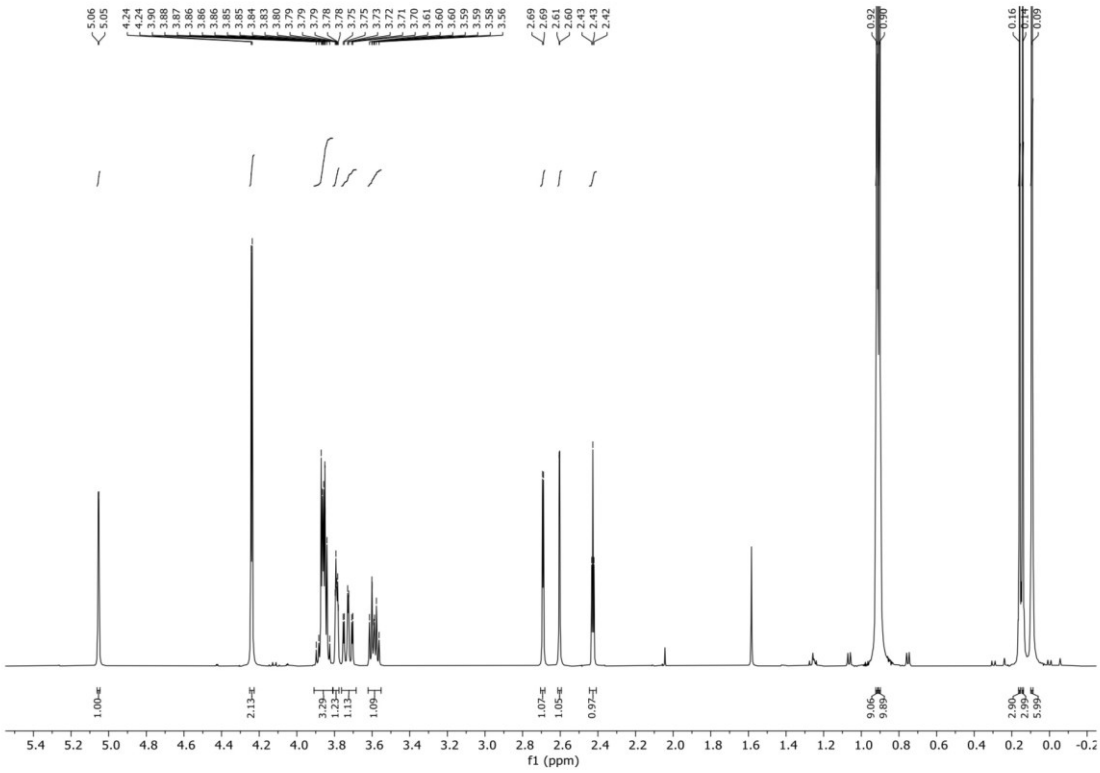

^{13}C-NMR, (100.6 MHz, $CDCl_3$): **(I2)**

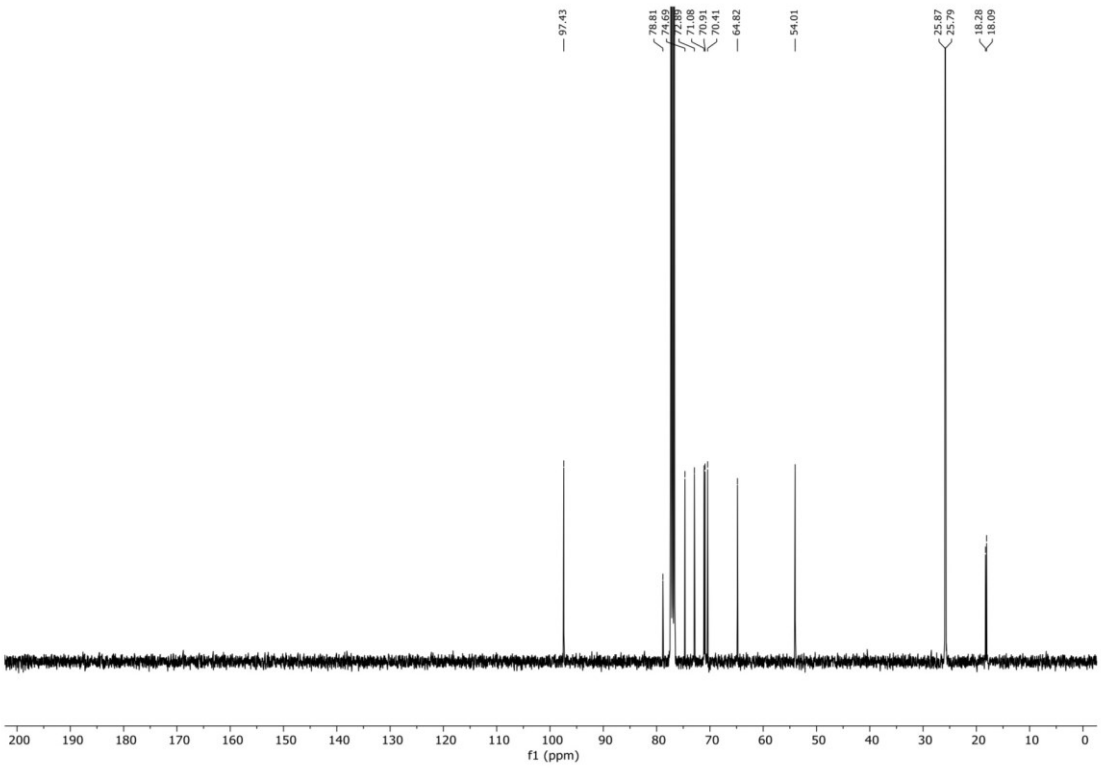

Supporting Information

^{1}H-NMR, (400 MHz, $CDCl_3$): **(I3)**

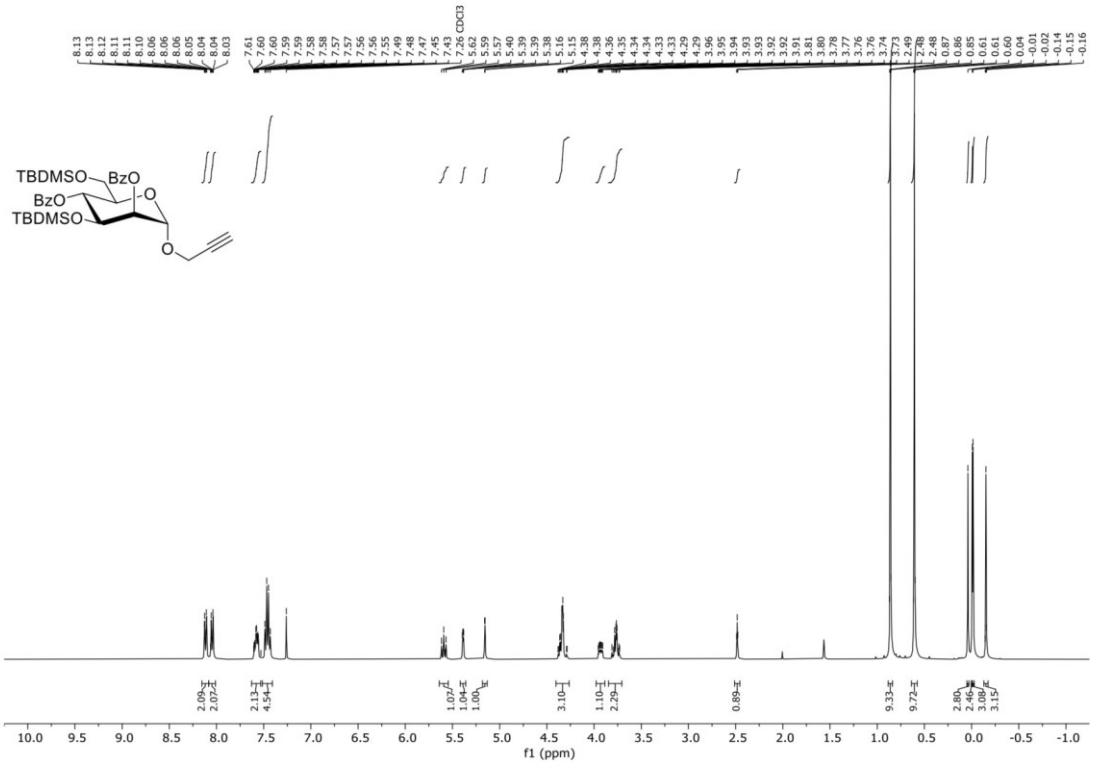

^{1}H-NMR Zoom, (400 MHz, $CDCl_3$): **(I3)**

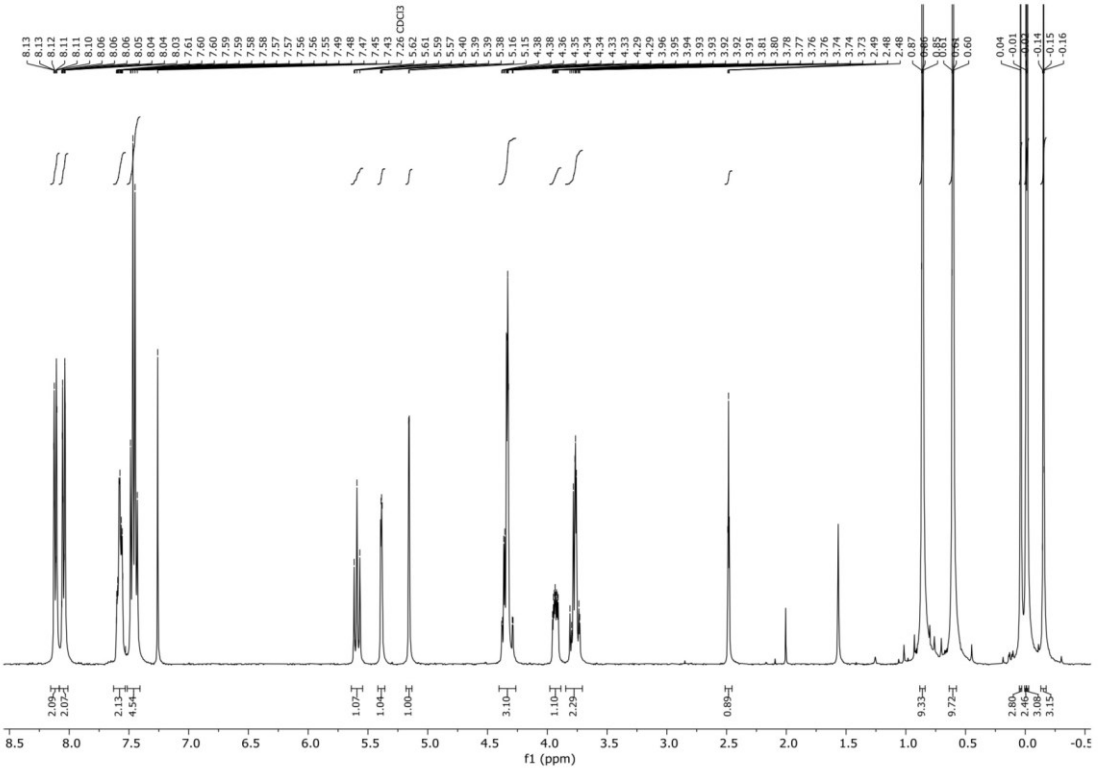

Supporting Information

^{13}C-NMR, (100.6 MHz, $CDCl_3$): **(I3)**

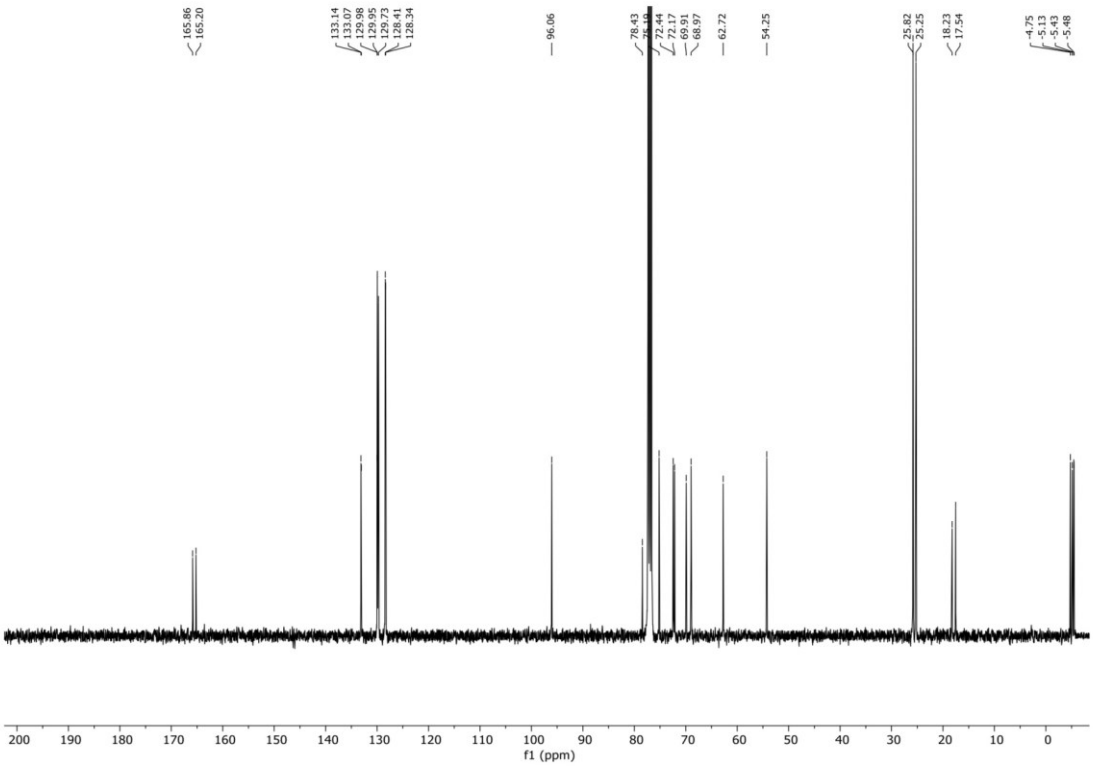

^{1}H-NMR, (400 MHz, $CDCl_3$): **(2)**

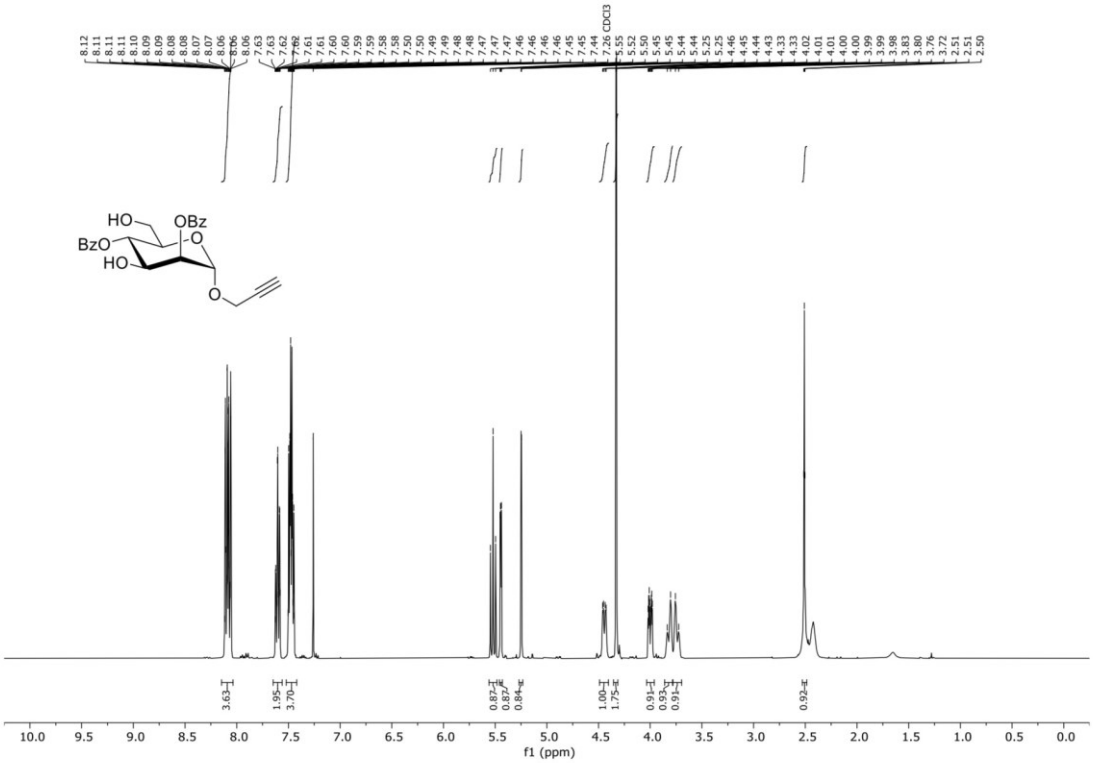

Supporting Information

^{1}H-NMR Zoom, (400 MHz, $CDCl_3$): **(2)**

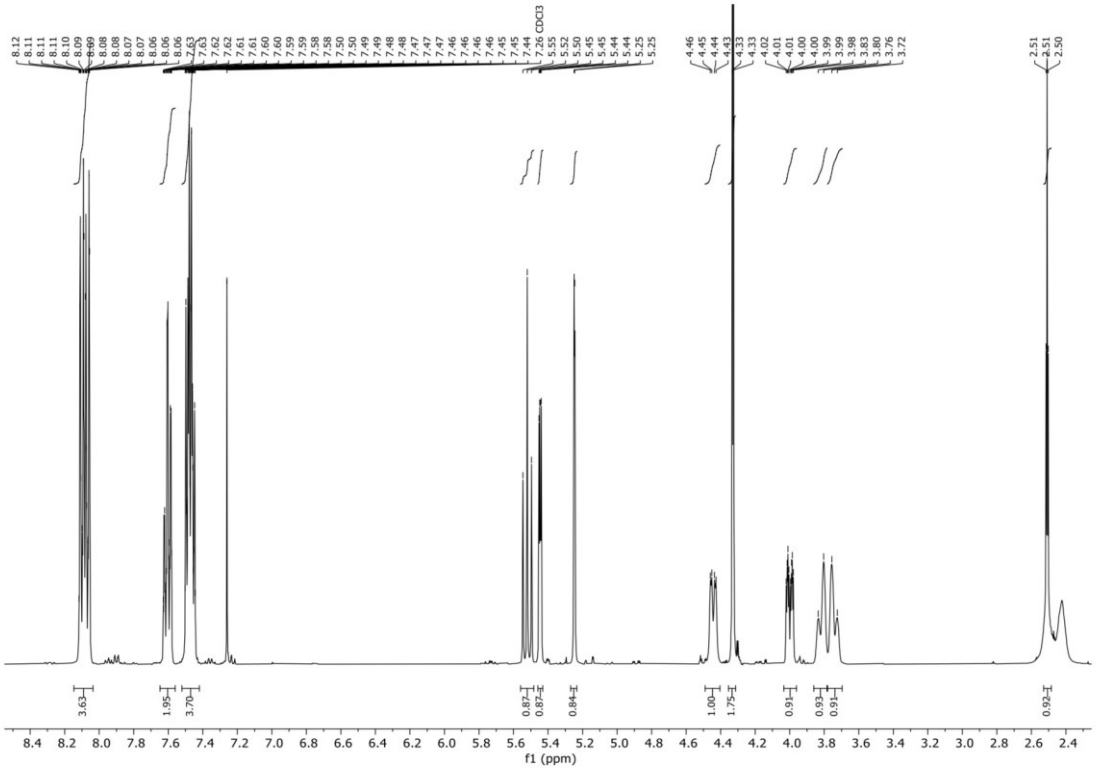

^{13}C-NMR, (100.6 MHz, $CDCl_3$): **(2)**

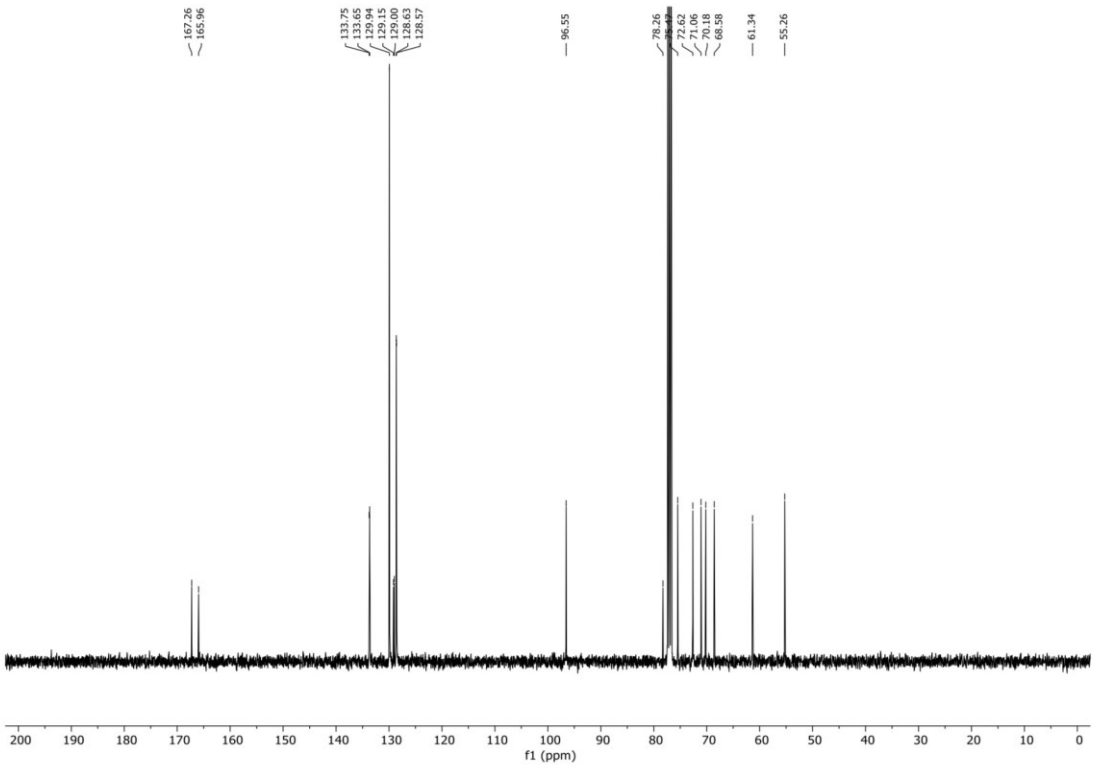

Supporting Information

^{1}H-NMR, (300 MHz, $CDCl_3$): **(3)**

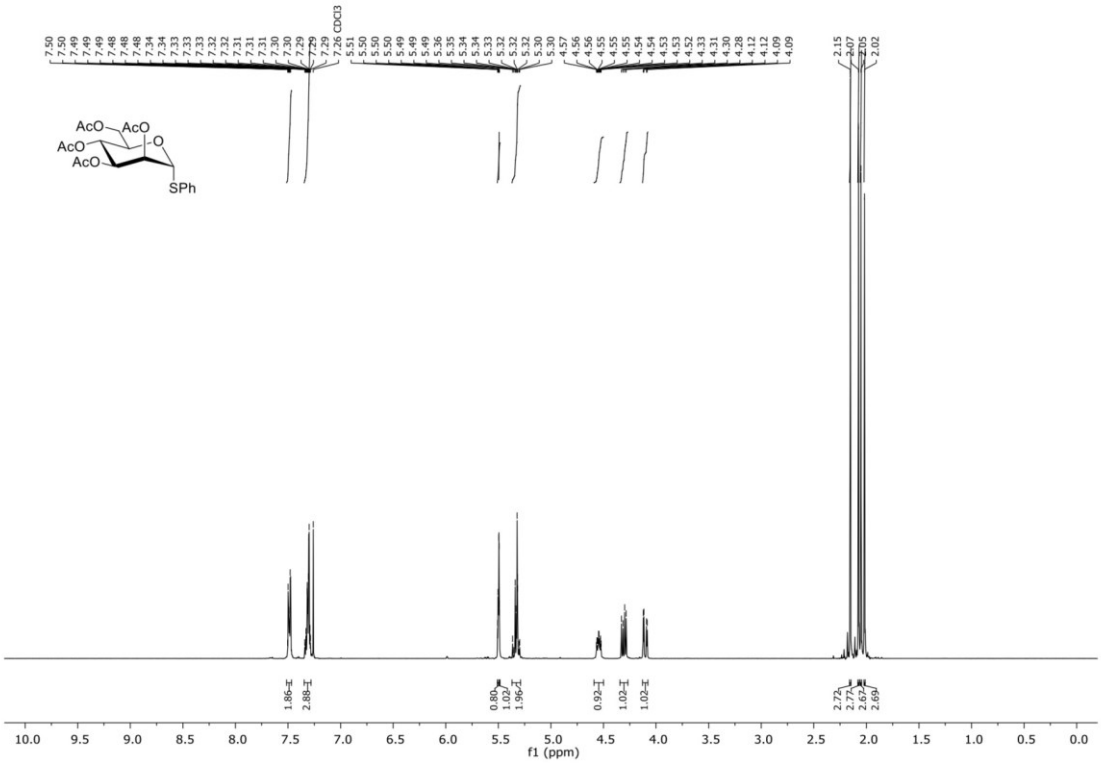

^{1}H-NMR Zoom, (300 MHz, $CDCl_3$): **(3)**

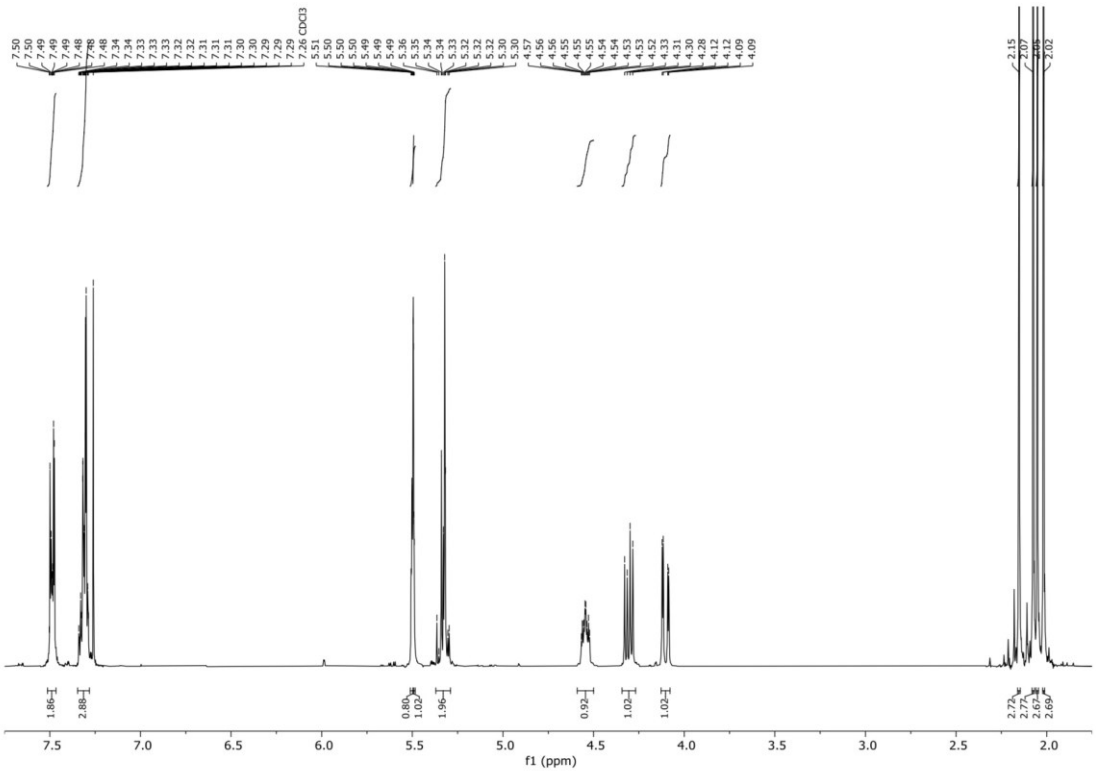

Supporting Information

^{13}C-NMR, (75.5 MHz, $CDCl_3$): **(3)**

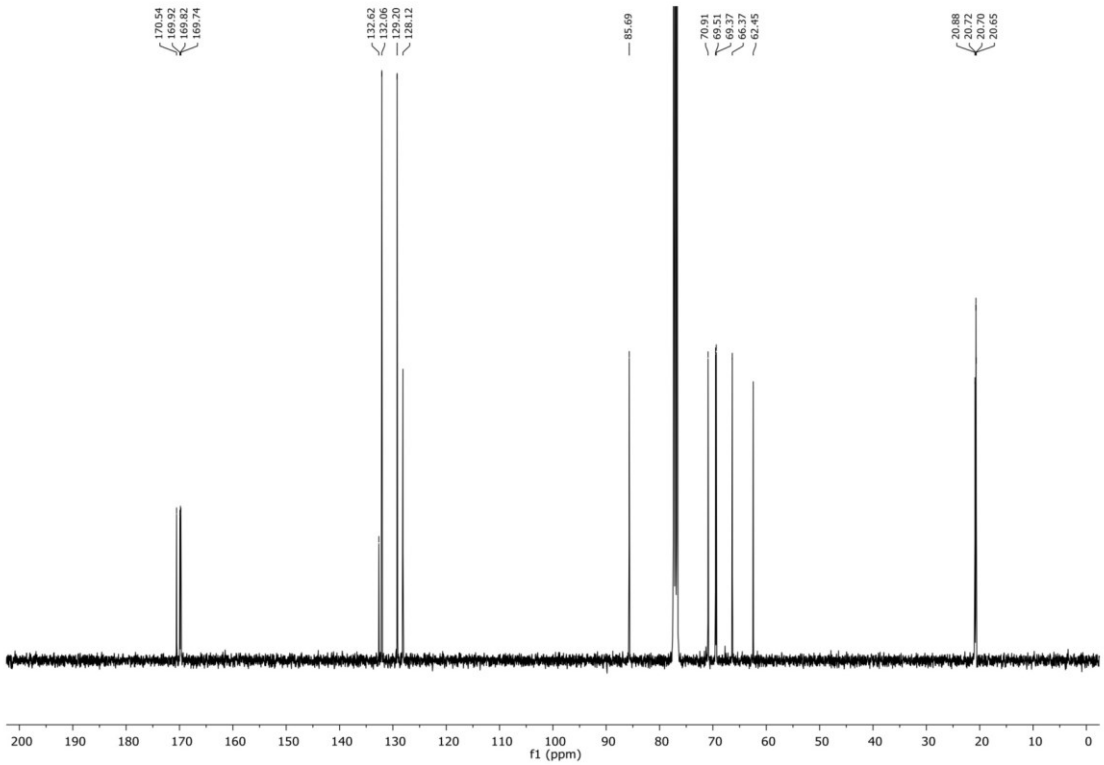

^{1}H-NMR, (600 MHz, $CDCl_3$): **(4)**

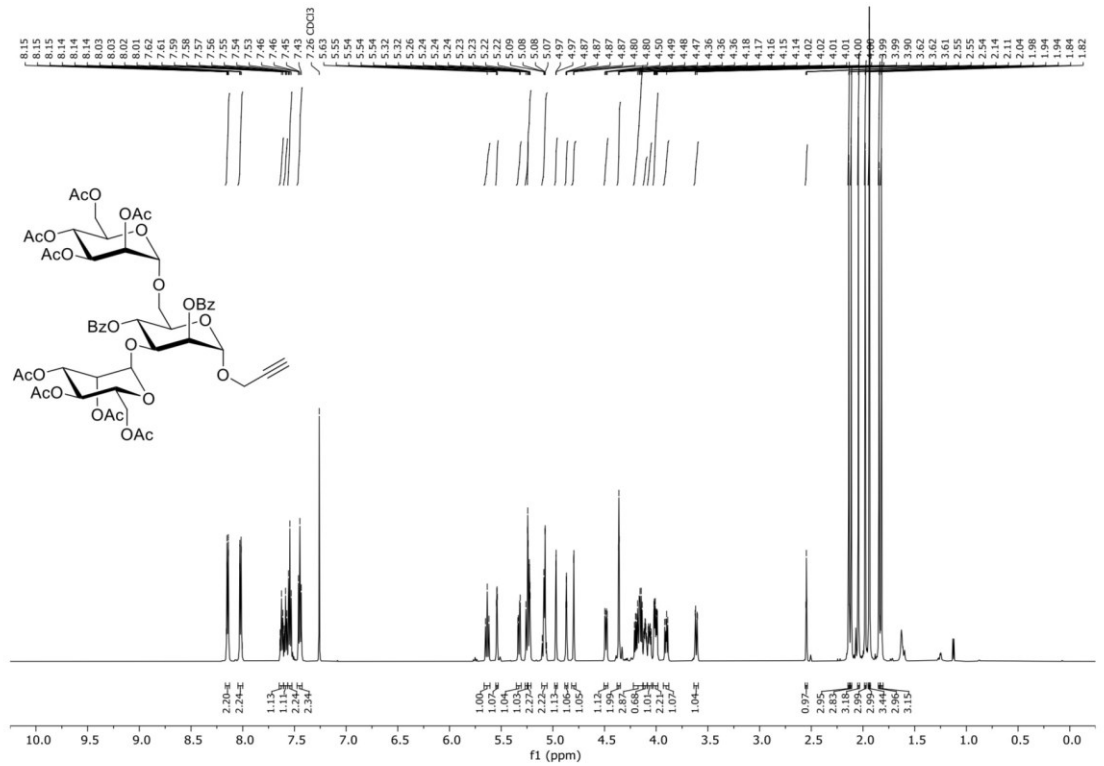

Supporting Information

^{1}H-NMR Zoom, (600 MHz, $CDCl_3$): **(4)**

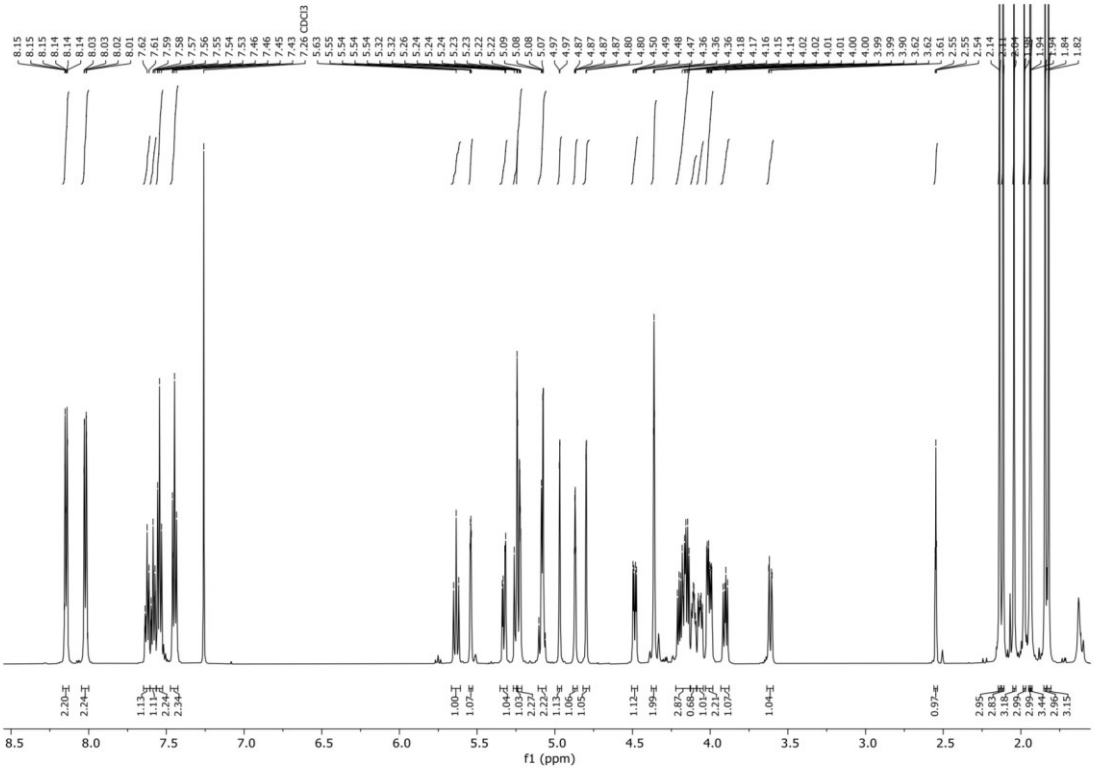

^{13}C-NMR, (151.0 MHz, $CDCl_3$): **(4)**

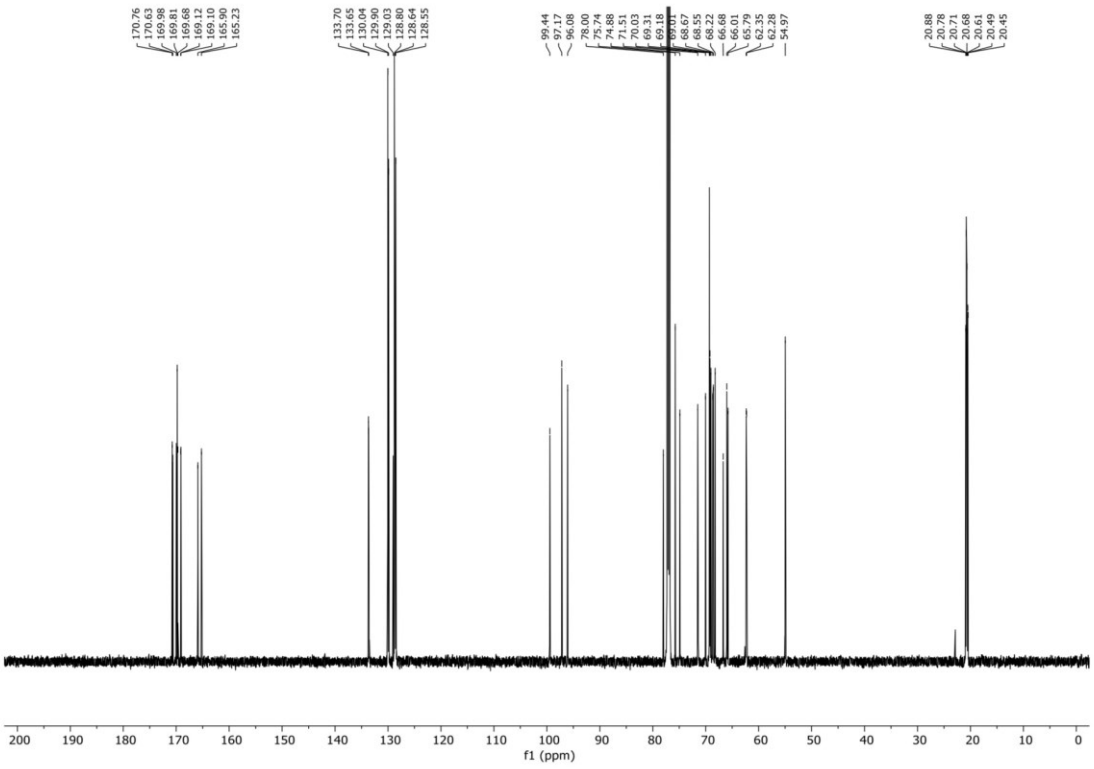

Supporting Information

^{1}H-NMR, (400 MHz, $CDCl_3$): **(S2)**

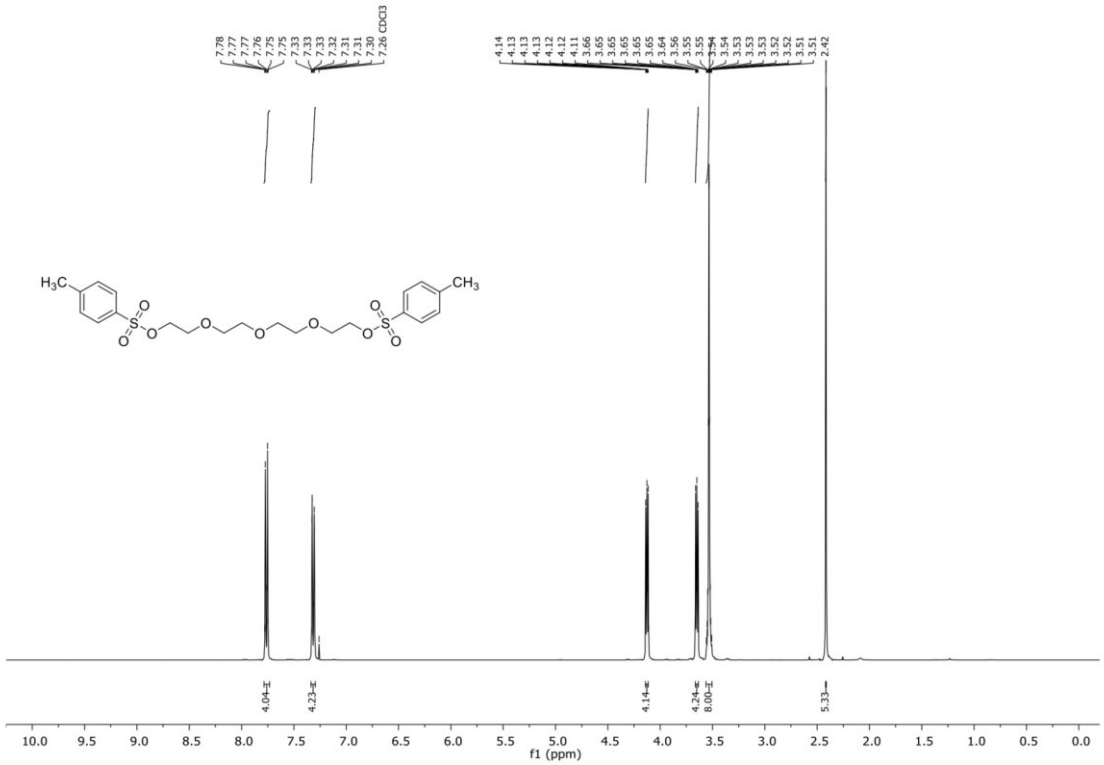

^{1}H-NMR Zoom, (400 MHz, $CDCl_3$): **(S2)**

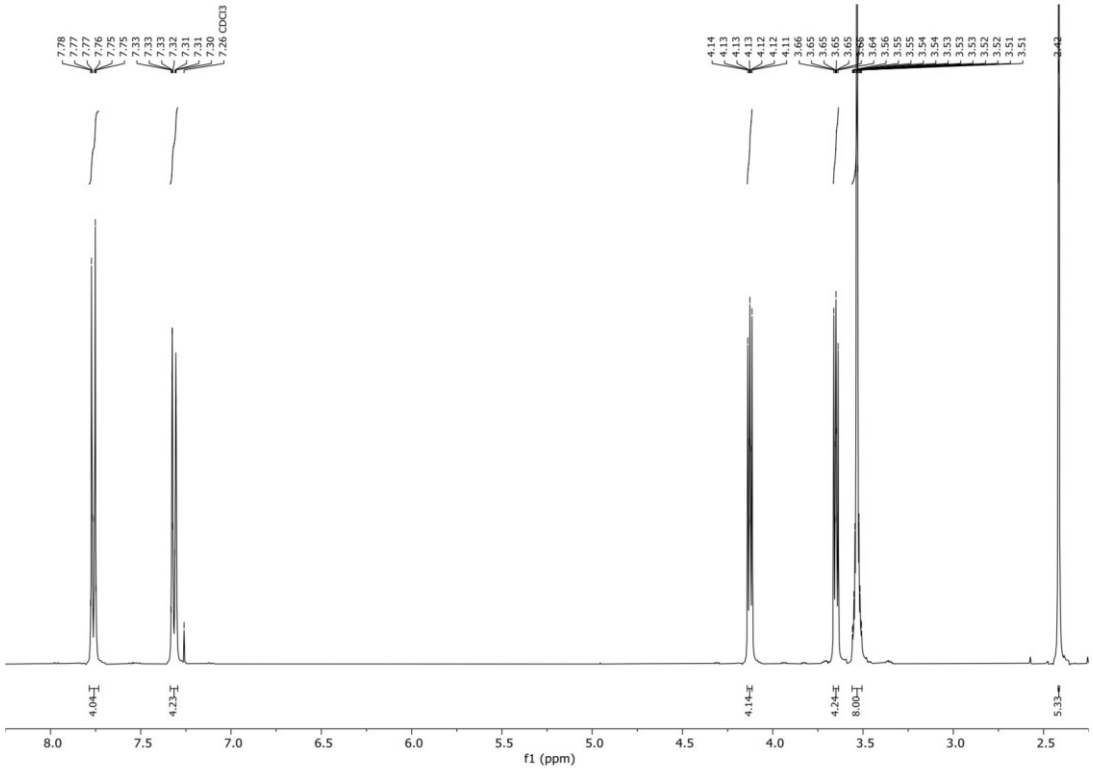

Supporting Information

^{13}C-NMR, (100.6 MHz, $CDCl_3$): **(S2)**

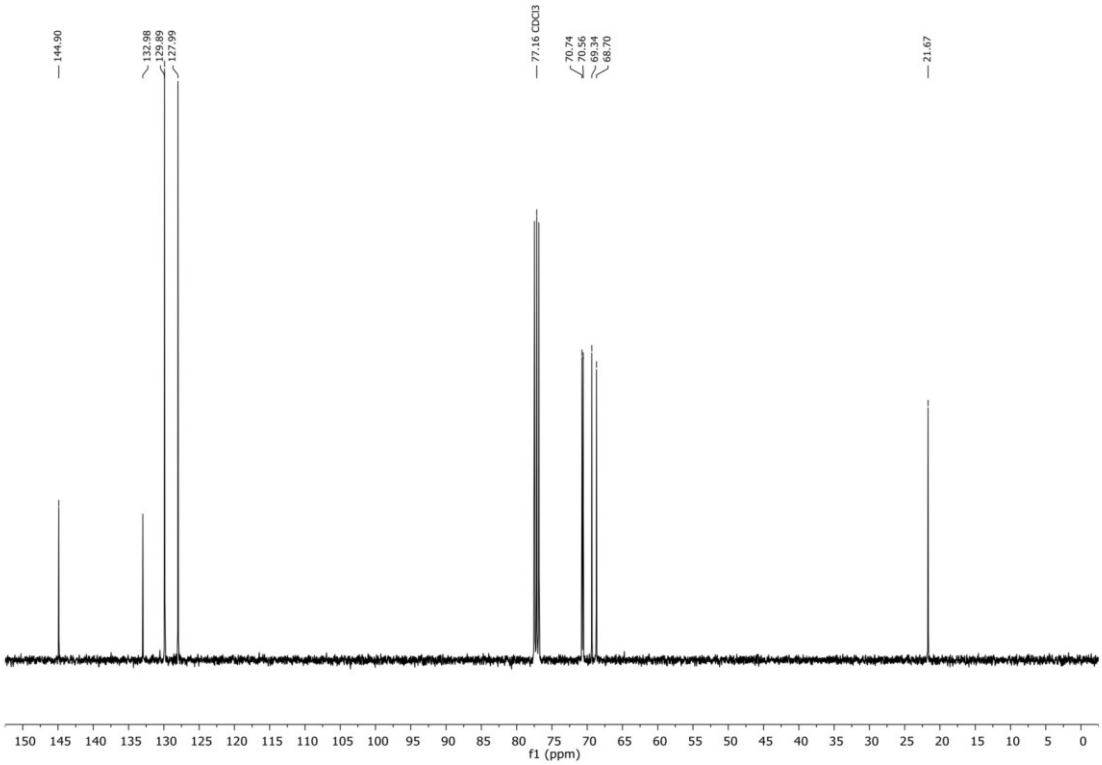

^{1}H-NMR, (400 MHz, $CDCl_3$): **(5)**

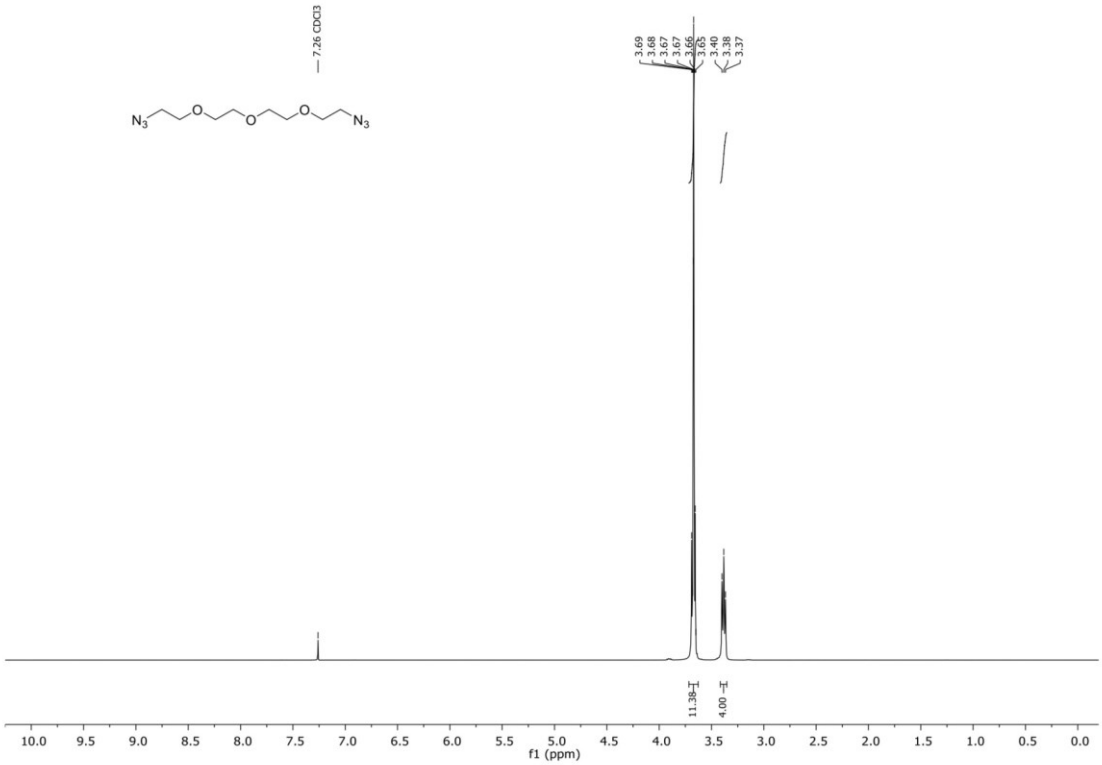

Supporting Information

^{1}H-NMR Zoom, (400 MHz, $CDCl_3$): **(5)**

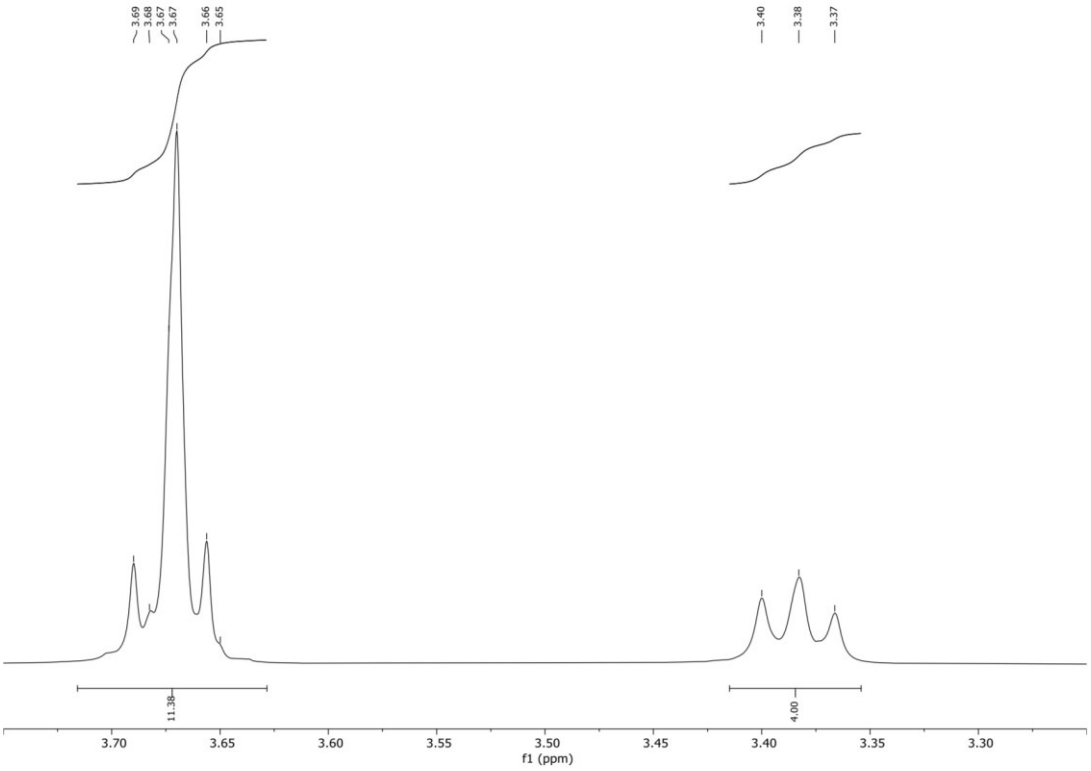

^{13}C-NMR, (100.6 MHz, $CDCl_3$): **(5)**

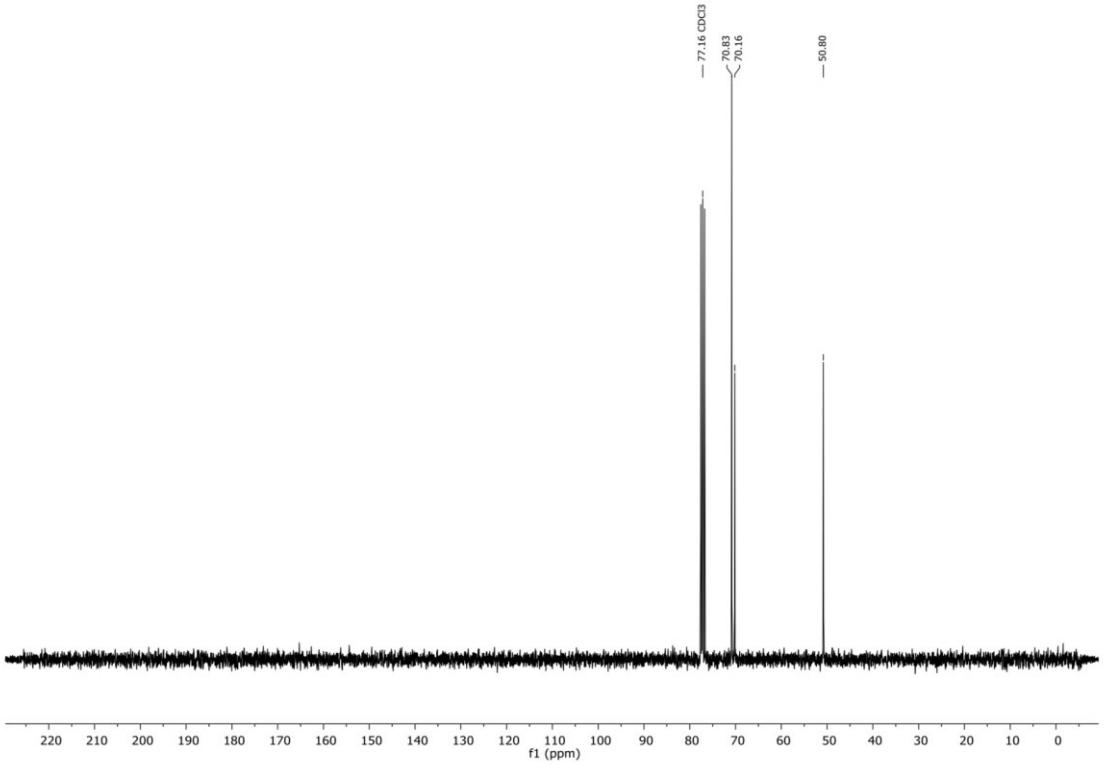

Supporting Information

^{1}H-NMR, (600 MHz, $CDCl_3$): **(6)**

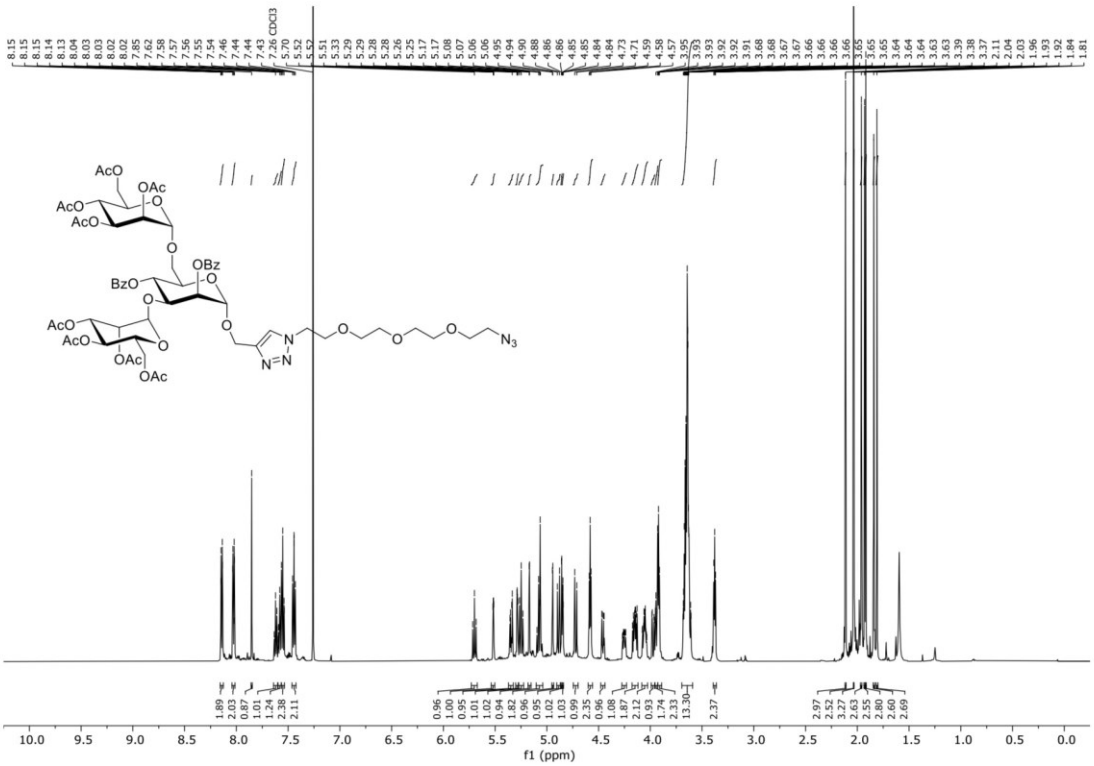

^{1}H-NMR Zoom, (600 MHz, $CDCl_3$): **(6)**

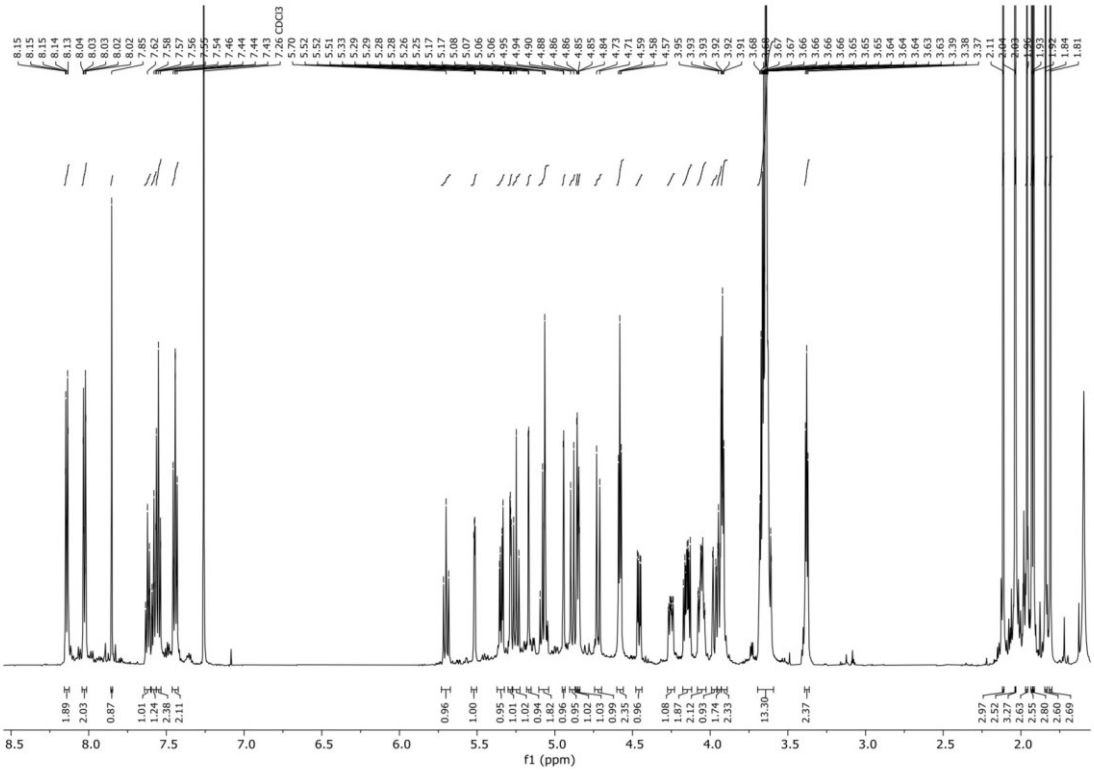

Supporting Information

^{13}C-NMR, (151.0 MHz, $CDCl_3$): **(6)**

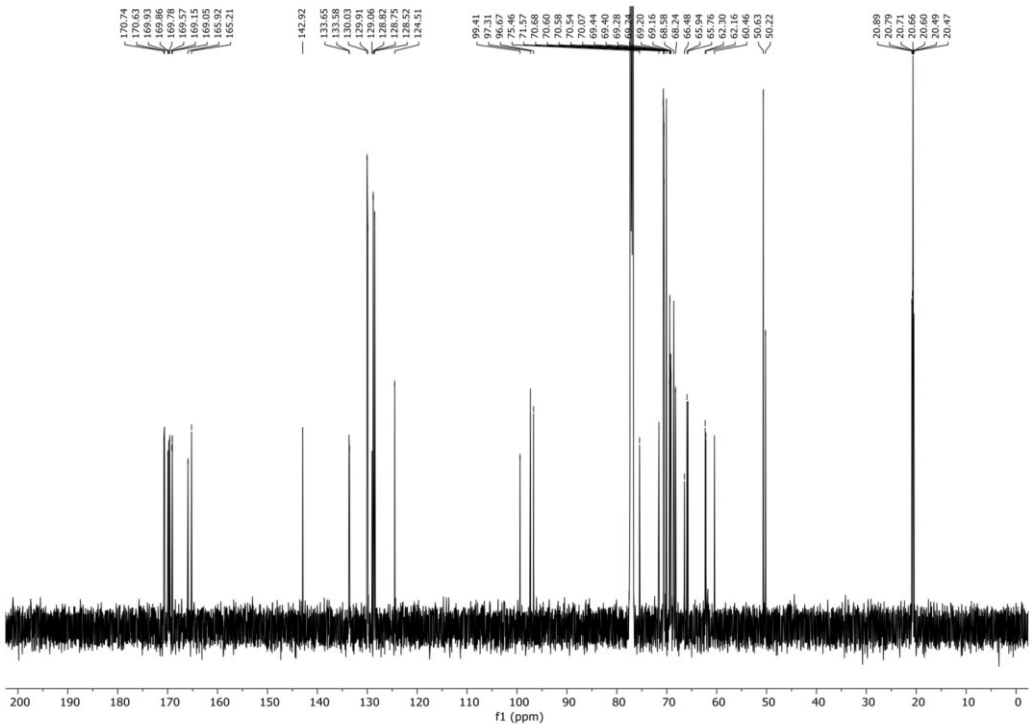

^{1}H-NMR, (600 MHz, D_2O): **(TM)**

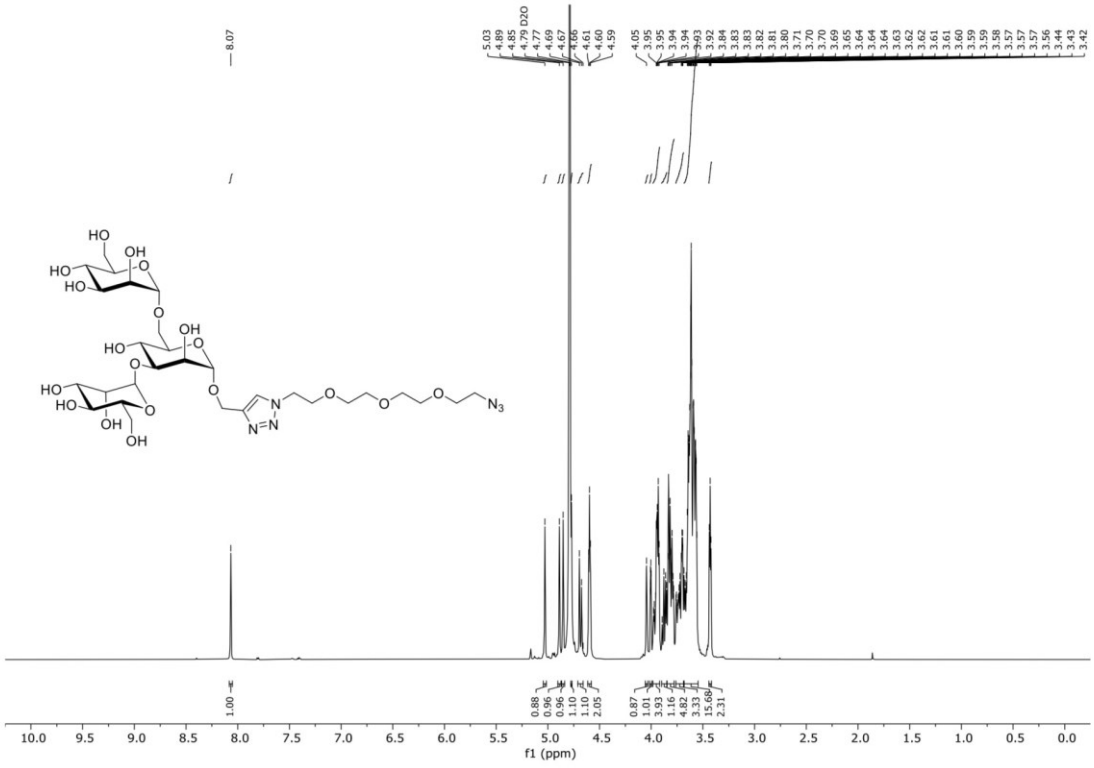

Supporting Information

^{1}H-NMR Zoom, (600 MHz, D_2O): **(TM)**

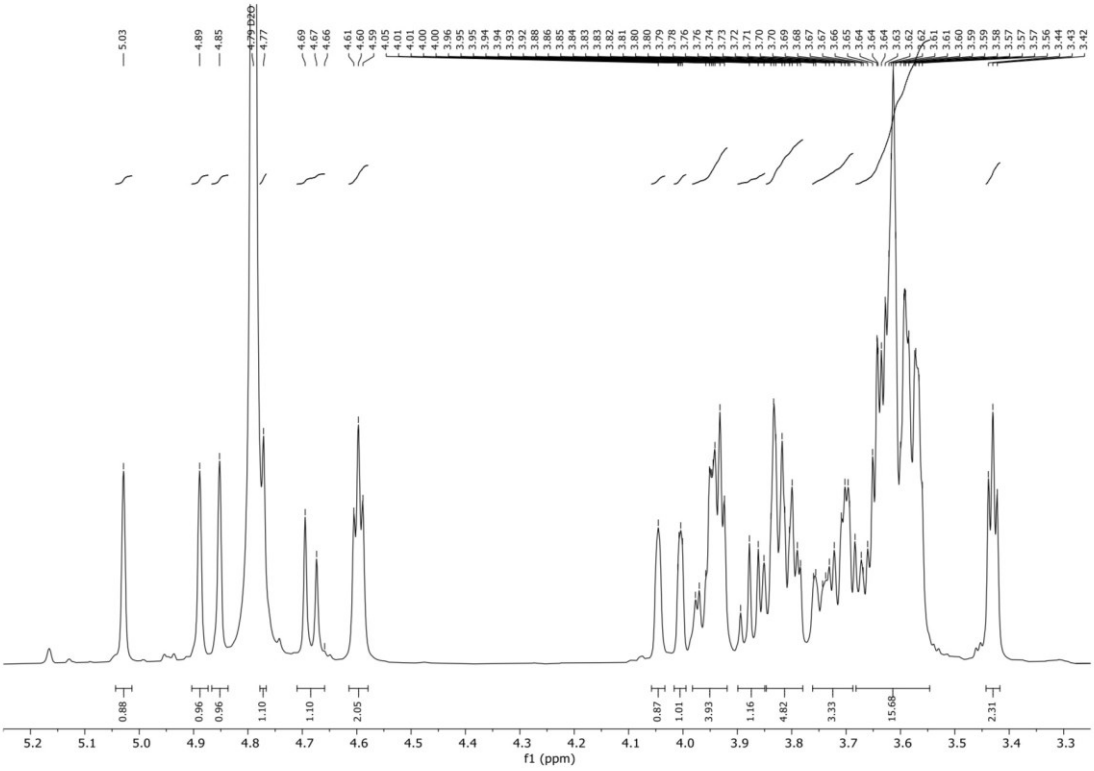

^{13}C-NMR, (151.0 MHz, D_2O): **(TM)**

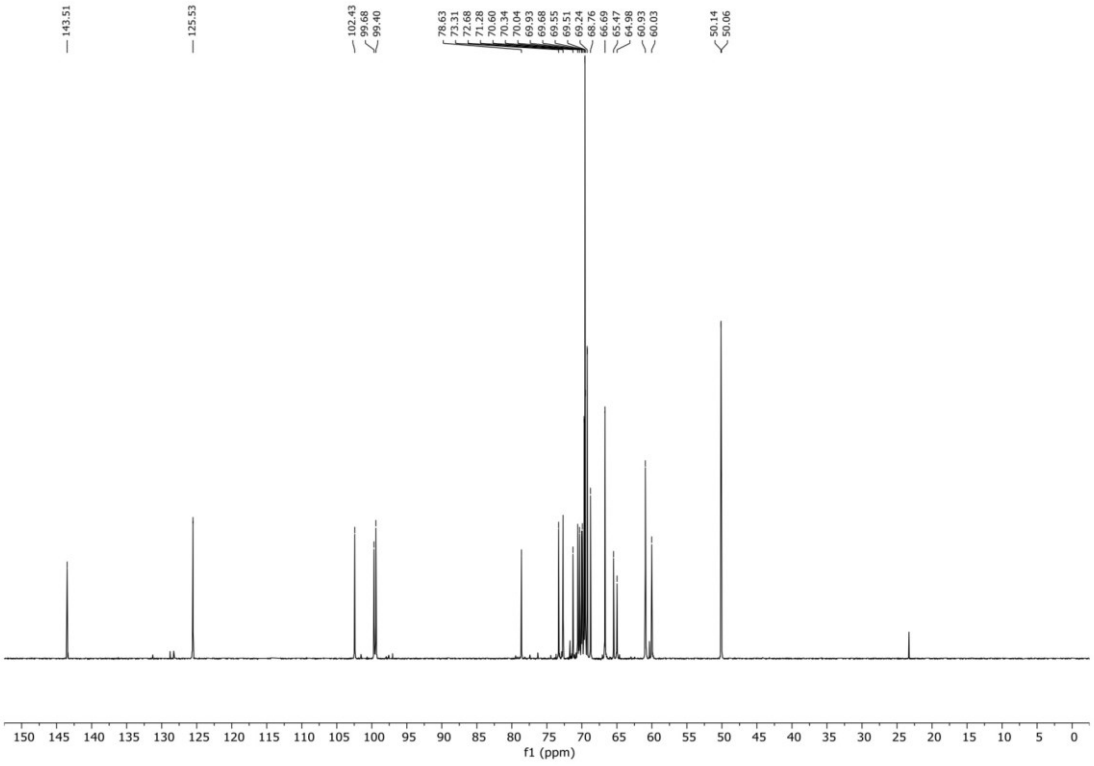

Supporting Information

^{1}H-NMR, (400 MHz, CD_2Cl_2): **2-(pyridine-2-yldisulfanyl)ethan-1-ol (S3)**

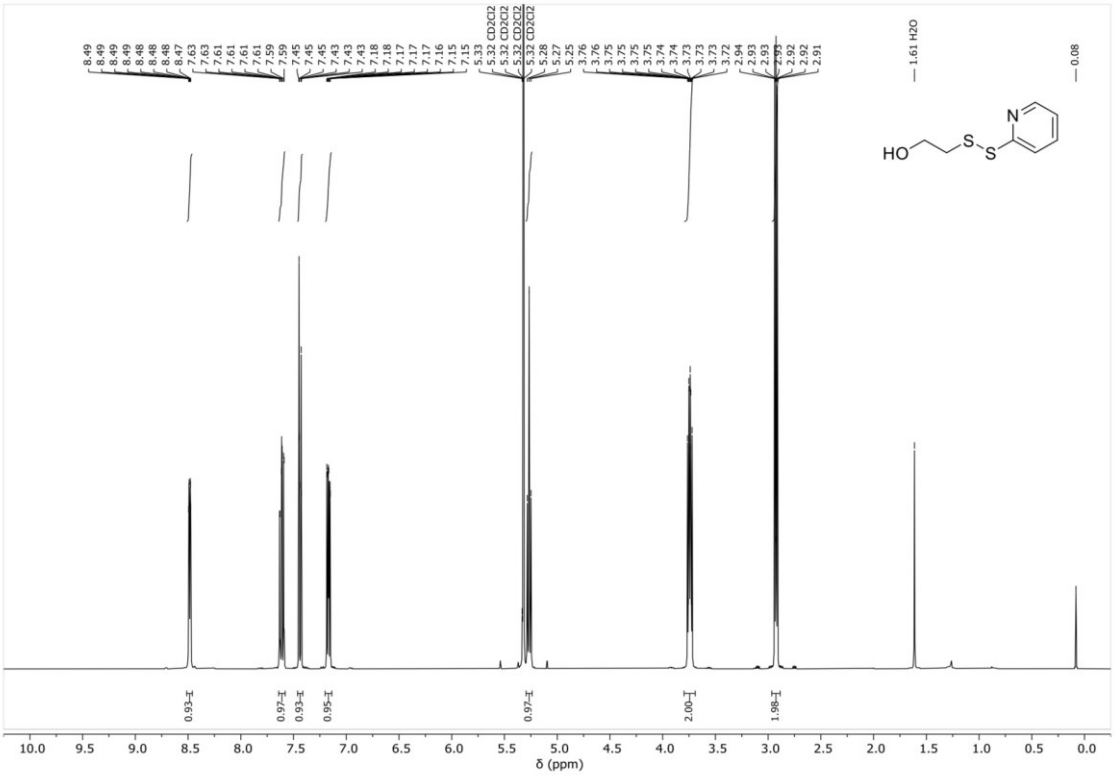

^{13}C-NMR, (101 MHz, CD_2Cl_2): **2-(pyridine-2-yldisulfanyl)ethan-1-ol (S3)**

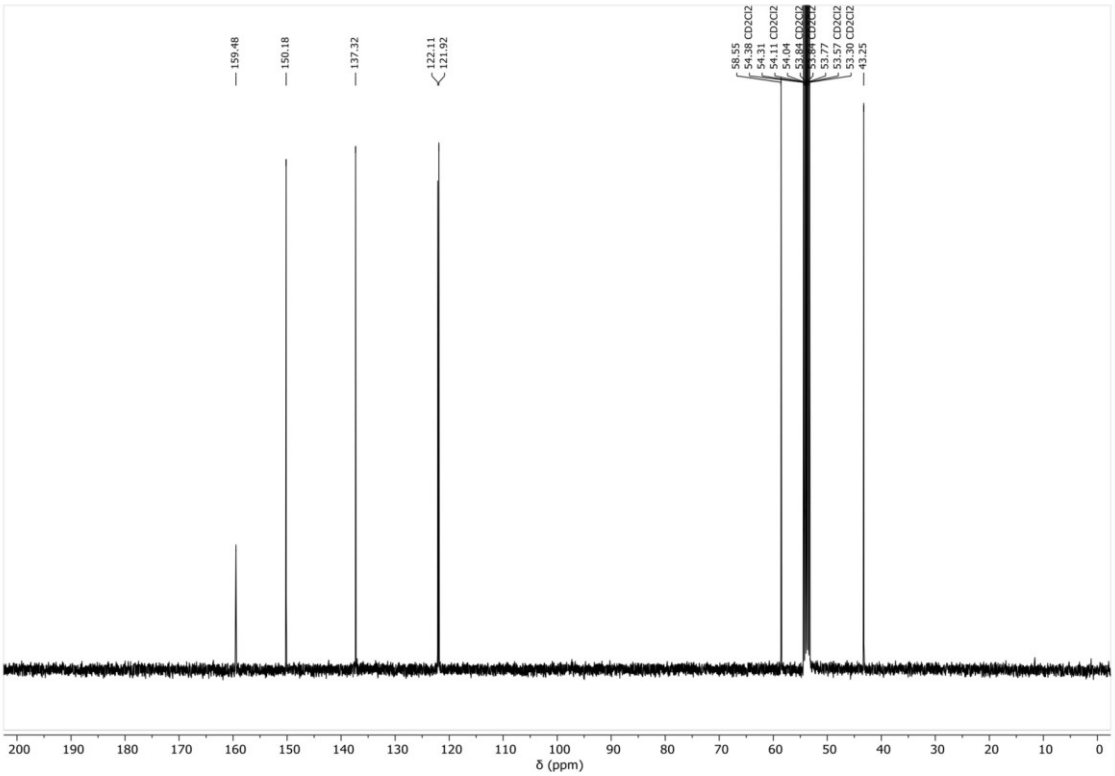

Supporting Information

^{1}H-NMR, (400 MHz, CD_2Cl_2): **4-nitrophenyl (2-(pyridin-2-yldisulfanyl)ethyl) carbonate (S4)**

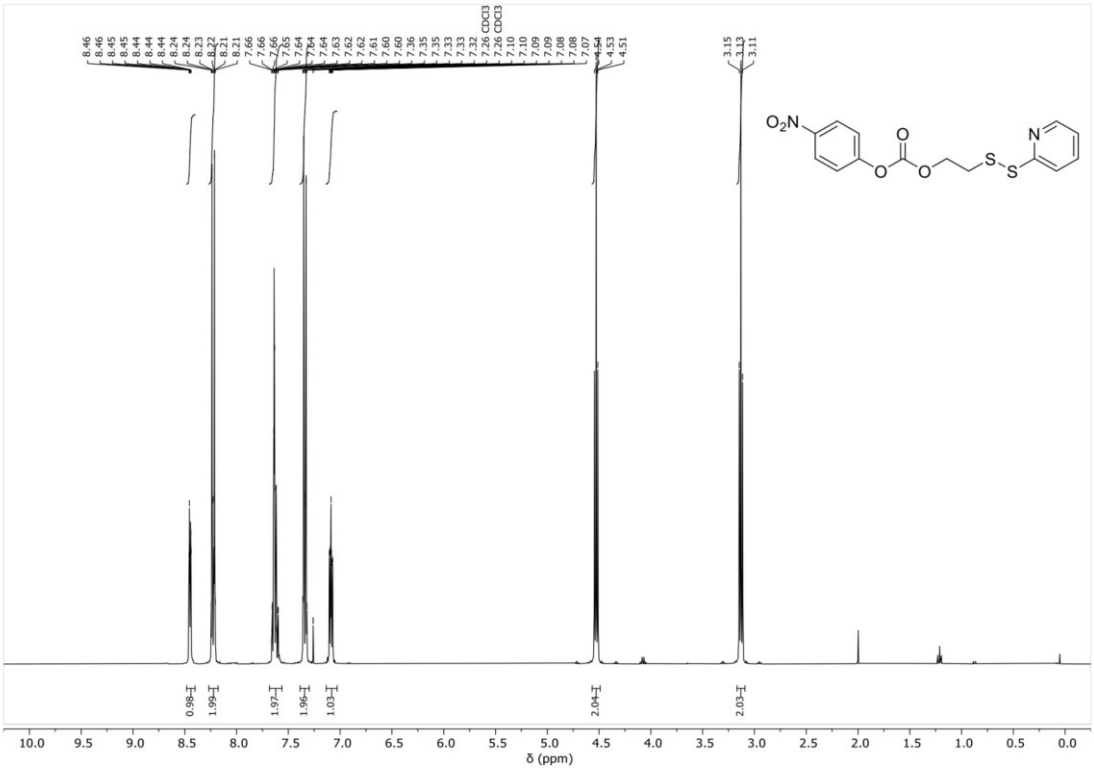

^{13}C-NMR, (101 MHz, CD_2Cl_2): **4-nitrophenyl (2-(pyridin-2-yldisulfanyl)ethyl) carbonate (S4)**

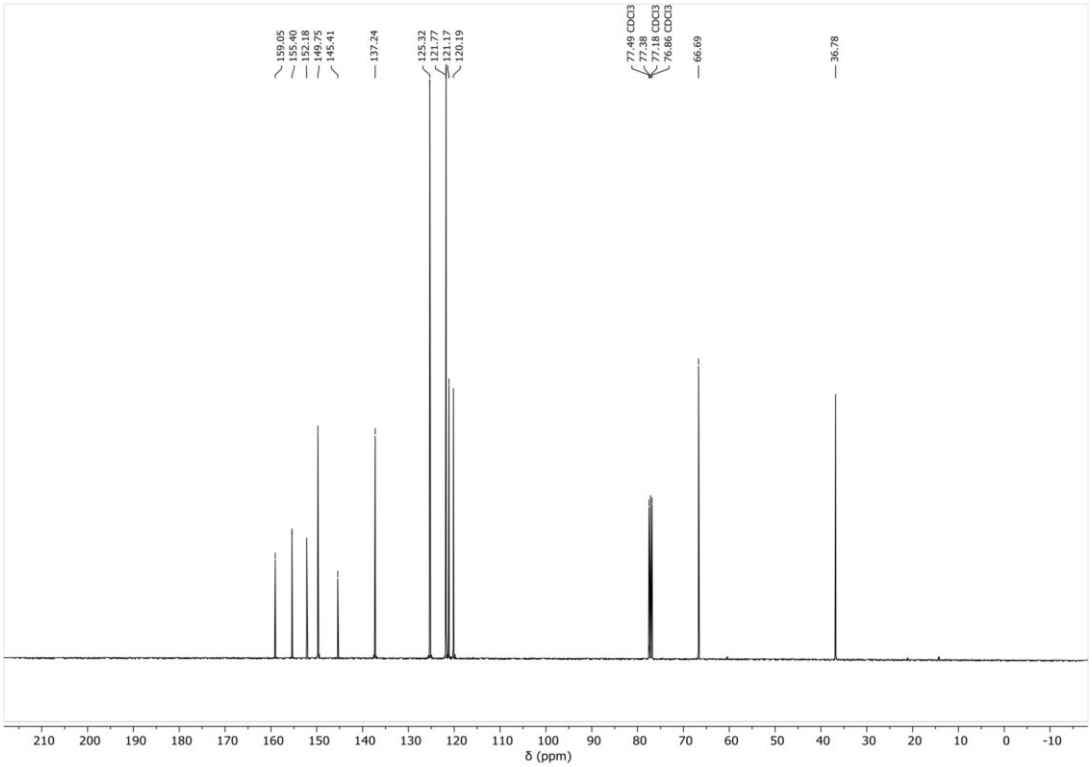

Supporting Information

^{1}H-NMR, (700 MHz, CD_2Cl_2): **(Pyr-S-S-Benzyl)**

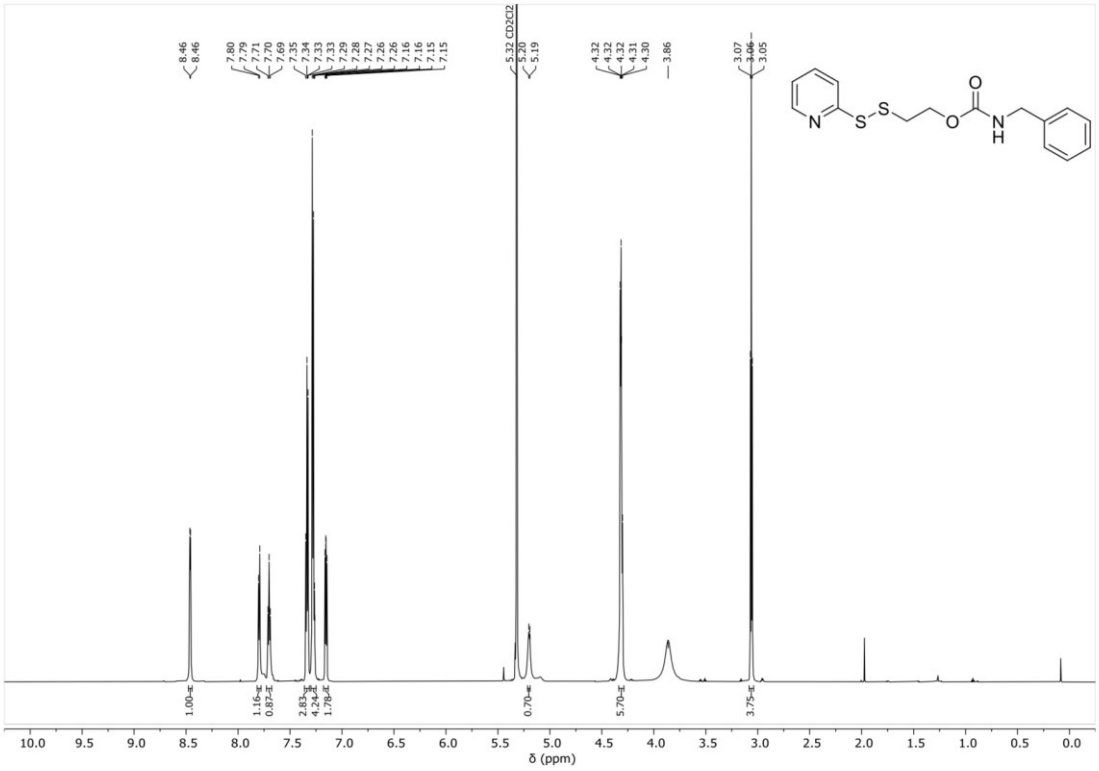

^{13}C-NMR, (101 MHz, CD_2Cl_2): **(Pyr-S-S-Benzyl)**

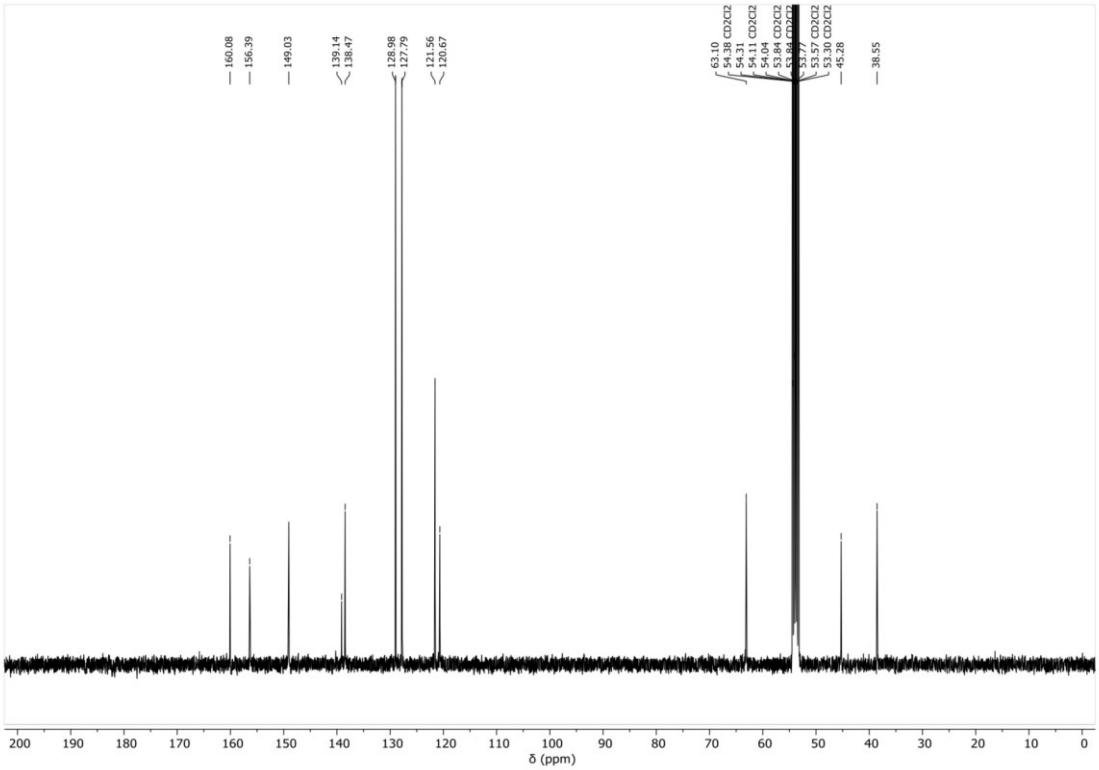

70

Supporting Information

^{1}H-NMR, (700 MHz, DMF-d_7): **(Pyr-S-S-TLR7/8a·TFA)**

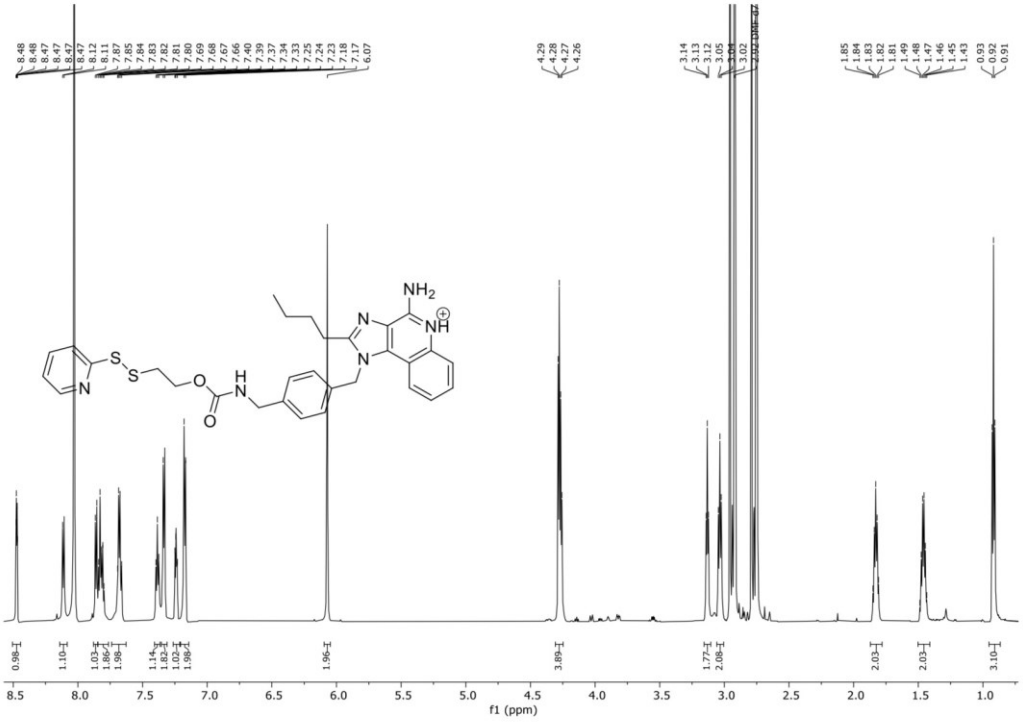

^{1}H-NMR Zoom, (700 MHz, DMF-d_7): **(Pyr-S-S-TLR7/8a·TFA)**

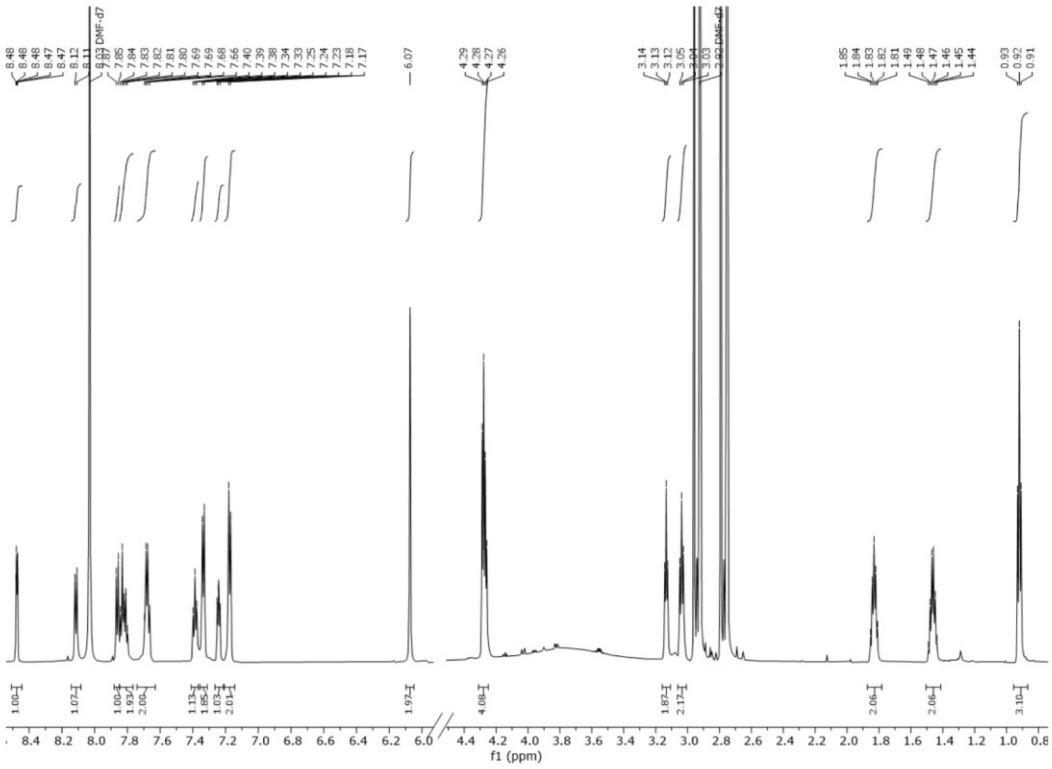

Supporting Information

9.4 LC-ESI-MS spectra

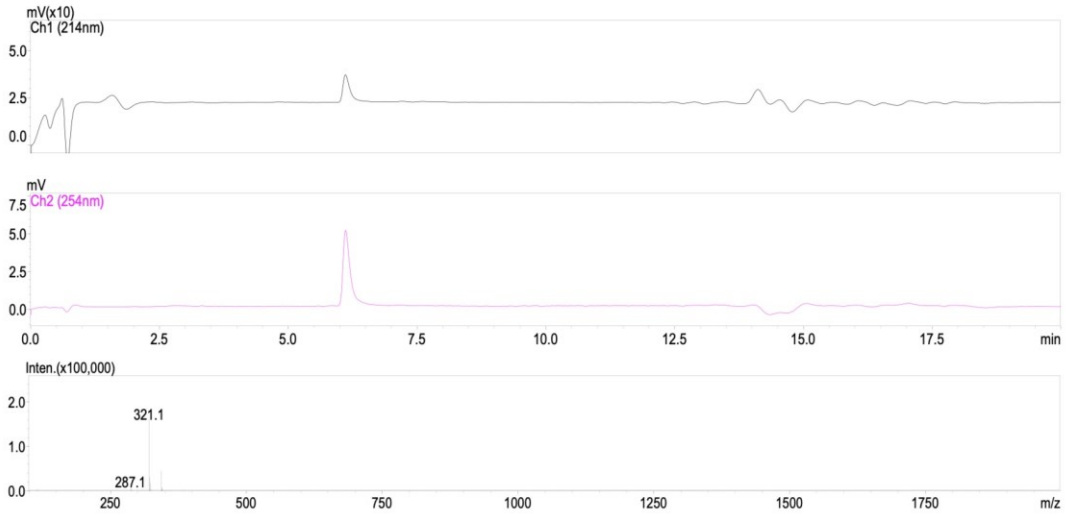

Figure S28: LC chromatogram (214 nm top, 254 nm middle; t_R = 6.118 min) and TIC of ESI$^+$-MS of Pyr-S-S-Benzyl. Found m/z = 321.1 $[M+H]^+$. calc. 321.1 $[M+H]^+$ formula: $C_{15}H_{316}N_2O_2S_2$.

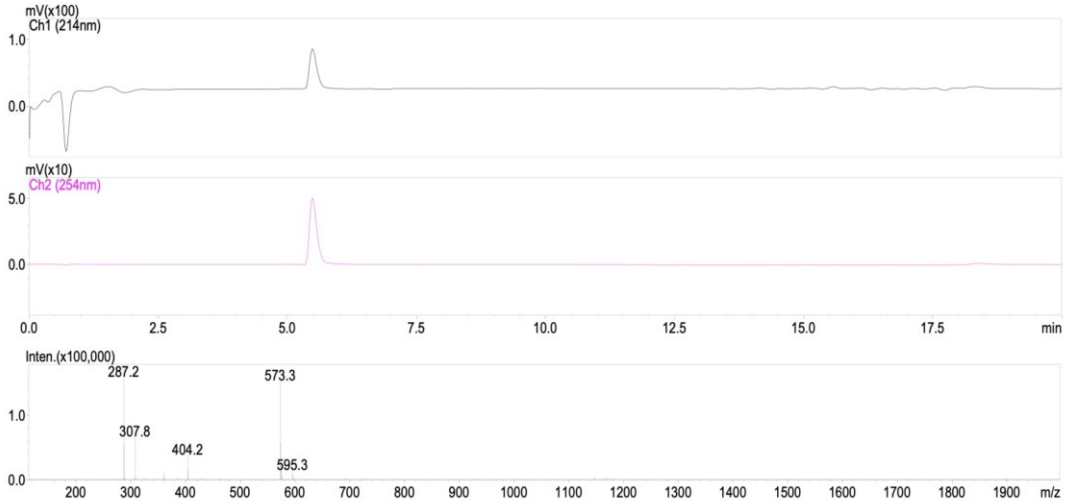

Figure S29: LC chromatogram (214 nm top, 254 nm middle; t_R = 5.491 min) and TIC of ESI$^+$-MS of Pyr-S-S-TLR7/8a. Found m/z = 573.3 $[M+H]^+$. calc. 573.2 $[M+H]^+$, formula: $C_{30}H_{32}N_6O_2S_2$.

Supporting Information

9.5 MALDI-ToF-MS spectra

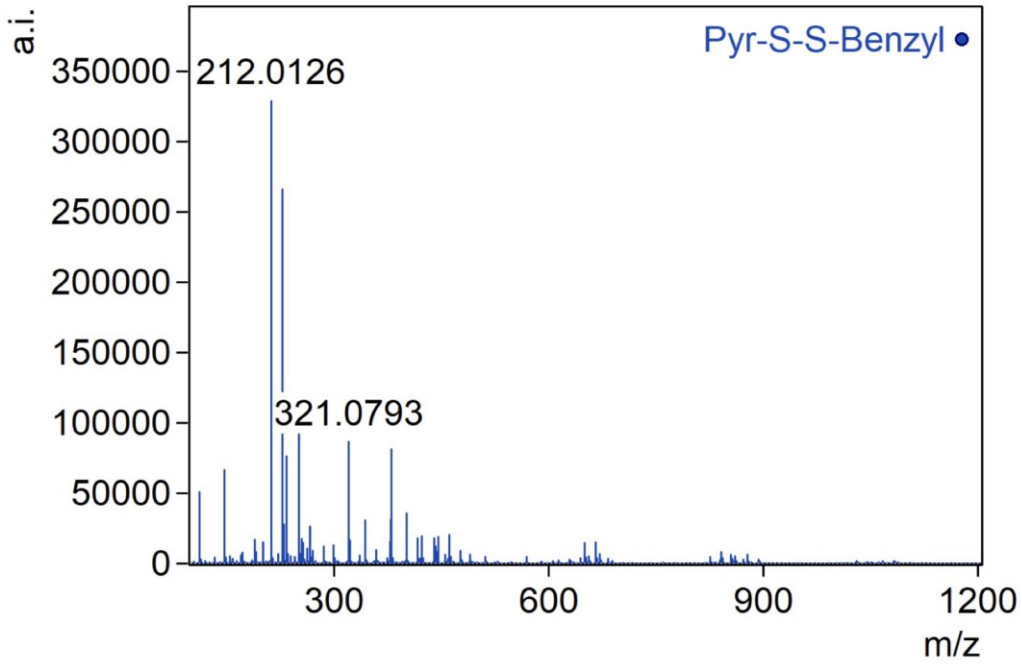

Figure S30: MALDI-ToF-spectrum of Pyr-S-S-Benzyl (matrix: α-Cyano-4-hydroxycinnamic acid). Found *m/z* = 321.0793 $[M+H]^+$, calc. 321.0726 $[M+H]^+$ formula: $C_{15}H_{316}N_2O_2S_2$.

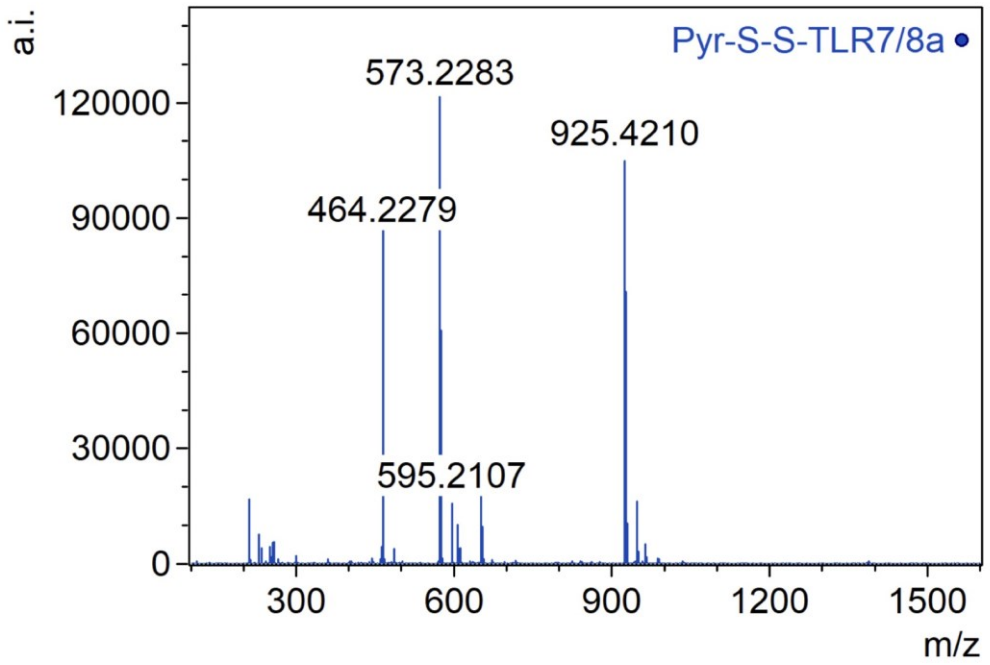

Figure S31: MALDI-ToF-spectrum of Pyr-S-S-TLR7/8a (matrix: α-Cyano-4-hydroxycinnamic acid). Found *m/z* = 573.2283 $[M+H]^+$, 595.2107 $[M+Na]^+$, 464.2279 $[M+2H\text{-}Pyr\text{-}S]^+$, 925.4210 $[2M+H\text{-}Pyr\text{-}S]^+$; calc. 573.2101 $[M+H]^+$, formula: $C_{30}H_{32}N_6O_2S_2$.

Supporting Information

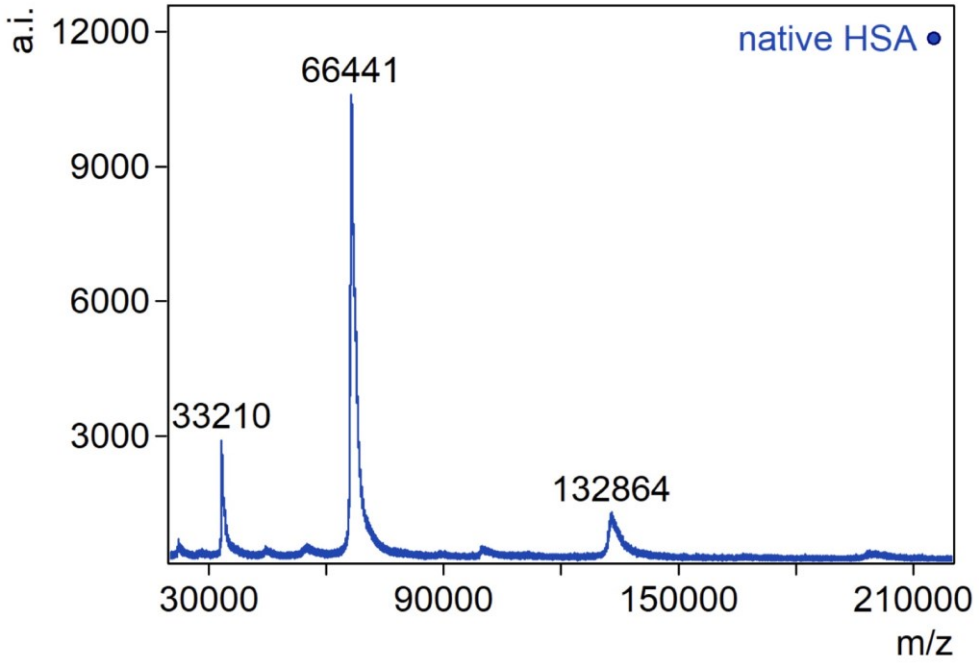

Figure S32: MALDI-ToF-spectrum of native HSA. Found *m/z* = 66441 $[M+H]^+$. Peaks at half mass and dimer are also observed.

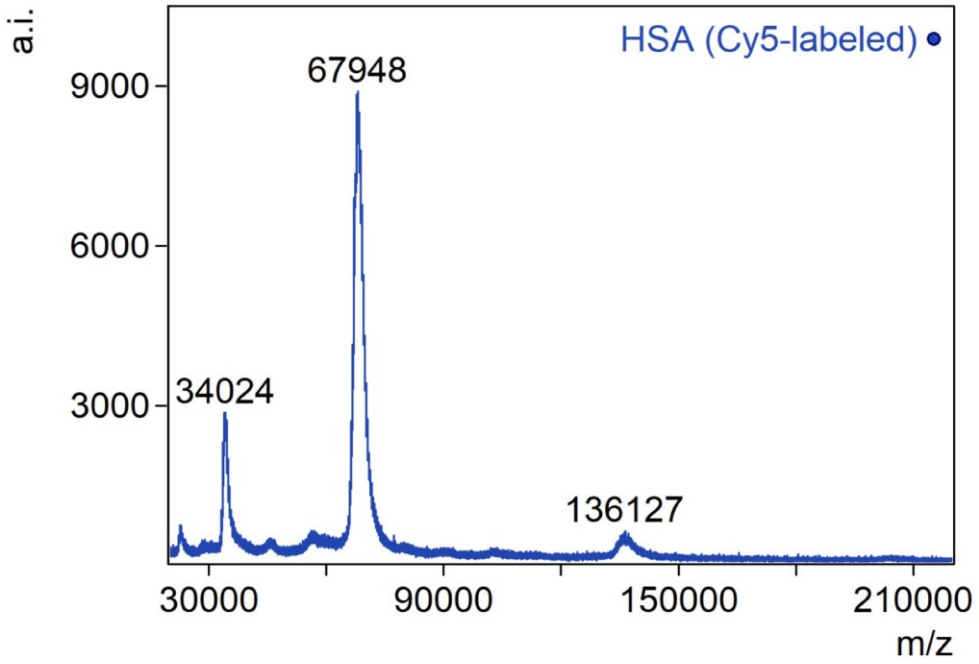

Figure S33: MALDI-ToF-spectrum of Cy5 labeled HSA. Found *m/z* = 67948 $[M+H]^+$.

Supporting Information

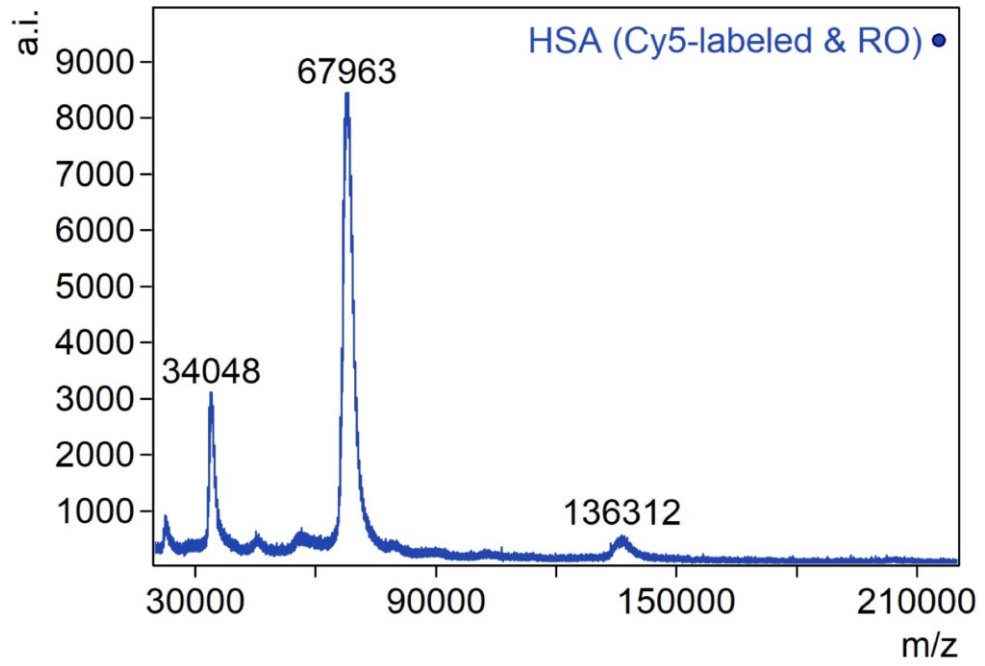

Figure S34: MALDI-ToF-spectrum of Cy5 labeled HSA after maleimide ring opening (RO). Found m/z = 67963 $[M+H]^+$.

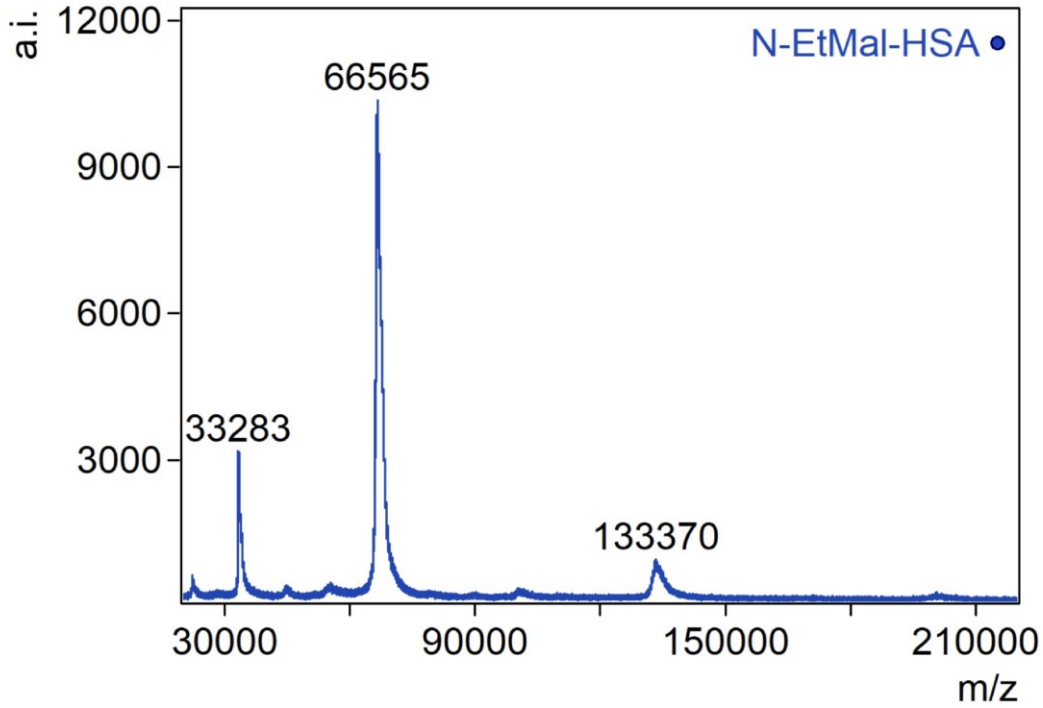

Figure S35: MALDI-ToF-spectrum of *N*-ethylmaleimide capped HSA. Found m/z = 66565 $[M+H]^+$.

Supporting Information

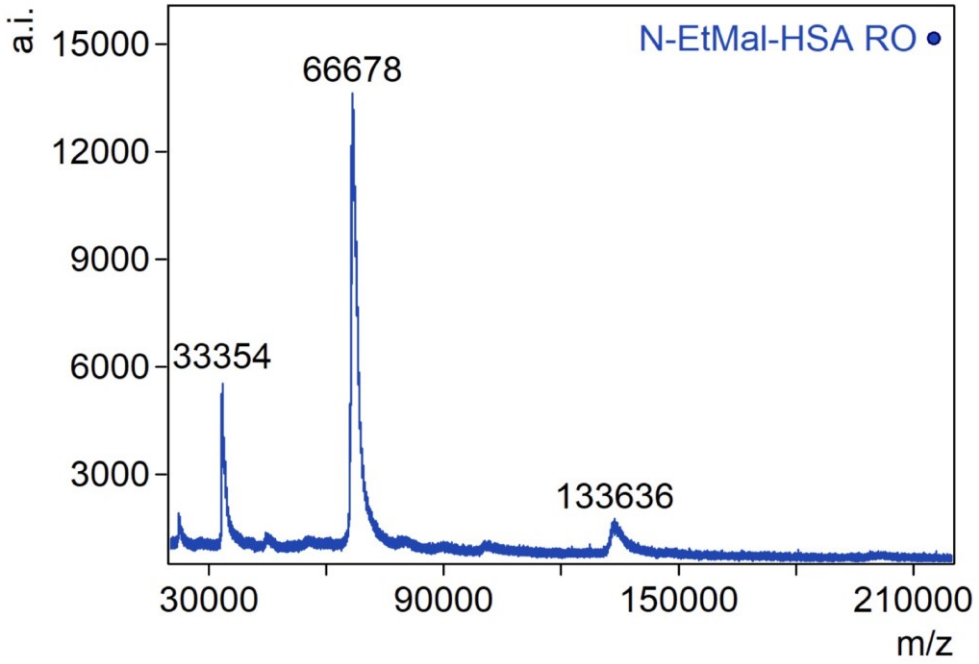

Figure S36: MALDI-ToF-spectrum of N-ethylmaleimide capped HSA after maleimide ring opening. Found *m/z* = 66678 $[M+H]^+$.

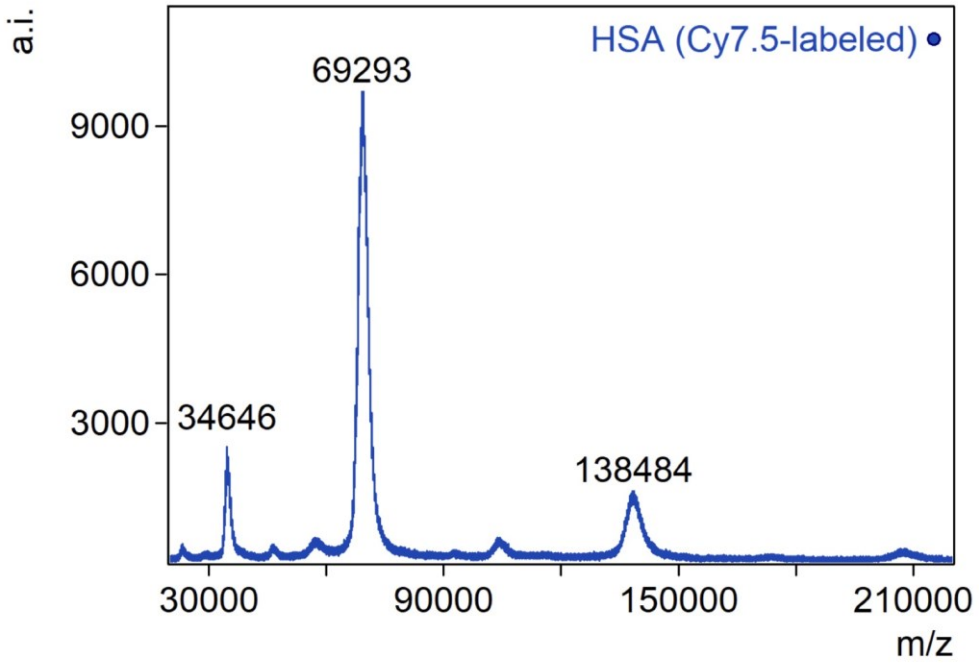

Figure S37: MALDI-ToF-spectrum of Cy7.5 labeled HSA. Found *m/z* = 69293 $[M+H]^+$.

Supporting Information

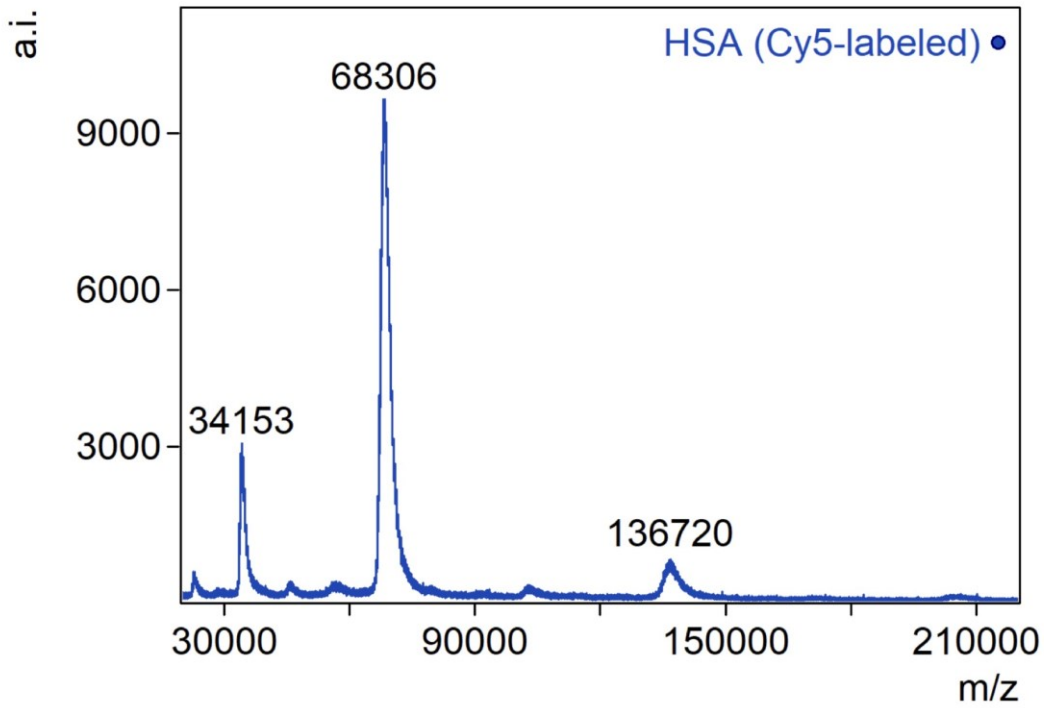

Figure S38: MALDI-ToF-spectrum of Cy5-labeled HSA. Found *m/z* = 68306 $[M+H]^+$.

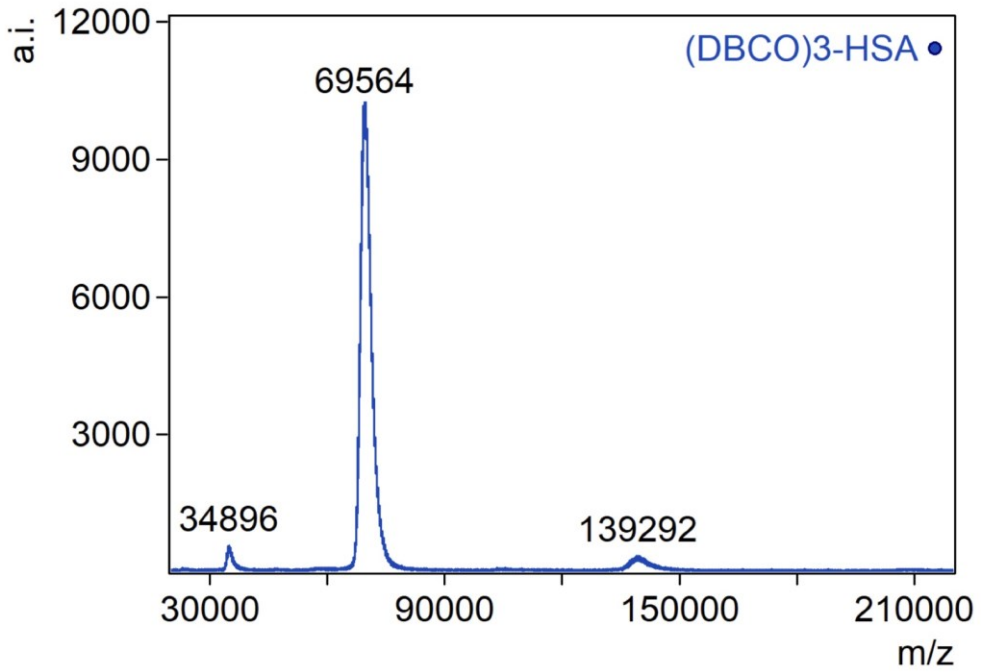

Figure S39: MALDI-ToF-spectrum of Cy5-labeled, DBCO-modified HSA. Found *m/z* = 69564 $[M+H]^+$.

Supporting Information

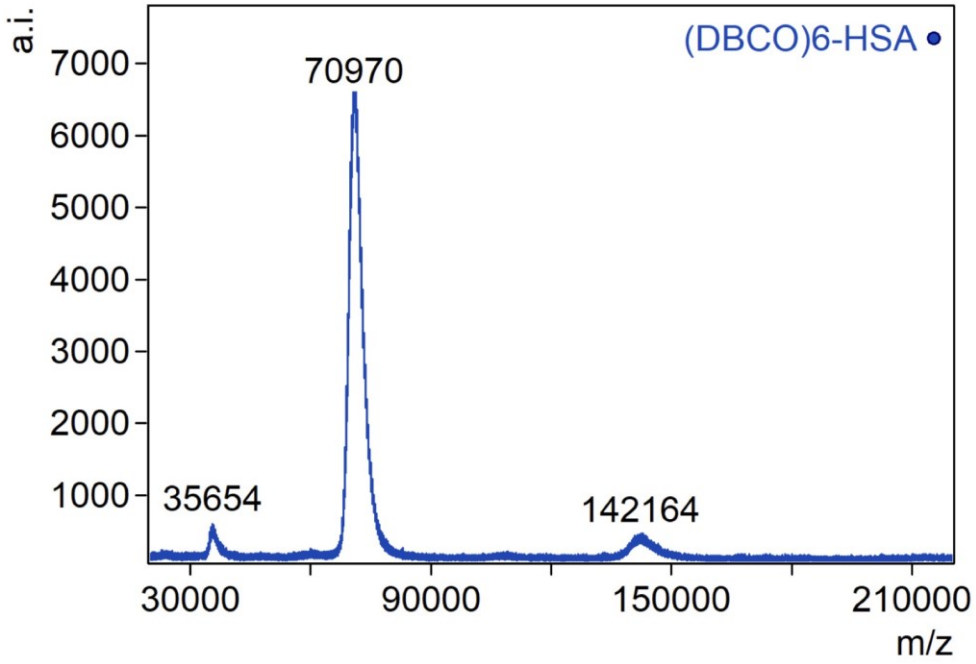

Figure S40: MALDI-ToF-spectrum of Cy5-labeled, DBCO-modified HSA. Found *m/z* = 70970 $[M+H]^+$.

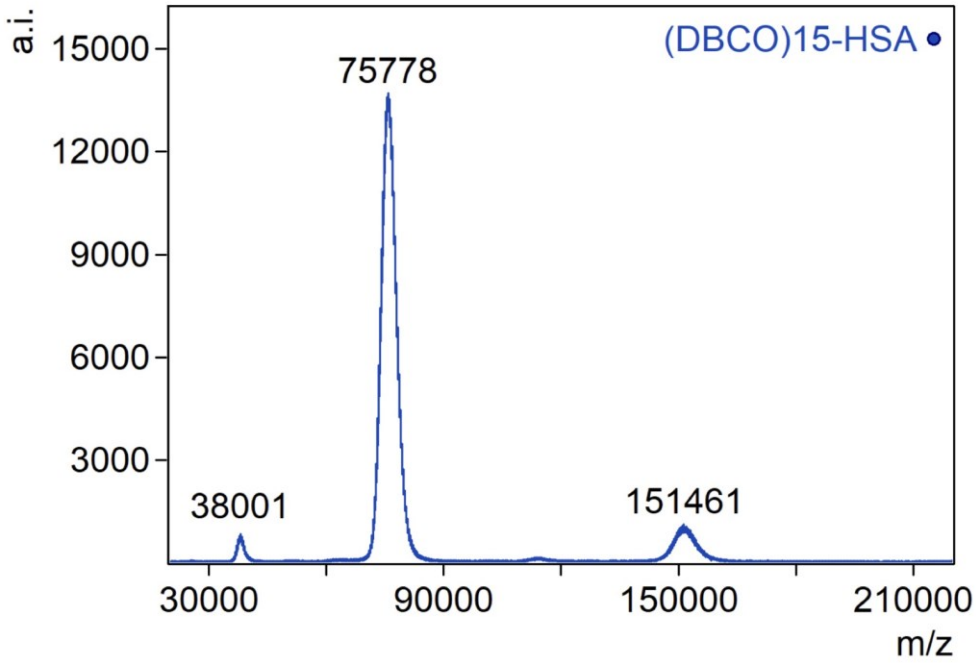

Figure S41: MALDI-ToF-spectrum of Cy5-labeled, DBCO-modified HSA. Found *m/z* = 75778 $[M+H]^+$.

Supporting Information

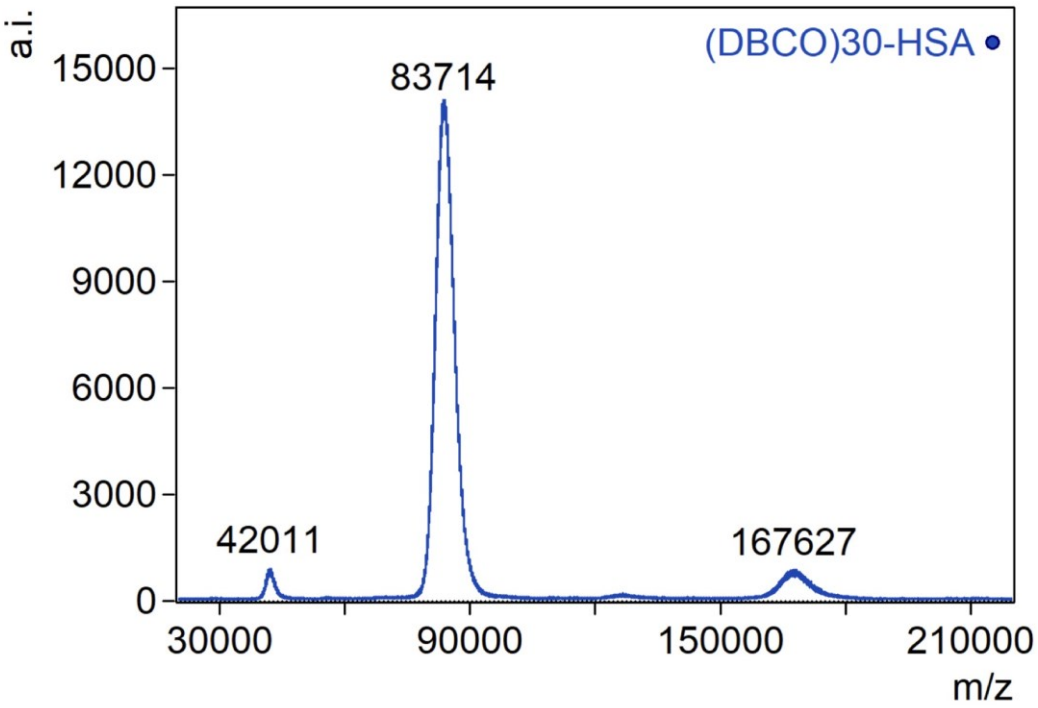

Figure S42: MALDI-ToF-spectrum of Cy5-labeled, DBCO-modified HSA. Found *m/z* = 83714 $[M+H]^+$.

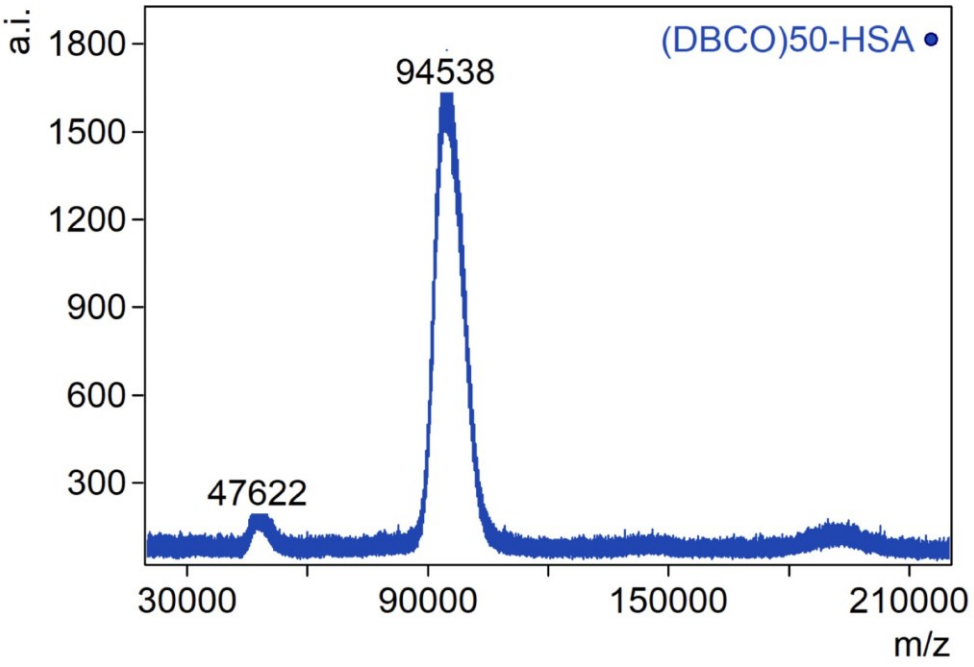

Figure S43: MALDI-ToF-spectrum of Cy5-labeled, DBCO-modified HSA. Found *m/z* = 94538 $[M+H]^+$.

Supporting Information

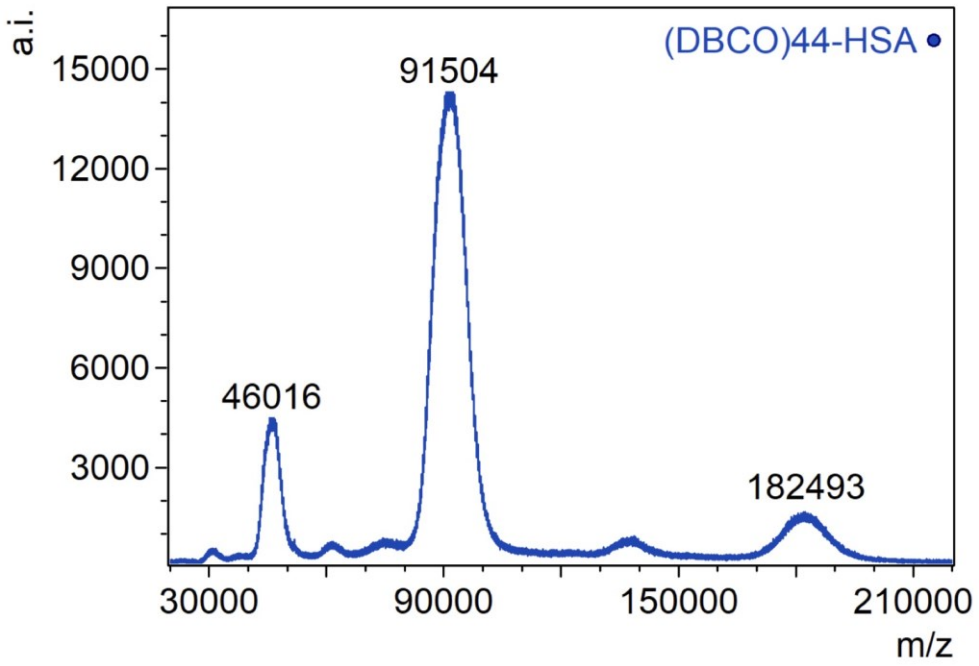

Figure S44: MALDI-ToF-spectrum of Cy5-labeled, DBCO-modified HSA. Found *m/z* = 91504 $[M+H]^+$.

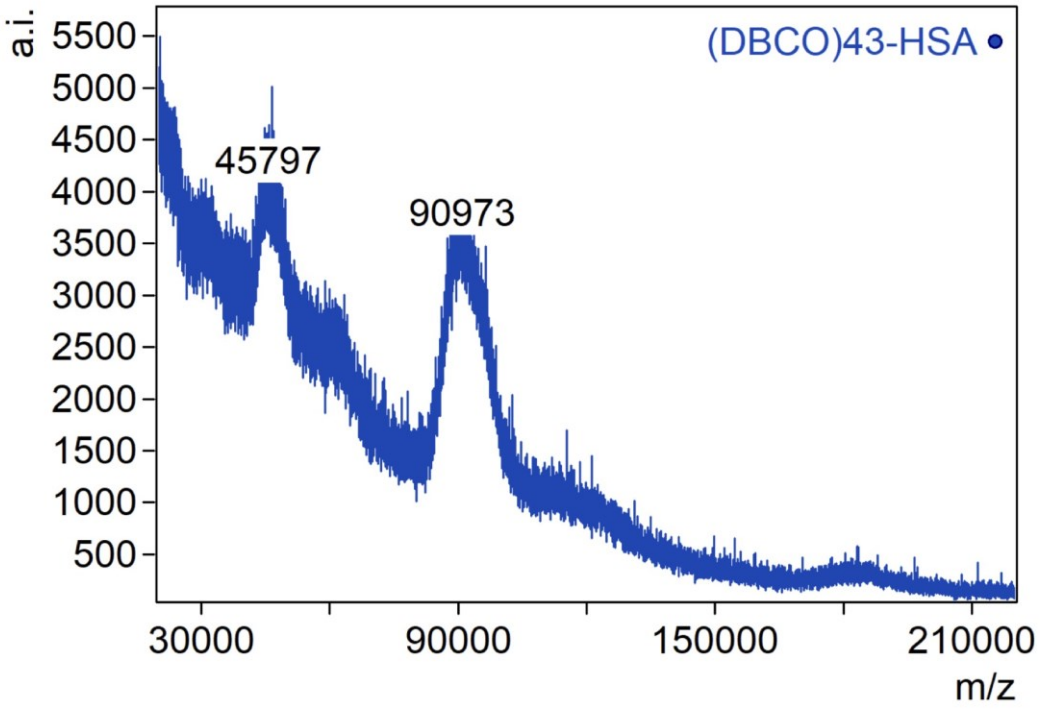

Figure S45: MALDI-ToF-spectrum of Cy5-labeled, DBCO-modified HSA. Found *m/z* = 90973 $[M+H]^+$.

Supporting Information

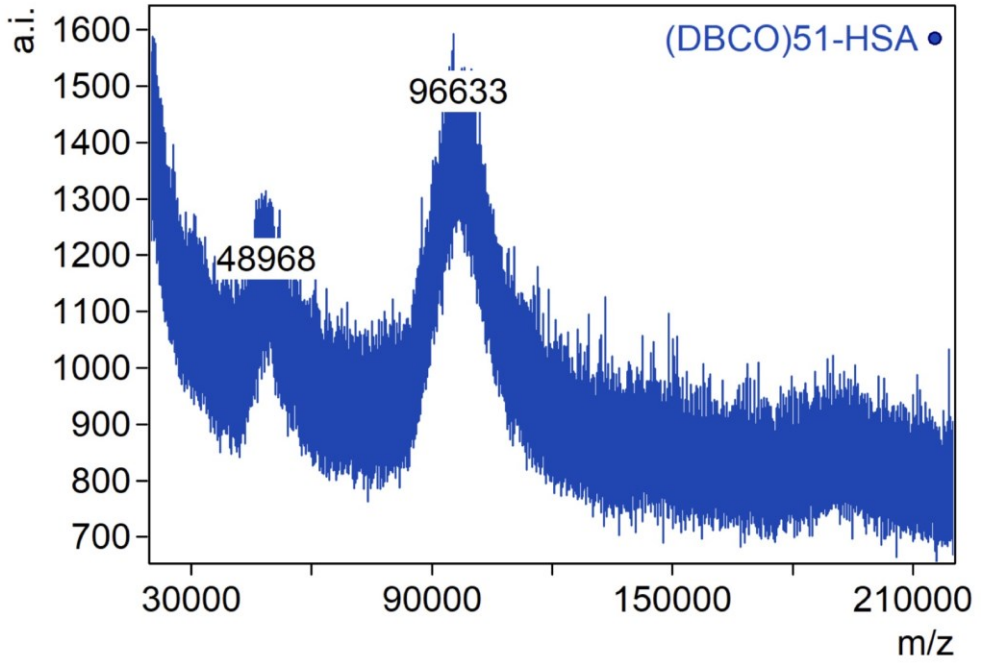

Figure S46: MALDI-ToF-spectrum of Cy7.5-labeled, DBCO-modified HSA. Found *m/z* = 96633 $[M+H]^+$.

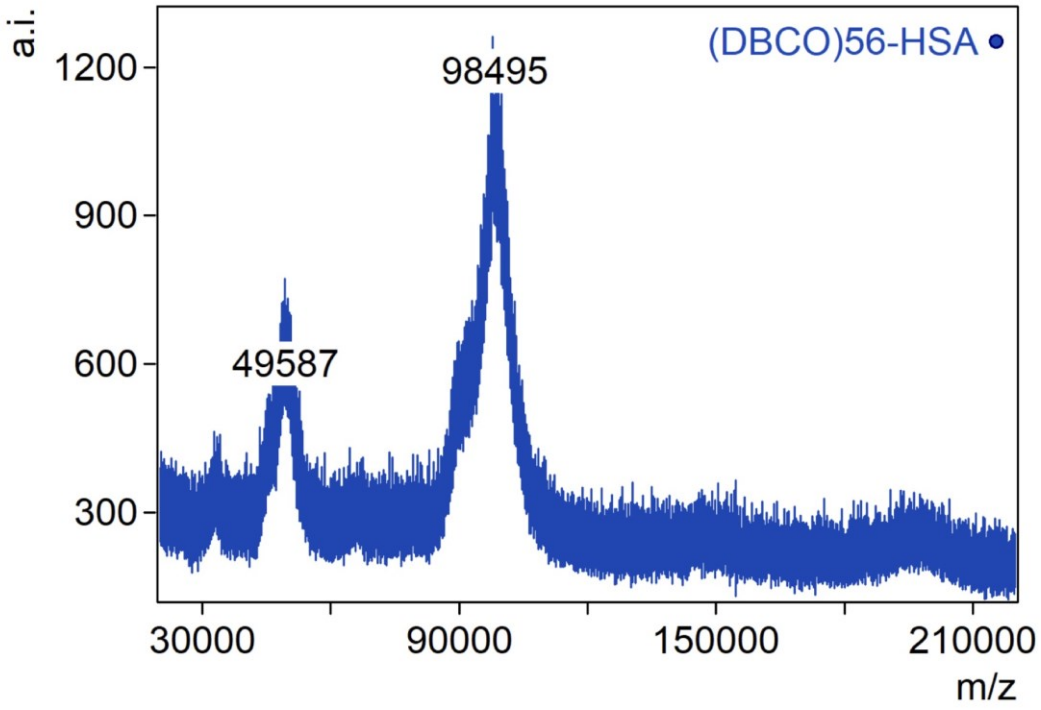

Figure S47: MALDI-ToF-spectrum of Cy5-labeled, DBCO-modified HSA. Found *m/z* = 98495 $[M+H]^+$.

Supporting Information

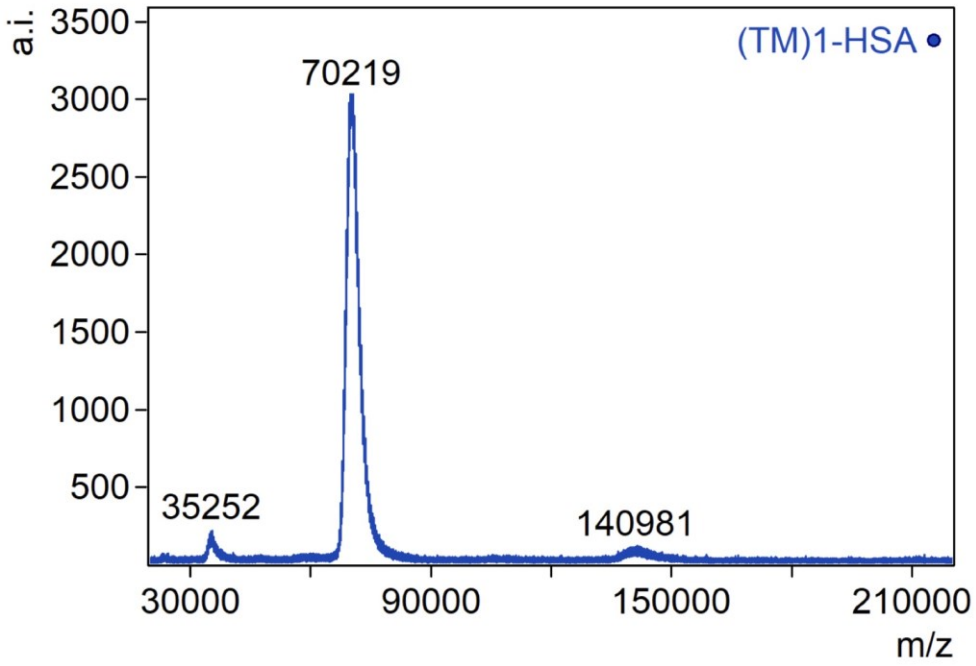

Figure S48: MALDI-ToF-spectrum of Cy5-labeled, TM-modified HSA. Found *m/z* = 70219 $[M+H]^+$.

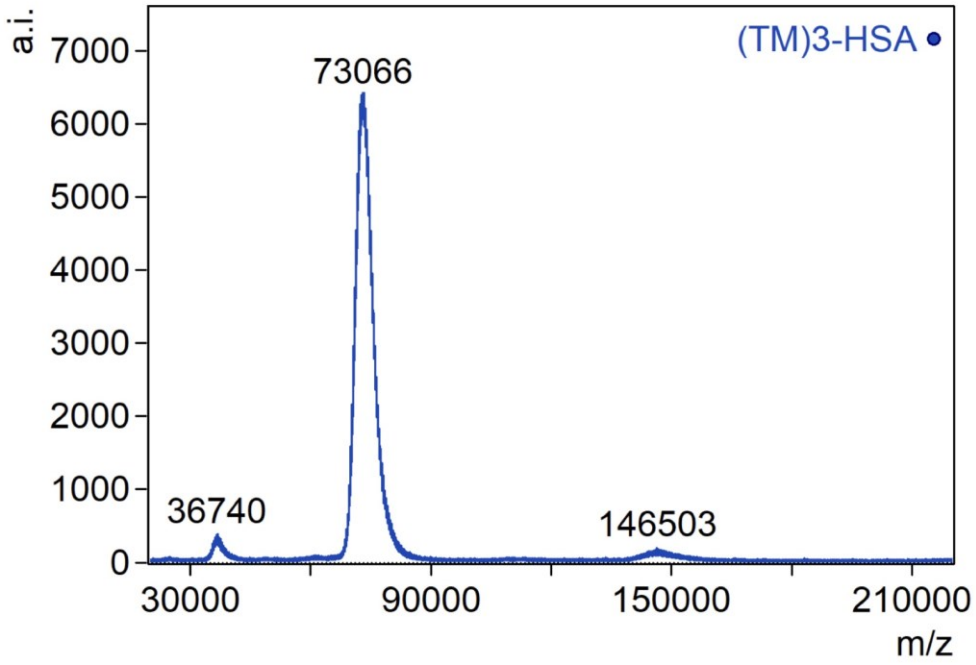

Figure S49: MALDI-ToF-spectrum of Cy5-labeled, TM-modified HSA. Found *m/z* = 73066 $[M+H]^+$.

Supporting Information

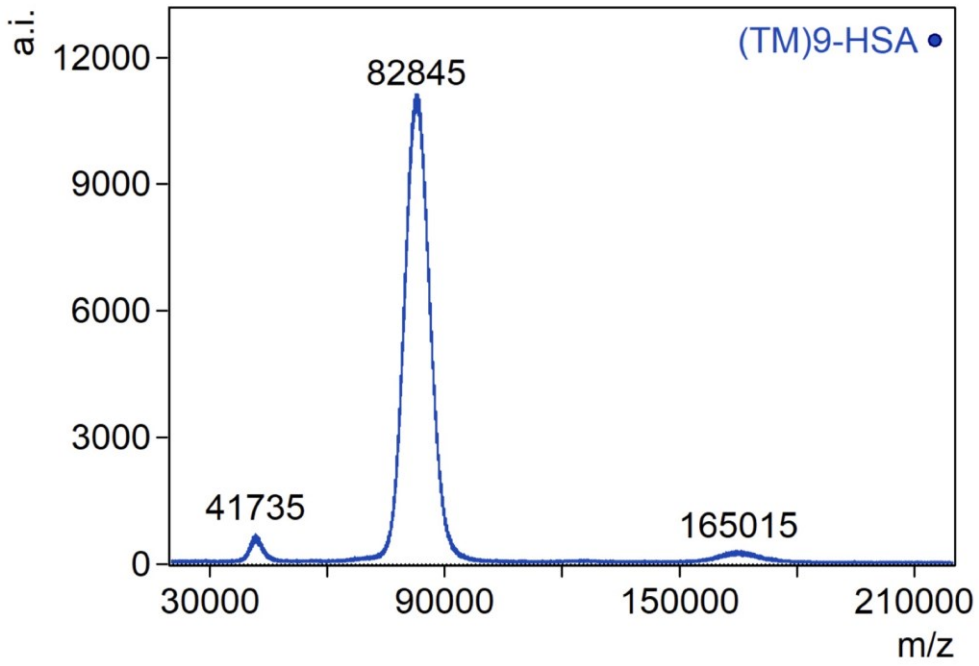

Figure S50: MALDI-ToF-spectrum of Cy5-labeled, TM-modified HSA. Found *m/z* = 82845 $[M+H]^+$.

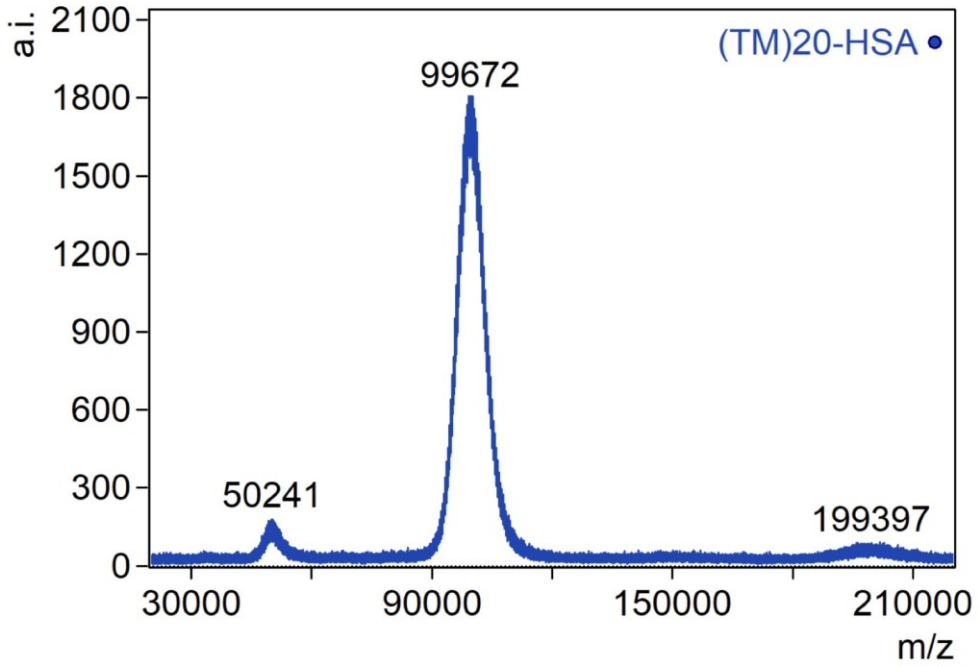

Figure S51: MALDI-ToF-spectrum of Cy5-labeled, TM-modified HSA. Found *m/z* = 99672 $[M+H]^+$.

Supporting Information

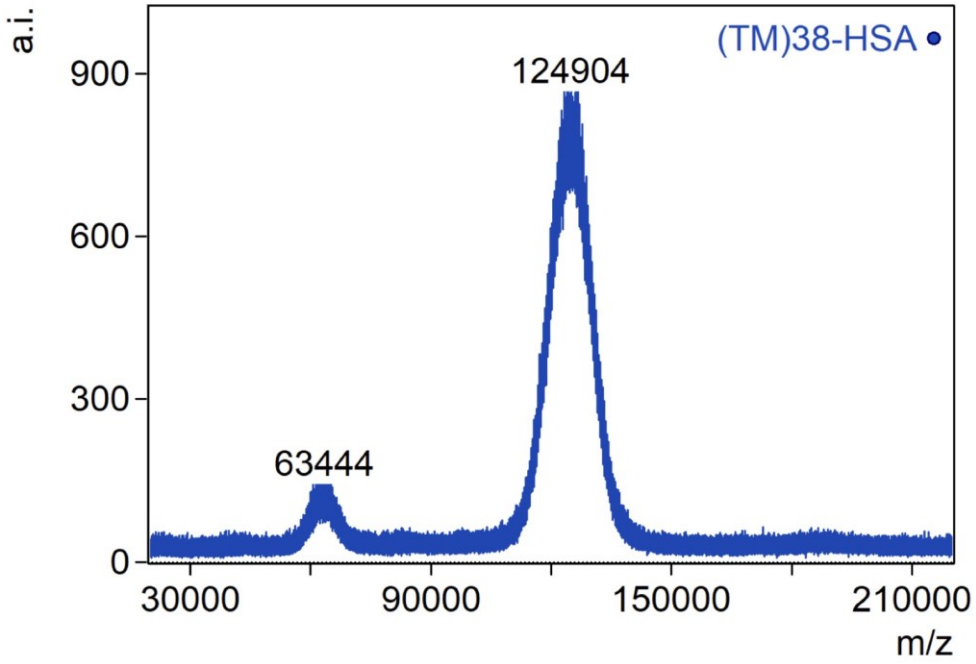

Figure S52: MALDI-ToF-spectrum of Cy5-labeled, TM-modified HSA. Found *m/z* = 124904 $[M+H]^+$.

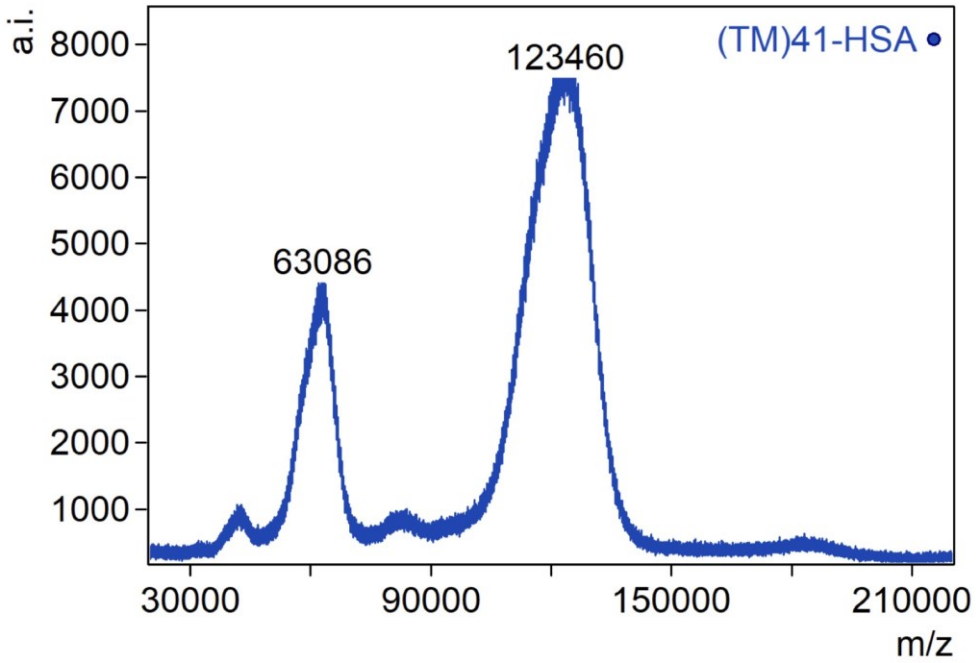

Figure S53: MALDI-ToF-spectrum of Cy5-labeled, TM-modified HSA. Found *m/z* = 123460 $[M+H]^+$.

Supporting Information

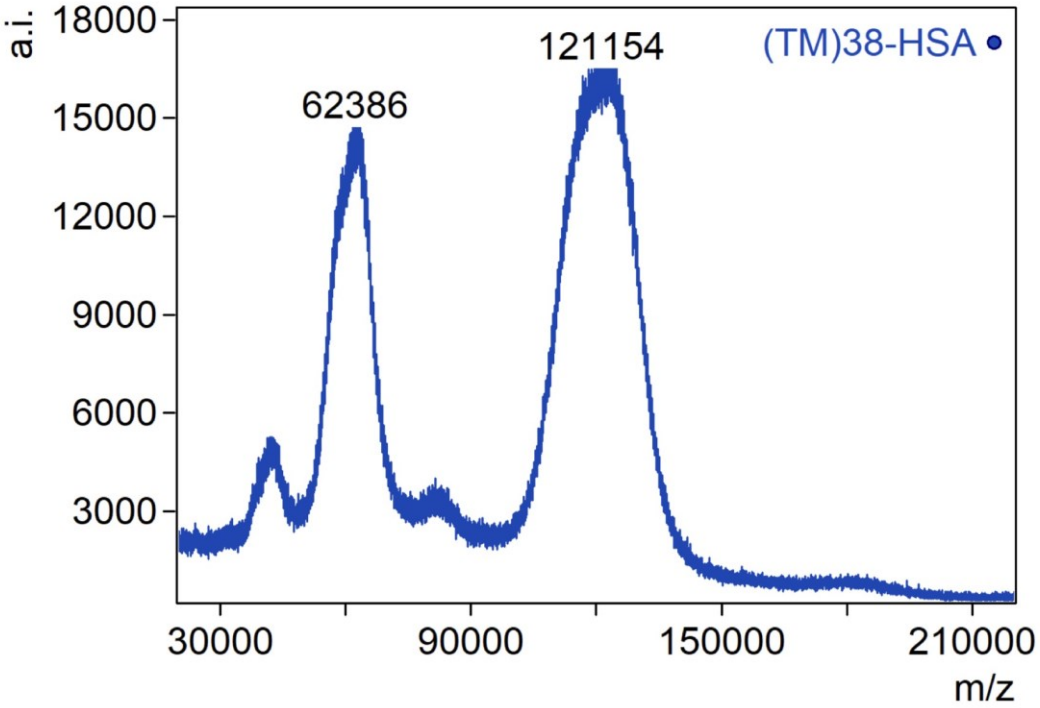

Figure S54: MALDI-ToF-spectrum of Cy5-labeled, TM-modified HSA. Found *m/z* = 121154 $[M+H]^+$.

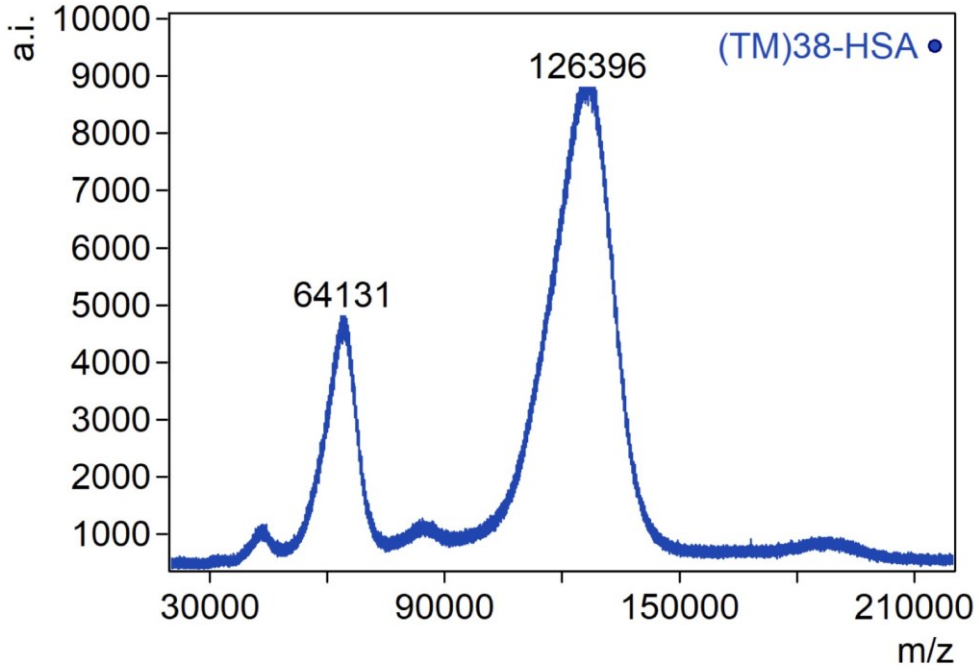

Figure S55: MALDI-ToF-spectrum of Cy7.5-labeled, TM-modified HSA. Found *m/z* = 126396 $[M+H]^+$.

Supporting Information

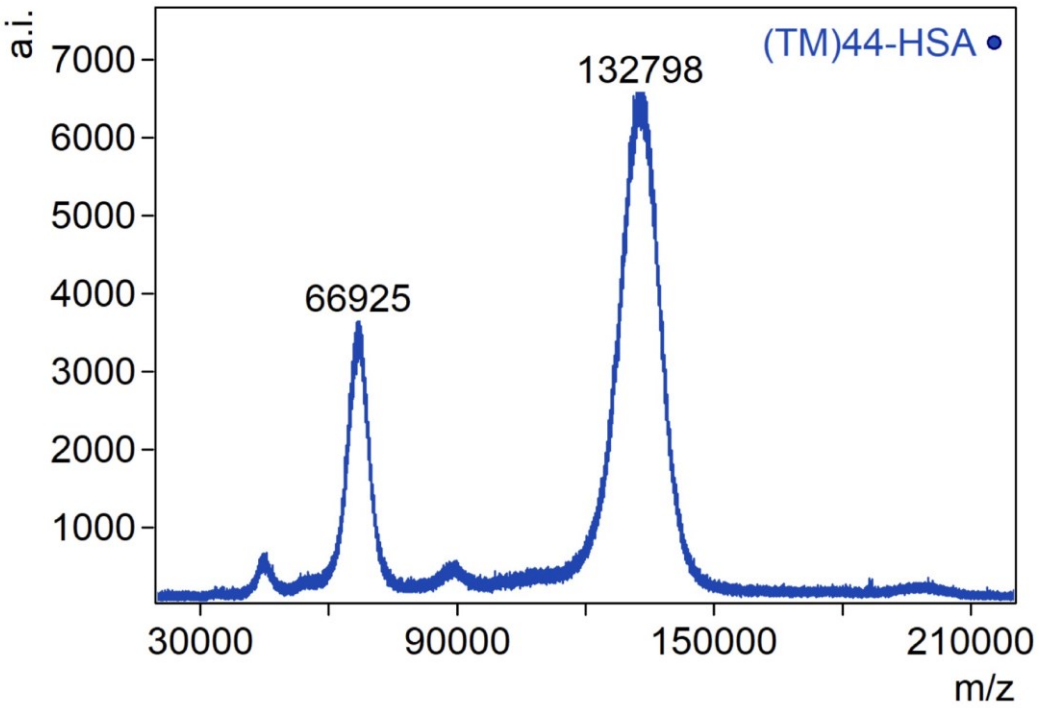

Figure S56: MALDI-ToF-spectrum of Cy5-labeled, TM-modified HSA. Found *m/z* = 132798 $[M+H]^+$.

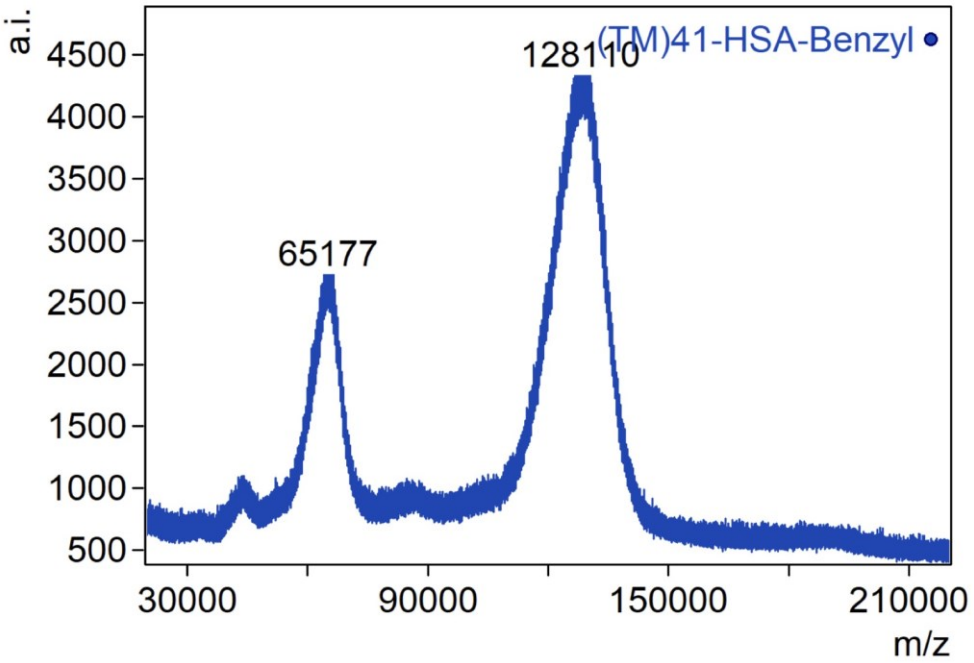

Figure S57: MALDI-ToF-spectrum of Cy5-labeled, benzyl loaded HSA nanocarrier. Found *m/z* = 128110 $[M+H]^+$.

Supporting Information

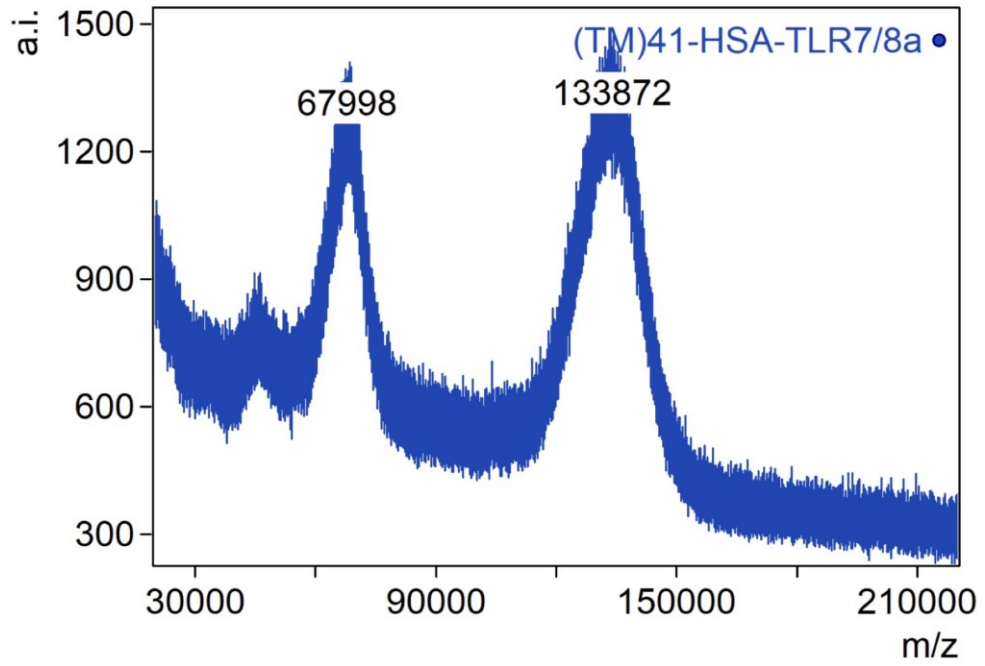

Figure S58: MALDI-ToF-spectrum of Cy5-labeled, TLR7/8a loaded HSA nanocarrier. Found *m/z* = 133872 $[M+H]^+$.

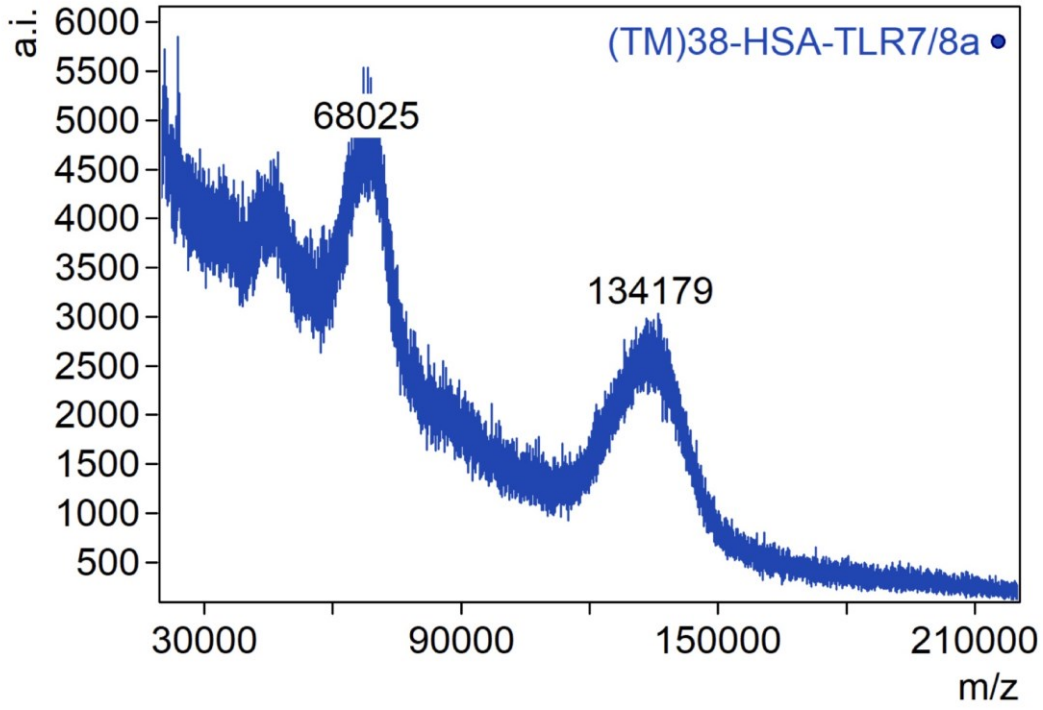

Figure S59: MALDI-ToF-spectrum of Cy5-labeled, TLR7/8a loaded HSA nanocarrier. Found *m/z* = 134179 $[M+H]^+$.

Supporting Information

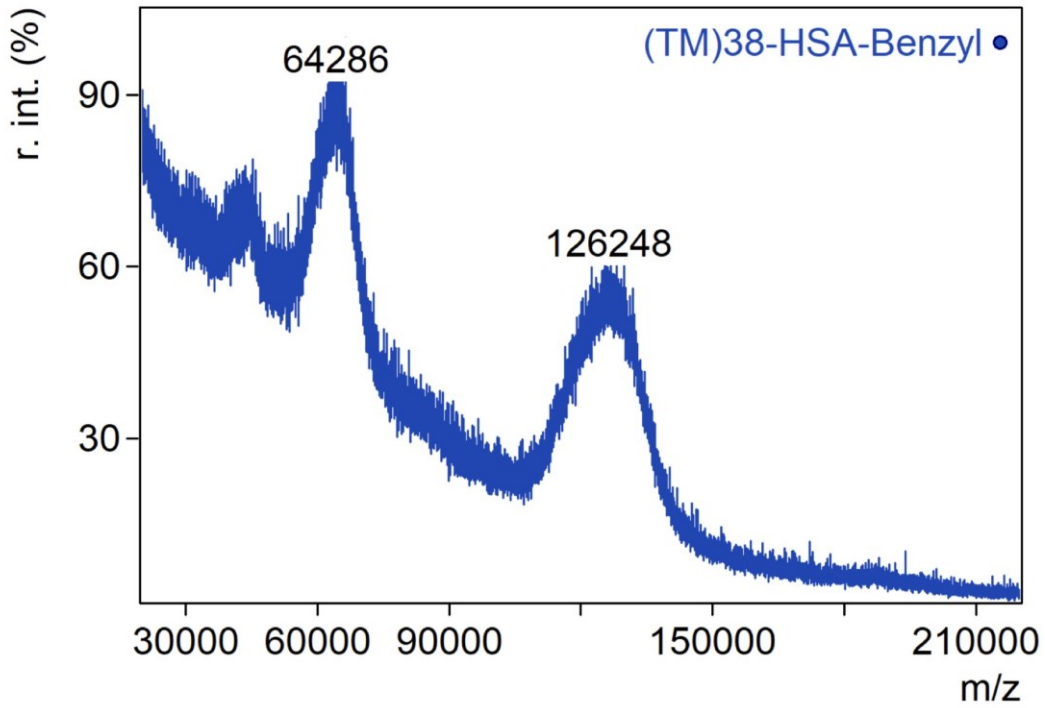

Figure S60: MALDI-ToF-spectrum of Cy5-labeled, benzyl loaded HSA nanocarrier. Found *m/z* = 126248 $[M+H]^+$.

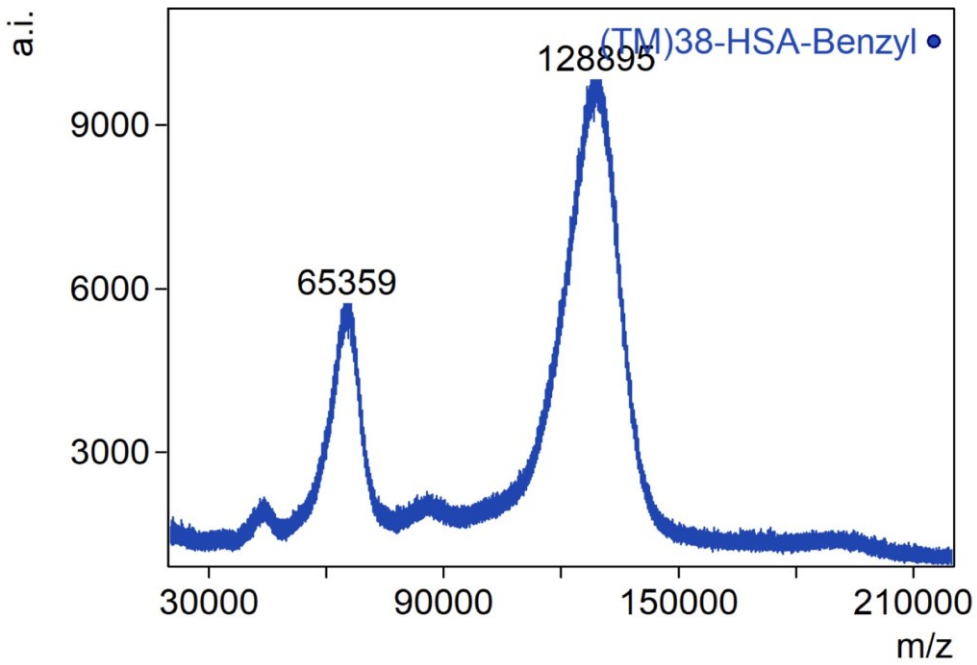

Figure S61: MALDI-ToF-spectrum of Cy7.5-labeled, benzyl loaded HSA nanocarrier. Found *m/z* = 128895 $[M+H]^+$.

Supporting Information

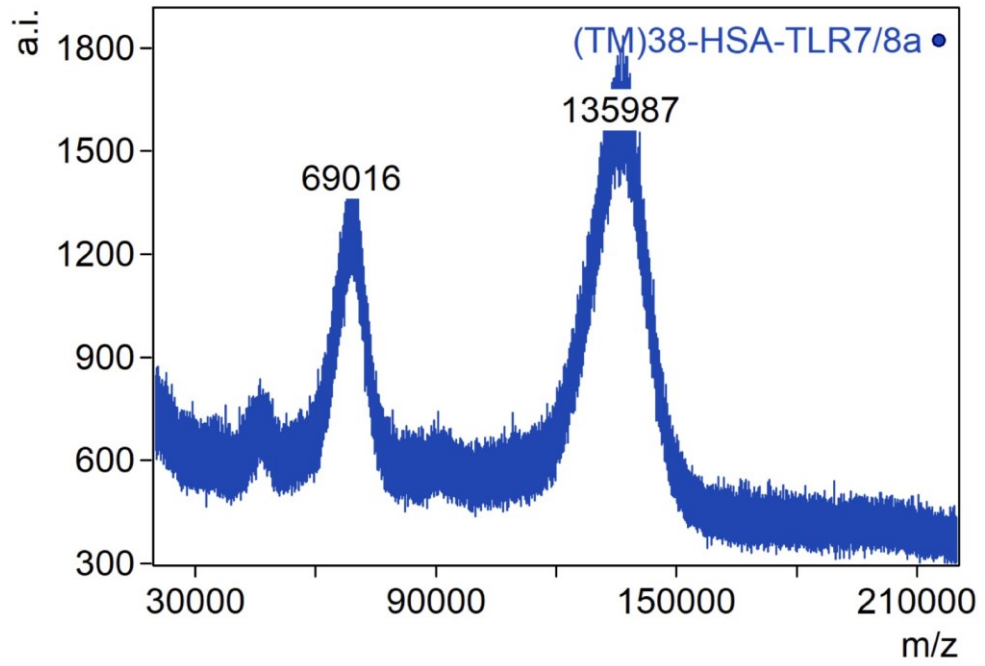

Figure S62: MALDI-ToF-spectrum of Cy7.5-labeled, TLR7/8a loaded HSA nanocarrier. Found *m/z* = 135987 $[M+H]^+$.

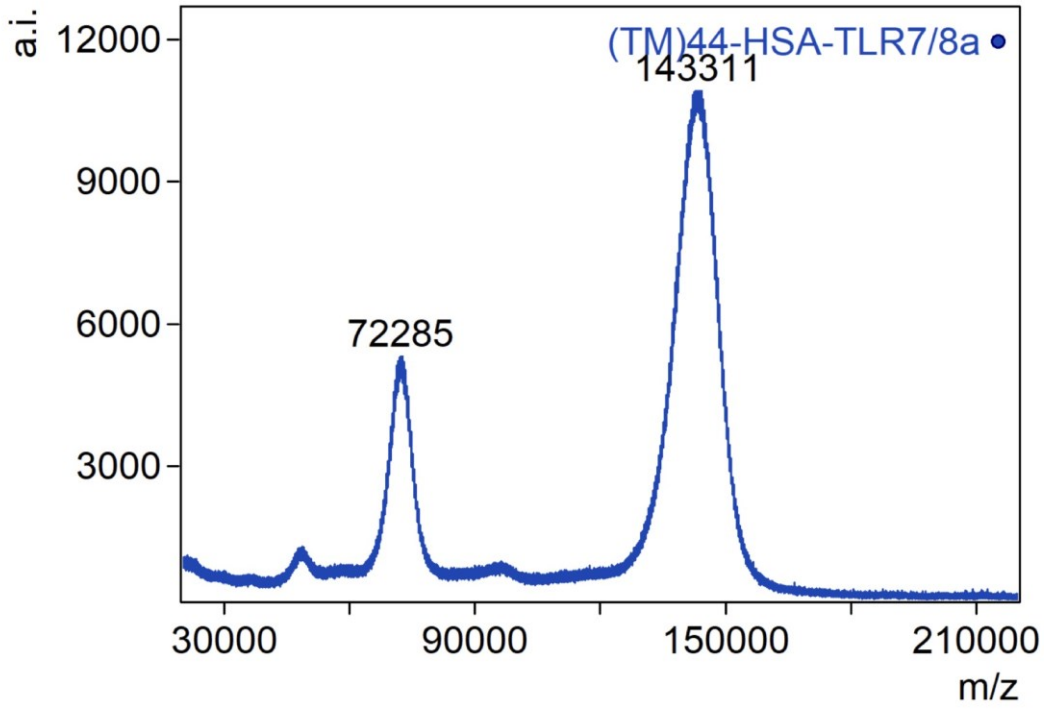

Figure S63: MALDI-ToF-spectrum of Cy5-labeled, TLR7/8a loaded HSA nanocarrier. Found *m/z* = 143311 $[M+H]^+$.

Supporting Information

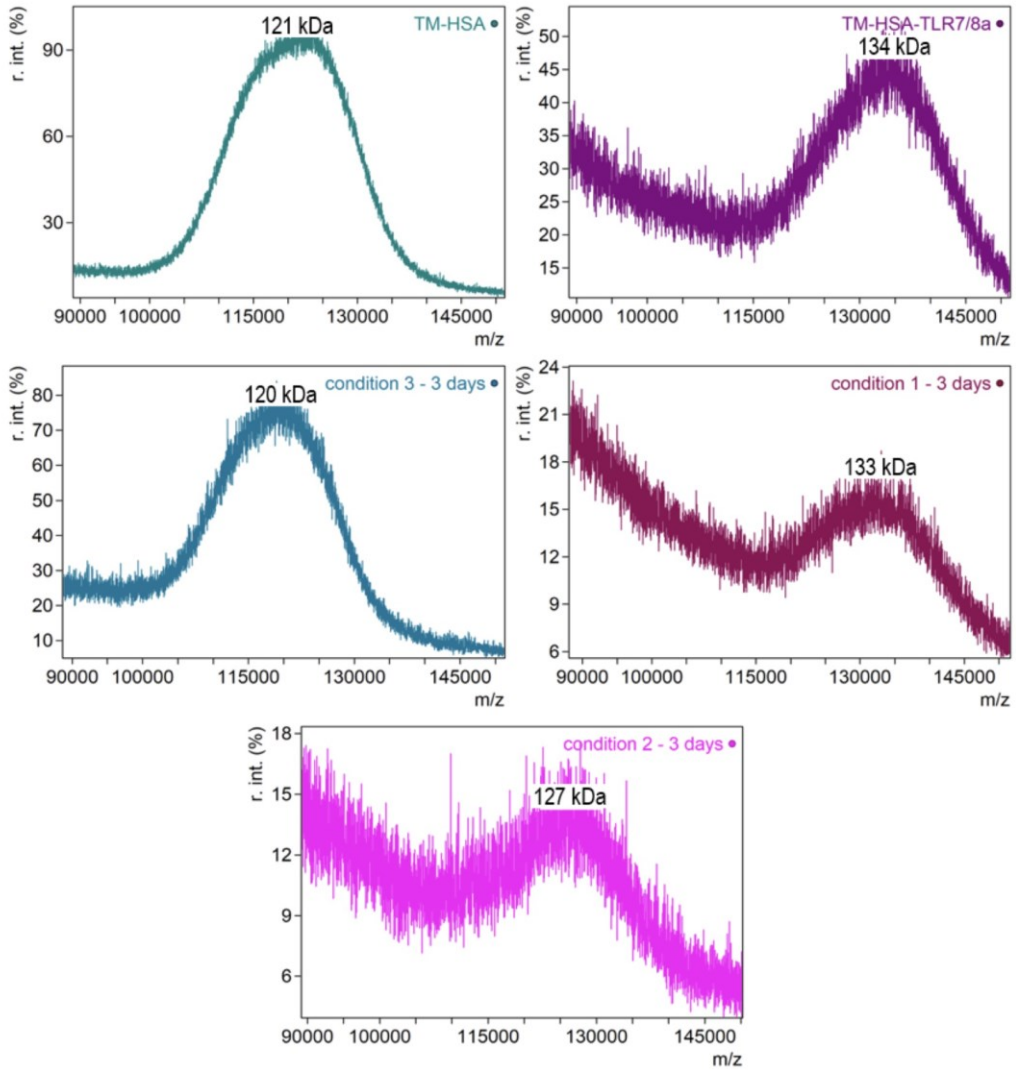

Figure S64: Normalized MALDI-ToF-MS spectra of nanocarrier of drug release from TM-HSA-TLR7/8a (see section 6.5.1) incubated at conditions 1 (middle right), 2 (bottom) and 3 (middle left) as well as used nanocarrier TM-HSA-TLR7/8a (top right) and precursor conjugate TM-HSA (top left) for comparison. Nanocarriers under release conditions 1-3 were directly taken from reaction solutions and diluted in sinapinic acid matrix 1:5, 1:6 or 1:12 for MALDI-ToF-MS analysis.

Supporting Information

9.6 LC-HRMS spectra

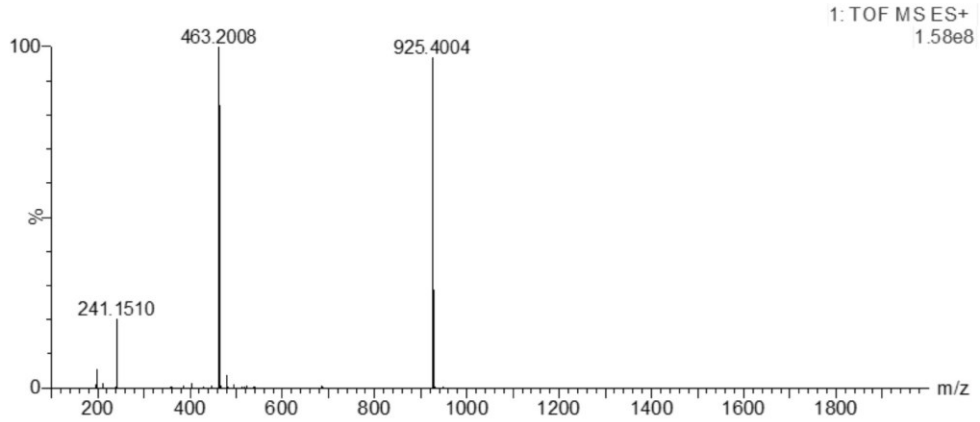

Figure S65: Dimerized TLR7/8a with linker **(a)** (calc. *m/z* 925.4000 $[M+H]^+$, found 925.4004; calc *m/z* 463.2037 $[M+2H]^{2+}$, found 463.2008).

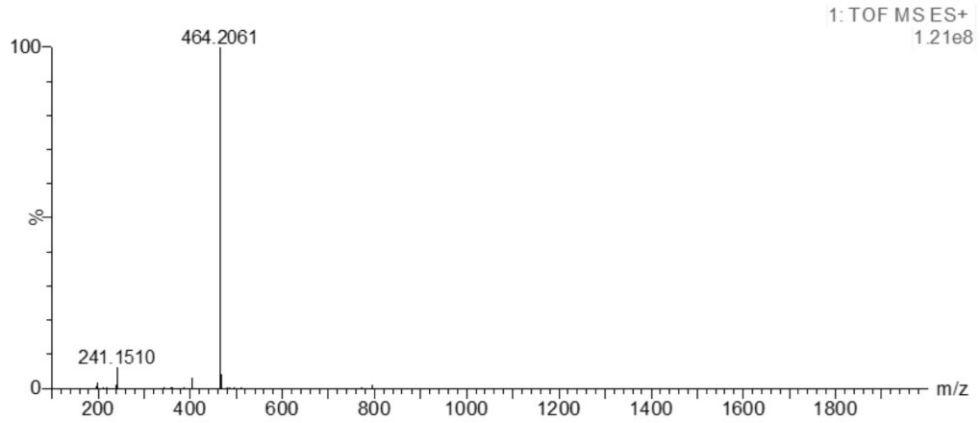

Figure S66: TLR7/8a with linker (**b**) (calc. *m/z* 464.2115 $[M+H]^+$, found 464.2061).

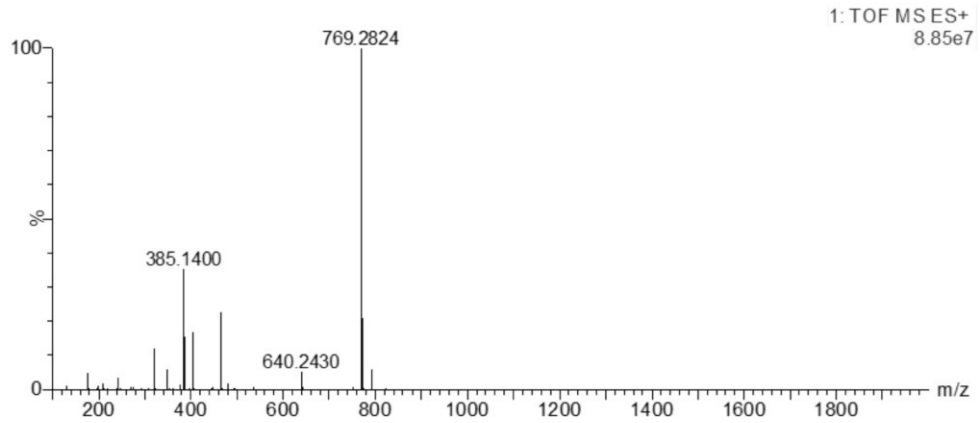

Figure S67: GSH adduct to TLR7/8a with linker (**c**) (calc. *m/z* 769.2796 $[M+H]^+$, found 769.2824; calc. *m/z* 385.1435 $[M+2H]^{2+}$, found 385.1400).

Supporting Information

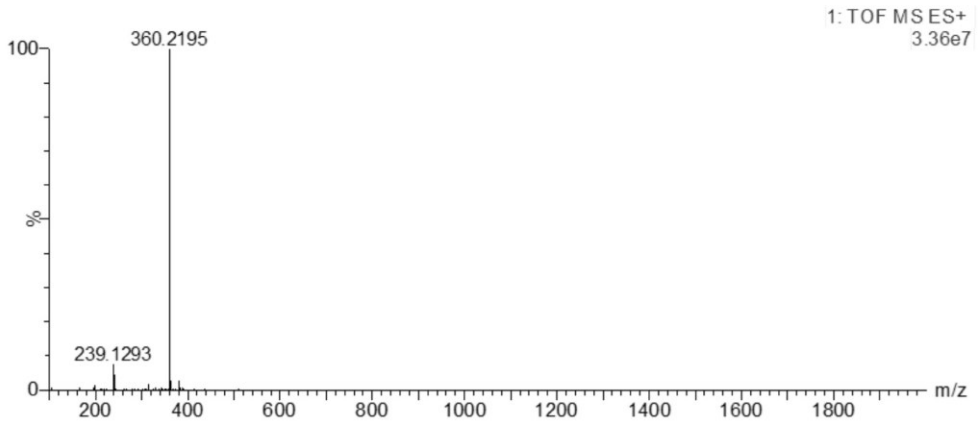

Figure S68: Released TLR7/8a (**d**) (calc. *m/z* 360.2183 $[M+H]^+$, found 360.2195).

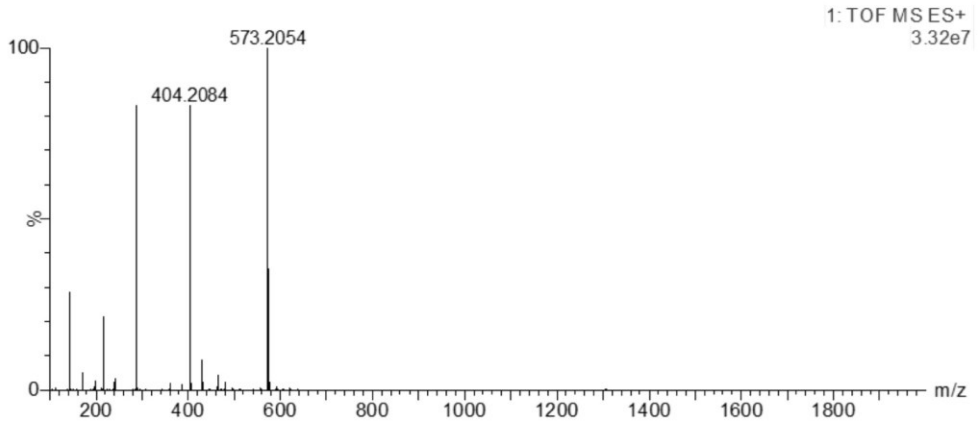

Figure S69: TLR7/8a with linker (**e**) (calc. *m/z* 573.2101 $[M+H]^+$, found 573.2054).

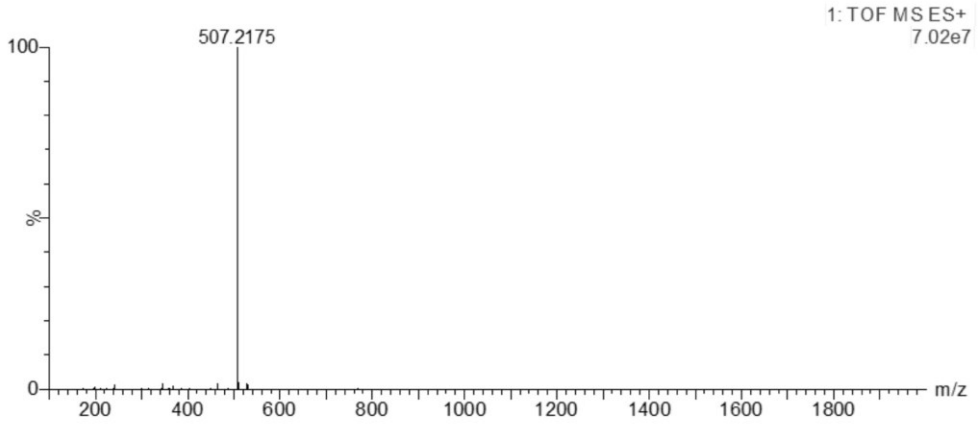

Figure S70: Urea related adduct of TLR7/8a with linker (**f**) (calc. *m/z* 507.2173 $[M+H]^+$, found 507.2175).

Supporting Information

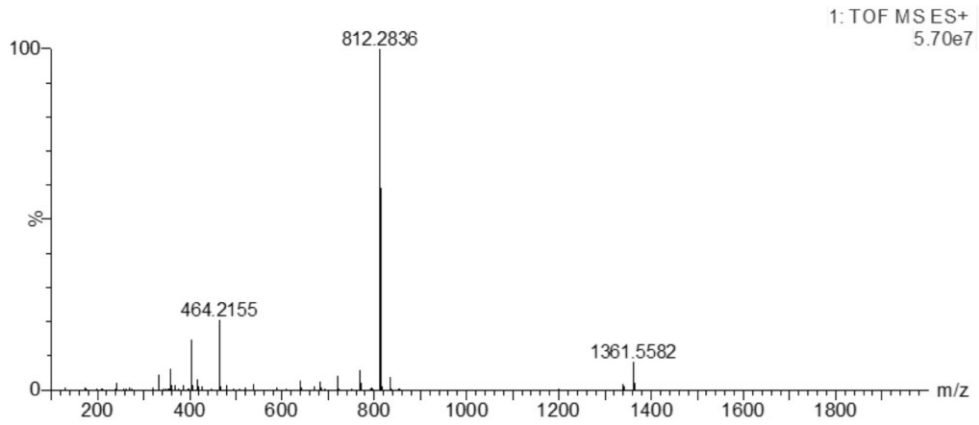

Figure S71: Urea related adduct of TLR7/8a with linker and GSH (**g**) (calc. *m/z* 812.2854, found 812.2836).

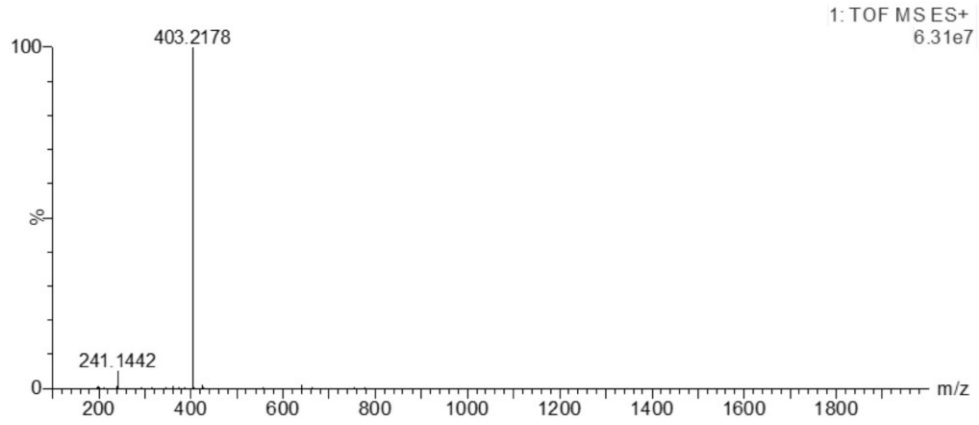

Figure S72: Urea related adduct of TLR7/8a with linker (**h**) (calc. *m/z* 403.2241 $[M+H]^+$, found 403.2178).

4. Surface density of mono- and trivalent high-mannan derived targeting structures with different affinity impacts cellular uptake of human serum albumin derived nanocarriers

The second project focused on systematically analyzing ligand-receptor interactions of mannose-based targeting structures with the lectins CD206 and CD209 by varying ligand type, valency, and density, to broaden the applicability of the biomacromolecular nanocarrier design of Chapter 3 in an immunotherapeutic context. Interactions were studied using both isolated molecules (the carbohydrate recognition domains of CD206/CD209 with the targeting structure) and ligand-decorated HSA nanocarriers. A comparative, multi-method investigation was performed to provide insight into, and partially differentiate between, ligand-specific effects and nanocarrier-mediated influences, with the aim of deriving broader design principles for carbohydrate-decorated nanocarriers.

Authors

R. Forster‡, **B. Lantzberg**‡, A. Weldert‡, L. Rosenberger, Y. Zeyn, D. Kowalczyk, S. L. Kuan, C. Kersten*, M. Bros*, T. Weil*, T. Schirmeister* and T. Opatz*

‡ Authors contributed equally to this work.

* Corresponding author

Published in Biomacromolecules 2025, 26, 11, 8087 – 8102

DOI: 10.1021/acs.biomac.5c01510

Date of Publication: 7th of October 2025

Contributions

As co-first author, **Bellinda Lantzberg** conceptualized the chemical design of the HSA conjugates and conducted the synthetic and analytical experiments, including MALDI-ToF-

MS, DLS, and agarose gel electrophoresis. She planned the *in vitro* experiments, analyzed the data, and performed formal analysis. Furthermore, she prepared the respective figures and drafted the corresponding parts of the manuscript and supplementary information. She also reviewed and edited the manuscript.

As co-first author, Robert Forster conducted all synthetic and analytical experiments regarding the saccharide targeting structures, analyzed and processed the data. He prepared figures and drafted the original manuscript as well as the supplementary information. As co-first author, Annabelle Weldert used molecular docking to predict binding modes. She recombinantly expressed and purified the CRDs of CD206 and CD209, performed NanoDSF studies, processed and analyzed the data, and performed formal analysis. Furthermore, she prepared the respective figures and drafted the corresponding parts of the manuscript and supplementary information. Laura Rosenberger and Yanira Zeyn conducted all *in vitro* experiments, processed the data, and reviewed the manuscript. Danuta Kowalczyk conducted synthetic and analytical experiments regarding saccharide targeting structures. Seah Ling Kuan supervised Bellinda Lantzberg and reviewed and edited the manuscript. Christian Kersten supervised Annabelle Weldert, generated a set of targeting structure conformers using Omega and reviewed and edited the manuscript. Matthias Bros provided resources, supervised Laura Rosenberger and Yanira Zeyn, and reviewed and edited the manuscript. Tanja Weil, Tanja Schirmeister, and Till Opatz provided resources, acquired funding for the project, and reviewed and edited the manuscript. Furthermore, Tanja Weil supervised Bellinda Lantzberg, Tanja Schirmeister supervised Annabelle Weldert, and Till Opatz was involved in conceptualization and administration of the project and supervised Robert Forster.

BioMACROMOLECULES

pubs.acs.org/Biomac
Article

Surface Density of Mono- and Trivalent High-Mannan-Derived Targeting Structures with Different Affinities Impacts Cellular Uptake of Human Serum Albumin-Derived Nanocarriers

Robert Forster,[#] Bellinda Lantzberg,[#] Annabelle Weldert,[#] Laura Rosenberger, Yanira Zeyn, Danuta Kowalczyk, Seah Ling Kuan, Christian Kersten,* Matthias Bros,* Tanja Weil,* Tanja Schirmeister,* and Till Opatz*

Cite This: *Biomacromolecules* 2025, 26, 8087−8102

Read Online

ACCESS | Metrics & More | Article Recommendations | Supporting Information

ABSTRACT: Actively targeted delivery of nanocarriers (NC) modified with targeting structures (TS) binding to cell surface receptors, specific to target cells, enables enhanced selectivity and efficacy of cellular uptake. This is influenced by the ligand density on the NC surface. Herein, the impact of type, valency, and surface density of high-mannan derived TS on the C-type lectin receptor (CLR)-mediated uptake of human serum albumin (HSA)-based NCs in immune cell populations was investigated. Monovalent and trivalent TSs were prepared via efficient synthesis protocols and investigated regarding their affinity versus isolated carbohydrate recognition domains (CRD) of CD206 and CD209 within a NanoDSF study. Conjugation to HSA resulted in low valency and saturated NCs with a well-defined mannose epitope count. An *in vitro* study with bone-marrow-derived dendritic cells and splenic immune cells revealed the impact of the NC surface modification on cellular uptake and cell selectivity, allowing insights into the design of TSs and NCs.

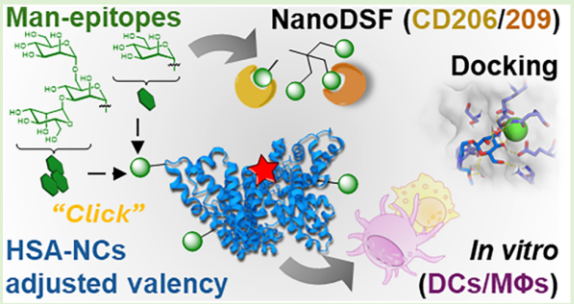

1. INTRODUCTION

Actively targeted drug delivery in immunotherapy aims at modulating immune responses by using drug-loaded nanoparticulate carriers (NCs) functionalized with targeting structures (TS).[1−4] Such polymer-, lipid-, or protein-based NCs protect the cargo, improve biodistribution and therapeutic efficacy.[5−9] Mannose-based TS enable selective delivery to antigen-presenting cells (APC) like dendritic cells (DC) or macrophages (MΦ) mediated by C-type lectin receptors (CLR).[10,11] CLR engagement allows internalization and intracellular distribution of NCs prior to the release and processing, as well as presentation of NC-derived antigens and, in the case of sufficient APC activation, downstream T-cell responses. This makes them attractive targets for APC-specific therapies (e.g., tumor immunotherapy).[12−18] Targeting of DCs or M2-polarized MΦs focuses on highly expressed CLRs like CD206 (MMR-1) and CD209 (DC-SIGN), due to involvement of either CLR in antigen internalization and subsequent presentation via major histocompatibility complex (MHC) molecules for T-cell activation.[19−29] CD206 contains eight carbohydrate recognition domains (CRD), with CRD4 being responsible for most of the binding activity.[30−33] CD209 contains one CRD and forms a homotetramer (Figure 1A).[34−36] Glycan array studies revealed binding of epitopes of a nonamannose substructure from naturally occurring high-mannan-type glycans,[37−44] with CD206 preferring shorter, terminally α-(1→2)-linked and CD209 internal α-(1→2)- and α-(1→3)-linked epitopes with canonical binding modes engaging hydroxyl groups 3 and 4 of the mannose units (Man).[45−49] Increased affinity for the α-(1→3)- and α-(1→6)-branched trisaccharide (Man_3) epitopes results from secondary contacts (Figure 1A).[31] CLR targeting thus strongly depends on epitope geometry.[50−52] Singular binding interactions of isolated epitopes and CRDs provide low intrinsic affinity and specificity (K_D in the mM range).[53−56] Presentation of multiple CRDs and formation of oligomers and cell surface clusters by CLRs offer extended binding regions[57−59] and enable multivalent interactions with multimerized epitopes for high functional affinity (avidity) and specificity (K_D in the μM to pM range) due to avidity effects such as clustering, chelation, and statistical rebinding (compare Figure 1C for avidity effects

Received: July 28, 2025
Revised: September 22, 2025
Accepted: September 23, 2025
Published: October 7, 2025

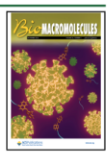

https://doi.org/10.1021/acs.biomac.5c01510
Biomacromolecules 2025, 26, 8087−8102

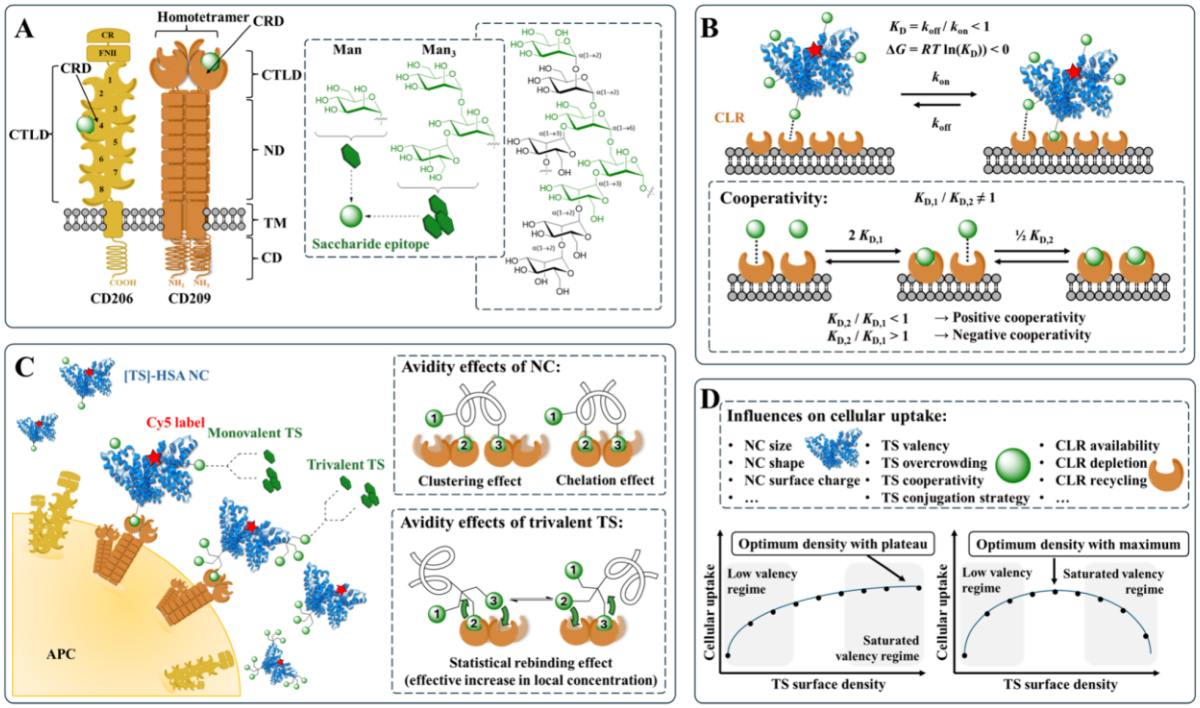

Figure 1. (A) Functional domains of CD206 and CD209: Cysteine-rich (CR), fibronectin type II (FNII), C-type lectin (CTLD), carbohydrate recognition (CRD), neck (ND), transmembrane (TM), and cytoplasmic domain (CD).[11,104,105] Saccharide epitopes Man and Man_3 of the nonasaccharide substructure from high-mannan glycans chosen as TS for CLR binding. (B) Multivalent interactions of NC and cell surface form multiple TS-CRD complexes governed by avidity of NC as a product of intrinsic affinities of individual TS and valency of NC resulting in avidity effects. Formation of initial complex exerts influence on subsequent formations.[81] (C) APC targeting with HSA-NCs presenting mono- and trivalent TSs carrying Man or Man_3 epitopes.[11] Cooperative avidity effects like simultaneous clustering of one CRD of two different CLRs or chelation of two CRDs of one respective CLR (NC multivalency) as well as an effective increase in the local concentration of epitopes by statistical rebinding (TS multivalency) influence uptake.[64−70] (D) Further properties of NCs and TS influencing cellular uptake, with dependency on TS surface density resulting in two trends: (a) increase until constant threshold or (b) increase until maximum, followed by decline.[76]

of potential relevance for the present study). Clustering refers to the ability of multivalent ligands to simultaneously bind to multiple receptors, while chelation enables binding to oligomeric receptors via simultaneous occupation of multiple binding sites. Statistical rebinding refers to the ability of a multivalent ligand to reform individual ligand−receptor bonds upon dissociation using adjacent epitopes, resulting in an increased probability of binding interactions. Acting as an effective increase in local epitope concentration, this leads to a higher apparent binding affinity.[60−70] Similar considerations apply for engagement of CLRs with multivalent NCs presenting mannose TSs, as biodistribution and cellular uptake are markedly influenced not only by size, surface charge and valency of the NC, but also by surface density, conjugation strategy, and orientation of the TSs.[71−82] Formation of TS-CLR complexes (Figure 1B) resulting from multivalent interactions between NCs, presenting multimerized TSs, and cell surfaces, expressing multiple CLRs can be described in thermodynamic terms by the Gibbs free energy, ΔG, which is related to avidity of the system via the dissociation constant, K_D ($\Delta G = RT \ln(K_D)$).[81,83] Models describing ΔG in terms of multivalent binding interactions highlight the number of formed complexes as the main driving force, with each contributing favorable binding enthalpy ΔH to overcompensate the unfavorable decrease in entropy ΔS upon binding ($\Delta G = \Delta H - T\Delta S$).[64,84] Negative values of ΔG describe the equilibrium of the binding process to favor the TS-CRD complex ($\Delta G < 0$ kJ/mol → $K_D < 1$ M). The entropy loss, ΔS, results from the mobility restriction for TSs entering the bound state. Being smaller for TSs already constrained by high surface density or conjugation via rigid linkers, the usage of flexible linkers, which offer the mobility required for adaptation to the target and efficient binding, imparts higher entropic penalties.[85−87] Based on thermodynamic considerations, targeting efficacy of multivalent NCs is assumed to benefit from high TS numbers (TS valency) and CLR expression (receptor availability).[81] On the contrary, targeting efficacy is hampered on the NC level by its size increase inherent to higher surface modification and further impacted by its shape and surface charge.[88] On the cellular level, targeting efficacy is decreased by steric hindrance of closely packed TSs (TS overcrowding), higher consumption of cell membrane receptors per NC binding event (receptor depletion) and slow recycling kinetics of such receptors (receptor recycling).[89] Thus, cellular uptake follows two general trends depending on TSs density: (a) "optimum density with a plateau" and (b) "optimum density with a maximum" (Figure 1D). The underlying mechanisms governing these trends have been comprehensively analyzed by Alkilany et al.[76] Steric hindrance of TSs on NCs with saturated surface also depends on the conjugation strategy employed,[90] with nonoriented TSs experiencing reduced steric hindrance resulting in trend (a) and with oriented, closely packed ligands

https://doi.org/10.1021/acs.biomac.5c01510
Biomacromolecules 2025, 26, 8087−8102

Biomacromolecules pubs.acs.org/Biomac Article

Scheme 1. Retrosynthesis of Building Blocks (Grey Highlight) Involving Mannoses (1) and (2), Linkers (3), (4), and (5), and Predendron (6) for Assembly of Monovalent and Trivalent TSs (Orange Highlight) with Abbreviated Residues (Green Highlight)[a]

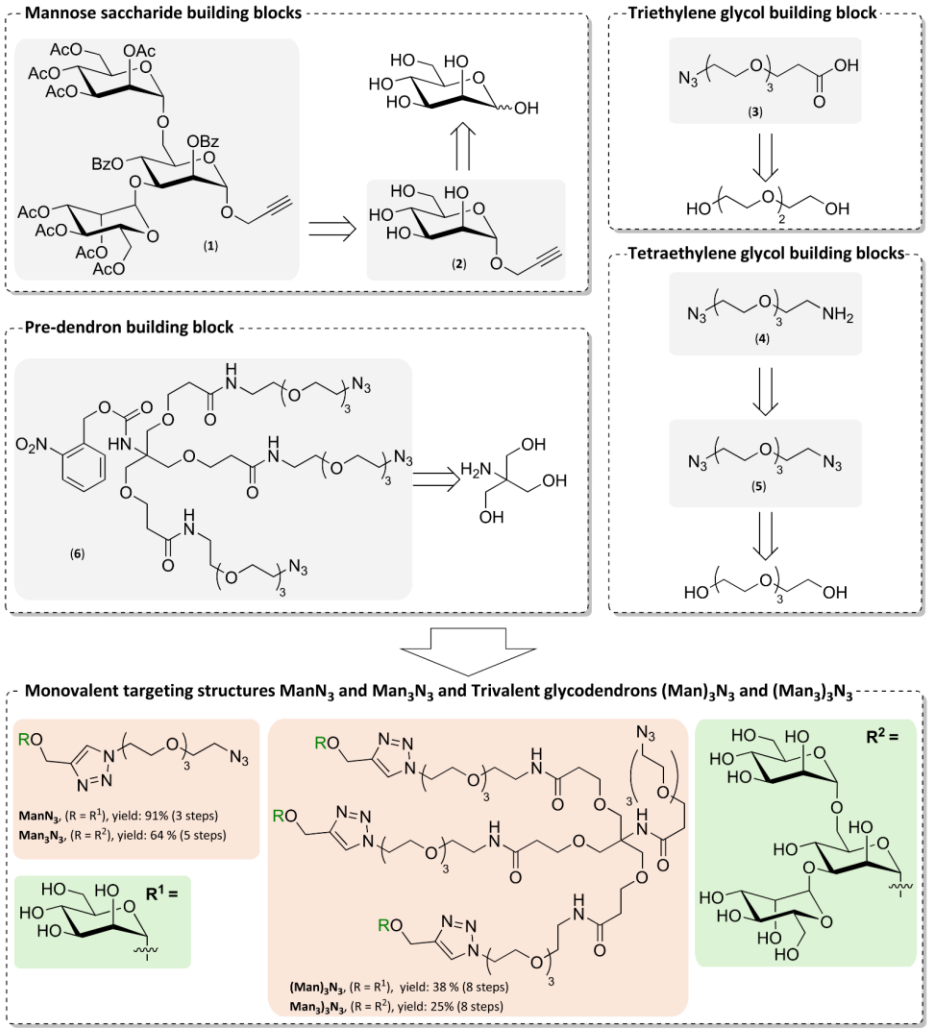

[a]Yields and step count are stated for each TS. Synthesis and analytical data are displayed in section 4.1 of the Supporting Information.

experiencing overcrowding effects resulting in trend (b).[76] Ligand density furthermore influences the operating uptake mechanism responsible for internalization of NCs.[91−93] Thus, avidity of NCs represents not a simple "additive" phenomenon summing up intrinsic affinities of TS,[94] as already formed binding interactions influence subsequent formations (Figure 1B), either by positive (first favors second interaction) or negative cooperativity (first hinders second interaction) (TS cooperativity), with avidity effects falling into the first category.[81,83,95] This complex interplay determining biodistribution and cellular uptake of targeted NCs is sensitive to small changes in NC valency and TS surface density with the major contributors summarized in Figure 1D. Chung et al. demonstrated low-valency human serum albumin (HSA)-derived NCs with six Man TSs achieving high uptake in lung metastases via selective CD206-mediated targeting of tumor-associated MΦs, while slightly higher valency of eight TSs shifted accumulation to the liver.[96] Such investigations of targeted delivery approaches are often directed at systemic distribution with limited focus on interactions of multivalent NCs at the cellular level.[81] The latter are often studied in experiments using surface plasmon resonance (SPR)[63,97,98] on artificial or isolated membranes,[99−101] to model the disposition of natural cellular membranes.[81] Given the relevance of low-valency NCs and limited understanding of multivalent interactions occurring at the cellular level, the impact of TS surface density and NC valency on cellular uptake, being a crucial step for targeted delivery approaches, needs to be investigated.[76] Heading out from reported HSA-NCs presenting monovalent TSs with the Man_3-epitope for CLR targeted transport of a toll-like receptor (TLR) 7/8 agonist for APC selective uptake,[102] we used similar systems to present quantifiable amounts of well-defined monovalent and trivalent TSs with Man and Man_3 epitopes at low and high degree of

https://doi.org/10.1021/acs.biomac.5c01510
Biomacromolecules 2025, 26, 8087−8102

functionalization for this study. HSA as basis of NCs enables surface modification with controlled stoichiometry.[103] Quantification of the number of TS per NC was a prerequisite to investigate which effect (i) TS surface density and NC valency, (ii) epitope type, and (iii) epitope clustering have on targeting properties. First, a docking study for both epitopes allowed insights into TS conformation and potential epitope binding modes (sections 3.1 and 3.3). Then, a NanoDSF study revealed binding affinities of all unconjugated TSs for isolated CRDs of CD206 and CD209 (section 3.2). Furthermore, an *in vitro* study of bone marrow-derived DCs (BMDC) allowed the investigation of cellular uptake of TS-HSA conjugates with low degree of functionalization (low valency) and high degree of functionalization (saturated valency) under consideration of influences (i)−(iii) (compare Figure 1D). Cellular uptake levels served as a measure of binding strength to determine the cell targeting ability of NCs within a biologically relevant environment and enabled interpretation in the context of the discussed trends (a) and (b). Finally, an *in vitro* study of splenic immune cells enabled comparisons within a more heterogeneous cell population and indications about APC targeting selectivity in the presence of off-target immune cells.

2. EXPERIMENTAL SECTION

2.1. General Experimental Conditions. For the synthesis of the HSA-based compounds, all reactions were performed without taking precautions to exclude air and moisture, unless stated otherwise. Organic solvents (CH_3CN, HPLC grade; CH_2Cl_2, HPLC grade; DMF, peptide grade; DMSO, analysis grade) were obtained from Thermo Fisher Scientific (Waltham, MA, USA) and used without further purification. Milli-Q water (MQ) was obtained from a Millipore purification system. For the synthesis of carbohydrate-based compounds, reactions involving sensitive and reactive species were conducted under an atmosphere of argon-gas in dried glass ware utilizing the standard Schlenk technique. Dried solvents were used, obtained from a SPS 5 solvent drying system (M. Braun Inertgas-Systeme, Garching, BY, Germany) for toluene and DCM. Further dried solvents were obtained from Acros Organics (Geel, Belgium) in AcroSeal bottles over molecular sieves for DMF, MeOH and pyridine. Glycosylation reactions were conducted in the presence of activated spherical molecular sieve beads (diameter 1−2 mm, pore size 3 Å) supplied from Alfa Aesar (Haverhill, MA, USA). The stated temperatures refer to the temperatures measured with a contact thermometer in the used heating mantle or cooling bath. Heated reactions were conducted in an aluminum block placed on the stirring plate. Glycosylation reactions conducted in a temperature range between −40 °C to −20 °C were placed in an acetone bath, which had its temperature adjusted using a FT902 cryostat (Julabo, Seelbach, BW, Germany). Zemplén-deacylations were neutralized with the ion-exchange resin Amberlite IR 120 (*H*-Form) supplied by Merck Millipore (Burlington, MA, USA). The resin was thoroughly washed with MeOH, H_2O, 1 M HCl, and MeOH in that order prior to use utilizing a glass frit. To remove molecular sieves, ion-exchange resin, and other solids prior to reaction work up, reaction mixtures were filtered through a glass frit using Celite Hyflo Super Cel diatomaceous earth, supplied from Sigma-Aldrich (St. Louis, MO, USA).

2.2. Synthesis of Saccharide Targeting Structures. To present one or three Man or Man_3 epitopes, the clickable monovalent TSs $ManN_3$, Man_3N_3, and the Newkome-type[106] glycodendrons $(Man)_3N_3$, and $(Man_3)_3N_3$ were prepared (Scheme 1). The contained flexible ethylene glycol-based linkers enable conjugation to dibenzocyclooctyne (DBCO)-modified HSA derived NCs via strain-promoted azide alkyne cycloaddition (SPAAC). Their synthesis involves the preparation of saccharide, linker, and predendron building blocks using a set of efficient and scalable synthesis protocols evolving around the copper-catalyzed azide alkyne cycloaddition (CuAAC) reaction for their assembly (Scheme S1 in the Supporting Information for details on the synthesis steps and reaction conditions). The building blocks are summarized in the upper part and the assembled TS in the lower part of Scheme 1. The TSs were obtained with significantly improved yields compared to prior reports (e.g., Man_3N_3: 4% over eight steps).[75] Higher efficiency and robustness of the synthesis route up to the multigram scale results from telescoped reaction protocols (two-step propargylation and Zemplén-deacylation sequence[107] and three-step silylation, benzoylation, desilylation sequence[108]). All building blocks and intermediates were characterized by ^1H NMR, ^{13}C NMR, 2D NMR, and high-resolution mass spectrometry (HR-MS). The unconjugated TSs were used in the NanoDSF study and for conjugation to the [DBCO]-HSA precursor.

2.3. Differential Scanning Fluorimetry (NanoDSF) Study of Unconjugated TS. Thermal shift experiments were performed by using a Prometheus NanoDSF instrument (NanoTemper, Munich, Germany). Each sample, containing 12 μM CD209 CRD or CD206 CRD4 (recombinant protein expression and purification displayed in section 6.1 of the Supporting Information) together with varying ligand concentrations in binding buffer (150 mM NaCl, 25 mM Tris-Cl, pH 7.8, and 25 mM $CaCl_2$), was loaded into NanoDSF capillaries. Each ligand concentration was measured in triplicate. Samples were subjected to a controlled temperature increase from 20 to 85 °C at a rate of 1.5 °C per minute. Protein unfolding was monitored by measuring the fluorescence emission ratio at 350 and 330 nm. The FoldAffinity tool developed by Niebling et al.[109] was used to analyze the melting curves (data displayed on section 6.2 of the Supporting Information) and determine the unfolded fraction at each ligand concentration, evaluated at 53 °C for CD206 and at 63 °C for CD209. Data were analyzed according to the vertical slice method developed by Bai et al.[110] The unfolded fraction was plotted against the ligand concentration, and EC_{50} values were determined by fitting the data to the Hill equation using GraphPad Prism 8.0.1. K_D values were calculated using eq 1[110] based on the unfolded fraction in the absence of ligand (f_{uo}) and the total protein concentration ([*P*]). Associated errors were determined according to the standard error propagation rules.

$$K_D = (1 - f_{uo}) \times \left(EC_{50} - \frac{[P]}{2}\right) \quad (1)$$

2.4. Matrix-Assisted Laser Desorption Ionization − Time of Flight Mass Spectrometry (MALDI-ToF-MS). Mass spectra for HSA-based compounds were acquired on a ToF MS rapifleX spectrometer (Bruker Corporation, Ettlingen, BW, Germany) using sinapinic acid as the matrix. The molecular mass for all compounds was calculated as the m/z value using the peak center representing the singly charged species.

2.5. Agarose Gel Electrophoresis. An 1% agarose gel (0.5 g agarose, 50 mL 1 × TAE buffer) was prepared, and protein (~1−3 μg) samples were loaded. The gel was run at 150 V for 33 min. The gel was imaged using the Cyanine 5 (Cy5)-channel and stained with coomassie brilliant blue before imaging using a ChemiDoc Imaging system (Bio-Rad Laboratories, Hercules, CA, USA) using the coomassie brilliant blue channel.[111]

2.6. Dynamic Light Scattering (DLS). Measurements of HSA-based compounds (10 μM in MQ) were performed at 25 °C using a Zetasizer Nano S (Malvern Instruments, Malvern, England) equipped with a He/Ne Laser (λ = 633 nm) and a narrow band filter at a fixed scattering angle of 173 °. Volume distribution of DLS measurements of compounds were used to determine the compounds size distribution.

2.7. Synthesis of HSA Conjugates. Synthesis procedures were adapted[102] and modified, as provided in detail in the SI (section 4.2 in the SI). Briefly, native HSA was dye-labeled using Sulfo-Cy5-Maleimide at Cys34 in 50 mM PB, pH 7.4, followed by ring-opening for stabilization in 50 mM borate buffer, pH 9.2 (HSA). The HSA was purified via spin filtration (Vivaspin, 10 kDa cutoff). A fixed number of DBCO-groups (13 or 47, as determined by the average molecular weight from MALDI-ToF-MS analysis) were statistically attached to

https://doi.org/10.1021/acs.biomac.5c01510
Biomacromolecules 2025, 26, 8087−8102

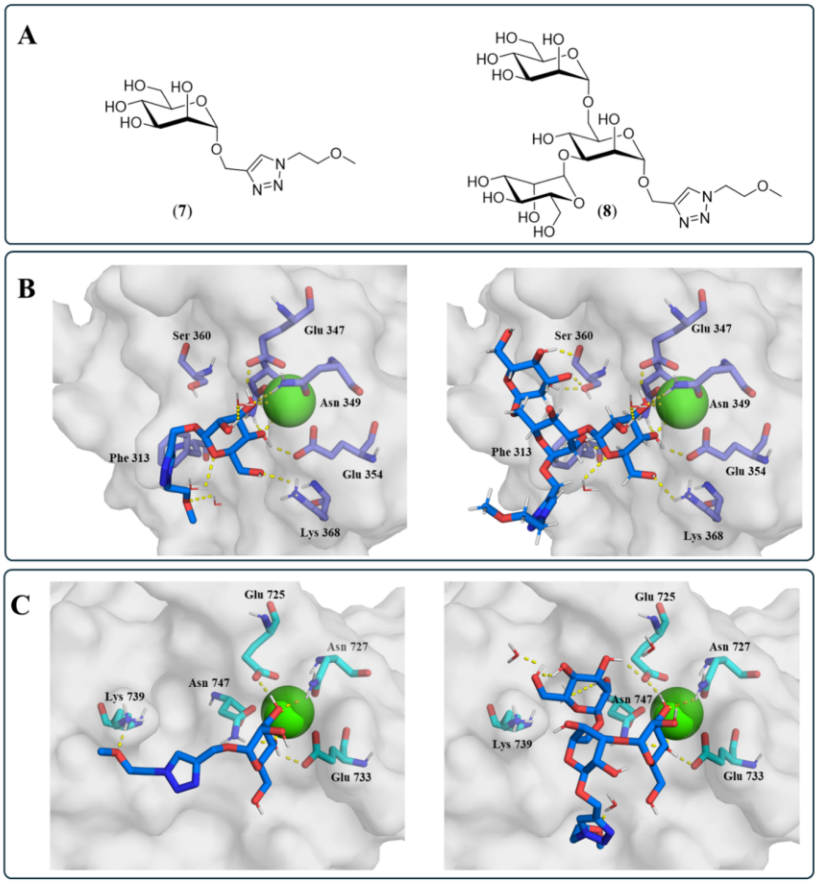

Figure 2. (A) TS Man (**7**) and Man_3 (**8**) with truncated linkers used for the in silico binding mode study. (B) Predicted binding modes for TS Man (**7**) (left) and TS Man_3 (**8**) (right) in complex with CD209 (PDB: 1SL4).[112] (C) Predicted binding mode for TS Man (**7**) (left) and TS Man_3 (**8**) (right) in complex with CD206 (PDB: 7JUF).[31] TS displayed as sticks with blue C-atoms, protein surfaces in light gray, selected amino acid residues inside the CRD as sticks with purple (CD209) or light blue (CD206) C-atoms and label, Ca^{2+}-cations as green spheres, water molecules as lines, and polar interactions as yellow dashed lines.

lysine residues randomly distributed on the NC surface via DBCO-PEG_4-NHS in 50 mM PB, pH 7.4 yielding DBCO-HSA. Subsequently, synthetic azide-functionalized TS ($ManN_3$, Man_3N_3, $(Man)_3N_3$, or $(Man_3)_3N_3$; MQ, 10 mg/mL) was added to DBCO-HSA (1 mg/mL) in 50 mM PB, 8 M urea, 2 mM EDTA. Equivalents of TS and reaction time were strictly controlled and adjusted based on reaction progress monitoring via MALDI-ToF-MS. For conjugates with n(TS) = 1−9, remaining free DBCO groups were capped using excess N_3−PEG_3−OH. All HSA conjugates were purified via spin filtration (Vivaspin, 10 kDa cutoff) and obtained with recovery rates ranging from 38% to quantitative. The degree of modification of HSA with TS was controlled qualitatively via agarose gel electrophoresis (Figure S1 in the Supporting Information) and quantitatively via MALDI-ToF-MS analysis. In total, five groups of NCs were prepared following the described procedure, involving the control group C [C I = Cy5-labeled HSA, C II = DBCO-HSA with 13 DBCO groups attached, and C III = HO-PEG_3-HSA, in which the 13 DBCO groups were saturated with capping reagent], the $ManN_3$ modified group M [M I, M II, M III, M VI, M IX, M_{sat}], the $(Man)_3N_3$ modified group [MD I, MD II, MD III, MD_{sat}], the Man_3N_3 modified group (TM I, TM II, TM III, TM IV, TM IX, TM_{sat}] and the $(Man_3)_3N_3$ modified group [TMD I, TMD II, TMD III, TMD_{sat}], where the Roman numeral always represents the number of TS groups attached. This systematic matrix of NCs with known amounts of epitopes of different structures at variable TS density and NC valency enables the subsequent interpretation of in vitro experiments.

2.8. Cell Culture. Murine bone marrow cells ($2{\cdot}10^5$/mL for GM-CSF supplemented culture) were seeded in 12-well suspension culture plates (Greiner Bio-One, Frickenhausen, BW, Germany) in culture medium (IMDM, 2 mM L-glutamine, 100 U/mL penicillin G, 100 μg/mL streptomycin (Sigma-Aldrich, Deisenhofen, BY, Germany) and 50 μM β-mercaptoethanol (Carl Roth, Karlsruhe, BW, Germany) containing 5% FBS (PAN-Biotech, Aidenbach, BY, Germany)) supplemented with recombinant murine GM-CSF (10 ng/mL) (Miltenyi Biotec, Bergisch Gladbach, NRW, Germany). Cells were kept at 37 °C, 95% relative humidity, and 5% CO_2. Culture media was replenished on day 3 and 6 with GM-CSF supplemented cell culture medium.

2.9. Spleen Cell Isolation. Murine spleens were mechanically disrupted with a pestle and pressed through a cell strainer with a pore size of 40 μm (Greiner Bio-One, Frickenhausen, BW, Germany) to obtain a single-cell suspension. Erythrocytes were lysed using 2.00 mL of Gey's Red Cell Lysis buffer (H_2O dest., 100 μM EDTA, 10.0 mM $KHCO_3$ and 155 mM NH_4Cl) for 1 min at room temperature. Subsequently, cells were washed using an IMDM-based culture medium containing 5% FBS (PAN Biotech, Aidenbach, Germany), 2.00 mM L-glutamine, 100 IU/mL penicillin, 100 μg/mL streptomycin, and 50.0 μM β-mercaptoethanol. Isolated splenocytes

https://doi.org/10.1021/acs.biomac.5c01510
Biomacromolecules 2025, 26, 8087−8102

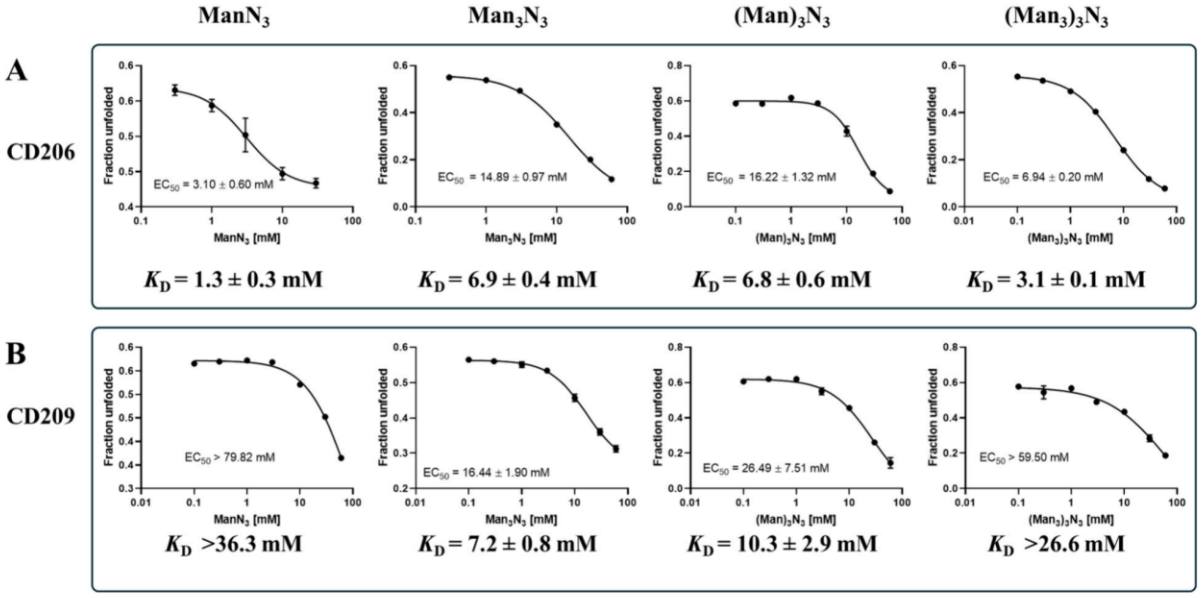

Figure 3. NanoDSF study for binding of mono- and trivalent TSs $ManN_3$, Man_3N_3, $(Man)_3N_3$, and $(Man_3)_3N_3$ to the CRDs of CD206 and CD209. (A) Affinity of mono- and trivalent TSs for CRD4 of CD206. (B) Affinity of mono- and trivalent TSs for CRD of CD209. The unfolded fraction of each CRD at different TS concentrations was determined at 53 °C for CD206 and at 63 °C for CD209. The unfolded fraction was plotted against TS concentration, and EC_{50} values were determined using GraphPad Prism 8.0.1. The respective K_D values were calculated from EC_{50}, as described in section 2.3, and are given for each case.

(2×10^6/500 μL) were used for *in vitro* experiments and stained for FACS analysis.

2.10. Fluorescence Activated Cell Sorting (FACS). After treatment, GM-CSF BMDCs and splenocytes were harvested, washed with staining buffer (PBS, 1% FBS, 0.5 mM EDTA) and incubated with rat antimouse CD16/CD32 antibody (clone 2.4G2; 15 min, 4 °C) to prevent antibody binding to Fcγ receptors. Following this, the samples were incubated with fluorescence-labeled antibodies (20 min, 4 °C). Then, samples were washed with PBS and incubated with a flexible viability dye (FVD, 1:1000 in PBS, 30 min, 4 °C) to identify live/dead cells. Measurements were carried out using an Attune NxT flow cytometer and data were analyzed using Attune NxT software (both are from Thermo Fisher, Waltham, MA, USA).

3. RESULTS AND DISCUSSION

3.1. Prediction of Binding Modes for Monovalent TSs. Predicted binding modes for the TS Man (**7**) and Man_3 (**8**), with a truncated linker unit (Figure 2A), were generated by molecular docking to investigate potential influences of linker placement on binding mode. The molecular docking-predicted binding mode of the TS Man (**7**) to the CRD of CD209 showed polar interactions between the Man epitope and the Ca^{2+}-cation inside the principal Ca^{2+}-binding site, as well as to the surrounding amino acids Glu347, Asn349, Glu354, Lys368, and Asn365 (Figure 2B). The truncated linker is oriented toward the protein surface and interacts with water molecules inside the pocket. The predicted binding mode of the TS Man_3 (**8**) with the CRD of CD209, indicates that the Man_3 epitope predominantly binds through the terminally α-(1→3)-connected mannose residue, with the same interactions as the Man epitope in the prior case. The central mannose moiety forms no additional hydrogen bonds to the CRD, while the terminal α-(1→6)-linked mannose residue forms additional polar interactions with Ser360 in the secondary binding site, consistent with previous crystal structures of similar compounds (Figure 2B).[112] Molecular docking of the TS Man (**7**) to the CRD of CD206, showed that the Man epitope similarly engages in polar interactions with the central Ca^{2+}-cation and surrounding amino acids Glu725, Asn727, Glu733, and Asn747 (Figure 2C). The linker forms a hydrogen bond to Lys739. In the predicted binding mode of the TS Man_3 (**8**) with the CRD of CD206, the characteristic polar interactions again arise from the α-(1→3)-linked mannose residue, with an additional polar interaction between the α-(1→6)-linked mannose and Glu725. The linker interacts with a binding-site water molecule. All linkers are found at the solvent-exposed protein surface, with their orientation pointing away from the primary binding site. Therefore, this attachment point seems to be suitable for linking Man moieties for glycodendrons.

3.2. NanoDSF Binding Study for Mono- and Trivalent TSs. The binding affinity of CRD4 of CD206 to saccharide ligands has been mainly investigated by NMR titration and competition binding assays, yielding high μM to low mM affinities.[31,113] For CD209, surface plasmon resonance (SPR), isothermal titration calorimetry (ITC), and solid-phase competition assays have been employed to measure the affinity of both the tetrameric extracellular domain (ECD) and the monomeric carbohydrate recognition domain (CRD) toward different mannose variations, with reported values ranging from the low millimolar range to being too weak to detect.[35,50,63,114−117] Notably, the isolated CRD is known to have weaker affinities to its ligands than the tetrameric ECD.[36] A growing body of literature has demonstrated that (Nano)-DSF can be utilized to obtain affinity values even in the mM range, which is challenging for other biophysical methods, while having a relatively low sample consumption.[109,110,118,119] The method has previously been used to screen possible ligands of CD209.[115]

https://doi.org/10.1021/acs.biomac.5c01510
Biomacromolecules 2025, 26, 8087−8102

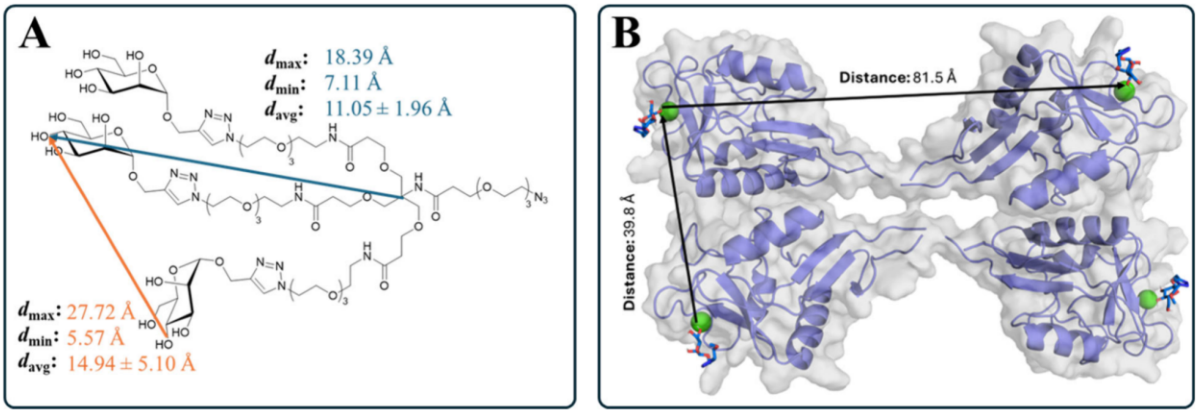

Figure 4. (A) Minimal, maximal, and average distances spanned by two Man epitopes measured between hydroxy groups at C-4 (orange line), as well as minimal, maximal, and average distances of one epitope from the focal point of the glycodendron measured between central carbon and hydroxy groups at C-4 (blue line) obtained from a set of conformers (n = 1000) of TS $(Man)_3N_3$. (B) Model of tetrameric CD209 using CD209 monomers (PDB: 1SL4)[112] aligned on tetrameric DC-SIGNR (PDB: 1XAR, C_α RMSD: 0.41 Å).[104]

In this study, NanoDSF was used to investigate the binding affinity of unconjugated monovalent TSs $ManN_3$ and Man_3N_3, as well as the trivalent TSs $(Man)_3N_3$ and $(Man_3)_3N_3$ for isolated CRDs of CD206 and CD209. Utilization of isolated CRDs instead of the complete tetrameric and octameric receptors allowed an investigation of the affinity without the potential occurrence of avidity effects taking place on the receptor side. For the interaction of $ManN_3$ and $(Man_3)_3N_3$ with the CRD of CD209, only a lower affinity estimate could be obtained, as the tested concentrations of TSs did not achieve sufficient saturation to determine a definitive EC_{50} value. The observed binding affinities to the isolated CRDs were in the low millimolar range, with all ligands showing stabilizing effects. This confirms that the presence of linkers does not prevent interactions between the mannose epitopes and the CRD. For the monovalent TSs, CD206 showed a slight preference for the Man over the Man_3 epitope (1.3 mM vs 6.9 mM; Figure 3), with the affinity of the TS $ManN_3$ being in accordance with K_i values measured via binding competition and NMR assays.[31,113] Notably, the K_D value of the TS Man_3N_3 is slightly higher than what was determined in a solid phase competition assay for a similar structure (K_i = 0.3 mM).[31,113] The difference might originate from differences in the methods. In the solid-phase assay, the biotinylated CRDs were immobilized on streptavidin-coated plates in a defined orientation, likely enhancing the effective presentation of the binding site.[113] In contrast, NanoDSF measurements were conducted with isolated, solubilized monomeric CRDs without surface- or orientation-related effects. Additionally, steric effects and interactions arising from the linker moiety may also impact binding affinity.[115]

For binding to CD209, the opposite trend compared to CD206 could be observed, favoring Man_3N_3 over $ManN_3$ (>36.3 mM vs 7.2 mM), which is consistent with previous publications.[114,117] The preference of CD209 for Man_3N_3 might result from the additional interactions formed by the α-(1→6)-connected mannose unit in Man_3 observed in the docking studies (Figure 2). The multivalent presentation of carbohydrate residues did not lead to a large increase in the affinity. For CD206, the affinities of the trivalent TSs were in the same range as for the monovalent TSs, with $(Man)_3$ having slightly lower affinity than $(Man_3)_3$ (6.8 mM vs 3.1 mM, Figure 3). For CD209, there was a slight trend indicating an increase in affinity of the trivalent $(Man)_3$-TS compared to the monovalent Man-TS (10.3 mM vs >36.3 mM, Figure 3). However, for the Man_3 epitope, the trivalent $(Man_3)_3$-TS exhibited reduced affinity compared to the monovalent Man_3-TS (>26.6 mM vs 7.2 mM, Figure 3). Li et al. reported comparable, monovalent Man and Man_3-TSs involving a triazole moiety used for an SPR assay with tetrameric extracellular domains (ECDs) of CD209 immobilized and all four CRDs oriented toward the solvent, thus mimicking the natural presentation on cell surfaces.[117] The affinities determined for the monovalent TSs were in a similar range to those measured by NanoDSF (Man too weak to detect and Man_3 with IC_{50} = 1.5 mM). However, when the TSs were presented in a trivalent manner, an increase in binding affinity was observed (e.g.: 1.5 mM monovalent vs 2.4 μM trivalent for trimannose),[117] which was not the case in the NanoDSF experiments. Overall, these results suggest that the multivalent presentation of the receptors is crucial to benefit from avidity effects that cannot result from the multivalent ligand presentation alone (Figure 1C). Additionally, in solution, steric hindrance between individual CRDs may limit their simultaneous engagement with a multivalent ligand. The binding interaction between a CRD and a carbohydrate epitope could reduce the accessibility of the remaining epitopes for binding to additional CRDs, also constricted by an increased entropy penalty in comparison to immobilized or preorganized tetrameric CRDs. Intramolecular interactions between the carbohydrate moieties could further interfere with receptor recognition or present key epitopes in suboptimal orientations. In summary, all tested TSs demonstrated measurable binding to the isolated CRDs, confirming that overall, the mannose epitopes remained accessible and functional despite linker modifications and multivalent presentation.

3.3. Prediction of Distances of Mannose Epitopes of a Trivalent TS. As initial prediction for the avidity effects expected of the trivalent TSs (Figure 1C) interacting with the tetrameric CD209 receptor, a set of conformers (n = 1000) of the TS $(Man)_3N_3$ was generated using Omega.[120,121] This set of conformers allowed measurement of the possible distances spanned by two of the involved mannose epitopes (measured

https://doi.org/10.1021/acs.biomac.5c01510
Biomacromolecules 2025, 26, 8087−8102

between hydroxy groups at C-4) as well as minimal and maximal distance of one epitope from the focal point of the glycodendron (measured between central carbon and hydroxy groups at C-4) within the set of conformers (Figure 4, overall distribution shown in Figure S8 in the Supporting Information). Calculation of average distances, for all epitopes, enabled a comparison with the average distance between two Ca^{2+}-ions within the two closest CRDs of the CD209 homotetramer. For chelation effects to originate from the trivalent TS, the distance of about 40 Å needs to be spanned by the glycodendron to enable interaction of two mannose epitopes at two CRDs at the same time, based on a model of the CD209 tetramer (Figure 4B), which is in line with SAXS and MD studies.[98] With the conformers of the TS $(Man)_3N_3$ spanning shorter distances on average (Figure 4A), the glycodendrons should not be capable of engaging in chelating effects. The occurrence of clustering effects involving multiple CD209 homotetramers originating from trivalent TS is highly unlikely. In line with this, NanoDSF, with isolated, monomeric CRDs did not reveal a pronounced affinity gain for trivalent ligands (Figure 3). While this experiment cannot provide a direct test of chelation, because only single-site binding events per CRD are monitored, the NanoDSF data do not contradict the modeling prediction. Therefore, potential increases in binding strengths in a biological setting with correctly immobilized full receptors are most likely a result of increased local concentration of mannose epitopes at one CRD via statistical rebinding (Figure 1C).[87] Avidity effects originating from NCs cannot be predicted within this simplified model and could possibly involve clustering or chelation effect (Figure 1C). Within a biological setting, cellular uptake of NCs could benefit from avidity effects originating from the TSs boosting the effects resulting from the NCs themselves.[98]

3.4. Targeting Capability of TS-Decorated NCs *In Vitro*. To investigate the influence of the designed TSs in a more application-focused setting, we proceeded with *in vitro* experiments using receptors organized in their natural form. For this purpose, we synthesized different HSA-based NCs decorated with all tested TSs (section 4.2 in the Supporting Information) either within the low-valency regime carrying one to three mono- and trivalent TSs (TS I–III), six and nine monovalent TSs (TS VI, TS IX) per NC or within the saturated valency regime saturated with the maximum possible number of TSs per NC (38–45, TS_{sat}). The resulting systems thus contain comparable amounts of Man and Man_3 epitopes per NC, either monovalent or clustered within the glycodendrons, statistically distributed on the surface. The low degrees of modification are supposed to allow a systematic study of potential contributions of avidity effects of the trivalent TSs to receptor interaction and cellular uptake, which would be otherwise superimposed by avidity effects originating from NCs with high valency. Untreated cells (UT) or cells treated with the TLR7/8 agonist R848 as well as cells treated with control conjugates, which are Cy5-labeled only (C I), DBCO-modified (13 groups, C II) or DBCO-modified and capped via SPAAC with triethylene glycol residues (C III), were used as controls for comparison. An *in vitro* study comprising overnight incubation of Granulocyte macrophage colony-stimulating factor (GM-CSF) BMDCs together with the Cy5-labeled TS-HSA conjugates and following FACS analysis was conducted (Figure 5 and Figure 6). Generally, cellular uptake of TS-HSA conjugates resulted from the attachment of TSs, with the untargeted HSA-derived NCs

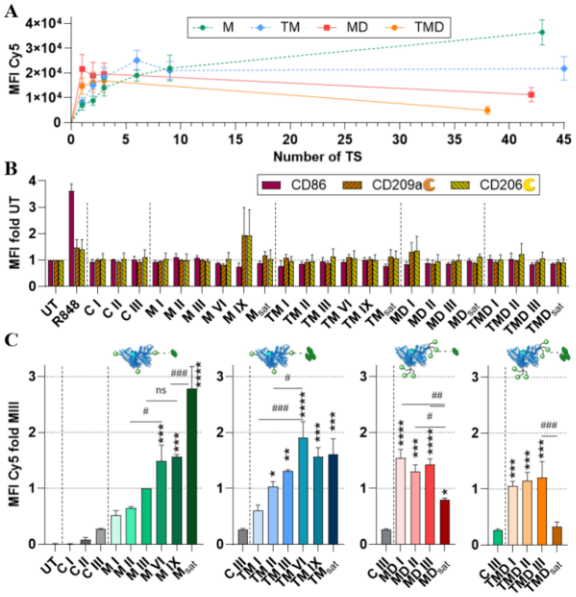

Figure 5. FACS analysis of cellular uptake in GM-CSF BMDCs after incubation overnight with different HSA conjugates (50 nM). (A) Linear plot of the cellular TS-HSA conjugate uptake versus the number of ligands attached. (B) Receptor expression of targeted CLRs (CD206, CD209) and activation marker CD86 upon treatment. (C) Normalized cellular TS-HSA conjugate uptake comparing the NC valency and surface density within each TS type. Data represented as mean ± SEM, n = 3; statistical differences are indicated between conjugates #, and vs control conjugate C III* (one-way ANOVA, Tukey test). *,# $p < 0.05$, **,# $p < 0.01$, ***,# $p < 0.001$, ****,# $p < 0.0001$. UT = Untreated control.

providing only limited unspecific uptake, as seen from controls C I, C II, and C III (Figure 5C). Cellular uptake of the TS-HSA conjugates does not induce changes in expression levels of the CLRs CD206 and CD209, as well as of the activation marker CD86 (Figure 5B), ensuring consistent receptor availability upon treatment and supporting NCs potential immunocompatibility. Observed effects on uptake levels thus are assumed not to be impacted by receptor availability. Also, an influence of slow receptor recycling, which affects their availability, is unlikely for CD206 and CD209 due to the reported rapid recycling kinetics and the long incubation time overnight.[122,123] Additionally, receptor depletion, which is most relevant for nano rods and large NCs (>60 nm), is supposed to be neglectable as well due to the size (~7 nm) and globular shape of the HSA-NCs.[76,124−126] In the following, the cellular uptake as a measure of targeting capability and thus indirectly also binding strength of the four groups of TS-HSA conjugates (M, TM, MD, TMD, Figure 5C) is analyzed and evaluated regarding their general uptake trend and the influence of (i) TS surface density and NC valency, (ii) the epitope type, and (iii) epitope clustering. The general uptake trends of NCs in BMDCs functionalized with increasing numbers of statistically attached TSs are visualized with a linear plot of the cellular uptake against the number of TSs per NC for all conjugates (Figure 5A) and by plots grouping respective conjugates to enable comparison of NC valency and surface density within each TS type (Figure 5C). For Man-decorated NCs, the addition of statistically distributed TS

https://doi.org/10.1021/acs.biomac.5c01510
Biomacromolecules 2025, 26, 8087−8102

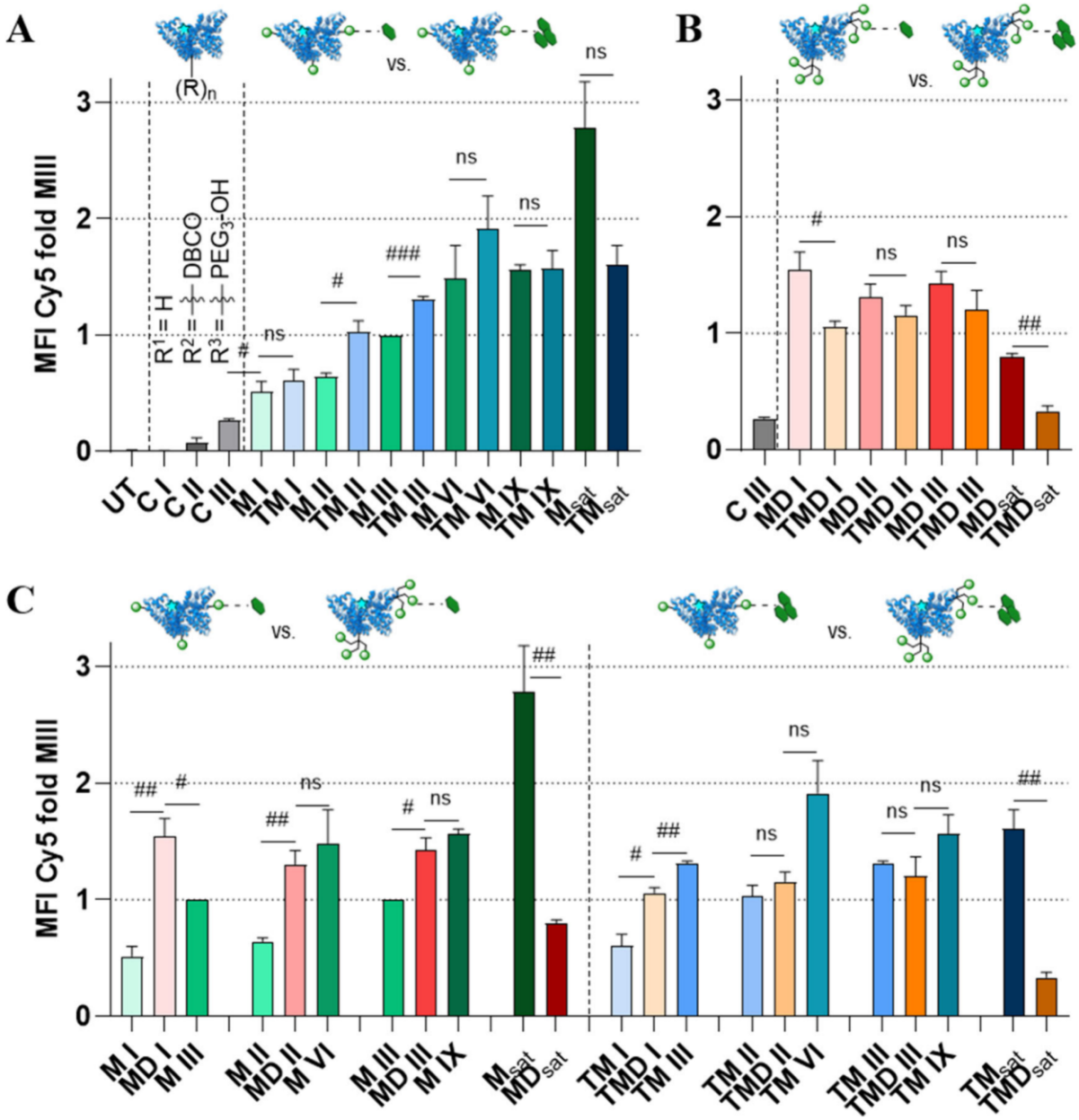

Figure 6. FACS analysis of cellular uptake in GM-CSF BMDCs after incubation overnight with different HSA conjugates (50 nM). Normalized cellular TS-HSA conjugate uptake was calculated by comparing epitope type in (A) M/TM conjugates and (B MD/TMD conjugates and (C) epitope clustering. Data are presented as mean ± SEM, $n = 3$; statistical differences are indicated between conjugates # (*t* test). # $p < 0.05$, # $p < 0.01$, # $p < 0.001$, # $p < 0.0001$. UT = Untreated control.

increases the surface density and leads to an approximately logarithmic increase in cellular uptake at the beginning of the low-valency regime with a significant benefit from M VI onward compared to control conjugate C III. However, the benefit of each additional Man decreases as the total number increases, and the uptake rate slows down. Although a significant increase continues into the saturated valency regime, it becomes less pronounced relative to the TS number and eventually approaches a plateau. For the herein tested Man-decorated NCs, M_{sat} showed the highest cellular uptake. For Man_3-decorated NCs, increasing surface density is also accompanied by an increase in cellular uptake with a significant benefit for TM II. However, a plateau in cell uptake is already reached at a lower TS number from conjugate TM VI onward with no additional significant increase afterward. The onset of this plateau was suggested to occur around a modification rate of 9 TM groups in similar conjugates in GM-CSF BMDC at the same applied concentration prior to this study.[102] In summary, increased surface density of our monovalent TSs results in increased cellular uptake, with the greatest gain in the

https://doi.org/10.1021/acs.biomac.5c01510
Biomacromolecules 2025, 26, 8087−8102

low valency regime and maximum cellular uptake being achieved from conjugate TM VI onward. The observed situation resembles the trend of "optimum density with plateau" (Figure 1D). For NCs decorated with our trivalent TS $(Man)_3$ and $(Man_3)_3$, there is a significantly enhanced cell uptake compared with unmodified NCs for the conjugates MD I and TMD I, respectively. The further increase in the number of TS in the low-valency regime is not accompanied by any significant changes in cellular uptake. At the transition into the saturated valency regime, both conjugate MD_{sat} and conjugate TMD_{sat} show a significant decrease in cellular uptake; in the case of TMD even to the same level as control conjugate C III. Since no visual precipitation or signs of increased aggregation via DLS (Table S2 and Table S4 in the Supporting Information) could be detected, this strong decrease in cellular uptake could reflect the decline in the trend "optimum density with maximum" (Figure 1D) triggered by effects discussed above, like steric overcrowding or negative cooperativity of TSs, superimposing potential avidity effects by clustering or by the NC itself. However, the precise occurrence of the optimum surface density cannot be determined due to the minimal variation in uptake within the low-valency regime and the possibility that the optimum is already reached with the attachment of a single trivalent TS in the form of the conjugates MD I and TMD I.

The difference in cellular uptake mediated by epitope type (Man vs Man_3) is evident from the direct comparison of the respective conjugates decorated with these NCs, as plotted in Figure 6A. Within the low-valency regime, there is a consistent trend that the structurally more complex Man_3 epitope induces a slightly higher cellular uptake, which is statistically significant in a direct comparison of conjugates M II/TM II and M III/TM III, respectively. This is in accordance with literature reports attributing higher affinity to Man_3[31,51] and with our docking studies (Figure 2). These differences in cellular uptake are attenuated for conjugates M IX/TM IX and the ones with a higher degree of functionalization, with TM conjugates reaching the onset of the observed plateau already within the low-valency regime and at lower MFI levels (Figure 5A and C). This earlier onset of negative effects, like overcrowding, for the TM conjugates could be due to the higher steric demands of the larger epitope. This is also supported by a comparison of the conjugates carrying the different epitope types in their trivalent form (Figure 6B). Conjugates from the TMD group tend to have lower cellular uptake compared with the MD group throughout both regimes of valency, with statistically significant differences between MD I/TMD I and MD_{sat}/TMD_{sat}, respectively. This is presumably due to the higher steric hindrance for the larger Man_3-epitopes when clustered within the glycodendrons, thereby superimposing the inherently higher binding affinity of the Man_3 epitope. The effects of epitope clustering become apparent when conjugates carrying the glycodendron are compared with conjugates carrying the same number of monovalent TS or the same overall number of epitopes presented (Figure 6C). With increasing TS surface density, the ratio of presented epitopes per NC between the groups M vs MD and TM vs TMD remains the same (1:3), but the absolute difference in epitope number increases from 2 to 4 to 6. The conjugate MD I, with one trivalent TS, thus presenting three clustered Man epitopes, shows significantly higher cellular uptake than M I, which has one monovalent TS and thus a single Man epitope. Compared to conjugate M III, which carries three randomly distributed monovalent TSs and thus the same number of epitopes, MD I still achieves higher uptake. This suggests that clustering of epitopes enhances uptake through avidity effects here.

However, while the trivalent Man is superior to the monovalent Man in the subsequent low-valency regime with equivalent TS modification rate (e.g., MD II > M II), this does not apply to conjugates with equivalent epitope count (e.g., MD II vs M VI). And since the conjugates with clustered Man (MD) do not show a significant increase in the cell uptake trend with increasing TS density (Figure 5A), the conjugates with monovalent Man prove to be more effective from a modification rate of two to three onward and especially in the saturated valency regime. For the Man_3 epitope, e.g., when comparing conjugates TM I vs TMD I vs TM III, enhancing cellular uptake comes with epitope count (e.g., TM I vs TMD I), but not with clustering of the epitopes (e.g., TMD I vs TM III) until TM conjugates enter the region of saturated cellular uptake from TM VI onward. In the saturated valency regime, TM_{sat} outperforms TMD_{sat} because of the above-mentioned negative effects, hampering cellular uptake. In summary, when evaluating the targeting capability of the four investigated TSs on our HSA-based NCs in BMDCs, monovalent TSs lead to a general cellular uptake trend "optimum density with plateau", with TM conjugates reaching cellular uptake saturation within the low-valency regime and M conjugates demonstrating the overall highest absolute cellular uptake within the saturated regime. Trivalent TSs on our NCs appear to induce negative effects, which increasingly outweigh the intended avidity benefits of epitope clustering early on and with increasing modification rate. Since this trend appears for both trivalent TSs independent of the type of epitope attached, the design of the dendron backbone may be the cause, potentially a result of excessive flexibility, spatially unfavorable arrangement of epitopes, or a too limited span of dendron arms to enable avidity effects. This results in a general trend of "optimum density with a maximum". Regarding the epitope type, TM conjugates show a higher uptake at the beginning of the low valency regime, but this advantage diminishes with increasing TS count and reverses in the saturated regime.

To test the robustness of the general uptake trends derived for the tested TS-decorated NCs as well as the cell-type selectivity, we performed an additional *in vitro* experiment using a more heterogeneous cell population. We incubated spleen cells derived from murine spleens with TS-conjugates (50 nM) overnight, followed by FACS analysis (Figure 7). In general, the data reveals a higher variability, as expected, and a higher cellular uptake of the control conjugate C III. Among nontargeted splenic immune cells, comprising PMN-, NK-, B-, and T-cells, PMNs exhibit some uptake of TS-conjugates, presumably due to their role as rapid-acting phagocytes in innate immunity. This tendency is slightly more pronounced in M conjugates than in TM/MD/TMD conjugates. However, the absolute cellular uptake among nontargeted splenic immune cells remains low compared to targeted cells. For targeted APCs (DCs and MΦ), the mono- and trivalent TS-conjugates show uptake trends similar to those of BMDCs. It is noteworthy that slight variations occur during the onset of the saturated regime. MD conjugates show a decreased uptake into target cells, whereas M, TM, and TMD conjugates show a similar relative efficiency as in BMDCs.

https://doi.org/10.1021/acs.biomac.5c01510
Biomacromolecules 2025, 26, 8087−8102

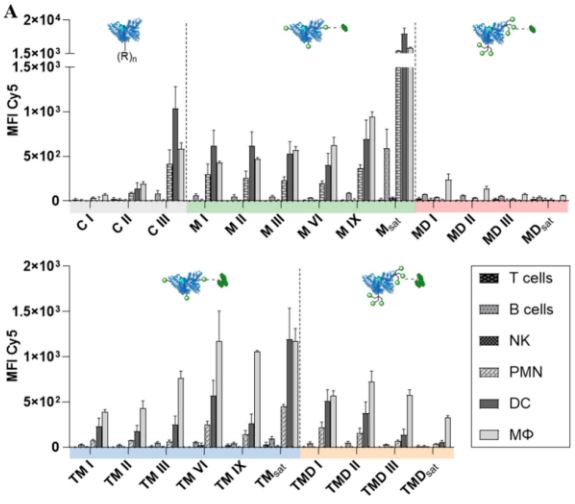

Figure 7. FACS analysis of cellular uptake in spleen cells after overnight incubation with different HSA conjugates (50 nM, (top) M/MD- and (bottom(TM/TMD-HSA conjugates) differentiated into cell types (target cells: macrophages MΦ, DCs; nontarget immune cells: T cells, B cells, NK, and PMN). Data are presented as mean ± SEM, n = 3.

4. CONCLUSION

Within the present study, mono- and trivalent TSs, presenting the Man- and Man_3-epitopes, were synthesized using robust and high yielding procedures. Successful conjugation using SPAAC reactions allowed the preparation of HSA-derived NCs presenting a defined number of randomly dispersed TSs. A NanoDSF investigation provided an approach to measure carbohydrate−lectin interactions in homogeneous solution, revealing binding interactions of unconjugated TSs and isolated CRDs of CD206 and CD209, with affinities in the millimolar range, consistent with earlier reports.[17,55,56] Due to the absence of multivalent CRD presentation, no increase in avidity was observed for the trivalent TSs, stressing the requirement of membrane-like CRD presentation for the investigation of avidity effects.[127] Thus, investigating cellular uptake of HSA conjugates using *in vitro* studies provided a realistic, biological environment to test immunocompatibility and to measure cellular uptake efficiency of the NCs under the influences of epitope type, TS surface density, clustering of epitopes, and overall valency. TS-mediated cellular uptake revealed a strong dependency from respective surface density following two trends as a result of the interplay between additional epitopes favorably contributing to and negative steric or cooperativity effects hindering binding interactions. Growing numbers of monovalent TSs lead to an increase in cellular uptake leveling out into a plateau. Growing numbers of trivalent TSs lead ultimately to a decrease in cellular uptake. Within the design of the studied conjugates, exploitation of the higher intrinsic affinity of the Man_3- over the simpler Man-epitope is beneficial only at low surface densities, providing slight improvements in cellular uptake, with the situation reversed at saturated surface densities, due to mitigation by negative effects, potentially steric overcrowding. Furthermore, trivalent TSs cannot improve cellular uptake of the employed HSA-based NCs by induction of avidity effects due to being hampered by negative effects, especially in the saturated valency regime. To dissect the contributions of either steric overcrowding, negative cooperativity, or other unfavorable effects, which may be the cause of hampered cellular uptake upon using trivalent targeting structures, will require further investigation. Avidity effects originating from a trivalent TS carrying the Man-epitope can only be observed in the low-valency regime. Thus, utilization of these trivalent TSs seems to be beneficial in combination with low valency NCs, which offer only a few connection sites for chemical surface functionalization. In spleen cell populations, all tested TS-HSA conjugates show selectivity for CD206 and CD209 expressing target cells, namely, DCs and macrophages,[19−29] over nontargeted splenic immune cells, with the monovalent Man showing a slightly higher off-target uptake. On a general note, for the design of targeted NCs, the optimization of TSs and surface density always needs to account for the specificities, such as size and flexibility of the NC, impacting steric hindrance and cooperativity effects. Thus, spatially demanding, multivalent TSs seem to be better adapted for use on surfaces of larger NCs, and less demanding, monovalent TSs on the surfaces of smaller NCs.[75] A better understanding of the complex interplay between NC valency and TS surface density *in vitro* may improve the efficacy of targeted delivery approaches by providing means to influence biodistribution and cellular uptake. Thus, this investigation sheds some light on the impact of incremental changes in NC surface modification on cellular uptake and cell selectivity, allowing insights into the design of TSs and NCs.

■ ASSOCIATED CONTENT

Data Availability Statement

Additional information is available from the corresponding authors on request.

Supporting Information

The Supporting Information is available free of charge at https://pubs.acs.org/doi/10.1021/acs.biomac.5c01510.

General conditions and purification methods, analytical methods, synthesis procedures, and analytical data for all steps of saccharide TS preparation and HSA conjugate preparation; Binding modes for monovalent TSs; Recombinant protein expression and purification; NanoDSF melting curves; Histograms for distance distribution of mannose epitopes in a trivalent TS; ^{1}H and ^{13}C NMR spectra of carbohydrate compounds; MALDI spectra of HSA conjugates (PDF)

■ AUTHOR INFORMATION

Corresponding Authors

Till Opatz − *Department of Chemistry, Johannes Gutenberg-University Mainz, 55128 Mainz, Germany;* orcid.org/0000-0002-3266-4050; Email: opatz@uni-mainz.de

Tanja Schirmeister − *Department for Pharmaceutical and Biomedical Sciences, Johannes Gutenberg-University Mainz, 55128 Mainz, Germany*; Email: schirmei@uni-mainz.de

Tanja Weil − *Max Planck Institute for Polymer Research, 55128 Mainz, Germany*; Email: weil@mpip-mainz.mpg.de

Matthias Bros − *Department of Dermatology, University Medical Center of the Johannes Gutenberg-University Mainz, 55131 Mainz, Germany*; Email: mbros@uni-mainz.de

Christian Kersten − *Department for Pharmaceutical and Biomedical Sciences, Johannes Gutenberg-University Mainz,*

https://doi.org/10.1021/acs.biomac.5c01510
Biomacromolecules 2025, 26, 8087−8102

55128 Mainz, Germany; orcid.org/0000-0001-9976-7639; Email: kerstec@uni-mainz.de

Authors

Robert Forster − *Department of Chemistry, Johannes Gutenberg-University Mainz, 55128 Mainz, Germany;* orcid.org/0009-0008-7954-5711

Bellinda Lantzberg − *Max Planck Institute for Polymer Research, 55128 Mainz, Germany;* orcid.org/0009-0006-9323-5897

Annabelle Weldert − *Department for Pharmaceutical and Biomedical Sciences, Johannes Gutenberg-University Mainz, 55128 Mainz, Germany;* orcid.org/0009-0001-5016-0286

Laura Rosenberger − *Department of Dermatology, University Medical Center of the Johannes Gutenberg-University Mainz, 55131 Mainz, Germany*

Yanira Zeyn − *Department of Dermatology, University Medical Center of the Johannes Gutenberg-University Mainz, 55131 Mainz, Germany*

Danuta Kowalczyk − *Department of Chemistry, Johannes Gutenberg-University Mainz, 55128 Mainz, Germany*

Seah Ling Kuan − *Max Planck Institute for Polymer Research, 55128 Mainz, Germany;* orcid.org/0000-0003-3945-4491

Complete contact information is available at: https://pubs.acs.org/10.1021/acs.biomac.5c01510

Author Contributions

[#]These authors contributed equally to this work (R.F., B.L., and A.W.). R.F.: Investigation, Formal analysis, Methodology, Data Curation, Writing - Original Draft, Visualization; B.L.: Investigation, Formal analysis, Methodology, Data Curation, Writing - Original Draft, Visualization; A.W.: Investigation, Formal analysis, Methodology, Data Curation, Writing - Original Draft, Visualization; L.R.: Investigation, Formal analysis; Y.Z.: Investigation, Formal analysis; D.K.: Investigation, Formal analysis; S.L.K.: Supervision, Writing - Review and Editing; C.K.: Supervision, Writing - Review and Editing; M.B.: Resources, Supervision, Funding acquisition; T.W.: Resources, Supervision, Funding acquisition, Writing - Review and Editing; T.S.: Resources, Supervision, Funding acquisition, Writing - Review and Editing; T.O.: Resources, Conceptualization, Project administration, Supervision, Funding acquisition, Writing - Review and Editing. The manuscript was written through contributions of all authors. All authors have given approval to the final version of the manuscript.

Funding

The authors would like to thank the Max Planck Society and the Deutsche Forschungsgemeinschaft (DFG, German Research Foundation) project number 213555243 − SFB 1066 (Q05, B16, B05) for financial support.

Notes

The authors declare the following competing financial interest(s): B.L., Y.Z., R.F., S.L.K., M.B., T.O., and T.W. are coinventors of a pending patent that claims to use mannosylated human serum albumin-based NCs for targeted immunotherapy.

■ ACKNOWLEDGMENTS

The authors would like to thank Dr. Maureen Taylor for providing the plasmid for the CRD4 of CD206, Professor Franck Fieschi for providing the plasmid for the CRD of CD209 and the Group of Professor Heermann for access to the NanoDSF instrument. The authors are grateful to Dr. David Y. W. Ng for valuable discussions regarding analysis of the *in vitro* experiments. We thank the JGU NMR spectroscopy and mass spectrometry department as well as the MPI-P mass spectrometry department for the conducted measurements. OpenAI ChatGPT (GPT-4o) and Grammarly were used for text editing and proofreading purposes. Responsibility for the content rests solely with the authors.

■ ABBREVIATIONS

NC, nanocarrier; TS, targeting structure; CLR, C-type lectin receptor; HSA, human serum albumin; CRD, carbohydrate recognition domain; CD206, cluster of differentiation 206; CD209, cluster of differentiation 209; NanoDSF, Nano differential scanning fluorimetry; APC, antigen-presenting cell; DC, dendritic cell; MΦ, macrophage; MMR-1, macrophage mannose receptor; DC-SIGN, dendritic cell specific ICAM-3 grabbing nonintegrin; MHC, major histocompatibility complex; Man, terminal mannose-monosaccharide; Man_3, α-(1→3)- and α-(1→6)-branched trimannose; SPR, surface plasmon resonance; UT, untreated cells; TLR, toll-like receptor; BMDC, bone marrow-derived dendritic cell; CR, cysteine-rich domain; FNII, fibronectin type II domain; CTLD, C-type lectin domain; ND, neck domain; TM, transmembrane domain; CD, cytoplasmic domain; HPLC, high performance liquid chromatography; SPAAC, strain-promoted azide alkyne cycloaddition; DBCO, dibenzocyclooctyne; CuAAC, copper-catalyzed azide alkyne cycloaddition; TRIS, tris(hydroxymethyl)aminomethane; HRMS, high-resolution mass spectrometry; MALDI-ToF, matrix assisted laser desorption ionization − time of flight mass spectrometry; DLS, dynamic light scattering; C, control conjugate; M, mannose conjugate; TM, trimannose conjugate; MD, mannose glycodendron conjugate; TMD, trimannose glycodendron conjugate; FACS, fluorescence-activated cell sorting; ITC, isothermal titration calorimetry; ECD, tetrameric extracellular domain; NMR, nuclear magnetic resonance; EC_{50}, half maximal effective concentration; Cy5, cyanine 5 dye; GM-CSF, Granulocyte macrophage colony-stimulating factor; MFI, mean fluorescence intensity; PMN-cell, polymorphonuclear neutrophil; NK-cell, natural killer cell

■ REFERENCES

(1) Wang, F.; Ullah, A.; Fan, X.; Xu, Z.; Zong, R.; Wang, X.; Chen, G. Delivery of nanoparticle antigens to antigen-presenting cells: from extracellular specific targeting to intracellular responsive presentation. *J. Controlled Release* **2021**, *333*, 107−128.

(2) Nahar, U. J.; Toth, I.; Skwarczynski, M. Mannose in vaccine delivery. *J. Controlled Release* **2022**, *351*, 284−300.

(3) Suvarna, V.; Sawant, N.; Desai, N. A Review on Recent Advances in Mannose-Functionalized Targeted Nanocarrier Delivery Systems in Cancer and Infective Therapeutics. *Crit. Rev. Ther. Drug Carrier Syst.* **2023**, *40* (2), 43−82.

(4) Zhao, Y.; Guo, Y.; Tang, L. Engineering cancer vaccines using stimuli-responsive biomaterials. *Nano Research* **2018**, *11* (10), 5355−5371.

(5) Feng, X.; Xu, W.; Li, Z.; Song, W.; Ding, J.; Chen, X. Immunomodulatory Nanosystems. *Adv. Sci.* **2019**, *6* (17), No. 1900101.

(6) Kim, C. G.; Kye, Y.-C.; Yun, C.-H. The Role of Nanovaccine in Cross-Presentation of Antigen-Presenting Cells for the Activation of CD8+ T Cell Responses. *Pharmaceutics* **2019**, *11* (11), 612.

(7) Li, S.; Feng, X.; Wang, J.; He, L.; Wang, C.; Ding, J.; Chen, X. Polymer nanoparticles as adjuvants in cancer immunotherapy. *Nano Research* **2018**, *11* (11), 5769−5786.
(8) Wang, J.; Li, Z.; Wang, Z.; Yu, Y.; Li, D.; Li, B.; Ding, J. Nanomaterials for Combinational Radio−Immuno Oncotherapy. *Adv. Funct. Mater.* **2020**, *30* (30), No. 1910676.
(9) Prabahar, K.; Alanazi, Z.; Qushawy, M. Targeted drug delivery system: Advantages, carriers and strategies. *Indian J. Pharm. Educ. Res.* **2021**, *55*, 346−353.
(10) Patil, T. S.; Deshpande, A. S. Mannosylated nanocarriers mediated site-specific drug delivery for the treatment of cancer and other infectious diseases: A state of the art review. *J. Controlled Release* **2020**, *320*, 239−252.
(11) Paurević, M.; Šrajer Gajdošik, M.; Ribić, R. Mannose Ligands for Mannose Receptor Targeting. *Int. J. Mol. Sci.* **2024**, *25* (3), 1370.
(12) Banchereau, J.; Steinman, R. M. Dendritic cells and the control of immunity. *Nature* **1998**, *392*, 245.
(13) Sancho, D.; Reis e Sousa, C. Signaling by Myeloid C-Type Lectin Receptors in Immunity and Homeostasis. *Annu. Rev. Immunol.* **2012**, *30* (1), 491−529.
(14) Tacken, P. J.; de Vries, I. J. M.; Torensma, R.; Figdor, C. G. Dendritic-cell immunotherapy: from ex vivo loading to in vivo targeting. *Nat. Rev. Immunol.* **2007**, *7* (10), 790−802.
(15) Lang, R.; Schoenen, H.; Desel, C. Targeting Syk-Card9-activating C-type lectin receptors by vaccine adjuvants: Findings, implications and open questions. *Immunobiology* **2011**, *216* (11), 1184−1191.
(16) Tang, C.-K.; Sheng, K.-C.; Apostolopoulos, V.; Pietersz, G. A Protein/peptide and DNA vaccine delivery by targeting C-type lectin receptors. *Expert Rev. Vaccines* **2008**, *7* (7), 1005−1018.
(17) Lepenies, B.; Lee, J.; Sonkaria, S. Targeting C-type lectin receptors with multivalent carbohydrate ligands. *Adv. Drug Delivery Rev.* **2013**, *65* (9), 1271−1281.
(18) Rosenblum, D.; Joshi, N.; Tao, W.; Karp, J. M.; Peer, D. Progress and challenges towards targeted delivery of cancer therapeutics. *Nat. Commun.* **2018**, *9* (1), 1410.
(19) Apostolopoulos, V.; Thalhammer, T.; Tzakos, A. G.; Stojanovska, L. Targeting Antigens to Dendritic Cell Receptors for Vaccine Development. *J. Drug Delivery* **2013**, *2013*, No. 1.
(20) Apostolopoulos, V.; Mckenzie, I. f. c. Role of the Mannose Receptor in the Immune Response. *Curr. Mol. Med.* **2001**, *1* (4), 469−474.
(21) East, L.; Isacke, C. M. The mannose receptor family. *Biochim. Biophys. Acta - Gen. Subj.* **2002**, *1572* (2), 364−386.
(22) Reddy, S. T.; Swartz, M. A.; Hubbell, J. A. Targeting dendritic cells with biomaterials: developing the next generation of vaccines. *Trends Immunol.* **2006**, *27* (12), 573−579.
(23) Wilson, D. S.; Hirosue, S.; Raczy, M. M.; Bonilla-Ramirez, L.; Jeanbart, L.; Wang, R.; Kwissa, M.; Franetich, J.-F.; Broggi, M. A. S.; Diaceri, G.; Quaglia-Thermes, X.; Mazier, D.; Swartz, M. A.; Hubbell, J. A. Antigens reversibly conjugated to a polymeric glyco-adjuvant induce protective humoral and cellular immunity. *Nat. Mater.* **2019**, *18* (2), 175−185.
(24) Wang, F.; Xiao, W.; Elbahnasawy, M. A.; Bao, X.; Zheng, Q.; Gong, L.; Zhou, Y.; Yang, S.; Fang, A.; Farag, M. M. S.; Wu, J.; Song, X. Optimization of the Linker Length of Mannose-Cholesterol Conjugates for Enhanced mRNA Delivery to Dendritic Cells by Liposomes. *Front. Pharmacol.* **2018**, *9*, na.
(25) van Kooyk, Y. C-type lectins on dendritic cells: key modulators for the induction of immune responses. *Biochem. Soc. Trans.* **2008**, *36* (6), 1478−1481.
(26) McKenzie, E. J.; Taylor, P. R.; Stillion, R. J.; Lucas, A. D.; Harris, J.; Gordon, S.; Martinez-Pomares, L. Mannose Receptor Expression and Function Define a New Population of Murine Dendritic Cells1. *J. Immunol.* **2007**, *178* (8), 4975−4983.
(27) Engering, A.; Geijtenbeek, T. B. H.; van Vliet, S. J.; Wijers, M.; van Liempt, E.; Demaurex, N.; Lanzavecchia, A.; Fransen, J.; Figdor, C. G.; Piguet, V.; van Kooyk, Y. The Dendritic Cell-Specific Adhesion Receptor DC-SIGN Internalizes Antigen for Presentation to T Cells1. *J. Immunol.* **2002**, *168* (5), 2118−2126.
(28) Tacken, P. J.; de Vries, I. J. M.; Gijzen, K.; Joosten, B.; Wu, D.; Rother, R. P.; Faas, S. J.; Punt, C. J. A.; Torensma, R.; Adema, G. J.; Figdor, C. G. Effective induction of naive and recall T-cell responses by targeting antigen to human dendritic cells via a humanized anti−DC-SIGN antibody. *Blood* **2005**, *106* (4), 1278−1285.
(29) Geijtenbeek, T. B. H.; Torensma, R.; van Vliet, S. J.; van Duijnhoven, G. C. F.; Adema, G. J.; van Kooyk, Y.; Figdor, C. G. Identification of DC-SIGN, a Novel Dendritic Cell−Specific ICAM-3 Receptor that Supports Primary Immune Responses. *Cell* **2000**, *100* (5), 575−585.
(30) Stahl, P. D.; Ezekowitz, R. A. B. The mannose receptor is a pattern recognition receptor involved in host defense. *Curr. Opin. Immunol.* **1998**, *10* (1), 50−55.
(31) Feinberg, H.; Jégouzo, S. A. F.; Lasanajak, Y.; Smith, D. F.; Drickamer, K.; Weis, W. I.; Taylor, M. E. Structural analysis of carbohydrate binding by the macrophage mannose receptor CD206. *J. Biol. Chem.* **2021**, *296*, No. 100368.
(32) Taylor, M. E.; Bezouska, K.; Drickamer, K. Contribution to ligand binding by multiple carbohydrate-recognition domains in the macrophage mannose receptor. *J. Biol. Chem.* **1992**, *267* (3), 1719−1726.
(33) Taylor, M. E.; Drickamer, K. Structural requirements for high affinity binding of complex ligands by the macrophage mannose receptor. *J. Biol. Chem.* **1993**, *268* (1), 399−404.
(34) Švajger, U.; Anderluh, M.; Jeras, M.; Obermajer, N. C-type lectin DC-SIGN: An adhesion, signalling and antigen-uptake molecule that guides dendritic cells in immunity. *Cell. Signal.* **2010**, *22* (10), 1397−1405.
(35) Mitchell, D. A.; Fadden, A. J.; Drickamer, K. A novel mechanism of carbohydrate recognition by the C-type lectins DC-SIGN and DC-SIGNR: subunit organization and binding to multivalent ligands. *J. Biol. Chem.* **2001**, *276* (31), 28939−28945.
(36) Tabarani, G.; Thépaut, M.; Stroebel, D.; Ebel, C.; Vivès, C.; Vachette, P.; Durand, D.; Fieschi, F. DC-SIGN Neck Domain Is a pH-sensor Controlling Oligomerization: SAXS and Hydrodynamic studies of extracellular domain. *J. Biol. Chem.* **2009**, *284* (32), 21229−21240.
(37) Azad, A. K.; Rajaram, M. V.; Schlesinger, L. S. Exploitation of the macrophage mannose receptor (CD206) in infectious disease diagnostics and therapeutics. *JCMB* **2014**, *1* (1), No. 1000003.
(38) Nguyen, D. G.; Hildreth, J. E. K. Involvement of macrophage mannose receptor in the binding and transmission of HIV by macrophages. *Eur. J. Immunol.* **2003**, *33* (2), 483−493.
(39) Monteiro, J. T.; Lepenies, B. Myeloid C-Type Lectin Receptors in Viral Recognition and Antiviral Immunity. *Viruses* **2017**, *9* (3), 59.
(40) Martinez-Pomares, L.; Linehan, S. A.; Taylor, P. R.; Gordon, S. Binding Properties of the Mannose Receptor. *Immunobiology* **2001**, *204* (5), 527−535.
(41) Martinez-Pomares, L. The mannose receptor. *J. Leukocyte Biol.* **2012**, *92* (6), 1177−1186.
(42) Osorio, F.; Reis e Sousa, C. Myeloid C-type Lectin Receptors in Pathogen Recognition and Host Defense. *Immunity* **2011**, *34* (5), 651−664.
(43) van Kooyk, Y.; Unger, W. W. J.; Fehres, C. M.; Kalay, H.; García-Vallejo, J. J. Glycan-based DC-SIGN targeting vaccines to enhance antigen cross-presentation. *Mol. Immunol.* **2013**, *55* (2), 143−145.
(44) Valverde, P.; Martínez, J. D.; Cañada, F. J.; Arda, A.; Jiménez-Barbero, J. Molecular recognition in C-type lectins: the cases of DC-SIGN, Langerin, MGL, and L-sectin. *ChemBioChem.* **2020**, *21* (21), 2999−3025.
(45) Chatterjee, D.; Khoo, K. H. The surface glycopeptidolipids of mycobacteria: structures and biological properties. *Cell. Mol. Life Sci.* **2001**, *58* (14), 2018−2042.
(46) Shibata, N.; Ikuta, K.; Imai, T.; Satoh, Y.; Satoh, R.; Suzuki, A.; Kojima, C.; Kobayashi, H.; Hisamichi, K.; Suzuki, S. Existence of Branched Side Chains in the Cell Wall Mannan of Pathogenic Yeast,

https://doi.org/10.1021/acs.biomac.5c01510
Biomacromolecules 2025, 26, 8087−8102

Candida albicans: Structure-antigenicity relationship between the cell wall mannans of candida albicans and candida parapsilosis. *J. Biol. Chem.* **1995**, *270* (3), 1113−1122.
(47) Feinberg, H.; Mitchell, D. A.; Drickamer, K.; Weis, W. I. Structural Basis for Selective Recognition of Oligosaccharides by DC-SIGN and DC-SIGNR. *Science* **2001**, *294* (5549), 2163−2166.
(48) Adams, E. W.; Ratner, D. M.; Bokesch, H. R.; McMahon, J. B.; O'Keefe, B. R.; Seeberger, P. H. Oligosaccharide and Glycoprotein Microarrays as Tools in HIV Glycobiology: Glycan-Dependent gp120/Protein Interactions. *Chem. Biol.* **2004**, *11* (6), 875−881.
(49) Reina, J. J.; Díaz, I.; Nieto, P. M.; Campillo, N. E.; Páez, J. A.; Tabarani, G.; Fieschi, F.; Rojo, J. Docking, synthesis, and NMR studies of mannosyl trisaccharide ligands for DC-SIGN lectin. *Org. Biomol. Chem.* **2008**, *6* (15), 2743−2754.
(50) van Liempt, E.; Bank, C. M. C.; Mehta, P.; Garci′a-Vallejo, J. J.; Kawar, Z. S.; Geyer, R.; Alvarez, R. A.; Cummings, R. D.; Kooyk, Y. v.; van Die, I. Specificity of DC-SIGN for mannose- and fucose-containing glycans. *FEBS Lett.* **2006**, *580* (26), 6123−6131.
(51) Holla, A.; Skerra, A. Comparative analysis reveals selective recognition of glycans by the dendritic cell receptors DC-SIGN and Langerin. *Protein Eng., Des. Sel.* **2011**, *24* (9), 659−669.
(52) van Montfort, T.; Eggink, D.; Boot, M.; Tuen, M.; Hioe, C. E.; Berkhout, B.; Sanders, R. W. HIV-1 N-glycan composition governs a balance between dendritic cell-mediated viral transmission and antigen presentation. *J. Immunol.* **2011**, *187* (9), 4676−4685.
(53) Lee, R. T.; Lee, Y. C. Affinity enhancement by multivalent lectin−carbohydrate interaction. *Glycoconjugate J.* **2000**, *17* (7), 543−551.
(54) Monsigny, M.; Mayer, R.; Roche, A.-C. Sugar-lectin interactions: sugar clusters, lectin multivalency and avidity. *Carbohydr. Lett.* **2000**, *4*, 35−52.
(55) Lepenies, B.; Seeberger, P. H. The promise of glycomics, glycan arrays and carbohydrate-based vaccines. *Immunopharmacol. Immunotoxicol.* **2010**, *32* (2), 196−207.
(56) Lepenies, B.; Yin, J.; Seeberger, P. H. Applications of synthetic carbohydrates to chemical biology. *Curr. Opin. Chem. Biol.* **2010**, *14* (3), 404−411.
(57) Drickamer, K. Multiplicity of lectin-carbohydrate interactions. *Nat. Struct. Mol. Biol.* **1995**, *2* (6), 437−439.
(58) Brewer, C. F. Multivalent lectin-carbohydrate cross-linking interactions. *Chemtracts-Biochem. Mol. Biol.* **1996**, *6*, 165−179.
(59) Lundquist, J. J.; Toone, E. J. The Cluster Glycoside Effect. *Chem. Rev.* **2002**, *102* (2), 555−578.
(60) Sharon, N. Lectins: past, present and future. *Biochem. Soc. Trans.* **2008**, *36* (6), 1457−1460.
(61) Sharon, N.; Lis, H. *Lectins*; Springer: Dordrecht, 2003. DOI: 10.1007/978-1-4020-6953-6.
(62) Sharon, N.; Lis, H. History of lectins: from hemagglutinins to biological recognition molecules. *Glycobiol.* **2004**, *14* (11), 53R−62R.
(63) Porkolab, V.; Pifferi, C.; Sutkeviciute, I.; Ordanini, S.; Taouai, M.; Thépaut, M.; Vivès, C.; Benazza, M.; Bernardi, A.; Renaudet, O.; Fieschi, F. Development of C-type lectin-oriented surfaces for high avidity glycoconjugates: towards mimicking multivalent interactions on the cell surface. *Org. Biomol. Chem.* **2020**, *18* (25), 4763−4772.
(64) Kitov, P. I.; Bundle, D. R. On the Nature of the Multivalency Effect: A Thermodynamic Model. *J. Am. Chem. Soc.* **2003**, *125* (52), 16271−16284.
(65) Müller, C.; Despras, G.; Lindhorst, T. K. Organizing multivalency in carbohydrate recognition. *Chem. Soc. Rev.* **2016**, *45* (11), 3275−3302.
(66) Fasting, C.; Schalley, C. A.; Weber, M.; Seitz, O.; Hecht, S.; Koksch, B.; Dernedde, J.; Graf, C.; Knapp, E.-W.; Haag, R. Multivalency as a Chemical Organization and Action Principle. *Angew. Chem., Int. Ed.* **2012**, *51* (42), 10472−10498.
(67) Jayaraman, N. Multivalent ligand presentation as a central concept to study intricate carbohydrate−protein interactions. *Chem. Soc. Rev.* **2009**, *38* (12), 3463−3483.
(68) Kiessling, L. L.; Gestwicki, J. E.; Strong, L. E. Synthetic multivalent ligands in the exploration of cell-surface interactions. *Curr. Opin. Chem. Biol.* **2000**, *4* (6), 696−703.
(69) Kiessling, L. L.; Gestwicki, J. E.; Strong, L. E. Synthetic Multivalent Ligands as Probes of Signal Transduction. *Angew. Chem., Int. Ed.* **2006**, *45* (15), 2348−2368.
(70) Vorup-Jensen, T. On the roles of polyvalent binding in immune recognition: Perspectives in the nanoscience of immunology and the immune response to nanomedicines. *Adv. Drug Delivery Rev.* **2012**, *64* (15), 1759−1781.
(71) Bellato, F.; Feola, S.; Dalla Verde, G.; Bellio, G.; Pirazzini, M.; Salmaso, S.; Caliceti, P.; Cerullo, V.; Mastrotto, F. Mannosylated Polycations Target CD206+ Antigen-Presenting Cells and Mediate T-Cell-Specific Activation in Cancer Vaccination. *Biomacromolecules* **2022**, *23* (12), 5148−5163.
(72) Chae, J.; Kang, S. H.; Kim, J.; Choi, Y.; Kang, S. H.; Choi, J. Targeted and efficient delivery of rifampicin to macrophages involved in non-tuberculous mycobacterial infection via mannosylated solid lipid nanoparticles. *Nanoscale Adv.* **2023**, *5* (17), 4536−4545.
(73) Heck, A. G.; Schwiertz, D.; Lantzberg, B.; Nguyen, H.-C.; Forster, R.; Scherger, M.; Opatz, T.; Van Ginderachter, J. A.; Nuhn, L. Introducing Targeting Units or pH-Releasable Immunodrugs into Core-Clickable Nanogels. *Eur. Polym. J.* **2024**, *214*, No. 113150.
(74) Kvakova, K.; Ondra, M.; Schimer, J.; Petrik, M.; Novy, Z.; Raabova, H.; Hajduch, M.; Cigler, P. Visualization of Sentinel Lymph Nodes with Mannosylated Fluorescent Nanodiamonds. *Adv. Funct. Mater.* **2022**, *32* (23), No. 2109960.
(75) Krumb, M.; Frey, M.-L.; Langhanki, J.; Forster, R.; Kowalczyk, D.; Mailänder, V.; Landfester, K.; Opatz, T. Multivalency Beats Complexity: A Study on the Cell Uptake of Carbohydrate Functionalized Nanocarriers to Dendritic Cells. *Cells* **2020**, *9* (9), 2087.
(76) Alkilany, A. M.; Zhu, L.; Weller, H.; Mews, A.; Parak, W. J.; Barz, M.; Feliu, N. Ligand density on nanoparticles: A parameter with critical impact on nanomedicine. *Adv. Drug Delivery Rev.* **2019**, *143*, 22−36.
(77) Gao, J.; Chen, P.; Singh, Y.; Zhang, X.; Szekely, Z.; Stein, S.; Sinko, P. J. Novel Monodisperse PEGtide Dendrons: Design, Fabrication, and Evaluation of Mannose Receptor-Mediated Macrophage Targeting. *Bioconjugate Chem.* **2013**, *24* (8), 1332−1344.
(78) Herrera-González, I.; González-Cuesta, M.; Thépaut, M.; Laigre, E.; Goyard, D.; Rojo, J.; García Fernández, J. M.; Fieschi, F.; Renaudet, O.; Nieto, P. M.; Ortiz Mellet, C. High-Mannose Oligosaccharide Hemimimetics that Recapitulate the Conformation and Binding Mode to Concanavalin A, DC-SIGN and Langerin. *Chem.—Eur. J.* **2024**, *30* (2), No. e202303041.
(79) Herrera-González, I.; Thépaut, M.; Sánchez-Fernández, E. M.; di Maio, A.; Vivès, C.; Rojo, J.; García Fernández, J. M.; Fieschi, F.; Nieto, P. M.; Ortiz Mellet, C. Mannobioside biomimetics that trigger DC-SIGN binding selectivity. *Chem. Commun.* **2022**, *58* (86), 12086−12089.
(80) Sedaghat, B.; Stephenson, R. J.; Giddam, A. K.; Eskandari, S.; Apte, S. H.; Pattinson, D. J.; Doolan, D. L.; Toth, I. Synthesis of Mannosylated Lipopeptides with Receptor Targeting Properties. *Bioconjugate Chem.* **2016**, *27* (3), 533−548.
(81) Zimmer, O.; Goepferich, A. On the uncertainty of the correlation between nanoparticle avidity and biodistribution. *Eur. J. Pharm. Biopharm.* **2024**, *198*, No. 114240.
(82) Tjandra, K. C.; Thordarson, P. Multivalency in Drug Delivery−When Is It Too Much of a Good Thing? *Bioconjugate Chem.* **2019**, *30* (3), 503−514.
(83) Erlendsson, S.; Teilum, K. Binding Revisited—Avidity in Cellular Function and Signaling. *Front. Mol. Biosci.* **2021**, *7*, No. 615565.
(84) Krishnamurthy, V. M.; Estroff, L. A.; Whitesides, G. M. Multivalency in Ligand Design. *Fragment-Based Approaches in Drug Discovery*, 2006; pp 11−53.
(85) Dam, T. K.; Oscarson, S.; Roy, R.; Das, S. K.; Pagé, D.; Macaluso, F.; Brewer, C. F. Thermodynamic, Kinetic, and Electron

https://doi.org/10.1021/acs.biomac.5c01510
Biomacromolecules 2025, 26, 8087−8102

Microscopy Studies of Concanavalin A and Dioclea grandiflora Lectin Cross-linked with Synthetic Divalent Carbohydrates. *J. Biol. Chem.* **2005**, *280* (10), 8640−8646.
(86) Maslanka Figueroa, S.; Fleischmann, D.; Beck, S.; Goepferich, A. The Effect of Ligand Mobility on the Cellular Interaction of Multivalent Nanoparticles. *Macromol. Biosci.* **2020**, *20* (4), No. 1900427.
(87) Ordanini, S.; Varga, N.; Porkolab, V.; Thépaut, M.; Belvisi, L.; Bertaglia, A.; Palmioli, A.; Berzi, A.; Trabattoni, D.; Clerici, M.; Fieschi, F.; Bernardi, A. Designing nanomolar antagonists of DC-SIGN-mediated HIV infection: ligand presentation using molecular rods. *Chem. Commun.* **2015**, *51* (18), 3816−3819.
(88) Reuter, K. G.; Perry, J. L.; Kim, D.; Luft, J. C.; Liu, R.; DeSimone, J. M. Targeted PRINT Hydrogels: The Role of Nanoparticle Size and Ligand Density on Cell Association, Biodistribution, and Tumor Accumulation. *Nano Lett.* **2015**, *15* (10), 6371−6378.
(89) Elias, D. R.; Poloukhtine, A.; Popik, V.; Tsourkas, A. Effect of ligand density, receptor density, and nanoparticle size on cell targeting. *Nanomedicine: Nanotechnology, Biology and Medicine* **2013**, *9* (2), 194−201.
(90) Tang, P. S.; Sathiamoorthy, S.; Lustig, L. C.; Ponzielli, R.; Inamoto, I.; Penn, L. Z.; Shin, J. A.; Chan, W. C. W. The Role of Ligand Density and Size in Mediating Quantum Dot Nuclear Transport. *Small* **2014**, *10* (20), 4182−4192.
(91) Akhter, A.; Hayashi, Y.; Sakurai, Y.; Ohga, N.; Hida, K.; Harashima, H. Ligand density at the surface of a nanoparticle and different uptake mechanism: Two important factors for successful siRNA delivery to liver endothelial cells. *Int. J. Pharm.* **2014**, *475* (1), 227−237.
(92) Dalal, C.; Saha, A.; Jana, N. R. Nanoparticle Multivalency Directed Shifting of Cellular Uptake Mechanism. *J. Phys. Chem. C* **2016**, *120* (12), 6778−6786.
(93) Song, X.; Li, R.; Deng, H.; Li, Y.; Cui, Y.; Zhang, H.; Dai, W.; He, B.; Zheng, Y.; Wang, X.; Zhang, Q. Receptor mediated transcytosis in biological barrier: The influence of receptor character and their ligand density on the transmembrane pathway of active-targeting nanocarriers. *Biomaterials* **2018**, *180*, 78−90.
(94) Wang, J.; Tian, S.; Petros, R. A.; Napier, M. E.; DeSimone, J. M. The Complex Role of Multivalency in Nanoparticles Targeting the Transferrin Receptor for Cancer Therapies. *J. Am. Chem. Soc.* **2010**, *132* (32), 11306−11313.
(95) Hunter, C. A.; Anderson, H. L. What is Cooperativity? *Angew. Chem., Int. Ed.* **2009**, *48* (41), 7488−7499.
(96) Chung, H.; Park, J. Y.; Kim, K.; Yoo, R. J.; Suh, M.; Gu, G. J.; Kim, J. S.; Choi, T. H.; Byun, J. W.; Ju, Y. W.; Han, W.; Ryu, H. S.; Chung, G.; Hwang, D. W.; Kim, Y.; Kang, H.-R.; Na, Y. R.; Choi, H.; Im, H.-J.; Lee, Y.-S.; Seok, S. H. Circulation Time-Optimized Albumin Nanoplatform for Quantitative Visualization of Lung Metastasis via Targeting of Macrophages. *ACS Nano* **2022**, *16* (8), 12262−12275.
(97) Silpe, J. E.; Sumit, M.; Thomas, T. P.; Huang, B.; Kotlyar, A.; van Dongen, M. A.; Banaszak Holl, M. M.; Orr, B. G.; Choi, S. K. Avidity Modulation of Folate-Targeted Multivalent Dendrimers for Evaluating Biophysical Models of Cancer Targeting Nanoparticles. *ACS Chem. Biol.* **2013**, *8* (9), 2063−2071.
(98) Porkolab, V.; Lepšík, M.; Ordanini, S.; St John, A.; Le Roy, A.; Thépaut, M.; Paci, E.; Ebel, C.; Bernardi, A.; Fieschi, F. Powerful Avidity with a Limited Valency for Virus-Attachment Blockers on DC-SIGN: Combining Chelation and Statistical Rebinding with Structural Plasticity of the Receptor. *ACS Cent. Sci.* **2023**, *9* (4), 709−718.
(99) Cuellar-Camacho, J. L.; Bhatia, S.; Reiter-Scherer, V.; Lauster, D.; Liese, S.; Rabe, J. P.; Herrmann, A.; Haag, R. Quantification of Multivalent Interactions between Sialic Acid and Influenza A Virus Spike Proteins by Single-Molecule Force Spectroscopy. *J. Am. Chem. Soc.* **2020**, *142* (28), 12181−12192.
(100) Di Iorio, D.; Verheijden, M. L.; van der Vries, E.; Jonkheijm, P.; Huskens, J. Weak Multivalent Binding of Influenza Hemagglutinin Nanoparticles at a Sialoglycan-Functionalized Supported Lipid Bilayer. *ACS Nano* **2019**, *13* (3), 3413−3423.
(101) Jung, H.; Robison, A. D.; Cremer, P. S. Multivalent ligand−receptor binding on supported lipid bilayers. *J. Struct. Biol.* **2009**, *168* (1), 90−94.
(102) Lantzberg, B.; Zeyn, Y.; Forster, R.; Jian, L.; Schauenburg, D.; Hieber, C.; Nuhn, L.; Zhou, T.; Silva, M. J. S. A.; Koynov, K.; Jiang, H.-L.; Kuan, S. L.; Bros, M.; Opatz, T.; Weil, T. Glycogen-inspired trimannosylated serum albumin nanocarriers for targeted delivery of toll-like receptor 7/8 agonists to immune cells and liver. *J. Controlled Release* **2025**, *382*, No. 113705.
(103) Karimi, M.; Bahrami, S.; Ravari, S. B.; Zangabad, P. S.; Mirshekari, H.; Bozorgomid, M.; Shahreza, S.; Sori, M.; Hamblin, M. R. Albumin nanostructures as advanced drug delivery systems. *Expert Opinion on Drug Delivery* **2016**, *13* (11), 1609−1623.
(104) Feinberg, H.; Guo, Y.; Mitchell, D. A.; Drickamer, K.; Weis, W. I. Extended Neck Regions Stabilize Tetramers of the Receptors DC-SIGN and DC-SIGNR. *J. Biol. Chem.* **2005**, *280* (2), 1327−1335.
(105) Khoo, U.-S.; Chan, K. Y. K.; Chan, V. S. F.; Lin, C. L. S. DC-SIGN and L-SIGN: the SIGNs for infection. *J. Mol. Med.* **2008**, *86* (8), 861−874.
(106) Cardona, C. M.; Gawley, R. E. An improved synthesis of a trifurcated newkome-type monomer and orthogonally protected two-generation dendrons. *J. Org. Chem.* **2002**, *67* (4), 1411−1413.
(107) Krabicová, I.; Dolenský, B.; Řezanka, M. Selectivity of 1-O-Propargyl-d-Mannose Preparations. *Molecules* **2022**, *27* (5), 1483.
(108) Ramos-Soriano, J.; de la Fuente, M. C.; de la Cruz, N.; Figueiredo, R. C.; Rojo, J.; Reina, J. J. Straightforward synthesis of Man9, the relevant epitope of the high-mannose oligosaccharide. *Org. Biomol. Chem.* **2017**, *15* (42), 8877−8882.
(109) Niebling, S.; Burastero, O.; Bürgi, J.; Günther, C.; Defelipe, L. A.; Sander, S.; Gattkowski, E.; Anjanappa, R.; Wilmanns, M.; Springer, S.; Tidow, H.; García-Alai, M. FoldAffinity: binding affinities from nDSF experiments. *Sci. Rep.* **2021**, *11* (1), 9572.
(110) Bai, N.; Roder, H.; Dickson, A.; Karanicolas, J. Isothermal Analysis of ThermoFluor Data can readily provide Quantitative Binding Affinities. *Sci. Rep.* **2019**, *9* (1), 2650.
(111) Mesapogu, S.; Jillepalli, C. M.; Arora, D. K. Agarose Gel Electrophoresis and Polyacrylamide Gel Electrophoresis: Methods and Principles. In *Analyzing Microbes: Manual of Molecular Biology Techniques*; Arora, D. K., Das, S., Sukumar, M., Eds.; Springer: Berlin; Heidelberg, 2013; pp 73−91.
(112) Guo, Y.; Feinberg, H.; Conroy, E.; Mitchell, D. A.; Alvarez, R.; Blixt, O.; Taylor, M. E.; Weis, W. I.; Drickamer, K. Structural basis for distinct ligand-binding and targeting properties of the receptors DC-SIGN and DC-SIGNR. *Nat. Struct. Mol. Biol.* **2004**, *11* (7), 591−598.
(113) Hitchen, P. G.; Mullin, N. P.; Taylor, M. E. Orientation of sugars bound to the principal C-type carbohydrate-recognition domain of the macrophage mannose receptor. *Biochem. J.* **1998**, *333* (3), 601−608.
(114) Feinberg, H.; Castelli, R.; Drickamer, K.; Seeberger, P. H.; Weis, W. I. Multiple modes of binding enhance the affinity of DC-SIGN for high mannose N-linked glycans found on viral glycoproteins. *J. Biol. Chem.* **2007**, *282* (6), 4202−4209.
(115) Cramer, J.; Lakkaichi, A.; Aliu, B.; Jakob, R. P.; Klein, S.; Cattaneo, I.; Jiang, X.; Rabbani, S.; Schwardt, O.; Zimmer, G.; Ciancaglini, M.; Abreu Mota, T.; Maier, T.; Ernst, B. Sweet Drugs for Bad Bugs: A Glycomimetic Strategy against the DC-SIGN-Mediated Dissemination of SARS-CoV-2. *J. Am. Chem. Soc.* **2021**, *143* (42), 17465−17478.
(116) Sutkeviciute, I.; Thépaut, M.; Sattin, S.; Berzi, A.; McGeagh, J.; Grudinin, S.; Weiser, J.; Le Roy, A.; Reina, J. J.; Rojo, J.; Clerici, M.; Bernardi, A.; Ebel, C.; Fieschi, F. Unique DC-SIGN Clustering Activity of a Small Glycomimetic: A Lesson for Ligand Design. *ACS Chem. Biol.* **2014**, *9* (6), 1377−1385.
(117) Li, R.-J. E.; Hogervorst, T. P.; Achilli, S.; Bruijns, S. C.; Arnoldus, T.; Vivès, C.; Wong, C. C.; Thépaut, M.; Meeuwenoord, N. J.; van den Elst, H.; Overkleeft, H. S.; van der Marel, G. A.; Filippov, D. V.; van Vliet, S. J.; Fieschi, F.; Codée, J. D. C.; van Kooyk, Y.

https://doi.org/10.1021/acs.biomac.5c01510
Biomacromolecules 2025, 26, 8087−8102

Systematic Dual Targeting of Dendritic Cell C-Type Lectin Receptor DC-SIGN and TLR7 Using a Trifunctional Mannosylated Antigen. *Front. Chem.* **2019**, *7*, 650.
(118) Khan, M. F.; Rahman, M. M.; Xin, Y.; Mustafa, A.; Smith, B. J.; Ottemann, K. M.; Roujeinikova, A. Determination of Protein−Ligand Binding Affinities by Thermal Shift Assay. *ACS Pharamcol. Transl. Sci.* **2024**, *7* (10), 3096−3107.
(119) Niesen, F. H.; Berglund, H.; Vedadi, M. The use of differential scanning fluorimetry to detect ligand interactions that promote protein stability. *Nat. Protoc.* **2007**, *2* (9), 2212−2221.
(120) OMEGA 5.0.0.3: OpenEye, Cadence Molecular Sciences, Santa Fe, NM, http://www.eyesopen.com.
(121) Hawkins, P. C. D.; Skillman, A. G.; Warren, G. L.; Ellingson, B. A.; Stahl, M. T. Conformer Generation with OMEGA: Algorithm and Validation Using High Quality Structures from the Protein Databank and Cambridge Structural Database. *J. Chem. Inf. Model.* **2010**, *50* (4), 572−584.
(122) Schetters, S. T. T.; Kruijssen, L. J. W.; Crommentuijn, M. H. W.; Kalay, H.; Ochando, J.; den Haan, J. M. M.; Garcia-Vallejo, J. J.; van Kooyk, Y. Mouse DC-SIGN/CD209a as Target for Antigen Delivery and Adaptive Immunity. *Front. Immunol.* **2018**, *9*, No. 990.
(123) Mastrotto, F.; Pirazzini, M.; Negro, S.; Salama, A.; Martinez-Pomares, L.; Mantovani, G. Sulfation at Glycopolymer Side Chains Switches Activity at the Macrophage Mannose Receptor (CD206) In Vitro and In Vivo. *J. Am. Chem. Soc.* **2022**, *144* (50), 23134−23147.
(124) Zhang, S.; Gao, H.; Bao, G. Physical Principles of Nanoparticle Cellular Endocytosis. *ACS Nano* **2015**, *9* (9), 8655−8671.
(125) Behzadi, S.; Serpooshan, V.; Tao, W.; Hamaly, M. A.; Alkawareek, M. Y.; Dreaden, E. C.; Brown, D.; Alkilany, A. M.; Farokhzad, O. C.; Mahmoudi, M. Cellular uptake of nanoparticles: journey inside the cell. *Chem. Soc. Rev.* **2017**, *46* (14), 4218−4244.
(126) Hoshyar, N.; Gray, S.; Han, H.; Bao, G. The Effect of Nanoparticle Size on In Vivo Pharmacokinetics and Cellular Interaction. *Nanomedicine* **2016**, *11* (6), 673−692.
(127) Budhadev, D.; Poole, E.; Nehlmeier, I.; Liu, Y.; Hooper, J.; Kalverda, E.; Akshath, U. S.; Hondow, N.; Turnbull, W. B.; Pöhlmann, S.; Guo, Y.; Zhou, D. Glycan-Gold Nanoparticles as Multifunctional Probes for Multivalent Lectin−Carbohydrate Binding: Implications for Blocking Virus Infection and Nanoparticle Assembly. *J. Am. Chem. Soc.* **2020**, *142* (42), 18022−18034.

https://doi.org/10.1021/acs.biomac.5c01510
Biomacromolecules 2025, 26, 8087−8102

Supporting Information

Surface Density of Mono- and Trivalent High-Mannan Derived Targeting Structures with Different Affinity Impacts Cellular Uptake of Human Serum Albumin Derived Nanocarriers

Robert Forster[†,#], Bellinda Lantzberg[‡,#], Annabelle Weldert[§,#], Laura Rosenberger[‖], Yanira Zeyn[‖], Danuta Kowalczyk[†], Seah Ling Kuan[‡], Christian Kersten[§,], Matthias Bros[‖,*], Tanja Weil[‡,*], Tanja Schirmeister[§,*], Till Opatz[†,*]*

[†] Department of Chemistry, Johannes Gutenberg-University Mainz, Duesbergweg 10 – 14, 55128 Mainz, Germany.

[‡] Max Planck Institute for Polymer Research, Ackermannweg 10, 55128 Mainz, Germany.

[§] Department for Pharmaceutical and Biomedical Sciences, Johannes Gutenberg-University Mainz, Staudingerweg 5, 55128 Mainz, Germany.

[‖] Department of Dermatology, University Medical Center of the Johannes Gutenberg-University Mainz, Obere Zahlbacher Straße 63, 55131 Mainz, Germany.

[#] Equal contribution

[*] E-mail: opatz@uni-mainz.de; schirmei@uni-mainz.de; weil@mpip-mainz.mpg.de; mbros@uni-mainz.de; kerstec@uni-mainz.de.

Supporting Information

1 Table of contents

Supporting Information

2 General conditions and purification methods

Chemicals: All chemicals were purchased from ABCR (Karlsruhe, BW, Germany), *Acros Organics* (Geel, Belgium), *Alfa Aesar* (Haverhill, MA, USA), *Arctom Scientific* (Westlake Village, CA, USA), *Carbolution* (St. Ingbert, SL, Germany), *Carl Roth* (Karlsruhe, BW, Germany), *Sigma Aldrich* (St. Louis, MO, USA), *TCI* (Tokyo, Japan), *Thermo Fisher Scientific* (Waltham, MA, USA) or *VWR* (Radnor, PA, USA) and used without further purification. Deuterated solvents for NMR experiments were obtained from *Deutero* (Kastellaun, RP, Germany) for $CDCl_3$, CD_3OD and D_2O. Deuterated chloroform was stored over molecular sieves and powdered, basic aluminum oxide (Brockmann activity I, pore size 58 Å) supplied from *Sigma Aldrich* (St. Louis, MO, USA).

Materials: PE- or PE-Cy7-labeled anti-CD11c (clone N418), eFl450- or FITC-CD86 (GL-1), PerCP-eFl710-CD80 (16-10A1), eFl506-CD3 (17A2), SB600-CD11b (M1/70), SB702-CD19 (eBio1D3), PE-NK1.1 (PK136), PE-eFl610-Ly6G (1A8-L6g), FITC-CD209a (MMD3), PE-Cy7-CD206 (C068C2), and eFl780-FVD used for flow cytometric analysis were purchased from BD Biosciences (Franklin Lakes, NJ, USA), Bio Legend (San Diego, CA, USA) or Thermo Fisher Scientific (Waltham, MA, USA).

Analytical high performance liquid chromatography (HPLC-ELS-MS): For carbohydrate synthesis monitoring of reaction progress was accomplished utilizing a 1260 Infinity II HPLC system, consisting of a 1260 Infinity Solvent rack, 1260 Infinity HiP Degasser (G4225A), 1260 Infinity Binary Pump (G1312B) operated at a flow rate of 0.7 mL/min, 1260 Infinity II Vial sampler (G7129A) adjusted to an injection volume of 1.5 µL., 1260 Infinity TCC (G1316A) operated at 40 °C, 1260 Infinity II DAD HS (G7117C) for multiple wavelength detection in combination with an 1290 Infinity II ELSD (G7102A) and an Infinity Lab 6100 Series LCMSD (G6125B) via electro spray ionization (ESI) (*Agilent Technologies Deutschland GmbH*, Waldbronn, BW, Germany). Separation was conducted using an analytical reversed phase Ascentis Express C_{18}-column (30 mm x 2.1 mm, 2.7 µm) (*Supelco Deutschland GmbH*, Bad Homburg v. d. Höhe, HE, Germany). The mobile phase was composed of a gradient mixture consisting of A = H_2O with 0.1 % HCOOH and B = MeCN using a gradient profile starting with ratio A:B = 10:90 until t = 0.2 min, followed by a linear increase to ratio A:B = 90:10 until t = 7.5 min followed by an isocratic hold until t = 10 min. Solvents were obtained from commercial suppliers in optima HPLC-MS grade quality: MeCN (*VWR*, Radnor, PA, USA), H_2O (*VWR*, Radnor, PA, USA) and HCOOH (*Thermo Fisher Scientific*, Waltham, MA, USA).

Flash column chromatography (FCC): For carbohydrate synthesis purification of larger amounts of crude products via manual normal phase flash column chromatography was accomplished with nitrogen overpressure following the method of *Still et al.*[1] Silica gel (particle size 35–70 µm) obtained from *Acros Organics* (Geel, Belgium) was utilized as stationary phase and binary, isocratic mixtures of cyclohexane (^{c}Hex) and ethyl acetate (EtOAc) as mobile phase. The solvents were obtained with "technical grade" quality and purified via distillation prior to use. Purification of small amounts of crude products via normal phase flash column chromatography was accomplished utilizing an Isolera Four Flash Purification System (*Biotage,* Uppsala, Sweden) equipped with pumps for variable gradient mixtures at flow rates of 1–200 mL/min, a DAD for detection at wavelengths between 200 – 800 nm and an integrated fraction collector. Normal phase separation was conducted using SNAP KP-SIL cartridges (*Biotage*, Uppsala, Sweden) packed with 10 g, 25 g, 50 g and 100 g of silica gel suitable for the separation of < 0.20 g, 0.20 – 0.50, 0.50 – 1.00 g or > 1.00 g of crude material. Binary eluent mixtures consisting of cyclohexane, ethyl acetate or DCM and MeOH were used. Purification of small amounts of crude products via reversed phase flash column chromatography was accomplished utilizing an

Supporting Information

Isolera One Flash Purification System (*Biotage*, Uppsala, Sweden) equipped with pumps for variable gradient mixtures at flow rates of 1–200 mL/min, a DAD for detection at wavelengths between 200 – 400 nm and an integrated fraction collector. Reversed phase separation used SNAP C_{18} cartridges (*Biotage*, Uppsala, Sweden) packed with 12 g, 30 g and 60 g of stationary phase suitable for the separation of < 0.20 g, 0.20 – 0.50 or > 1.00 g of crude material. Binary eluent mixtures consisting of MeCN and H_2O were used. Isolation of purified material was accomplished via lyophilization utilizing an Alpha 2-4LDPlus freeze dryer (*Martin Christ Gefriertrocknungsanlagen*, Osterode, NI, Germany).

Preparative high performance liquid chromatography (HPLC): HPLC purifications were carried out using a Shimadzu HPLC system equipped with a semi preparative reversed phase Eclipse XBD-C_{18}-column (9.4 mm x 250 mm, 5 µm) (*Agilent Technologies Deutschland GmbH*, Waldbronn, BW, Germany).

Thin layer chromatography (TLC): For carbohydrate synthesis monitoring of reaction progress and chromatographic separation via normal phase TLC was conducted using silica gel 60 F_{254} modified aluminum plates and reversed phase TLC on silica gel 60 RP-18 F_{254S} modified aluminum plates (*Merck KGaA*, Darmstadt, Germany) containing manganese doted zinc silicate for detection upon UV irradiation. Mobile phases consisted of binary eluent mixtures as described below with the composition stated as volumetric ratio (*v*:*v*). For further substance detection the following staining reagents were applied, and the plates heated with a heat gun: "Potassium permanganate staining reagent": $KMnO_4$ (1.00 g), K_2CO_3 (7.00 g) dissolved in H_2O (100 mL) adding a NaOH-solution (5 %, 2.00 mL) and "Carbohydrate staining reagent": 3-Methoxyphenol (0.20 mL) dissolved in EtOH (100 mL) adding conc. H_2SO_4 (7.00 mL). Ratio of Fronts values (R_f) were stated for each compound.

3 Analytical methods

Absorbance spectroscopy measurements: The absorbance was measured using a NANODROP 2000c spectrophotometer (*Thermo Fisher scientific*, Waltham, MA, USA) or Spark 20M microplate reader (*Tecan*, Wiesbaden, HE, Germany).

High resolution mass spectrometry (HR-ESI-MS): HR-ESI-MS was recorded using a Synapt G2-Si mass spectrometer (*Waters Corporation*, Eschborn, HE, Germany). High resolution exact mass determination for carbohydrate structures was performed using a G6545A Q-ToF (*Agilent Technologies Deutschland GmbH*, Waldbronn, BW, Germany) via electro spray ionization (ESI). Sample injection was achieved using a 1260 Infinity II HPLC-System (*Agilent Technologies Deutschland GmbH*, Waldbronn, BW, Germany) with a G7111B 1260 Quaternary Pump, G7129A 1260 Vialsampler und G7116A 1260 Multicolumn Thermostat. Mass calibration was done on the day of sample measurement utilizing an external standard.

Infrared spectroscopy (IR): Infrared spectra were measured utilizing a Tensor 27 FT-IR spectrometer with built in Diamant-ATR-unit (*Bruker Corporation*, Ettlingen, BW, Germany). The absorption frequencies of characteristic oscillation bands are stated as wave number $\tilde{\nu}$ [cm^{-1}]. Spectra were processed using the Opus software (*Bruker Corporation*, Ettlingen, BW, Germany) for baseline correction and peak detection.

Melting range determination: For carbohydrate compounds obtained as crystalline solid the melting range Θ [°C] was determined using a KSP1N melting point meter (*A. Krüss Optronic*, Hamburg, HH, Germany). Samples were transferred into a capillary tube and heated with a rate of 1 °C/min. The melting process was observed and temperature values for onset and end of melting are given.

Supporting Information

Nuclear magnetic resonance spectroscopy (NMR): For carbohydrate structures NMR-spectra were recorded utilizing an AC300 (*Bruker Corporation*, Ettlingen, BW, Germany) with 5 mm Dual-^{13}C-head and B-ACS 60 sample changer for 300 MHz ^{1}H-NMR-, 75.5 MHz ^{13}C-NMR- as well as 2D-NMR-experiments, an Avance-II 400 (*Bruker Corporation*, Ettlingen, BW, Germany) with 5 mm BBFO-head with z-gradient and ATM as well as SampleXPress 60 sample changer for 400 MHz ^{1}H-NMR-, 100.6 MHz ^{13}C-NMR- and 2D-NMR experiments and an Avance-III 600 (*Bruker Corporation*, Ettlingen, BW, Germany) with 5 mm TCI-Cryoprobe with z-Gradient and ATM as well as SampleXPress Lite 16 sample changer for 600 MHz ^{1}H-NMR-, 151.0 MHz ^{13}C-NMR- and 2D-NMR experiments. Samples were dissolved in an appropriate deuterated solvent ($CDCl_3$, CD_3OD, D_2O). Spectra were processed using the MestReNova software (*Mestrelab Research*, Santiago de Compostela, Spain) for baseline correction (Whittaker smoother) and automated phase correction. Spectra were referenced to the signal of the respective deuterated solvent ($CDCl_3$: ^{1}H: δ = 7.26 ppm, CD_3OD: ^{1}H: δ = 3.31 ppm, D_2O: ^{1}H: δ = 4.79 ppm) and using the absolute reference function of the analysis software. Observed signals are described using their chemical shifts (δ) in ppm, multiplicity (s-singlet, d-doublet, t-triplet, dd-double of doublet, etc. and m-multiplet; app-apparent and br-broad), integral and locator of ^{1}H- and ^{13}C-position in the molecule. Signal assignment was supported utilizing 2D-NMR spectra: COSY, HSQC, HSQC-NoDec, HMBC, TOCSY, NOESY (data not shown).

Polarimetry: For carbohydrate compound specific optical rotation values $[\alpha]_D^\theta$ of all optical active carbohydrate compounds were determined using an automated 241 MC polarimeter (*PerkinElmer Inc.*, Waltham, MA, USA). Measurements were undertaken utilizing a sodium-vapor lamp at the sodium D-double line (λ_{D1} = 589.5924 nm und λ_{D2} = 588.9951 nm) with an aperture adjustment of 600 nm and a lid width of 2 nm. Optical rotation values α were determined at an integration time of 20 seconds. Measurements were carried out at ambient temperature with the actual value stated for each optical rotation value. Glass cuvettes (l = 10 cm, V = 1.00 mL) were filled with a sample solution (c = 0.01 g/mL) in an appropriate solvent ($CHCl_3$, MeOH, H_2O). The polarimeter was calibrated with the pure solvent prior to the measurement. The unit of the specific optical rotation $[\alpha]_\lambda^\theta$ of [°·cm^2/10·g] is neglected in the following.

Supporting Information

4 Synthesis procedures

4.1 Synthesis of the mono- and trivalent targeting structures

The synthesis of the mannose-based saccharide building blocks (**1**) and (**2**), the HOOC-PEG_3-N_3 building block (**3**), the H_2N-PEG_4-N_3 building block (**4**), the N_3-PEG_4-N_3 building block (**5**), and the trivalent pre-dendron (**6**) is summarized in Scheme S 1. The sequences include a total of 15 reaction steps involving three telescoped reaction procedures reducing needed purification steps and improving overall yield. Starting from D-mannose, glycosyl donor (**S1**) was prepared via a telescoped, two-step procedure involving a peracetylation using Ac_2O and pyridine[2, 3] as well as a glycosylation using PhSH and $BF_3{\cdot}OEt_2$ in DCM.[4, 5] Furthermore, the monosaccharide building block ManPrg (**2**) was prepared via a telescoped, three-step procedure involving a peracetylation using Ac_2O and pyridine, a glycosylation using PrgOH and $BF_3{\cdot}OEt_2$ in DCM as well as a Zemplén deacylation utilizing NaOMe in MeOH.[4, 6-13] Starting from this deprotected building block, glycosyl acceptor (**S2**) was prepared via a telescoped, three-step procedure involving a di-silylation using TBDMSCl and imidazole in DMF, a di-benzoylation using BzCl and DMAP in a mixture of DCM and pyridine as well as a di-desilylation using $(HF)_x{\cdot}$pyridine complex in AcOH and THF.[14-22] Glycosylation of glycosyl donor (**S1**) with glycosyl acceptor (**S2**) using a promotor system consisting of NIS and AgOTf in DCM delivered the trisaccharide building block Man_3Prg (**1**).[18, 19, 23] Starting with PEG_4, the N_3-PEG_4-N_3 building block (**5**) was obtained via a di-mesylation using MsCl and NEt_3 in DCM followed by a nucleophilic substitution using NaN_3 and TBAI in DMF.[6, 24-26] Staudinger reduction of one azide group using one equivalent of PPh_3 in a mixture of Et_2O, THF am 1 M HCl gave access to H_2N-PEG_4-N_3 building block (**4**).[24, 26] Starting with PEG_3, the protected precursor (**S3**) was prepared via a Micheal addition using TBA and Na in THF followed by a tosylation using TsCl and NEt_3 in DCM.[26-28] The HOOC-PEG_3-N_3 building block (**3**) was obtained via a nucleophilic addition using NaN_3 in DMF followed by cleavage of the tert-butyl ester using TFA in DCM.[26, 27, 29] Starting with TRIS, a Micheal addition using TBA and 5 M NaOH in DMSO yields the Lin's amine analogue (**S4**).[26, 30-32] Protection of the amine using the respective chloroformate ester, derived from *o*-NBA and TCF, gave access to the orthogonally protected precursor (**S5**).[26, 33, 34] Cleavage of the *tert*-butyl esters using TFA in DCM delivered the tricarboxylic acid (**S6**).[26, 29, 35] Finally, an amide coupling reaction using HATU and DIPEA in DMF allowed to connect the H_2N-PEG_4-N_3 building block (**4**) to obtain pre-dendron (**6**). The assembly of monovalent and trivalent TSs is summarized in Scheme S 2. The synthesis sequences include a total of 11 reaction steps to obtain all four TSs using similar reaction conditions. Synthesis of the TS $ManN_3$ was achieved by connecting the ManPrg (**2**) and the N_3-PEG_4-N_3 building blocks (**5**) via a CuAAC-reaction using Cu^IBr and PMDTA in DMF.[36-40] $ManN_3$ (**1**) was obtained with a total yield of 91 % over the longest linear sequence starting from HOOC-PEG_4-N_3 (**3**) containing three steps. The assembly of the TS Man_3N_3 was achieved by connecting the Man_3Prg (**1**) and the diazide tetraethylene glycol building blocks (**5**) via a CuAAC-reaction using Cu^IBr and PMDTA in DMF followed by a global Zemplén-deacylation using NaOMe and NaOH in MeOH.[6, 39-41] Man_3N_3 was obtained with a total yield of 64 % over the longest linear sequence starting from D-mannose containing five steps. The assembly of the trivalent glycodendrons of the Newkome-type[32] $(Man)_3N_3$ and $(Man_3)_3N_3$ was accomplished by connecting the respective fully protected building blocks (**S7**), which can be obtained by isolating the intermediat during the telescoped synthesis of the deprotected building block ManPrg (**2**) prior to the Zemplén-deacylation, and Man_3Prg (**1**) with pre-dendron (**6**) via a CuAAC-reaction using Cu^IBr and PMDTA in DMF resulting in (**S8**) and (**S9**).[26, 39] UV-A-Irradiation at an emission maximum of 350 nm allowed photolysis of the

Supporting Information

photocleavable NBA-carbamate in context of a Norrish-type-II fragmentation giving access to the deprotected amines (**S10**) and (**S11**).[26, 42, 43]

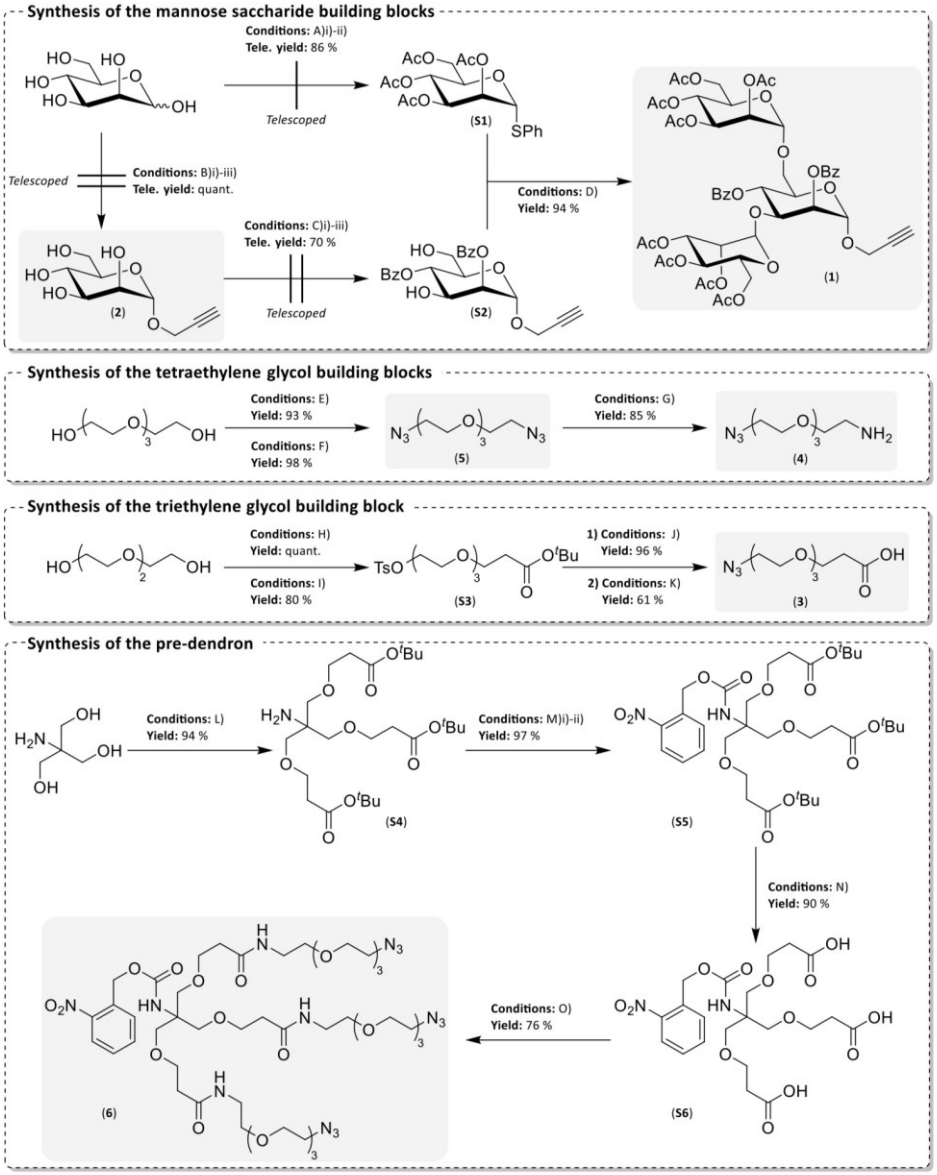

Scheme S 1: Synthesis of the mannose-based saccharide building blocks ManPrg (**2**) and Man_3Prg (**1**), H_2N-PEG_4-N_3 building block (**4**), HOOC-PEG_4-N_3 building block (**3**) and of the trivalent pre-dendron (**6**). The building blocks used to assemble the TSs are highlighted in grey. Reaction conditions: A)i) Ac_2O, pyr., Ar-atm., rt, 20 h; A)ii) $BF_3{\cdot}OEt_2$, PhSH, DCM, Ar-atm., 0 °C to rt, 24 h; B)i) Ac_2O, pyr., Ar-atm., rt, 20 h; B)ii) $BF_3{\cdot}EtO_2$, HOPrg, DCM, Ar-atm., 0 °C to rt, 20 h; B)iii) NaOMe, MeOH, Ar-atm., rt, 16 h; C)i) TBDMSCl, Imi., DMF, Ar-atm., MS 3Å, 0 °C, 4 h; C)ii) BzCl, pyr., DMAP, DCM, Ar-atm., MS 3Å, 0 °C to rt, 42 h; C)iii) $(HF)_X{\cdot}$pyr., AcOH, THF, 0 °C to rt, 24 h; D) NIS, AgOTf, DCM, Ar-atm., -40 °C to -20 °C, 4 h; E) MsCl, NEt_3, DCM, Ar-atm., 0 °C to rt, 3 h; F) NaN_3, TBAI, DMF, Ar-atm., 80 °C, 4 h; G) PPh_3, Et_2O/THF/1 M HCl (8:1:4), rt, 48 h; H) TBA, Na, THF, Ar-atm., rt, 22 h; I) TsCl, NEt_3, DCM, Ar-atm., rt, 23 h; J) NaN_3, DMF, Ar-atm., rt, 21 h; K) TFA, DCM, Ar-atm., rt, 22 h; L) TBA, NaOH (5M), DMSO, Ar-atm., 0 °C to rt, 96 h; M)i) NBA, TCF, THF, 66 °C, 4 h; M)ii) $NaHCO_3$, EtOAc/H_2O (2:1), rt, 18 h; N) TFA, DCM, rt, 72 h; O) (**4**), HATU, DIPEA, DMF, Ar-atm., rt, 48 h.

Via an amide coupling reaction using HATU and DIPEA in DMF the HOOC-PEG_4-N_3 building block (**3**) was connected to obtain the precursors (**S12**) and (**S13**).[26, 44] A global Zemplén-deacylation using NaOMe and NaOH in MeOH gave access to the deprotected glycodendrimers $(Man)_3N_3$ and $(Man_3)_3N_3$.[11, 26] Both structures were obtained with a total yield of 38 % and 25 % respectively over the

Supporting Information

longest linear sequence starting from tetraethylene glycol containing eight steps. Analytically pure samples of the intermediate products of telescope steps were isolated and used for characterization.

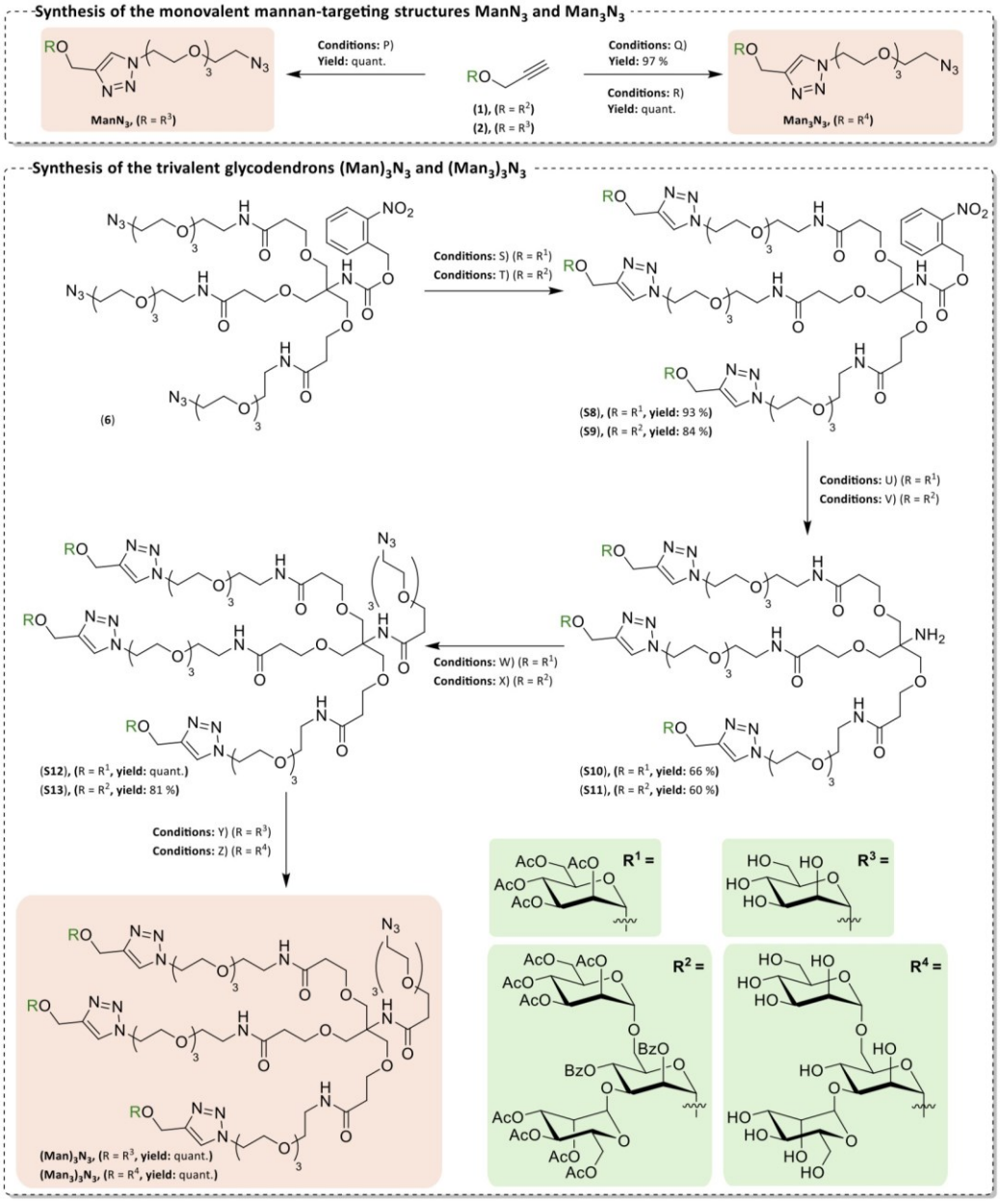

Scheme S 2: Assembly of the monovalent TSs $ManN_3$ and Man_3N_3 as well as of the trivalent glycodendrons $(Man)_3N_3$ and $(Man_3)_3N_3$. The mannose residues of the TSs are abbreviated and highlighted in green. The TSs used for NanoDSF studies and conjugation to the HSA-NC are highlighted in orange. Reaction conditions: P) Cu^IBr, NaAsc, DMF, Ar-atm., 45 °C, 20 h; Q) Cu^IBr, PMDTA, DMF, Ar-atm., 45 °C, 3 h; R) NaOMe, NaOH, MeOH, Ar-atm., rt, 24 h; S) (**S7**), Cu^IBr, PMDTA, DMF, Ar-atm., 45 °C, 4 h; T) (**1**), Cu^IBr, PMDTA, DMF, Ar-atm., 45 °C, 5 h; U) UV-A, MeCN, Ar-atm., rt, 15 h; V) UV-A, MeCN, Ar-atm., rt, 15 h; W) (**3**), HATU, DIPEA, Ar-atm., DMF, rt, 48 h; X) (**3**), HATU, DIPEA, Ar-Atm., DMF, rt, 48 h; Y) NaOMe, MeOH, Ar-atm., rt, 2 h; Z) NaOMe, NaOH, MeOH, Ar-atm., rt, 18 h.

Supporting Information

4.1.1 Synthesis of Phenyl 2,3,4,6-Tetra-*O*-acetyl-1-thio-α-D-mannopyranoside

The title compound was synthesized utilizing a telescoped two-step protocol according to Scheme S 3 following synthesis protocols by *Krabicová et al.*[13] and *Ekholm et al.*[4]

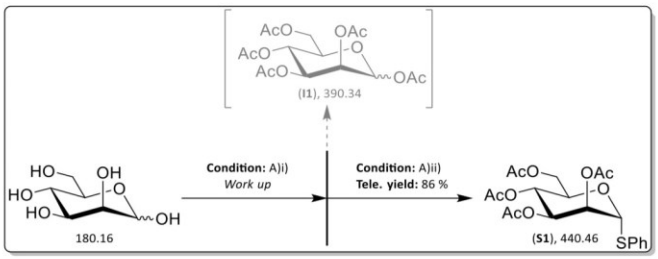

Scheme S 3: Synthesis of Phenyl 2,3,4,6-Tetra-*O*-acetyl-1-thio-α-D-mannopyranoside (**S1**). Reaction conditions A)i) Ac_2O, Pyr., Ar-atm., rt, 20 h; A)ii) $BF_3{\cdot}OEt_2$, PhSH, DCM, Ar-atm., 0 °C to rt, 24 h; telescoped yield: 86 %.

Both reaction steps were carried out in dried Schlenk vessels, which were previously equipped with magnetic stirring bars. D-Mannose (2.00 g, 11.1 mmol, 1.00 eq.) was dissolved in absolute pyridine (10.0 mL) under an atmosphere of argon and the slightly turbid solution was cooled to a temperature of 0 °C in an ice bath. Ac_2O (11.5 g, 10.5 mL, 111 mmol, 10.0 eq.) was added with a syringe. The yellowish reaction mixture was stirred for 20 hours while slowly warming up to room temperature. Complete conversion of the limiting substrate and formation of the desired product were determined by reaction control via TLC and HPLC-ELS-MS. The mixture was poured onto H_2O (1 x 100 mL) and extracted with EtOAc (3 x 100 mL). The collected organic phases were washed with saturated $NaHCO_3$ solution (3 x 100 mL), 1M HCl solution (3 x 100 mL), H_2O (3 x 100 mL) and saturated NaCl solution (1 x 100 mL). The organic phase was dried over anhydrous Na_2SO_4 and filtered. All volatile components were removed in vacuo. Toluene (3 x 20.0 mL) was added to the residue and all volatile components were again removed in vacuo. The residue was dried in fine vacuum. The first intermediate (4.60 g) was obtained in the form of colorless oil and dissolved in absolute DCM (20.0 mL) under an atmosphere of argon. PhSH (1.96 g, 1.81 mL, 17.8 mmol, 1.60 eq.) was added with a syringe and molecular sieves (MS 3Å, 0.50 g) were added successively. The mixture was stirred for 30 minutes at room temperature. The brownish solution was cooled to a temperature of 0 °C in an ice bath and $BF_3{\cdot}OEt_2$ (7.88 g, 7.03 mL, 55.5 mmol, 5.00 eq.) was added dropwise. The resulting yellowish reaction mixture was stirred for 24 hours while slowly warming up to room temperature, with a deep red solution resulting. Complete conversion of the limiting substrate and formation of the desired product were determined by reaction control via TLC and HPLC-ELS-MS. The mixture was diluted with DCM (1 x 100 mL) and poured onto ice-cold H_2O (1 x 150 mL) with stirring. The organic phase was washed with saturated $NaHCO_3$ solution (1 x 100 mL) and added to an ice-cooled 1 M NaOH solution (1 x 150 mL) while stirring vigorously. The two-phase mixture was stirred for one hour at a temperature of 0 °C. The organic phase was washed again with saturated $NaHCO_3$ solution (1 x 150 mL), 1 M NaOH solution (1 x 150 mL) and saturated NaCl solution (1 x 150 mL), dried over anhydrous Na_2SO_4 and filtered. All volatile components were removed in vacuo and the residue was dried in fine vacuum. The crude product (6.35 g) was obtained in the form of an orange oil and purified by FCC (^{c}Hex/EtOAc, isocratic at 33 % EtOAc). The pure product (**S1**) was obtained as α-anomer in the form of a colorless solid.

Yield: 4.21 g (9.55 mmol, 86 %), (Lit.[4]: 95 %), colorless solid.

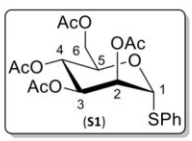

^{1}H-NMR (400 MHz, $CDCl_3$, 25 °C)**:** δ (ppm) = 7.51–7.47 (m, 2H, C-1-S-Ph, H_{ortho}), 7.35–7.28 (m, 3H, C-1-S-Ph, H_{meta}, H_{para}), 5.55 (dd, ^3J = 3.1, 1.6 Hz, 1H, H-2), 5.49 (d, ^3J = 1.6 Hz, 1H, H-1), 5.33 (dd, ^3J = 9.9, 9.8 Hz, 1H, H-4), 5.32 (dd, ^3J = 9.8, 3.1 Hz, 1H, H-3), 4.55 (ddd, ^3J = 9.9, 5.9, 2.4 Hz, 1H, H-5), 4.31 (dd,

^2J = 12.2, ^3J = 5.9 Hz, 1H, H-6a), 4.10 (dd, ^2J = 12.2, ^3J = 2.4 Hz, 1H, H-6b), 2.15 (s, 3H, C-4-O(C=O)CH_3), 2.07 (s, 3H, C-6-O(C=O)CH_3), 2.05 (s, 3H, C-3-O(C=O)CH_3), 2.02 (s, 3H, C-2-O(C=O)CH_3). **^{13}C-NMR** (101 MHz, $CDCl_3$, 25 °C)**:** δ (ppm) = 170.5 (1C, C-6-O(*C*=O)CH_3), 169.9 (1C, C-3-O(*C*=O)CH_3), 169.8 (1C, C-4-O(*C*=O)CH_3), 169.7 (1C, C-2-O(*C*=O)CH_3), 132.6 (1C, C-1-SPh, C_{ipso}), 132.1 (2C, C-1-SPh, C_{ortho}), 129.2 (2C, C-1-SPh, C_{meta}), 128.1 (1C, C-1-SPh, C_{para}), 85.7 (1C, C-1), 70.9 (1C, C-2), 69.5 (1C, C-5) 69.4 (1C, C-3), 66.4 (1C, C-4), 62.5 (1C, C-6), 20.9 (1C, C-4-O(C=O)*C*H_3), 20.7 (1C, C-6-O(C=O)*C*H_3), 20.7 (1C, C-3-O(C=O)*C*H_3), 20.7 (1C, C-2-O(C=O)*C*H_3). **HR-MS** (ESI$^+$)**:** $m/z_{cal.}$ = 463.1033 $[M+Na]^+$, $m/z_{exp.}$ = 463.1031 $[M+Na]^+$; $m/z_{cal.}$ = 331.1029 $[M-SPh]^+$, $m/z_{exp.}$ = 331.1022 $[M-SPh]^+$. R_f (NP) = 0.33 (^{c}Hex/EtOAc 2:1). **Melting range:** Θ (°C) = 79.5 – 81.1 (EtOAc). **Optical rotation** (LM)**:** $[\alpha]_D^{21}$ = +104 ($CHCl_3$). **IR** (ATR)**:** $\tilde{\nu}$ (cm^{-1}) = 1745, 1440, 1369, 1221, 1106, 1050, 976, 915, 749, 692.

The analytical data follows literature data.[4]

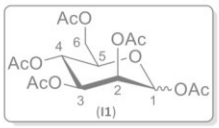

NMR-signals of major α-anomer: ^{1}H-NMR (400 MHz, $CDCl_3$, 25 °C)**:** δ (ppm) = 6.07 (d, ^3J = 2.0 Hz, 1H, H-1), 5.35 – 5.32 (m, 2H, H-2, H-3), 5.26 – 5.23 (m, 1H, H-4), 4.27 (dd, ^2J = 12.4, ^3J = 4.9 Hz, 1H, H-6a), 4.08 (dd, ^2J = 12.4, ^3J = 2.4 Hz, 1H, H-6b), 4.06 – 4.01 (m, 1H, H-5), 2.16 (s, 3H, C-4-O(C=O)CH_3), 2.15 (s, 3H, C-1-O(C=O)CH_3), 2.08 (s, 3H, C-6-O(C=O)CH_3), 2.04 (s, 3H, C-2-O(C=O)CH_3), 1.99 (s, 3H, C-3-O(C=O)CH_3). **^{13}C-NMR** (101 MHz, $CDCl_3$, 25 °C)**:** δ (ppm) = 170.7 (C-6-O(*C*=O)CH_3), 170.1 (C-3-O(*C*=O)CH_3), 169.8 (C-4-O(*C*=O)CH_3), 169.6 (C-2-O(*C*=O)CH_3), 168.2 (C-1-O(*C*=O)CH_3), 90.7 (C-1), 70.7 (C-5), 68.8 (C-3), 68.4 (C-2), 65.6 (C-4), 62.2 (C-6), 21.0 (C-4-O(C=O)*C*H_3), 20.9 (C-1-O(C=O)*C*H_3), 20.8 (C-6-O(C=O)*C*H_3), 20.8 (C-2-O(C=O)*C*H_3), 20.7 (C-3-O(C=O)*C*H_3). **NMR-signals of minor β-anomer: ^{1}H-NMR** (400 MHz, $CDCl_3$, 25 °C)**:** δ (ppm) = 5.85 (d, ^3J = 1.2 Hz, 1H, H-1), 5.47 (dd, ^3J = 3.3, 1.2 Hz, 1H, H-2), 5.31–5.27 (m, 1H, H-4), 5.12 (dd, ^3J = 10.0, 3.3 Hz, 1H, H-3), 4.29 (dd, ^2J = 12.3 Hz, ^3J = 5.3 Hz, 1H, H-6a), 4.14 (dd, ^2J = 12.3 Hz, ^3J = 2.4 Hz, 1H, H-6b), 3.79 (ddd, ^3J = 9.9, 5.3, 2.4 Hz, 1H, H-5), 2.20 (s, 3H, C-4-O(C=O)CH_3), 2.09 (s, 3H, C-1-O(C=O)CH_3), 2.08 (s, 3H, C-6-O(C=O)CH_3), 2.04 (s, 3H, C-2-O(C=O)CH_3), 1.99 (s, 3H, C-3-O(C=O)CH_3). **^{13}C-NMR** (101 MHz, $CDCl_3$, 25 °C)**:** δ (ppm) = 170.7 (1C, C-6-O(*C*=O)-CH_3), 170.3 (1C, C-3-O(*C*=O)-CH_3), 169.9 (1C, C-4-O(*C*=O)-CH_3), 169.7 (1C, C-2-O(*C*=O)-CH_3), 168.5 (1C, C-1-O(*C*=O)-CH_3), 90.5 (1C, C-1), 73.4 (1C, C-5), 70.7 (1C, C-3), 68.3 (1C, C-2), 65.5 (1C, C-4), 62.2 (1C, C-6), 21.0 (1C, C-4-O(C=O)*C*H_3), 20.9 (1C, C-1-O(C=O)*C*H_3), 20.8 (1C, C-6-O(C=O)*C*H_3), 20.8 (1C, C-2-O(C=O)*C*H_3), 20.6 (1C, C-3-O(C=O)*C*H_3). **Analytical data of obtained anomeric mixture (α:β 4.2:1): HR-MS** (ESI$^+$)**:** $m/z_{cal.}$ = 413.1054 $[M+Na]^+$, $m/z_{exp.}$ = 413.1058 $[M+Na]^+$. R_f (NP) = 0.45 (^{c}Hex/EtOAc 1:1), 0.25 (^{c}Hex/EtOAc 2:1). **Melting range:** Θ (°C) = 60.0 – 61.0 (DCM). **Optical rotation** (LM)**:** $[\alpha]_D^{21}$ = +48.0 ($CHCl_3$). **IR** (ATR)**:** (cm^{-1}) = 2991, 1745, 1434, 1370, 1213, 1148, 1088, 1052, 1026, 974, 912, 786, 732, 686, 601, 562, 500, 467, 449.

The analytical data follows literature data.[6, 11, 45, 46]

Supporting Information

4.1.2 Synthesis of Propargyl α-D-Mannopyranoside

The title compound was synthesized utilizing a telescoped three-strep protocol according to Scheme S 4 following synthesis protocols by *Krabicová et al.*[13], *Poláková et al.*[10] and *Reintjens et al.*[12].

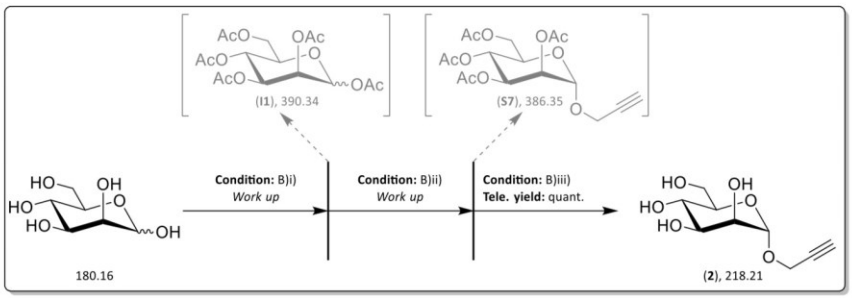

Scheme S 4: Synthesis of Propargyl α-D-Mannopyranoside (**2**). Reaction conditions: B)i) Ac_2O, Pyr., Ar-atm., rt, 20 h; B)ii) $BF_3{\cdot}EtO_2$, HOPrg, DCM, Ar-atm., 0 °C to rt, 20 h; B)iii) NaOMe, MeOH, Ar-atm., rt, 16 h; telescoped yield: quant.

All three reaction steps were carried out in dried Schlenk vessels, which were previously equipped with magnetic stirring bars. D-Mannose (1.00 g, 5.55 mmol, 1.00 eq.) was dissolved in absolute pyridine (5.00 mL) under an atmosphere of argon and the slightly turbid solution was cooled to a temperature of 0 °C in an ice bath. Ac_2O (5.67 g, 5.23 mL, 55.5 mmol, 10.0 eq.) was added with a syringe. The yellowish reaction mixture was stirred for 20 hours while slowly warming up to room temperature. Complete conversion of the limiting substrate and formation of the desired product were determined by reaction control via TLC and HPLC-ELS-MS. The mixture was poured onto H_2O (1 x 50.0 mL) and extracted with EtOAc (3 x 50.0 mL). The collected organic phases were washed with saturated $NaHCO_3$ solution (3 x 50.0 mL), 1M HCl solution (3 x 50.0 mL), H_2O (3 x 50.0 mL) and saturated NaCl solution (1 x 50.0 mL). The organic phase was dried over anhydrous Na_2SO_4 and filtered. All volatile components were removed in vacuo. Toluene (3 x 10.0 mL) was added to the residue and all volatile components were again removed in vacuo. The residue was dried in fine vacuum. The first intermediate (2.23 g) was obtained in the form of colorless oil and dissolved in absolute DCM (20.0 mL) under argon atmosphere. The colorless solution was cooled to a temperature of 0 °C in an ice bath. PrgOH (1.56 g, 1.60 mL, 27.8 mmol, 5.00 eq.) and $BF_3{\cdot}OEt_2$ (7.88 g, 7.03 mL, 55.5 mmol, 10.0 eq.) were added successively with a syringe. The resulting yellowish reaction mixture was stirred for 20 hours with slow warming to room temperature, during which time the solution turned dark red. Complete conversion of the limiting substrate and formation of the desired product were determined by reaction control via TLC and HPLC-ELS-MS. The mixture was diluted with DCM (1 x 100 mL) and washed with H_2O (3 x 100 mL), saturated $NaHCO_3$ solution (3 x 100 mL) and saturated NaCl solution (1 x 100 mL). The organic phase was dried over anhydrous Na_2SO_4 and filtered. All volatile components were removed in vacuo. The second intermediate (2.25 g) was obtained in the form of yellowish oil and dissolved in a mixture of absolute DCM (5.00 mL) and absolute MeOH (20.0 mL) under argon atmosphere. NaOMe (71.0 mg, 2.22 mmol, 0.40 eq.) was added in argon countercurrent and the reaction mixture was stirred for 20 hours at room temperature. Complete conversion of the limiting substrate and formation of the desired product were determined by reaction control via TLC and HPLC-ELS-MS. The reaction was terminated by adding the ion exchange resin Amberlite IR 120 (200 mg). The mixture was stirred for ten minutes until a constant pH-value (pH = 6 – 7) was reached. The reaction mixture was filtered over Celite through a glass frit and eluted with MeOH (1 x 100 mL). All volatile components were removed in vacuo and the residue was dried in fine vacuum. The crude product (1.54 g) was obtained in the form of a yellowish foam, dissolved in H_2O (1 x 50.0 mL) and extracted with a mixture of ^{c}Hex and EtOAc (2 x 50.0 mL, 10:1v:v) and purified after lyophilization of the aqueous phase by FCC (liquid feed from

MeOH, DCM/MeOH, gradient from 0 % to 20 % MeOH, Isolera Four Purification System, SNAP KP-Sil 100 g cartridge). The pure product (**2**) was obtained as an α-anomer in the form of a colorless solid.

Yield: 1.21 g (5.55 mmol, quant.), (Lit.[6, 11]: 98 %), colorless solid.

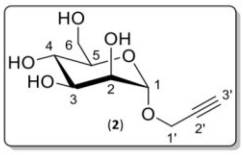

^{1}H-NMR (400 MHz, CD_3OD, 25 °C)**:** δ (ppm) = 4.96 (d, ^3J = 1.7 Hz, 1H, H-1), 4.27 (d, ^4J = 2.4 Hz, 2H, H-1‘), 3.84 (dd, ^2J = 11.8, ^3J = 2.3 Hz, 1H, H-6a), 3.79 (dd, ^2J = 3.2, 1.7 Hz, 1H, H-2), 3.70 (dd, ^2J = 11.8 Hz, ^3J = 5.9 Hz, 1H, H-6b), 3.67 (dd, ^3J = 9.1, 3.2 Hz, 1H, H-3), 3.62 (t_{app}, ^3J = 9.4 Hz, 1H, H-4), 3.51 (ddd, ^3J = 8.8, 5.9, 2.3 Hz, 1H, H-5), 2.86 (t, ^4J = 2.4 Hz, 1H, H-3‘). **^{13}C-NMR** (101 MHz, CD_3OD, 25 °C)**:** δ (ppm) = 99.8 (1C, C-1), 80.0 (1C, C-2‘), 76.0 (1C, C-3‘), 75.1 (1C, C-5), 72.5 (1C, C-3), 72.0 (1C, C-2), 68.5 (1C, C-4), 62.8 (1C, C-6), 54.8 (1C, C-1‘). **HR-MS** (ESI^+)**:** $m/z_{cal.}$ = 241.0683 $[M+Na]^+$, $m/z_{exp.}$ = 241.0682 $[M+Na]^+$. $\boldsymbol{R_f}$ (NP) = 0.13 (DCM/MeOH 10:1). **Melting range:** Θ (°C) = 119.0 – 120.1 °C (H_2O). **Optical rotation** (LM)**:** $[\boldsymbol{\alpha}]_{\mathbf{D}}^{\mathbf{20}}$ = +116.7 ° (MeOH). **IR** (ATR)**:** (cm^{-1}) = 3288, 2929, 2118, 1599, 1351, 1213, 1131, 1058, 1008, 970, 919, 881, 813, 683. The analytical data follows literature data.[6, 11, 12]

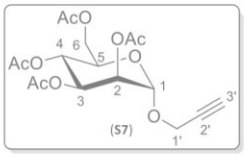

^{1}H-NMR (400 MHz, $CDCl_3$, 25 °C)**:** δ (ppm) = 5.35 (dd, ^3J = 9.5, 3.2 Hz, 1H, H-3), 5.31 (dd, ^3J = 9.5, 9.3 Hz, 1H, H-4), 5.28 (dd, ^3J = 3.2, 1.7 Hz, 1H, H-2), 5.03 (d, ^3J = 1.7 Hz, 1H, H-1), 4.29 (dd, ^2J = 12.3 Hz, ^3J = 5.1 Hz, 1H, H-6a), 4.27 (d, ^2J = 12.6 Hz, ^4J = 2.4 Hz, 2H, H-1‘), 4.11 (dd, ^2J = 12.3, ^3J = 2.5 Hz, 1H, H-6b), 4.02 (ddd, ^3J = 9.3, 5.1, 2.5 Hz, 1H, H-5), 2.47 (t, ^4J = 2.4 Hz, 1H, H-3‘), 2.16 (s, 3H, C-3-O(C=O)CH_3), 2.11 (s, 3H, C-6-O(C=O)CH_3), 2.04 (s, 3H, C-2-O(C=O)CH_3), 1.99 (s, 3H, C-4-O(C=O)CH_3). **^{13}C-NMR** (101 MHz, $CDCl_3$, 25 °C)**:** δ (ppm) = 170.8 (1C, C-6-O(*C*=O)CH_3), 170.1 (1C, C-3-O(*C*=O)CH_3), 170.0 (1C, C-4-O(*C*=O)CH_3), 169.8 (1C, C-2-O(*C*=O)CH_3), 96.4 (1C, C-1), 78.1 (1C, C-2‘), 75.7 (1C, C-3‘), 69.5 (1C, C-2), 69.1 (1C, C-5), 69.1 (1C, C-3), 66.2 (1C, C-4), 62.5 (1C, C-6), 55.1 (1C, C-1‘), 21.0 (1C, C-3-O(C=O)*C*H_3), 20.9 (1C, C-6-O(C=O)*C*H_3), 20.8 (1C, C-2-O(C=O)*C*H_3), 20.8 (1C, C-4-O(C=O)*C*H_3). **HR-MS** (ESI^+)**:** $m/z_{cal.}$ = 409.1105 $[M+Na]^+$, $m/z_{exp.}$ = 409.1104 $[M+Na]^+$. $\boldsymbol{R_f}$ (NP) = 0.59 (^{c}Hex/EtOAc 1:1). **Melting range** (°C) = 103.0 – 104.5 (EtOAc). **Optical rotation** (LM)**:** $[\boldsymbol{\alpha}]_{\mathbf{D}}^{\mathbf{19}}$ = +58.3 ($CHCl_3$). **IR** (ATR)**:** (cm^{-1}) = 3272, 2958, 1747, 1437, 1371, 1224, 1137, 1078, 1050, 982, 919, 797, 691, 601.

The analytical data follows literature data.[6-9]

Supporting Information

4.1.3 Synthesis of Propargyl 2,4-Di-*O*-benzoyl-α-D-mannopyranoside

The title compound was synthesized utilizing a telescoped three-strep protocol according to Scheme S 5 following modified synthesis protocols by *Ramos-Soriano et al.*[18], *Teumelsan et al.*[19], *van den Bos et al.*[21] and *Zhang et al.*[22]

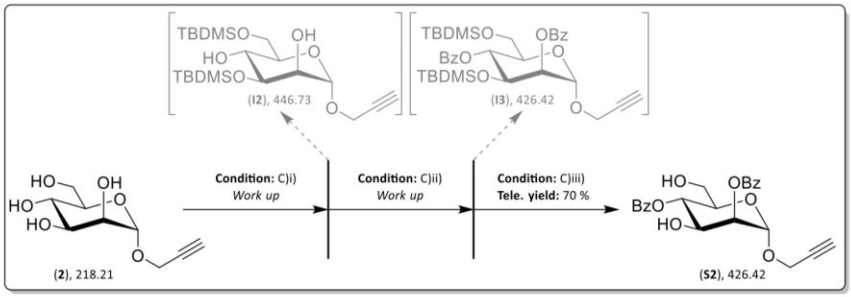

Scheme S 5: Synthesis of Propargyl 2,4-Di-*O*-benzoyl-α-D-mannopyranoside (**S2**). Reaction conditions: C)i) TBDMSCl, Imi., DMF, Ar-atm., MS 3Å, 0 °C, 4 h; C)ii) BzCl, Pyr., DMAP, DCM, Ar-atm., MS 3Å, 0 °C to rt, 42 h; C)iii) $(HF)_X$·Pyr., AcOH, THF, 0 °C to rt, 24 h; telescoped yield: 70 %.

The first two reaction steps were carried out in dried Schlenk vessels, the third in a Teflon vessel, which had previously been fitted with magnetic stirring bars. Propargyl α-D-mannopyranoside (**2**, 0.10 g, 0.46 mmol, 1.00 eq.) was dissolved in absolute DMF (1.00 mL) under an atmosphere of argon and the mixture was cooled to a temperature of 0 °C in an ice bath. Successively TBDMSCl (0.21 g, 1.37 mmol, 3.00 eq.) and imidazole (0.19 g, 2.75 mmol, 6.00 eq.) were added. The yellowish reaction mixture was stirred at this temperature for three hours. Complete conversion of the limiting substrate and formation of the desired product were determined by reaction control via TLC and HPLC-ELS-MS. The mixture was diluted with DCM (1 x 50.0 mL) and the organic phase was washed with saturated $NaHCO_3$ solution (1 x 30.0 mL), H_2O (2 x 30.0 mL) and saturated NaCl solution (1 x 30.0 mL). The collected aqueous phases were extracted with DCM (1 x 30.0 mL). The collected organic phases were dried over anhydrous Na_2SO_4 and filtered. All volatiles were removed in vacuo. Toluene (2 x 5.00 mL) was added to the residue and again all volatiles were removed in vacuo. The residue was dried in fine vacuum. The first intermediate (0.24 g) was obtained in the form of colorless oil and was dissolved in absolute DCM (2.00 mL) under an atmosphere of argon and molecular sieves (MS 3 Å, 0.25 g) were added. The mixture was stirred for ten minutes at room temperature and then cooled to a temperature of 0 °C in an ice bath. Absolute pyridine (0.50 mL), DMAP (11.2 mg, 92.0 µmol, 0.20 eq.) and benzoyl chloride (0.36 g, 0.29 mL, 2.53 mmol, 5.50 eq.) were added successively. Cooling was removed and the reaction mixture was stirred at room temperature for 24 hours to obtain a cloudy suspension. Complete conversion of the limiting substrate and formation of the desired product were determined by reaction control via TLC and HPLC-ELS-MS. The cloudy reaction mixture was filtered through a glass frit via Celite and eluted with EtOAc (1 x 100 mL). The organic phase was washed with H_2O (2 x 50.0 mL), 1 M HCl solution (1 x 50.0 mL), saturated $NaHCO_3$ solution (1 x 50.0 mL) and saturated NaCl solution (1 x 30.0 mL). The organic phase was dried over anhydrous Na_2SO_4 and filtered. All volatiles were removed in vacuo. Toluene (2 x 5.00 mL) was added to the residue and again all volatiles were removed in vacuo. The residue was dried in fine vacuum. The second intermediate (0.49 g) was obtained in the form of yellowish oil and dissolved in THF (5.00 mL). The resulting colorless solution was cooled to a temperature of 0 °C in an ice bath. AcOH (0.20 mL) and $(HF)_X$·Pyr. (70 %, 1.31 g, 1.19 mL, 46.0 mmol, 100 eq.) were added with a syringe and the resulting yellowish solution was stirred for 24 hours while slowly warming up to room temperature. Complete conversion of the limiting substrate and formation of the desired product were determined by reaction control via TLC and HPLC-ELS-MS. The solution

was diluted with DCM (1 x 100 mL) and the organic phase was poured onto an ice-cooled, saturated $NaHCO_3$ solution (100 mL). The organic phase was washed with saturated $NaHCO_3$ solution (2 x 50.0 mL), 1 M HCl solution (1 x 50.0 mL), saturated $NaHCO_3$ solution (1 x 50.0 mL) and saturated NaCl solution (1 x 50.0 mL). The collected organic phases were dried over anhydrous Na_2SO_4 and filtered. All volatiles were removed in vacuo. Toluene (2 x 5.00 mL) was added to the residue and again all volatiles were removed in vacuo. The residue was dried in fine vacuum. The crude product (0.17 g) was obtained in the form of a yellowish oil and purified using RP-FCC (MeCN/H_2O, gradient 5 % to 55 % to 100 % MeCN, Isolera One Flash Purification System, SNAP C_{18} 30 g cartridge). The pure product (**S2**) was obtained in the form of a colorless lyophilizate.

Yield: 0.14 g (0.32 mmol, 70 %), colorless lyophilizate.

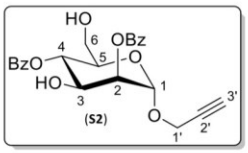

^{1}H-NMR (400 MHz, $CDCl_3$, 25 °C)**:** δ (ppm) = 8.15 – 8.04 (m, 4H, H_{ortho}), 7.65 – 7.56 (m, 2H, H_{para}), 7.52 – 7.42 (m, 4H, H_{meta}), 5.52 (t, ^3J = 10.0 Hz, 1H, H-4), 5.45 (dd, ^3J = 3.5, 1.7 Hz, 1H, H-2), 5.25 (d, ^3J = 1.7 Hz, 1H, H-1), 4.44 (dd, ^3J = 9.9, 3.5 Hz, 1H, H-3), 4.33 (d, ^4J = 2.4 Hz, 2H, H-1‘), 4.00 (ddd, ^3J = 10.1, 4.2, 2.3 Hz, 1H, H-5), 3.82 (dd, ^2J = 12.7 Hz, ^3J = 2.3 Hz, 1H, H-6a), 3.74 (d, ^2J = 12.7 Hz, ^3J = 4.2 Hz, 1H), 2.51 (t, ^4J = 2.4 Hz, 1H). **^{13}C-NMR** (101 MHz, $CDCl_3$, 25 °C)**:** δ (ppm) = 167.3 (1C, C-4-O(*C*=O)Ph), 166.0 (1C, C-2-O(*C*=O)Ph), 133.8 (1C, C-2-O(C=O)Ph, C_{para}), 133.6 (1C, C-4-O(C=O)Ph, C_{para}), 129.9 (2C, C-2-O(C=O)Ph, C_{ortho}), 129.1 (1C, C-2-O(C=O)Ph, C_{ipso}), 129.0 (1C, C-4-O(C=O)Ph, C_{ipso}), 128.6 (2C, C-2-O(C=O)Ph, C_{meta}), 128.6 (2C, C-4-O(C=O)Ph, C_{meta}), 96.6 (1C, C-1), 78.3 (1C, C-2‘), 75.5 (1C, C-3‘), 72.6 (1C, C-2), 71.1 (1C, C-5), 70.2 (1C, C-4), 68.6 (1C, C-3), 61.3 (1C, C-6), 55.3 (1C, C-1‘). **HR-MS** (ESI$^+$)**:** $m/z_{cal.}$ = 449.1207 [M+Na]$^+$, $m/z_{exp.}$ = 449.1206 [M+Na]$^+$. **Optical rotation** (LM)**:** $[\alpha]_D^{20}$ = -16.2 ($CHCl_3$). R_f (NP) = 0.30 (^{c}Hex/EtOAc 2:1). **IR** (ATR)**:** (cm^{-1}) = 3491, 3297, 2927, 1720, 1602, 1452, 1318, 1265, 1178, 1114, 1069, 1027, 1012, 971, 912, 794, 711, 686.

The analytical data follows literature data.[6]

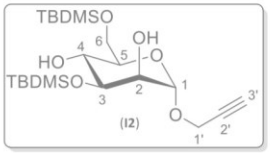

^{1}H-NMR (400 MHz, $CDCl_3$, 25 °C)**:** δ (ppm) = 5.05 (d, ^3J = 1.5 Hz, 1H, H-1), 4.24 (d, ^4J = 2.4 Hz, 2H, H-1‘), 3.91 – 3.81 (m, 3H, H-3, H-6a, H-6b), 3.79 (ddd, ^3J = 3.7, 1.5, 1.2 Hz, 1H, H-2), 3.73 (td, ^3J = 9.1, 8.6, 2.1 Hz, 1H, H-4), 3.60 (dt, ^3J = 9.1, 5.5 Hz, 1H, H-5), 2.69 (d, ^3J = 2.1 Hz, 1H, C-4-O*H*), 2.60 (d, ^3J = 1.2 Hz, 1H, C-2-O*H*), 2.43 (t, ^4J = 2.4 Hz, 1H, H-3‘), 0.92 (s, 9H, C-3-O-Si-C(CH_3)$_3$), 0.90 (s, 9H, C-6-O-Si-C(CH_3)$_3$), 0.16 (s, 3H, C-3-O-Si-CH_3), 0.14 (s, 3H, C-3-O-Si-CH_3), 0.09 (s, 6H, C-6-O-Si-CH_3). **^{13}C-NMR** (101 MHz, $CDCl_3$, 25 °C)**:** δ (ppm) = 97.6 (1C, C-1), 79.0 (1C, C-2‘), 74.9 (1C, C-3‘), 73.1 (1C, C-3), 71.2 (1C, C-2), 71.1 (1C, C-5), 70.6 (1C, C-4), 65.0 (1C, C-6), 54.2 (1C, C-1‘), 26.0 (3C, C-6-O-Si-C(*C*H$_3$)$_3$), 26.0 (3C, C-3-O-Si-C(*C*H$_3$)$_3$), 18.4 (1C, C-6-O-Si-*C*(CH$_3$)$_3$), 18.2 (1C, C-3-O-Si-*C*(CH$_3$)$_3$), -4.3 (1C, C-3-O-Si-*C*H$_3$), -4.7 (1C, C-3-O-Si-*C*H$_3$), -5.3 (1C, C-6-O-Si-*C*H$_3$), -5.3 (1C, C-6-O-Si-*C*H$_3$). **HR-MS** (ESI$^+$)**:** $m/z_{cal.}$ = 469.2412 [M+Na]$^+$, $m/z_{exp.}$ = 469.2414 [M+Na]$^+$. R_f (NP) = 0.41 (^{c}Hex/EtOAc 4:1). **Melting range:** Θ (°C) = 78.5 – 80.0 (EtOAc). **Optical rotation** (LM)**:** $[\alpha]_D^{20}$ = +58.7 ($CHCl_3$). **IR** (ATR)**:** (cm^{-1}) = 3508, 3312, 2953, 2929, 2858, 1472, 1254, 1215, 1138, 1108, 1048, 1012, 970, 916, 868, 836, 779, 671.

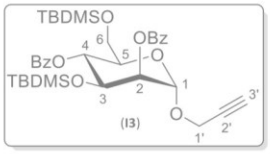

^{1}H-NMR (400 MHz, $CDCl_3$, 25 °C)**:** δ (ppm) = 8.14 – 8.10 (m, 2H, C-2-O(C=O)Ph, H_{ortho}), 8.07 – 8.02 (m, 2H, C-4-O(C=O)Ph, H_{ortho}), 7.61 – 7.54 (m, 2H, H_{para}), 7.50 – 7.41 (m, 4H, H_{meta}), 5.60 (t_{app}, ^3J = 9.8 Hz, 1H, H-4), 5.39 (dd, ^3J = 3.6, 1.8 Hz, 1H, H-2), 5.16 (d, ^3J = 1.8 Hz, 1H, H-1), 4.35 (dd, ^3J = 9.8, 3.6 Hz, 1H, H-3), 4.34 (d, ^4J = 2.4 Hz, C-1‘) 3.94 (ddd, ^3J = 9.8, 5.7, 2.8 Hz, 1H, H-5), 3.79 (dd, ^2J = 11.3 Hz, ^3J = 5.7 Hz, 1H, H-6a), 3.75 (dd, ^2J = 11.3 Hz,

^3J = 2.8 Hz, 1H, H-6b), 2.49 (t, ^4J = 2.4 Hz, 1H, H-3'), 0.86 (s, 9H, C-6-O-Si-C(CH_3)$_3$), 0.61 (s, 9H, C-3-O-Si-C(CH_3)$_3$), 0.04 (s, 3H, C-3-O-Si-CH_3), 0.00 (s, 3H, C-6-O-Si-CH_3), -0.01 (s, 3H, -C-6-O-Si-CH_3), -0.15 (s, 3H, C-3-O-Si-CH_3). **^{13}C-NMR** (101 MHz, $CDCl_3$, 25 °C)**:** δ (ppm) = 166.0 (1C, C-2-O(*C*=O)Ph), 165.3 (1C, C-4-O(*C*=O)Ph), 133.3 (1C, C-2-O(C=O)Ph, C_{para}), 133.2 (1C, C-4-O(C=O)Ph, C_{para}), 130.1 (2C, C-2-O(C=O)Ph, C_{ortho}), 130.0 (1C, C-2-O(C=O)Ph, C_{ipso}), 129.9 (1C, C-4-O(C=O)Ph, C_{ipso}), 129.9 (2C, C-4-O(C=O)Ph, C_{ortho}), 128.6 (2C, C-2-O(C=O)Ph, C_{meta}), 128.5 (2C, C-4-O(C=O)Ph, C_{meta}), 96.2 (1C, C-1), 78.6 (1C, C-2'), 75.4 (1C, C-3'), 72.6 (1C, C-2), 72.3 (1C, C-5), 70.1 (1C, C-4), 69.1 (1C, C-3), 62.9 (1C, C-6), 54.4 (1C, C-1'), 26.0 (3C, C-6-O-Si-C(CH_3)$_3$), 25.4 (3C, C-3-O-Si-C(CH_3)$_3$), 18.4 (1C, C-6-O-Si-*C*(CH_3)$_3$), 17.7 (1C, C-3-O-Si-*C*(CH_3)$_3$), -4.60 (1C, C-3-O-Si-*C*H_3), -4.98 (1C, C-3-O-Si-*C*H_3), -5.28 (1C, C-6-O-Si-*C*H_3), -5.33 (1C, C-6-O-Si-*C*H_3). **HR-MS** (ESI$^+$)**:** $m/z_{cal.}$ = 677.2936 [M+Na]$^+$, $m/z_{exp.}$ = 677.2929 [M+Na]$^+$. R_f (NP) = 0.53 (^{c}Hex/EtOAc 10:1). **Optical rotation** (LM)**:** $[\alpha]_D^{20}$ = -10.4 ($CHCl_3$). **IR** (ATR)**:** (cm^{-1}) = 2929, 2857, 1728, 1602, 1452, 1389, 1361, 1323, 1261, 1108, 1062, 1028, 990, 878, 837, 778, 710, 677.

4.1.4 Synthesis of Propargyl 2,4-Di-*O*-benzoyl-3,6-di-*O*-(2,3,4,6-tetra-*O*-acetyl-α-D-mannopyranosyl)-α-D-mannopyranoside

The title compound was synthesized according to following modified synthesis protocols by *Kanaya et al.*[23], *Ramos-Soriano et al.*[18] and *Teumelsan et al.*[19]

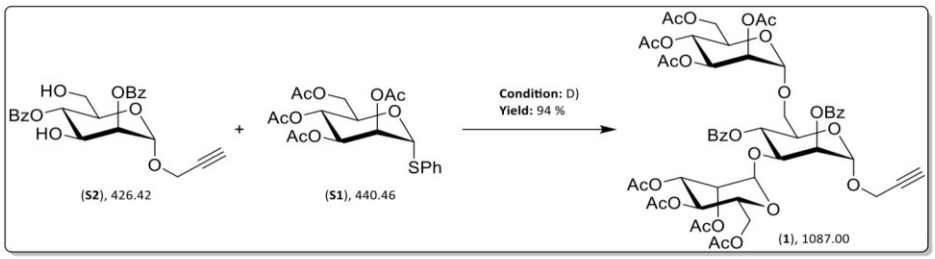

Scheme S 6: Synthesis of Propargyl 2,4-Di-*O*-benzoyl-3,6-di-*O*-(2,3,4,6-tetra-*O*-acetyl-α-D-mannopyranosyl)-α-D-mannopyranoside (1). Reaction conditions: D) NIS, AgOTf, DCM, Ar-atm., -40 °C to -20 °C, 4 h; yield: 94 %.

The reaction was carried out in a dried Schlenk vessel, which was previously fitted with a magnetic stir bar. Propargyl 2,4-Di-O-benzoyl-α-D-mannopyranoside (**1**, 0.10 g, 0.23 mmol, 1.00 eq.) and phenyl 2,3,4,6-tetra-O-acetyl-1-thio-α-D-mannopyranoside (**S1**, 0.31 g, 0.70 mmol, 3.00 eq.) were added toluene (3 x 2.50 mL) and all volatiles were removed in vacuo. The residue was dried in fine vacuum for half an hour and dissolved in absolute DCM (5.00 mL) under an atmosphere of argon. Molecular sieves (MS 3 Å, 0.25 g) were added and the solution stirred for half an hour at room temperature. The solution was cooled down to a temperature of -40 °C in an acetone bath using a cryostat. NIS (0.24 g, 1.06 mmol, 4.50 eq.) was added to the mixture in small portions. AgOTf (28.0 mg, 0.11 mmol, 0.45 eq.) was dissolved in absolute toluene (0.50 mL) under an atmosphere of argon in another dried Schlenk vessel and the solution was added to the cooled reaction mixture with a syringe. The resulting colorless suspension was stirred for two hours while slowly warming up to a temperature of -20 °C, whereby a red suspension was obtained. The reaction mixture was stirred for a further two hours at this temperature. Complete conversion of the limiting substrate and formation of the desired product were determined by reaction control via TLC and HPLC-ELS-MS. The reaction was terminated by addition of NEt_3 (0.07 g, 0.10 mL, 0.70 mmol, 3.00 eq.). The resulting orange suspension was filtered through a glass frit over *Celite* and eluted with DCM (1 x 50.0 mL). The organic phase was washed with saturated $Na_2S_2O_3$ solution (2 x 50.0 mL), saturated $NaHCO_3$ solution (2 x 50.0 mL) and saturated NaCl solution (1 x 50.0 mL), dried over anhydrous Na_2SO_4 and filtered. All volatiles were removed in vacuo and the residue was dried in fine vacuum. The crude product (0.51 g) was obtained in the form of a dark orange

oil and purified using FCC (^{c}Hex/EtOAc, gradient 0 % to 70 % to 100 % EtOAc, Isolera Four Flash Purification System, SNAP KP Sil 50 g cartridge) and RP-FCC (MeCN/H_2O, gradient 10 % to 70 % to 100 % MeCN, Isolera One Flash Purification System, SNAP C_{18} 30 g cartridge). The pure product (**1**) was obtained in the form of a colorless lyophilizate.

Yield: 0.24 g (0.22 mmol, 94 %), colorless lyophilizate.

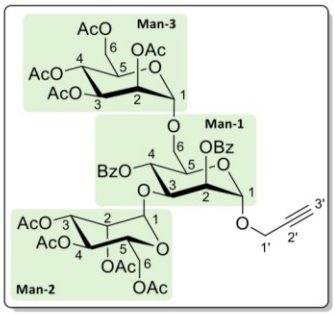

^{1}H-NMR (600 MHz, $CDCl_3$, 25 °C)**:** δ (ppm) = 8.17 – 8.13 (m, 2H, C-2$_{Man-1}$-O(C=O)Ph, H$_{ortho}$), 8.05 – 8.00 (m, 2H, C-4$_{Man-1}$-O(C=O)Ph, H$_{ortho}$), 7.65 – 7.61 (m, 1H, C-2$_{Man-1}$-O(C=O)Ph, H$_{para}$), 7.60 – 7.57 (m, 1H, C-4$_{Man-1}$-O(C=O)Ph, H$_{para}$), 7.56 – 7.52 (m, 2H, C-2$_{Man-1}$-O(C=O)Ph, H$_{meta}$), 7.47 – 7.43 (m, 2H, C-4$_{Man-1}$-O(C=O)Ph, H$_{meta}$), 5.63 (t_{app}, ^3J = 10.0 Hz, 1H, H-4$_{Man-1}$), 5.54 (dd, ^3J = 3.5, 1.8 Hz, 1H, H-2$_{Man-1}$), 5.33 (dd, ^3J = 10.1, 3.4 Hz, 1H, H-3$_{Man-3}$), 5.24 (d, ^3J = 1.8 Hz, 1H, H-1$_{Man-1}$), 5.27 – 5.21 (m, 2H, H-2$_{Man-3}$, H-4$_{Man-3}$), 5.11 – 5.06 (dd, 2H, H-3$_{Man-2}$, H-4$_{Man-2}$), 4.97 (d, ^3J = 1.9 Hz, 1H, H-1$_{Man-2}$), 4.88 – 4.85 (m, 1H, H-2$_{Man-2}$), 4.80 (d, ^3J = 1.8 Hz, 1H, H-1$_{Man-3}$), 4.49 (dd, ^3J = 9.8, 3.4 Hz, 1H, H-3$_{Man-1}$), 4.36 (d, ^4J = 2.4 Hz, 2H, H-1‘), 4.22 – 4.13 (m, 3H, H-5$_{Man-1}$, H-6a$_{Man-2}$, H-6a$_{Man-3}$), 4.11 (ddd, ^3J = 9.4, 5.7, 1.8 Hz, 1H, H-5$_{Man-2}$), 4.06 (ddd, ^3J = 10.2, 5.5, 2.1 Hz, 1H, H-5$_{Man-3}$), 4.01 (ddd, ^2J = 12.2, ^3J = 5.7, 2.0 Hz, 2H, H-6b$_{Man-2}$, H-6b$_{Man-3}$), 3.90 (dd, ^2J = 10.8 Hz, ^3J = 6.8 Hz, 1H, H-6a$_{Man-1}$), 3.61 (dd, ^2J = 10.8 Hz, ^3J = 2.2 Hz, 1H, H-6b$_{Man-1}$), 2.55 (t, ^4J = 2.4 Hz, 1H, H-3‘), 2.14 (s, 3H, C-6$_{Man-3}$-O(C=O)CH_3), 2.11 (s, 3H, C-4$_{Man-3}$-O(C=O)CH_3), 2.04 (s, 3H, C-3$_{Man-3}$-O(C=O)CH_3), 1.98 (s, 3H, C-3$_{Man-2}$-O(C=O)CH_3), 1.94 (s, 3H, C-6$_{Man-2}$-O(C=O)CH_3), 1.94 (s, 3H, C-4$_{Man-2}$-O(C=O)CH_3), 1.84 (s, 3H, C-2$_{Man-3}$-O(C=O)CH_3), 1.82 (s, 3H, C-2$_{Man-2}$-O(C=O)CH_3). **^{13}C-NMR** (151 MHz, $CDCl_3$, 25 °C)**:** δ (ppm) = 170.8 (1C, C-6$_{Man-2}$-O(*C*=O)CH$_3$), 170.6 (1C, C-6$_{Man-3}$-O(*C*=O)CH$_3$), 170.0 (1C, C-4$_{Man-3}$-O(*C*=O)CH$_3$), 169.8 (1C, C-3$_{Man-3}$-O(*C*=O)CH$_3$), 169.8 (1C, C-3$_{Man-2}$-O(*C*=O)CH$_3$), 169.7 (1C, C-4$_{Man-2}$-O(*C*=O)CH$_3$), 169.1 (1C, C-2$_{Man-3}$-O(*C*=O)CH$_3$), 169.1 (1C, C-2$_{Man-2}$-O(*C*=O)CH$_3$), 165.9 (1C, C-2$_{Man-1}$-O(*C*=O)Ph), 165.2 (1C, C-4$_{Man-1}$-O(*C*=O)Ph), 133.7 (1C, C-2$_{Man-1}$-O(C=O)Ph, C$_{para}$), 133.6 (1C, C-4$_{Man-1}$-O(C=O)Ph, C$_{para}$), 130.0 (2C, C-2$_{Man-1}$-O(C=O)Ph, C$_{ortho}$), 129.9 (2C, C-4$_{Man-1}$-O(C=O)Ph, C$_{ortho}$), 129.0 (1C, C-2$_{Man-1}$-O(C=O)Ph, C$_{ipso}$), 128.8 (2C, C-2$_{Man-1}$-O(C=O)Ph, C$_{meta}$), 128.6 (1C, C-4$_{Man-1}$-O(C=O)Ph, C$_{ipso}$), 128.5 (2C, C-4$_{Man-1}$-O(C=O)Ph, C$_{meta}$), 99.4 (1C, C-1$_{Man-2}$), 97.2 (1C, C-1$_{Man-3}$), 96.1 (1C, C-1$_{Man-1}$), 78.0 (1C, C-2‘), 75.7 (1C, C-3‘), 74.9 (1C, C-3$_{Man-1}$), 71.5 (1C, C-2$_{Man-1}$), 70.0 (1C, C-5$_{Man-1}$), 69.3 (2C, C-5$_{Man-2}$, C-2$_{Man-3}$), 69.2 (1C, C-2$_{Man-2}$), 69.0 (1C, C-3$_{Man-3}$), 68.7 (1C, C-4$_{Man-1}$), 68.6 (1C, C-5$_{Man-3}$), 68.2 (1C, C-3$_{Man-2}$), 66.7 (1C, C-6$_{Man-1}$), 66.0 (1C, C-4$_{Man-2}$), 65.8 (1C, C-4$_{Man-3}$), 62.4 (1C, C-6$_{Man-2}$), 62.3 (1C, C-6$_{Man-3}$), 55.0 (1C, C-1‘), 20.9 (1C, C-4$_{Man-3}$-O(C=O)*C*H$_3$), 20.8 (1C, C-6$_{Man-3}$-O(C=O)*C*H$_3$), 20.8 (1C, C-3$_{Man-3}$-O(C=O)*C*H$_3$), 20.7 (1C, C-6$_{Man-2}$-O(C=O)*C*H$_3$), 20.7 (1C, C-3$_{Man-2}$-O(C=O)*C*H$_3$), 20.6 (1C, C-4$_{Man-2}$-O(C=O)*C*H$_3$), 20.5 (1C, C-2$_{Man-2}$-O(C=O)*C*H$_3$), 20.5 (1C, C-2$_{Man-3}$-O(C=O)*C*H$_3$). **HR-MS** (ESI$^+$)**:** $m/z_{cal.}$ = 1109.3117 [M+Na]$^+$, $m/z_{exp.}$ = 1109.3117 [M+Na]$^+$. **Optical rotation** (LM)**:** $[\alpha]_D^{20}$ = + 12.0 ($CHCl_3$). R_f (NP) = 0.19 (^{c}Hex/EtOAc 1:1). **IR** (ATR)**:** (cm^{-1}) = 3278, 2948, 1750, 1602, 1452, 1370, 1319, 1225, 1139, 1046, 981, 916, 715, 601.

4.1.5 Synthesis of 1,11-Di[(methanesulfonyl)oxy]-3,6,9-trioxaundecane

The title compound was synthesized according to Scheme S 7 following modified synthesis protocols by *Bakleh et al.*[24] and *Kramer et al.*[6]

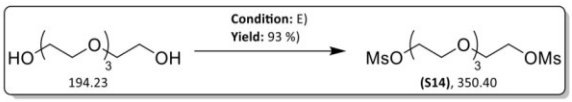

Scheme S 7: Synthesis of 1,11-Di[(methanesulfonyl)oxy]-3,6,8-trioxaundecane (**S14**). Reaction control: E) MsCl, NEt_3, DCM, Ar-atm., 0 °C to rt, 3 h; yield: 93 %.

The reaction was carried out in a dried Schlenk vessel, which was previously fitted with a magnetic stirring rod. Tetraethylene glycol (5.00 g, 25.7 mmol, 1.00 eq.) was dried in fine vacuum for half an hour with stirring and then dissolved in absolute DCM (125 mL) under an atmosphere of argon. The mixture was cooled to a temperature of 0 °C in an ice bath. Successively, MsCl (6.49 g, 4.38 mL, 56.6 mmol, 2.20 eq.) and NEt_3 (7.81 g, 10.8 mL 77.2 mmol, 3.00 eq.) were added slowly with stirring. The reaction mixture was stirred for three hours while slowly warming up to room temperature. Complete conversion of the limiting substrate and formation of the desired product were determined by reaction control via TLC and HPLC-ELS-MS. The reaction was terminated by the addition of ice-cooled H_2O (1 x 125 mL). The organic phase was separated and washed with ice-cooled 2 M HCl (1 x 125 mL), saturated $NaHCO_3$ solution (1 x 125 mL) and saturated NaCl solution (1 x 125 mL). The organic phase was dried over anhydrous Na_2SO_4, filtered and all volatile components were removed in vacuo. The residue was dried in a fine vacuum. The pure product (**S14**) was obtained in the form of yellowish oil.

Yield: 8.37 g (23.9 mmol, 93 %), (Lit.[6, 24]: 98 %), yellowish oil.

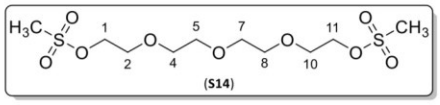

^{1}H-NMR (400 MHz, $CDCl_3$, 25 °C)**:** δ (ppm) = 4.38 – 4.34 (m, 4H, H-1, H-11), 3.77 – 3.73 (m, 4H, H-2, H-10), 3.67 – 3.60 (m, 8H, H-4, H-5, H-7, H-8), 3.06 (s, 6H, -C*H*$_3$). **^{13}C-NMR** (101 MHz, $CDCl_3$, 25 °C)**:** δ (ppm) = 70.7 (2C, C-5, C-7), 70.6 (2C, C-4, C-8), 69.4 (2C, C-2, C-10), 69.1 (2C, C-1, C-11), 37.7 (2C, -*C*H$_3$). **HR-MS** (ESI$^+$)**:** $m/z_{cal.}$ = 373.0597 [M+Na]$^+$, $m/z_{exp.}$ = 373.0600 [M+Na]$^+$. R_f (NP) = 0.08 (^{c}Hex/EtOAc 1:2). **IR** (ATR)**:** (cm^{-1}) = 3026, 2877, 1454, 1346, 1249, 1172, 1134, 1108, 1015, 974, 919, 803, 732, 528, 483, 456, 420.

The analytical data follows literature data.[6, 24]

4.1.6 Synthesis of 1,11-Diazido-3,6,9-trioxaundecane

The title compound was synthesized according to Scheme S 8 following modified synthesis protocols by *Bakleh et al.*[24] and *Kramer et al.*[6]

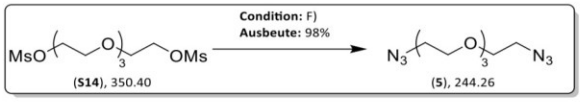

Scheme S 8: Synthesis of 1,11-Diazido-3,6,9-trioxaundecane (**5**). Reaction conditions: F) NaN_3, TBAI, DMF, Ar-atm., 80 °C, 4 h; yield: 98 %.

The reaction was carried out in a dried Schlenk vessel, which was previously fitted with a magnetic stir bar. 1,11-Di[(methanesulfonyl)oxy]-3,6,9-trioxaundecane (**S14**, 2.00 g, 5.71 mmol, 1.00 eq.) was dissolved in absolute DMF (10.0 mL) under atmosphere of argon. NaN_3 (0.93 g, 14.3 mmol, 2.50 eq.) and TBAI (0.11 g, 0.29 mmol, 0.05 eq.) were added. The orange reaction mixture was stirred for four hours at a temperature of 80 °C, resulting in a colorless precipitation. Complete conversion of the limiting substrate and formation of the desired product were determined by reaction control via TLC and HPLC-ELS-MS. The mixture was filtered over *Celite* and eluted with Et_2O (1 x 50.0 mL). All

volatiles were removed first in vacuo and then in fine vacuum. Toluene (3 x 50.0 mL) was added to the residue and again all volatiles were removed in fine vacuum. The residue was dissolved in Et_2O (1 x 50.0 mL) and filtered through *Celite* to remove insoluble salts. All volatiles were removed in vacuo and the residue was dried in fine vacuum. The pure product (**5**) was obtained in the form of yellowish oil.

Yield: 1.37 g (5.61 mmol, 98 %), (Lit.[6, 24]: 98 %), yellowish oil.

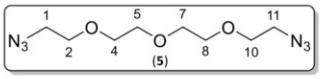

^{1}H-NMR (300 MHz, $CDCl_3$, 25 °C)**:** δ (ppm) = 3.72 – 3.63 (m, 12H, H-2, H-4, H-5, H-7, H-8, H-10), 3.38 (t, ^3J = 5.1 Hz, 4H, H-1, H-11). **^{13}C-NMR** (75.5 MHz, $CDCl_3$, 25 °C)**:** δ (ppm) = 70.8 (4C, C-4, C-5, C-7, C-8), 70.2 (2C, C-2, C-10), 50.8 (2C, C-1, C-11). **HR-MS** (ESI^+)**:** $m/z_{cal.}$ = 267.1176 $[M+Na]^+$, $m/z_{exp.}$ = 267.1175 $[M+Na]^+$. R_f (NP) = 0.37 (cHex/EtOAc 2:1). **IR** (ATR)**:** (cm^{-1}) = 2868, 2097, 1443, 1346, 1285, 1122, 992, 936, 853, 648, 556, 436, 419.

The analytical data follows literature data.[6, 24-26]

4.1.7 Synthesis of 11-Amino-1-azido-3,6,9-trioxaundecane

The title compound was synthesized according to Scheme S 9 following modified synthesis protocols *Bakleh et al.*[24] and *Krumb et al.*[26]

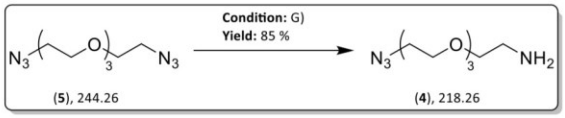

Scheme S 9: Synthesis of 11-Amino-1-azido-3,6,9-trioxaundecane (**4**). Reaction conditions: A) PPh_3, Et_2O/THF/1 M HCl (8:1:4), rt, 48 h; yield: 85 %.

The reaction was carried out in a reaction vessel, which was previously equipped with a magnetic stirring bar. 1,11-Diazido-3,6,9-trioxaundecane (**5**, 3.00 g, 12.3 mmol, 1.00 eq.) was dissolved in a mixture of Et_2O (20.0 mL) and THF (5.00 mL). An aqueous 1 M HCl solution (20.0 mL) was added to the yellowish solution. PPh_3 (3.22 g, 12.3 mmol, 1.00 eq.) was dissolved in Et_2O (20.0 mL) and added to the mixture within one hour using a dropping funnel, accompanied by decolorization of the reaction mixture. The reaction solution was stirred for 48 hours at room temperature. Complete conversion of the limiting substrate and formation of the iminophosphorane intermediate and the byproduct triphenylphosphine oxide were observed by reaction control via TLC and HPLC-ELS-MS. A two-phase mixture with colorless organic and yellowish aqueous phase was obtained. The organic phase was discarded, and the aqueous phase extracted with Et_2O (5 x 50.0 mL) until the byproduct could no longer be detected by TLC. The aqueous phase was adjusted to a pH of 14 while stirring using ground NaOH pellets and then extracted with DCM (5 x 50.0 mL). The collected organic phases were dried over anhydrous Na_2SO_4 and filtered. All volatile components were removed in a vacuum and the residue was dried in fine vacuum. The crude product (3.56 g) was obtained in the form of yellowish oil and purified by FCC (DCM/MeOH + NEt_3, isocratic at 5 % MeOH and 1 $\%_{v/v}$ additive). The pure product (**4**) was obtained in the form of yellowish oil.

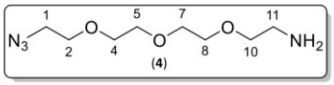

^{1}H-NMR (300 MHz, $CDCl_3$, 25 °C)**:** δ (ppm) = 3.67 – 3.55 (m, 10H, H-2, H-4, H-5, H-7, H-8), 3.48 (t, ^3J = 5.2 Hz, 2H, H-11), 3.36 (t, ^3J = 5.1 Hz, 2H, H-1), 2.83 (t, ^3J = 5.2 Hz, 2H, H-10), 1.89 (s, 2H, $-NH_2$). **^{13}C-NMR** (75.5 MHz, $CDCl_3$, 25 °C)**:** δ (ppm) = 73.1 (1C, C-11), 70.7, 70.6, 70.6, 70.2, 70.0 (5C, C-2, C-4, C-5, C-7, C-8), 50.6 (1C, C-1), 41.6 (1C, C-10). **HR-MS** (ESI^+)**:** $m/z_{cal.}$ = 219.1452 $[M+H]^+$, $m/z_{exp.}$ = 219.1457 $[M+H]^+$. R_f (NP) = 0.25 (DCM/MeOH + NEt_3 20:1 + 1 $\%_{v/v}$ additive). **IR** (ATR)**:** (cm^{-1}) = 3366, 2866, 2098, 1593, 1454, 1348, 1286, 1105, 932, 851, 729, 644, 557.

The analytical data follows literature data.[24, 26]

4.1.8 Synthesis of *tert*-Butyl-12-Hydroxy-4,7,10-trioxadodecanoate

The title compound was synthesized according to Scheme S 10 following modified synthesis protocols by *Tavernaro et al.*[27] and *Krumb et al.*[26]

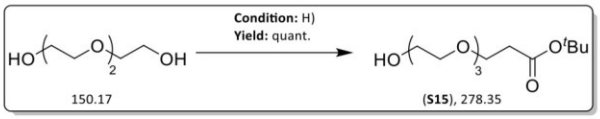

Scheme S 10: Synthesis of *tert*-Butyl-12-Hydroxy-4,7,10-trioxadodecanoate (**S15**). Reaction conditions H) TBA, Na, THF, Ar-atm., rt, 22 h; yield: quant.

The reaction was carried out in a dried Schlenk vessel, which was previously fitted with a magnetic stirring bar. Triethylene glycol (5.00 g, 4.46 mL, 33.3 mmol, 3.30 eq.) was dried in fine vacuum for half an hour with stirring and then dissolved in absolute THF (25.0 mL) under an atmosphere of argon. Elemental sodium (23.0 mg, 1.00 mmol, 0.03 eq.) was added with stirring and completely dissolved. TBA (1.29 g, 1.47 mL, 10.1 mmol, 1.00 eq.) was then added dropwise with syringe to the yellowish solution. The reaction was stirred for 22 hours in the absence of light at room temperature. Complete conversion of the limiting substrate and formation of the desired product were determined by reaction control via TLC and HPLC-ELS-MS. A 1 M HCl solution (1 x 1.30 mL) was added while stirring. All volatile components were removed in vacuo and the residue was dried in fine vacuum. The crude product (6.40 g) was obtained in the form of yellowish oil and dissolved in saturated NaCl solution (50.0 mL). The aqueous phase was extracted with EtOAc (4 x 50 mL). The collected organic phases were dried over anhydrous Na_2SO_4 and filtered. All volatiles were removed in vacuo and the residue was dried in a fine vacuum. The pure product (**S15**) was obtained in the form of colorless oil.

Yield: 2.81 g (10.1 mmol, quant.), (Lit.[26, 27]: 86 – 100 %), colorless oil.

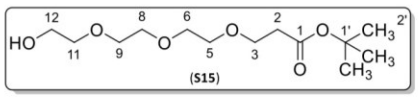

^{1}H-NMR (300 MHz, $CDCl_3$, 25 °C)**:** δ (ppm) = 3.77 – 3.73 (m, 2H, H-12), 3.73 – 3.71 (m, 2H, H-3), 3.71 – 3.62 (m, 8H, H-5, H-6, H-8, H-9), 3.62 – 3.59 (m, 2H, H-11), 2.51 (t, ^3J = 6.6 Hz, 2H, H-2), 1.44 (s, 9H, H-2'). **^{13}C-NMR** (75.5 MHz, $CDCl_3$, 25 °C)**:** δ (ppm) = 170.9 (1C, C-1), 80.6 (1C, C-1'), 72.5 (1C, C-11), 70.6, 70.5, 70.4, 70.4 (4C, C-5, C-6, C-8, C-9), 66.9 (1C, C-3), 61.8 (1C, C-12), 36.2 (1C, C-2), 28.1 (3C, C-2'). **HR-MS** (ESI$^+$)**:** $m/z_{cal.}$ = 279.1802 $[M+H]^+$, $m/z_{exp.}$ = 279.1803 $[M+H]^+$; $m/z_{cal.}$ = 301.1622 $[M+Na]^+$, $m/z_{exp.}$ = 301.1629 $[M+Na]^+$. R_f (NP) = 0.13 (^{c}Hex/EtOAc 1:1). **IR** (ATR)**:** (cm^{-1}) = 3459, 2872, 1729, 1456, 1393, 1368, 1254, 1160, 1120, 1069, 939, 887, 847, 475.

The analytical data follows literature data.[26, 27]

4.1.9 Synthesis of *tert*-Butyl-12-[(*p*-toluenesulfonyl)oxy]-4,7,10-trioxadodecanoate

The title compound was synthesized according to Scheme S 11 following modified synthesis protocols by *Tsakama et al.*[28] and *Krumb et al.*[26]

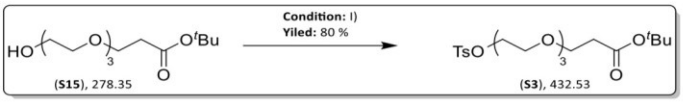

Scheme S 11: Synthesis of *tert*-Butyl-12-[(*p*-toluenesulfonyl)oxy]-4,7,10-trioxadodecanoate (**S3**). Reaction conditions: A) TsCl, NEt_3, DCM, Ar-atm., rt, 23 h; yield: 80 %.

The reaction was carried out in a dried Schlenk vessel, which was previously fitted with a magnetic stirring bar. *tert*-Butyl-12-Hydroxy-4,7,10-trioxadodecanoate (**S15**, 2.66 g, 9.56 mmol, 1.00 eq.) was

dissolved in absolute DCM (12.0 mL) under an atmosphere of argon and NEt_3 (2.32 g, 3.17 mL, 22.9 mmol, 2.40 eq.) was added. The solution was cooled to a temperature of 0 °C in an ice bath and TsCl (3.64 g, 19.1 mmol, 2.00 eq.) was added slowly. The reaction mixture was stirred for 23 hours at room temperature, resulting in a dark orange solution and formation of a colorless precipitate. Complete conversion of the limiting substrate and formation of the desired product were determined by reaction control via TLC and HPLC-ELS-MS. The precipitate was separated by filtration over *Celite* through a glass frit and eluted with DCM (1 x 100 mL). The resulting organic phase was washed with H_2O (3 x 100 mL) and saturated NaCl solution (1 x 100 mL). The collected aqueous phases were extracted with DCM (2 x 100 mL) and the collected organic phases were dried over anhydrous Na_2SO_4 and filtered. All volatile components were removed in vacuo and the residue was dried in fine vacuum. The crude product (5.43 g) was obtained in the form of an orange oil and purified using FCC (^{c}Hex/EtOAc, gradient 0 % to 35 % to 100 % EtOAc, Isolera Four Flash Purification System, SNAP KP-Sil 100 g cartridge). The pure product (**S3**) was obtained in the form of yellowish oil.

Yield: 3.32 g (7.65 mmol, 80 %), (Lit.[26, 28]: 69 %), yellowish oil.

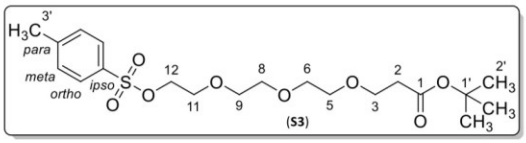

^{1}H-NMR (400 MHz, $CDCl_3$, 25 °C)**:** δ (ppm) = 7.82 – 7.77 (m, 2H, H_{ortho}), 7.36 – 7.32 (m, 2H, H_{meta}), 4.18 – 4.11 (m, 2H, H-12), 3.72 – 3.62 (m, 4H, H-3, H-11), 3.62 – 3.51 (m, 8H, H-5, H-6, H-8, H-9), 2.49 (t, ^3J = 6.6 Hz, 2H, H-2), 2.45 (s, 3H, H-5'), 1.44 (s, 9H, H-2'). **^{13}C-NMR** (101 MHz, $CDCl_3$, 25 °C)**:** δ (ppm) = 170.9 (1C, C-1), 144.8 (1C, C_{para}), 133.0 (1C, C_{ipso}), 129.8 (2C, C_{meta}), 128.0 (2C, C_{ortho}), 80.5 (1C, C-1'), 70.8, 70.5, 70.3, 69.2 (5C, C-5, C-6, C-8, C-9, C-12), 68.7 (1C, C-11), 66.9 (1C, C-3), 36.2 (1C, C-2), 28.1 (1C, C-2'), 21.6 (1C, C-3'). **HR-MS** (ESI^+)**:** $m/z_{cal.}$ = 455.1710 $[M+Na]^+$, $m/z_{exp.}$ = 455.1710 $[M+Na]^+$. R_f (NP) = 0.22 (^{c}Hex/EtOAc 2:1). **IR** (ATR)**:** (cm^{-1}) = 2875, 1728, 1598, 1454, 1359, 1290, 1253, 1190, 1177, 1118, 1098, 1018, 923, 817, 776, 664, 583, 555.

The analytical data follows literature data.[26, 28]

4.1.10 Synthesis of *tert*-Butyl-12-azido-4,7,10-trioxadodecanoate

The title compound was synthesized according to Scheme S 12 following modified synthesis protocols by *Tavernaro et al.*[27] and *Krumb et al.*[26]

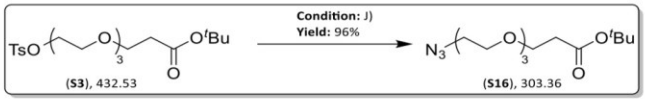

Scheme S 12: Synthesis of *tert*-Butyl-12-azido-4,7,10-trioxadodecanoate (**S16**). Reaction conditions: J) NaN_3, DMF, Ar-atm., rt, 21 h; yield: 96 %.

The reaction was carried out in a dried Schlenk vessel previously equipped with a magnetic stirring bar. *tert*-Butyl-12-[(p-toluenesulfonyl)oxy]-4,7,10-trioxadodecanoate (**S3**, 3.14 g, 7.26 mmol, 1.00 eq) was dissolved in absolute DMF (30.0 mL) under an atmosphere of argon. NaN_3 (0.61 g, 9.44 mmol, 1.30 eq.) was added. The reaction mixture was stirred for 21 hours at 60 °C, resulting in a yellowish solution. Complete conversion of the limiting substrate and formation of the desired product were determined by reaction control via TLC and HPLC-ELS-MS. All volatiles were removed in fine vacuum. Toluene (3 x 10.0 mL) was added to the residue and all volatiles were again removed in fine vacuum. The crude product (3.86 g) was obtained in the form of orange oil and dissolved in H_2O (1 x 100 mL). The aqueous phase was extracted with Et_2O (3 x 50.0 mL). The collected organic phases were dried over anhydrous Na_2SO_4 and filtered. All volatiles were removed in vacuo, and the residue was dried in fine vacuum. The pure product (**S16**) was obtained in the form of yellowish oil.

Yield: 2.11 g (6.97 mmol, 96 %), (Lit.[26, 27]: 57 – 91 %), yellowish oil.

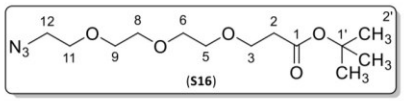

^{1}H-NMR (400 MHz, $CDCl_3$, 25 °C)**:** δ (ppm) = 3.73 – 3.69 (m, 2H, H-3), 3.69 – 3.66 (m, 2H, H-11), 3.66 – 3.58 (m, 8H, H-5, H-6, H-8, H-9), 3.38 (t, ^3J = 5.1 Hz, 2H, H-12), 2.49 (t, ^3J = 6.6 Hz, 2H, H-2), 1.44 (s, 9H, H-2‘). **^{13}C-NMR** (101 MHz, $CDCl_3$, 25 °C)**:** δ (ppm) = 170.9 (1C, C-1), 80.5 (1C, C-1‘), 70.7, 70.6, 70.6, 70.4 (4C, C-5, C-6, C-8, C-9), 70.0 (1C, C-11), 66.9 (1C, C-3), 50.7 (1C, C-12), 36.3 (1C, C-2), 28.1 (1C, C-2‘). **HR-MS** (ESI$^+$)**:** $m/z_{cal.}$ = 326.1686 $[M+Na]^+$, $m/z_{exp.}$ = 326.1692 $[M+Na]^+$; $m/z_{cal.}$ = 327.1716 $[M(^{13}C)+Na]^+$, $m/z_{exp.}$ = 327.1720 $[M(^{13}C)+Na]^+$. R_f (NP) = 0.26 (^{c}Hex/EtOAc 3:1). **IR** (ATR)**:** (cm^{-1}) = 2870, 2104, 1729, 1456, 1393, 1367, 1283, 1255, 1120, 940, 848, 557.

The analytical data follows literature data.[26, 27]

4.1.11 Synthesis of 12-Azido-4,7,10-trioxadodecanic acid

The title compound was synthesized according to Scheme S 13 following modified synthesis protocols by *Landeros et al.*[29] sowie *Krumb et al.*[26]

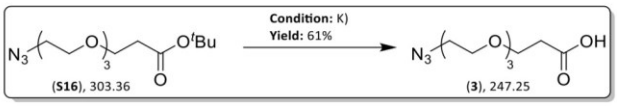

Scheme S 13: Synthesis of 12-Azido-4,7,10-trioxadodecanic acid (**3**). Reaction conditions: K) TFA, DCM, Ar-atm., rt, 22 h; yield: 61 %.

The reaction was carried out in a dried Schlenk vessel previously equipped with a magnetic stirring bar. *tert*-Butyl-12-azido-4,7,10-trioxadodecanoic acid (**S16**, 1.00 g, 3.30 mmol, 1.00 eq.) was dissolved in absolute DCM (5.00 mL) under an atmosphere of argon. TFA (1.51 g, 1.02 mL, 13.2 mmol, 4.00 eq.) was added dropwise to the yellowish solution using a syringe. The reaction mixture was stirred for 22 hours. Complete conversion of the limiting substrate and the formation of the desired product were determined by reaction control via TLC and HPLC-ELS-MS. All volatiles were removed in fine vacuum. Toluene (3 x 10.0 mL) was added to the residue and all volatiles were again removed in fine vacuum. The crude product (0.62 g) was obtained as an orange oil and purified by FCC (^{c}Hex/EtOAc + HCOOH, isocratic at 75 % EtOAc and 1 %$_{v/v}$ additive). The pure product (**3**) was obtained in the form of colorless oil.

Yield: 0.50 g (2.02 mmol, 61 %), (Lit.[26, 29]: 41 – 94 %), colorless oil.

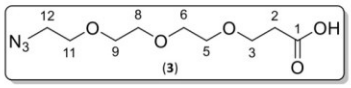

^{1}H-NMR (300 MHz, $CDCl_3$, 25 °C)**:** δ (ppm) = 3.76 (t, ^3J = 6.3 Hz, 2H, H-3), 3.71 – 3.62 (m, 10H, H-5, H-6, H-8, H-9, H-11), 3.39 (t, ^3J = 5.1 Hz, 2H, H-12), 2.64 (t, ^3J = 6.3 Hz, 2H, H-2). **^{13}C-NMR** (75.5 MHz, $CDCl_3$, 25 °C)**:** δ (ppm) = 176.2 (1C, C-1), 70.6, 70.6, 70.4 (4C, C-5, C-6, C-8, C-9), 70.0 (1C, C-11), 66.3 (1C, C-3), 50.7 (1C, C-12), 34.8 (1C, C-2). **HR-MS** (ESI$^+$)**:** $m/z_{ber.}$ = 270.1060 $[M+Na]^+$, $m/z_{exp.}$ = 270.1072 $[M+Na]^+$, $m/z_{Dif.}$ = 4.44 ppm. R_f (NP) = 0.30 (^{c}Hex/EtOAc + HCOOH 1:3 + 1 % additive). **IR** (ATR)**:** (cm^{-1}) = 3489, 2876, 2195, 2105, 1960, 1731, 1442, 1349, 1285, 1192, 1118, 938, 835.

The analytical data follows literature data.[26, 29]

4.1.12 Synthesis of *tert*-Butyl-6-amino-6-(1-*tert*-butyl-4-oxapentanoate-5-yl)-4,8-dioxa-undecane-1,11-dioate

The title compound was synthesized according to Scheme S 14 following modified synthesis protocols by *Cardona et al.*[32], *Appel et al.*[31] sowie *Krumb et al.*[26]

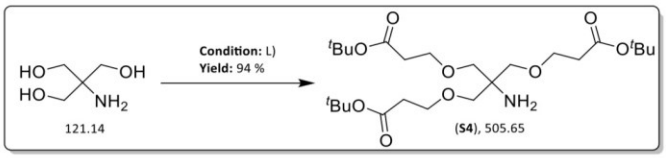

Scheme S 14: Synthesis of *tert*-Butyl-6-amino-6-(1-*tert*-butyl-4-oxapentanoate-5-yl)-4,8-dioxaundecane-1,11-dioate (**S4**). Reaction conditions: L) TBA, NaOH (5 M), DMSO, Ar-atm., 0 °C to rt, 96 h; yield: 94 %.

The reaction was carried out in a dried Schlenk flask previously equipped with a magnetic stirring bar. NaOH (0.10 g, 2.50 mmol, 0.12 eq.) was dissolved in H_2O (0.50 mL) under an atmosphere of argon and this 5 M NaOH solution was degassed in an ultrasonic bath with an argon stream for 30 minutes. TRIS (2.50 g, 20.6 mmol, 1.00 eq.) was dissolved in absolute DMSO (5.00 mL) under an atmosphere of argon and the solution was degassed in an ultrasonic bath with an argon stream for 30 minutes. The latter solution was cooled to 0 °C in an ice bath, and the ice bath was removed. Once the solidified solution had melted, the 5 M NaOH solution was added with stirring using a syringe. After the addition was complete, TBA (26.4 g, 29.9 mL, 206 mmol, 10.0 eq.) was added dropwise to the mixture. The reaction mixture was stirred at room temperature under exclusion of light for 96 hours, resulting in a milky, cloudy solution. Complete conversion of the limiting substrate and the formation of the desired product were determined by reaction control via TLC and HPLC-ELS-MS. All volatiles were removed in fine vacuum. Toluene (3 x 10.0 mL) was added to the residue and all volatiles were again removed under medium vacuum. Further volatiles were removed by lyophilization. The residue was dissolved in EtOAc (1 x 100 mL), and the organic phase was washed with saturated NaCl solution (3 x 100 mL), dried over anhydrous Na_2SO_4, and filtered. All volatiles were removed under reduced pressure, and the residue was dried in fine vacuum. The crude product (10.6 g) was obtained as a colorless oil and purified by FCC (^{c}Hex/EtOAc + NEt_3, isocratic at 25 % EtOAc and 5 %$_{v/v}$ additive). The pure product (**S4**) was obtained in the form of colorless oil.

Yield: 9.81 g (19.4 mmol, 94 %), (Lit.[26, 31, 32]: 33-50 %), colorless oil.

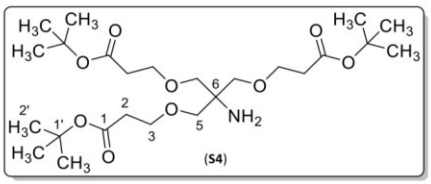

^{1}H-NMR (400 MHz, $CDCl_3$, 25 °C)**:** δ (ppm) = 3.63 (t, ^3J = 6.4 Hz, 6H, H-3), 3.30 (s, 6H, H-5), 2.45 (t, ^3J = 6.4 Hz, 6H, H-2), 1.65 (s, 2H, -N*H*$_2$), 1.44 (s, 27H, H-2'). **^{13}C-NMR** (101 MHz, $CDCl_3$, 25 °C)**:** δ (ppm) = 171.1 (3C, C-1), 80.6 (3C, C-1'), 73.0 (3C, C-5), 67.3 (3C, C-3), 56.1 (1C, C-6), 36.5 (3C, C-2), 28.2 (9C, C-2'). **HR-MS** (ESI$^+$)**:** $m/z_{cal.}$ = 506.3324 $[M+H]^+$, $m/z_{exp.}$ = 506.3318 $[M+H]^+$; $m/z_{cal.}$ = 507.3357 $[M(^{13}C)+H]^+$, $m/z_{exp.}$ = 507.3348 $[M(^{13}C)+H]^+$; $m/z_{cal.}$ = 528.3143 $[M+Na]^+$, $m/z_{exp.}$ = 528.3134 $[M+Na]^+$; $m/z_{cal.}$ = 529.3176 $[M(^{13}C)+Na]^+$, $m/z_{exp.}$ = 529.3167 $[M(^{13}C)+Na]^+$. R_f = 0.46 (^{c}Hex/EtOAc + NEt_3 3:1 + 5 %$_{v/v}$ additive). **IR** (ATR)**:** (cm^{-1}) = 2979, 2874, 2255, 1725, 1458, 1393, 1367, 1331, 1255, 1157, 1110, 1069, 907, 846, 728, 648, 464.

The analytical data follows literature data.[26, 31]

Supporting Information

4.1.13 Synthesis of 2-Nitrobenzyl-(6-(1-*tert*-butyl-4-oxapentanoat-5-yl)-4,8-dioxa-1,11-di-*tert*-butylundecanoat-6-yl)-carbamate

The title compound was synthesized utilizing a telescoped two-step procedure according to Scheme S 15 following modified synthesis protocols by *Odaka et al.*[34], *Baldoli et al.*[33] and *Krumb et al.*[26]

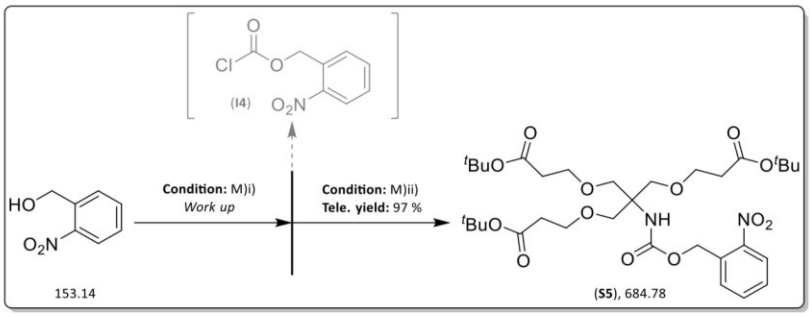

Scheme S 15: Synthesis of 2-Nitrobenzyl-(6-(1-*tert*-butyl-4-oxapentanoate-5-yl)-4,8-dioxa-1,11-di-*tert*-butylundecanoate-6-yl)-carbamate (**S5**). Reaction conditions: M)i) TCF, THF, 66 °C, 4 h; M)ii) (**S4**), $NaHCO_3$, EtOAc/H_2O (2:1), RT, 18 h; telescoped yield: 97 %.

The reaction was carried out in a dried Schlenk vessel previously equipped with a magnetic stirring bar. (2-Nitrophenyl)methanol (0.45 g, 2.94 mmol, 1.50 eq.) was dissolved in absolute THF (20.0 mL) under an atmosphere of argon. TCF (0.58 g, 0.35 mL, 2.94 mmol, 1.50 eq.) was slowly added dropwise with a syringe. The yellow reaction solution was stirred for four hours while heated to reflux, with a color change to orange occurring. Complete conversion of the limiting substrate and the formation of the desired product were determined by reaction control via TLC and HPLC-ELS-MS. All volatiles were removed in vacuo and the residue was dried in fine vacuum. The residue (1.12 g) was obtained in the form of an orange oil and dissolved in DCM (50.0 mL). The organic phase was washed with H_2O (2 x 25.0 mL) and saturated NaCl solution (1 x 25.0 mL), dried over anhydrous Na_2SO_4, and filtered. All volatiles were removed in vacuo, and the residue was dried in fine vacuum. The intermediate (0.69 g) was obtained in the form of yellow oil and dissolved in EtOAc (1.00 mL). *tert*-Butyl-6-amino-6-(1-*tert*-butyl-4-oxapentanoate-5-yl)-4,8-dioxaundecane-1,11-dioate (**S4**, 1.00 g, 1.98 mmol, 1.00 eq.) and $NaHCO_3$ (0.33 g, 3.93 mmol, 2.00 eq.) were dissolved in a mixture of EtOAc (2.60 mL) and H_2O (1.80 mL) with stirring. The solution of the intermediate was added dropwise via syringe. The resulting yellow reaction mixture was stirred for 18 hours at room temperature. Complete conversion of the limiting substrate and the formation of the desired product were determined by reaction control via TLC and HPLC-ELS-MS. The reaction mixture was diluted with EtOAc (1 x 50.0 mL) and washed with H_2O (1 x 10.0 mL). The aqueous phase was extracted with EtOAc (3 x 30.0 mL). The collected organic phases were washed with H_2O (1 x 30.0 mL) and saturated NaCl solution (1 x 30.0 mL), dried over anhydrous Na_2SO_4, and filtered. All volatiles were removed in vacuo, and the residue was dried in fine vacuum. The crude product (1.52 g) was obtained as a yellowish oil and purified by FCC (^{c}Hex/EtOAc, isocratic at 20 % EtOAc). The pure product (**S5**) was obtained in the form of colorless oil.

Yield: 1.31 g (1.91 mmol, 97 %), colorless oil.

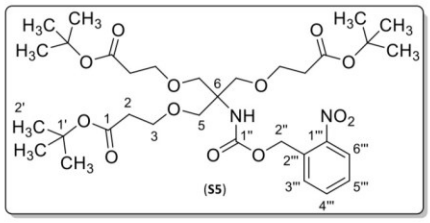

^{1}H-NMR (400 MHz, $CDCl_3$, 25 °C)**:** δ (ppm) = 8.15 – 8.08 (m, 1H, H-6'''), 7.67 – 7.66 (m, 1H, H-5'''), 7.66 – 7.64 (m, 1H, H-3'''), 7.50 – 7.38 (m, 1H, H-4'''), 5.51 (s, 1H, -N*H*-), 5.47 (s, 2H, H-2''), 3.66 (s, 6H, H-5), 3.64 (d, ^3J = 6.3 Hz, 6H, H-3), 2.45 (t, ^3J = 6.3 Hz, 6H, H-2), 1.44 (s, 27H, H-2'). **^{13}C-NMR** (101 MHz, $CDCl_3$, 25 °C)**:** δ (ppm) = 170.8 (3C, C-1), 154.4 (1C, C-1''), 147.0 (1C,

C-1'''), 134.0 (1C, C-2'''), 133.8 (1C, C-3'''), 128.2 (1C, C-5'''), 128.1 (1C, C-4'''), 124.9 (1C, C-6'''), 80.5 (1C, C-1'), 69.3 (1C, C-5), 67.1 (1C, C-3), 62.6 (1C, C-2''), 58.8 (1C, C-6), 36.2 (1C, C-2), 28.1 (1C, C-2'). **HR-MS** (ESI$^+$)**:** $m/z_{cal.}$ = 707.3362 $[M+Na]^+$, $m/z_{exp.}$ = 707.3352 $[M+Na]^+$. R_f (NP) = 0.28 (^{c}Hex/EtOAc 5:1). **IR** (ATR)**:** (cm^{-1}) = 2978, 2930, 2870, 2252, 2246, 1725, 1528, 1440, 1347, 1266, 1159, 1109, 905, 860, 808, 786, 725, 649, 480.

The analytical data follows literature data.[26]

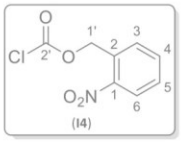

^{1}H-NMR (400 MHz, $CDCl_3$, 25 °C)**:** δ (ppm) = 8.21 – 8.18 (m, 1H, H-6), 7.77 – 7.70 (m, 1H, H-4), 7.67 – 7.63 (m, 1H, H-3), 7.61 – 7.54 (m, 1H, H-5), 5.75 (s, 2H, H-1'). **^{13}C-NMR** (101 MHz, $CDCl_3$, 25 °C)**:** δ (ppm) = 150.5 (1C. C-2''), 147.1 (1C, C-1), 134.3 (1C, C-4), 129.7 (1C, C-5), 129.6 (1C, C-2), 129.0 (1C, C-3), 125.5 (1C, C-6), 69.5 (1C, C-1'). **HR-MS** (ESI$^+$)**:** $m/z_{cal.}$ = 136.0399 $[M-O(C=O)Cl]^+$, $m/z_{exp.}$ = 136.0396 $[M-O(C=O)Cl]^+$. R_f (NP) = 0.65 (^{c}Hex/DCM 1:3). **IR** (ATR)**:** (cm^{-1}) = 1775, 1526, 1344, 1309, 1138, 857, 791, 729, 686.

The analytical data follows literature data.[47]

4.1.14 Synthesis of 2-Nitrobenzyl-(6-(1-carboxy-4-oxapentan-5-yl)-4,8-dioxa-1-11-dicarboxyundecan-6-yl)-carbamate

The title compound was synthesized according to Scheme S 16 following modified synthesis protocols by *Landeros et al.*[29], *Spritzer et al.*[35] and *Krumb et al.*[26]

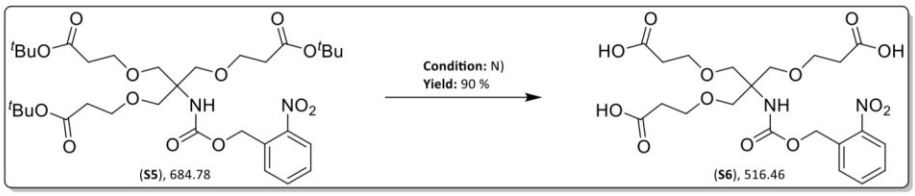

Scheme S 16: Synthesis of 2-Nitrobenzyl-(6-(1-carboxy-4-oxapentan-5-yl)-4,8-dioxa-1-11-dicarboxyundecan-6-yl)-carbamate (**S6**). Reaction conditions: N) TFA, DCM, rt, 72 h; yield: 90 %.

The reaction was carried out in a dried Schlenk vessel previously equipped with a magnetic stirring bar. 2-Nitrobenzyl-(6-(1-*tert*-butyl-4-oxapentanoate-5-yl)-4,8-dioxa-1,11-di-*tert*-butylundecanoate-6-yl)-carbamate (**S5**, 3.25 g, 4.75 mmol, 1.00 eq.) was dissolved in absolute DCM (20.0 mL) under an atmosphere of argon. TFA (5.42 g, 3.66 mL, 47.5 mmol, 10.0 eq.) was slowly added dropwise via syringe, and the reaction mixture was stirred for 72 hours at room temperature. Complete conversion of the limiting substrate and the formation of the desired product were determined by reaction control via TLC and HPLC-ELS-MS. All volatiles were removed under in vacuo. Toluene (3 x 20.0 mL) was added to the residue and all volatiles were again removed under reduced pressure and the residue dried in fine vacuum. The crude product (2.54 g) was obtained in the form of a yellowish oil and purified by FCC (^{c}Hex/EtOAc + HCOOH, isocratic at 66 % EtOAc and 1 %$_{v/v}$ additive). The pure product (**S6**) was obtained in the form of colorless oil.

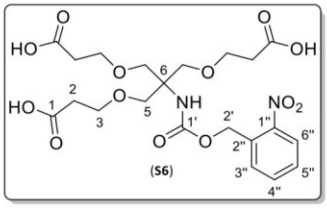

^{1}H-NMR (400 MHz, $(CD_3)_2SO$, 25 °C)**:** δ (ppm) = 8.16 – 8.09 (m, 1H, H-6''), 7.85 – 7.75 (m, 1H, H-4''), 7.71 – 7.64 (m, 1H, H-3''), 7.64 – 7.55 (m, 1H, H-5''), 6.85 (s, 1H, -N*H*-), 5.34 (s, 2H, H-2'), 3.57 (t, ^3J = 6.3 Hz, 6H, H-3), 3.49 (s, 6H, H-5), 3.17 (s, 3H, -OH), 2.42 (t, ^3J = 6.3 Hz, 6H, H-2). **^{13}C-NMR** (101 MHz, $(CD_3)_2SO$, 25 °C)**:** δ (ppm) = 172.6 (3C, C-1), 154.0 (1C, C-1'), 146.8 (1C, C-1''), 134.1 (1C, C-4''), 133.3 (1C, C-2''), 128.7 (1C, C-5''), 128.3 (1C, C-3''), 124.7 (1C, C-6''), 67.9 (3C, C-5), 66.6 (3C, C-3), 61.5 (1C, C-2'), 58.9 (1C, C-6), 34.5 (3C, C-2). **HR-MS** (ESI$^-$)**:** $m/z_{cal.}$ = 515.1519

$[M-H]^-$, $m/z_{exp.}$ = 515.1517 $[M-H]^-$. R_f (NP) = 0.21 (^{c}Hex/EtOAc + HCOOH 1:2 + 1 %$_{v/v}$ additive). **IR** (ATR): (cm^{-1}) = 2927, 2881, 1709, 1524, 1422, 1343, 1236, 1188, 1094, 1068, 859, 791, 732, 702, 590, 474.

The analytical data follows literature data.[26]

4.1.15 Synthesis of 2-Nitrobenzyl-(1,35-diazido-18-(17-azido-5-oxo-2,9,12,15-tetraoxa-6-azaheptadecyl)-13,23-dioxo-3,6,9,16,20,27,30,33-octaoxa-12,24-diazapentatriacontan-18-yl)-carbamate

The title compound was synthesized according to Scheme S 17 following modified synthesis protocols by *Appel et al.*[31], *Krumb et al.*[26] and *Zhou et al.*[48]

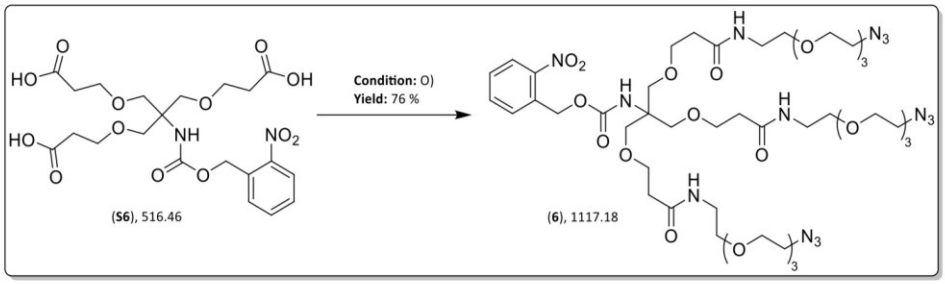

Scheme S 17: Synthesis of 2-Nitrobenzyl-(1,35-diazido-18-(17-azido-5-oxo-2,9,12,15-tetraoxa-6-azaheptadecyl)-13,23-dioxo-3,6,9,16,20,27,30,33-octaoxa-12,24-diazapentatriacontan-18-yl)-carbamate (**6**). Reaction conditions: O) (**4**), HATU, DIPEA, DMF, Ar-atm., rt, 48 h; yield: 76 %.

The reaction was carried out in a dried Schlenk vessel previously equipped with a magnetic stirring bar. 2-Nitrobenzyl-(6-(1-carboxy-4-oxapentan-5-yl)-4,8-dioxa-1-11-dicarboxyundecan-6-yl)-carbamate (**S6**, 0.97 g, 1.88 mmol, 1.00 eq.) was dissolved in absolute DMF (25.0 mL) under an atmosphere of argon. HATU (2.14 g, 5.64 mmol, 3.00 eq.) was added, followed by DIPEA (0.97 g, 1.28 mL, 7.52 mmol, 4.00 eq.). The reaction mixture was stirred for half an hour at room temperature. 11-Amino-1-azido-3,6,9-trioxaundecane (**4**, 1.64 g, 7.52 mmol, 4.00 eq.) was dissolved in absolute DMF (5.00 mL) under an atmosphere of argon and slowly added dropwise to the yellowish reaction mixture using a syringe. The mixture was stirred at room temperature for 48 hours. Complete conversion of the limiting substrate and the formation of the desired product were determined by reaction control via TLC and HPLC-ELS-MS. All volatiles were removed in fine vacuum. Toluene (3 x 20.0 mL) was added to the residue and all volatiles were again removed under fine vacuum. The crude product (4.02 g) was obtained in the form of an orange oil and purified by FCC (EtOAc/MeOH, gradient from 10 % to 30 % MeOH) followed by RP-FCC ($MeCN/H_2O$, gradient from 10 % to 60 % to 100 % MeCN, Isolera One Purification System, SNAP C_{18} 60 g cartridge). The pure product (**6**) was obtained in the form of colorless oil

Yield: 1.60 g (1.43 mmol, 76 %), colorless oil.

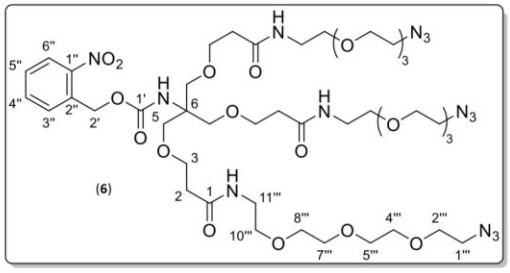

^{1}H-NMR (600 MHz, $CDCl_3$, 25 °C): δ (ppm) = 8.15 – 8.02 (m, 1H, H-6''), 7.69 – 7.64 (m, 2H, H-3'', H-4''), 7.49 – 7.45 (m, 1H, H-5''), 6.70 (t, ^3J = 5.4 Hz, 3H, -N*H*-C-11'''), 5.71 (s, 1H, -N*H*-C-6), 5.45 (s, 2H, H-2'), 3.70 (t, ^3J = 5.9 Hz, 6H, H-2), 3.67 – 3.60 (m, 36H, H-5, H-2''', H-4''', H-5''', H-7''', H-8'''), 3.54 (t, ^3J = 5.4 Hz, 6H, H-10'''), 3.43 (q, ^3J = 5.4 Hz, 6H, H-11'''), 3.38 (t, ^3J = 5.1 Hz, 6H, H-1'''), 2.42 (t, ^3J = 5.9 Hz, 6H, H-3). **^{13}C-NMR** (151 MHz, $CDCl_3$, 25 °C): δ (ppm)

= 171.2 (3C, C-1), 154.6 (1C, C-1'), 147.2 (1C, C-1''), 133.9 (1C, C-4''), 133.4 (1C, C-2''), 128.7 (1C, C-3''), 128.5 (1C, C-5''), 125.0 (3C, C-6''), 70.7, 70.6, 70.5, 70.2, 70.0 (15C, C-2''', C-4''', C-5''', C-7''', C-8'''), 69.8 (3C, C-10'''), 69.2 (3C, C-5), 67.4 (3C, C-2), 62.9 (1C, C-2'), 58.9 (1C, C-6), 50.6 (3C, C-1'''), 39.2 (3C, C-11'''), 36.6 (3C, C-3). **HR-MS** (ESI)**:** $m/z_{cal.}$ = 581.2598 $[M+2Na]^{2+}$, $m/z_{exp.}$ = 581.2600 $[M+2Na]^{2+}$; $m/z_{cal.}$ = 1139.5303 $[M+Na]^{+}$, $m/z_{exp.}$ = 1139.5307 $[M+Na]^{+}$. R_f (NP) = 0.44 (EtOAc/MeOH 7:3). **IR** (ATR)**:** (cm^{-1}) = 3310, 2872, 2101, 1726, 1651, 1525, 1344, 1283, 1092, 912, 858, 793, 729, 646, 556.

The analytical data follows literature data.[26]

4.1.16 Synthesis of (1-(11-Azido-3,6,9-trioxaundec-1-yl)-1*H*-1,2,3-triazol-4-yl)-methyl α-D-Mannopyranoside

The title compound was synthesized according to Scheme S 18 following a modified synthesis protocol by *Yamamoto et al.*[39]

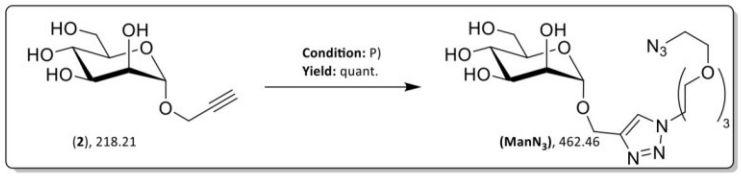

Scheme S 18: Synthesis of (1-(11-Azido-3,6,9-trioxaundec-1-yl)-1*H*-1,2,3-triazol-4-yl)-methyl α-D-Mannopyranoside (**ManN$_3$**). Reaction conditions: P) Cu^{I}Br, NaAsc, DMF, Ar-atm., 45 °C, 20 h; yield: quant.

The reaction was carried out in a dried Schlenk vessel previously equipped with a magnetic stirring bar. Propargyl α-D-mannopyranoside (**2**, 0.10 g, 0.46 mmol, 1.00 eq.) and 1,11-diazido-3,6,9-trioxaundecane (**5**, 0.56 g, 2.29 mmol, 5.00 eq.) were dissolved under an atmosphere of argon in absolute DMF (10.0 mL), which had previously been degassed for half an hour in an ultrasonic bath with an argon stream. The mixture was degassed by three freeze-pump-thaw cycles and then brought under an atmosphere of argon. PDMTA (4.00 mg, 5.00 µL, 23.0 µmol, 0.05 eq.) was added using an Eppendorf pipette. The mixture was warmed up to a temperature of 45 °C, and Cu^{I}Br (3.30 g, 23.0 µmol, 0.05 eq.) was added. The turquoise-colored reaction mixture was stirred at this temperature for 20 hours. Complete conversion of the limiting substrate and the formation of the desired product were determined by reaction control via TLC and HPLC-ELS-MS. The solution was cooled to room temperature. All volatiles were removed in fine vacuum. Toluene (3 x 5.00 mL) was added to the residue, and all volatiles were again removed in fine vacuum. The crude product (0.74 g) was obtained as a yellow liquid and purified by FCC (EtOAc/MeOH, gradient from 0 % to 5 % to 10 % MeOH, Isolera Four Purification System, SNAP KP-Sil 50 g cartridge) and RP-FCC (MeCN/H_2O, gradient from 3 % to 5 % to 100 % MeCN, Isolera One Purification System, SNAP C_{18} 30 g cartridge). The pure product (**ManN$_3$**) was obtained in the form of colorless oil. The excess of the starting material 1,11-diazido-3,6,9-trioxaundecane (**5**) was also recovered with a recovery rate of 92 %.

Yield: 0.21 g (0.46 mmol, quant.), colorless oil.

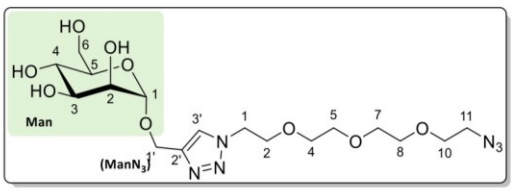

^{1}H-NMR (600 MHz, CD_3OD, 25 °C)**:** δ (ppm) = 8.08 (s, 1H, H-3'), 4.85 (d, ^3J = 1.7 Hz, 1H, H-1$_{Man}$), 4.80 (d, ^2J = 12.4 Hz, 1H, H-1a'), 4.65 (d, ^2J = 12.4 Hz, 1H, H-1b'), 4.59 (t, ^3J = 5.3 Hz, 2H, H-1), 3.90 (t, ^3J = 5.1 Hz, 2H, H-2), 3.85 (dd, ^2J = 11.8 Hz, ^3J = 2.2 Hz, 1H, H-6a$_{Man}$), 3.78 (dd, ^3J = 3.4, 1.7 Hz, 1H, H-2$_{Man}$), 3.72 (dd, ^2J = 11.8 Hz, ^3J = 5.9 Hz, 1H, H-6b$_{Man}$), 3.67 (dd, ^3J = 9.1, 3.4 Hz, 1H, H-3$_{Man}$), 3.67 – 3.65 (m, 2H, H-10), 3.65 – 3.59 (m, 9H, H-4$_{Man}$, H-4, H-5, H-7, H-8),

3.57 (ddd, ^3J = 9.7, 5.8, 2.2 Hz, 1H, H-5$_{Man}$), 3.37 (t, ^3J = 4.9 Hz, 2H, H-11). **^{13}C-NMR** (151 MHz, CD_3OD, 25 °C)**:** δ (ppm) = 142.9 (1C, C-2'), 124.1 (1C, C-3'), 98.6 (1C, C-1$_{Man}$), 72.8 (1C, C-5$_{Man}$), 70.4 (1C, C-3$_{Man}$), 69.9 (1C, C-2$_{Man}$), 69.4, 69.4, 69.3 (4C, C-4, C-5, C-7, C-8), 69.0 (1C, C-10), 68.2 (1C, C-2), 66.4 (1C, C-4$_{Man}$), 60.8 (1C, C-6$_{Man}$), 58.5 (1C, C-1'), 49.6 (1C, C-11), 49.3 (1C, C-1). **HR-MS** (ESI$^+$)**:** $m/z_{cal.}$ = 485.1966 $[M+Na]^+$, $m/z_{exp.}$ = 485.1963 $[M+Na]^+$. R_f (NP) = 0.23 (EtOAc/MeOH 10:3). **Optical rotation** (LM)**:** $[\alpha]_D^{22}$ = +50.1 (MeOH). **IR** (ATR)**:** (cm^{-1}) = 3370, 2875, 2108, 1452, 1350, 1300, 1127, 1100, 1060, 816, 680, 557, 511.

The analytical data follows literature data.[37]

4.1.17 Synthesis of (1-(11-Azido-3,6,9-trioxaundec-1-yl)-1*H*-1,2,3-triazol-4-yl)-methyl 2,4-Di-*O*-benzoyl-3,6-di-*O*-(2,3,4,6-tetra-*O*-acetyl-α-D-mannopyranosyl)-α-D-mannopyranoside

The title compound was synthesized according to Scheme S 19 following modified synthesis protocols by *Kramer et al.*[6] and *Yamamoto et al.*[39]

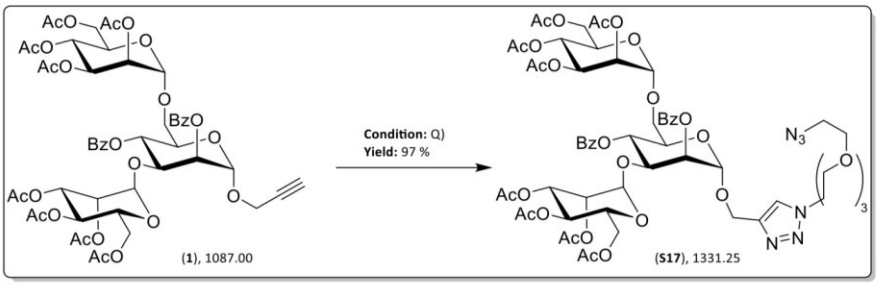

Scheme S 19: Synthesis of (1-(11-Azido-3,6,9-trioxaundec-1-yl)-1*H*-1,2,3-triazol-4-yl)-methyl 2,4-Di-*O*-benzoyl-3,6-di-*O*-(2,3,4,6-tetra-*O*-acetyl-α-D-mannopyranosyl)-α-D-mannopyranoside (**S17**). Reaction conditions: Q) (**5**), Cu^{I}Br, PMDTA, DMF, Ar-atm., 45 °C, 3 h; yield: 97 %

The reaction was carried out in a dried Schlenk vessel previously equipped with a magnetic stirring bar. Propargyl 2,4-di-O-benzoyl-3,6-di-O-(2,3,4,6-tetra-O-acetyl-α-D-mannopyranosyl)-α-D-mannopyranoside (**1**, 0.50 g, 0.46 mmol, 1.00 eq.) was dissolved together with 1,11-diazido-3,6,9-trioxaundecane (**5**, 1.69 g, 6.90 mmol, 15.0 eq.) under an atmosphere of argon in absolute DMF (45.0 mL), which had previously been degassed for half an hour in an ultrasonic bath with an argon stream. The mixture was degassed using three freeze-pump-thaw cycles and returned to an argon atmosphere. PDMTA (0.07 g, 0.08 mL, 0.39 mmol, 0.85 eq.) was added using an Eppendorf pipette. The mixture was warmed up to a temperature of 45 °C, and Cu^{I}Br (0.03 g, 0.23 mmol, 0.50 eq.) was added. The turquoise-colored reaction solution was stirred at this temperature for three hours. Complete conversion of the limiting substrate and formation of the desired product were determined by reaction control via TLC and HPLC-ELS-MS. The solution was cooled to room temperature, diluted with EtOAc (1 x 100 mL), and washed with saturated NH_4Cl solution (2 x 50.0 mL). The aqueous phase was diluted with H_2O (1 x 50.0 mL) until all salts were dissolved and extracted with EtOAc (1 x 50.0 mL). The collected organic phases were washed with saturated NaCl solution (1 x 100 mL), dried over anhydrous Na_2SO_4, and filtered. All volatiles were removed in fine vacuum. The crude product (2.56 g) was obtained in the form of a yellowish liquid and purified by FCC (^{c}Hex/EtOAc, gradient 0 % to 100 % EtOAc, Isolera Four Flash Purification System, SNAP KP-Sil 100 g cartridge). The pure product (**S17**) was obtained in the form of yellowish oil. The excess of the starting material 1,11-diazido-3,6,9-trioxaundecane (**5**) was also recovered with a recovery rate of 90 %.

Yield: 0.60 g (0.45 mmol, 97 %), yellowish oil.

Supporting Information

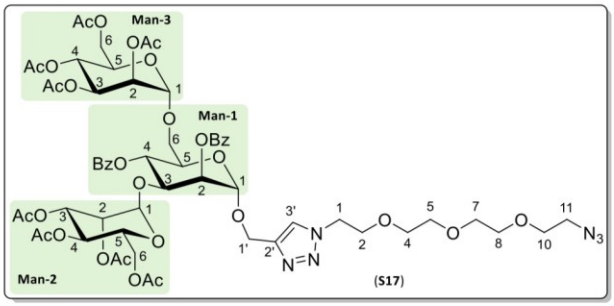

^{1}H-NMR (600 MHz, $CDCl_3$, 25 °C): δ (ppm) = 8.16 – 8.13 (m, 2H, C-2$_{Man-1}$-O(C=O)Ph, H$_{ortho}$), 8.04 – 8.01 (m, 2H, C-4$_{Man-1}$-O(C=O)Ph, H$_{ortho}$), 7.85 (s, 1H, H-3‘), 7.64 – 7.60 (m, 1H, C-2$_{Man-1}$-O(C=O)Ph, H$_{para}$), 7.60 – 7.57 (m, 1H, C-4$_{Man-1}$-O(C=O)Ph, H$_{para}$), 7.57 – 7.53 (m, 2H, C-2$_{Man-1}$-O(C=O)Ph, H$_{meta}$), 7.46 – 7.42 (m, 2H, C-4$_{Man-1}$-O(C=O)Ph, H$_{meta}$), 5.70 (t$_{app}$, ^3J = 10.0 Hz, 1H, H-4$_{Man-1}$), 5.52 (dd, ^3J = 3.4, 1.8 Hz, 1H, H-2$_{Man-1}$), 5.34 (dd, ^3J = 10.1, 3.5 Hz, 1H, H-3$_{Man-3}$), 5.28 (dd, ^3J = 3.5, 1.7 Hz, 1H, H-2$_{Man-3}$), 5.25 (t$_{app}$, ^3J = 10.1 Hz, 1H, H-4$_{Man-3}$), 5.17 (d, ^3J = 1.8 Hz, 1H, H-1$_{Man-1}$), 5.10 – 5.04 (m, 2H, H-3$_{Man-2}$, H-4$_{Man-2}$), 4.94 (d, ^3J = 1.9 Hz, 1H, H-1$_{Man-2}$), 4.89 (d, ^2J = 12.1 Hz, 1H, H-1a‘), 4.86 (d, ^3J = 1.7 Hz, 1H, H-1$_{Man-3}$), 4.85 (dd, ^3J = 3.0, 1.9 Hz, 1H, H-2$_{Man-2}$), 4.72 (d, ^2J = 12.1 Hz, 1H, H-1b‘), 4.58 (t, ^3J = 5.2 Hz, 2H, H-1), 4.46 (dd, ^3J = 10.0, 3.4 Hz, 1H, H-3$_{Man-1}$), 4.25 (ddd, ^3J = 10.0, 6.1, 2.3 Hz, 1H, H-5$_{Man-1}$), 4.18 – 4.12 (m, 2H, H-6a$_{Man-2}$, H-6a$_{Man-3}$), 4.08 – 4.03 (m, 2H, H-5$_{Man-2}$, H-5$_{Man-3}$), 3.97 (dd, ^2J = 12.2, ^3J = 2.1 Hz, 1H, H-6b$_{Man-3}$), 3.96 – 3.93 (m, 2H, H-6a$_{Man-1}$, H-6b$_{Man-2}$), 3.93 – 3.89 (m, 2H, H-2), 3.69 – 3.59 (m, 11H, H-6b$_{Man-1}$, H-4, H-5, H-7, H-8, H-10), 3.38 (t, ^3J = 5.0 Hz, 2H, H-11), 2.11 (s, 3H, C-2$_{Man-3}$-O(C=O)CH_3), 2.04 (s, 3H, C-4$_{Man-3}$-O(C=O)CH_3), 2.03 (s, 3H, C-6$_{Man-3}$-O(C=O)CH_3), 1.96 (s, 3H, C-3$_{Man-3}$-O(C=O)CH_3), 1.93 (s, 3H, C-6$_{Man-2}$-O(C=O)CH_3), 1.92 (s, 3H, C-4$_{Man-2}$-O(C=O)CH_3), 1.84 (s, 3H, C-2$_{Man-2}$-O(C=O)CH_3), 1.81 (s, 3H, C-3$_{Man-2}$-O(C=O)CH_3). **^{13}C-NMR** (151 MHz, $CDCl_3$, 25 °C): δ (ppm) = 170.7 (1C, C-6$_{Man-2}$-O(*C*=O)CH$_3$), 170.6 (1C, C-6$_{Man-3}$-O(*C*=O)CH$_3$), 169.9 (1C, C-2$_{Man-3}$-O(*C*=O)CH$_3$), 169.9 (1C, C-4$_{Man-3}$-O(*C*=O)CH$_3$), 169.8 (1C, C-4$_{Man-2}$-O(*C*=O)CH$_3$), 169.6 (1C, C-3$_{Man-3}$-O(*C*=O)CH$_3$), 169.1 (1C, C-2$_{Man-2}$-O(*C*=O)CH$_3$), 169.1 (1C, C-3$_{Man-2}$-O(*C*=O)CH$_3$), 165.9 (1C, C-2$_{Man-1}$-O(*C*=O)Ph), 165.2 (1C, C-4$_{Man-1}$-O(*C*=O)Ph), 142.9 (1C, C-2‘), 133.6 (1C, C-2$_{Man-1}$-O(C=O)Ph, C$_{para}$), 133.6 (1C, C-4$_{Man-1}$-O(C=O)Ph, C$_{para}$), 130.0 (2C, C-2$_{Man-1}$-O(C=O)Ph, C$_{ortho}$), 129.9 (2C, C-4$_{Man-1}$-O(C=O)Ph, C$_{ortho}$), 129.1 (1C, C-4$_{Man-1}$-O(C=O)Ph, C$_{ipso}$), 128.8 (2C, C-2$_{Man-1}$-O(C=O)Ph, C$_{meta}$), 128.7 (1C, C-2$_{Man-1}$-O(C=O)Ph, C$_{ipso}$), 128.5 (2C, C-4$_{Man-1}$-O(C=O)Ph, C$_{meta}$), 124.5 (1C, C-3‘), 99.4 (1C, C-1$_{Man-2}$), 97.3 (1C, C-1$_{Man-3}$), 96.7 (1C, C-1$_{Man-1}$), 75.5 (1C, C-3$_{Man-1}$), 71.6 (1C, C-2$_{Man-1}$), 70.7, 70.6, 70.6, 70.5, 70.1 (5C, C-4, C-5, C-7, C-8, C-10), 69.4 (1C, C-5$_{Man-1}$), 69.4 (1C, C-2), 69.3 (1C, C-5$_{Man-2}$), 69.2 (1C, C-2$_{Man-3}$), 69.2 (1C, C-2$_{Man-2}$), 69.2 (1C, C-3$_{Man-3}$), 68.6 (1C, C-5$_{Man-3}$), 68.2 (1C, C-3$_{Man-2}$), 66.5 (1C, C-6$_{Man-1}$), 65.9 (1C, C-4$_{Man-2}$), 65.8 (1C, C-4$_{Man-3}$), 62.3 (1C, C-6$_{Man-3}$), 62.2 (1C, C-6$_{Man-2}$), 60.5 (1C, C-1‘), 50.6 (1C, C-11), 50.2 (1C, C-1), 20.9 (1C, C-2$_{Man-3}$-O(C=O)*C*H$_3$), 20.8 (1C, C-6$_{Man-3}$-O(C=O)*C*H$_3$), 20.7 (1C, C-3$_{Man-3}$-O(C=O)*C*H$_3$), 20.7 (1C, C-4$_{Man-3}$-O(C=O)*C*H$_3$), 20.6 (1C, C-6$_{Man-2}$-O(C=O)*C*H$_3$), 20.5(1C, C-2$_{Man-2}$-O(C=O)*C*H$_3$), 20.5 (1C, C-3$_{Man-2}$-O(C=O)*C*H$_3$). **HR-MS** (ESI$^+$): $m/z_{cal.}$ = 1353.4392 [M+Na]$^+$, $m/z_{exp.}$ = 1353.4375 [M+Na]$^+$. R_f (NP) = 0.25 (EtOAc). **Optical rotation** (LM): $[\alpha]_D^{20}$ = 10.6 ($CHCl_3$). **IR** (ATR): (cm^{-1}) = 2942, 2103, 1749, 1451, 1370, 1226, 1134, 1087, 1070, 1048, 980, 936, 715, 653, 600, 529, 479, 466, 450.

4.1.18 Synthesis of (1-(11-Azido-3,6,9-trioxaundec-1-yl)-1*H*-1,2,3-triazol-4-yl)-methyl 3,6-Di-*O*-(α-D-mannopyranosyl)-α-D-mannopyranoside

The title compound was synthesized according to Scheme S 20 following modified synthesis protocols by *Kramer et al.*[6], *Lindhorst et al.*[40] and *Reina et al.*[41]

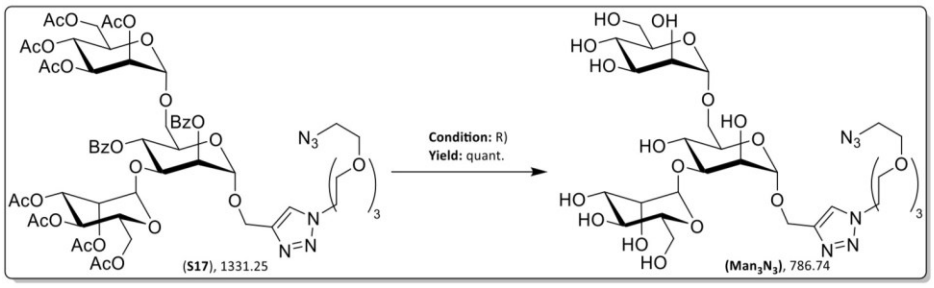

Scheme S 20: Synthesis of (1-(11-Azido-3,6,9-trioxaundec-1-yl)-1*H*-1,2,3-triazol-4-yl)-methyl 3,6-Di-*O*-(α-D-mannopyranosyl)-α-D-mannopyranoside (**Man$_3$N$_3$**). Reaction conditions: R) NaOMe, NaOH, MeOH, Ar-atm., rt, 24 h; yield: quant.

The reaction was carried out in a dried Schlenk vessel previously equipped with a magnetic stirring bar. 1-(11-Azido-3,6,9-trioxaundec-1-yl)-1H-1,2,3-triazol-4-yl)-methyl 2,4-Di-O-benzoyl-3,6-di-O-(2,3,4,6-tetra-O-acetyl-α-D-mannopyranosyl)-α-D-mannopyranoside (**S17**, 0.27 g, 0.21 mmol, 1.00 eq.) was dissolved in absolute MeOH (5.00 mL) under an atmosphere of argon. NaOMe (11.3 mg, 0.21 mmol, 1.00 eq.) and NaOH (8.40 mg, 0.21 mmol, 1.00 eq.) were added successively. The reaction mixture was stirred for four hours at a temperature of 40 °C. Complete conversion of the limiting substrate and formation of the desired product were determined by TLC and HPLC-ELS-MS. The reaction was terminated by adding the ion exchange resin *Amberlite IR 120* (0.20 g), and the mixture was stirred for ten minutes until a constant pH value (pH = 6–7) was reached. The reaction mixture was filtered through a glass frit with *Celite* and eluted with MeOH (1 x 100 mL). All volatiles were removed in vacuo. The residue was obtained as a yellowish oil, dissolved in H_2O (1 x 20.0 mL), and extracted with Et_2O (3 x 20.0 mL). The crude product (0.10 g) was obtained as a yellowish oil by lyophilization of the aqueous phase and purified by RP-FCC (MeCN/H_2O, gradient from 5 % to 60 % to 100 % MeCN, Isolera One Flash Purification System, SNAP C_{18} 12 g cartridge). The pure product (**Man$_3$N$_3$**) was obtained in the form of a colorless lyophilizate.

Yield: 0.17 g (0.21 mmol, quant.), colorless lyophilizate.

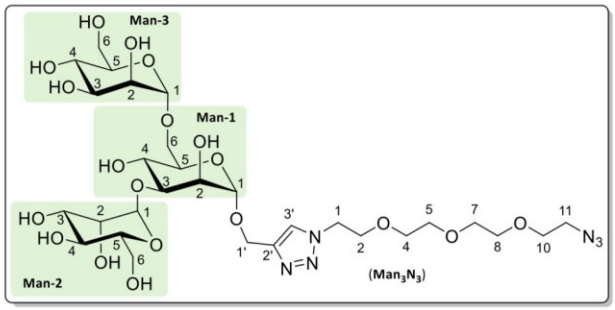

^{1}H-NMR (600 MHz, D_2O, 25 °C)**:** δ (ppm) = 8.07 (s, 1H, H-3‘), 5.03 (s, 1H, H-1$_{Man-2}$), 4.89 (s, 1H, H-1$_{Man-1}$), 4.85 (s, 1H, H-1$_{Man-3}$), 4.78 – 4.77 (m, 1H, H-1a‘), 4.68 (d, ^2J = 12.6 Hz, 1H, H-1b‘), 4.60 (t, ^3J = 5.0 Hz, 2H, H-1), 4.05 (s, 1H, H-2$_{Man-1}$), 4.01 (dd, ^3J = 3.5, 1.6 Hz, 1H, H-2$_{Man-2}$), 3.98 – 3.92 (m, 4H, H-2, H-2$_{Man-3}$, H-6a$_{Man-1}$), 3.90 – 3.85 (m, 1H, H-4$_{Man-1}$), 3.85 – 3.78 (m, 4H, H-3$_{Man-1}$, H-3$_{Man-2}$, H-3$_{Man-3}$, H-6a$_{Man-3}$), 3.76 – 3.69 (m, 3H, H-5$_{Man-1}$, H-5$_{Man-2}$, H-6b$_{Man-3}$), 3.68 – 3.55 (m, 16H, H-4, H-5, H-7, H-8, H-10, H-6b$_{Man-1}$, H-4$_{Man-2}$, H-6$_{Man-2}$, H-4$_{Man-3}$, H-5$_{Man-3}$), 3.43 (t, ^3J = 4.9 Hz, 2H, H-11). **^{13}C-NMR** (151 MHz, D_2O, 25 °C)**:** δ (ppm) = 143.5 (1C, C-2‘), 125.5 (1C, C-3‘), 102.4 (1C, C-1$_{Man-2}$), 99.7 (1C, C-1$_{Man-1}$), 99.4 (1C, C-1$_{Man-3}$), 78.6 (1C, C-3$_{Man-1}$), 73.3 (1C, C-5$_{Man-2}$), 72.7 (1C, C-5$_{Man-3}$), 71.3 (1C, C-5$_{Man-1}$), 70.6 (1C, C-3$_{Man-3}$), 70.3 (1C, C-3$_{Man-2}$), 70.0 (1C, C-2$_{Man-2}$), 69.9 (1C, C-2$_{Man-3}$), 69.7 (1C, C-6$_{Man-2}$), 69.6 (4C, C-4, C-5, C-7, C-8),

69.5 (1C, C-2_{Man-1}), 69.2 (1C, C-10), 68.8 (1C, C-2), 66.7 (2C, C-4_{Man-2}, C-4_{Man-3}), 65.5 (1C, C-4_{Man-1}), 65.0 (1C, C-6_{Man-1}), 60.9 (1C, C-6_{Man-3}), 60.0 (1C, C-1'), 50.1 (1C, C-11), 50.1 (1C, C-1). **HR-MS** (ESI^+): $m/z_{cal.}$ = 809.3032 $[M+Na]^+$, $m/z_{exp.}$ = 809.3024 $[M+Na]^+$. R_f (RP) = 0.60 ($MeCN/H_2O$ 1:4). **Optical rotation** (LM): $[\alpha]_D^{23}$ = +45.6 (MeOH). **IR** (ATR): (cm^{-1}) = 3327, 2921, 2107, 1592, 1349, 1025, 979, 807, 501.

The analytical data follows literature data.[6]

4.1.19 Synthesis of 2-Nitrobenzyl (1,35-Bis(4-(2,3,4,6-tetra-*O*-acetyl-α-D-mannopyranosyloxymethyl)-1*H*-1,2,3-triazol-1-yl)-18-(17-(4-(2,3,4,6-tetra-*O*-acetyl-α-D-mannopyranosyloxymethyl)-1*H*-1,2,3-triazol-1-yl))-5-oxo-2,9,12,15-tetraoxa-6-azaheptadec-1-yl)-13,23-dioxo-3,6,9,16,20,27,30,33-octaoxa-12,24-diazapentatriacontan-18-yl)carbamate

The title compound was synthesized according to Scheme S 21 following modified synthesis protocols by *Yamamoto et al.*[39] and *Krumb et al.*[26]

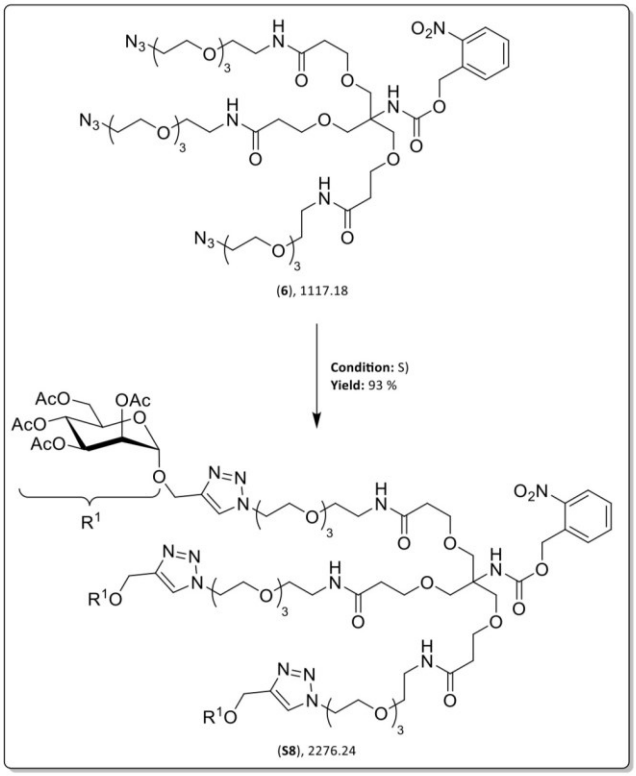

Scheme S 21: Synthesis of 2-Nitrobenzyl (1,35-Bis(4-(2,3,4,6-tetra-*O*-acetyl-α-D-mannopyranosyloxymethyl)-1*H*-1,2,3-triazol-1-yl)-18-(17-(4-(2,3,4,6-tetra-*O*-acetyl-α-D-mannopyranosyloxymethyl)-1*H*-1,2,3-triazol-1-yl))-5-oxo-2,9,12,15-tetraoxa-6-azaheptadec-1-yl)-13,23-dioxo-3,6,9,16,20,27,30,33-octaoxa-12,24-diazapentatriacontan-18-yl)carbamate (**S8**). Reaction conditions S) (**S7**), CuBr, PMDTA, DMF, Ar-atm., 45 °C, 4 h; yield: 93 %.

The reaction was carried out in a dried Schlenk vessel, which was previously equipped with a magnetic stirring bar. 2-Nitrobenzyl-(1,35-diazido-18-(17-azido-5-oxo-2,9,12,15-tetraoxa-6-azaheptadecyl)-13,23-dioxo-3,6,9,16,20,27,30,33-octaoxa-12,24-diazapentatria-contan-18-yl)-carbamate (**6**, 0.28 g, 0.25 mmol, 1.00 eq.) and Propargyl 2,3,4,6-Tetra-*O*-acetyl-α-D-mannopyranoside (**S7**, 0.34 g, 0.88 mmol, 3.50 eq.) were dissolved under an atmosphere of argon in absolute DMF (20.0 mL), which had previously been purged for half an hour with an argon gas stream in an ultrasonic bath. PMDTA (0.09 g, 0.10 mL, 0.50 mmol, 2.00 eq.) was added via syringe. The yellowish solution was degassed for

half an hour with an argon gas stream in an ultrasonic bath and then warmed to a temperature of 45 °C. $Cu^{I}Br$ (0.01 g, 0.06 mmol, 0.25 eq.) was added. The greenish reaction mixture was stirred at this temperature for four hours. Complete conversion of the limiting substrate and the formation of the desired product were determined by reaction control via TLC and HPLC-ELS-MS. All volatiles were removed in fine vacuum. Toluene (3 x 10.0 mL) was added to the residue and all volatiles were again removed in fine vacuum. The residue was taken up in EtOAc (1 x 50.0 mL), and the organic phase was washed with saturated NH_4Cl solution (3 x 50.0 mL). The collected aqueous phases were diluted with H_2O (1 x 50.0 mL) until all salts were dissolved and extracted with EtOAc (3 x 50.0 mL). The collected organic phases were dried over anhydrous Na_2SO_4 and filtered. All volatiles were removed in vacuo, and the residue was dried in fine vacuum. The crude product (0.64 g) was obtained in the form of yellowish oil and purified by RP-FCC ($MeCN/H_2O$, gradient from 10 % to 40 % to 100 % MeCN, Isolera One Purification System, SNAP C_{18} 60 g cartridge). The pure product (**S8**) was obtained in the form of colorless oil.

Yield: 0.53 g (0.23 mmol, 93 %), colorless oil.

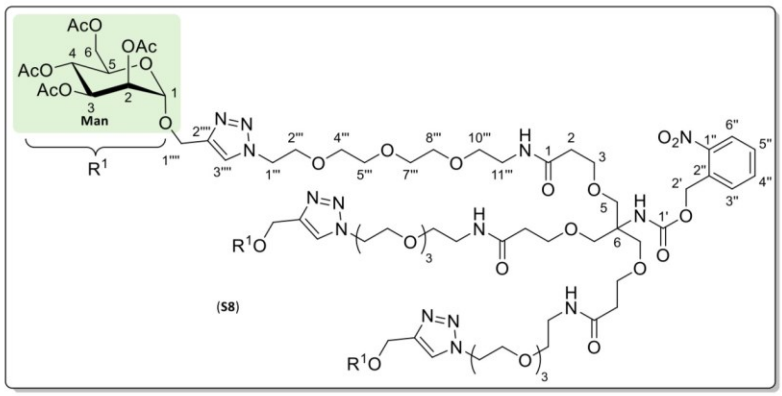

^{1}H-NMR (600 MHz, $CDCl_3$, 25 °C)**:** δ (ppm) = 8.09 – 8.07 (m, 1H, H-6‘‘), 7.76 (s, 3H, H-3‘‘‘‘), 7.68 – 7.63 (m, 2H, H-4‘‘, H-5‘‘), 7.48 – 7.44 (m, 1H, H-3‘‘), 6.73 (t, ^{3}J = 5.7 Hz, 3H, -N*H*-C-11‘‘‘), 5.74 (s, 1H, -N*H*-C-6), 5.43 (s, 2H, H-2‘), 5.31 – 5.28 (m, 6H, H-3$_{Man}$, H-4$_{Man}$), 5.22 (t$_{app}$, ^{3}J = 2.2 Hz, 3H, H-2$_{Man}$), 4.96 (d, ^{3}J = 1.7 Hz, 3H, H-1$_{Man}$), 4.82 (d, ^{2}J = 12.2 Hz, 3H, H-1a‘‘‘‘), 4.66 (d, ^{2}J = 12.2 Hz, 3H, H-1b‘‘‘‘), 4.55 (t, ^{3}J = 5.1 Hz, 6H, H-1‘‘‘), 4.29 (dd, ^{2}J = 12.2 Hz, ^{3}J = 5.0 Hz, 3H, H-6a$_{Man}$), 4.10 (dd, ^{2}J = 12.2 Hz, ^{3}J = 2.5 Hz, 3H, H-6b$_{Man}$), 4.08 – 4.05 (m, 3H, H-5$_{Man}$), 3.88 (t, ^{3}J = 5.1 Hz, 6H, H-2‘‘‘), 3.68 (t, ^{3}J = 5.8 Hz, 6H, H-2), 3.64 – 3.57 (m, 30H, H-4‘‘‘, H-5‘‘‘, H-7‘‘‘, H-8‘‘‘, H-5), 3.53 (t, ^{3}J = 5.4 Hz, 6H, H-10‘‘‘), 3.41 (q, ^{3}J = 5.4 Hz, 6H. H-11‘‘‘), 2.40 (t, ^{3}J = 5.8 Hz, 6H, H-3), 2.14 (s, 9H, C-2$_{Man}$-O(C=O)C*H*$_3$), 2.11 (s, 9H, C-6$_{Man}$-O(C=O)C*H*$_3$), 2.02 (s, 9H, C-3$_{Man}$-O(C=O)C*H*$_3$), 1.96 (s, 9H, C-4$_{Man}$-O(C=O)C*H*$_3$). **^{13}C-NMR** (151 MHz, $CDCl_3$, 25 °C)**:** δ (ppm) = 171.2 (3C, C-1), 170.7 (3C, C-6$_{Man}$-O(*C*=O)CH$_3$), 170.1 (3C, C-2$_{Man}$-O(*C*=O)CH$_3$), 169.9 (3C, C-3$_{Man}$-O(*C*=O)CH$_3$), 169.7 (3C, C-4$_{Man}$-O(*C*=O)CH$_3$), 154.6 (1C, C-1‘), 147.2 (1C, C-1‘‘), 143.3 (3C, C-2‘‘‘‘), 133.9 (1C, C-4‘), 133.3 (1C, C-2‘), 128.8 (1C, C-5‘), 128.5 (1C, C-3‘), 125.0 (1C, C-5‘), 124.2 (3C, C-3‘‘‘‘), 96.8 (3C, C-1$_{Man}$), 70.5, 70.4, 70.4, 70.1 (12C, C-4‘‘‘, C-5‘‘‘, C-7‘‘‘, C-8‘‘‘), 69.8 (3C, C-10‘‘‘), 69.4 (3C, C-5), 69.4 (3C, C-2‘‘‘), 69.3 (3C, C-2$_{Man}$), 69.0 (3C, C-4$_{Man}$), 68.6 (3C, C-5$_{Man}$), 67.4 (3C, C-2), 66.0 (3C, C-3$_{Man}$), 62.9 (1C, C-2‘), 62.3 (3C, C-6$_{Man}$), 60.9 (3C, C-1‘‘‘‘), 58.9 (1C, C-6), 50.3 (3C, C-1‘‘‘), 39.2 (3C, C-11‘‘‘), 36.6 (3C, C-3), 20.9 (3C, C-2$_{Man}$-O(C=O)*C*H$_3$), 20.8 (3C, C-6$_{Man}$-O(C=O)*C*H$_3$), 20.7 (3C, C-4$_{Man}$-O(C=O)*C*H$_3$), 20.7 (3C, C-3$_{Man}$-O(C=O)*C*H$_3$). **HR-MS** (ESI^{+})**:** $m/z_{cal.}$ = 1138.4598 $[M+2H]^{2+}$, $m/z_{exp.}$ = 1138.4606 $[M+2H]^{2+}$; $m/z_{cal.}$ = 1138.9615 $[M+2H]^{2+}$, $m/z_{exp.}$ = 1138.9626 $[M+2H]^{2+}$; $m/z_{cal.}$ = 2298.8942 $[M+Na]^{+}$, $m/z_{exp.}$ = 2298.9003 $[M+Na]^{+}$; $m/z_{cal.}$ = 2298.8976 $[M+Na]^{+}$, $m/z_{exp.}$ = 2298.9020 $[M+Na]^{+}$. R_f (NP) = 0.25 (DCM/MeOH 15:1). **Optical rotation** (LM)**:** $[\alpha]_D^{26}$ = +30.6 ($CHCl_3$). **IR** (ATR)**:** (cm^{-1}) = 3378, 2878, 2184, 2102, 1998, 1746, 1656, 1528, 1434, 1370, 1226, 1132, 1087, 1048, 979, 920, 734.

Supporting Information

The analytical data follows literature data.[26]

4.1.20 Synthesis of *N*-(1-(4-(2,3,4,6-Tetra-*O*-acetyl-α-D-mannopyranosyloxymethyl)-1*H*-1,2,3-triazol-1-yl)-3,6,9-trioxaundec-11-yl)-6-amino-6-(17-(4-(2,3,4,6-tetra-*O*-acetyl-α-D-mannopyranosyloxymethyl)-1*H*-1,2,3-triazol-1-yl)-5-oxo-2,9,12,15-tetraoxa-6-azaheptadec-1-yl)-11-oxo-4,8,15,18,21-pentaoxa-12-aza-(23-(4-(2,3,4,6-tetra-*O*-acetyl-α-D-mannopyranosyloxymethyl)-1*H*-1,2,3-triazol-1-yl)-tricosanamide

The title compound was synthesized according to Scheme S 22 following modified synthesis protocols by *Amit et al.*[42, 43] and *Krumb et al.*[26]

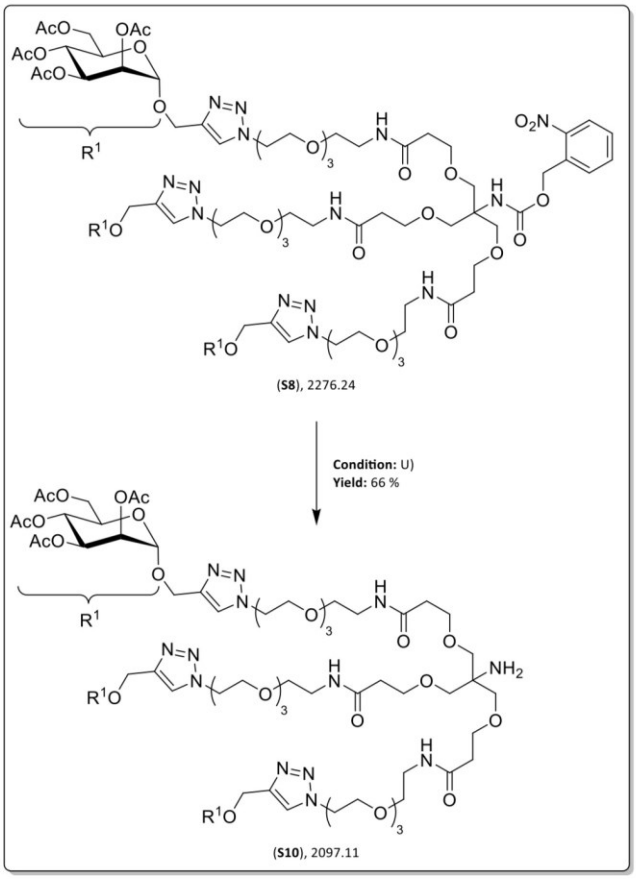

Scheme S 22: Synthesis of *N*-(1-(4-(2,3,4,6-Tetra-*O*-acetyl-α-D-mannopyranosyloxymethyl)-1*H*-1,2,3-triazol-1-yl)-3,6,9-trioxaundec-11-yl)-6-amino-6-(17-(4-(2,3,4,6-tetra-*O*-acetyl-α-D-mannopyranosyloxymethyl)-1*H*-1,2,3-triazol-1-yl)-5-oxo-2,9,12,15-tetraoxa-6-azaheptadec-1-yl)-11-oxo-4,8,15,18,21-pentaoxa-12-aza-(23-(4-(2,3,4,6-tetra-*O*-acetyl-α-D-mannopyranosyloxymethyl)-1*H*-1,2,3-triazol-1-yl)-tricosanamide (**S10**). Reaction conditions U) UV-A, MeCN, Ar-atm., rt, 15 h; yield: 70 %.

The reaction was carried out in a quartz tube which had previously been equipped with a magnetic stirring bar. 2-Nitrobenzyl (1,35-Bis(4-(2,3,4,6-tetra-*O*-acetyl-α-D-mannopyranosyloxymethyl)-1*H*-1,2,3-triazol-1-yl)-18-(17-(4-(2,3,4,6-tetra-*O*-acetyl-α-D-mannopyranosyloxymethyl)-1*H*-1,2,3-triazol-1-yl))-5-oxo-2,9,12,15-tetraoxa-6-azaheptadec-1-yl)-13,23-dioxo-3,6,9,16,20,27,-30,33-octaoxa-12,24-diazapentatriacontan-18-yl)carbamate (**S8**, 0.45 g, 0.20 mmol, 1.00 eq.) was dissolved under an atmosphere or argon in a mixture of MeCN and H_2O (1:1$_{v/v}$, 10.0 mL) that had previously been degassed for half an hour with an argon gas stream in an ultrasonic bath. The colorless solution was again degassed for half an hour with an argon gas stream in an ultrasonic bath. The reaction mixture was irradiated with

Supporting Information

UV-A radiation (λ_{max} = 350 nm) with stirring at room temperature for 15 hours in a Rayonet photoreactor. Complete conversion of the limiting substrate and formation of the desired product were determined by TLC and HPLC-ELS-MS. The orange solution was diluted with MeCN (10.0 mL) and H_2O (10.0 mL) and transferred into a flask. All volatile components were removed by lyophilization. The crude product (0.34 g) was obtained in the form of an orange lyophilizate and purified by FCC (DCM/MeOH, isocratic at 10 % MeOH). The pure product (**S10**) was obtained in the form of orange oil.

Yield: 0.29 g (0.14 mmol, 70 %), orange oil.

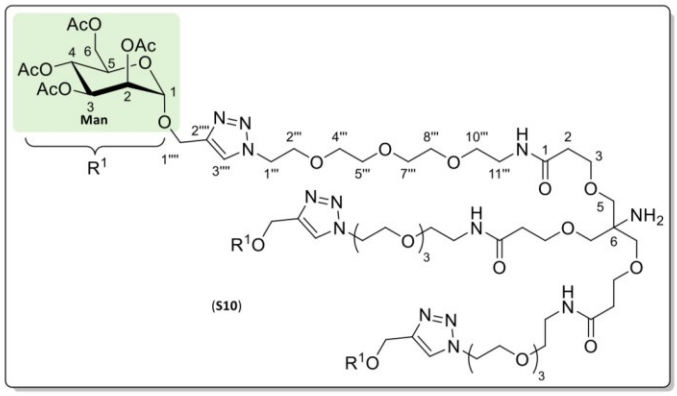

^{1}H-NMR (600 MHz, $CDCl_3$, 25 °C)**:** δ (ppm) = 7.77 (s, 3H, H-3‘‘‘), 7.17 (s, 2H, C-6-NH_2), 6.77 (t, ^3J = 5.7 Hz, 3H, -N*H*-C-11‘‘‘), 5.30 – 5.28 (m, 6H, H-3$_{Man}$, H-4$_{Man}$), 5.21 (dd, ^3J = 2.9, 1.7 Hz, 3H, H-2$_{Man}$), 4.95 (d, ^3J = 1.7 Hz, 3H, H-1$_{Man}$), 4.82 (d, ^2J = 12.2 Hz, 3H, H-1a‘‘‘‘), 4.66 (d, ^2J = 12.2 Hz, 3H, H-1b‘‘‘‘), 4.55 (t, ^3J = 5.3 Hz, 6H, H-1‘‘‘), 4.29 (dd, ^2J = 12.2 Hz, ^3J = 5.0 Hz, 3H, H-6a$_{Man}$), 4.10 (dd, ^2J = 12.2 Hz, ^3J = 2.4 Hz, 3H, H-6b$_{Man}$), 4.08 – 4.04 (m, 3H, H-5$_{Man}$), 3.88 (t, ^3J = 5.1 Hz, 6H, H-2‘‘‘), 3.70 (t, ^3J = 5.9 Hz, 6H, H-2), 3.65 – 3.55 (m, 12H, H-4‘‘‘, H-5‘‘‘, H-7‘‘‘, H-8‘‘‘), 3.53 (t, ^3J = 5.1 Hz, 6H, H-10‘‘‘), 3.43 (s, 6H. H-5), 3.42 – 3.39 (m, 6H, H-11‘‘‘), 2.41 (t, ^3J = 5.9 Hz, 6H, H-3), 2.14 (s, 9H, C-2$_{Man}$-O(C=O)C*H*$_3$), 2.11 (s, 9H, C-6$_{Man}$-O(C=O)C*H*$_3$), 2.02 (s, 9H, C-3$_{Man}$-O(C=O)C*H*$_3$), 1.96 (s, 9H, C-4$_{Man}$-O(C=O)C*H*$_3$). **^{13}C-NMR** (151 MHz, $CDCl_3$, 25 °C)**:** δ (ppm) = 171.5 (3C, C-1), 170.8 (3C, C-6$_{Man}$-O(*C*=O)CH$_3$), 170.1 (3C, C-2$_{Man}$-O(*C*=O)CH$_3$), 170.0 (3C, C-3$_{Man}$-O(*C*=O)CH$_3$), 169.7 (3C, C-4$_{Man}$-O(*C*=O)CH$_3$), 143.2 (3C, C-2‘‘‘‘), 124.3 (3C, C-3‘‘‘‘), 96.8 (3C, C-1$_{Man}$), 70.4, 70.4, 70.3, 70.1 (12C, C-4‘‘‘, C-5‘‘‘, C-7‘‘‘, C-8‘‘‘), 69.9 (3C, C-5), 69.7 (3C, C-10‘‘‘), 69.4 (3C, C-2‘‘‘), 69.4 (3C, C-2$_{Man}$), 69.1 (3C, C-4$_{Man}$), 68.6 (3C, C-5$_{Man}$), 67.5 (3C, C-2), 66.0 (3C, C-3$_{Man}$), 62.3 (3C, C-6$_{Man}$), 60.8 (3C, C-1‘‘‘‘), 58.7 (3C, C-6), 50.3 (3C, C-1‘‘‘), 39.1 (3C, C-11‘‘‘), 36.5 (3C, C-3), 20.9 (3C, C-2$_{Man}$-O(C=O)*C*H$_3$), 20.8 (3C, C-6$_{Man}$-O(C=O)*C*H$_3$), 20.7 (3C, C-4$_{Man}$-O(C=O)*C*H$_3$), 20.7 (3C, C-3$_{Man}$-O(C=O)*C*H$_3$). **HR-MS** (ESI$^+$)**:** $m/z_{cal.}$ = 1048.9489 $[M+2H]^{2+}$, $m/z_{exp.}$ = 1048.9513 $[M+2H]^{2+}$; $m/z_{cal.}$ = 1049.4505 $[M+2H]^{2+}$, $m/z_{exp.}$ = 1049.4531 $[M+2H]^{2+}$. R_f (NP) = 0.41 (DCM/MeOH 10:1). **Optical rotation** (LM)**:** $[\alpha]_D^{26}$ = +30.6 ($CHCl_3$). **IR** (ATR)**:** (cm^{-1}) = 3384, 2874, 2175, 2106, 2017, 1745, 1650, 1547, 1435, 1370, 1224, 1131, 1085, 1048, 980, 913, 796, 728, 601, 502, 466, 440, 421.

The analytical data follows literature data.[26]

Supporting Information

4.1.21 Synthesis of *N*-(1-Bis(17-(4-(2,3,4,6-tetra-*O*-acetyl-α-D-mannopyranosyloxy-methyl)-1*H*-1,2,3-triazol-1-yl)-5-oxo-2,9,12,15-tetraoxa-6-azaheptadec-1-yl)-18-(4-(2,3,4,6-tetra-*O*-acetyl-α-D-mannopyranosyloxymethyl)-1*H*-1,2,3-triazol-1-yl)-6-oxo-3,10,13,16-tetraoxa-7-azaoctadec-1-yl)-12-azido-4,7,10-pentaoxadodecanamide

The title compound was synthesized according to Scheme S 23 following modified synthesis protocols by *Cheng et al.*[44] and *Krumb et al.*[26]

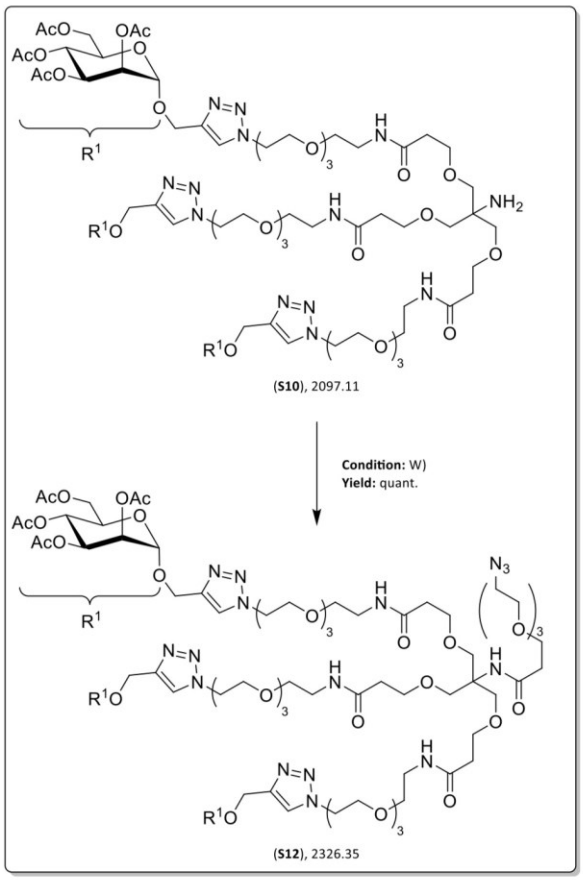

Scheme S 23: Synthesis of *N*-(1-Bis(17-(4-(2,3,4,6-tetra-*O*-acetyl-α-D-manno-pyranosyloxymethyl)-1*H*-1,2,3-triazol-1-yl)-5-oxo-2,9,12,15-tetraoxa-6-aza-hepta-dec-1-yl)-18-(4-(2,3,4,6-tetra-*O*-acetyl-α-D-mannopyranosyloxymethyl)-1H-1,2,3-triazol-1-yl)-6-oxo-3,10,13,16-tetraoxa-7-azaoctadec-1-yl)-12-azido-4,7,10-pentaoxadodecanamide (**S12**). Reaction conditions: A) (**3**), HATU, DIPEA, Ar-atm., DMF, rt, 48 h; yield: quant.

The reaction was carried out in a dried Schlenk vessel previously equipped with a magnetic stirring bar. 12-Azido-4,7,10-trioxadodecanoic acid (**3**, 1.20 g, 4.80 mmol, 10.0 eq.) was dissolved in absolute DMF (10.0 mL) under an atmosphere of argon. HATU (1.83 g, 4.80 mmol, 10.0 eq.) was added, followed by DIPEA (0.81 g, 1.10 mL, 6.24 mmol, 13.0 eq.) via syringe. The reaction mixture was stirred for half an hour at room temperature. *N*-(1-(4-(2,3,4,6-tetra-*O*-acetyl-α-D-mannopyranosyloxymethyl)-1*H*-1,2,3-triazol-1-yl)-3,6,9-trioxaundec-11-yl)-6-amino-6-(17-(4-(2,3,4,6-tetra-*O*-acetyl-α-D-manno-pyranosyl-oxymethyl)-1*H*-1,2,3-triazol-1-yl)-5-oxo-2,9,12,15-tetraoxa-6-azaheptadec-1-yl)-11-oxo-4,8,15,18,21-pentaoxa-12-aza-(23-(4-(2,3,4,6-tetra-*O*-acetyl-α-D-mannopyranosyloxy-methyl)-1*H*-1,2,3-triazol-1-yl)-tricosanamide (**S10**, 1.00 g, 0.48 mmol, 1.00 eq.) was dissolved in absolute DMF (10.0 mL) under an atmosphere of argon and slowly added dropwise to the yellowish reaction mixture using a syringe. The mixture was stirred at room temperature for 48 hours. Complete conversion of the limiting substrate

Supporting Information

and the formation of the desired product were determined by reaction control via TLC and HPLC-ELS-MS. All volatiles were removed in fine vacuum. Toluene (3 x 20.0 mL) was added to the residue and all volatiles were again removed in fine vacuum. The crude product (3.42 g) was obtained in the form of an orange oil and purified by FCC (DCM/MeOH, isocratic at 10 % MeOH) followed by RP-FCC ($MeCN/H_2O$, gradient from 10 % to 50 % to 100 % MeCN, Isolera One Purification System, SNAP C_{18} 60 g cartridge). The pure product (**S12**) was obtained in the form of yellowish oil.

Yield: 1.12 g (0.48 mmol, quant.), yellowish oil.

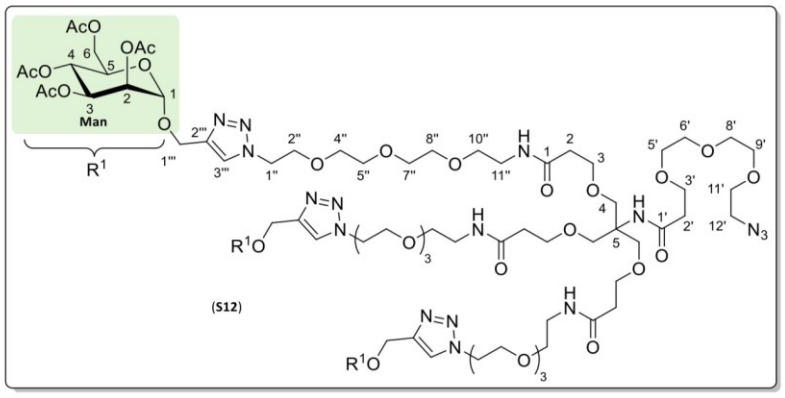

^{1}H-NMR (600 MHz, $CDCl_3$, 25 °C)**:** δ (ppm) = 7.77 (s, 3H, H-3‘‘‘), 6.76 (t, ^3J = 5.6 Hz, 3H, -N*H*-C-11‘‘), 6.58 (s, 1H, -N*H*-C-5), 5.33 – 5.26 (m, 6H, H-3$_{Man}$, H-4$_{Man}$), 5.22 (dd, ^3J = 2.4, 0.7 Hz, 3H, H-2$_{Man}$), 4.96 (d, ^3J = 1.7 Hz, 3H, H-1$_{Man}$), 4.83 (d, ^2J = 12.2 Hz, 3H, H-1a‘‘‘), 4.67 (d, ^2J = 12.2 Hz, 3H, H-1b‘‘‘), 4.56 (t, ^3J = 5.1 Hz, 6H, H-1‘‘), 4.30 (dd, ^2J = 12.2 Hz, ^3J = 4.9 Hz, 3H, H-6a$_{Man}$), 4.10 (dd, ^2J = 12.2 Hz, ^3J = 2.5 Hz, 3H, H-6b$_{Man}$), 4.09 – 4.05 (m, 3H, H-5$_{Man}$), 3.89 (t, ^3J = 5.1 Hz, 6H, H-2‘‘), 3.72 – 3.58 (m, 42H, H-4, H-3‘, H-5‘, H-6‘, H-8‘, H-9‘, H-11‘, H-4‘‘, H-5‘‘, H-7‘‘, H-8‘‘), 3.54 (t, ^3J = 5.5 Hz, 6H, H-10‘‘), 3.42 (q, ^3J = 5.5 Hz, 6H, H-11‘‘), 3.38 (t, ^3J = 5.0 Hz, 2H, H-12‘), 2.44 (t, ^3J = 6.1 Hz, 2H, H-2‘), 2.40 (t, ^3J = 5.9 Hz, 6H, H-3), 2.15 (s, 9H, C-2$_{Man}$-O(C=O)C*H*$_3$), 2.12 (s, 9H, C-6$_{Man}$-O(C=O)C*H*$_3$), 2.03 (s, 9H, C-4$_{Man}$-O(C=O)C*H*$_3$), 1.97 (s, 9H, C-3$_{Man}$-O(C=O)C*H*$_3$). **^{13}C-NMR** (151 MHz, $CDCl_3$, 25 °C)**:** δ (ppm) = 171.6 (1C, C-1‘), 171.3 (3C, C-1), 170.88 (3C, C-6$_{Man}$-O(*C*=O)CH$_3$), 170.18 (3C, C-2$_{Man}$-O(*C*=O)CH$_3$), 169.98 (3C, C-3$_{Man}$-O(*C*=O)CH$_3$), 169.78 (3C, C-4$_{Man}$-O(*C*=O)CH$_3$), 143.3 (3C, C-2‘‘‘), 124.2 (3C, C-3‘‘‘), 96.8 (3C, C-1$_{Man}$), 70.6, 70.5, 70.5, 70.5, 70.4, 70.2, 70.1, 70.0 (16C, C-5‘, C-6‘, C-8‘, C-9‘, C-4‘‘, C-5‘‘, C-7‘‘, C-8‘‘), 69.8 (6C, C-5, C-10‘‘), 69.4 (6C, C-2‘‘, C-2$_{Man}$), 69.2 (1C, C-11‘), 69.0 (3C, C-4$_{Man}$), 68.6 (3C, C-5$_{Man}$), 67.4 (3C, C-2), 67.3 (1C, C-3‘), 66.0 (3C, C-3$_{Man}$), 62.3 (3C, C-6$_{Man}$), 60.9 (3C, C-1‘‘‘), 59.7 (1C, C-5), 50.6 (1C, C-12‘), 50.3 (3C, C-1‘‘), 39.2 (3C, C-11‘‘), 37.4 (1C, C-2‘), 36.6 (3C, C-3), 20.9 (3C, C-2$_{Man}$-O(C=O)C*H*$_3$), 20.8 (3C, C-6$_{Man}$-O(C=O)C*H*$_3$), 20.7 (3C, C-4$_{Man}$-O(C=O)C*H*$_3$), 20.7 (3C, C-3$_{Man}$-O(C=O)C*H*$_3$). **HR-MS** (ESI$^+$)**:** $m/z_{cal.}$ = 797.9857 $[M+3Na]^{3+}$, $m/z_{exp.}$ = 797.9858 $[M+3Na]^{3+}$; $m/z_{cal.}$ = 798.3201 $[M+3Na]^{3+}$, $m/z_{exp.}$ = 798.3200 $[M+Na]^{3+}$; $m/z_{cal.}$ = 1185.4839 $[M+2Na]^{2+}$, $m/z_{exp.}$ = 1185.4848 $[M+2Na]^{2+}$; $m/z_{cal.}$ = 1185.9856 $[M+2Na]^{2+}$, $m/z_{exp.}$ = 1185.9840 $[M+2Na]^{2+}$. R_f (NP) = 0.23 (DCM/MeOH 15:1), 0.47 (DCM/MeOH 10:1). **Optical rotation** (LM)**:** $[\alpha]_D^{27}$ = +26.5 ($CHCl_3$).**IR** (ATR)**:** (cm^{-1}) = 3311, 2877, 2101, 1748, 1656, 1547, 1436, 1370, 1227, 1132, 1087, 1049, 980.

The analytical data follows literature data.[26]

4.1.22 Synthesis of *N*-(1-Bis(17-(4-(α-D-mannopyranosyloxymethyl)-1*H*-1,2,3-triazol-1-yl)-5-oxo-2,9,12,15-tetraoxa-6-azaheptadec-1-yl)-18-(4-(α-D-mannopyranosyloxymethyl)-1*H*-1,2,3-triazol-1-yl)-6-oxo-3,10,13,16-tetraoxa-7-azaoctadec-1-yl)-12-azido-4,7,10-pentaoxadodecanamide

The title compound was synthesized according to Scheme S 24 following modified synthesis protocols by *Percec et al.*[11] and *Krumb et al.*[26]

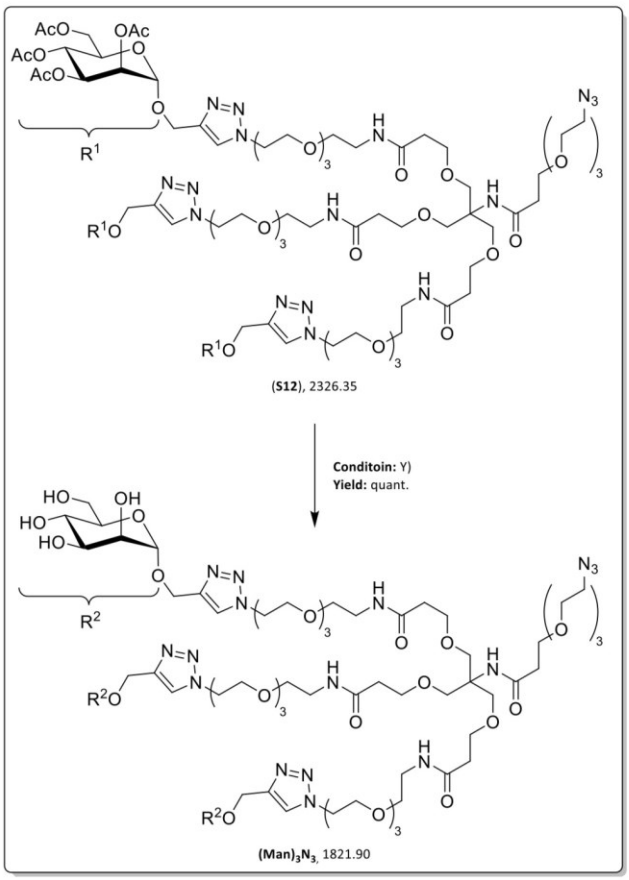

Scheme S 24: Synthesis of *N*-(1-Bis(17-(4-(α-D-mannopyranosyloxymethyl)-1*H*-1,2,3-triazol-1-yl)-5-oxo-2,9,12,15-tetraoxa-6-azaheptadec-1-yl)-18-(4-(α-D-mannopyranosyloxymethyl)-1*H*-1,2,3-triazol-1-yl)-6-oxo-3,10,13,16-tetraoxa-7-azaoctadec-1-yl)-12-azido-4,7,10-pentaoxadodecanamide **(Man)$_3$N$_3$**. Reaction conditions: Y) NaOMe, MeOH, Ar-atm., RT, 2 h; yield: quant.

The reaction was carried out in a dried Schlenk vessel, which was previously equipped with a magnetic stirring bar. *N*-(1-bis(17-(4-(2,3,4,6-tetra-*O*-acetyl-α-D-manno-pyranosyloxymethyl)-1*H*-1,2,3-triazol-1-yl)-5-oxo-2,9,12,15-tetraoxa-6-azaheptadec-1-yl)-18-(4-(2,3,4,6-tetra-*O*-acetyl-α-D-mannopyranosyloxymethyl)-1*H*-1,2,3-triazol-1-yl)-6-oxo-3,10,-13,16-tetra-oxa-7-azaoctadec-1-yl)-12-azido-4,7,10-penta¬oxa¬dodecan¬amide (**S12**, 0.10 g, 0.04 mmol, 1.00 eq.) was dissolved in absolute MeOH (10.0 mL) under an atmosphere of argon. NaOMe (2.60 mg, 0.05 mmol, 1.20 eq.) was added and the resulting solution was stirred for two hours at room temperature. Complete conversion of the limiting substrate and the formation of the desired product were determined by reaction control via TLC and HPLC-ELS-MS. The reaction was ended by addition of the ion exchange resin *Amberlite IR 120* (0.10 g), and the mixture was stirred for ten minutes until a constant pH value (pH = 6–7) was reached. The reaction mixture was filtered through a glass frit with *Celite* and eluted with MeOH (1 x 50.0 mL). All volatiles were removed in vacuo. The crude product (0.08 g) was obtained in the form of yellowish

Supporting Information

oil and purified by RP-FCC (MeCN/H_2O, gradient from 5 % to 25 % to 100 % MeCN, Isolera One Flash Purification System, SNAP C_{18} 12 g cartridge). The pure product **$(Man)_3N_3$** was obtained in the form of colorless oil.

Yield: 0.07 g (0.04 mmol, quant.), colorless oil.

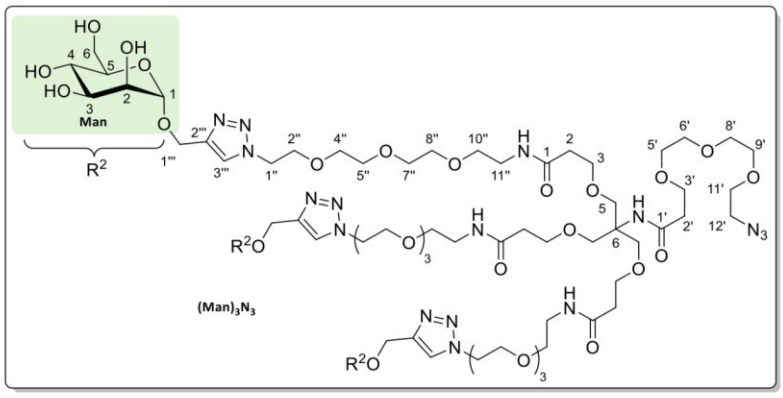

^{1}H-NMR (600 MHz, D_2O, 25 °C)**:** δ (ppm) = 8.07 (s, 3H, H-3‘‘‘), 4.92 (d, ^3J = 1.7 Hz, 3H, H-1$_{Man}$), 4.78 (d, ^2J = 12.4 Hz, 3H, H-1a‘‘‘), 4.66 (d, ^2J = 12.4 Hz, 3H, H-1a‘‘‘), 4.59 (t, ^3J = 5.0 Hz, 6H, H-1‘‘), 3.93 (t, ^3J = 5.0 Hz, 6H, H-2‘‘), 3.87 (dd, ^3J = 3.5, 1.7 Hz, 3H, H-2$_{Man}$), 3.80 (dd, ^2J = 12.2 Hz, ^3J = 2.0 Hz, 3H, H-6a$_{Man}$), 3.75 – 3.69 (m, 3H, H-3$_{Man}$), 3.69 – 3.53 (m, 66H, H-4$_{Man}$, H-5$_{Man}$, H-6b$_{Man}$, H-2, H-5, H-3‘, H-5‘, H-6‘, H-8‘, H-11‘, H-9‘, H-4‘‘, H-5‘‘, H-7‘‘, H-8‘‘, H-10‘‘), 3.44 (t, ^3J = 4.9 Hz, 2H, H-12‘), 3.34 (t, ^3J = 5.5 Hz, 6H, H-11‘‘), 2.46 (t, ^3J = 6.1 Hz, 2H, H-2‘), 2.44 (t, ^3J = 6.1 Hz, 6H, H-3). **^{13}C-NMR** (151 MHz, D_2O, 25 °C)**:** δ (ppm) = 174.1 (3C, C-1), 173.8 (1C, C-1‘), 143.5 (3C, C-2‘‘‘), 125.6 (3C, C-3‘‘‘), 99.4 (3C, C-1$_{Man}$), 73.0 (3C, C-5$_{Man}$), 70.5 (3C, C-3$_{Man}$), 69.9 (3C, C-2$_{Man}$), 69.6, 69.6, 69.6, 69.6, 69.5, 69.5 (16C, C-4‘‘, C-5‘, C-6‘, C-8‘, C-9‘, C-5‘‘, C-7‘‘, C-8‘‘), 69.4 (3C, C-5), 69.3, (1C, C-11‘) 68.8 (3C, C-10‘‘), 68.7 (3C, C-2‘‘), 68.4 (1C, C-3‘), 67.5 (3C, C-2), 66.6 (3C, C-4$_{Man}$), 60.8 (3C, C-6$_{Man}$), 60.3 (1C, C-6), 59.7 (3C, C-1‘‘‘), 50.1 (1C, C-12‘), 50.0 (3C, C-1‘‘), 39.0 (3C, C-11‘‘), 36.4 (1C, C-2‘), 36.1 (3C, C-3). **HR-MS** (ESI$^+$)**:** $m/z_{cal.}$ = 629.9434 $[M+3Na]^{3+}$, $m/z_{exp.}$ = 629.9433 $[M+3Na]^{3+}$; $m/z_{cal.}$ = 630.2779 $[M+3Na]^{3+}$, $m/z_{exp.}$ = 630.2773 $[M+3Na]^{3+}$; $m/z_{cal.}$ = 933.4205 $[M+2Na]^{2+}$, $m/z_{exp.}$ = 933.4188 $[M+3Na]^{3+}$; $m/z_{cal.}$ = 933.9222 $[M+2Na]^{2+}$, $m/z_{exp.}$ = 933.9205 $[M+3Na]^{3+}$. R_f (NP) = 0.17 (DCM/MeOH + AcOH 5:1 +0.1 %$_{v/v}$ additive); (RP) = 0.43 (MeCN/H_2O 3:7). **Optical rotation** (LM)**:** $[\alpha]_D^{22}$ = +34.0 (MeOH). **IR** (ATR)**:** (cm^{-1}) = 3628, 3348, 2915, 2875, 2114, 1652, 1596, 1457, 1352, 1305, 1249, 1099, 913, 846, 773, 741, 692, 679, 667, 639, 607, 561, 538, 516, 500, 482, 473, 457, 432, 415.

The analytical data follows literature data.[26]

Supporting Information

4.1.23 Synthesis of 2-Nitrobenzyl (1,35-Bis(4-(2,4-di-*O*-benzoyl-3,6-di-*O*-(2,3,4,6-tetra-*O*-acetyl-α-D-mannopyranosyl)-α-D-mannopyranosyloxymethyl)-1*H*-1,2,3-triazol-1-yl)-18-(17-(4-(2,4-di-*O*-benzoyl-3,6-di-*O*-(2,3,4,6-tetra-*O*-acetyl-α-D-mannopyranosyl)-α-D-mannopyranosyloxymethyl)-1*H*-1,2,3-triazol-1-yl))-5-oxo-2,9,12,15-tetraoxa-6-azaheptadec-1-yl)-13,23-dioxo-3,6,9,16,20,-27,30,33-octaoxa-12,24-diazapentatriacontan-18-yl)carbamate

The title compound was synthesized according to Scheme S 25 following modified synthesis protocols by *Krumb et al.*[26] and *Yamamoto et al.*[39]

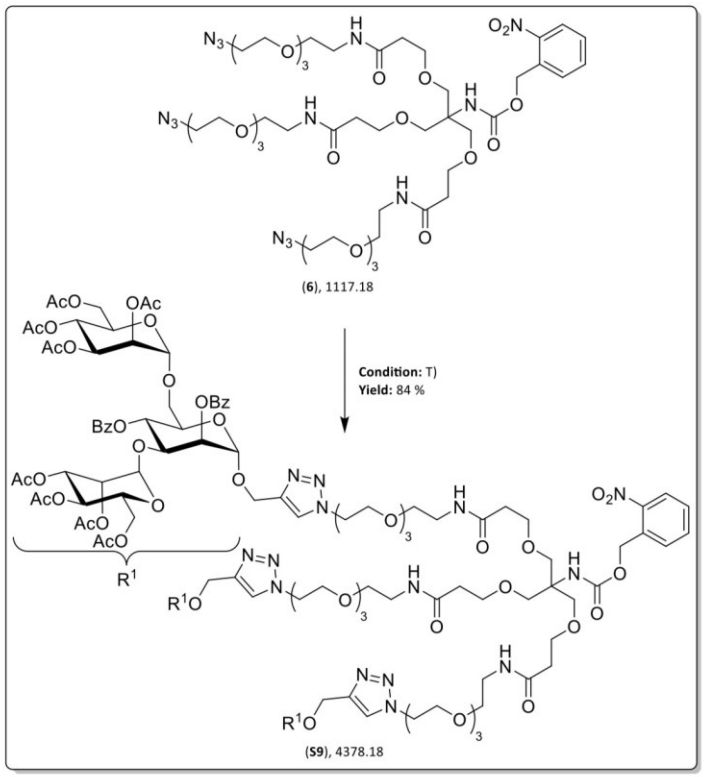

Scheme S 25: Synthesis of 2-Nitrobenzyl (1,35-Bis(4-(2,4-di-*O*-benzoyl-3,6-di-*O*-(2,3,4,6-tetra-*O*-acetyl-α-D-mannopyranosyl)-α-D-mannopyranosyloxymethyl)-1*H*-1,2,3-triazol-1-yl)-18-(17-(4-(2,4-di-*O*-benzoyl-3,6-di-*O*-(2,3,4,6-tetra-*O*-acetyl-α-DD-mannopyranosyl)-α-D-mannopyranosyloxymethyl)-1*H*-1,2,3-triazol-1-yl))-5-oxo-2,9,12,15-tetraoxa-6-azaheptadec-1-yl)-13,23-dioxo-3,6,9,16,20,27,30,33-octaoxa-12,24-diazapentatriacontan-18-yl)carbamate (**6**). Reaction condition: T) (**1**), Cu^{I}Br, PMDTA, DMF, Ar-Atm., 45 °C, 5 h; yield: 84 %.

The reaction was carried out in a dried Schlenk vessel, which was previously equipped with a magnetic stirring bar. 2-Nitrobenzyl-(1,35-diazido-18-(17-azido-5-oxo-2,9,12,15-tetraoxa-6-azaheptadecyl)-13,23-dioxo-3,6,9,16,20,27,30,33-octaoxa-12,24-diazapentatria-contan-18-yl)carbamate (**6**, 0.20 g, 0.18 mmol, 1.00 eq.) and Propargyl 2,4-di-*O*-benzoyl-3,6-di-*O*-(2,3,4,6-tetra-*O*-acetyl-α-D-manno¬pyranosyl)-α-D-manno¬pyranosyloxymethyl (**1**, 0.68 g, 0.63 mmol, 3.50 eq.) were dissolved under an atmosphere of argon in absolute DMF (10.0 mL), which had previously been degassed for half an hour with an argon gas stream in an ultrasonic bath. PMDTA (0.06 g, 0.08 mL, 0.36 mmol, 2.00 eq.) was added via syringe. The yellowish solution was again degassed for half an hour with an argon gas stream in an ultrasonic bath and then warmed to a temperature of 45 °C. Cu^{I}Br (7.20 mg, 0.05 mmol, 0.25 eq.) was added. The greenish reaction mixture was stirred at this temperature for five hours. Complete conversion of the limiting substrate and the formation of the desired product were determined by reaction control via TLC and HPLC-ELS-MS. All volatile components were removed in fine vacuum. Toluene (3 x 10.0 mL) was added to the residue and all volatiles were again removed in fine vacuum.

Supporting Information

The residue was taken up in EtOAc (1 x 50.0 mL), and the organic phase was washed with saturated NH_4Cl solution (3 x 50.0 mL). The collected aqueous phases were diluted with H_2O (1 x 50.0 mL) until all salts were dissolved and extracted with EtOAc (3 x 50.0 mL). The collected organic phases were dried over anhydrous Na_2SO_4 and filtered. All volatiles were removed under vacuum, and the residue was dried in fine vacuum. The crude product (0.62 g) was obtained in the form of yellowish oil and purified by FCC (DCM/MeOH, isocratic at 5 % MeOH). The pure product (**S9**) was obtained in the form of colorless oil.

Yield: 0.66 g (0.15 mmol, 84 %), colorless oil.

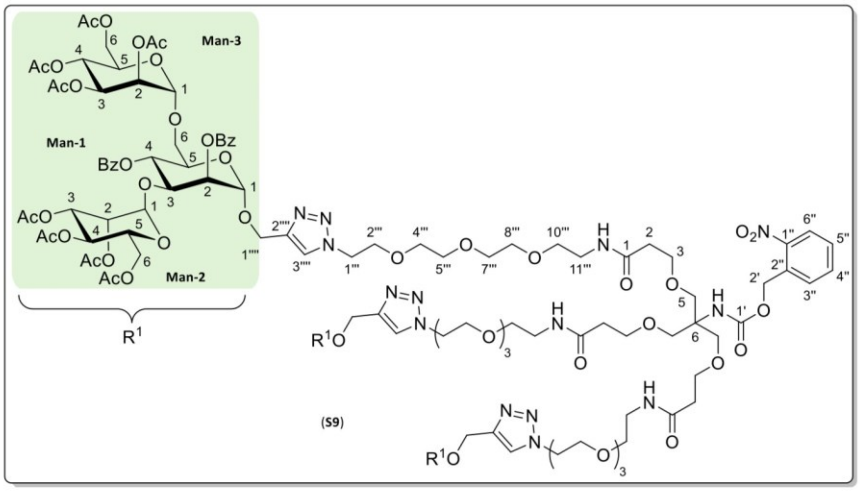

^{1}H-NMR (600 MHz, $CDCl_3$, 25 °C)**:** δ (ppm) = 8.16 – 8.12 (m, 6H, C-2$_{Man\text{-}1}$-O(C=O)Ph, H$_{ortho}$), 8.10 – 8.07 (m, 1H, H-6‘‘), 8.05 – 8.00 (m, 6H, C-4$_{Man\text{-}1}$-O(C=O)Ph, H$_{ortho}$), 7.83 (s, 3H, H-3‘‘‘‘), 7.68 – 7.53 (m, 14H, H-4‘‘, H-5‘‘, C-2$_{Man\text{-}1}$-O(C=O)Ph, H$_{meta}$, H$_{para}$, C-4$_{Man\text{-}1}$-O(C=O)Ph, H$_{para}$), 7.51 – 7.46 (m, 1H, H-3‘‘), 7.46 – 7.42 (m, 6H, C-4$_{Man\text{-}1}$-O(C=O)Ph, H$_{meta}$), 6.70 (t, ^3J = 5.5 Hz, 3H, -N*H*-C-11‘‘‘), 5.74 (s, 1H, -N*H*-C-6), 5.70 (t$_{app}$, ^3J = 10.0 Hz, 3H, H-4$_{Man\text{-}1}$), 5.51 (dd, ^3J = 3.5, 1.8 Hz, 3H, H-2$_{Man\text{-}1}$), 5.44 (s, 2H, H-2‘), 5.34 (dd, ^3J = 10.1, 3.4 Hz, 3H, H-3$_{Man\text{-}3}$), 5.31 – 5.27 (m, 3H, H-2$_{Man\text{-}3}$), 5.24 (t, ^3J = 10.1 Hz, 3H, H-4$_{Man\text{-}3}$), 5.16 (d, ^3J = 1.7 Hz, 3H, H-1$_{Man\text{-}1}$), 5.10 – 5.04 (m, 6H, H-3$_{Man\text{-}2}$, H-4$_{Man\text{-}2}$), 4.94 (d, ^3J = 1.9 Hz, 3H, H-1$_{Man\text{-}2}$), 4.88 (d, ^2J = 12.1 Hz, 3H, H-1a‘‘‘‘), 4.85 (d, ^3J = 1.8 Hz, 3H, H-1$_{Man\text{-}3}$), 4.84 (t$_{app}$, ^3J = 2.4 Hz, 3H, H-2$_{Man\text{-}2}$), 4.72 (d, ^2J = 12.1 Hz, 3H, H-1b‘‘‘‘), 4.57 (t, ^3J = 5.3 Hz, 6H, H-1‘‘‘), 4.45 (dd, ^3J = 9.8, 3.4 Hz, 3H, H-3$_{Man\text{-}1}$), 4.25 (ddd, ^3J = 10.3, 6.0, 2.2 Hz, 3H, H-5$_{Man\text{-}1}$), 4.16 – 4.11 (m, 6H, H-6a$_{Man\text{-}2}$, H-6a$_{Man\text{-}3}$), 4.07 – 4.02 (m, 6H, H-5$_{Man\text{-}2}$, H-5$_{Man\text{-}3}$), 3.98 – 3.90 (m, 15H, H-5a, H-2a‘‘‘, H-6a$_{Man\text{-}1}$, H-6b$_{Man\text{-}2}$, H-6b$_{Man\text{-}3}$), 3.70 (t, ^3J = 5.9 Hz, 6H, H-2), 3.66 – 3.56 (m, 33H, H-5b, H-2b‘‘‘, H-4‘‘‘, H-5‘‘‘, H-7‘‘‘, H-8‘‘‘, H-6b$_{Man\text{-}1}$), 3.53 (t, ^3J = 5.4 Hz, 6H, H-10‘‘‘), 3.43 (q, ^3J = 5.5 Hz, 6H, H-11‘‘‘), 2.42 (t, ^3J = 5.9 Hz, 6H, H-3), 2.11 (s, 9H, C-4$_{Man\text{-}3}$-O(C=O)C*H*$_3$), 2.04 (s, 9H, C-6$_{Man\text{-}3}$-O(C=O)C*H*$_3$), 2.03 (s, 9H, C-3$_{Man\text{-}3}$-O(C=O)C*H*$_3$), 1.96 (s, 9H, C-6$_{Man\text{-}2}$-O(C=O)C*H*$_3$), 1.92 (s, 9H, C-3$_{Man\text{-}2}$-O(C=O)C*H*$_3$), 1.91 (s, 9H, C-4$_{Man\text{-}1}$-O(C=O)C*H*$_3$), 1.84 (s, 9H, C-2$_{Man\text{-}2}$-O(C=O)C*H*$_3$), 1.81 (s, 9H, C-2$_{Man\text{-}3}$-O(C=O)C*H*$_3$). **^{13}C-NMR** (151 MHz, $CDCl_3$, 25 °C)**:** δ (ppm) = 171.2 (3C, C-1), 170.8 (3C, C-6$_{Man\text{-}2}$-O(*C*=O)CH$_3$), 170.6 (3C, C-6$_{Man\text{-}3}$-O(*C*=O)CH$_3$), 170.0 (3C, C-4$_{Man\text{-}3}$-O(*C*=O)CH$_3$), 169.9 (3C, C-3$_{Man\text{-}3}$-O(*C*=O)CH$_3$), 169.8 (3C, C-3$_{Man\text{-}2}$-O(*C*=O)CH$_3$), 169.6 (3C, C-4$_{Man\text{-}2}$-O(*C*=O)CH$_3$), 169.2 (3C, C-2$_{Man\text{-}3}$-O(*C*=O)CH$_3$), 169.1 (3C, C-2$_{Man\text{-}2}$-O(*C*=O)CH$_3$), 165.9 (3C, C-2$_{Man\text{-}1}$-O(*C*=O)Ph), 165.2 (3C, C-4$_{Man\text{-}1}$-O(*C*=O)Ph), 154.6 (1C, C-1‘), 147.2 (1C, C-1‘‘), 142.9 (3C, C-2‘‘‘‘), 133.9 (1C, C-4‘‘), 133.7 (3C, C-2$_{Man\text{-}1}$-O(C=O)Ph, C$_{para}$), 133.6 (3C, C-4$_{Man\text{-}1}$-O(C=O)Ph, C$_{para}$), 133.3 (1C, C-2‘‘), 133.0 (6C, C-2$_{Man\text{-}1}$-O(C=O)Ph, C$_{ortho}$), 129.9 (6C, C-4$_{Man\text{-}1}$-O(C=O)Ph, C$_{ortho}$), 129.0 (3C, C-2$_{Man\text{-}1}$-O(C=O)Ph, C$_{ipso}$), 128.8 (6C,

Supporting Information

C-2$_{Man-1}$-O(C=O)Ph, C$_{meta}$), 128.8 (1C, C-5‘‘), 128.7 (3C, C-4$_{Man-1}$-O(C=O)Ph, C$_{ipso}$), 128.5 (1C, C-2‘‘), 128.5 (6C, C-4$_{Man-1}$-O(C=O)Ph, C$_{meta}$), 125.0 (1C, C-6‘‘), 124.4 (3C, C-3‘‘‘‘), 99.4 (3C, C-1$_{Man-2}$), 97.3 (3C, C-1$_{Man-3}$), 96.6 (3C, C-1$_{Man-1}$), 75.5 (3C, C-3$_{Man-1}$), 71.6 (3C, C-2$_{Man-1}$), 70.5, 70.5, 70.4, 70.1 (12C, C-4‘‘‘, C-5‘‘‘, C-7‘‘‘, C-8‘‘‘), 69.8 (3C, C-10‘‘‘), 69.5 (3C, C-5$_{Man-1}$), 69.4 (3C, C-5), 69.3 (3C, C-2‘‘‘), 69.2 (3C, C-2$_{Man-2}$), 69.2 (3C, C-2$_{Man-3}$), 69.2 (3C, C-3$_{Man-3}$), 68.6 (3C, C-5$_{Man-2}$), 68.5 (3C, C-4$_{Man-1}$), 68.2 (3C, C-3$_{Man-2}$), 67.4 (3C, C-2), 66.4 (3C, C-6$_{Man-1}$), 65.9 (3C, C-4$_{Man-2}$), 65.7 (3C, C-4$_{Man-3}$), 62.9 (1C, C-2‘), 62.3 (3C, C-6$_{Man-2}$), 62.2 (3C, C-6$_{Man-3}$), 60.4 (3C, C-1‘‘‘‘), 58.9 (3C, C-6), 50.2 (3C, C-1‘‘‘), 39.2 (3C, C-11‘‘‘), 36.6 (3C, C-3), 20.9 (3C, C-4$_{Man-3}$-O(C=O)*C*H$_3$), 20.8 (3C, C-6$_{Man-3}$-O(C=O)*C*H$_3$), 20.7 (3C, C-3$_{Man-3}$-O(C=O)*C*H$_3$), 20.7 (3C, C-6$_{Man-2}$-O(C=O)*C*H$_3$), 20.7 (3C, C-3$_{Man-2}$-O(C=O)*C*H$_3$), 20.6 (3C, C-4$_{Man-2}$-O(C=O)*C*H$_3$), 20.5 (3C, C-2$_{Man-2}$-O(C=O)*C*H$_3$), 20.5 (3C, C-2$_{Man-3}$-O(C=O)*C*H$_3$). **HR-MS** (ESI$^+$)**:** $m/z_{cal.}$ = 1459.8437 $[M+3H]^{3+}$, $m/z_{exp.}$ = 1459.8437 $[M+3H]^{3+}$; $m/z_{cal.}$ = 1460.1782 $[M+3H]^{3+}$, $m/z_{exp.}$ = 1460.1718 $[M+3H]^{3+}$; $m/z_{cal.}$ = 2189.2620 $[M+2H]^{2+}$, $m/z_{exp.}$ = 2189.2609 $[M+2H]^{2+}$; $m/z_{cal.}$ = 2189.7636 $[M+2H]^{2+}$, $m/z_{exp.}$ = 2189.7631 $[M+2H]^{2+}$. $\boldsymbol{R_f}$ (NP) = 0.23 (EtOAc/MeOH 5:1), 0.43 (DCM/MeOH 10:1). **Optical rotation** (LM)**:** $[\boldsymbol{\alpha}]_{\mathbf{D}}^{\mathbf{22}}$ = +9.50 ($CHCl_3$). **IR** (ATR)**:** (cm^{-1}) = 2925, 2869, 1749, 1667, 1529, 1452, 1370, 1226, 1047, 981, 753, 714.

Supporting Information

4.1.24 Synthesis of *N*-(1-(4-(2,4-Di-*O*-benzoyl-3,6-di-*O*-(2,3,4,6-tetra-*O*-acetyl-α-D-mannopyranosyl)-α-D-mannopyranosyloxymethyl)-1*H*-1,2,3-triazol-1-yl)-3,6,9-trioxaundec-11-yl)-6-amino-6-(17-(4-(2,4-di-*O*-benzoyl-3,6-di-*O*-(2,3,4,6-tetra-*O*-acetyl-α-D-mannopyranosyl)-α-D-mannopyranosyloxymethyl)-1*H*-1,2,3-triazol-1-yl)-5-oxo-2,9,12,15-tetraoxa-6-azaheptadec-1-yl)-11-oxo-4,8,15,18,-21-pentaoxa-12-aza-(23-(4-(2,4-di-*O*-benzoyl-3,6-di-*O*-(2,3,4,6-tetra-*O*-acetyl-α-D-mannopyranosyl)-α-D-mannopyranosyloxymethyl)-1*H*-1,2,3-triazol-1-yl)-tricosanamide

The title compound was synthesized according to Scheme S 26 following modified synthesis protocols by *Amit et al.*[42, 43] and *Krumb et al.*[26]

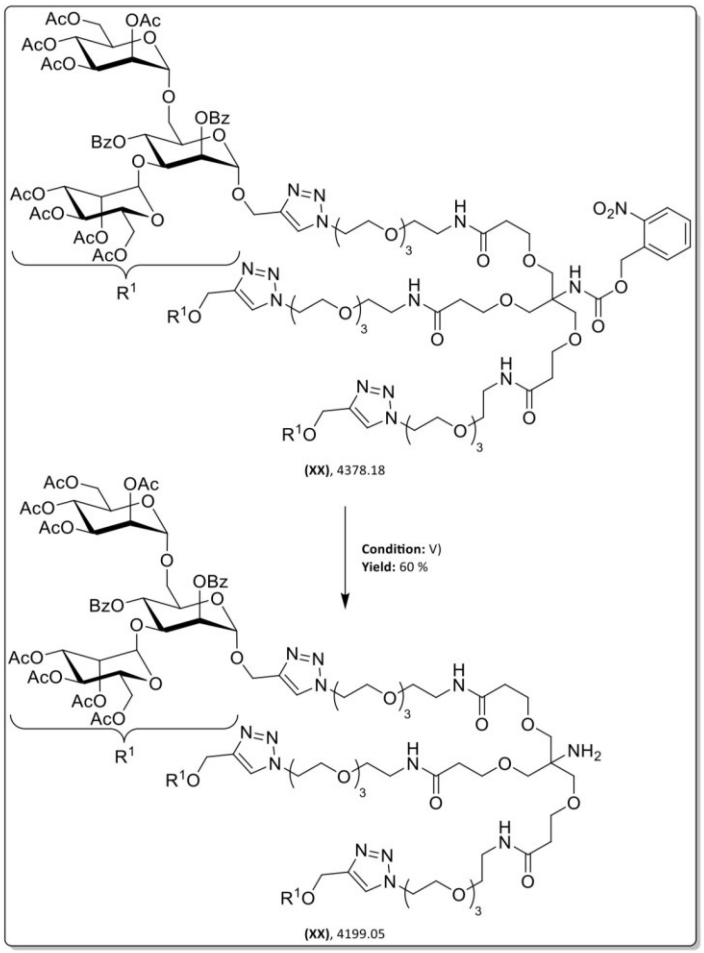

Scheme S 26: Synthesis of *N*-(1-(4-(2,4-Di-*O*-benzoyl-3,6-di-*O*-(2,3,4,6-tetra-*O*-acetyl-α-D-mannopyranosyl)-α-D-mannopyranosyloxymethyl)-1*H*-1,2,3-triazol-1-yl)-3,6,9-trioxaundec-11-yl)-6-amino-6-(17-(4-(2,4-di-*O*-benzoyl-3,6-di-*O*-(2,3,4,6-tetra-*O*-acetyl-α-D-mannopyranosyl)-α-D-mannopyranosyloxymethyl)-1*H*-1,2,3-triazol-1-yl)-5-oxo-2,9,12,15-tetraoxa-6-azaheptadec-1-yl)-11-oxo-4,8,15,18,21-pentaoxa-12-aza-(23-(4-(2,4-di-*O*-benzoyl-3,6-di-*O*-(2,3,4,6-tetra-*O*-acetyl-α-D-mannopyranosyl)-α-D-mannopyranosyloxymethyl)-1*H*-1,2,3-triazol-1-yl)tricosanamide (**S11**). Reaction conditions: V) UV-A, MeCN, Ar-atm., rt, 15 h; yield: 60 %.

The reaction was carried out in a quartz tube, which had previously been equipped with a magnetic stir bar. 2-Nitrobenzyl (1,35-Bis(4-(2,4-di-*O*-benzoyl-3,6-di-*O*-(2,3,4,6-tetra-*O*-acetyl-α-D-mannopyranosyl)-α-D-mannopyranosyloxymethyl)-1*H*-1,2,3-triazol-1-yl)-18-(17-(4-(2,4-di-*O*-benzoyl-3,6-di-*O*-(2,3,4,6-tetra-O-acetyl-α-D-mannopyranosyl)-α-D-mannopyranosyloxymethyl)-1*H*-1,2,3-triazol-1-yl))-

Supporting Information

5-oxo-2,9,12,15-tetraoxa-6-azaheptadec-1-yl)-13,23-dioxo-3,6,9,16,20,27,30,33-octaoxa-12,24-diaza-pentatriacontan-18-yl)¬carbamate (**S9**, 0.20 g, 0.05 mmol, 1.00 eq.) was dissolved under an atmosphere of argon in a mixture of MeCN and H_2O (1:1$_{v/v}$, 5.00 mL) that had previously been degassed for half an hour with an argon gas stream in an ultrasonic bath. The colorless solution was again degassed for half an hour with an argon gas stream in an ultrasonic bath. The reaction mixture was irradiated with UV-A radiation (λ_{max} = 350 nm) for 15 hours in a Rayonet photoreactor with stirring at room temperature. Complete conversion of the limiting substrate and formation of the desired product were determined by reaction control via TLC and HPLC-ELS-MS. The orange solution was diluted with MeCN (10.0 mL) and H_2O (10.0 mL) and transferred to a flask. All volatile components were removed by lyophilization. The crude product (0.18 g) was obtained in the form of an orange lyophilizate and purified by FCC (DCM/MeOH, isocratic at 5 % MeOH). The pure product (**S11**) was obtained in the form of orange oil.

Yield: 0.13 g (0.03 mmol, 60 %), orange oil.

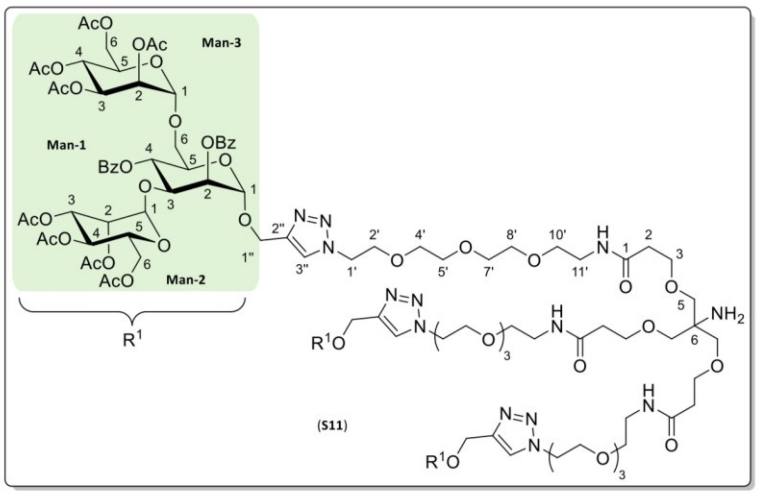

^{1}H-NMR (600 MHz, $CDCl_3$, 25 °C)**:** δ (ppm) = 8.19 – 8.10 (m, 6H, C-2$_{Man-1}$-O(C=O)Ph, H$_{ortho}$), 8.06 – 7.99 (m, 6H, C-4$_{Man-1}$-O(C=O)Ph, H$_{ortho}$), 7.83 (s, 3H, H-3‘‘), 7.64 – 7.60 (m, 3H, C-2$_{Man-1}$-O(C=O)Ph, H$_{para}$), 7.60 – 7.57 (m, 3H, C-4$_{Man-1}$-O(C=O)Ph, H$_{para}$), 7.56 – 7.53 (m, 6H, C-2$_{Man-1}$-O(C=O)Ph, H$_{meta}$), 7.46 – 7.42 (m, 6H, C-4$_{Man-1}$-O(C=O)Ph, H$_{meta}$), 5.70 (t, ^3J = 10.0 Hz, 3H, H-2), 5.51 (dd, ^3J = 3.5, 1.7 Hz, 3H, H-2$_{Man-1}$), 5.34 (dd, ^3J = 10.1, 3.5 Hz, 3H, H-3$_{Man-3}$), 5.29 (dd, ^3J = 3.4, 1.7 Hz, 3H, H-2$_{Man-3}$), 5.24 (t$_{app}$, ^3J = 10.1 Hz, 3H, H-4$_{Man-3}$), 5.16 (d, ^3J = 1.7 Hz, 3H, H-1$_{Man-1}$), 5.10 – 5.04 (m, 6H, H-3$_{Man-2}$, H-4$_{Man-2}$), 4.94 (d, ^3J = 1.9 Hz, 3H, H-1$_{Man-2}$), 4.88 (d, ^2J = 12.2 Hz, 3H, H-1a‘‘), 4.85 (d, ^3J = 1.7 Hz, 3H, H-1$_{Man-3}$), 4.84 (dd, ^3J = 2.9, 1.9 Hz, 3H, H-2$_{Man-2}$), 4.72 (d, ^2J = 12.2 Hz, 3H, H-1b‘‘), 4.58 (t, ^3J = 5.3 Hz, 6H, H-1‘), 4.45 (dd, ^3J = 9.8, 3.6 Hz, 3H, H-3$_{Man-1}$), 4.25 (ddd, ^3J = 10.3, 5.9, 2.1 Hz, 3H, H-5$_{Man-1}$), 4.17 – 4.11 (m, 6H, H-6a$_{Man-2}$, H-6a$_{Man-3}$), 4.07 – 4.01 (m, 6H, H-5$_{Man-2}$, H-5$_{Man-3}$), 3.99 – 3.90 (m, 18H, H-5a, H-2a‘, H-6a$_{Man-1}$, H-6b$_{Man-2}$, H-6b$_{Man-3}$), 3.70 (t, ^3J = 5.9 Hz, 6H, H-2), 3.67 – 3.57 (m, 36H, H-5b, H-2b‘, H-4‘, H-5‘, H-7‘, H-8‘, H-6a$_{Man-1}$), 3.55 (t, ^3J = 5.5 Hz, 6H, H-10‘), 3.44 (q, ^3J = 5.5 Hz, 6H, H-11‘), 2.43 (t, ^3J = 5.0 Hz, 3H, H-3), 2.11 (s, 9H, C-4$_{Man-3}$-O(C=O)CH_3), 2.04 (s, 9H, C-6$_{Man-3}$-O(C=O)CH_3), 2.03 (s, 9H, C-3$_{Man-3}$-O(C=O)CH_3), 1.96 (s, 9H, C-6$_{Man-2}$-O(C=O)CH_3), 1.92 (s, 9H, C-3$_{Man-2}$-O(C=O)CH_3), 1.91 (s, 9H, C-4$_{Man-2}$-O(C=O)CH_3), 1.84 (s, 9H, C-2$_{Man-2}$-O(C=O)CH_3), 1.81 (s, 9H, C-2$_{Man-3}$-O(C=O)CH_3). **^{13}C-NMR** (151 MHz, $CDCl_3$, 25 °C)**:** δ (ppm) = 171.3 (3C, C-1), 170.8 (3C, C-6$_{Man-2}$-O(*C*=O)CH$_3$), 170.6 (3C, C-6$_{Man-3}$-O(*C*=O)CH$_3$), 170.0 (3C, C-4$_{Man-3}$-O(*C*=O)CH$_3$), 169.9 (3C, C-3$_{Man-3}$-O(*C*=O)CH$_3$), 169.8 (3C, C-3$_{Man-2}$-O(*C*=O)CH$_3$), 169.6 (3C, C-4$_{Man-2}$-O(*C*=O)CH$_3$), 169.2 (3C, C-2$_{Man-3}$-O(*C*=O)CH$_3$), 169.1 (3C, C-2$_{Man-2}$-O(*C*=O)CH$_3$), 165.9 (3C, C-2$_{Man-1}$-O(*C*=O)Ph), 165.2 (3C, C-4$_{Man-1}$-O(*C*=O)Ph),

142.9 (3C, C-2‘‘), 133.7 (3C, C-2_{Man-1}-O(*C*=O)Ph, C_{para}), 133.6 (3C, C-4_{Man-1}-O(*C*=O)Ph, C_{para}), 130.0 (6C, C-2_{Man-1}-O(*C*=O)Ph, C_{ortho}), 129.9 (6C, C-4_{Man-1}-O(*C*=O)Ph, C_{ortho}), 129.0 (3C, C-2_{Man-1}-O(*C*=O)Ph, C_{ipso}), 128.8 (6C, C-2_{Man-1}-O(*C*=O)Ph, C_{meta}), 128.7 (3C, C-4_{Man-1}-O(*C*=O)Ph, C_{ipso}), 128.5 (6C, C-4_{Man-1}-O(*C*=O)Ph, C_{meta}), 124.4 (3C, C-3‘‘), 99.4 (3C, C-1_{Man-2}), 97.3 (3C, C-1_{Man-2}), 96.6 (3C, C-1_{Man-1}), 75.5 (3C, C-3_{Man-1}), 71.6 (3C, C-2_{Man-1}), 70.5, 70.5, 70.4, 70.1 (12C, C-4‘, C-5‘, C-7‘, C-8‘), 69.8 (3C, C-10‘), 69.5 (3C, C-5_{Man-1}), 69.4 (3C, C-5), 69.3 (3C, C-2‘), 69.2 (3C, C-2_{Man-2}), 69.2 (3C, C-2_{Man-3}), 69.2 (3C, C-3_{Man-3}), 68.6 (3C, C-5_{Man-3}), 68.5 (3C, C-4_{Man-1}), 68.2 (3C, C-3_{Man-2}), 67.4 (3C, C-2), 66.5 (3C, C-6_{Man-1}), 65.9 (3C, C-4_{Man-2}), 65.7 (3C, C-4_{Man-3}), 62.3 (3C, C-6_{Man-2}), 62.2 (3C, C-6_{Man-3}), 60.4 (3C, C-1‘‘), 50.6 (3C, C-6), 50.2 (3C, C-1‘), 39.2 (3C, C-11‘), 36.7 (3C, C-3), 20.9 (3C, C-4_{Man-3}-O(C=O)CH_3), 20.8 (3C, C-6_{Man-3}-O(C=O)CH_3), 20.7 (3C, C-3_{Man-3}-O(C=O)CH_3), 20.7 (3C, C-6_{Man-2}-O(C=O)CH_3), 20.7 (3C, C-3_{Man-2}-O(C=O)CH_3), 20.6 (3C, C-4_{Man-2}-O(C=O)CH_3), 20.5 (3C, C-2_{Man-2}-O(C=O)CH_3), 20.5 (3C, C-2_{Man-3}-O(C=O)CH_3). **HR-MS** (ESI^+)**:** $m/z_{cal.}$ = 1400.1698 $[M+3H]^{3+}$, $m/z_{exp.}$ = 1400.1699 $[M+3H]^{3+}$; $m/z_{cal.}$ = 1400.5042 $[M+3H]^{3+}$, $m/z_{exp.}$ = 1400.5041 $[M+3H]^{3+}$. $\boldsymbol{R_f}$ (NP) = 0.30 (DCM/MeOH 20:1). **Optical rotation** (LM)**:** $[\boldsymbol{\alpha}]_{\mathbf{D}}^{\mathbf{22}}$ = +9.50 ($CHCl_3$). **IR** (ATR)**:** (cm^{-1}) = 2935, 1748, 1663, 1452, 1369, 1224, 1046, 979, 915, 715, 449.

Supporting Information

4.1.25 Synthesis of *N*-(1-Bis(17-(4-(2,4-di-*O*-benzoyl-3,6-di-*O*-(2,3,4,6-tetra-*O*-acetyl-α-D-mannopyranosyl)-α-D-mannopyranosyloxymethyl)-1*H*-1,2,3-triazol-1-yl)-5-oxo-2,9,12,15-tetraoxa-6-azaheptadec-1-yl)-18-(4-(2,4-di-*O*-benzoyl-3,6-di-*O*-(2,3,4,6-tetra-*O*-acetyl-α-D-mannopyranosyl)-α-D-mannopyranosyloxymethyl)-1*H*-1,2,3-triazol-1-yl)-6-oxo-3,10,13,16-tetraoxa-7-azaoctadec-1-yl)-12-azido-4,7,10-pentaoxadodecanamide

The title compound was synthesized according to Scheme S 27 following modified synthesis protocols by *Cheng et al.*[44] and *Krumb et al.*[26]

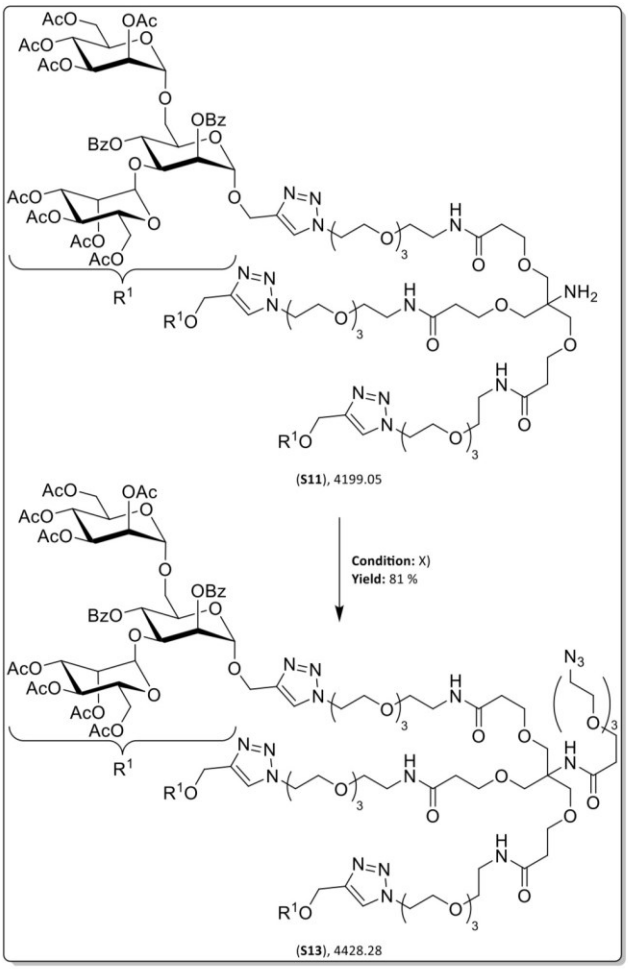

Scheme S 27: Synthesis of *N*-(1-Bis(17-(4-(2,4-di-*O*-benzoyl-3,6-di-*O*-(2,3,4,6-tetra-*O*-acetyl-α-D-mannopyranosyl)-α-D-mannopyranosyloxymethyl)-1*H*-1,2,3-triazol-1-yl)-5-oxo-2,9,12,15-tetraoxa-6-azaheptadec-1-yl)-18-(4-(2,4-di-*O*-benzoyl-3,6-di-*O*-(2,3,4,6-tetra-*O*-acetyl-α-D-mannopyranosyl)-α-D-mannopyranosyloxymethyl)-1*H*-1,2,3-triazol-1-yl)-6-oxo-3,10,13,16-tetraoxa-7-azaoctadec-1-yl)-12-azido-4,7,10-pentaoxadodecanamide (**S13**). Reaction condition X) (**3**), HATU, DIPEA, Ar-atm., DMF, rt, 48 h; yield: 81 %.

The reaction was carried out in a dried Schlenk vessel equipped with a magnetic stirring bar. 12-Azido-4,7,10-trioxadodecanoic acid (**3**, 0.11 g, 0.44 mmol, 10.0 eq.) was dissolved in absolute DMF (1.25 mL) under an atmosphere of argon. HATU (0.17 g, 0.44 mmol, 10.0 eq.) was added, followed by DIPEA (0.07 g, 0.09 mL, 0.52 mmol, 13.0 eq.) via syringe. The reaction mixture was stirred for half an hour at room temperature. *N*-(1-(4-(2,4-Di-*O*-benzoyl-3,6-di-*O*-(2,3,4,6-tetra-*O*-acetyl-α-D-mannopyranosyl)-α-D-mannopyranosyloxymethyl)-1*H*-1,2,3-triazol-1-yl)-3,6,9-trioxaundec-11-yl)-6-amino-6-(17-(4-

Supporting Information

(2,4-di-*O*-benzoyl-3,6-di-*O*-(2,3,4,6-tetra-*O*-acetyl-α-D-mannopyranosyl)-α-D-manno-pyranosyloxy-methyl)-1*H*-1,2,3-triazol-1-yl)-5-oxo-2,9,12,15-tetraoxa-6-azaheptadec-1-yl)-11-oxo-4,8,15,18,21-pentaoxa-12-aza-(23-(4-(2,4-di-*O*-benzoyl-3,6-di-*O*-(2,3,4,6-tetra-*O*-acetyl-α-D-mannopyranosyl)-α-D-mannopyranosyloxymethyl)-1*H*-1,2,3-triazol-1-yl)tricosanamide (**S11**, 0.17 g, 0.04 mmol, 1.00 eq.) was dissolved in absolute DMF (1.75 mL) under an atmosphere of argon and slowly added dropwise to the yellowish reaction mixture using a syringe. The mixture was stirred at room temperature for 48 hours. Complete conversion of the limiting substrate and the formation of the desired product were determined by reaction control via TLC and HPLC-ELS-MS. All volatiles were removed in fine vacuum. Toluene (3 x 5.00 mL) was added to the review and all volatiles were removed in fine vacuum. The crude product (0.49 g) was obtained in the form of orange oil and purified by FCC (DCM/MeOH, isocratic at 10 % MeOH) followed by RP-FCC (MeCN/H_2O, gradient from 10 % to 85 % to 100 % MeCN, Isolera One Purification System, SNAP C_{18} 12 g cartridge). The pure product (**S13**) was obtained in the form of yellowish oil.

Yield: 0.13 g (0.03 mmol, 81 %), colorless oil.

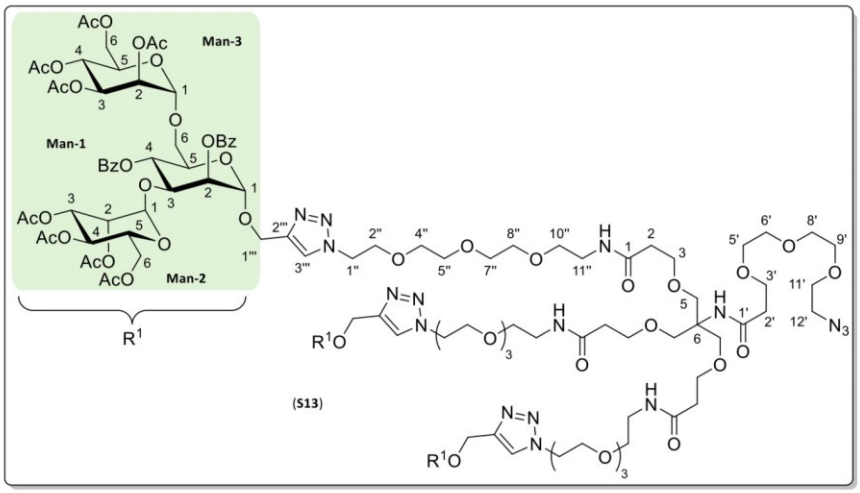

^{1}H-NMR (600 MHz, $CDCl_3$, 25 °C)**:** δ (ppm) = 8.15 – 8.12 (m, 6H, C-2$_{Man-1}$-O(C=O)Ph, H$_{ortho}$), 8.04 – 8.01 (m, 6H, C-4$_{Man-1}$-O(C=O)Ph, H$_{ortho}$), 7.83 (s, 3H, H-2‘‘‘), 7.64 – 7.60 (m, 3H, C-2$_{Man-1}$-O(C=O)Ph, H$_{para}$), 7.59 – 7.56 (m, 3H, C-4$_{Man-1}$-O(C=O)Ph, H$_{para}$), 7.56 – 7.53 (m, 6H, C-2$_{Man-1}$-O(C=O)Ph, H$_{meta}$), 7.46 – 7.42 (m, 6H, C-4$_{Man-1}$-O(C=O)Ph, H$_{meta}$), 6.72 (t, ^3J = 5.5 Hz, 3H, -N*H*-C-11‘‘), 6.60 (s, 1H, -N*H*-C-6), 5.70 (t$_{app}$, ^3J = 10.0 Hz, 3H, H-4$_{Man-1}$), 5.51 (dd, ^3J = 3.5, 1.8 Hz, 3H, H-2$_{Man-1}$), 5.34 (dd, ^3J = 10.1, 3.4 Hz, 3H, H-3$_{Man-3}$), 5.28 (dd, ^3J = 3.4, 1.7 Hz, 3H, H-2$_{Man-3}$), 5.24 (t, ^3J = 10.1 Hz, 3H, H-4$_{Man-3}$), 5.16 (d, ^3J = 1.7 Hz, 3H, H-1$_{Man-1}$), 5.10 – 5.04 (m, 6H, H-3$_{Man-2}$, H-4$_{Man-2}$), 4.94 (d, ^3J = 1.9 Hz, 3H, H-1$_{Man-2}$), 4.88 (d, ^2J = 12.1 Hz, 3H, H-1a‘‘‘), 4.85 (d, ^3J = 1.7 Hz, 3H, H-1$_{Man-3}$), 4.84 (dd, ^3J = 2.9, 1.9 Hz, 3H, H-2$_{Man-2}$), 4.71 (d, ^2J = 12.1 Hz, 3H, H-1b‘‘‘), 4.58 (t, ^3J = 5.3 Hz, 6H, H-1‘‘), 4.45 (dd, ^3J = 9.8, 3.4 Hz, 3H, H-3$_{Man-1}$), 4.25 (ddd, ^3J = 10.3, 6.0, 2.2 Hz, 3H, H-5$_{Man-1}$), 4.14 (ddd, ^2J = 12.2, 8.0, 5.5 Hz, 6H, H-6a$_{Man-2}$, H-6a$_{Man-3}$), 4.07 – 4.02 (m, 6H, H-5$_{Man-2}$, H-5$_{Man-3}$), 3.98 – 3.90 (m, 15H, H-5a, H-2a‘‘, H-6a$_{Man-1}$, H-6b$_{Man-2}$, H-6b$_{Man-3}$), 3.69 (t, ^3J = 5.6 Hz, 8H, H-2, H-3‘), 3.68 – 3.66 (m, 6H, H-5b, H-2b‘‘), 3.65 – 3.58 (m, 37H, H-5‘, H-6‘, H-8‘, H-9‘, H-11‘, H-4‘‘, H-5‘‘, H-7‘‘, H-8‘‘, H-6b$_{Man-1}$), 3.54 (t, ^3J = 5.5 Hz, 6H, H-10‘‘), 3.43 (q, ^3J = 5.5 Hz, 6H, H-11‘‘), 3.39 (t, ^3J = 5.0 Hz, 3H, H-12‘), 2.45 (t, ^3J = 6.0 Hz, 2H, H-2‘), 2.41 (t, ^3J = 5.9 Hz, 6H, H-3), 2.11 (s, 9H, C-4$_{Man-3}$-O(C=O)C*H*$_3$), 2.04 (s, 9H, C-6$_{Man-3}$-O(C=O)C*H*$_3$), 2.03 (s, 9H, C-3$_{Man-3}$-O(C=O)C*H*$_3$), 1.96 (s, 9H, C-6$_{Man-3}$-O(C=O)C*H*$_3$), 1.92 (s, 9H, C-3$_{Man-2}$-O(C=O)C*H*$_3$), 1.91 (s, 9H, C-4$_{Man-2}$-O(C=O)C*H*$_3$), 1.84 (s, 9H, C-2$_{Man-2}$-O(C=O)C*H*$_3$), 1.81 (s, 9H,

C-2$_{Man-3}$-O(C=O)CH_3). **^{13}C-NMR** (151 MHz, $CDCl_3$, 25 °C)**:** δ (ppm) = 171.7 (1C, C-1‘), 171.3 (3C, C-1), 170.7 (3C, C-6$_{Man-2}$-O(*C*=O)CH_3), 170.6 (3C, C-6$_{Man-3}$-O(*C*=O)CH_3), 170.0 (3C, C-4$_{Man-3}$-O(*C*=O)CH_3), 169.9 (3C, C-3$_{Man-3}$-O(*C*=O)CH_3), 169.8 (3C, C-3$_{Man-2}$-O(*C*=O)CH_3), 169.6 (3C, C-4$_{Man-2}$-O(*C*=O)CH_3), 169.2 (3C, C-2$_{Man-3}$-O(*C*=O)CH_3), 169.1 (3C, C-2$_{Man-2}$-O(*C*=O)CH_3), 165.9 (3C, C-2$_{Man-1}$-O(*C*=O)Ph), 165.2 (3C, C-4$_{Man-1}$-O(*C*=O)Ph), 142.9 (3C, C-2‘‘‘), 133.7 (3C, C-2$_{Man-1}$-O(*C*=O)Ph, C$_{para}$), 133.6 (3C, C-4$_{Man-1}$-O(*C*=O)Ph, C$_{para}$), 130.0 (6C, C-2$_{Man-1}$-O(*C*=O)Ph, C$_{ortho}$), 129.9 (6C, C-4$_{Man-1}$-O(*C*=O)Ph, C$_{ortho}$), 129.0 (3C, C-2$_{Man-1}$-O(*C*=O)Ph, C$_{ipso}$), 128.8 (6C, C-2$_{Man-1}$-O(*C*=O)Ph, C$_{meta}$), 128.7 (3C, C-4$_{Man-1}$-O(*C*=O)Ph, C$_{ipso}$), 128.5 (3C, C-4$_{Man-1}$-O(*C*=O)Ph, C$_{meta}$), 124.4 (3C, C-3‘‘‘), 99.4 (3C, C-1$_{Man-2}$), 97.3 (3C, C-1$_{Man-3}$), 96.6 (3C, C-1$_{Man-1}$), 75.5 (3C, C-3$_{Man-1}$), 71.6 (3C, C-2$_{Man-1}$), 70.6, 70.5, 70.5, 70.5, 70.4, 70.2, 70.1, 70.0 (16C, H-5‘, H-6‘, H-8‘, H-9‘, H-4‘‘, H-5‘‘, H-7‘‘, H-8‘‘), 69.8 (3C, C-10‘‘), 69.4 (3C, C-5$_{Man-1}$), 69.4 (3C, C-5), 69.3 (3C, C-2‘‘), 69.2 (3C, C-2$_{Man-2}$), 69.2 (3C, C-2$_{Man-3}$), 69.2 (3C, C-3$_{Man-3}$), 69.2 (1C, C-11‘), 68.6 (3C, C-5$_{Man-3}$), 68.5 (3C, C-4$_{Man-1}$), 68.2 (3C, C-3$_{Man-2}$), 67.3 (3C, C-2), 67.3 (3C, C-3‘), 66.4 (3C, C-6$_{Man-1}$), 65.9 (3C, C-4$_{Man-2}$), 65.7 (3C, C-4$_{Man-3}$), 62.3 (3C, C-6$_{Man-2}$), 62.2 (3C, C-6$_{Man-3}$), 60.4 (3C, C-1‘‘‘), 59.7 (1C, C-6), 50.6 (1C, C-12‘), 50.2 (3C, C-1‘‘), 39.2 (3C, C-11‘‘), 37.4 (1C, C-2‘), 36.6 (3C, C-3), 20.9 (3C, C-4$_{Man-3}$-O(C=O)*C*H_3), 20.8 (3C, C-6$_{Man-3}$-O(C=O)*C*H_3), 20.7 (3C, C-3$_{Man-3}$-O(C=O)*C*H_3), 20.7 (3C, C-6$_{Man-2}$-O(C=O)*C*H_3), 20.7 (3C, C-3$_{Man-2}$-O(C=O)*C*H_3), 20.6 (3C, C-4$_{Man-2}$-O(C=O)*C*H_3), 20.5 (3C, C-2$_{Man-2}$-O(C=O)*C*H_3), 20.5 (3C, C-2$_{Man-3}$-O(C=O)*C*H_3). **HR-MS** (ESI$^+$)**:** $m/z_{cal.}$ = 1476.5385 $[M+3H]^{3+}$, $m/z_{exp.}$ = 1476.5380 $[M+3H]^{3+}$; $m/z_{cal.}$ = 1476.8730 $[M+3H]^{3+}$, $m/z_{exp.}$ = 1476.8724 $[M+3H]^{3+}$; $m/z_{cal.}$ = 2214.3042 $[M+2H]^{2+}$, $m/z_{exp.}$ = 2214.3033 $[M+2H]^{2+}$; $m/z_{cal.}$ = 2214.8058 $[M+2H]^{2+}$, $m/z_{exp.}$ = 2214.8053 $[M+2H]^{2+}$. R_f (NP) = 0.20 (DCM/MeOH 25:1), 0.48 (DCM/MeOH 10:1). **Optical rotation** (LM)**:** $[\alpha]_D^{22}$ = +11.0 ($CHCl_3$). **IR** (ATR)**:** (cm^{-1}) = 2919, 2260, 2185, 2104, 2039, 2023, 1979, 1749, 1670, 1453, 1370, 1225, 1092, 1048, 983, 715, 598, 548, 537, 524, 497, 464, 456, 437, 422, 408.

4.1.26 Synthesis of *N*-(1-Bis(17-(4-(3,6-di-*O*-(α-D-mannopyranosyl)-α-D-mannopyranosyloxymethyl)-1*H*-1,2,3-triazol-1-yl)-5-oxo-2,9,12,15-tetraoxa-6-azaheptadec-1-yl)-18-(4-(3,6-di-*O*-(α-D-mannopyranosyl)-α-D-mannopyranosyloxymethyl)-1*H*-1,2,3-triazol-1-yl)-6-oxo-3,10,13,16-tetraoxa-7-azaoctadec-1-yl)-12-azido-4,7,10-pentaoxadodecanamide

The title compound was synthesized according to Scheme S 28 following modified synthesis protocols by *Krumb et al.*[26] sowie *Percec et al.*[11]

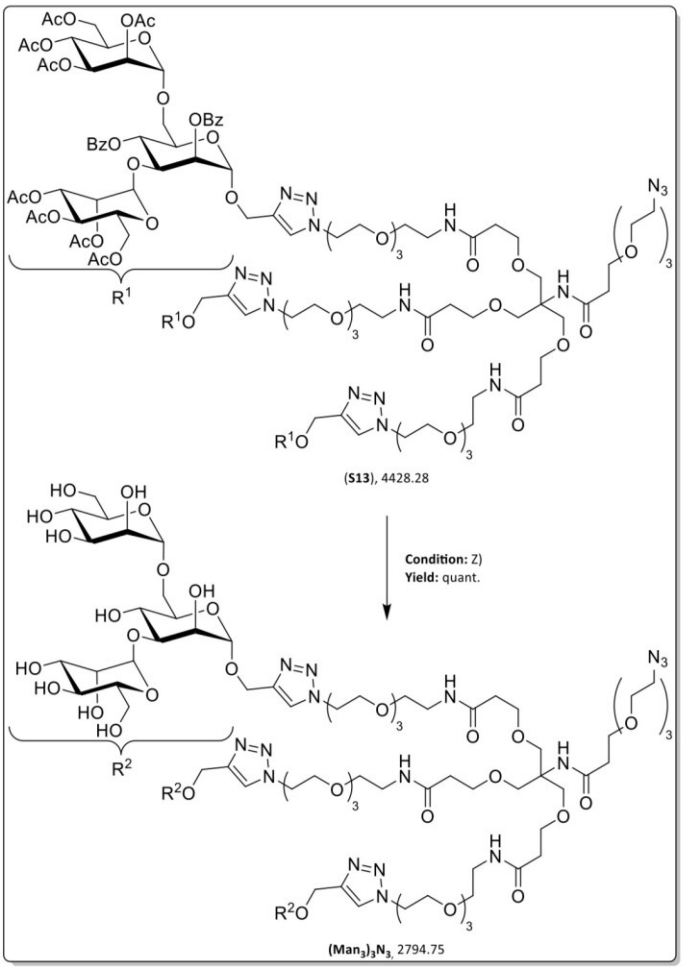

Scheme S 28: Synthesis of *N*-(1-Bis(17-(4-(3,6-di-*O*-(α-D-mannopyranosyl)-α-D-mannopyranosyloxymethyl)-1*H*-1,2,3-triazol-1-yl)-5-oxo-2,9,12,15-tetraoxa-6-azaheptadec-1-yl)-18-(4-(3,6-di-*O*-(α-D-mannopyranosyl)-α-D-mannopyranosyloxymethyl)-1*H*-1,2,3-triazol-1-yl)-6-oxo-3,10,13,16-tetraoxa-7-azaoctadec-1-yl)-12-azido-4,7,10-pentaoxadodecanamide **(Man$_3$)$_3$N$_3$**. Reaction conditions: Z) NaOMe, NaOH, MeOH, Ar-atm., rt, 18 h; yield: quant.

The reaction was carried out in a dried Schlenk vessel, which had previously been equipped with a magnetic stirring bar. *N*-(1-Bis(17-(4-(2,4-di-*O*-benzoyl-3,6-di-*O*-(2,3,4,6-tetra-*O*-acetyl-α-D-mannopyranosyl)-α-D-mannopyranosyloxymethyl)-1*H*-1,2,3-triazol-1-yl)-5-oxo-2,9,12,15-tetraoxa-6-azaheptadec-1-yl)-18-(4-(2,4-di-*O*-benzoyl-3,6-di-*O*-(2,3,4,6-tetra-*O*-acetyl-α-D-mannopyranosyl)-α-D-mannopyranosyloxymethyl)-1*H*-1,2,3-triazol-1-yl)-6-oxo-3,10,13,16-tetraoxa-7-azaoctadec-1-yl)-12-azido-4,7,10-pentaoxadodecanamide (**S13**, 0.10 g, 0.02 mmol, 1.00 eq.) was dissolved in absolute MeOH (10.0 mL) under an atmosphere of argon. NaOMe (4.00 mg, 0.07 mmol, 3.00 eq.) and freshly ground NaOH (3.00 mg, 0.07 mmol, 3.00 eq.) were added, and the resulting solution was stirred at room temperature for 18 hours. Complete conversion of the limiting substrate and the formation of the desired

Supporting Information

product were determined by reaction control via TLC and HPLC-ELS-MS. The reaction was ended by addition of the ion exchange resin *Amberlite IR 120* (0.20 g), and the mixture was stirred for 10 minutes until a constant pH (pH = 6 – 7) was reached. The reaction mixture was filtered through a glass frit with *Celite* and eluted with MeOH (1 x 50.0 mL). All volatiles were removed in vacuo. The crude product (0.18 g) was obtained in the form of yellowish oil and purified by RP-FCC (MeCN/H_2O, gradient from 5 % to 25 % to 100 % MeCN, Isolera One Flash Purification System, SNAP C_{18} 12 g cartridge). The pure product **$(Man_3)_3N_3$** was obtained in the form of a yellowish lyophilizate.

Yield: 0.06 g (0.02 mmol, quant.), yellowish lyophilizate.

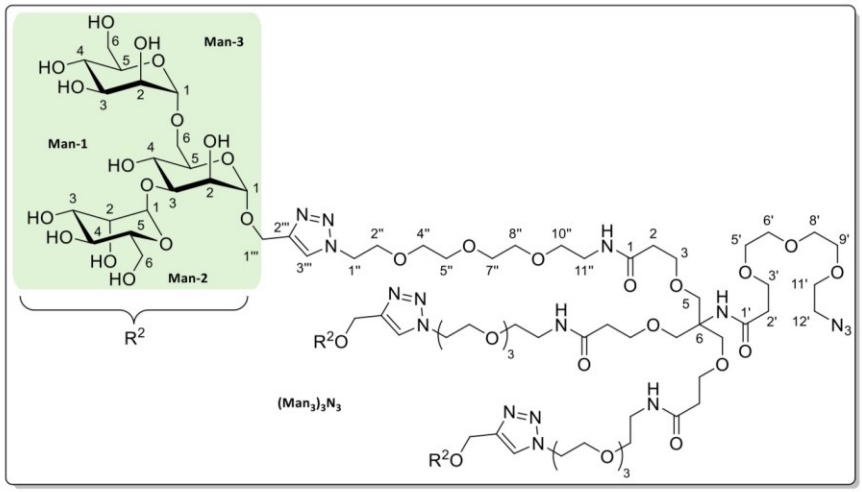

^{1}H-NMR (600 MHz, D_2O, 25 °C)**:** δ (ppm) = 8.07 (s, 3H, H-3‘‘‘), 5.01 (s, 3H, H-1_{Man-2}), 4.87 (s, 3H, H-1_{Man-3}), 4.83 (s, 3H, H-1_{Man-3}), 4.75 (d, ^2J = 12.5 Hz, 3H, H-1a‘‘‘), 4.66 (d, ^2J = 12.5 Hz, 3H, H-1b‘‘‘), 4.58 (t, ^3J = 5.0 Hz, 6H, H-1‘‘), 4.03 (s, 3H, H-2_{Man-1}), 3.99 (dd, ^3J = 3.5, 1.8 Hz, 3H, H-2_{Man-2}), 3.97 – 3.90 (m, 21H, H-2‘‘, H-10‘‘, H-2_{Man-3}, H-6_{Man-1}), 3.87 – 3.76 (m, 15H, H-3_{Man-1}, H-3_{Man-2}, H-3_{Man-3}, H-4_{Man-1}, H-$6a_{Man-3}$), 3.76 – 3.50 (m, 86H, H-2, H-5, H-3‘, H-5‘, H-6‘, H-8‘, H-9‘, H-11‘, H-2‘‘, H-4‘‘, H-5‘‘, H-7‘‘, H-8‘‘, H-10‘‘, H-4_{Man-2}, H-4_{Man-3}, H-5_{Man-1}, H-5_{Man-2}, H-5_{Man-3}, H-6_{Man-2}, H-$6b_{Man-3}$), 3.42 (t, ^3J = 4.9 Hz, 3H, H-12‘), 3.33 (t, ^3J = 5.5 Hz, 6H, H-11‘‘), 2.43 (t, ^3J = 6.3 Hz, 8H, H-3, H-2‘). **^{13}C-NMR** (151 MHz, D_2O, 25 °C)**:** δ (ppm) = 174.1 (3C, C-1), 173.7 (3C, C-1‘), 143.9 (3C, C-2‘‘‘), 125.7 (3C, C-3‘‘‘), 102.4 (3C, C-1_{Man-2}), 99.7 (3C, C-1_{Man-3}), 99.4 (3C, C-1_{Man-1}), 78.6 (3C, C-3_{Man-1}), 73.3 (3C, C-5_{Man-2}), 72.7 (3C, C-1_{Man-3}), 71.3 (3C, C-5_{Man-1}), 70.6 (3C, C-3_{Man-3}), 70.3 (3C, C-3_{Man-2}), 70.0 (3C, C-2_{Man-2}), 69.9 (3C, C-2_{Man-3}), 69.6, 69.6, 69.5, 69.5, 69.5, 69.5 (17C, C-5‘, C-6‘, C-8‘, C-9‘, C-4‘‘, C-5‘‘, C-7‘‘, C-8‘‘, H-2_{Man-1}), 69.4 (3C, C-5), 69.2 (1C, C-11‘), 68.8 (3C, C-10‘‘), 68.7 (3C, C-2‘‘), 68.4 (1C, C-3‘), 67.5 (3C, C-2), 66.7 (3C, C-4_{Man-3}), 66.6 (3C, C-6_{Man-2}), 65.4 (3C, C-4_{Man-1}), 64.9 (3C, C-6_{Man-1}), 60.9 (3C, C-6_{Man-3}), 60.3 (1C, C-6), 60.0 (3C, C-1‘‘‘), 50.1 (3C, C-1‘‘), 50.0 (1C, C-12‘), 39.0 (3C, C-11‘‘), 36.4 (1C, C-2‘), 36.1 (3C, C-3). **HR-MS** (ESI$^+$)**:** $m/z_{cal.}$ = 932.0671 $[M+3H]^{3+}$, $m/z_{exp.}$ = 932.0679 $[M+3H]^{3+}$; $m/z_{cal.}$ = 932.4016 $[M+3H]^{3+}$, $m/z_{exp.}$ = 932.4034 $[M+3H]^{3+}$; $m/z_{cal.}$ = 1419.5790 $[M+2Na]^{2+}$, $m/z_{exp.}$ = 1419.5789 $[M+2Na]^{2+}$; $m/z_{cal.}$ = 1420.0807 $[M+2Na]^{2+}$, $m/z_{exp.}$ = 1420.0812 $[M+2Na]^{2+}$. R_f (RP) = 0.79 (MeCN/H_2O 1:1). **Optical rotation** (LM)**:** $[\alpha]_D^{22}$ = +90.7 (H_2O). **IR** (ATR)**:** (cm^{-1}) = 3386, 2913, 2129, 1641, 1544, 1458, 1051, 809, 545, 443.

Supporting Information

4.2 Synthesis of the TS_n-HSA neoglycoalbumins

Prior to use, native HSA was dissolved in MQ-water, subjected to spin-filtration through a 300 kDa ultracentrifugation tube to remove large aggregates, and lyophilized. The mass of all HSA conjugates is expressed as the *m/z* value of the peak of the singly charged species and denoted as *M*. In the case of repeated synthesis, synthesis protocols are reported representatively. Scheme S 29 and Scheme S 30 show an overview of the synthesis route for all NCs.

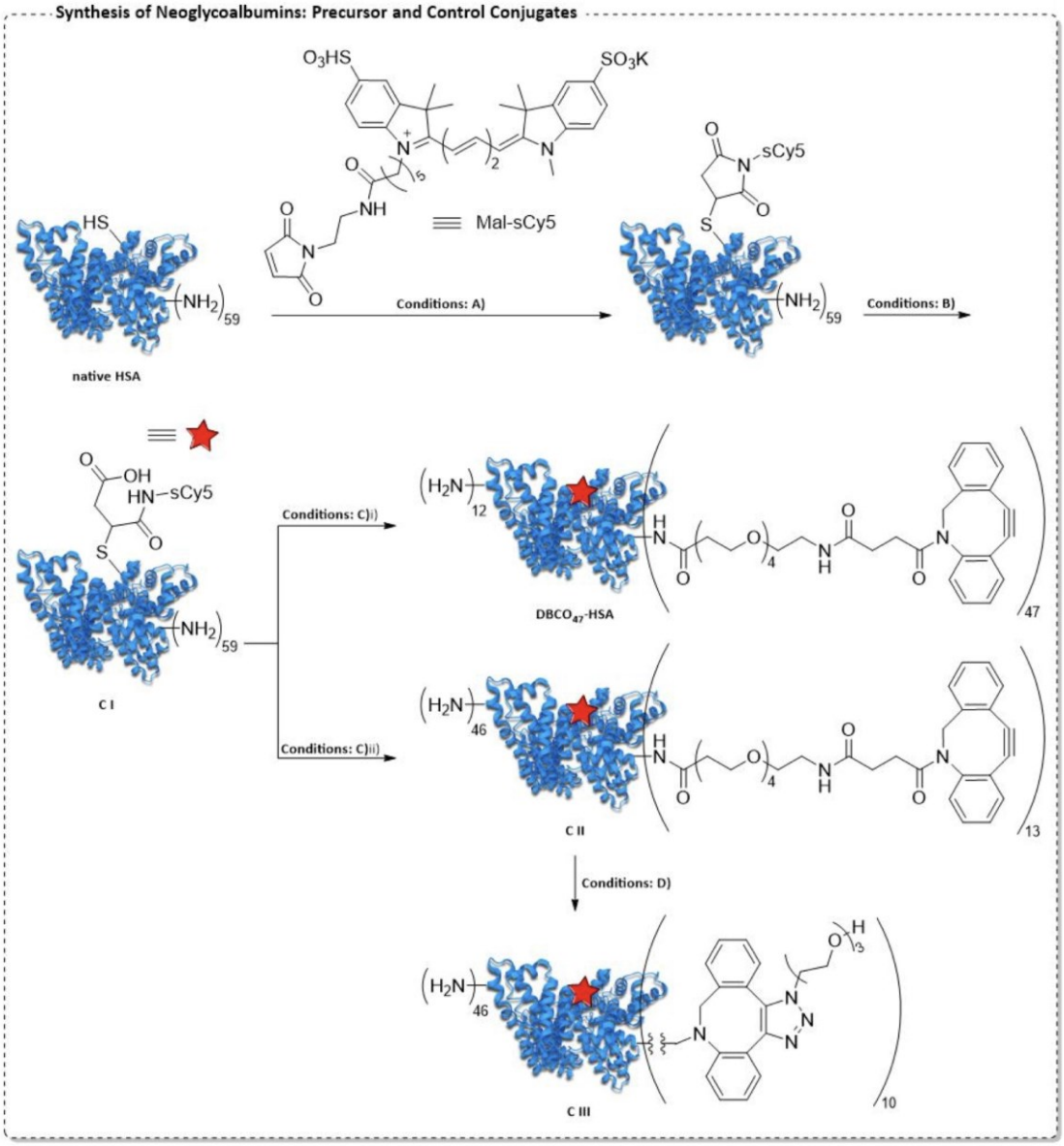

Scheme S 29: Synthesis of the precursor conjugates and control conjugates C I–III. Reaction conditions: A) 50 mM PB pH 7.4, RT, 4 h; B) 50 mM Na-borate buffer pH 9.2, 37 °C, o.n.; C) 50 mM PB pH 7.4, RT, 1 d; i) 19 eq. NHS-PEG_4-DBCO; ii) 150 eq. NHS-PEG_4-DBCO; D) N_3-PEG_3-OH, 50 mM PB (8 M urea, 2 mM EDTA) pH 8, RT.

Supporting Information

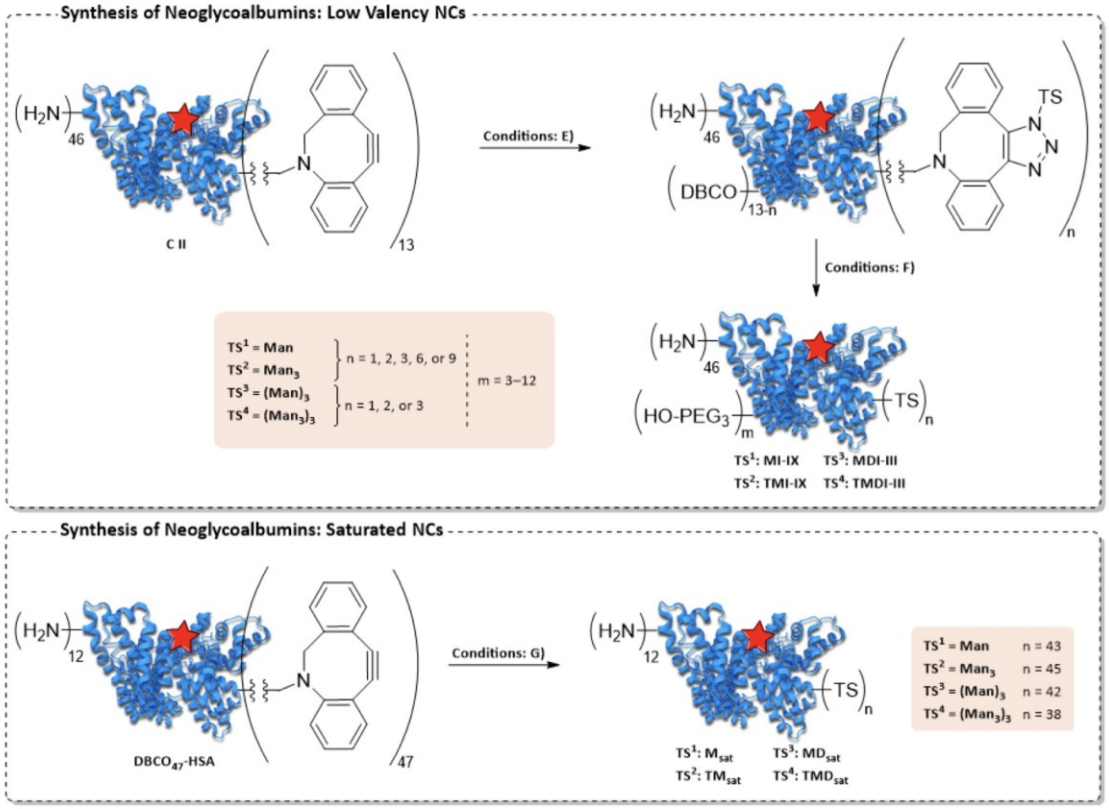

Scheme S 30: Synthesis of low (top) and high (bottom) valency NCs. Reaction conditions: 50 mM PB (8 M urea, 2 mM EDTA) pH 8, RT; E) 1–12 eq. TS; F) 63–100 eq. N_3-PEG_3-OH; G) 264 eq. TS.

Degree of TS modification via SPAAC was monitored with MALDI-ToF-MS and calculated with conjugate M III ([Man]$_3$-HSA) used as an example as follows:

$$\mathrm{DoM_{TS}} = \frac{(M_{MIII\ post\ glycosylation} - M_{CII})}{(M_{Man})} = \frac{(75815 g\cdot mol^{-1} - 74440 g\cdot mol^{-1})}{(462.46 g\cdot mol^{-1})} = \frac{1375 g\cdot mol^{-1}}{462.46 g\cdot mol^{-1}} = 3.0$$

$$\mathrm{DoM_{TS}} = 3.0$$

After glycosylation, residual DBCO groups were capped using 2-[2-(2-azidoethoxy)ethoxy]ethan-1-ol (N_3-PEG_3-OH). Conjugate masses *M* are always final, capped NCs unless otherwise noted.

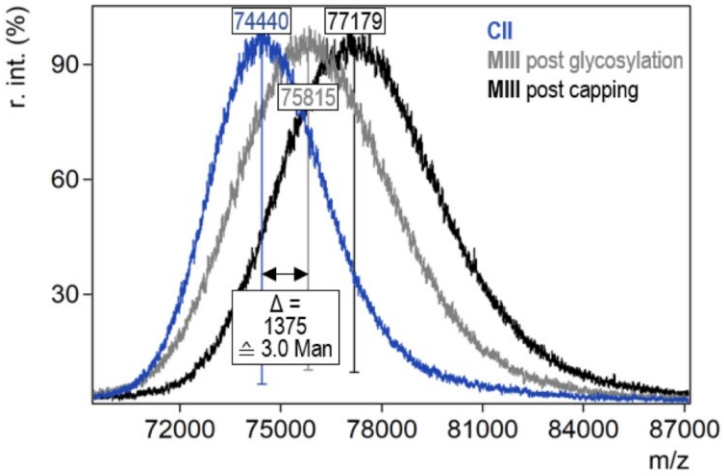

Supporting Information

4.2.1 Preparation of dye-labeled HSA via thiol-maleimide Michael addition

Native HSA (40 mg, 0.60 µmol, 1.0 eq.) was dissolved in 50 mM sodium phosphate buffer (pH = 7.4) to obtain a protein concentration of 5 mg/mL. Sulfo-Cy5 maleimide (967 µg, 1.20 µmol, 2.0 eq.) dissolved in MQ (25 mg/mL) was added to the native HSA. The reaction was shaken at room temperature for 4 hours and afterwards purified (5 x MQ) and concentrated *via* ultracentrifugation spin filter (Vivaspin, PES, 10 kDa). The product was lyophilized and obtained in the form of a blue lyophilizate.

Recovery rate: 31 mg (0.46 µmol, 77 %), blue lyophilizate.

MALDI-ToF-MS: m/z = 67474 $[M+H]^+$

4.2.2 Maleimide ring opening of labeled HSA (C I)

Labeled HSA (31 mg, 0.46 µmol) was diluted in 50 mM sodium borate buffer (pH = 9.2) to a final protein concentration of 1 mg/mL and shaken at 37 °C for 24 h. Afterwards, it was concentrated and purified (5 x MQ) *via* ultracentrifugation spin filter (Vivaspin, PES, 10 kDa). The product, henceforth referred to as HSA, was lyophilized and obtained in the form of a blue lyophilizate.

Recovery rate: 31 mg (0.46 µmol, quantitative), blue lyophilizate.

MALDI-ToF-MS: m/z = 67422 $[M+H]^+$

4.2.3 Preparation of $DBCO_{13}$-HSA *via* NHS-ester activated DBCO-linker (C II)

Labeled, ring-opened HSA (22.5 mg, 339 nmol, 1.0 eq) was diluted in 50mM phosphate buffer (pH = 7.4, 11.3 mL) to a protein concentration of 2 mg/mL. DBCO-PEG_4-NHS (4.19 mg, 6.44 µmol, 19 eq.) dissolved in DMSO (100 mg/mL) was diluted in 50mM phosphate buffer (pH = 7.4, 11.3 mL) and added. The reaction was shaken at room temperature for 1 day. Afterwards, the reaction solution was purified (5 x MQ) and concentrated *via* ultracentrifugation spin filter (Vivaspin, PES, 10 kDa). The product was lyophilized and obtained in the form of a blue lyophilizate.

Recovery rate: 22 mg (298 nmol, 88 %), blue lyophilizate.

MALDI-ToF-MS: m/z = 74440 $[M+H]^+$

4.2.4 Preparation of $DBCO_{47}$-HSA *via* NHS-ester activated DBCO-linker

Labeled, ring-opened HSA (2.0 mg, 30 nmol, 1.0 eq) was diluted in 50mM phosphate buffer (pH = 7.4, 0.75 mL) to a protein concentration of 2.7 mg/mL. DBCO-PEG_4-NHS (2.9 mg, 495 µmol, 149 eq.) dissolved in DMSO (100 mg/mL) was added in several portions and the reaction solution was shaken at room temperature for 1 day. Afterwards, the reaction solution was purified (5 x MQ) and concentrated *via* ultracentrifugation spin filter (Vivaspin, PES, 10 kDa). The product was lyophilized and obtained in the form of a blue lyophilizate.

Recovery rate: 2.9 mg (32 nmol, quantitative), blue lyophilizate.

MALDI-ToF-MS: m/z = 90973 $[M+H]^+$

4.2.5 Preparation of HO-PEG_3-HSA control C III

$DBCO_{13}$-HSA (0.50 mg, 6.72 nmol, 1.0 eq.) was dissolved in 50 mM phosphate buffer with 8 M urea and 2 mM EDTA (pH = 8) to a final protein concentration of 1 mg/mL. N_3-PEG_3-OH (295 nmol, 44.0 eq. or 3.4 eq/DBCO) diluted in DMSO (71 mM, 4.16 µL) was added in two portions and the reaction solution was inverted (10 rpm) at room temperature until no further functionalization could be observed. Afterwards, the reaction solution was purified (5 x MQ) and concentrated via

ultracentrifugation spin filter (Vivaspin, PES, 10 kDa). The product was lyophilized and obtained in the form of a blue lyophilizate.

Recovery rate: 0.45 mg (5.92 nmol, 88 %), blue lyophilizate.

MALDI-ToF-MS: *m/z* = 76184 $[M+H]^+$

4.2.6 Preparation of low valency TS-HSA neoglycoalbumins

General Procedure: $DBCO_{13}$-HSA (reaction scale: 0.5 – 1.0 mg, 6.7 – 13.4 nmol) was dissolved in 50 mM phosphate buffer with 8 M urea and 2 mM EDTA (pH = 8) to a final protein concentration of 1 mg/mL. The azide functionalized TS (1.2 – 12 eq., see Table S 1) dissolved in MQ (10 mg/mL) was added and the reaction solution was inverted (10 rpm) at room temperature. The reaction was closely monitored *via* Maldi-ToF-MS analysis until the desired modification rate was achieved (3 – 70 h). Afterwards, the reaction solution was purified (2 – 3 x reaction buffer) and capping reagent (71 mM in DMSO, 63 – 100 eq.) was added in excess overnight. The product was purified (1 x reaction buffer, 5 x MQ) and concentrated via ultracentrifugation spin filter (Vivaspin, PES, 10 kDa). The product was lyophilized and obtained in the form of a blue lyophilizate. All low valency conjugates were obtained with recovery rates ranging from 38 % to quantitative.

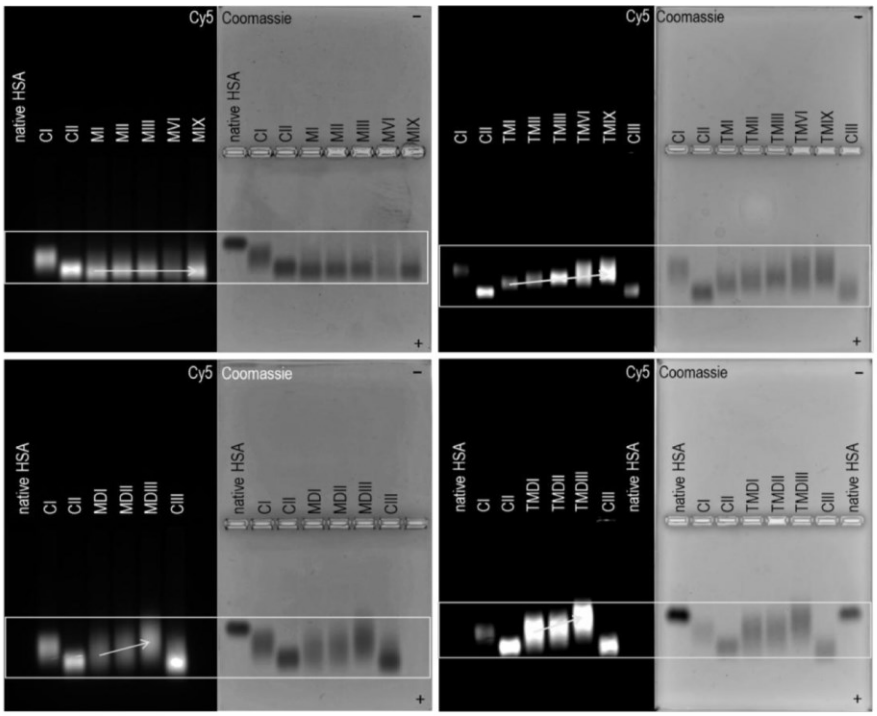

Figure S 1: Agarose gel electrophoresis of low valency NCs carrying varying amounts of different TSs (top left: Man, top right: Man_3, bottom left: $(Man)_3$, bottom right: $(Man_3)_3$) as well as control conjugates C I, C II and C III (always left Cy5-channel, right Coomassie brilliant blue staining).

Supporting Information

Table S 1: Summary of synthesized low valency conjugates with varying degrees of modification (DoM), number of TS equivalents used and Maldi-ToF-MS characterization.

Code	Conjugate	TS eq	MALDI-ToF-MS post glycosylation $[M+H]^+$ (*m/z*)	MALDI-ToF-MS post capping / final $[M+H]^+$ (*m/z*)	DoM: TS
MI	$[Man]_1$-HSA	1.2	75020	76340	1
MII	$[Man]_2$-HSA	2.3	75370	76681	2
MIII	$[Man]_3$-HSA	3.3	75815	77179	3
MVI	$[Man]_6$-HSA	6.3	77375	78061	6
MIX	$[Man]_9$-HSA	9.6	78485	78940	9
TMI	$[Man_3]_1$-HSA	3.3	75190	76648	1
TMII	$[Man_3]_2$-HSA	6.3	76163	77408	2
TMIII	$[Man_3]_3$-HSA	6.3	77100	78354	3
TMVI	$[Man_3]_6$-HSA	9.0	79086	79328	6
TMIX	$[Man_3]_9$-HSA	12.0	81503	81621	9
MDI	$[(Man)_3]_1$-HSA	2.5	76696	78893	1
MDII	$[(Man)_3]_2$-HSA	5.0	78220	79811	2
MDIII	$[(Man)_3]_3$-HSA	5.0	79910	81571	3
TMDI	$[(Man_3)_3]_1$-HSA	2.0	77087	78370	1
TMDII	$[(Man_3)_3]_2$-HSA	2.0	79471	79704	2
TMDIII	$[(Man_3)_3]_3$-HSA	4.0	82958	83200	3

Supporting Information

Table S 2: Sizes (d. nm) and PDIs of low valency TS-HSA conjugates determined by DLS measurements (10–20 uM in MQ). Measurements were performed in triplicates; errors are given as standard deviation.

Conjugate	Size d. nm	PDI
CI	6.8 ± 0.3	0.703
CII	5.7 ± 0.2	0.844
CIII	4.8 ± 0.5	0.975
MI	3.6 ± 1.2	0.966
MII	4.2 ± 1.4	1.000
MIII	2.8 ± 0.4	0.926
MVI	4.6 ± 1.3	1.000
MIX	7.0 ± 1.0	0.827
TMI	9.6 ± 1.0	0.978
TMII	6.2 ± 1.1	0.754
TMIII	6.7 ± 0.4	0.855
TMVI	6.3 ± 1.0	0.752
TMIX	5.4 ± 0.2	0.848
MDI	8.0 ± 1.0	0.628
MDII	7.7 ± 1.1	0.916
MDIII	3.7 ± 0.6	0.816
TMDI	6.2 ± 0.2	0.691
TMDII	7.6 ± 0.1	0.829
TMDIII	6.8 ± 0.8	0.697

Supporting Information

4.2.7 Preparation of saturated TS-HSA neoglycoalbumins

$DBCO_{47}$-HSA (0.3 mg, 3.24 nmol, 1 eq.) was dissolved in 50 mM phosphate buffer with 8 M urea and 2 mM EDTA (pH = 8) to a final protein concentration of 1 mg/mL. The azide functionalized TS (855 µmol, 264 eq. or 5.6 eq/DBCO) dissolved in MQ (10 mg/mL) was added and the reaction solution was inverted (10 rpm) at room temperature for 1 day. Afterwards, the reaction solution was purified (1 x reaction buffer, 5 x MQ) and concentrated via ultracentrifugation spin filter (Vivaspin, PES, 10 kDa). The product was lyophilized and obtained in the form of a blue lyophilizate quantitatively.

Table S 3: Summary table of synthesized conjugates of the saturated valency regime.

Code	Conjugate	MALDI-ToF-MS $[M+H]^+$ (*m/z*)	DoM: TS
M_{sat}	$[Man]_{43}$-HSA	112500	43
TM_{sat}	$[Man_3]_{45}$-HSA	127913	45
MD_{sat}	$[(Man)_3]_{42}$-HSA	169250	42
TMD_{sat}	$[(Man_3)_3]_{38}$-HSA	198400	38

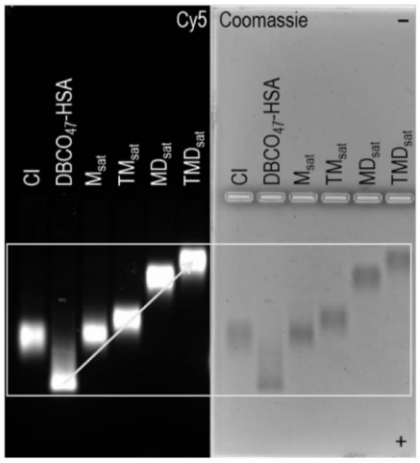

Figure S 2: Agarose gel electrophoresis of saturated NCs carrying different TSs (Number of Ts: Man: 43, Man_3: 45, $(Man)_3$: 42, $(Man_3)_3$: 38) as well as precursor conjugates $DBCO_{47}$-HSA and control conjugate C I (left Cy5-channel, right Coomassie brilliant blue staining).

Table S 4: Sizes (d. nm) and PDIs of saturated TS-HSA conjugates determined by DLS measurements (10–20 uM in MQ). Measurements were performed in triplicates; errors are given as standard deviation.

Conjugate	Size (d. nm)	PDI
M_{sat}	6.3 ± 1.3	0.581
TM_{sat}	6.8 ± 0.1	0.692
MD_{sat}	8.3 ± 0.1	0.570
TMD_{sat}	11.7 ± 0.8	0.697

Supporting Information

5 Prediction of binding modes for monovalent TSs

TS Man (**7**) and Man_3 (**8**) with a truncated linker were docked into the primary carbohydrate-recognition site (CRD) of either CD209 (PDB: 1SL4)[49] or CRD4 of CD206 (PDB: 7JUF)[50] using SeeSAR 13.01.1.[51-53] To recreate experimentally observed mannose-binding modes for CD209, the template docking mode was employed, while for CD206, a constraint to include any oxygen was applied to two oxygen atoms (Figure S 3A). For each ligand, ten poses were generated, ranked by the estimated binding affinity,[53] and the highest-ranked pose was selected for binding mode analysis. The crystallographic binding mode of the reference ligand was visually compared to the predicted pose to assess pose prediction accuracy (Figure S 3B, C). The root mean square deviation (RMSD) values were calculated as 0.41 Å for CD206 and 1.27 Å for CD209.

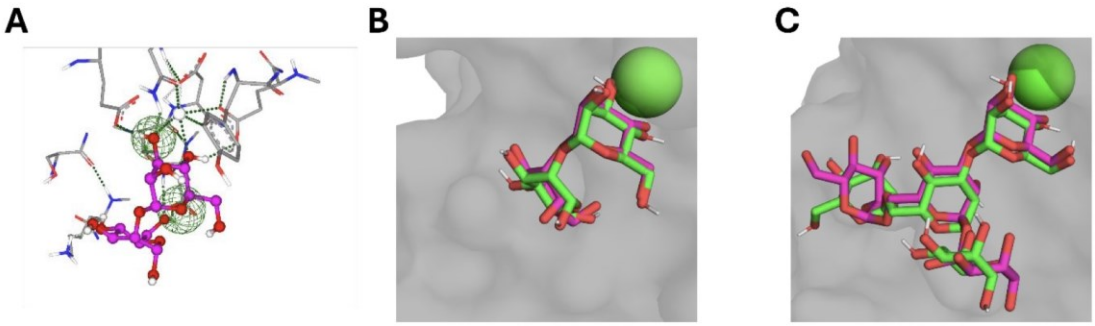

Figure S 3: **A)** Constraints (green spheres) put on reference ligand oxygen atoms for CD206 CRD4. **B)** Redocking the reference TSs for CD206 CRD4 (PDB: 7JUF, RMSD: 0.41 Å). **C)** Redocking the reference TSs for CD209 CRD (PDB: 1SL4, RMSD: 1.27 Å). The poses from the crystal structures are shown with pink carbon atoms, and the docking poses generated by SeeSAR 13.01.1 are shown with green carbon atoms. The protein surfaces are depicted in grey, and the Ca^{2+}-cation inside the binding pocket is represented as a green sphere.

6 NanoDSF binding study for mono- and trivalent TSs

6.1 Recombinant protein expression and purification.

6.1.1 Carbohydrate recognition domain 4 of CD206

CRD 4 of CD206 was expressed as described previously.[50] Briefly, a pT5T expression vector containing CRD4 of CD206 was transformed into competent *Escherichia coli* (E. coli) BL21 (DE3) cells. The cells were grown in LB medium containing 100 µg/mL ampicillin at 37 °C and 160 rpm until they reached an optical density (OD_{600}) of approximately 0.7. Overexpression was induced by adding 0.4 mM Isopropyl-β-D-thiogalactopyranoside (IPTG) for approximately 2.5 hours at 37 °C. Cells were harvested by centrifugation (10.000 × g at 4 °C for 15 minutes) and resuspended in cold buffer A (10 mM Tris-Cl, pH 7.8). Lysis was performed by thoroughly sonicating the cell pellets. Cell debris and inclusion bodies were collected by centrifugation (18,000 × g at 4 °C for 15 minutes), and the supernatant was discarded. The inclusion bodies were then solubilized in 100 mL of denaturing buffer B (6 M guanidine-HCl, 100 mM Tris-Cl, pH 7.0). After adding 2-mercaptoethanol (10 µL), the suspension was incubated at 4 °C on ice for 30 minutes. Insoluble impurities were removed by centrifugation (18,000 × g at 4 °C for 30 minutes). The supernatant was refolded by three-step dialysis against 2 L of buffer C (0.5 M NaCl, 25 mM Tris-Cl, pH 7.8, 25 mM $CaCl_2$) at 4 °C overnight. After centrifugation (18,000 × g at 4 °C for 30 minutes), the renatured CRD4 was purified using a 10 mL column of mannose-conjugated Sepharose prepared by divinyl sulfone coupling.[54] Finally, after washing with one column volume (CV) of buffer

D (150 mM NaCl, 25 mM Tris-Cl, pH 7.8, 25 mM $CaCl_2$), the bound protein was eluted with buffer E (150 mM NaCl, 25 mM Tris-Cl, pH 7.8, 2.5 mM EDTA).

6.1.2 Carbohydrate recognition domain of CD209

The recombinant CRD of CD209 was expressed as described previously.[55] Briefly, a pET-30 expression vector containing the CRD of CD209 was transformed into competent *Escherichia coli* (E. coli) BL21 (DE3) cells. The cells were grown in LB medium containing 100 µg/mL kanamycin at 37 °C and 160 rpm until they reached an optical density (OD_{600}) of approximately 0.7. Overexpression was induced by adding 0.5 mM IPTG for approximately 3 hours at 37 °C. Cells were harvested by centrifugation (10.000 × g at 4 °C for 15 minutes) and resuspended in cold buffer A (25 mM Tris-Cl, 150 mM NaCl, pH 8) supplemented with lysozyme, one tablet of protease inhibitor (cOmplete™, Roche), and DNase I. Lysis was performed by thoroughly sonicating the resuspended cell pellets. Cell debris and inclusion bodies were collected by centrifugation (20,000 × g at 4 °C for 1 hour), and the supernatant was discarded. The inclusion bodies were resuspended in buffer A supplemented with 2 M urea and 1% Triton X-100. After a second centrifugation step, the inclusion bodies were solubilized in buffer A supplemented with 6 M guanidine hydrochloride and 0.01 % 2-mercaptoethanol. Insoluble impurities were removed by centrifugation (20.000 × g at 4 °C for 1 hour). The resulting supernatant was dialyzed against 2 L of buffer B (25 mM Tris, pH 8) at 4 °C overnight. Next, refolding was performed by three-step dialysis against 2 L of buffer C (25 mM Tris-Cl, 150 mM NaCl, pH 8, 4 mM $CaCl_2$) at 4 °C overnight. After centrifugation (20.000 × g at 4 °C for 1 hour), the renatured CRD was purified using a HisTrap HP column pre-equilibrated with buffer D (150 mM NaCl, 25 mM Tris, pH 8, 4 mM $CaCl_2$, 10 mM imidazole). Unbound material was washed with 10 CV of buffer D, and the protein was eluted with buffer E (150 mM NaCl, 25 mM Tris, pH 8, 4 mM $CaCl_2$, 500 mM imidazole). Finally, functional protein was separated from non-functional protein by a 10 mL mannose-agarose column equilibrated with buffer C.

Supporting Information

6.2 Differential Scanning Fluorimetry (NanoDSF).

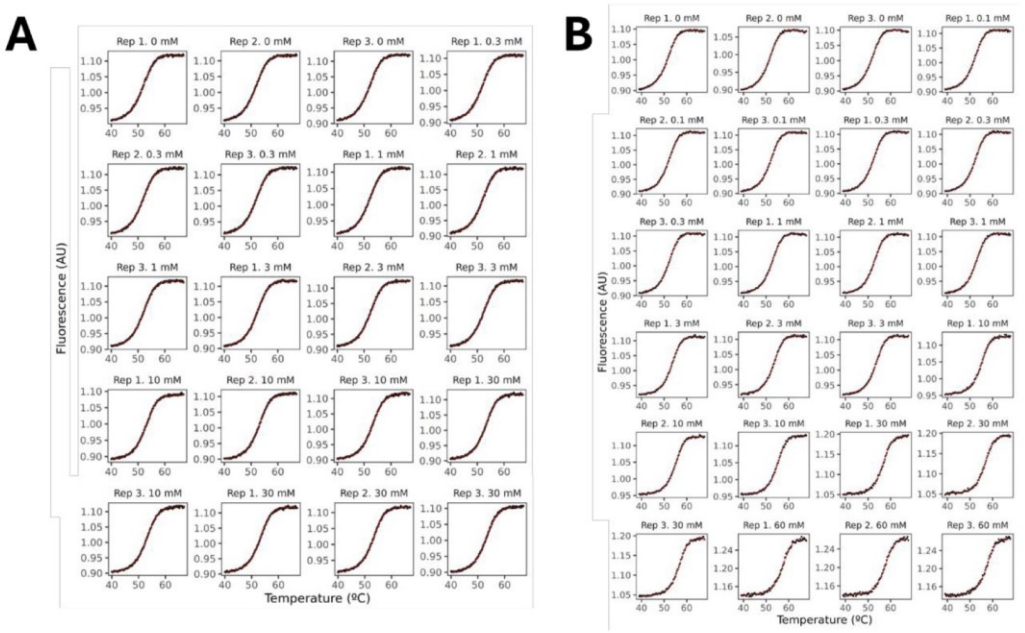

Figure S 4: **A)** Fitting of the fluorescence-based melting curves of protein CD206 CRD4 at different concentrations of the TS $ManN_3$. **B)** Fitting of the fluorescence-based melting curves of protein CD206 CRD4 at different concentrations of the TS Man_3N_3. Plot created by FoldAffinity (spc.embl-hamburg.de).[56]

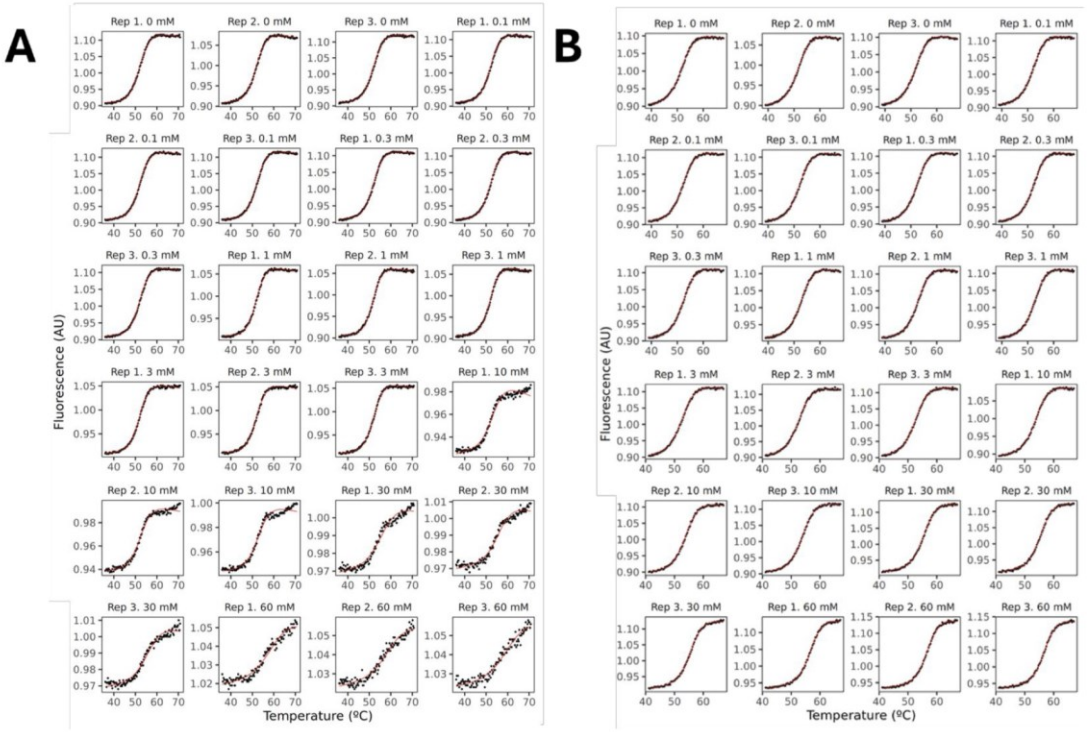

Figure S 5: **A)** Fitting of the fluorescence-based melting curves of protein CD206 CRD4 at different concentrations of the TS $(Man)_3N_3$. **B)** Fitting of the fluorescence-based melting curves of protein CD206 CRD4 at different concentrations of the TS $(Man_3)_3N_3$. Plot created by FoldAffinity (spc.embl-hamburg.de).[56]

Supporting Information

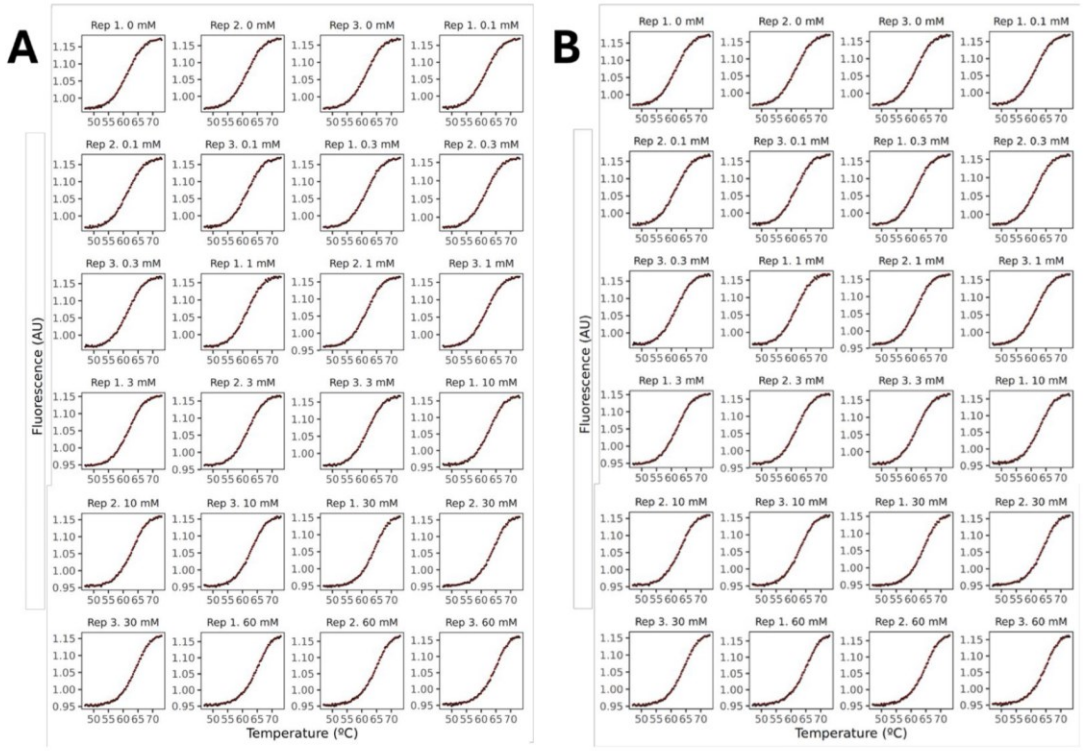

Figure S 6: **A)** Fitting of the fluorescence-based melting curves of protein CD209 CRD at different concentrations of the TS $ManN_3$. **B)** Fitting of the fluorescence-based melting curves of protein CD209 CRD at different concentrations of the TS Man_3N_3. Plot created by FoldAffinity (spc.embl-hamburg.de).[56]

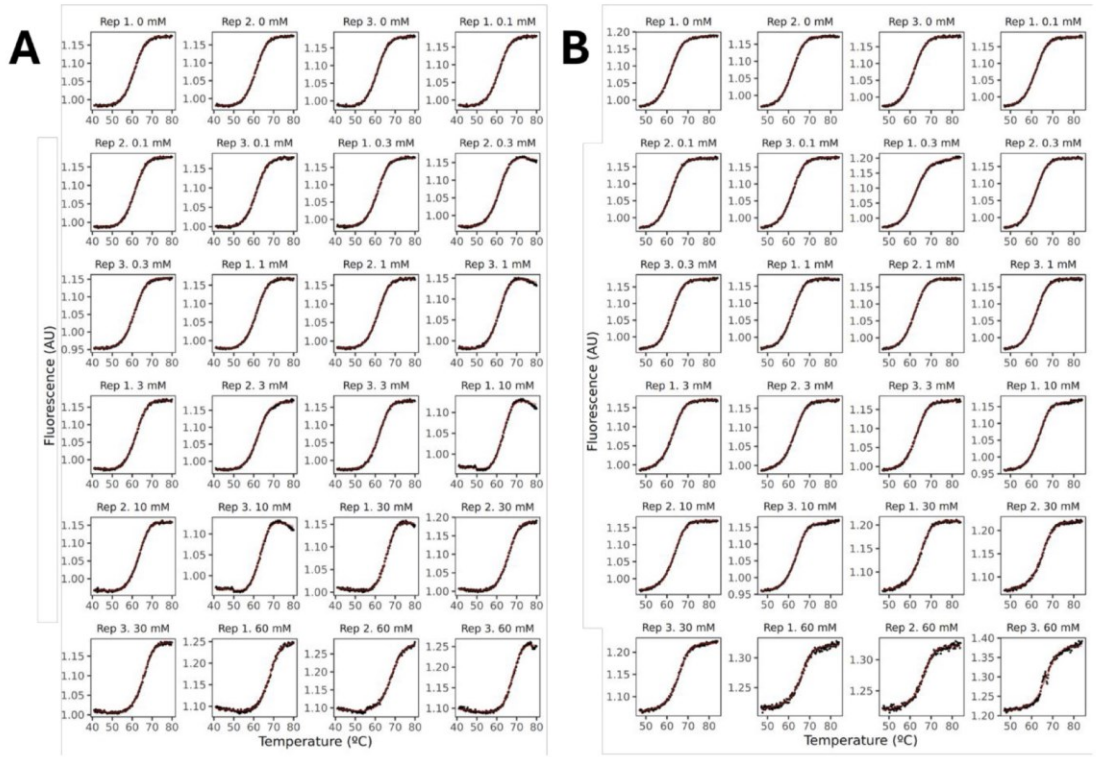

Figure S 7: **A)** Fitting of the fluorescence-based melting curves of protein CD209 CRD at different concentrations of the TS $(Man)_3N_3$. **B)** Fitting of the fluorescence-based melting curves of protein CD209 CRD at different concentrations of the TS $(Man_3)_3N_3$. Plot created by FoldAffinity (spc.embl-hamburg.de).[56]

Supporting Information

7 Prediction of distances of mannose epitopes of a trivalent TS

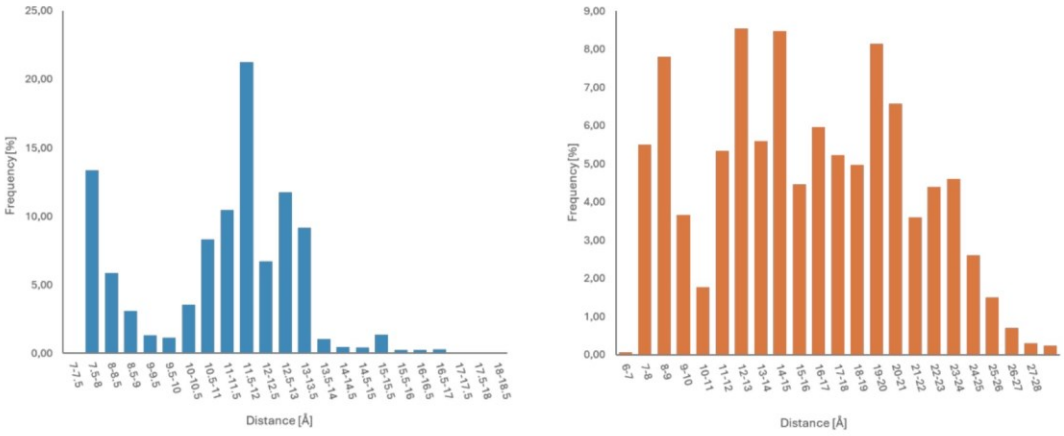

Figure S 8: Distribution of distances between one epitope and the focal point of the glycodendron measured between central carbon and hydroxy groups at *C*-4 (left). Distribution of distances spanned by two Man epitopes measured between hydroxy groups at *C*-4 (right).

8 Appendix

8.1 List of references

(1) Still, W. C.; Kahn, M.; Mitra, A. Rapid chromatographic technique for preparative separations with moderate resolution. *J. Org. Chem.* **1978**, *43* (14), 2923-2925. DOI: 10.1021/jo00408a041.

(2) Cavalli, E. S.; Mies, T.; Rzepa, H. S.; White, A. J. P.; Parsons, P. J.; Barrett, A. G. M. Pyrimidine Nucleosides Syntheses by Late-Stage Base Heterocyclization Reactions. *Org. Lett.* **2022**, *24* (49), 8931-8935. DOI: 10.1021/acs.orglett.2c03152.

(3) Kramer, J. R.; Deming, T. J. Glycopolypeptides via Living Polymerization of Glycosylated-l-lysine N-Carboxyanhydrides. *J. Am. Chem. Soc.* **2010**, *132* (42), 15068-15071. DOI: 10.1021/ja107425f.

(4) Ekholm, F. S.; Poláková, M.; Pawłowicz, A. J.; Leino, R. Synthesis of divalent 2, 2'-linked mannose derivatives by homodimerization. *Synth.* **2009**, *2009* (4), 567-576. DOI: 10.1055/s-0028-1083283.

(5) Nielsen, M. M.; Holmstrøm, T.; Pedersen, C. M. Stereoselective O-Glycosylations by Pyrylium Salt Organocatalysis. *Angew. Chem. Int. Ed.* **2022**, *61* (6), e202115394. DOI: 10.1002/anie.202115394.

(6) Kramer, S.; Langhanki, J.; Krumb, M.; Opatz, T.; Bros, M.; Zentel, R. HPMA-Based Nanocarriers for Effective Immune System Stimulation. *Macromol. Biosci.* **2019**, *19* (6), 1800481. DOI: 10.1002/mabi.201800481.

(7) León, E. I.; Martín, Á.; Pérez-Martín, I.; Quintanal, L. M.; Suárez, E. C–C Bond Formation by Sequential Intramolecular Hydrogen Atom Transfer/Intermolecular Radical Allylation Reaction in Carbohydrate Systems. *Eur. J. Org. Chem.* **2012**, *2012* (20), 3818-3829. DOI: 10.1002/ejoc.201200300.

(8) Schibilla, F.; Voskuhl, J.; Fokina, N. A.; Dahl, J. E. P.; Schreiner, P. R.; Ravoo, B. J. Host–Guest Complexes of Cyclodextrins and Nanodiamonds as a Strong Non-Covalent Binding Motif for Self-Assembled Nanomaterials. *Chem. Eur. J.* **2017**, *23* (63), 16059-16065. DOI: 10.1002/chem.201703392.

(9) Tanzi, L.; Robescu, M. S.; Marzatico, S.; Recca, T.; Zhang, Y.; Terreni, M.; Bavaro, T. Developing a Library of Mannose-Based Mono- and Disaccharides: A General Chemoenzymatic Approach to Monohydroxylated Building Blocks. *Molecules* **2020**, *25* (23), 5764. DOI: 10.3390/molecules25235764.

(10) Poláková, M.; Beláňová, M.; Mikušová, K.; Lattová, E.; Perreault, H. Synthesis of 1,2,3-Triazolo-Linked Octyl (1→6)-α-d-Oligomannosides and Their Evaluation in Mycobacterial Mannosyltransferase Assay. *Bioconjugate Chem.* **2011**, *22* (2), 289-298. DOI: 10.1021/bc100421g.

(11) Percec, V.; Leowanawat, P.; Sun, H.-J.; Kulikov, O.; Nusbaum, C. D.; Tran, T. M.; Bertin, A.; Wilson, D. A.; Peterca, M.; Zhang, S.; Heiney, P. A. Modular synthesis of amphiphilic Janus glycodendrimers and their self-assembly into glycodendrimersomes and other complex architectures with bioactivity to biomedically relevant lectins. *J. Am. Chem. Soc.* **2013**, *135* (24), 9055-9077. DOI: 10.1021/ja403323y.

(12) Reintjens, N. R. M.; Tondini, E.; Vis, C.; McGlinn, T.; Meeuwenoord, N. J.; Hogervorst, T. P.; Overkleeft, H. S.; Filippov, D. V.; van der Marel, G. A.; Ossendorp, F.; Codée, J. D. C. Multivalent, Stabilized Mannose-6-Phosphates for the Targeted Delivery of Toll-Like Receptor Ligands and Peptide Antigens. *ChemBioChem* **2021**, *22* (2), 434-440. DOI: 10.1002/cbic.202000538.

(13) Krabicová, I.; Dolenský, B.; Řezanka, M. Selectivity of 1-O-Propargyl-d-Mannose Preparations. *Molecules* **2022**, *27* (5), 1483. DOI: 10.3390/molecules27051483.

(14) Arias-Pérez, M.; Santos, M. An efficient approach to partially O-methylated α-D-mannopyranosides using bis-tert-butyldiphenylsilyl ethers as intermediates. *Tetrahedron* **1996**, *52* (32), 10785-10798. DOI: 10.1016/0040-4020(96)00600-X.

(15) Du, Y.; Zhang, M.; Kong, F. Highly efficient and practical synthesis of 3, 6-branched oligosaccharides. *Org. Lett.* **2000**, *2* (24), 3797-3800. DOI: 10.1021/ol000243w.

(16) Halmos, T.; Montserret, R.; Filippi, J.; Antonakis, K. Studies of the selective silylation of methyl α- and β-d-aldohexopyranosides: stability of the partially protected derivatives in polar solvents. *Carbohydr. Res.* **1987**, *170* (1), 57-69. DOI: 10.1016/0008-6215(87)85005-X.

(17) Mark, E.; Zbiral, E.; Brandstetter, H. H. Strukturelle Abwandlungen an partiell silylierten Kohlenhydraten mittels Triphenylphosphan/Azodicarbonsäurediethylester, 4. Mitt.: Transformationen an Mannose und Galaktose. *Monatsh. Chem.* **1980**, *111* (1), 289-307. DOI: 10.1007/BF00938735.

(18) Ramos-Soriano, J.; de la Fuente, M. C.; de la Cruz, N.; Figueiredo, R. C.; Rojo, J.; Reina, J. J. Straightforward synthesis of Man9, the relevant epitope of the high-mannose oligosaccharide. *Org. Biomol. Chem.* **2017**, *15* (42), 8877-8882. DOI: 10.1039/C7OB02286G.

(19) Teumelsan, N.; Huang, X. Synthesis of branched Man5 oligosaccharides and an unusual stereochemical observation. *J. Org. Chem.* **2007**, *72* (23), 8976-8979. DOI: 10.1021/jo7013824.

(20) Traboni, S.; Bedini, E.; Iadonisi, A. Orthogonal protection of saccharide polyols through solvent-free one-pot sequences based on regioselective silylations. *Beilstein J. Org. Chem.* **2016**, *12* (1), 2748-2756. DOI: 10.3762/bjoc.12.271.

(21) van den Bos, L. J.; Dinkelaar, J.; Overkleeft, H. S.; van der Marel, G. A. Stereocontrolled synthesis of β-D-mannuronic acid esters: synthesis of an alginate trisaccharide. *J. Am. Chem. Soc.* **2006**, *128* (40), 13066-13067. DOI: 10.1021/ja064787q.

(22) Zhang, Y.; Chen, C.; Jin, L.; Tan, H.; Wang, F.; Cao, H. Synthesis of unsymmetrical 3,6-branched Man5 oligosaccharide: a comparison between one-pot sequential glycosylation and stepwise synthesis. *Carbohydr. Res.* **2015**, *401*, 109-114. DOI: 10.1016/j.carres.2014.09.010.

(23) Kanaya, T.; Mashio, R.; Watanabe, T.; Schweizer, F.; Hada, N. Synthesis of glycosphingolipids from the fungus Hirsutella rhossiliensis. *Tetrahedron* **2017**, *73* (49), 6847-6855. DOI: 10.1016/j.tet.2017.10.034.

(24) Bakleh, M. E.; Sol, V.; Estieu-Gionnet, K.; Granet, R.; Déléris, G.; Krausz, P. An efficient route to VEGF-like peptide porphyrin conjugates via microwave-assisted 'click-chemistry'. *Tetrahedron* **2009**, *65* (36), 7385-7392. DOI: 10.1016/j.tet.2009.07.028.

(25) Davila, J.; Chassepot, A.; Longo, J.; Boulmedais, F.; Reisch, A.; Frisch, B.; Meyer, F.; Voegel, J.-C.; Mésini, P. J.; Senger, B.; Metz-Boutigue, M.-H.; Hemmerlé, J.; Lavalle, P.; Schaaf, P.; Jierry, L. Cyto-mechanoresponsive Polyelectrolyte Multilayer Films. *J. Am. Chem. Soc.* **2012**, *134* (1), 83-86. DOI: 10.1021/ja208970b.

(26) Krumb, M.; Frey, M.-L.; Langhanki, J.; Forster, R.; Kowalczyk, D.; Mailänder, V.; Landfester, K.; Opatz, T. Multivalency Beats Complexity: A Study on the Cell Uptake of Carbohydrate Functionalized Nanocarriers to Dendritic Cells. *Cells* **2020**, *9* (9), 2087. DOI: 10.3390/cells9092087.

(27) Tavernaro, I.; Hartmann, S.; Sommer, L.; Hausmann, H.; Rohner, C.; Ruehl, M.; Hoffmann-Roeder, A.; Schlecht, S. Synthesis of tumor-associated MUC1-glycopeptides and their multivalent presentation by functionalized gold colloids. *Org. Biomol. Chem.* **2015**, *13* (1), 81-97, 10.1039/C4OB01339E. DOI: 10.1039/C4OB01339E.

(28) Tsakama, M.; Shang, Y.; He, Y.; Fan, B.; Wang, F.; Chen, W.; Dai, X. Synthesis and optical properties of a novel sugar coated poly(p-phenyleneethynylene) effectively quenched by concanavalin A. *Tetrahedron Lett.* **2016**, *57* (16), 1739-1742. DOI: 10.1016/j.tetlet.2016.01.102.

(29) Landeros, J. M.; Silvestre, H. A.; Guadarrama, P. Synthesis of branched cores by poly-O-alkylation reaction under phase transfer conditions. A systematic study. *J. Mol. Struct.* **2013**, *1037*, 412-419. DOI: 10.1016/j.molstruc.2013.01.034.

(30) Newkome, G. R.; Lin, X. Symmetrical, four-directional, poly (ether-amide) cascade polymers. *Macromolecules* **1991**, *24* (6), 1443-1444. DOI: 10.1021/ma00006a042.

(31) Appel, R.; Fuchs, J.; Tyrrell, S. M.; Korevaar, P. A.; Stuart, M. C.; Voets, I. K.; Schonhoff, M.; Besenius, P. Steric Constraints Induced Frustrated Growth of Supramolecular Nanorods in Water. *Chemistry* **2015**, *21* (52), 19257-19264. DOI: 10.1002/chem.201503616.

(32) Cardona, C. M.; Gawley, R. E. An improved synthesis of a trifurcated newkome-type monomer and orthogonally protected two-generation dendrons. *J. Org. Chem.* **2002**, *67*(4), 1411-1413. DOI: 10.1021/jo0161678.

(33) Baldoli, C.; Rigamonti, C.; Maiorana, S.; Licandro, E.; Falciola, L.; Mussini, P. R. A New Triferrocenyl-tris(hydroxymethyl)aminomethane Derivative as a Highly Sensitive Electrochemical Marker of Biomolecules: Application to the Labelling of PNA Monomers and Their Electrochemical Characterization. *Chem. Eur. J.* **2006**, *12* (15), 4091-4100. DOI: 10.1002/chem.200501466.

(34) Odaka, M.; Furuta, T.; Kobayashi, Y.; Iwamura, M. Synthesis, Photoreactivity and Cytotoxic Activity of Caged Compounds of L-Leucyl-L-Leucine Methyl Ester, an Apoptosis Inducer. *Photochem. Photobiol.* **1996**, *63* (6), 800-806. DOI: 10.1111/j.1751-1097.1996.tb09633.x.

(35) Spitzer, D.; Rodrigues, L. L.; Straßburger, D.; Mezger, M.; Besenius, P. Tuneable Transient Thermogels Mediated by a pH- and Redox-Regulated Supramolecular Polymerization. *Angew. Chem. Int. Ed.* **2017**, *56* (48), 15461-15465. DOI: 10.1002/anie.201708857.

(36) André, S.; Cañada, F. J.; Shiao, T. C.; Largartera, L.; Diercks, T.; Bergeron-Brlek, M.; el Biari, K.; Papadopoulos, A.; Ribeiro, J. P.; Touaibia, M.; Solís, D.; Menéndez, M.; Jiménez-Barbero, J.; Roy, R.; Gabius, H.-J. Fluorinated Carbohydrates as Lectin Ligands: Biorelevant Sensors with Capacity to Monitor Anomer Affinity in 19F-NMR-Based Inhibitor Screening. *Eur. J. Org. Chem.* **2012**, *2012* (23), 4354-4364. DOI: 10.1002/ejoc.201200397.

(37) Hellmuth, I.; Freund, I.; Schlöder, J.; Seidu-Larry, S.; Thüring, K.; Slama, K.; Langhanki, J.; Kaloyanova, S.; Eigenbrod, T.; Krumb, M.; Röhm, S.; Peneva, K.; Opatz, T.; Jonuleit, H.; Dalpke, A. H.; Helm, M. Bioconjugation of Small Molecules to RNA Impedes Its Recognition by Toll-Like Receptor 7. *Front. Immunol.* **2017**, *8*, Original Research. DOI: 10.3389/fimmu.2017.00312.

(38) Lu, W.-Y.; Sun, X.-W.; Zhu, C.; Xu, J.-H.; Lin, G.-Q. Expanding the application scope of glycosidases using click chemistry. *Tetrahedron* **2010**, *66* (3), 750-757. DOI: 10.1016/j.tet.2009.11.044.

(39) Yamamoto, S.; Nakahama, S.; Yamaguchi, K. A Heterobifunctional Linker Bearing Azide-reactive Alkyne and Thiol-reactive Maleimide Connected with N-(2-Nitrobenzyl)imide to Synthesize Photocleavable Diblock Copolymers. *Chem. Lett.* **2013**, *42* (8), 791-793. DOI: 10.1246/cl.130235 (acccessed 2/11/2025).

(40) Lindhorst, T. K.; Bruegge, K.; Fuchs, A.; Sperling, O. A bivalent glycopeptide to target two putative carbohydrate binding sites on FimH. *Beilstein J. Org. Chem.* **2010**, *6*, 801-809. DOI: 10.3762/bjoc.6.90.

(41) Reina, J. J.; Rioboo, A.; Montenegro, J. Glycosyl Aldehydes: New Scaffolds for the Synthesis of Neoglycoconjugates via Bioorthogonal Oxime Bond Formation. *Synth.* **2018**, *50* (04), 831-845. DOI: 10.1055/s-0036-1591082.

(42) Amit, B.; Hazum, E.; Fridkin, M.; Patchornik, A. A photolabile protecting group for the phenolic hydroxyl function of tyrosine. *Int. J. Pept. Protein Res.* **1977**, *9* (2), 91-96. DOI: 10.1111/j.1399-3011.1977.tb03468.x.

(43) Amit, B.; Zehavi, U.; Patchornik, A. Photosensitive protecting groups of amino sugars and their use in glycoside synthesis. 2-Nitrobenzyloxycarbonylamino and 6-nitroveratryloxycarbonylamino derivatives. *J. Org. Chem.* **1974**, *39* (2), 192-196. DOI: 10.1021/jo00916a015.

(44) Cheng, S.; Feng, Y.; Li, W.; Liu, T.; Lv, X.; Tong, X.; Xi, G.; Ye, X.; Li, X. Development of novel antivrial agents that induce the degradation of the main protease of human-infecting coronaviruses. *Eur. J. Med. Chem.* **2024**, *275*, 116629. DOI: 10.1016/j.ejmech.2024.116629.

(45) Krumb, M.; Lucas, T.; Opatz, T. Visible Light Enables Aerobic Iodine Catalyzed Glycosylation. *Eur. J. Org. Chem.* **2019**, *2019* (28), 4517-4521. DOI: 10.1002/ejoc.201900143.

(46) Chakraborti, A. K.; Gulhane, R. Perchloric acid adsorbed on silica gel as a new, highly efficient, and versatile catalyst for acetylation of phenols, thiols, alcohols, and amines. *Chem. Commun.* **2003**, (15), 1896-1897. DOI: 10.1039/B304178F.

(47) Dyer, R. G.; Turnbull, K. D. Hydrolytic Stabilization of Protected p-Hydroxybenzyl Halides Designed as Latent Quinone Methide Precursors. *J. Org. Chem.* **1999**, *64* (21), 7988-7995. DOI: 10.1021/jo991085t.

(48) Zhou, K.; Li, G.; Pan, R.; Xin, S.; Wen, W.; Wang, H.; Luo, C.; Han, R. P. S.; Gu, Y.; Tu, Y. Preclinical evaluation of AGTR1-Targeting molecular probe for colorectal cancer imaging in orthotopic and liver metastasis mouse models. *Eur. J. Med. Chem.* **2024**, *271*, 116452. DOI: 10.1016/j.ejmech.2024.116452.

(49) Guo, Y.; Feinberg, H.; Conroy, E.; Mitchell, D. A.; Alvarez, R.; Blixt, O.; Taylor, M. E.; Weis, W. I.; Drickamer, K. Structural basis for distinct ligand-binding and targeting properties of the receptors DC-SIGN and DC-SIGNR. *Nat. Struct. Mol. Biol.* **2004**, *11* (7), 591-598. DOI: 10.1038/nsmb784.

(50) Feinberg, H.; Jégouzo, S. A.; Lasanajak, Y.; Smith, D. F.; Drickamer, K.; Weis, W. I.; Taylor, M. E. Structural analysis of carbohydrate binding by the macrophage mannose receptor CD206. *J. Biol. Chem.* **2021**, *296*, 100368. DOI: 10.1016/j.jbc.2021.100368

(51) SeeSAR, version 13.01.1 BioSolveIT GmbH, St. Augustin, Germany, https://www.biosolveit.de/SeeSAR.

(52) Rarey, M.; Kramer, B.; Lengauer, T.; Klebe, G. A Fast Flexible Docking Method using an Incremental Construction Algorithm. *J. Mol. Biol.* **1996**, *261* (3), 470-489. DOI: 10.1006/jmbi.1996.0477.

(53) Reulecke, I.; Lange, G.; Albrecht, J.; Klein, R.; Rarey, M. Towards an Integrated Description of Hydrogen Bonding and Dehydration: Decreasing False Positives in Virtual Screening with the HYDE Scoring Function. *ChemMedChem* **2008**, *3* (6), 885-897. DOI: 10.1002/cmdc.200700319.

(54) Fornstedt, N.; Porath, J. Characterization studies on a new lectin found in seeds of Vicia ervilia. *FEBS Lett.* **1975**, *57* (2), 187-191. DOI: 10.1016/0014-5793(75)80713-7.

(55) Thépaut, M.; Guzzi, C.; Sutkeviciute, I.; Sattin, S.; Ribeiro-Viana, R.; Varga, N.; Chabrol, E.; Rojo, J.; Bernardi, A.; Angulo, J.; Nieto, P. M.; Fieschi, F. Structure of a Glycomimetic Ligand in the Carbohydrate Recognition Domain of C-type Lectin DC-SIGN. Structural Requirements for Selectivity and Ligand Design. *J. Am. Chem. Soc.* **2013**, *135* (7), 2518-2529. DOI: 10.1021/ja3053305.

(56) Bai, N.; Roder, H.; Dickson, A.; Karanicolas, J. Isothermal Analysis of ThermoFluor Data can readily provide Quantitative Binding Affinities. *Sci. Rep.* **2019**, *9* (1), 2650. DOI: 10.1038/s41598-018-37072-x.

8.2 List of abbreviations

$(HF)_X \cdot Pyr$	Hydrogen fluoride pyridine complex
Ac_2O	Acetic anhydride
AgOTf	Silver triflate
Ar-atm.	Argon atmosphere
ATR	Attenuated total reflection
$BF_3 \cdot OEt_2$	Boron trifluoride diethyl etherate
BzCl	Benzoyl chloride
C_{18}	C_{18}-alkyl chains modified silica for RP chromatography
CDXX	Cluster of differentiation (number = XX)
CD_3CN	Deuterated Acetonitrile
CD_3OD	Deuterated methanol
$CDCl_3$	Deuterated Chloroform
^{c}Hex	Cyclohexane
COSY	Correlated spectroscopy
CRD	Carbohydrate recognition domain
CuBr	Copper(I)bromide
Cy5	Cyanine 5 dye
DC	Dendritic cell
D_2O	Deuterium oxide
DAD	Diode array detector
DBCO	Dibenzocyclooctyne
DCM	Dichloromethane
DIPEA	*N,N*-Diisopropylethylamine
DMAP	*N,N*-Dimethylpyridin-4-amine
DMF	Dimethylformamide
DMSO	Dimethyl sulfoxide
DoM	Degree of modification
EDTA	Ethylenediaminetetraacetic acid
ELS	Evaporative light scattering
Eq.	Equivalent
ESI	Electrospray ionization
Et_2O	Diethylether
EtOAc	Ethyl acetate
EtOH	Ethanol
FCC	Flash column chromatography
H_2O (MQ)	Ultrapure water
H_2SO_4	Sulfuric acid
HCl	Hydrochloric acid
HCOOH	Formic acid
HMBC	Heteronuclear multiple bond correlation
HOPrg	Propargyl alcohol
HPLC	High performance liquid chromatography
HR	High resolution
HSA	Human serum albumin
HSQC	Heteronuclear Single Quantum Coherence
HSQC-NoDec	HSQC without decoupling
I_2	Molecular iodine
ICAM-3	Intercellular adhesion molecule 3 (CD50)
IR	Infra-red
$KMnO_4$	Potassium permanganate
M	Molar mass
MALDI-ToF-MS	Matrix assisted laser desorption ionization with time-of-flight MS
MeOH	Methanol
MS	Mass spectrometry
MsCl	Mesylchloride
MS 3 Å	Molecular sieves (Pore size 3 Å)
$Na_2S_2O_3$	Sodium thiosulfate
Na_2SO_4	Sodium sulfate
NaCl	Sodium chloride
$NaHCO_3$	Sodium bicarbonate
NaN_3	Sodium azide
NanoDSF	Nano differential scanning fluorimetry
NaOH	Sodium hydroxide
NaOMe	Sodium methoxide
NEt_3	Triethylamine
NHS	*N*-Hydroxysuccinimide

Supporting Information

NIS	*N*-Iodosuccinimide
NMR	Nuclear magnetic resonance
NOESY	Nuclear Overhauser enhancement spectroscopy
NP	Normal phase chromatography
OVA	Ovalbumin
PEG	Polyethylene glycol
pH	Potentia hydrogenii
PhSH	Thiophenol
PMDTA	N^1-[2-(Dimethylamino)ethyl]-N^1,N^2,N^2-trimethylethane-1,2-diamine
Pyr.	Pyridine
R_f	Ratio of fronts
RP	Reversed phase chromate-graphy
TBAI	Tetrabutylammonium iodide
TBDMS	*tert*-Butyldimethylsilyl
TFA	Trifluoromethanesulfonic acid
THF	Tetrahydrofuran
TLC	Thin layer chromatography
TM	Trimannose
TOCSY	Total correlation spectroscopy
t_R	Retention time
TRIS	Tris(hydroxymethyl)amin
TS	Targeting structure
TsCl	Tosyl chloride

Supporting Information

8.3 NMR spectra

^{1}H-NMR, (400 MHz, $CDCl_3$): **(I1)**

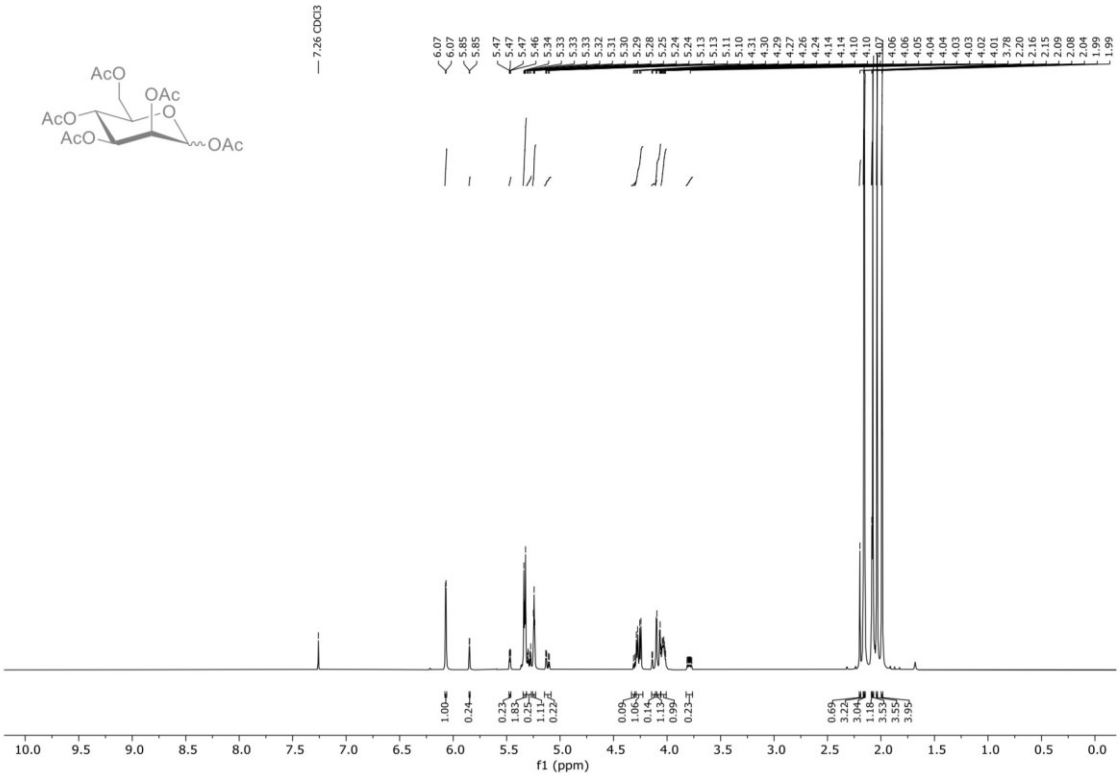

^{13}C-NMR, (101 MHz, $CDCl_3$): **(I1)**

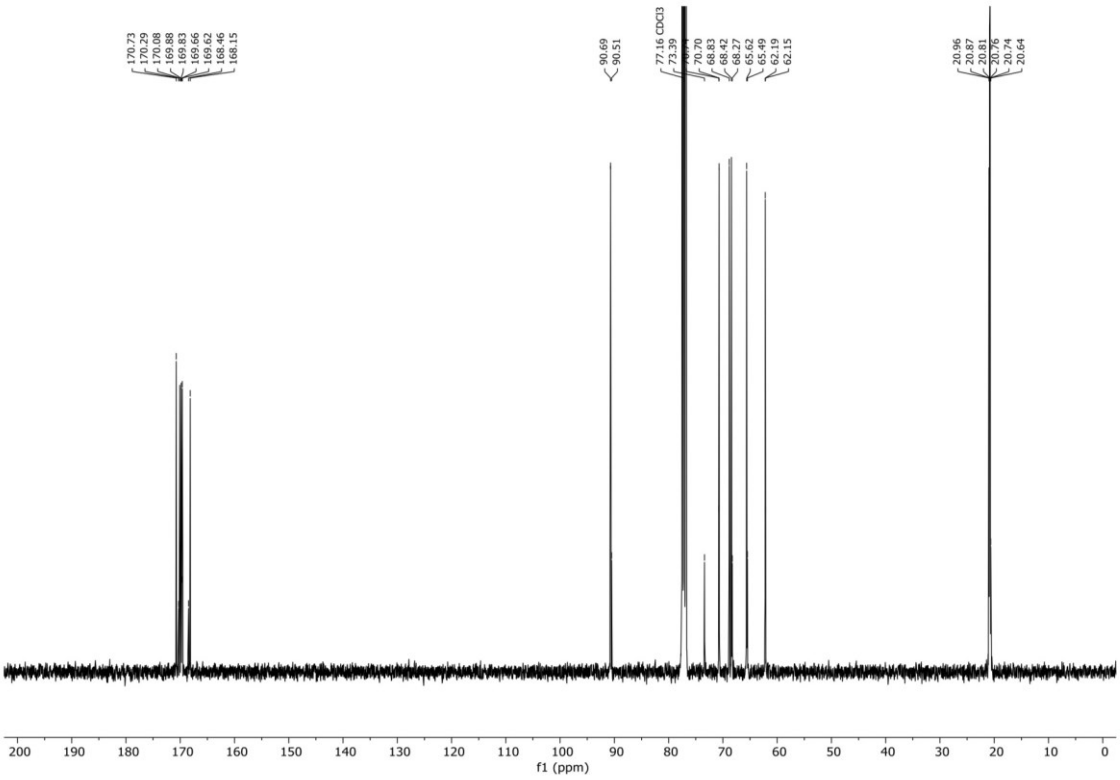

Supporting Information

^{1}H-NMR, (400 MHz, $CDCl_3$): **(S1)**

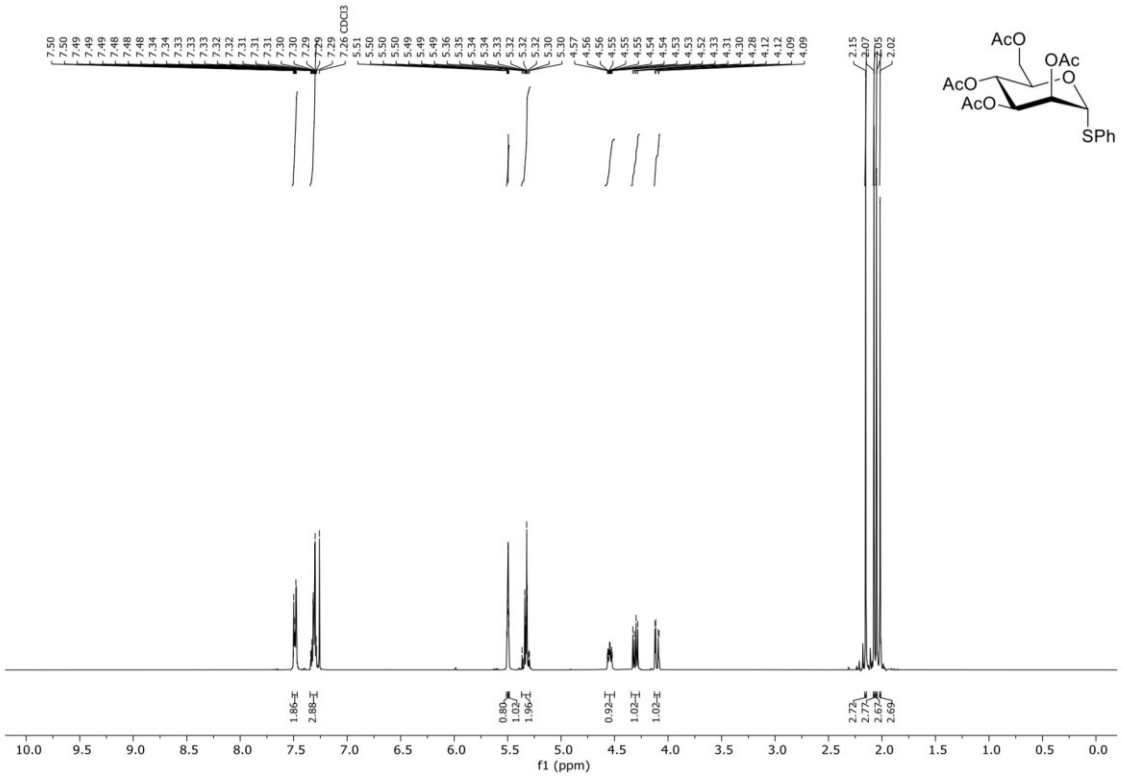

^{13}C-NMR, (101 MHz, $CDCl_3$): **(S1)**

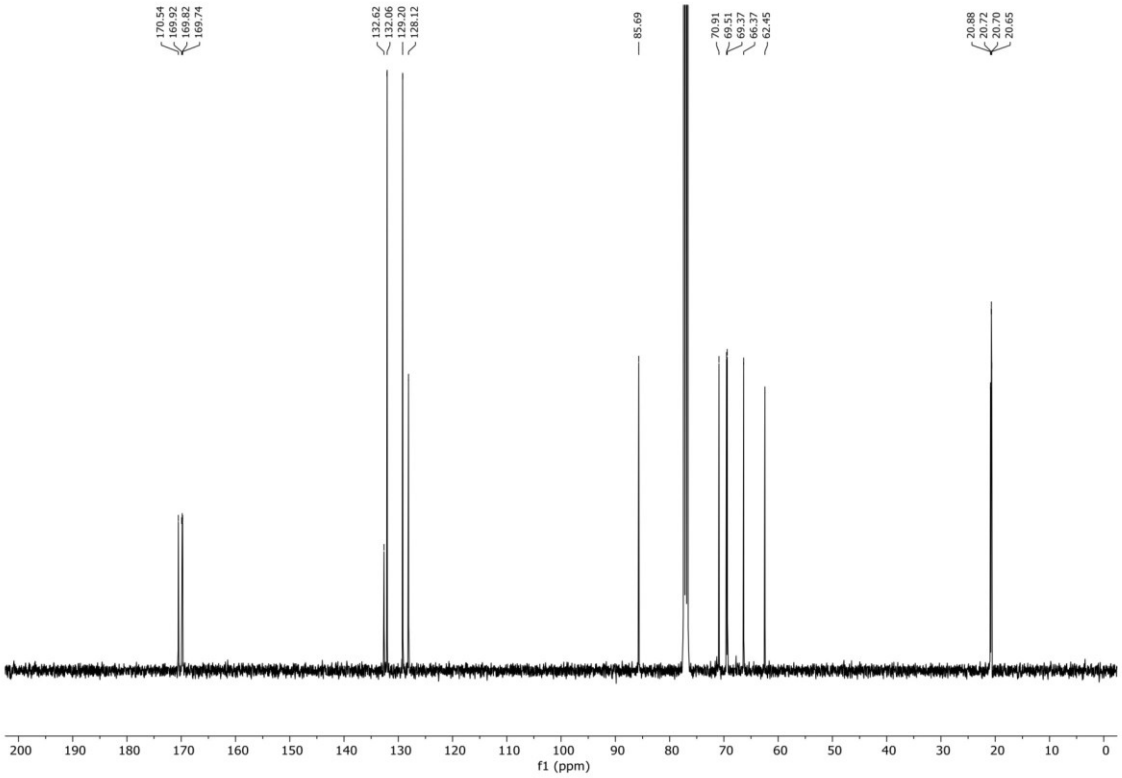

Supporting Information

^{1}H-NMR, (400 MHz, $CDCl_3$): (**S7**)

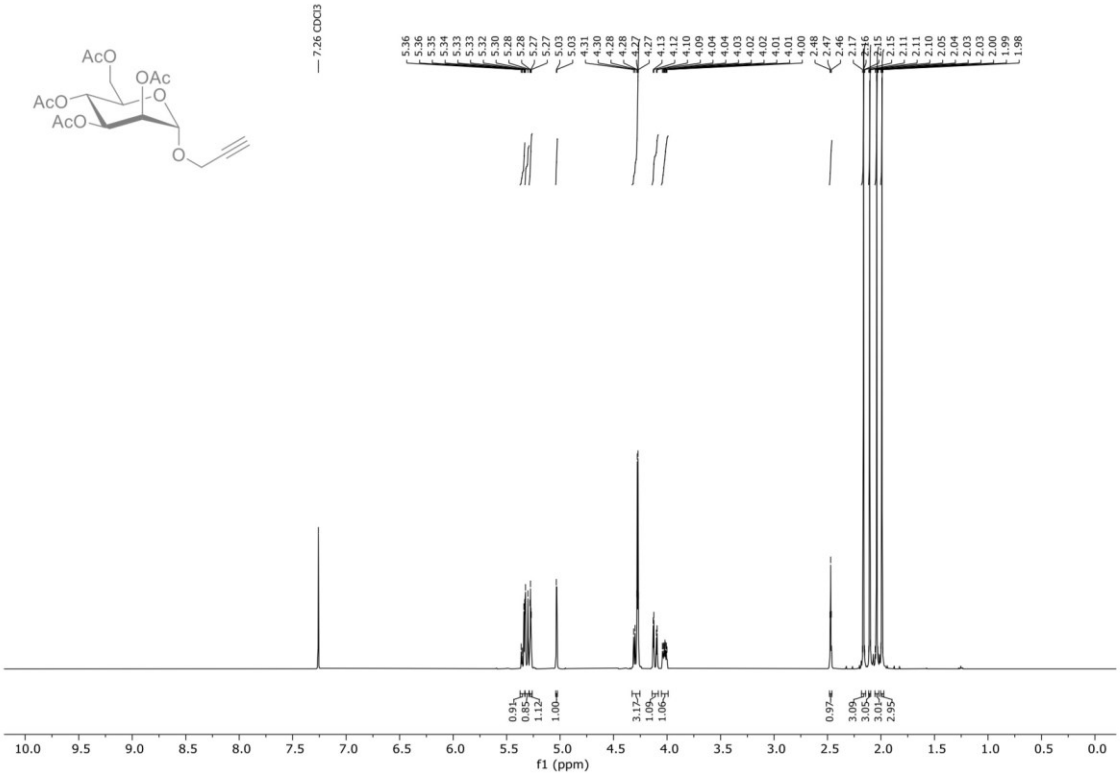

^{13}C-NMR, (101 MHz, $CDCl_3$): (**S7**)

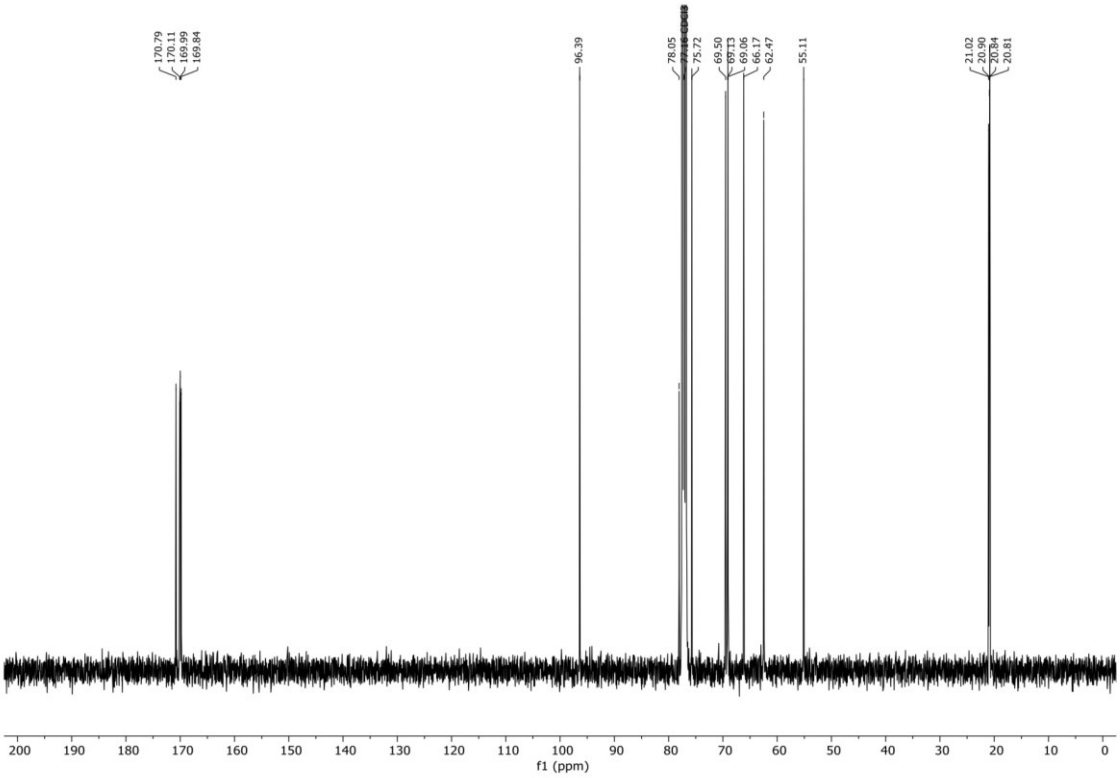

Supporting Information

^{1}H-NMR, (400 MHz, CD_3OD): (**1**)

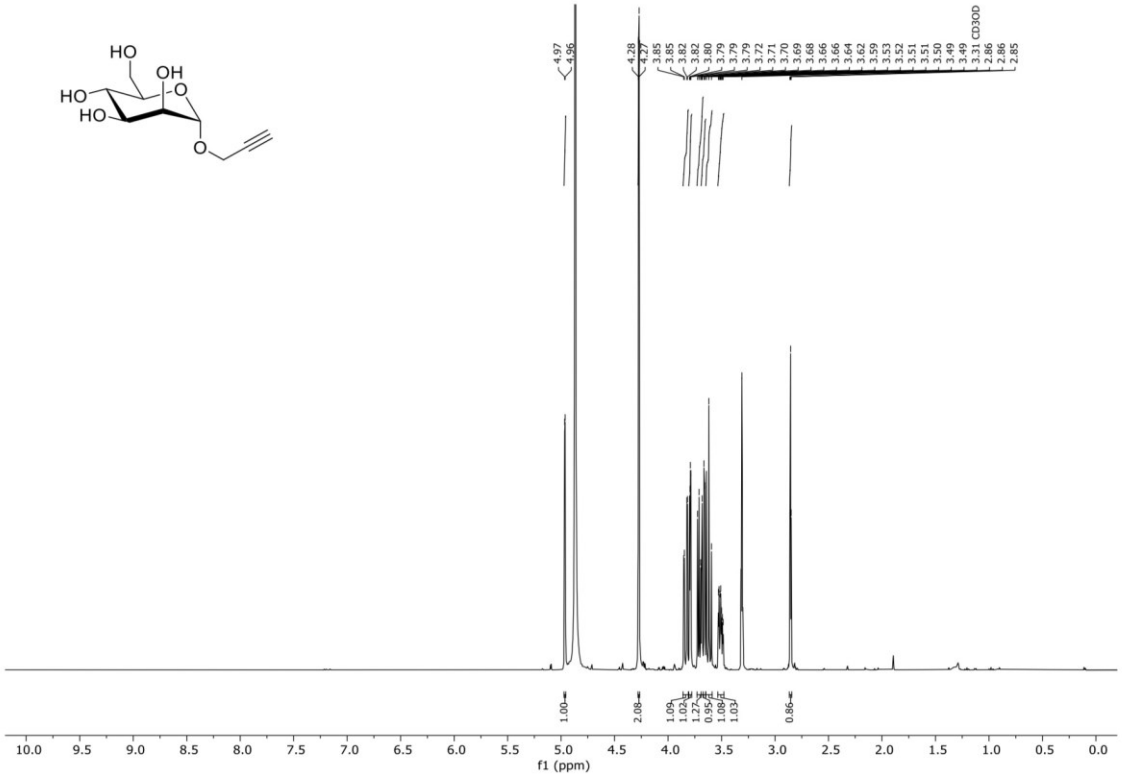

^{13}C-NMR, (101 MHz, CD_3OD): (**1**)

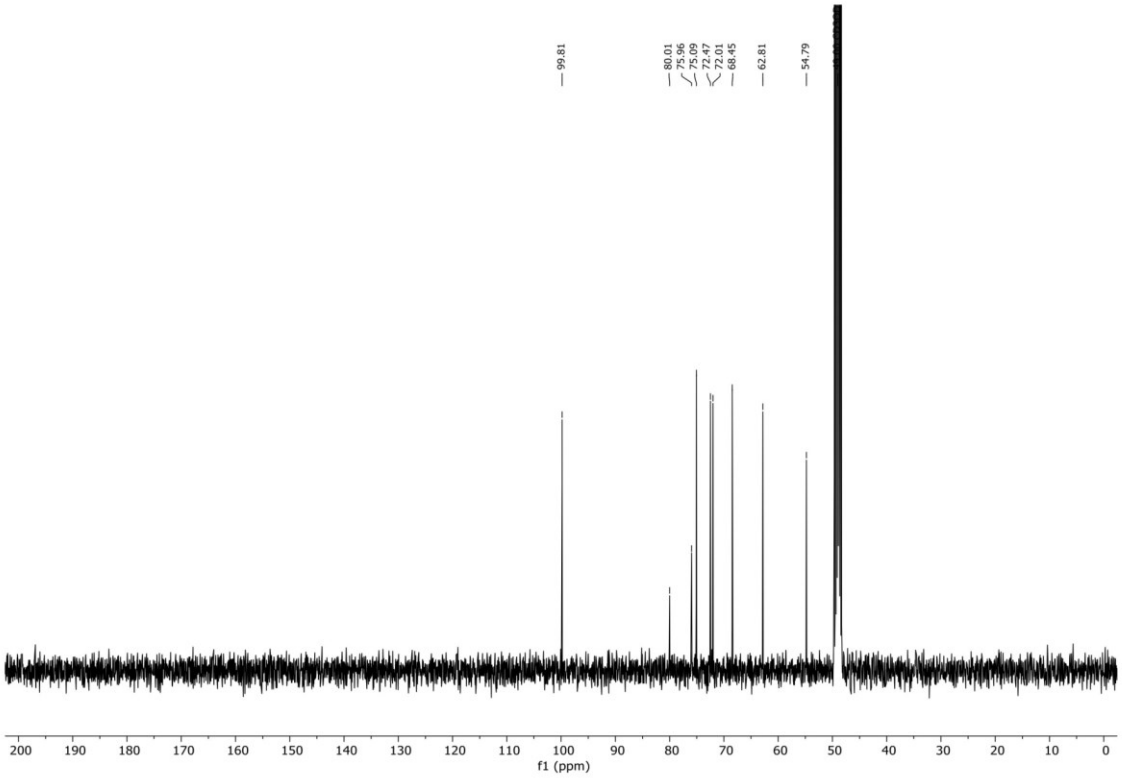

Supporting Information

^{1}H-NMR, (400 MHz, $CDCl_3$): (**I2**)

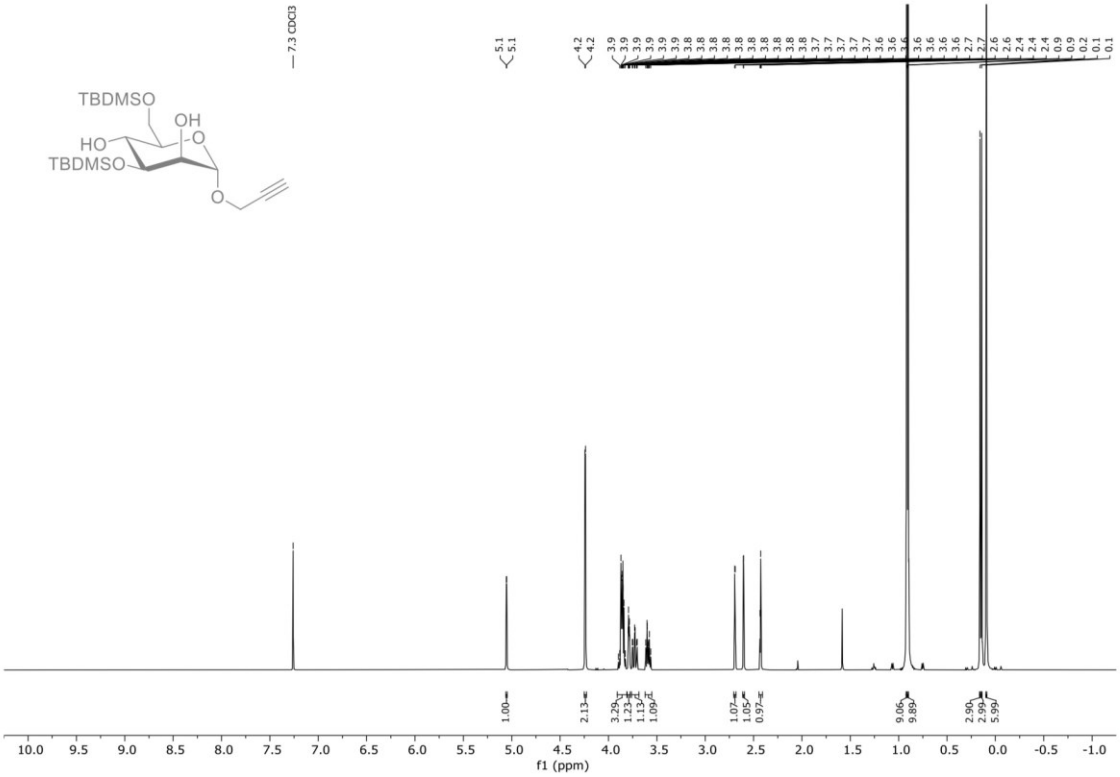

^{13}C-NMR, (101 MHz, $CDCl_3$): (**I2**)

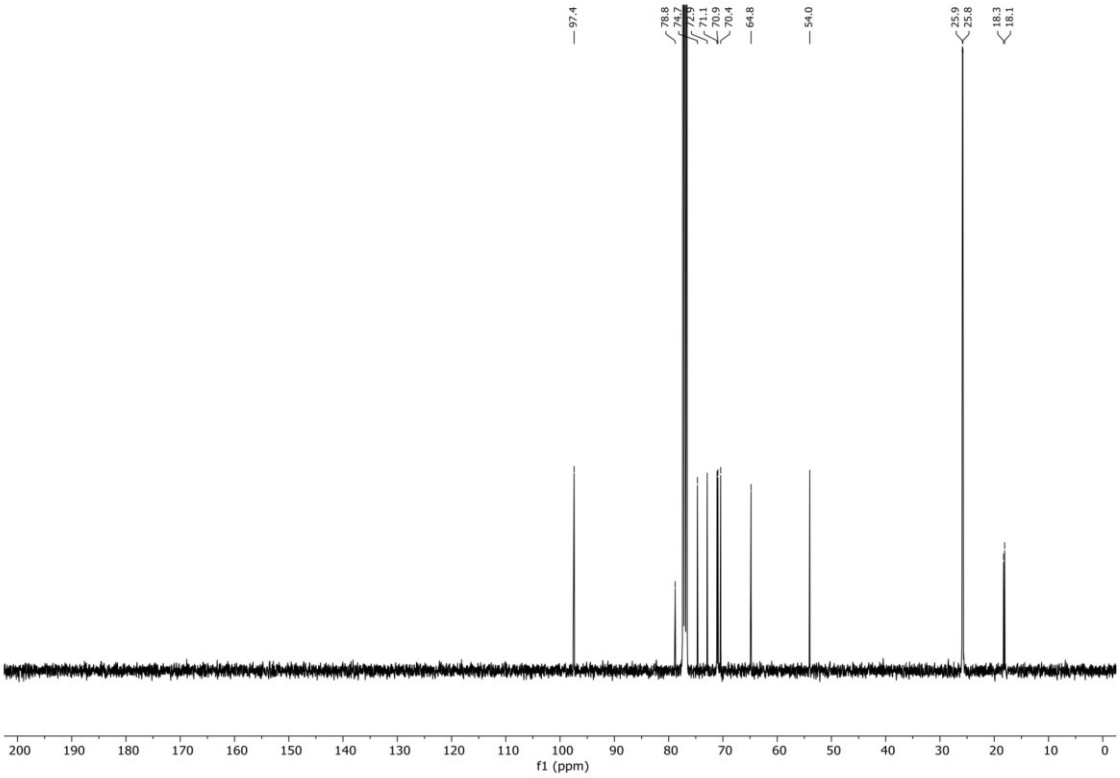

Supporting Information

^{1}H-NMR, (400 MHz, $CDCl_3$): (**I3**)

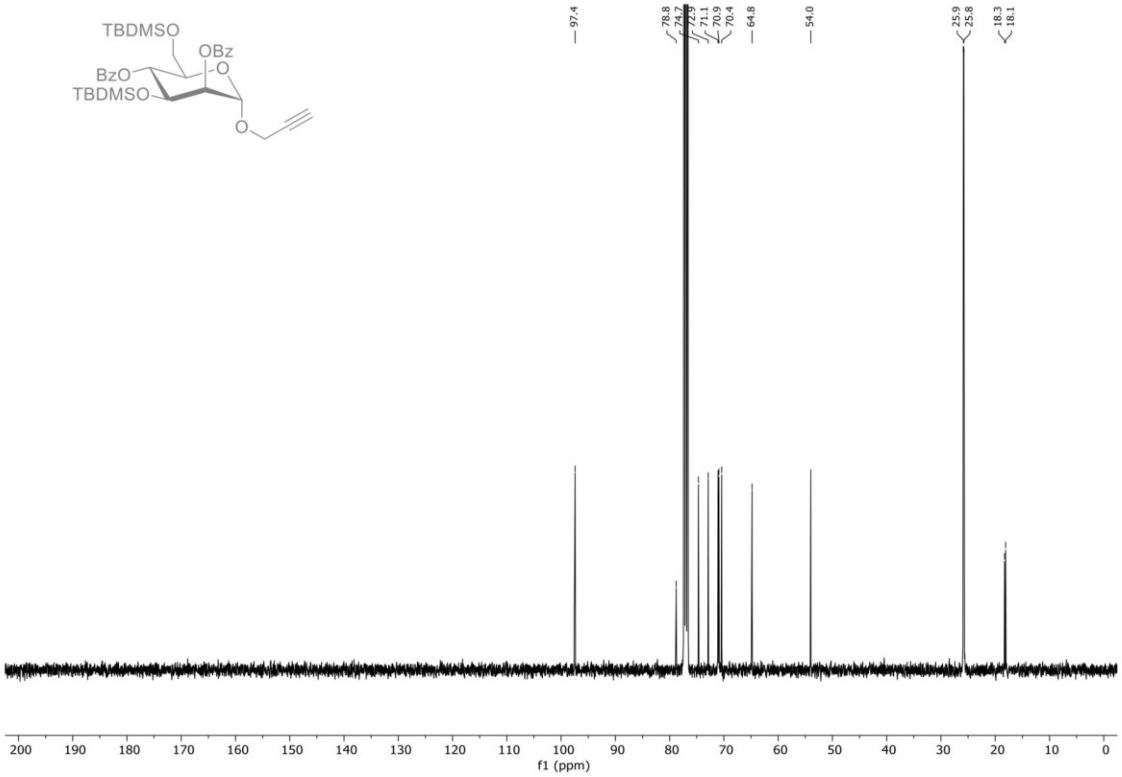

^{13}C-NMR, (101 MHz, $CDCl_3$): (**I3**)

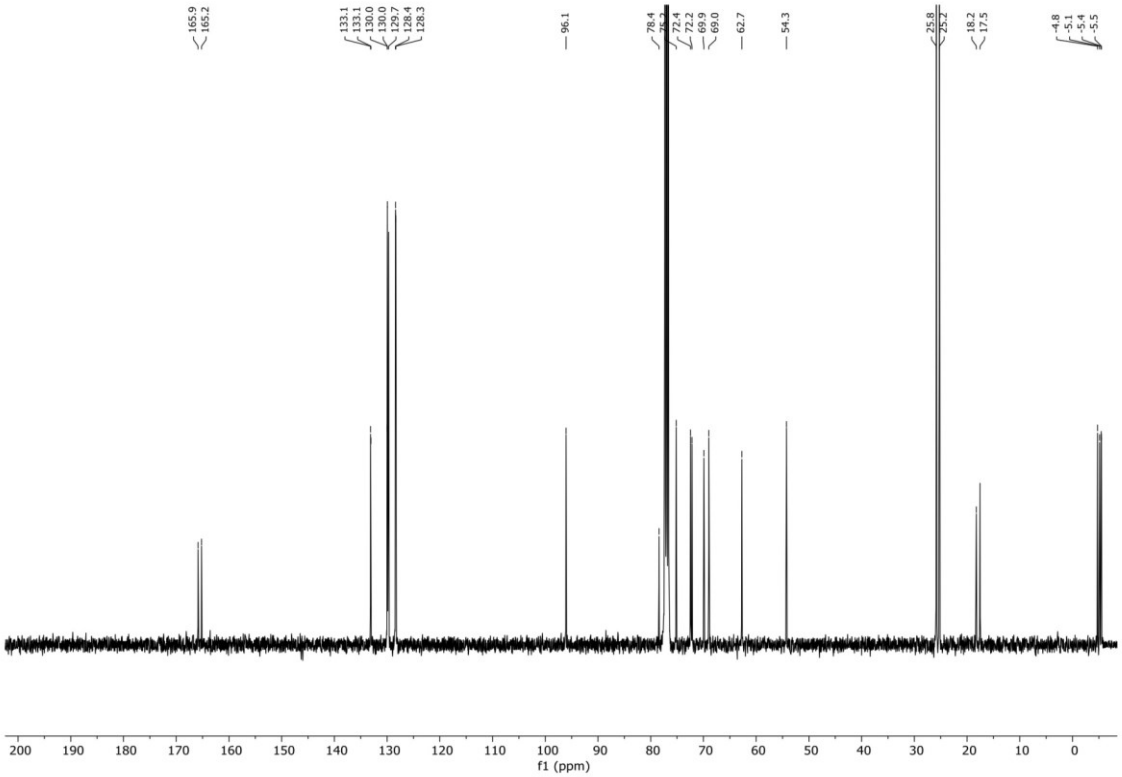

Supporting Information

^{1}H-NMR, (400 MHz, $CDCl_3$): (**S2**)

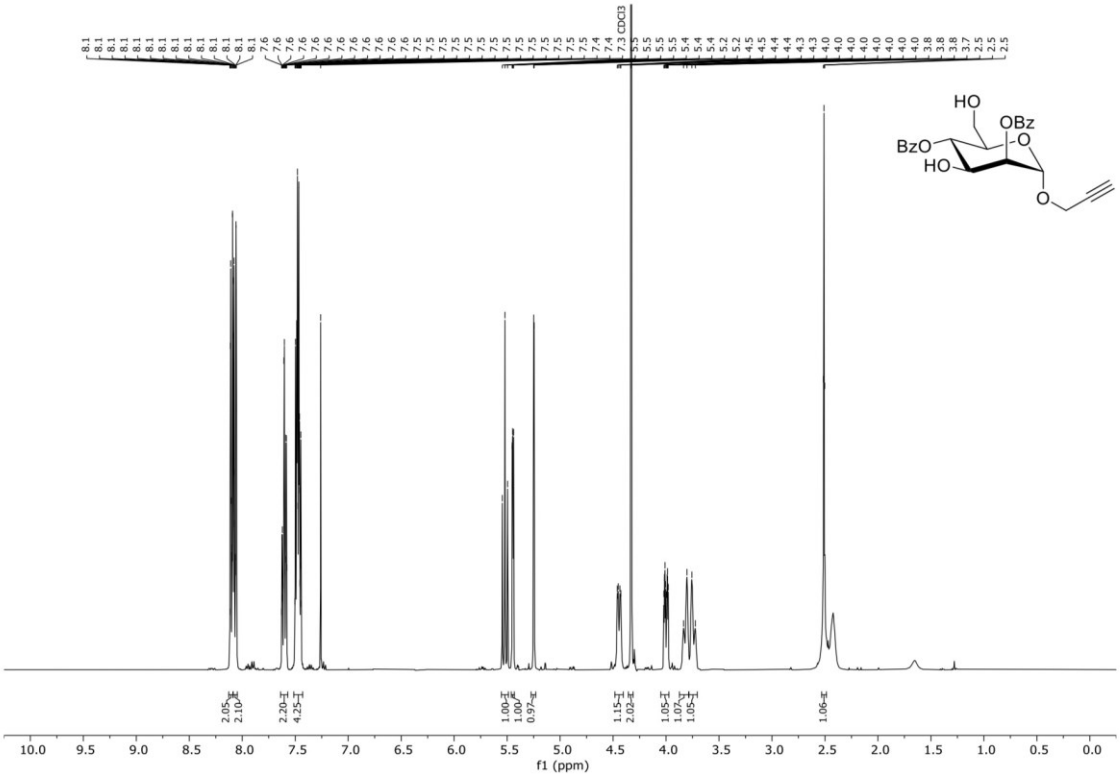

^{13}C-NMR, (101 MHz, $CDCl_3$): (**S2**)

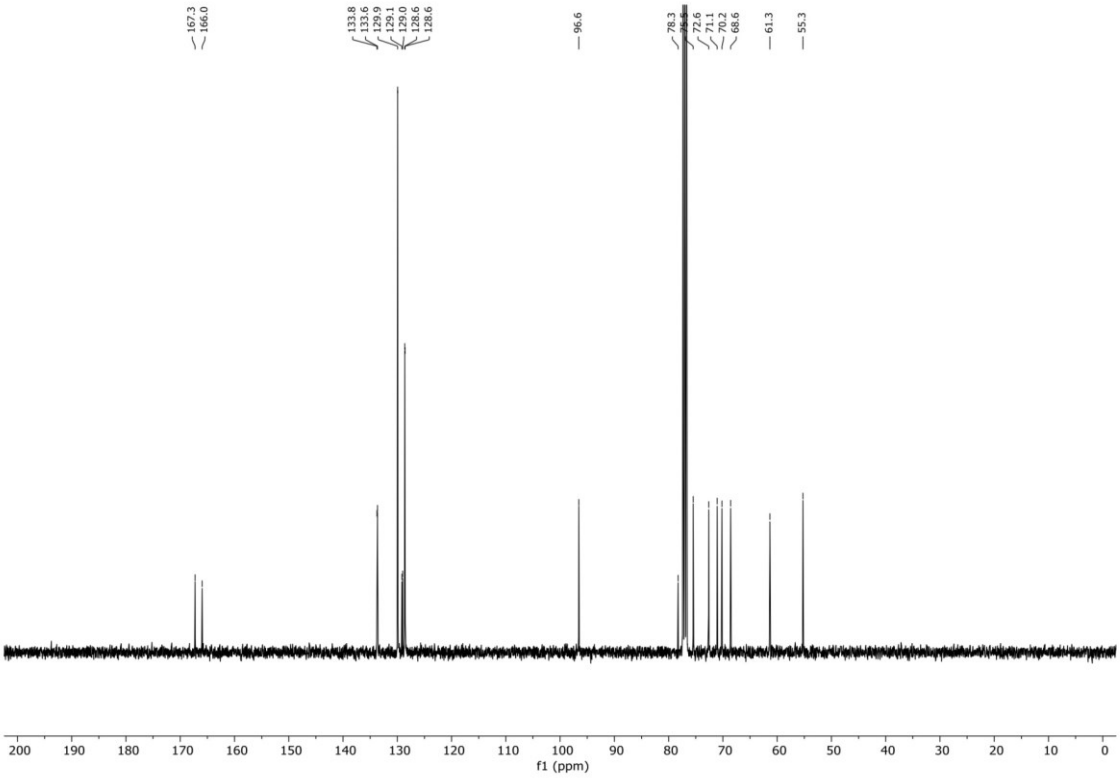

Supporting Information

^{1}H-NMR, (600 MHz, $CDCl_3$): (**1**)

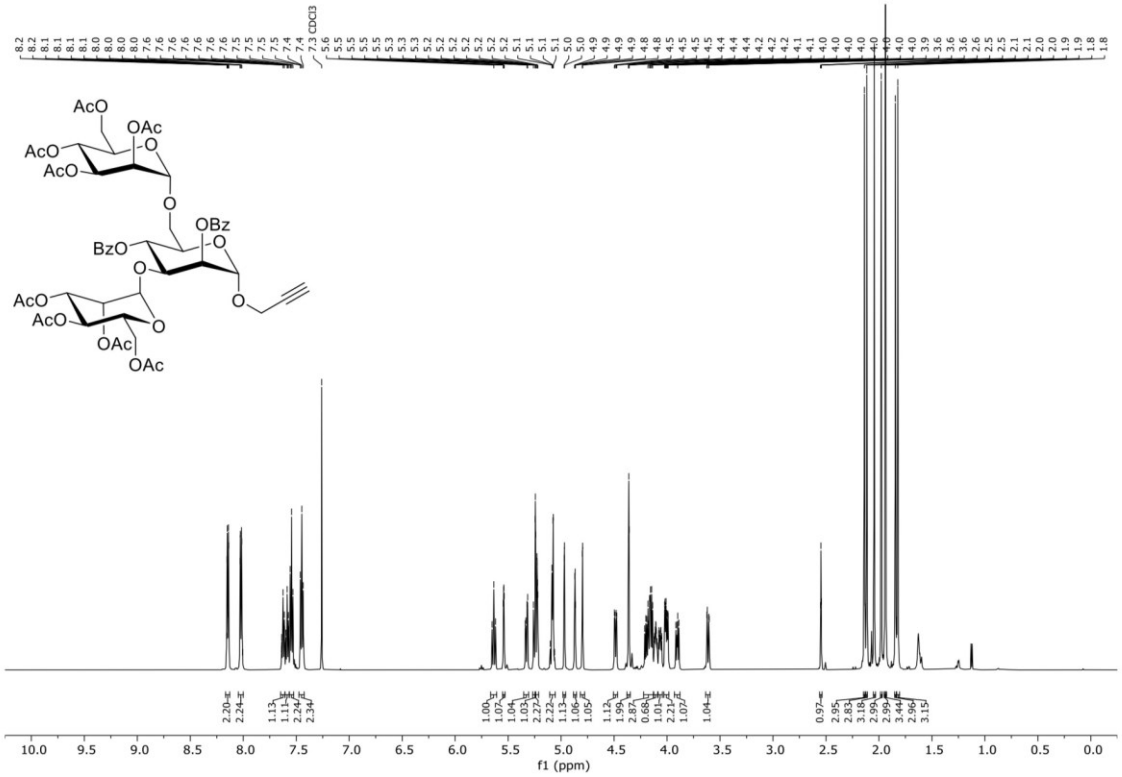

^{13}C-NMR, (151 MHz, $CDCl_3$): (**1**)

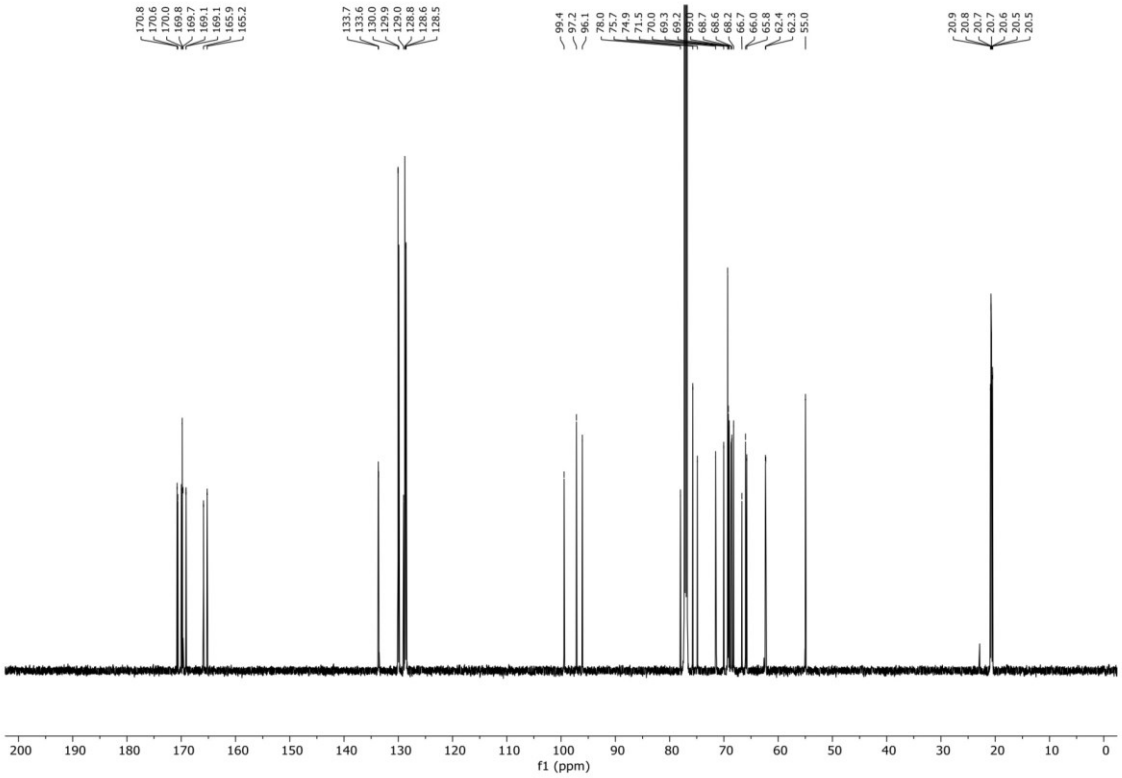

Supporting Information

^{1}H-NMR, (400 MHz, $CDCl_3$): (**S14**)

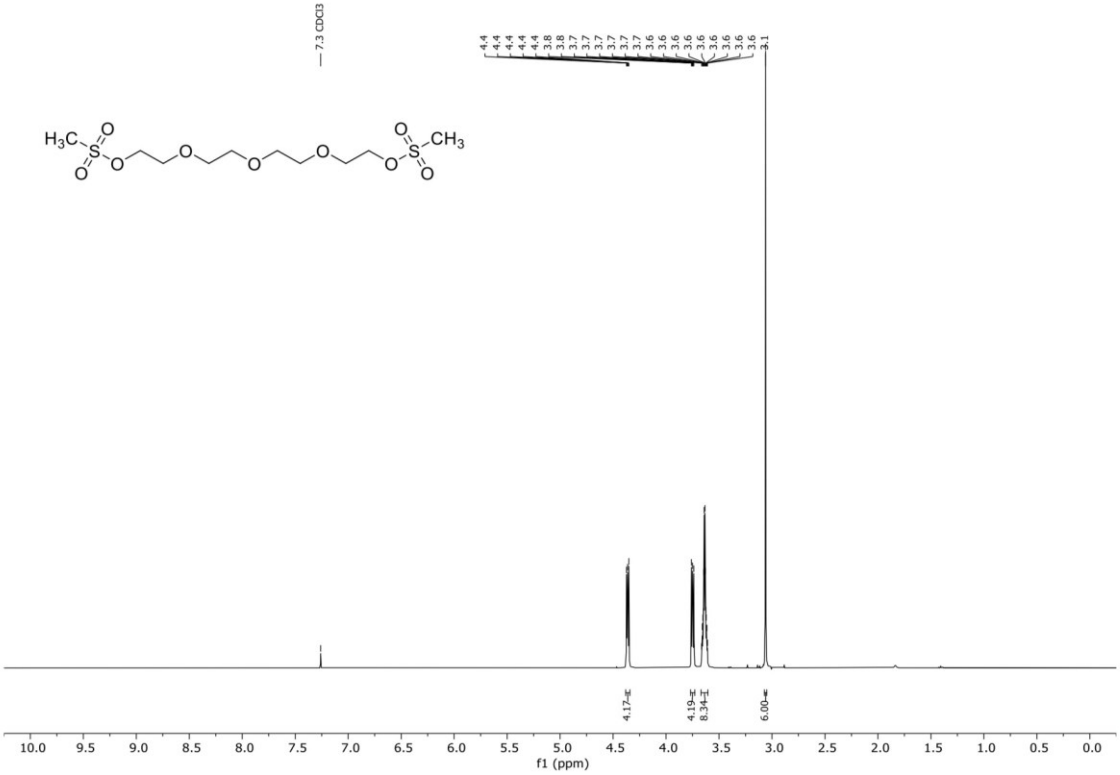

^{13}C-NMR, (101 MHz, $CDCl_3$): (**S14**)

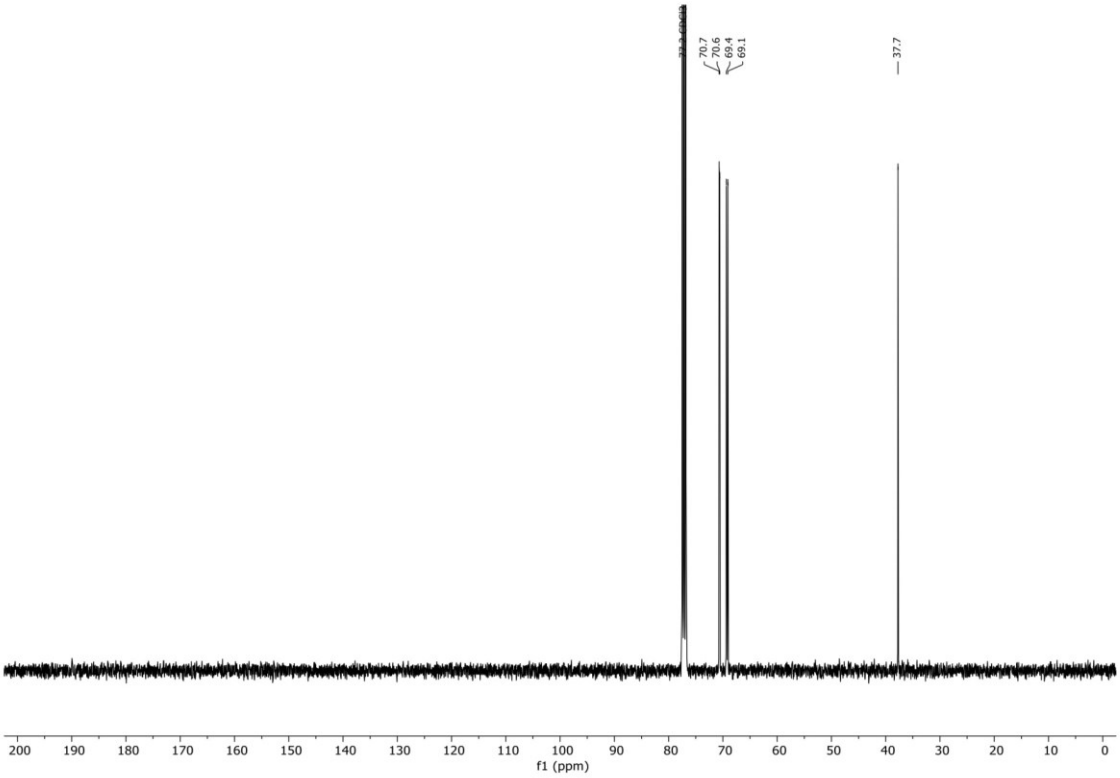

Supporting Information

^{1}H-NMR, (400 MHz, $CDCl_3$): (**5**)

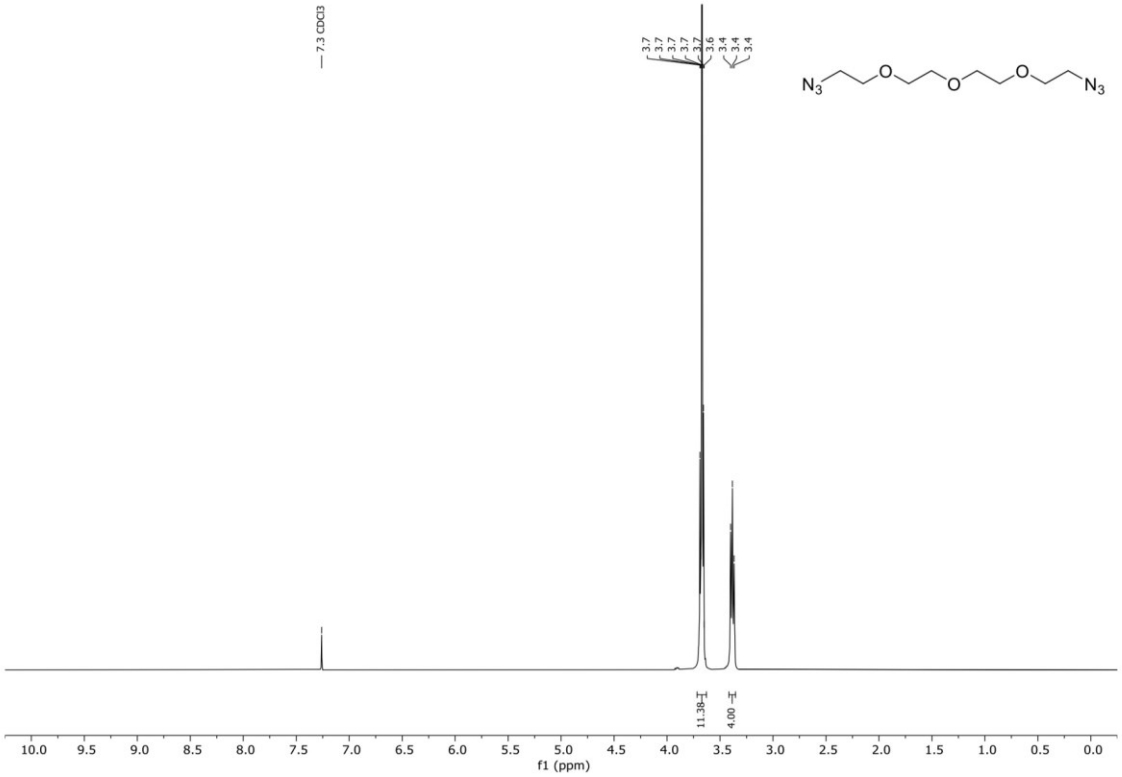

^{13}C-NMR, (101 MHz, $CDCl_3$): (**5**)

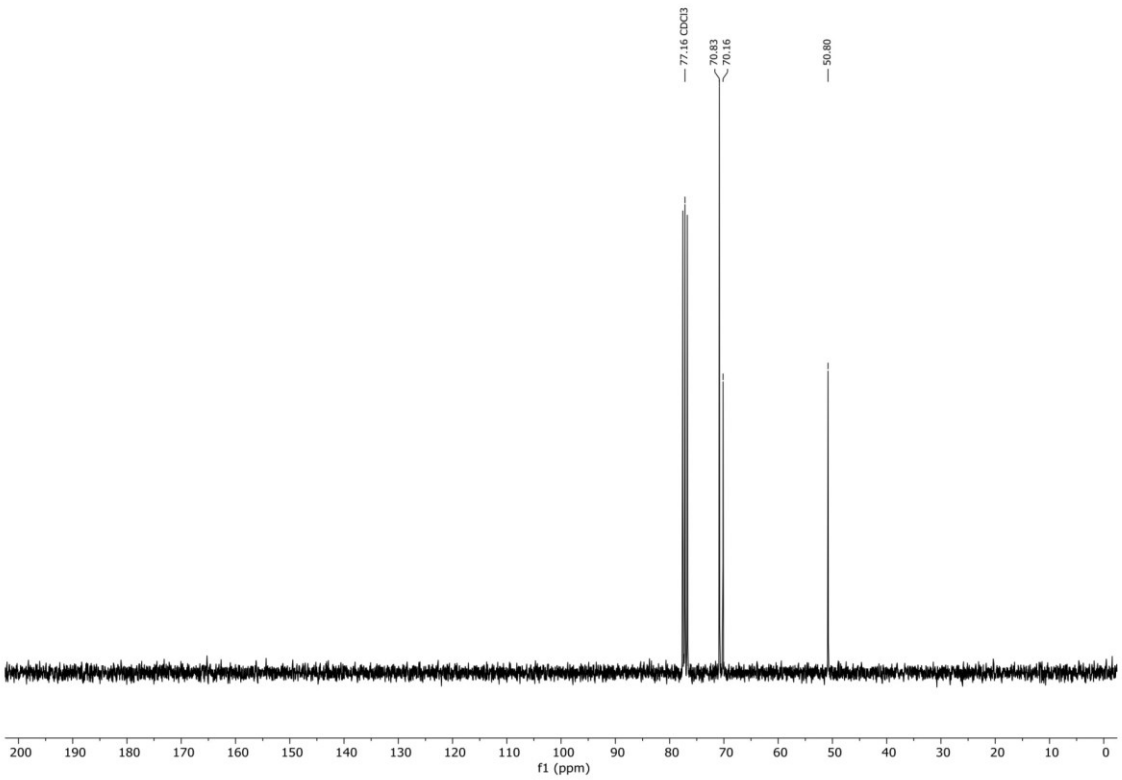

Supporting Information

^{1}H-NMR, (300 MHz, $CDCl_3$): (**4**)

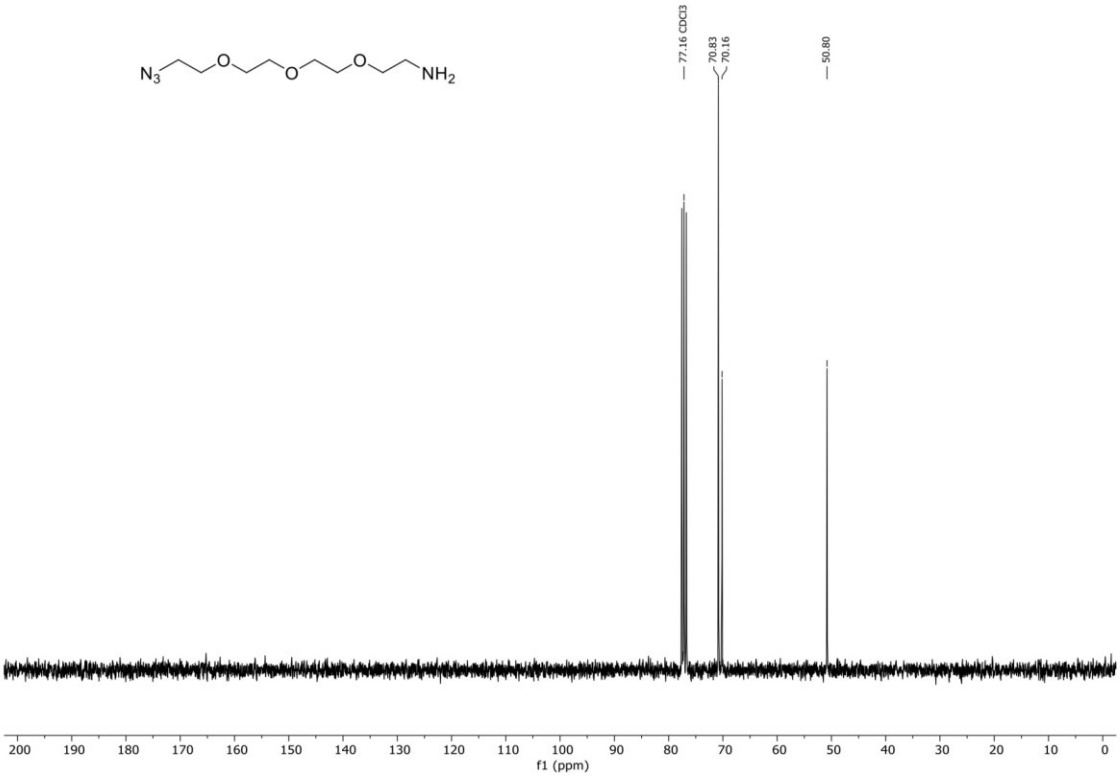

^{13}C-NMR, (75.5 MHz, $CDCl_3$): (**4**)

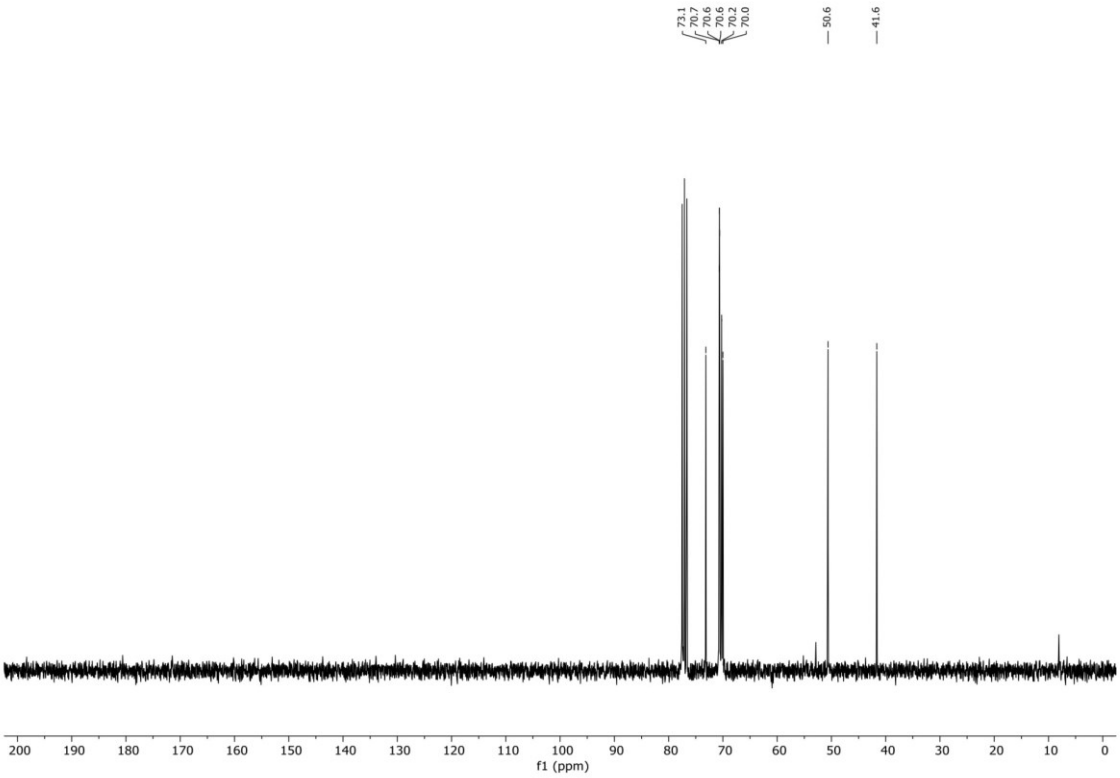

Supporting Information

^{1}H-NMR, (400 MHz, $CDCl_3$): (**S15**)

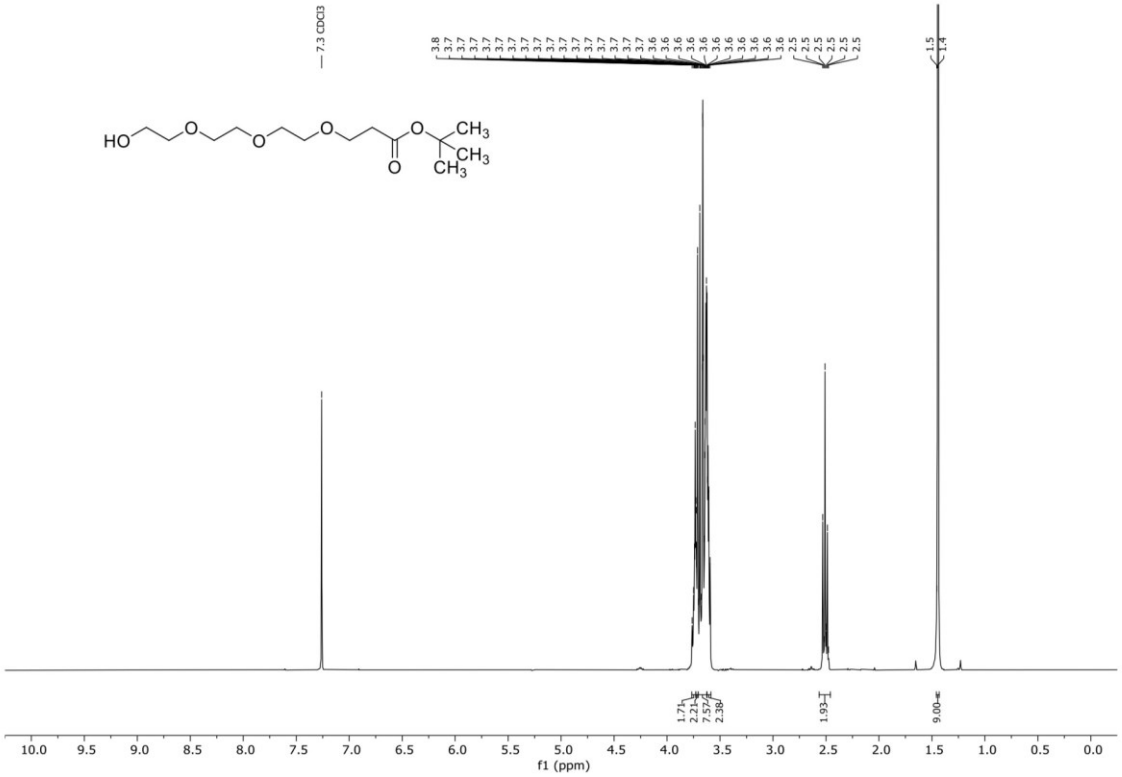

^{13}C-NMR, (101 MHz, $CDCl_3$): (**S15**)

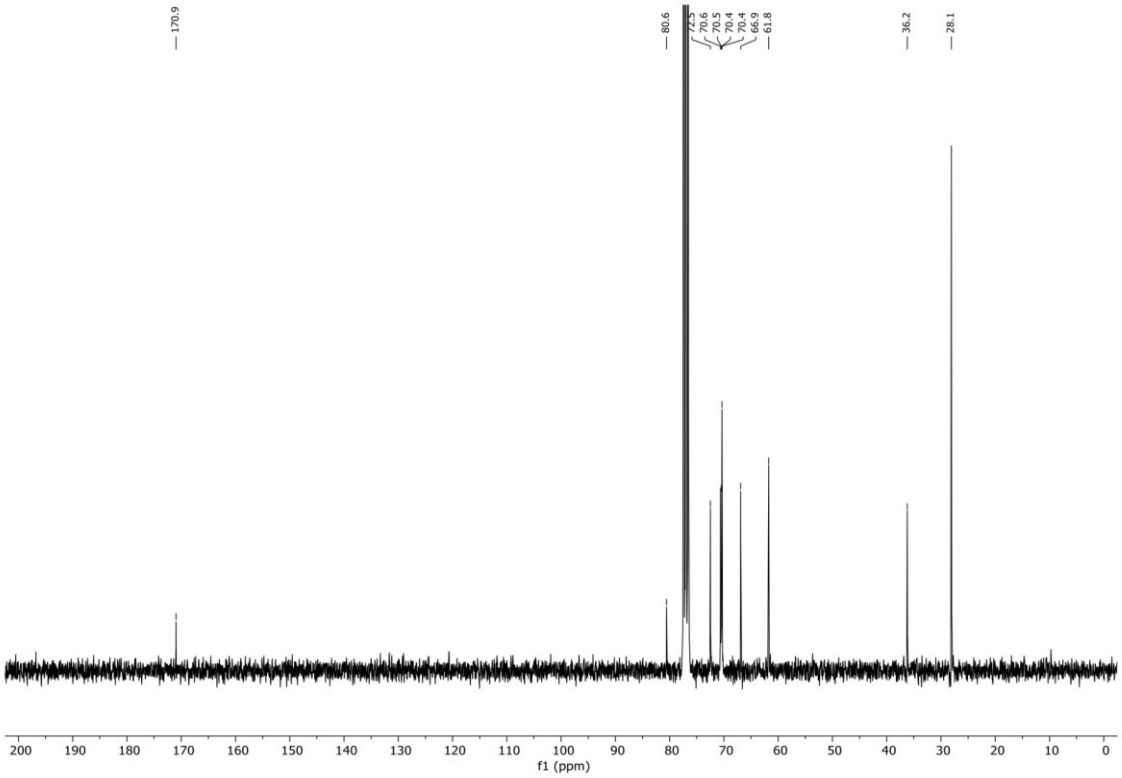

Supporting Information

^{1}H-NMR, (400 MHz, $CDCl_3$): (**S16**)

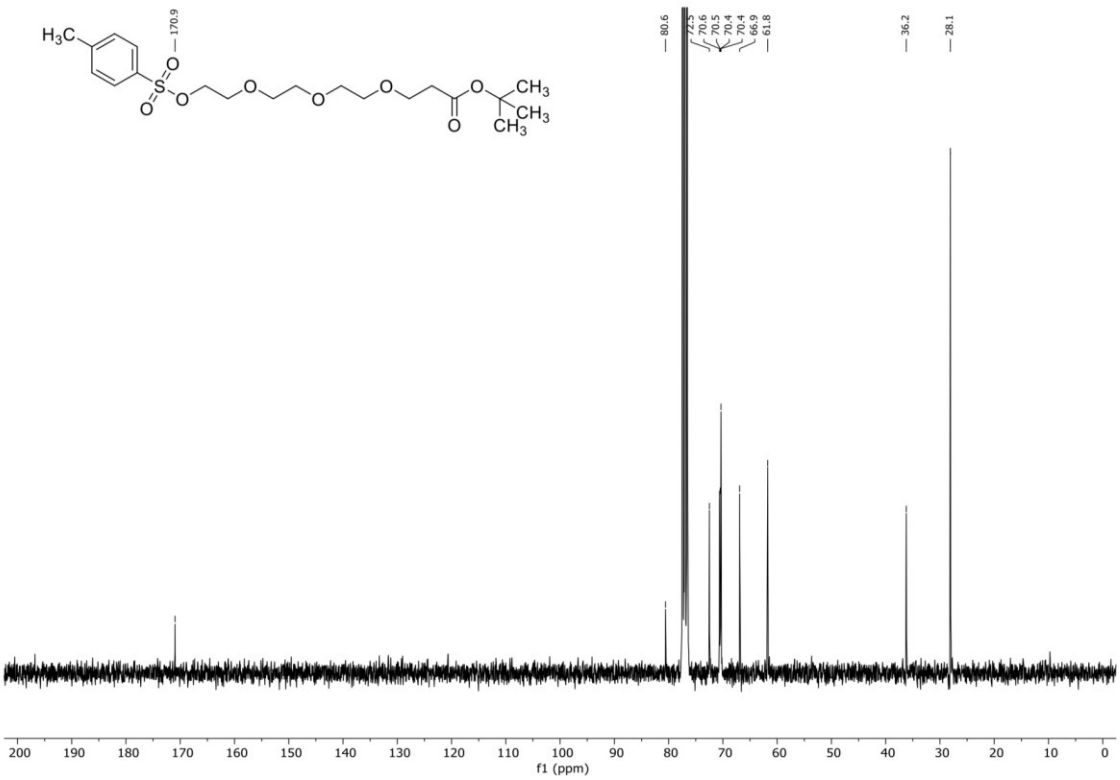

^{13}C-NMR, (101 MHz, $CDCl_3$): (**S16**)

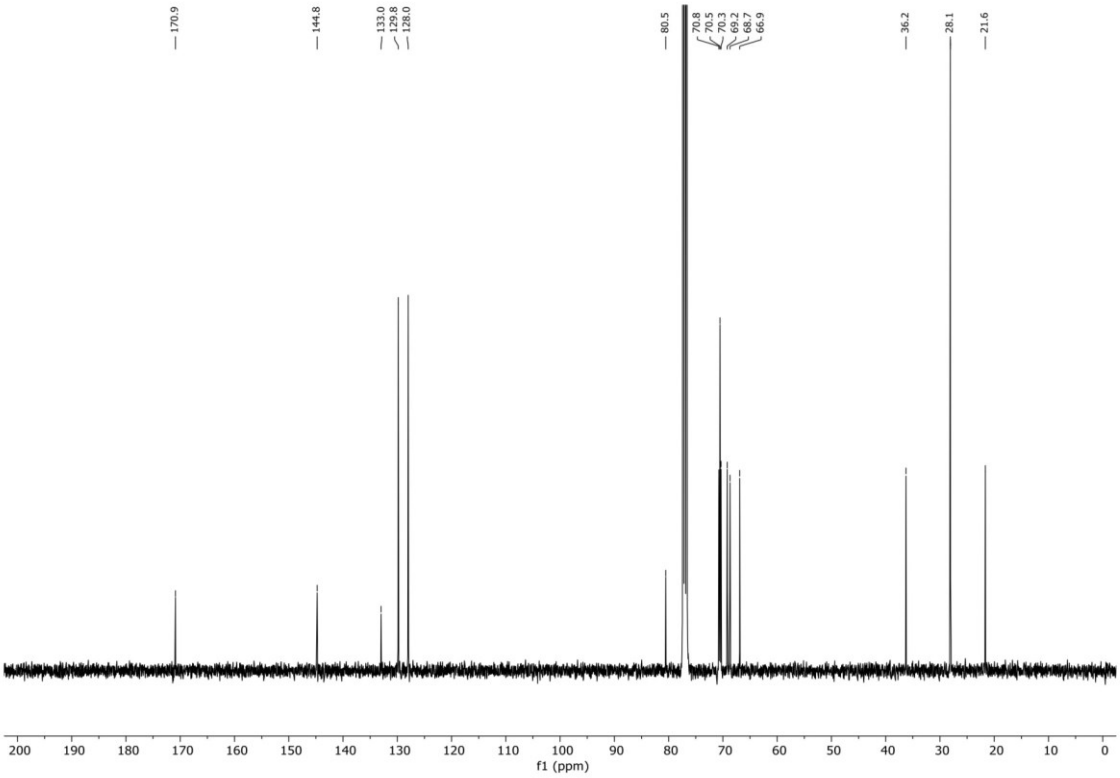

Supporting Information

^{1}H-NMR, (400 MHz, $CDCl_3$): (**S3**)

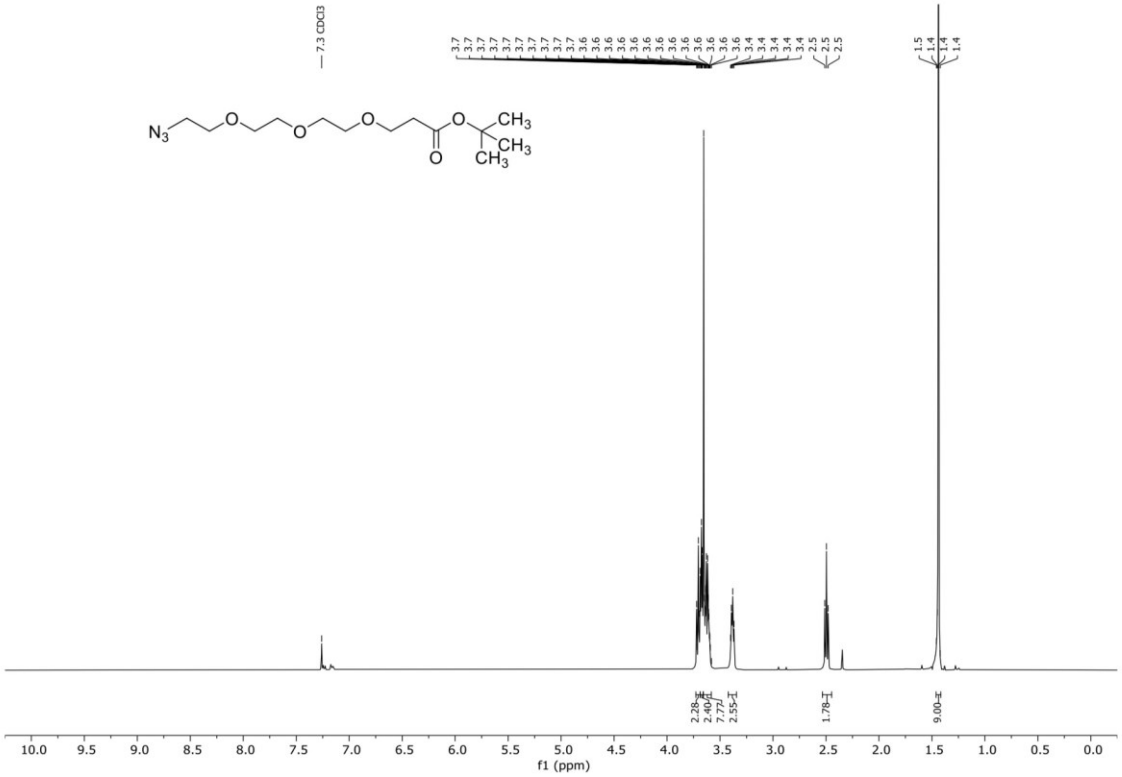

^{13}C-NMR, (101 MHz, $CDCl_3$): (**S3**)

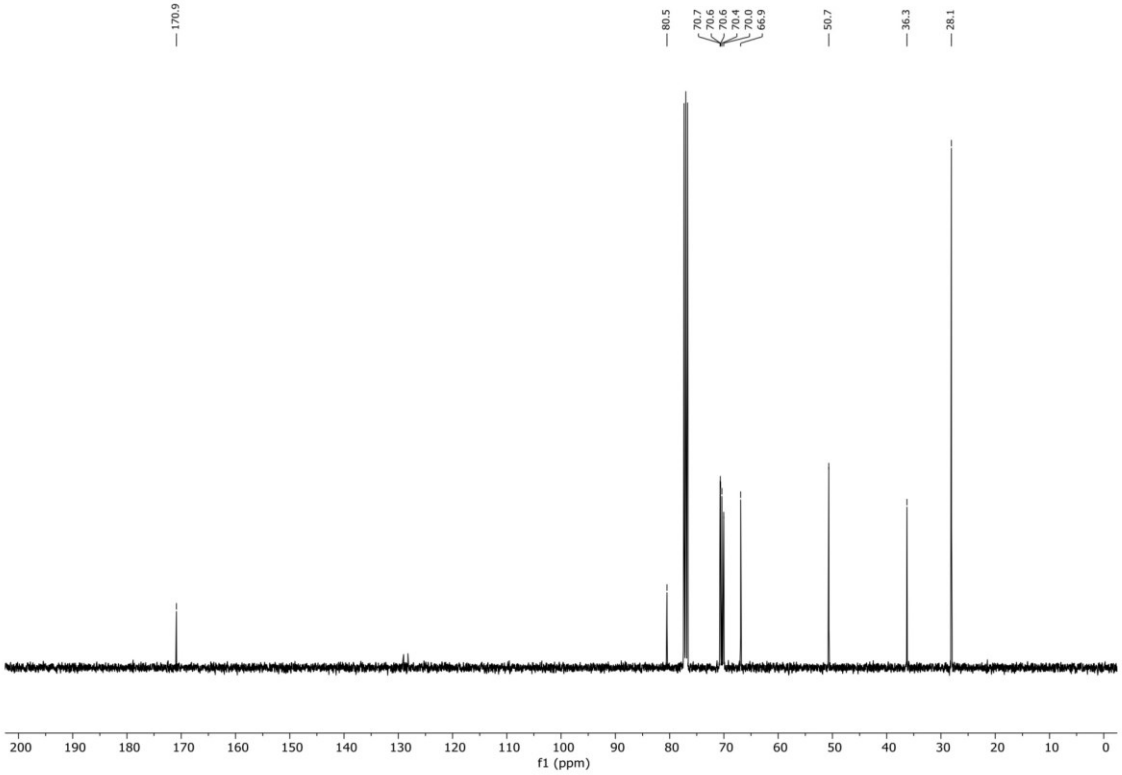

Supporting Information

^{1}H-NMR, (300 MHz, $CDCl_3$): (**3**)

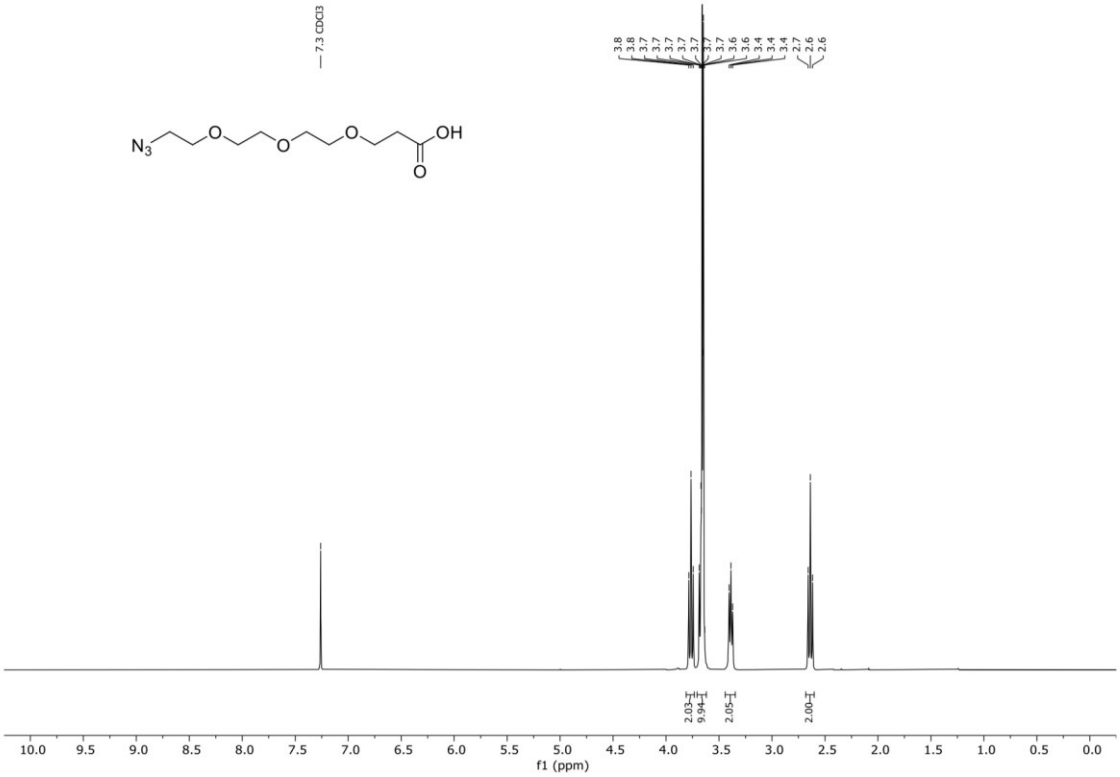

^{13}C-NMR, (75.5 MHz, $CDCl_3$): (**3**)

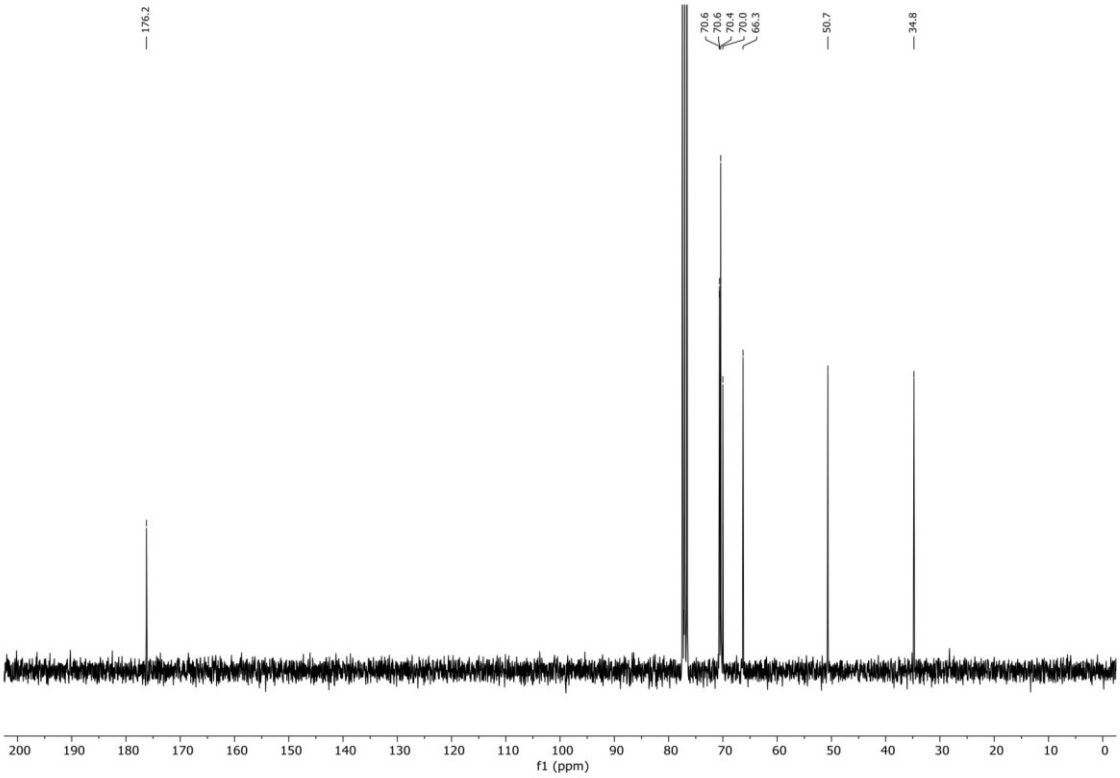

Supporting Information

^{1}H-NMR, (400 MHz, $CDCl_3$): (**S4**)

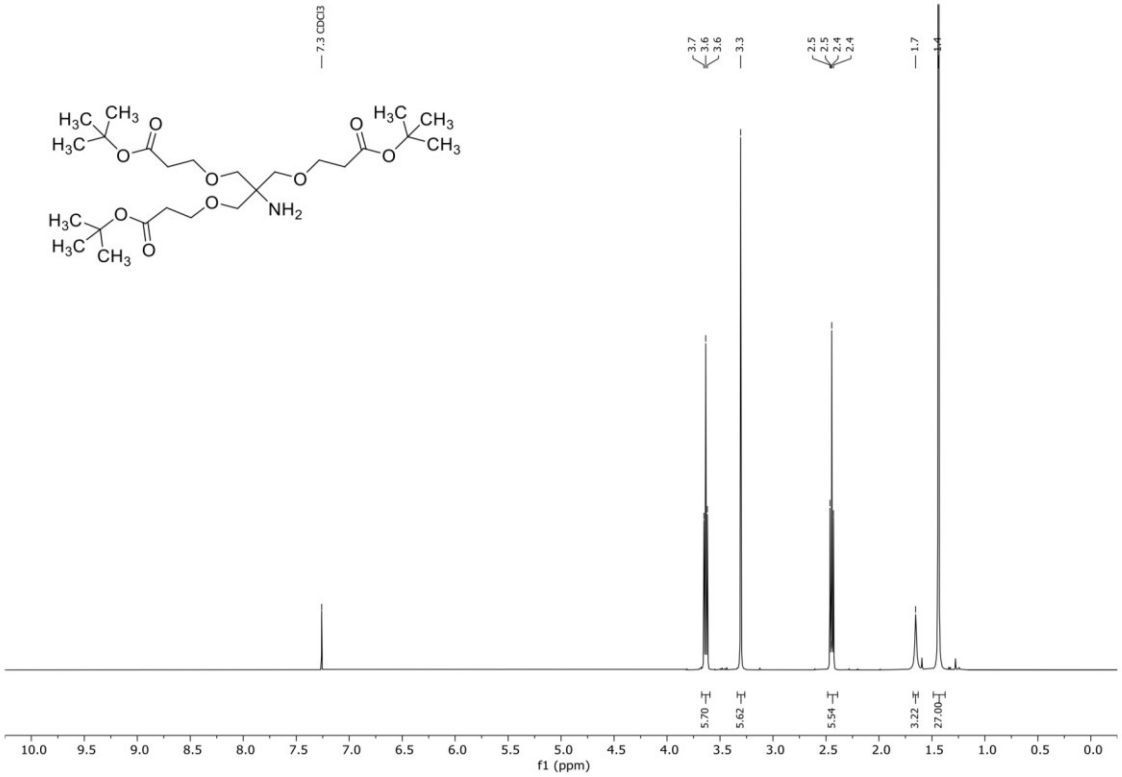

^{13}C-NMR, (101 MHz, $CDCl_3$): (**S4**)

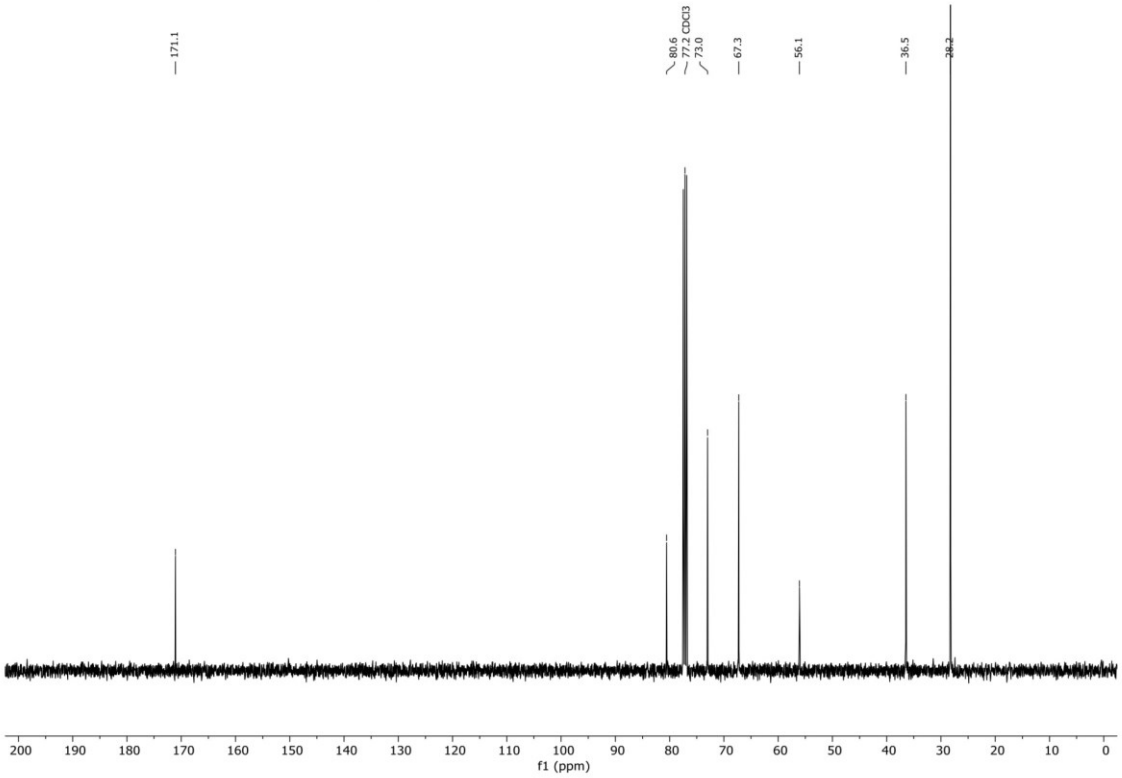

Supporting Information

^{1}H-NMR, (400 MHz, $CDCl_3$): (**I4**)

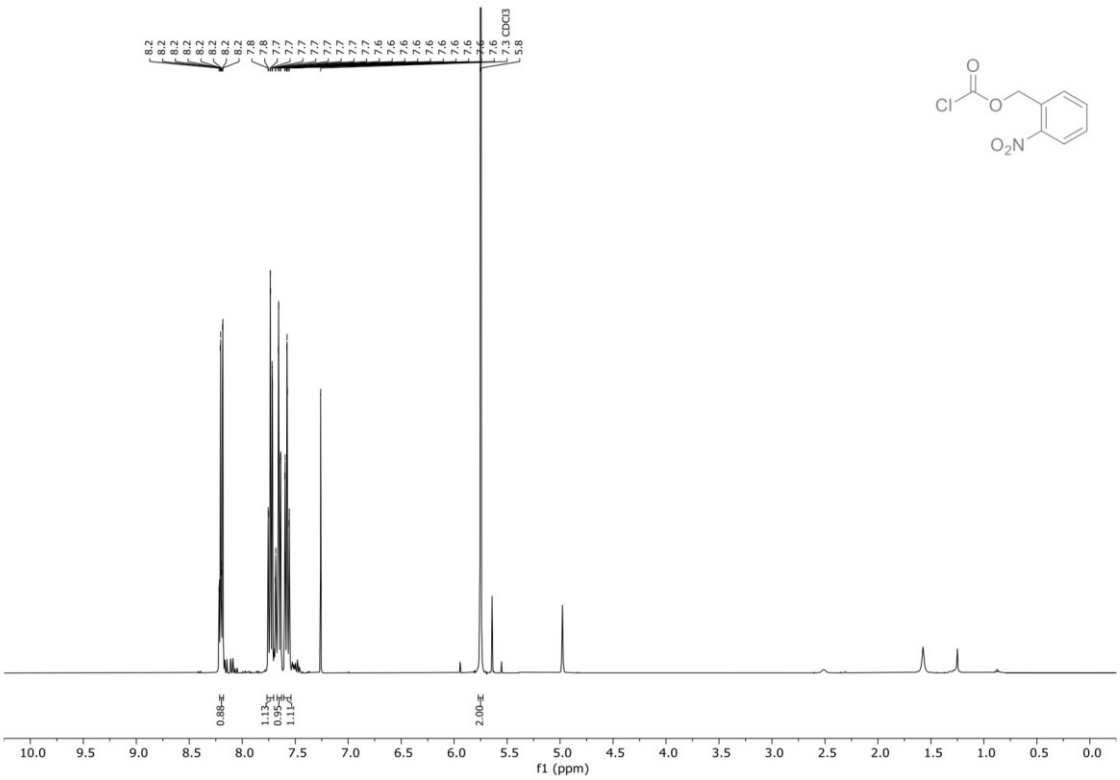

^{13}C-NMR, (101 MHz, $CDCl_3$): (**I4**)

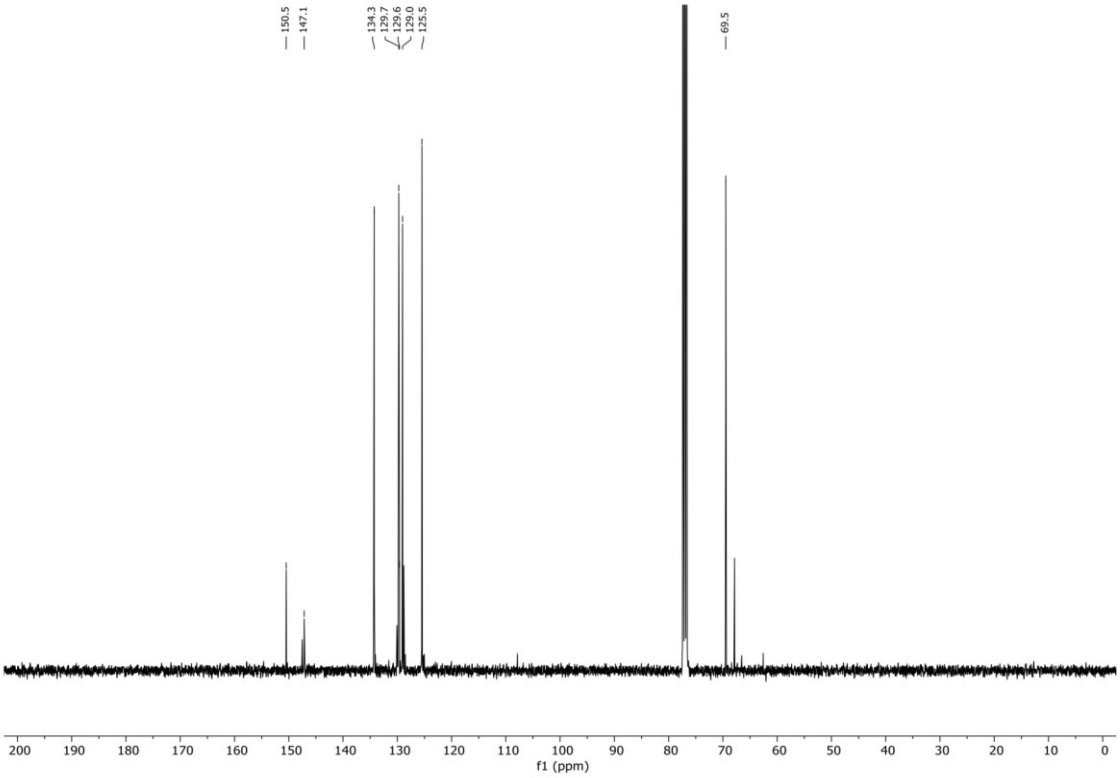

Supporting Information

^{1}H-NMR, (400 MHz, $CDCl_3$): (**S5**)

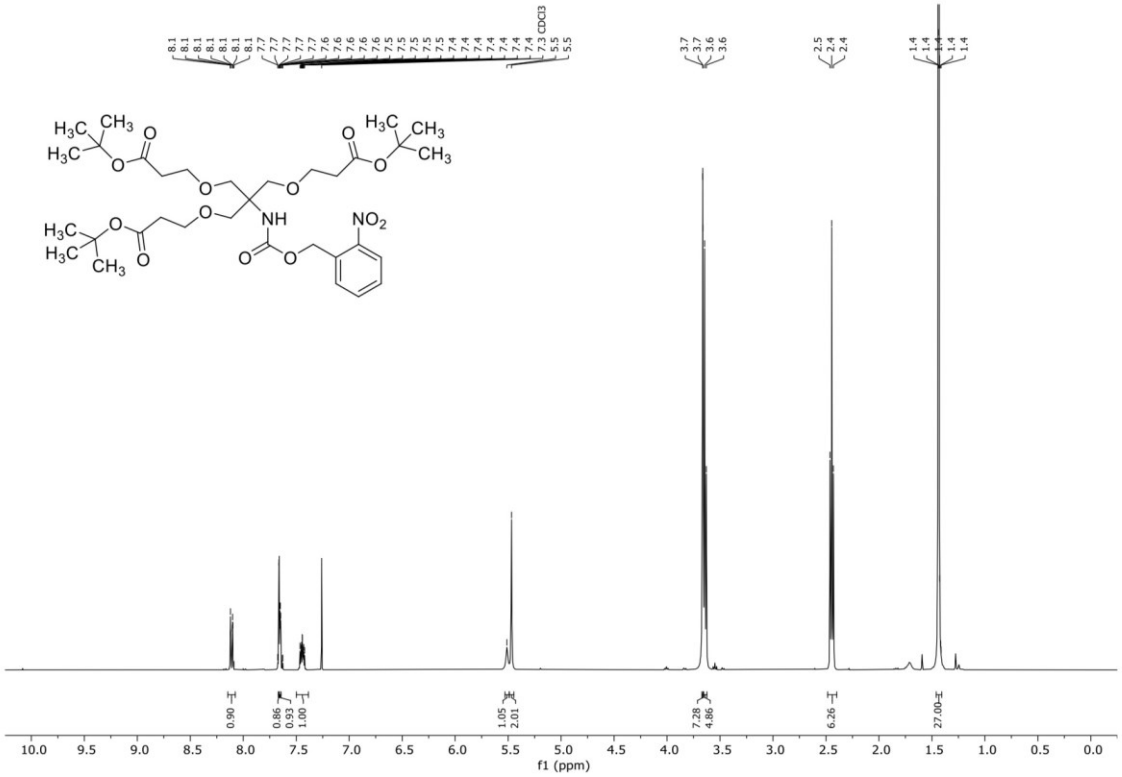

^{13}C-NMR, (101 MHz, $CDCl_3$): (**S5**)

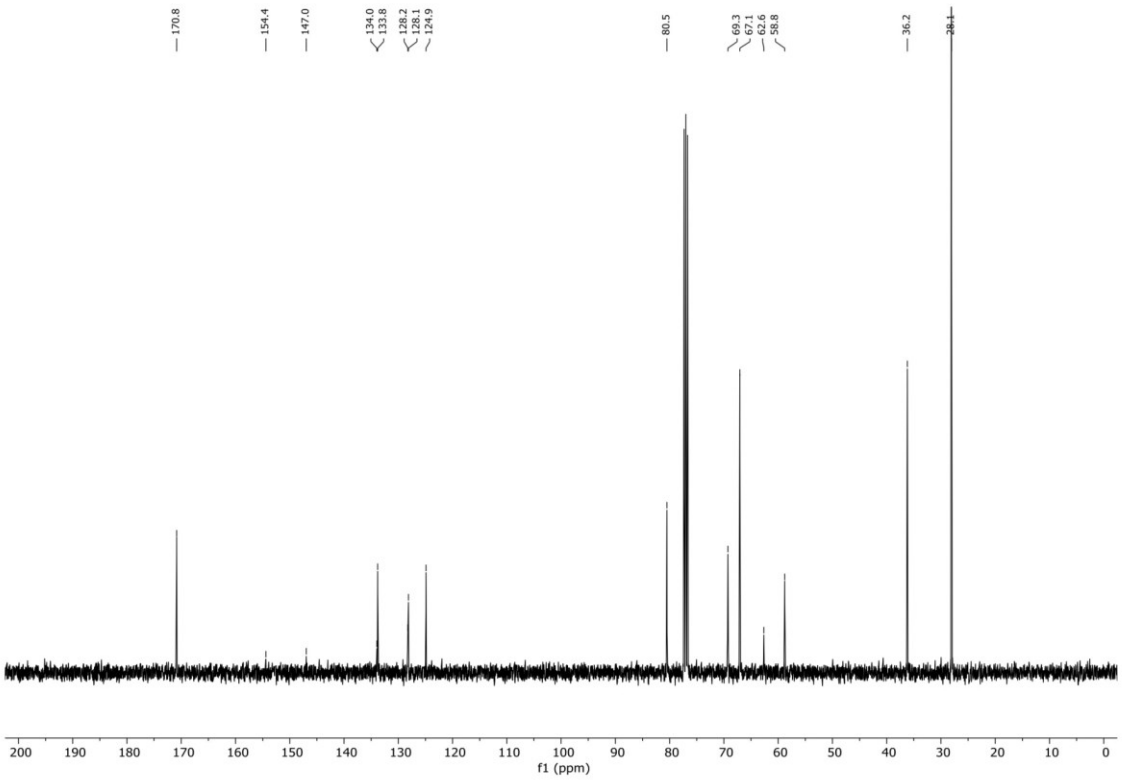

Supporting Information

^{1}H-NMR, (400 MHz, $(CD_3)_2SO$): (**S6**)

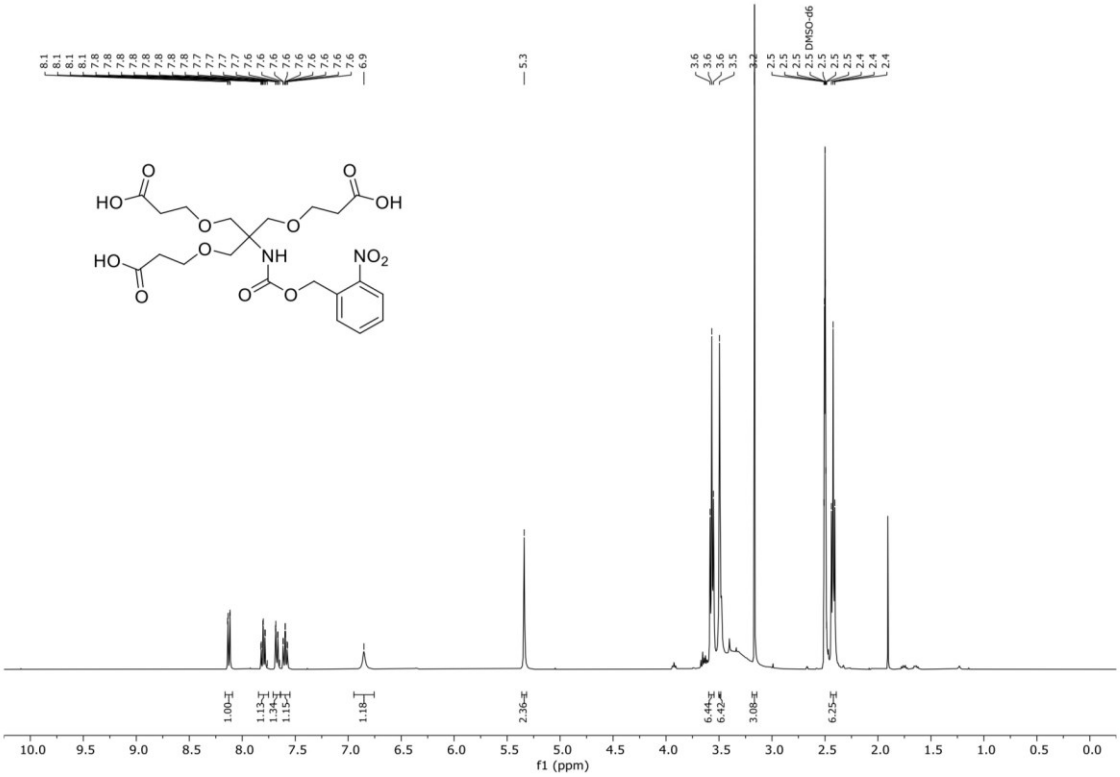

^{13}C-NMR, (101 MHz, $(CD_3)_2SO$): (**S6**)

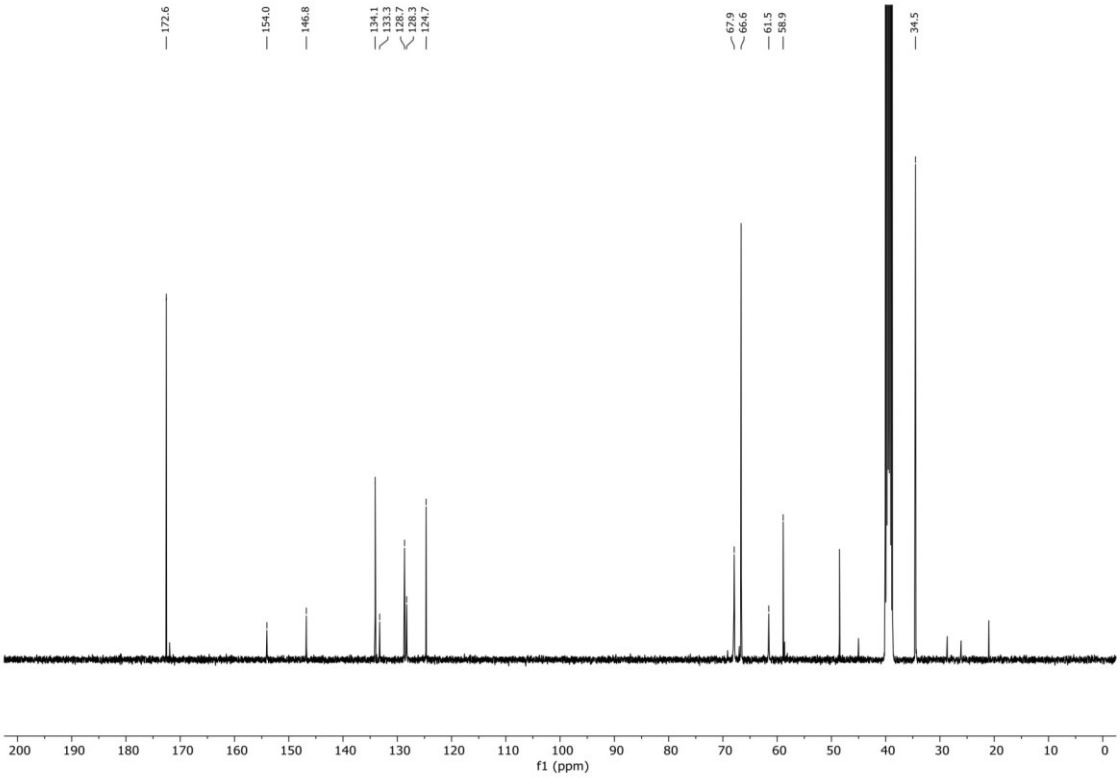

Supporting Information

^{1}H-NMR, (600 MHz, $CDCl_3$): (**6**)

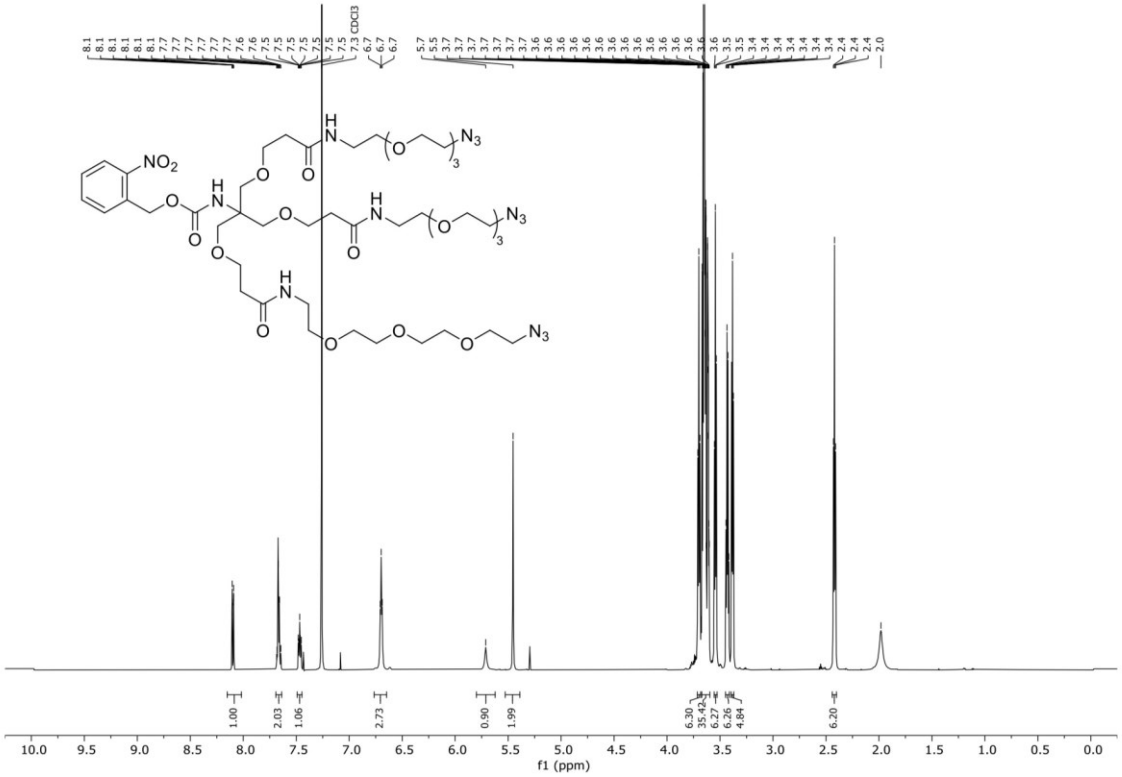

^{13}C-NMR, (151 MHz, $CDCl_3$): (**6**)

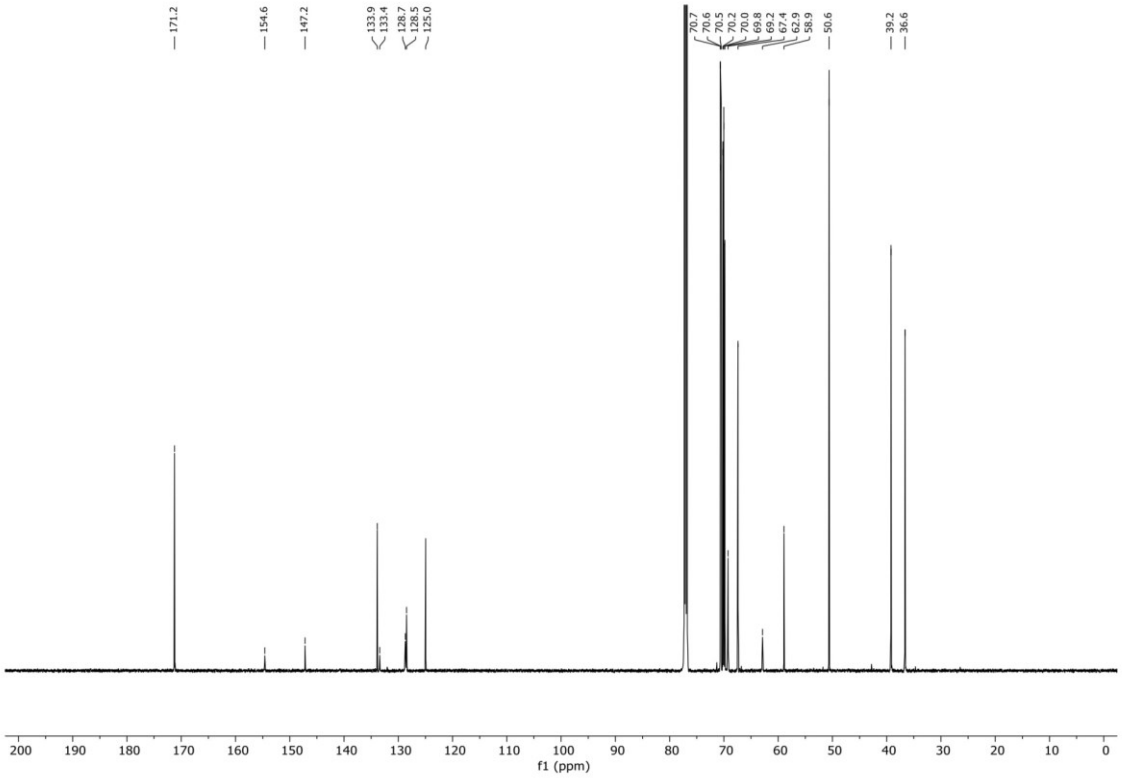

Supporting Information

^{1}H-NMR, (600 MHz, CD_3OD): (**Man_3N_3**)

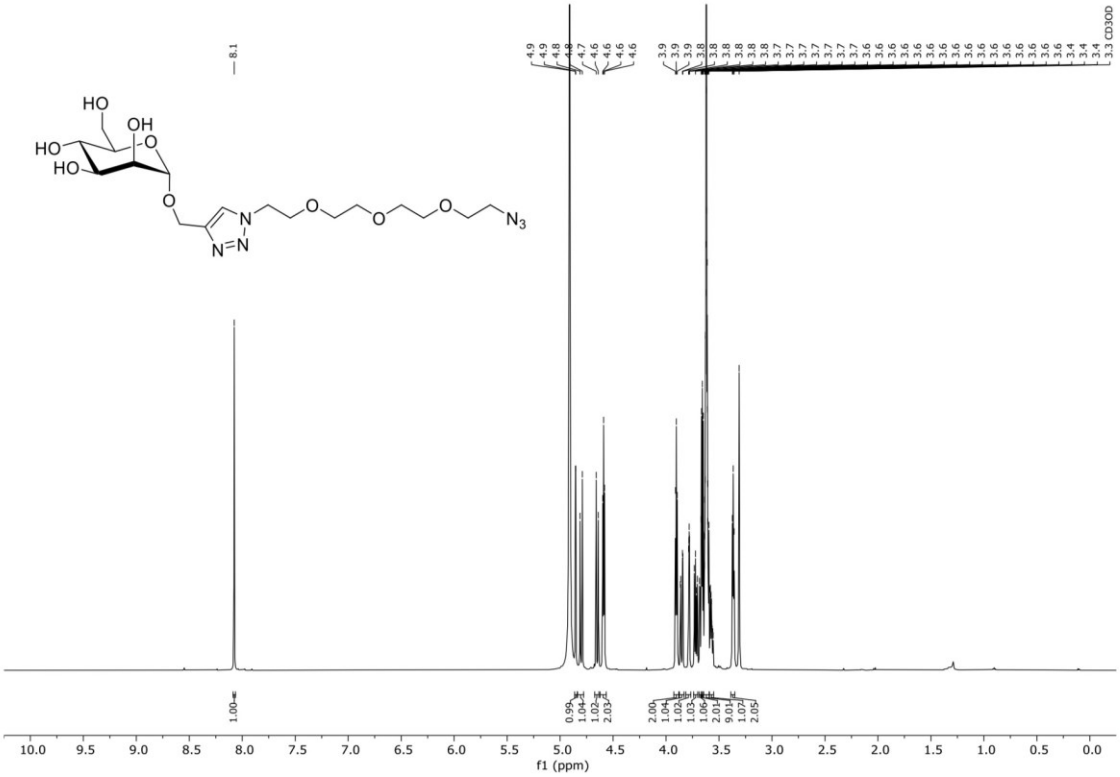

^{13}C-NMR, (151 MHz, CD_3OD): (**Man_3N_3**)

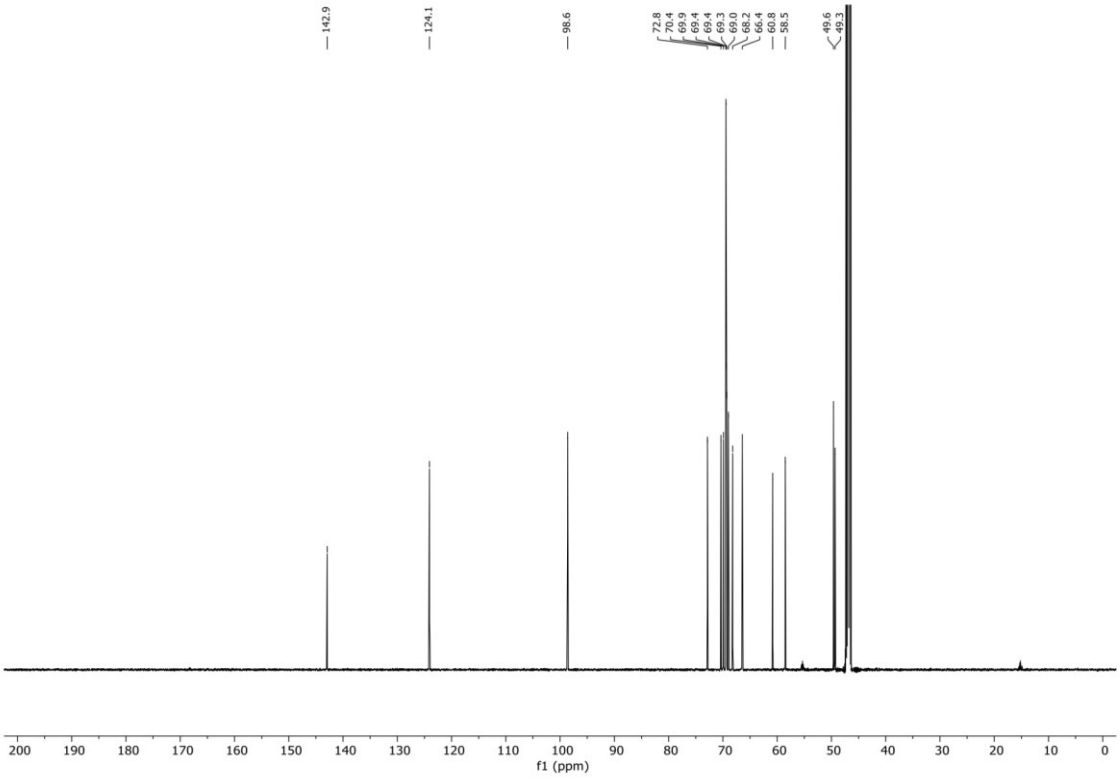

Supporting Information

^{1}H-NMR, (600 MHz, $CDCl_3$): (**S17**)

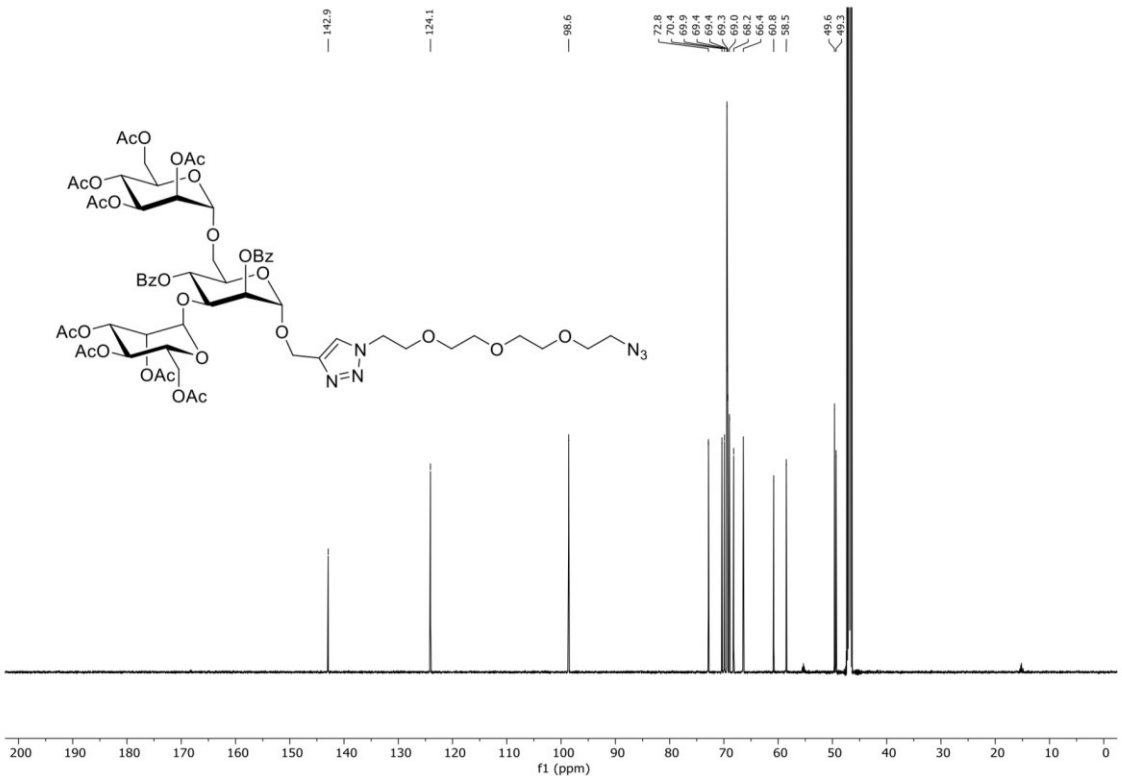

^{13}C-NMR, (151 MHz, $CDCl_3$): (**S17**)

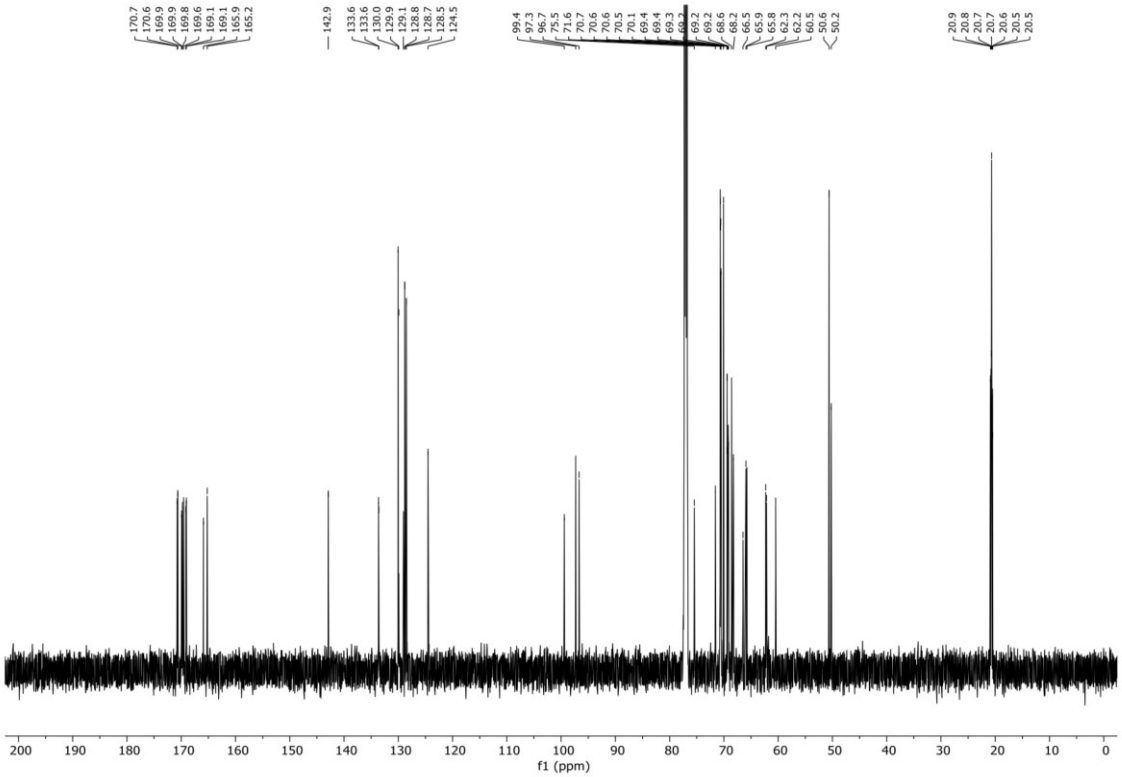

Supporting Information

^{1}H-NMR, (600 MHz, D_2O): (**Man_3N_3**)

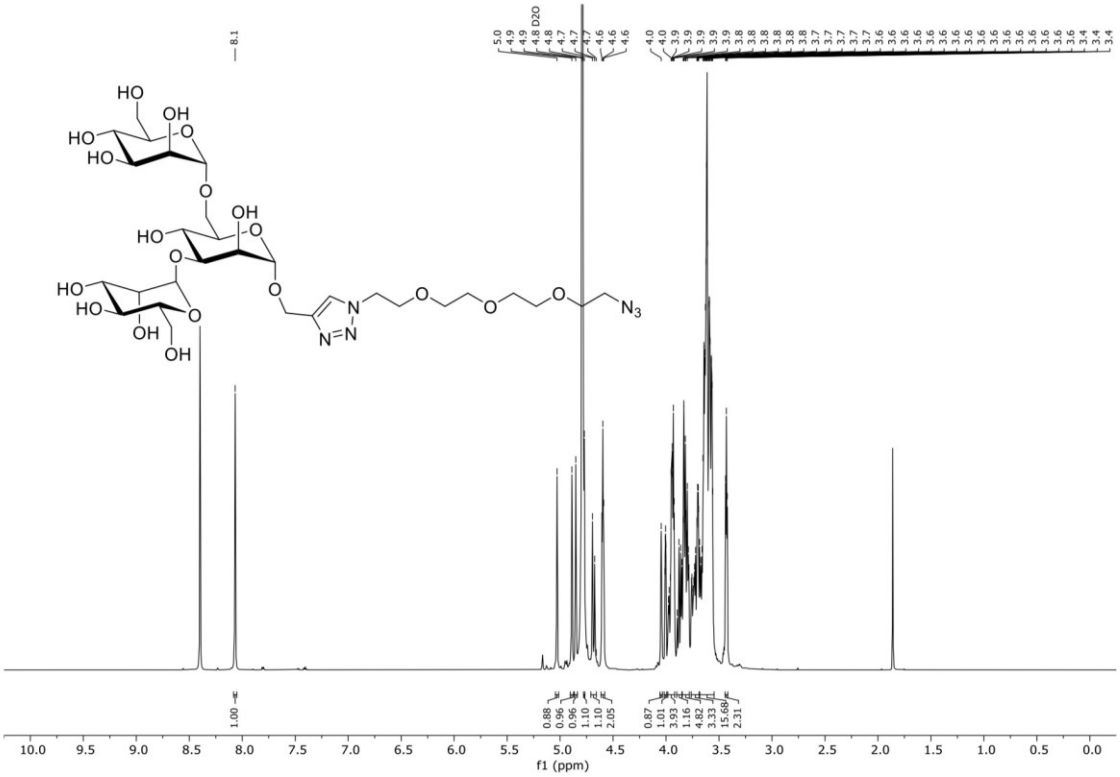

^{13}C-NMR, (151 MHz, D_2O): (**Man_3N_3**)

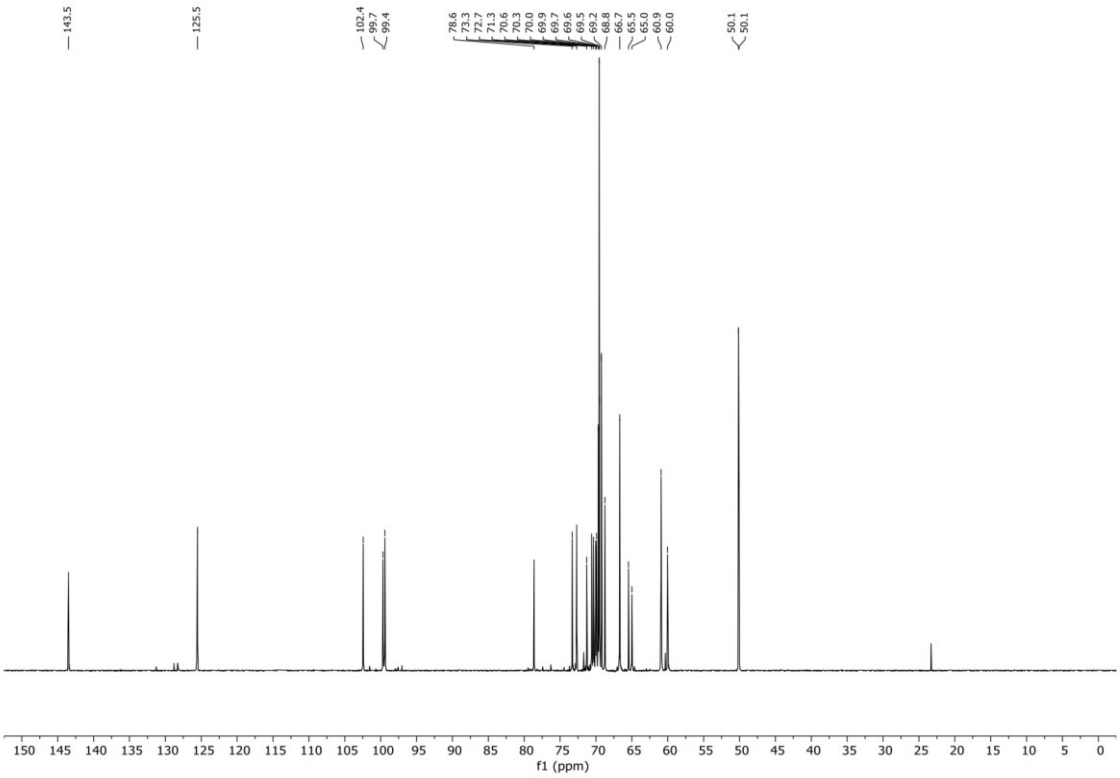

Supporting Information

^{1}H-NMR, (600 MHz, $CDCl_3$): (**S8**)

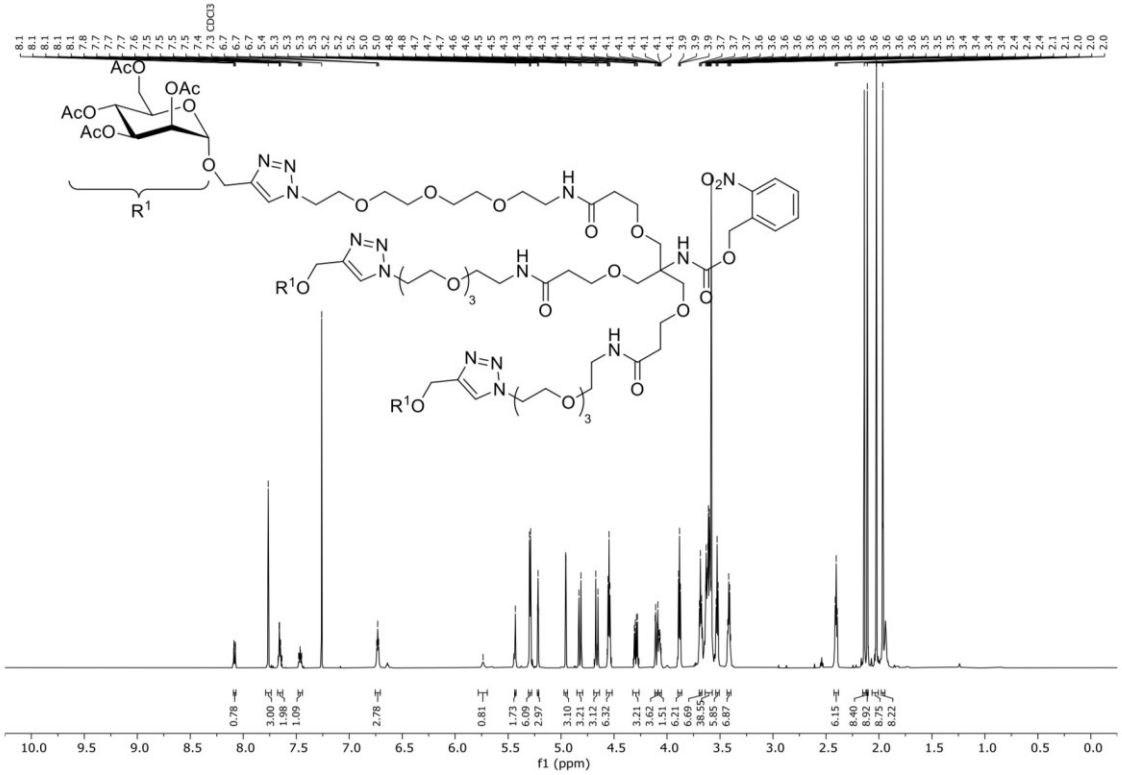

^{13}C-NMR, (151 MHz, $CDCl_3$): (**S8**)

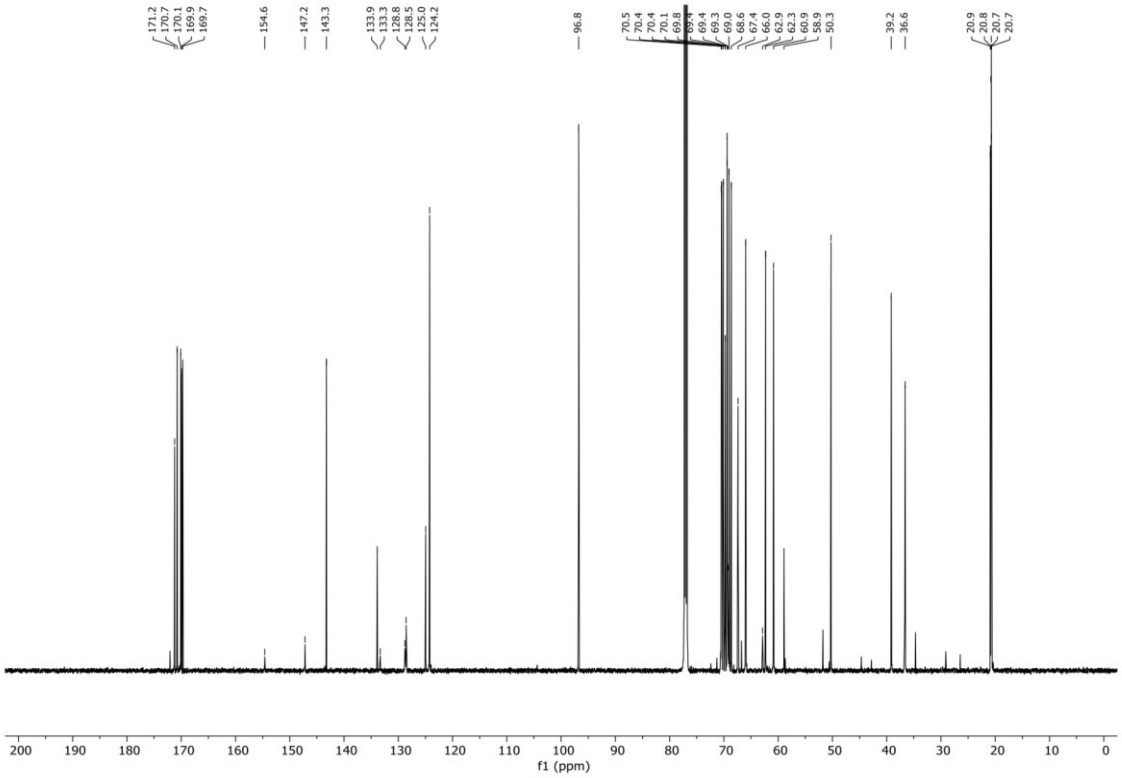

Supporting Information

^{1}H-NMR, (600 MHz, $CDCl_3$): (**S10**)

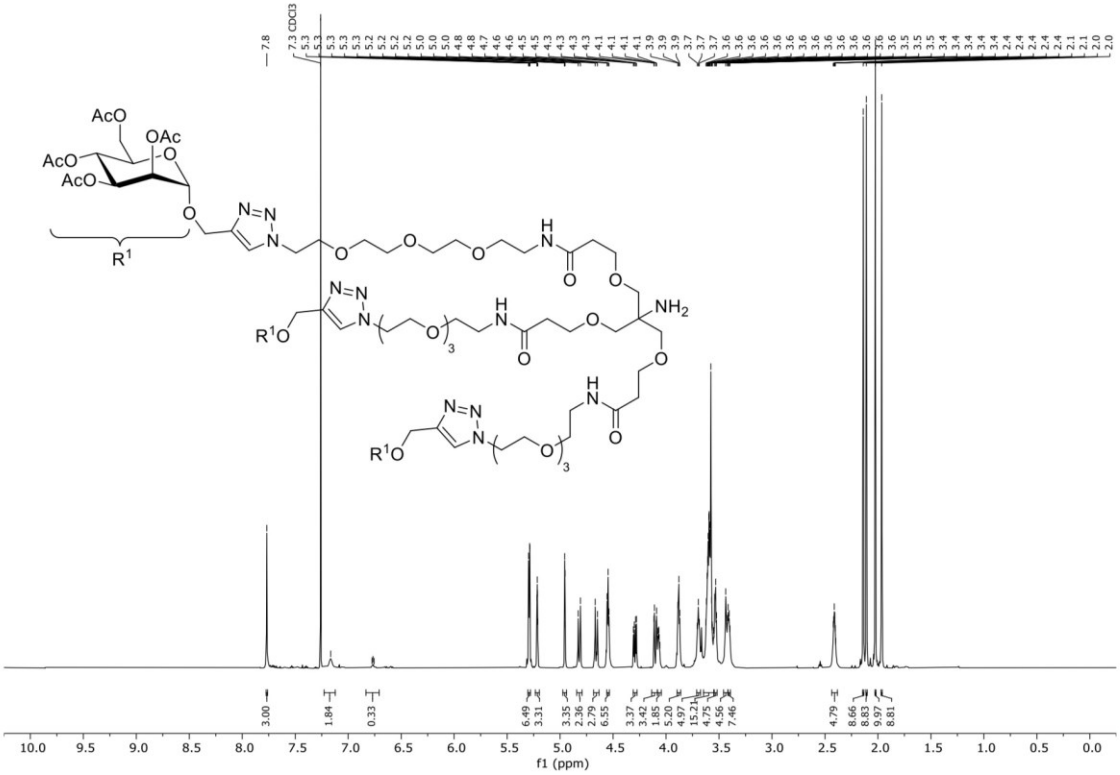

^{13}C-NMR, (151 MHz, $CDCl_3$): (**S10**)

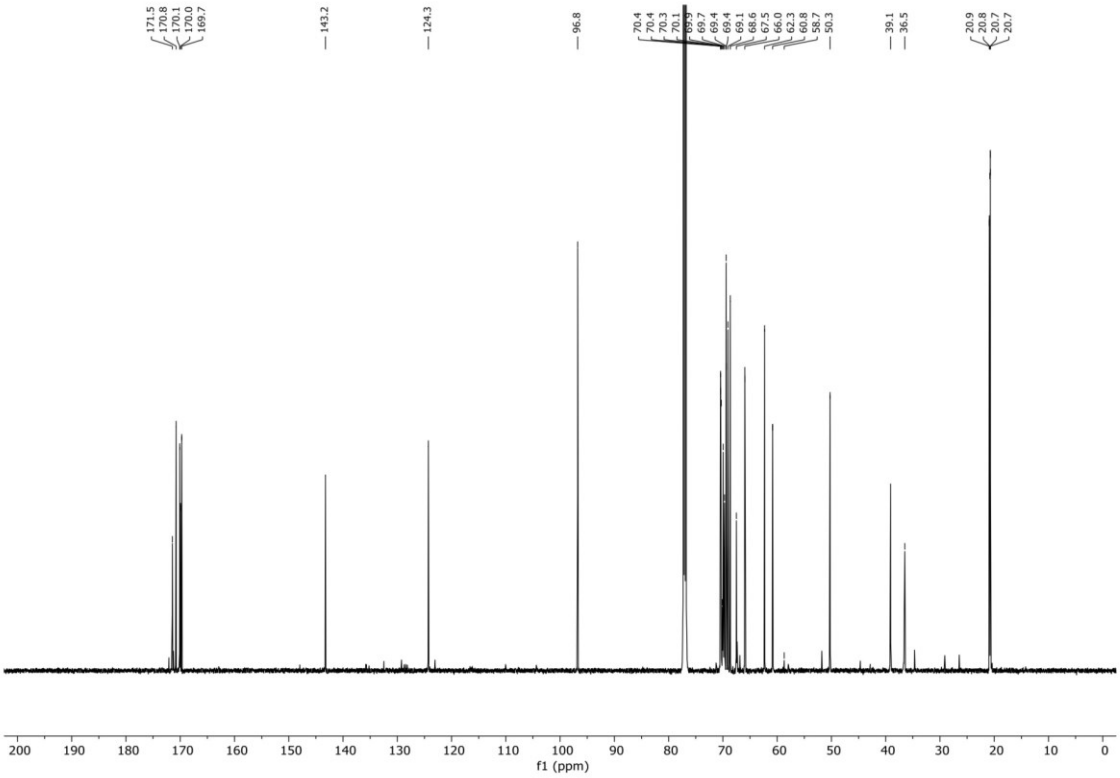

Supporting Information

^{1}H-NMR, (600 MHz, $CDCl_3$): (**S12**)

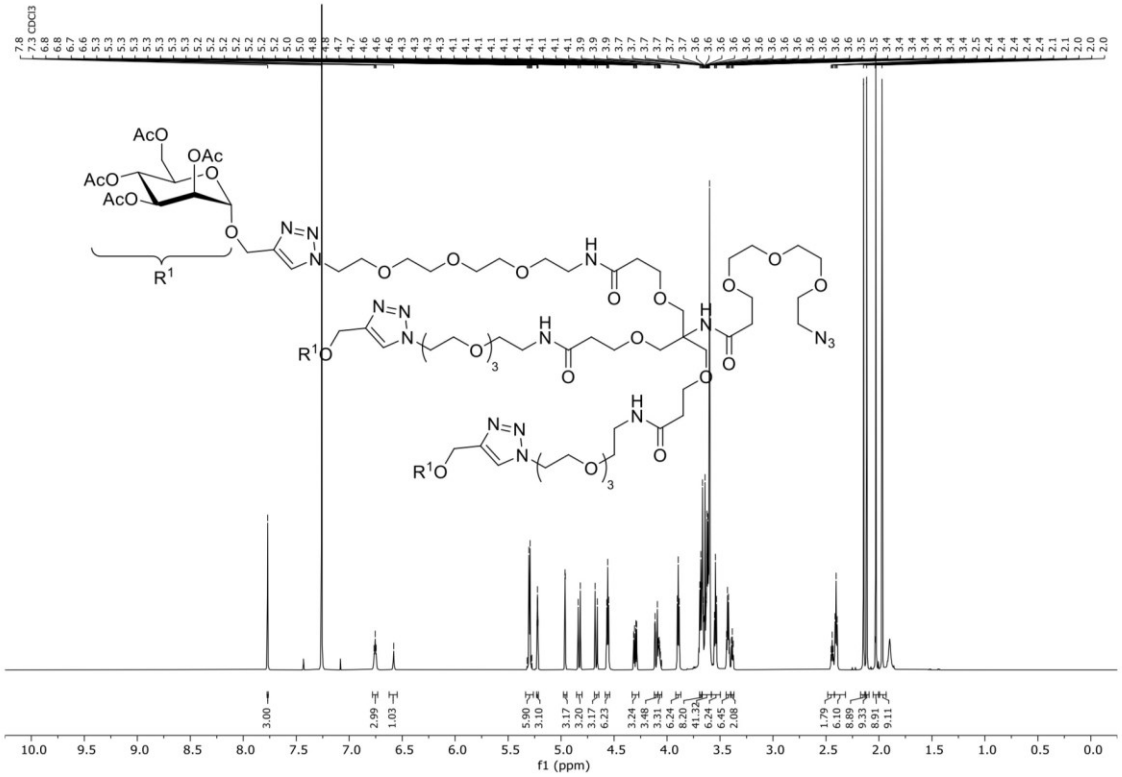

^{13}C-NMR, (151 MHz, $CDCl_3$): (**S12**)

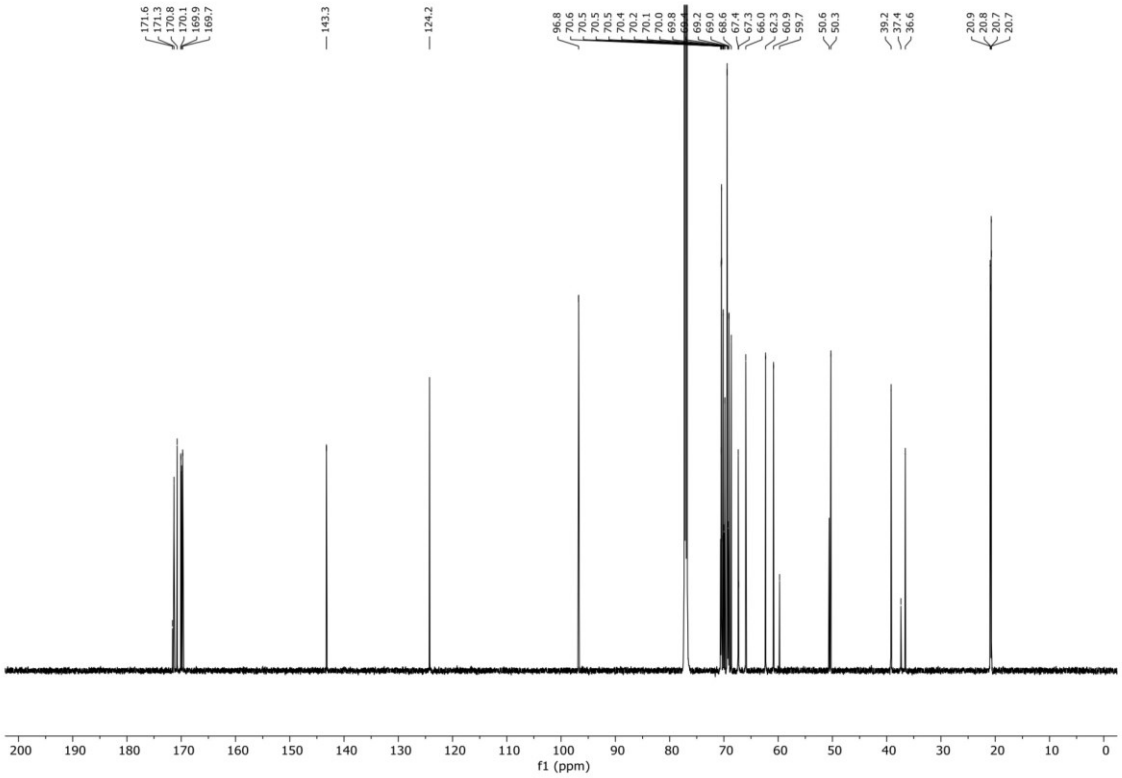

Supporting Information

^{1}H-NMR, (600 MHz, D_2O): **$(Man)_3N_3$**

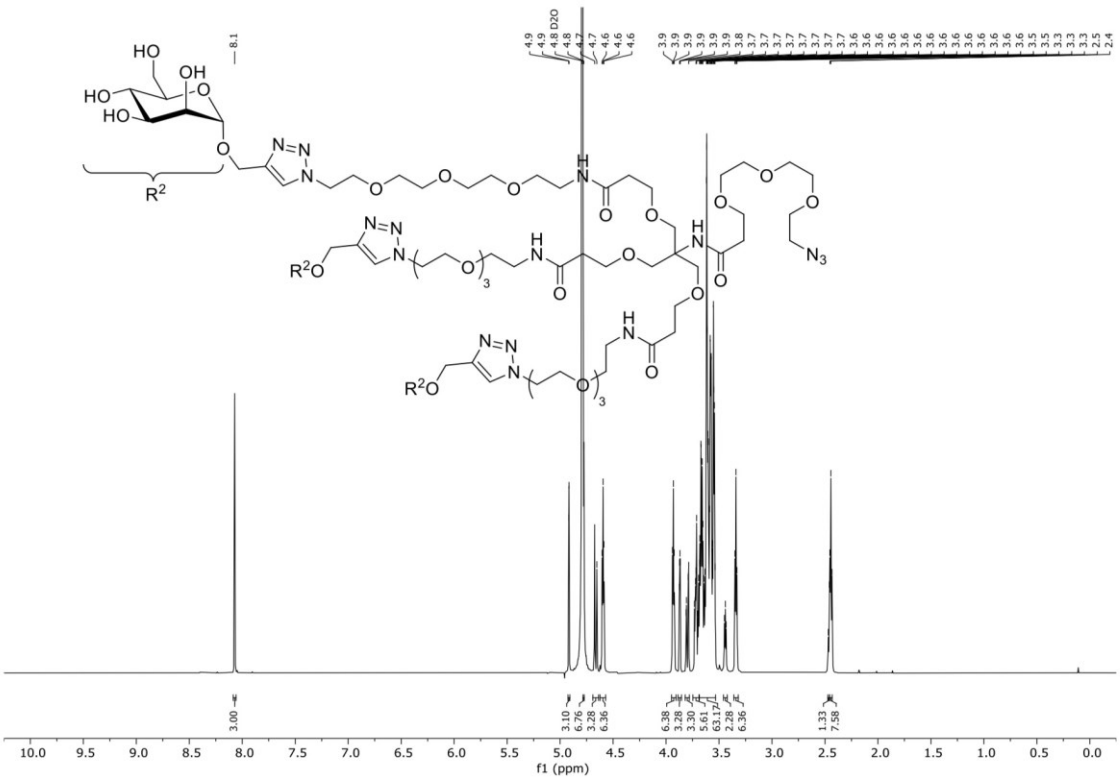

^{13}C-NMR, (151 MHz, $CDCl_3$): **$(Man)_3N_3$**

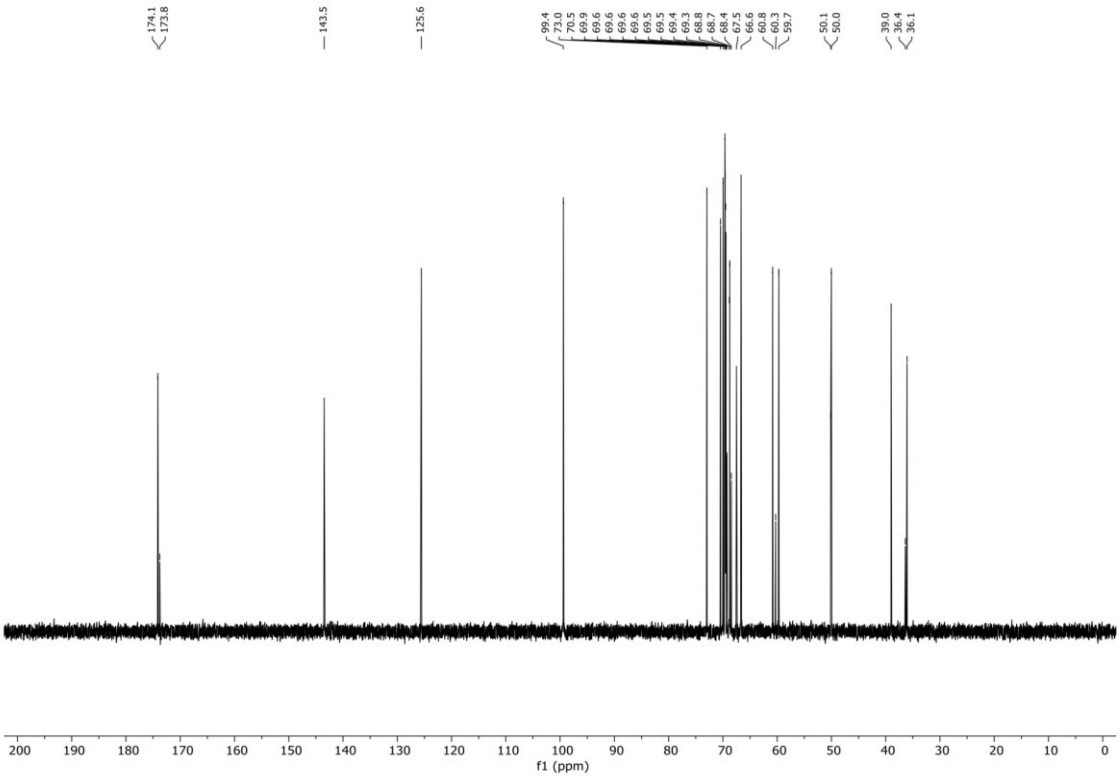

Supporting Information

^{1}H-NMR, (600 MHz, $CDCl_3$): (**S9**)

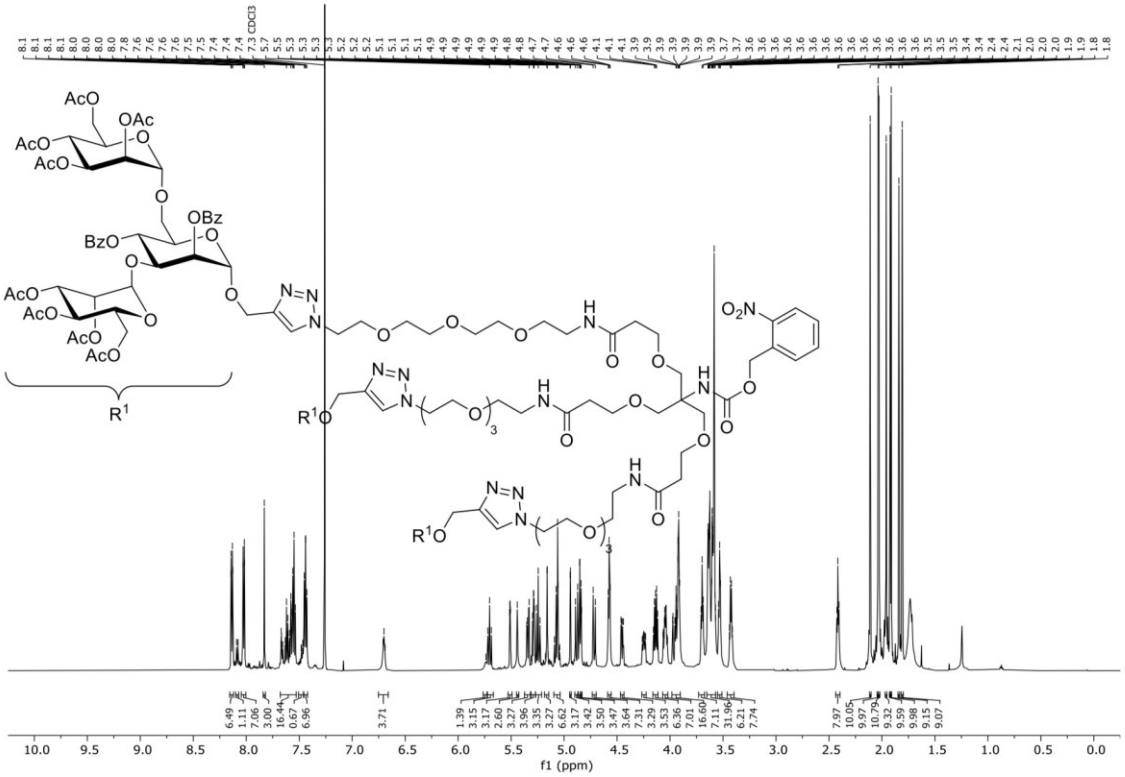

^{13}C-NMR, (151 MHz, $CDCl_3$): (**S9**)

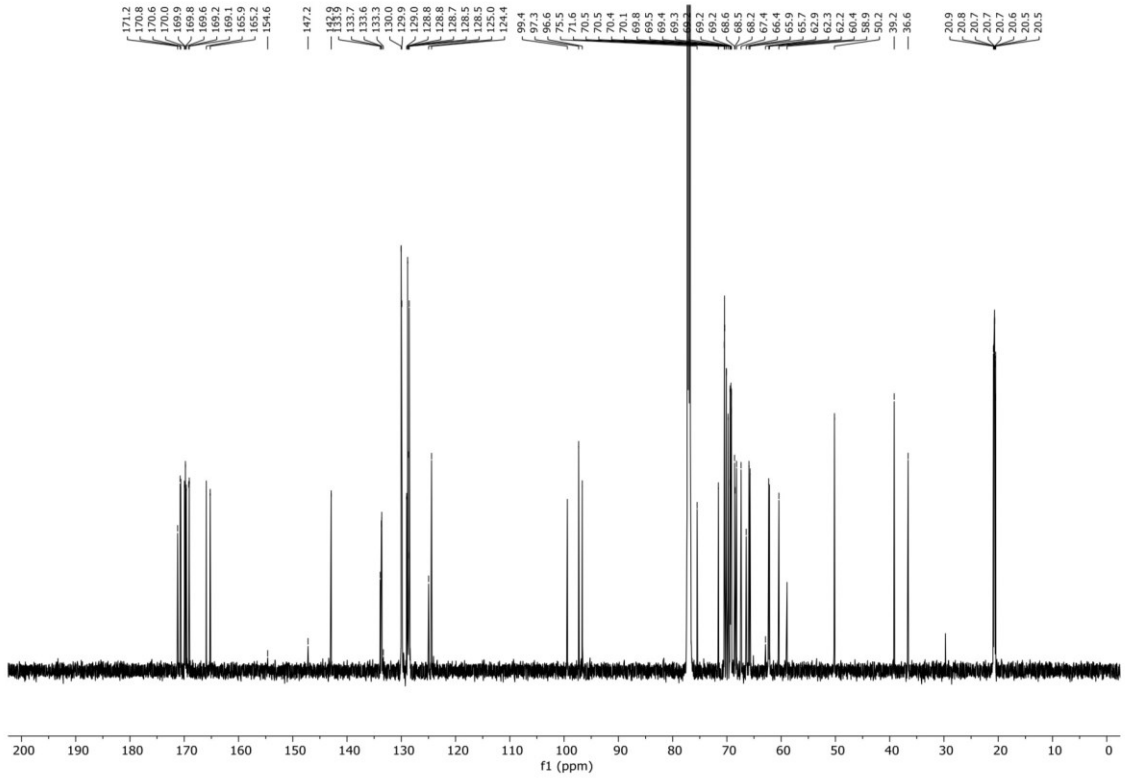

Supporting Information

^{1}H-NMR, (600 MHz, $CDCl_3$): (**S11**)

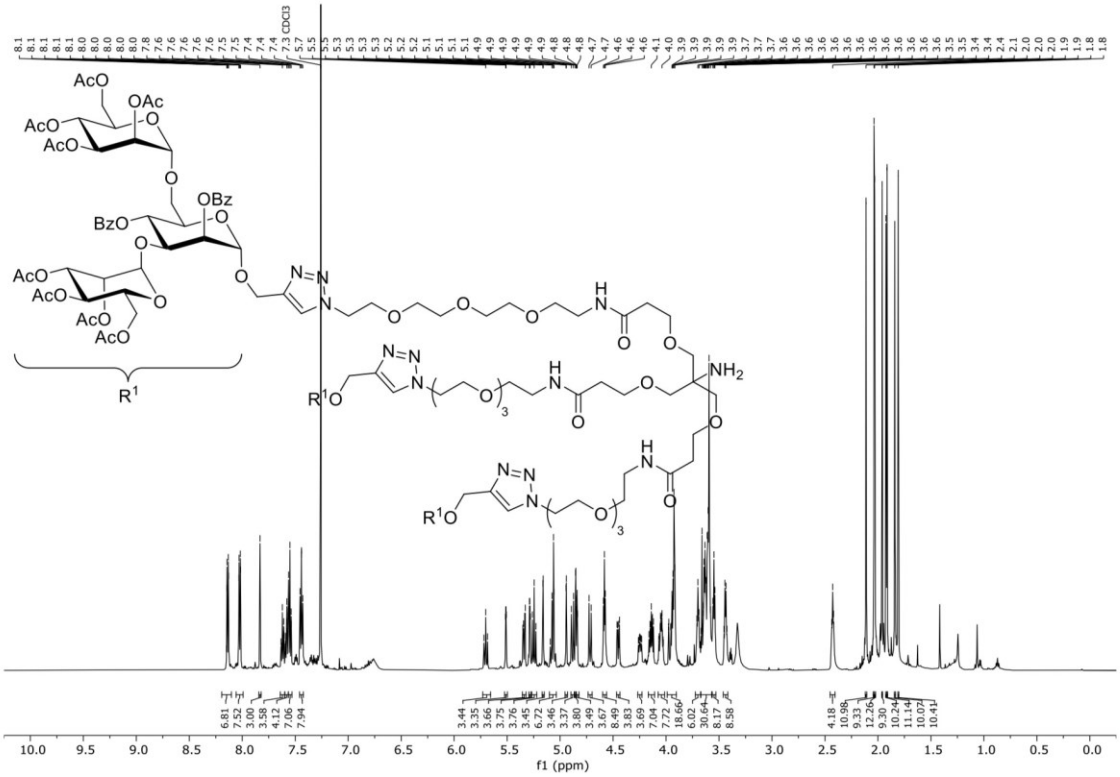

^{13}C-NMR, (151 MHz, $CDCl_3$): (**S11**)

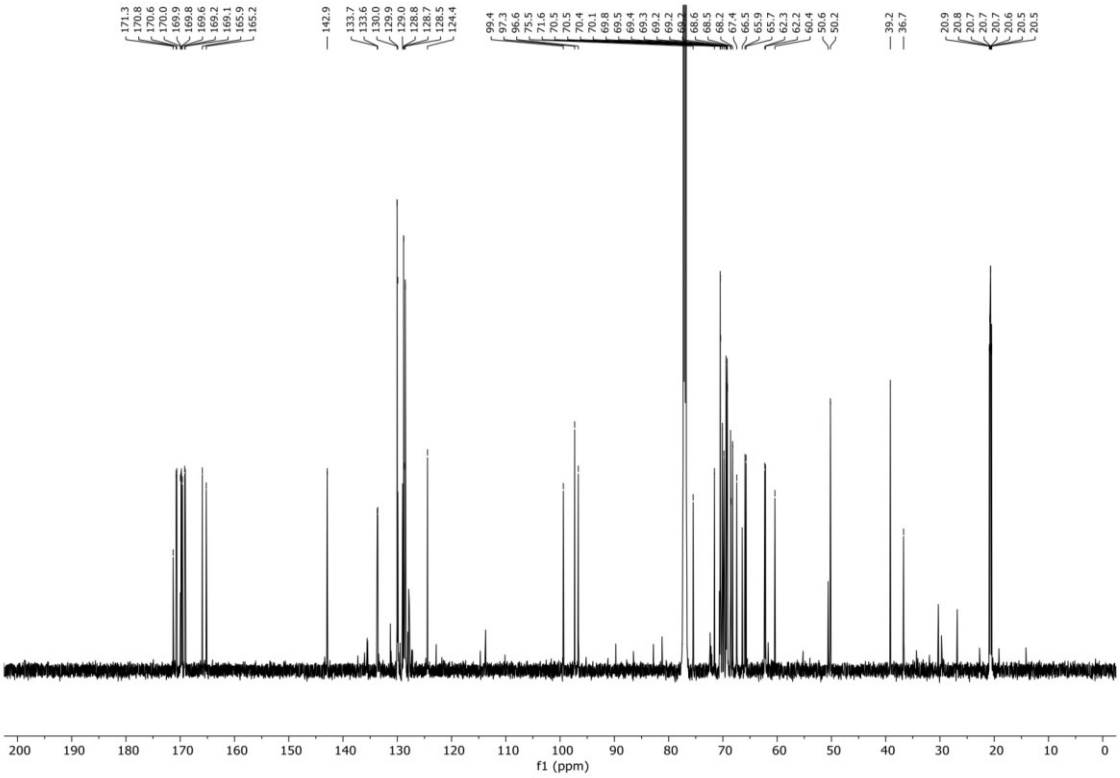

Supporting Information

^{1}H-NMR, (600 MHz, $CDCl_3$): (**S13**)

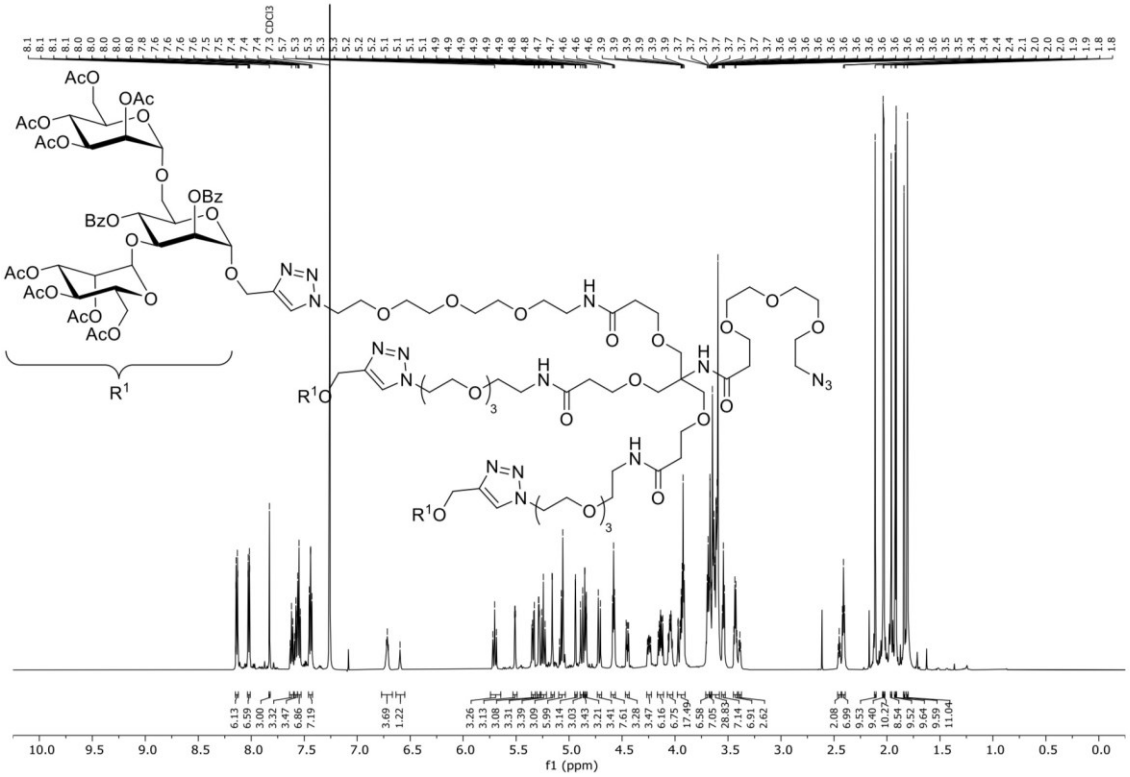

^{13}C-NMR, (151 MHz, $CDCl_3$): (**S13**)

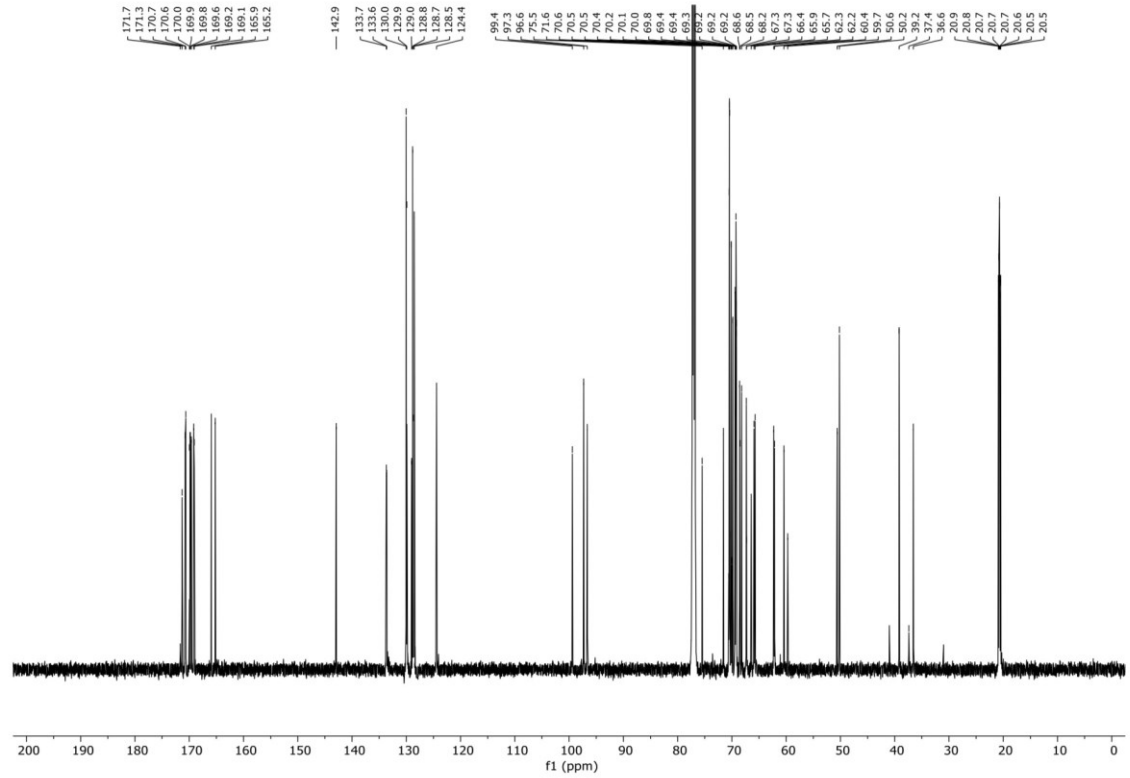

5. Dual stimuli-responsive dynamic covalent peptide tags: toward sequence-controlled release in tumor-like microenvironments

While Chapters 3 and 4 address targeting and cell-type-selective delivery, balancing the need for high drug conjugate stability in systemic circulation and the TME with the requirement for efficient intracellular drug release remains a major challenge in drug delivery approaches. Therefore, Chapter 5 focuses on the molecular design of a single, peptide-based drug linker system incorporating two different, complementary pairs of DCvC linkages. This combinatorial approach enables cooperative effects that overcome the inherent trade-off of single-linkage systems, leading to enhanced extracellular stability and reliable, stimuli-responsive intracellular release.

Authors

M. M. Zegota‡, M. A. Müller‡, **B. Lantzberg**, G. Kizilsavas, J. A. S. Coelho, P. Moscariello, M. Martínez-Negro, S. Morsbach, P. M. P. Gois, M. Wagner, D. Y. W. Ng, S. L. Kuan*, and T. Weil*

‡ Authors contributed equally to this work.

* Corresponding author

Published in Journal of American Chemical Society 2021, 382, 113705

DOI: 10.1021/jacs.1c06559

Date of Publication: 10th of October 2021

Contributions

As co-first author, Maksymilian M. Zegota designed and conducted the synthetic and experimental work regarding the peptides and peptide conjugates, analyzed and processed the data, and drafted the manuscript. As co-first author, Michael A. Müller performed the

synthesis and hybridization of peptide tags, carried out kinetics and stability studies in tumor-like microenvironments and bio-experiments together with Pierpaolo Moscariello, analyzed the data, and contributed to manuscript writing.

Bellinda Lantzberg optimized the peptide tag hybridization conditions regarding pH, buffer strength and equivalents of oxidizing reagent, and processed and analyzed the data. She prepared the manuscript figures, and assisted with manuscript corrections and revisions. Gönül Kizilsavas conducted NMR measurements and contributed to NMR data analysis and discussion. Jaime A. S. Coelho performed the DFT calculations and participated in their discussion. Pierpaolo Moscariello carried out the *in vitro* experiments, and María Martínez-Negro performed the ITC measurements, which were discussed with Svenja Morsbach. Pedro M. P. Gois contributed to discussions on the DFT calculations, and Manfred Wagner discussed the NMR experiments. David Y. W. Ng contributed to discussions on the concept and results and provided manuscript corrections, while Seah Ling Kuan co-designed and discussed the concept and results and assisted with manuscript revisions. Tanja Weil acquired funding for the project, co-designed and discussed the concept and results, and contributed to manuscript corrections.

JACS
JOURNAL OF THE AMERICAN CHEMICAL SOCIETY
pubs.acs.org/JACS
Article

Dual Stimuli-Responsive Dynamic Covalent Peptide Tags: Toward Sequence-Controlled Release in Tumor-like Microenvironments

Maksymilian Marek Zegota,[⊥] Michael Andreas Müller,[⊥] Bellinda Lantzberg, Gönül Kizilsavas, Jaime A. S. Coelho, Pierpaolo Moscariello, María Martínez-Negro, Svenja Morsbach, Pedro M. P. Gois, Manfred Wagner, David Y. W. Ng, Seah Ling Kuan,* and Tanja Weil*

Cite This: J. Am. Chem. Soc. 2021, 143, 17047−17058

Read Online

ACCESS | Metrics & More | Article Recommendations | Supporting Information

ABSTRACT: Dynamic covalent chemistry (DCvC) has emerged as a versatile synthetic tool for devising stable, stimuli-responsive linkers or conjugates. The interplay of binding affinity, association and dissociation constants exhibits a strong influence on the selectivity of the reaction, the conversion rate, as well as the stability in aqueous solutions. Nevertheless, dynamic covalent interactions often exhibit fast binding and fast dissociation events or vice versa, affecting their conversion rates or stabilities. To overcome the limitation in linker design, we reported herein dual responsive dynamic covalent peptide tags combining a pH responsive boronate ester with fast association and dissociation rates, and a redox-active disulfide with slow formation and dissociation rate. Precoordination by boronic acid−catechol interaction improves self-sorting and selectivity in disulfide formation into heterodimers. The resulting bis-peptide conjugate exhibited improved complex stability in aqueous solution and acidic tumor-like extracellular microenvironment. Furthermore, the conjugate responds to pH changes within the physiological range as well as to redox conditions found inside cancer cells. Such tags hold great promise, through cooperative effects, for controlling the stability of bioconjugates under dilution in aqueous media, as well as designing intelligent pharmaceutics that react to distinct biological stimuli in cells.

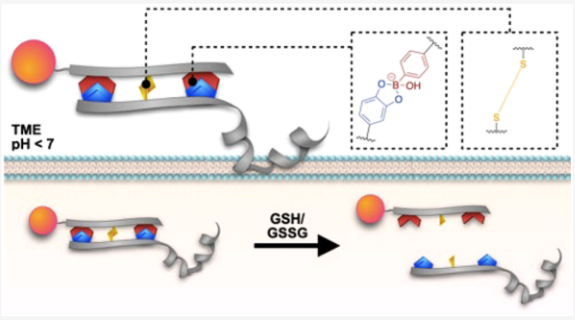

INTRODUCTION

Stimulus-responsive linker chemistry that can differentiate between the biochemical and physical differences manifested by tumor and normal tissues and respond accordingly has emerged as a central tool for the design of smart therapeutics and bioconjugates.[1−3] For example, systems that exploit the acidic extracellular matrix, acidic intracellular endosomes, elevated temperature, and higher glutathione concentrations found in cancer cells have been designed to trigger drug release selectively.[2,4] Nevertheless, the field is still fraught with challenges due to unsatisfactory systemic stability or premature drug release of most drug delivery systems.[1,2] In this regard, a fine balance between stability and reversibility, as well as sensitive response to small changes in the environmental parameters, are highly sought after features when designing linkers for biomedical applications. Dynamic covalent reactions (DCvR) are eminent candidates for new linker design since they are able to provide orthogonality, as well as combining high stability with reversibility at physiologically relevant conditions.[5,6] Ideally, the DCvRs should possess fast association (high on-rate, k_{on}) for rapid assembly and efficient conjugation even at lower concentrations, as well as a slow dissociation (low off-rate, k_{off}) so that the conjugates remain stable upon dilution.

An example of DCvR exhibiting fast k_{on} rates is based on phenylboronic acid chemistry with catechol groups, which proceed with fast k_{on} rates of about 10^3 M^{-1} s^{-1},[7,8] and is comparable to one of the fastest known bioorthogonal reactions, i.e., inverse electron demand Diels−Alder ($k_{on} > 10^3$ M^{-1} s^{-1}).[9] Moreover, the resultant boronate can achieve release at acidic pH,[8,10] rendering it attractive for preparing responsive bioconjugates. Nevertheless, fast binding often has its price—fast dissociation and the resultant conjugates usually lack hydrolytic stability.[7,8,11] For instance, conjugates with salicylhydroxamic acid exhibit high binding affinity ($K_D \sim 10$ μM) but fast dissociation was observed as well (estimated $k_{off} \sim 10^{-2}$ s^{-1}).[12,13] To improve the binding, two peptide strands each containing up to three noncanonical amino acids containing boronic acid and catechol side groups were shown to hybridize and the resultant double stranded peptide conjugates revealed

Received: June 24, 2021
Published: October 10, 2021

https://doi.org/10.1021/jacs.1c06559
J. Am. Chem. Soc. 2021, 143, 17047−17058

Journal of the American Chemical Society pubs.acs.org/JACS Article

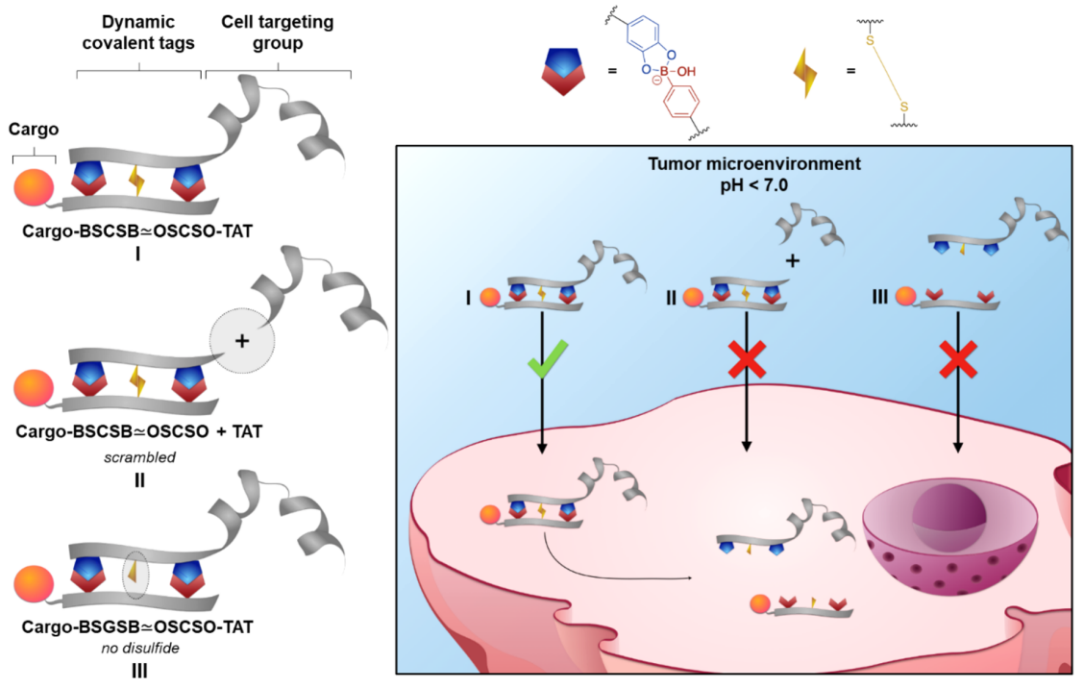

Figure 1. Conceptual overview of multivalent DCvRs based on cooperative boronic acid−catechol and thiol−thiol interaction imparting conjugate stability in the acidic tumor-like extracellular microenvironment as well as controlled release inside tumor cells. Illustrations were made with I−III for comparison.

Scheme 1. (a) Sequences of the Tripeptide; (b) Sequences of the Pentapeptide[a]

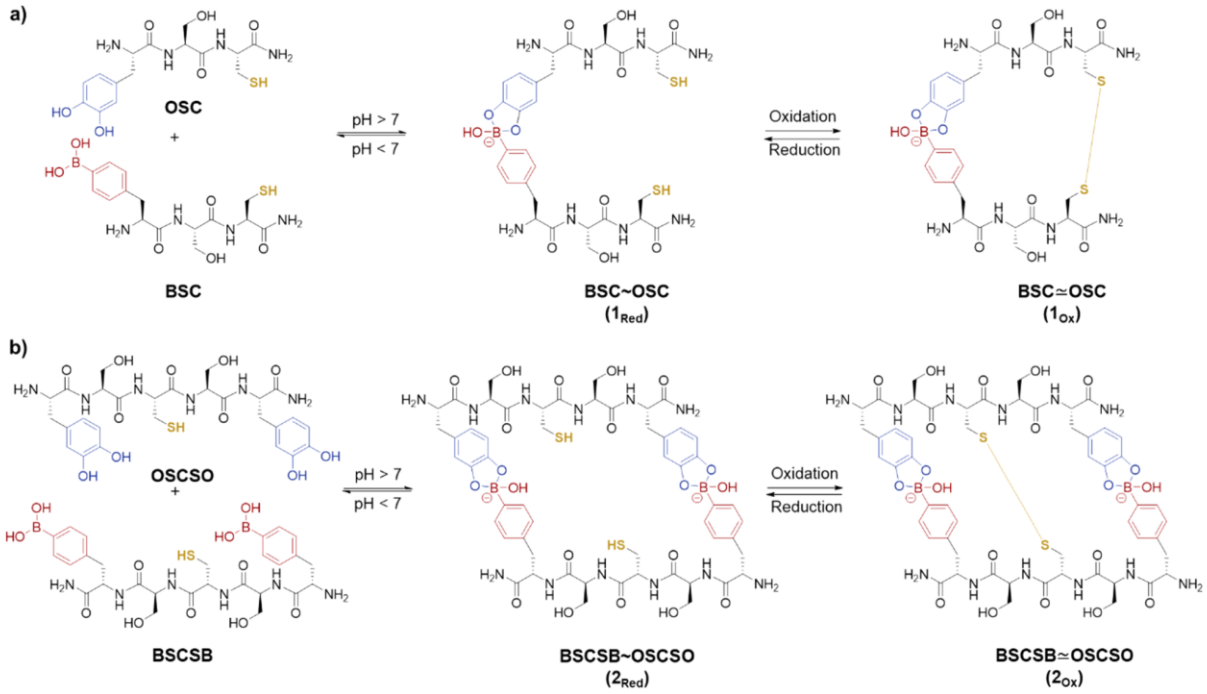

[a]All amino acids are represented by single letter code: 4-boronic acid-phenylalanine (B), cysteine (C), serine (S), and 3,4-dihydroxyphenylalanine (O). ~ denotes dynamic covalent boronate ester formation of B−O in two complementary peptide strands yielding $\mathbf{1}_{Red}$ and $\mathbf{2}_{Red}$, and ≃ denotes both B−O coordination and oxidation to form boronate ester and disulfide bridge formation leading to the dual stimuli-responsive peptide tags $\mathbf{1}_{Ox}$ and $\mathbf{2}_{Ox}$.

https://doi.org/10.1021/jacs.1c06559
J. Am. Chem. Soc. 2021, 143, 17047−17058

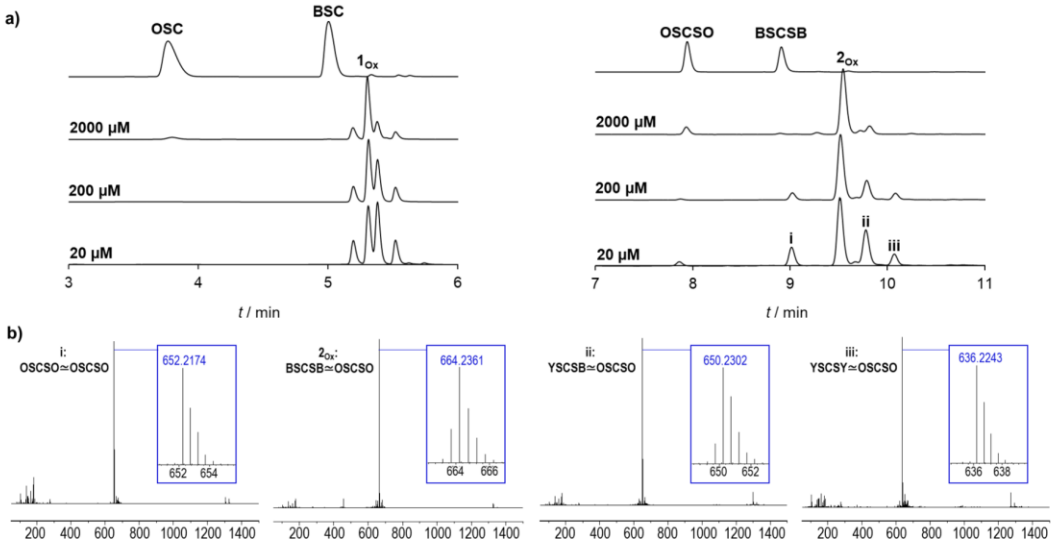

Figure 2. (a) Chromatograms of oxidation reactions using tripeptides (left) and pentapeptides (right) with varying concentrations of binding partners. Reactions were performed in 100 mM phosphate buffer pH = 7.4 by addition of 1.8 equiv of potassium peroxymonosulfate. (b) HR-ESI-MS analysis of purified $\mathbf{2}_{Ox}$ (measured m/z = 664.2361 $[M + 2H]^{2+}$, calc. m/z = 664.2343) and side products (i–iii), which were isolated.

low dissociation constants (the term hybridization is used in accordance with the process of joining two complementary strands of nucleic acids).[14] However, the limitation with fast dissociation remains unresolved. Conversely, conjugates with dynamic covalent hydrazones/hydrazides, oximes (pH-responsive), and disulfides (redox responsive)[15−17] showed slow association rates leading to prolonged reaction times, low conjugation yields,[18,19] and lack of true orthogonality due to homodimerization in the case of disulfides.[20,21] This can be partially resolved by intramolecular cyclization of disulfides in a single strand using the CXC (cysteine-any-cysteine) motifs but complementarity cannot be achieved.[22,23] Therefore, achieving fast association in combination with slow dissociation still represents a critical challenge in the design of DCv linkers.[6,24,25]

New strategies based on two complementary DCvRs compensating each other's weaknesses are, therefore, imperative to surmount the limitation of individual DCvR.[26] A DNA-mimetic dynamic covalent system, exploiting pH responsive boronic acid−catechol (fast) and hydrazine−aldehyde (slow) interactions, was devised for selective assembly of molecular ladders and grids from base-4-encoded oligo(peptoid)s.[27] Nevertheless, a combination of two orthogonal dynamic covalent interactions with two different stimuli on a peptide scaffold, their kinetics, and their stabilities have not been studied yet. In particular, a linker combining boronate esters and disulfides offers (1) fast preassembly due to high k_{on} of the boronic acid−catechol interactions, which will convert intermolecular to intramolecular disulfide formation, thereby compensating the slow and unspecific reactivity of thiols to form disulfide bonds; (2) stabilization of the resultant boronate esters due to low k_{off} of disulfide (Figure 1, Scheme 1). We demonstrate that short peptide tags containing both cysteine (C) and noncanonical amino acids, 4-boronic acid-phenylalanine (B) and 3,4-dihydroxyphenylalanine (O) residues on the complementary positions exhibit cooperative effects to form new DCv linkers with dissociation features that can be dictated by rationale sequence programming (Figure 2). In addition, targeting peptides such as cell penetrating TAT derived from human immunodeficiency virus can be easily extended on the peptide backbone through solid phase synthesis, and the N-terminal amine can be exploited to incorporate cargoes such as fluorescent dyes to form dual-responsive bioconjugates for drug delivery and bioimaging. Notably, the resultant dual responsive double-stranded bispeptide-linker exhibits stability and, at the same time, reacts to changes in pH or redox conditions, similar to that found in tumor microenvironments. The cooperative DCvR linker strategy presented herein holds immense promise for controlled drug delivery applications.

RESULTS AND DISCUSSION

Synthesis of Dynamic Covalent Peptide Tags. Four peptide sequences with varying boronic acid, catechol, and cysteine motifs were designed in this study. For clarity, new single letter codes were given for the noncanonical amino acids 4-boronic acid-phenylalanine (B) and 3,4-dihydroxyphenylalanine (or L-DOPA) (O), as depicted in Scheme 1. For solid-phase peptide synthesis (SPPS), the commercially available 4-boronophenylalanine (B) was protected in two steps with Fmoc and pinanediol on the amino and the BA functionality, respectively.[14]

To study the event of multiple boronic acid−catechol interactions, sequences with one or two B and O residues, as well as one cysteine (C) per peptide, were prepared, as shown in Scheme 1a and 1b. The polar amino acid serine (S) was selected as a short spacer that provides sufficient water-solubility with no charges to prevent potential electrostatic repulsion in the spacers in contrast to our previous studies using lysine as a spacer.[14] All the sequences used in this investigation (BSC, OSC, BSCSB, and OSCSO) and their oxidized heterodimers ($\mathbf{1}_{Ox}$, $\mathbf{2}_{Ox}$) are shown in Scheme 1. The monomeric sequences were synthesized using standard Fmoc-SPPS with *N*,*N*′-di-isopropylcarbodiimide/ethyl(hydroxyimino)cyanoacetate (DIC/Oxyma Pure) coupling chemistry, purified using RP-HPLC (>95% purity) and characterized by HR-ESI-MS and MALDI-TOF-MS (SI, Figures S1−S4).

https://doi.org/10.1021/jacs.1c06559
J. Am. Chem. Soc. 2021, 143, 17047−17058

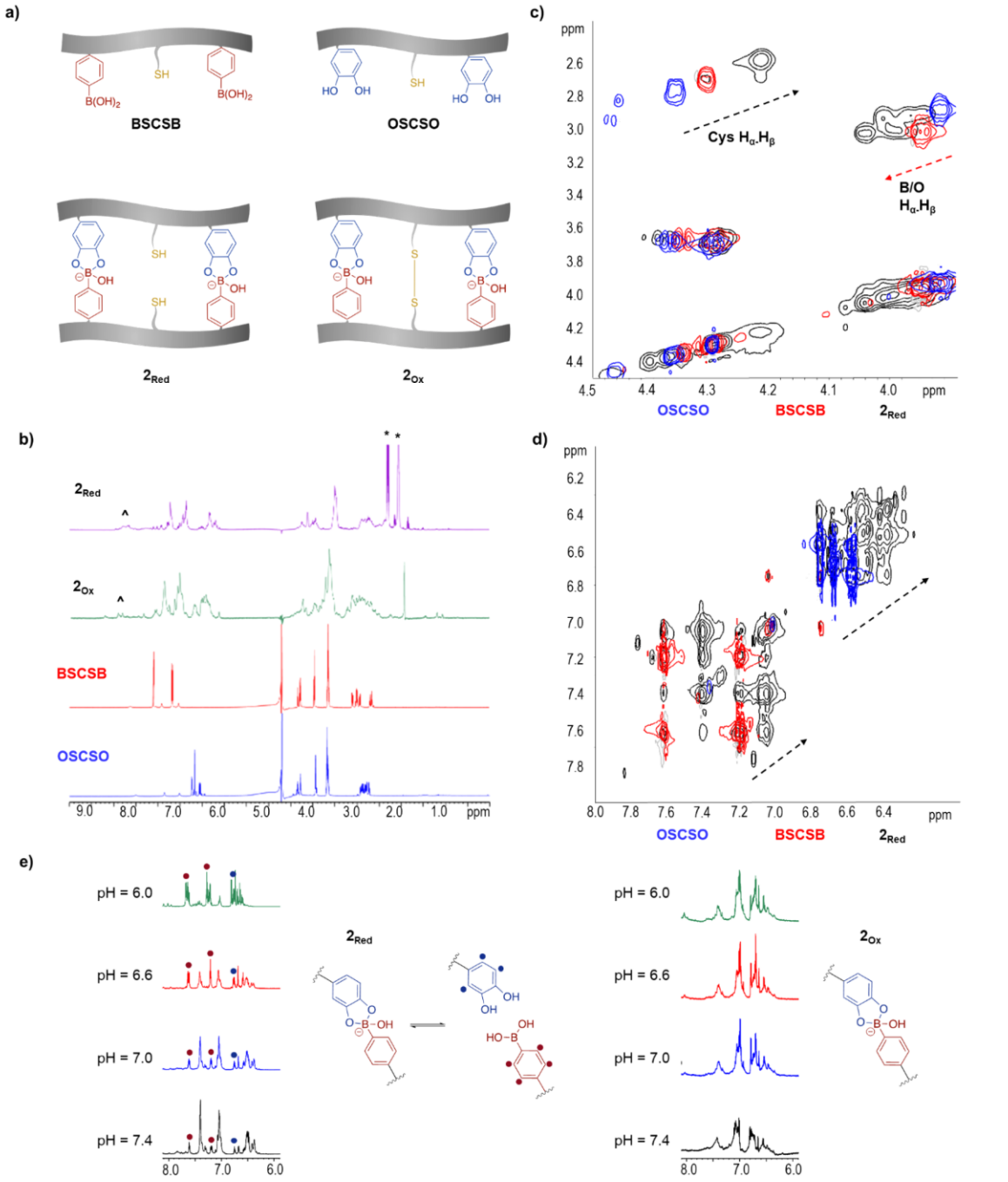

Figure 3. (a) Simplified scheme of the monomers as well as $\mathbf{2}_{Red}$ and $\mathbf{2}_{Ox}$. (b) ^{1}H NMR for peptide monomer and the hybridized double stranded peptide conjugate in reduced (2_{Red}) and oxidized ($\mathbf{2}_{Ox}$) form in 300 mM phosphate buffer, pH 7.4, 10% D2O in H_2O. * denotes signals due to the reducing reagent TCEP; ∧ are due to minor impurities, presumably due to homodimers and oxidized species. (c,d) ^{1}H−^{1}H TOCSY for single peptides and $\mathbf{2}_{Red}$ in 300 mM phosphate buffer, pH 7.4, 10% D_2O in H_2O (full ^{1}H−^{1}H TOCSY spectrum and the signal assignment for BSCSB and OSCSO available in the SI, Figures S26 and S27). (e) pH dependent chemical shifts of the aromatic protons in reduced and oxidized form.

In the following, we will use ~ to symbolize dynamic covalent boronate ester formation of two complementary peptide strands in their reduced form ($\mathbf{1}_{Red}$ and $\mathbf{2}_{Red}$), whereas ≃ denotes hybridization of complementary peptide strands with boronate ester formation and thiol oxidation to form a disulfide bridge ($\mathbf{1}_{Ox}$ and $\mathbf{2}_{Ox}$).

The hybridization conditions and the influence of B−O precoordination on disulfide formation of complementary tags were first investigated using HPLC. The reaction conditions, i.e.,

https://doi.org/10.1021/jacs.1c06559
J. Am. Chem. Soc. 2021, 143, 17047−17058

Journal of the American Chemical Society pubs.acs.org/JACS Article

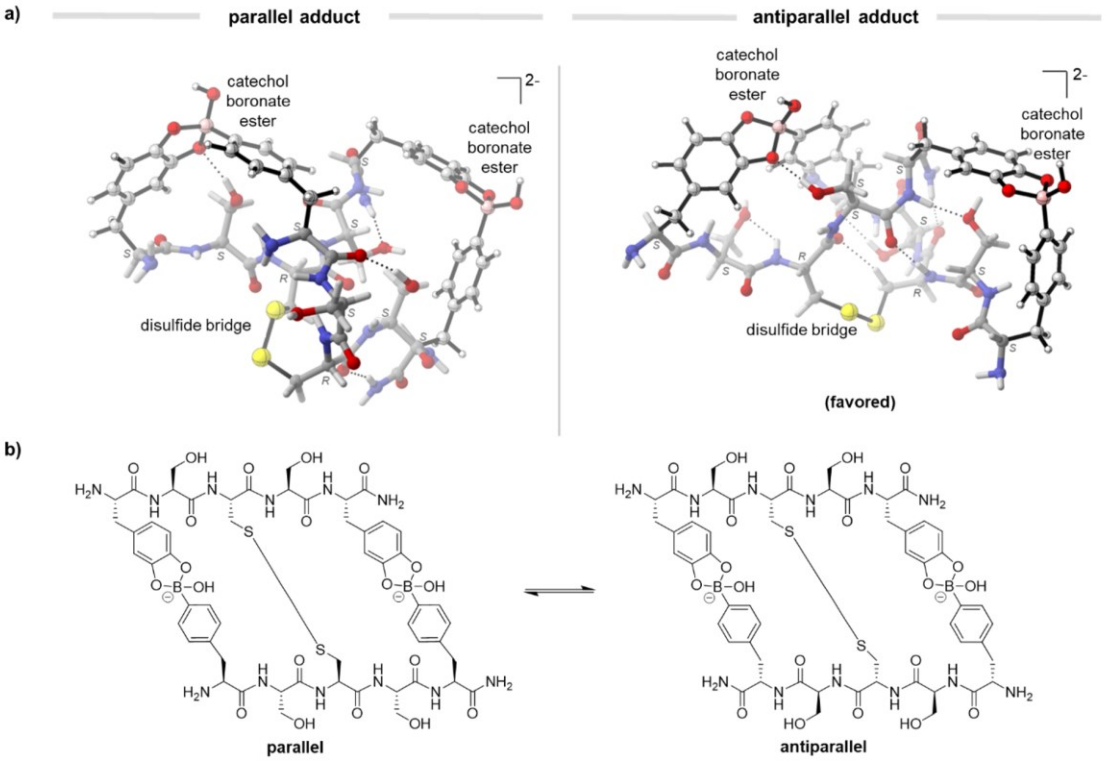

c)

Structure	S-S bond length / Å	E_{rel} / kcal mol^{-1}
2_{Ox} (BSCSB≃OSCSO) parallel	2.07	4.2
2_{Ox} (BSCSB≃OSCSO) antiparallel	2.08	0.0
BScSB≃OSCSO parallel	2.09	6.1
BScSB≃OSCSO antiparallel	2.10	0.0
bSCSb≃OSCSO parallel	2.07	5.6
bSCSb≃OSCSO antiparallel	2.10	0.0
fluorescein-BSCSB≃OSCSO-RGD parallel	2.07	3.3
fluorescein-BSCSB≃OSCSO-RGD antiparallel	2.08	0.0

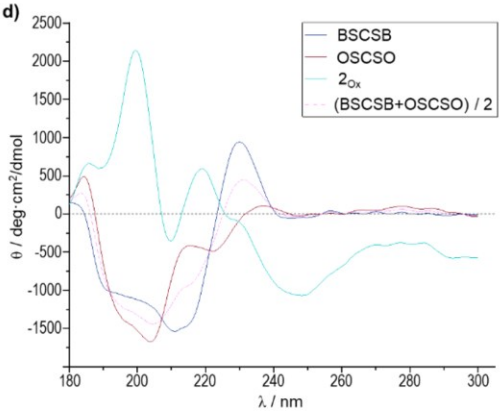

Figure 4. (a) DFT optimized structure of parallel and antiparallel $\mathbf{2}_{Ox}$ at B3LYP/6-31G(d) theory level (color coding: gray, carbon; white, hydrogen; red, oxygen; blue, nitrogen; yellow, sulfur; pink, boron). (b) Chemical structures of $\mathbf{2}_{Ox}$ in the parallel and antiparallel conformation. (c) Table showing calculated S−S bond distance and potential energy from DFT analysis. (d) Circular dichroism of $\mathbf{2}_{Ox}$, the individual pentapeptides and the average combined spectrum of both pentapeptides.

molar ratio of potassium peroxymonosulfate (Oxone), buffer strength, and pH, were optimized (SI, Figure S15a,b). 100 mM phosphate buffer (PB) at pH 7.4 and 1.8 mol equivalents of Oxone were applied for disulfide formation in all subsequent experiments, if not mentioned otherwise (SI, Figure S15a,b). Equimolar stock solutions (4000, 400, or 40 μM in 100 mM phosphate buffer, pH = 7.4) of complementary sequences were mixed in equal volumes and subsequently oxidized with Oxone resulting in final concentrations of 2000, 200, or 20 μM. Due to the sensitivity of the hybridization to pH, it is important to adjust the pH of the solution after dissolution before the oxidation with Oxone. For all studies, hybridized sequences of $\mathbf{1}_{Red}$ and $\mathbf{2}_{Red}$ were prepared by incubation of the individual components at 1 mM, while oxidation with Oxone in situ yield $\mathbf{1}_{Ox}$ and $\mathbf{2}_{Ox}$, as shown in the HPLC-chromatogram (Figure 2a). The reaction mixtures were immediately injected onto RP-HPLC. We observed less side products in the reaction mixture of the pentapeptides BSCSB ≃ OSCSO ($\mathbf{2}_{Ox}$) versus the tripeptides BSC ≃ OSC ($\mathbf{1}_{Ox}$). The incorporation of an additional boronic ester in $\mathbf{2}_{Ox}$ improves chemoselectivity by decreasing the amount of byproducts compared to $\mathbf{1}_{Ox}$ (Figure 2a). Further analysis by LC-MS (SI, Figures S11−S12) confirmed the formation of $\mathbf{1}_{Ox}$ and $\mathbf{2}_{Ox}$, with corresponding masses of 783 ($\mathbf{1}_{Ox}$, calc. m/z = 782.65) and 1328 ($\mathbf{2}_{Ox}$, calc. m/z = 1326.97). In addition, the

https://doi.org/10.1021/jacs.1c06559
J. Am. Chem. Soc. 2021, 143, 17047−17058

side products were isolated by HPLC and determined by high resolution-ESI-MS (HR-ESI-MS). The homodimer of the catechol sequence, OSCSO ~ OSCSO (i: measured m/z = 652.2174 $[M + 2H]^{2+}$; calc. m/z = 652.2162) was identified, as well as the partially oxidized form of the heterodimer of the boronic acid sequence, YSCSB ~ OSCSO (ii: measured m/z = 650.2302 $[M + 2H]^{2+}$; calc. m/z = 650.2278) and fully deborylated heterodimer YSCSY ~ OSCSO (iii: measured m/z = 636.2243 $[M + 2H]^{2+}$; calc. m/z = 636.2214) (Figure 2b) (SI, Table S1). Additionally we found traces of minor impurities, which were isolated but not characterized due to the quantity (see SI, Figure S15c for full chromatogram).

The benefit of the precoordination on disulfide formation of BSC ≃ OSC ($\mathbf{1}_{Ox}$) and BSCSB ≃ OSCSO ($\mathbf{2}_{Ox}$) is the most pronounced at 2000 μM, but it can be also seen at lower concentrations (200 and 20 μM). In the case of $\mathbf{2}_{Ox}$, fewer side products were formed most likely due to the higher percentage of fraction bound compared to $\mathbf{1}_{Ox}$. Thus, even though the boronic acid moiety is sensitive to oxidation, the amount of side products can be reduced by increasing the monomer concentration or the number of boronic acid−catechol interactions, as seen in the difference between the chromatograms of $\mathbf{1}_{Ox}$ and $\mathbf{2}_{Ox}$. Furthermore, two control sequences which are expected to show no binding were used, BSCSB and YSCSY. The oxidation leads mostly to homodimer with a very small fraction of heterodimer observed (SI, Figure S13), highlighting the importance of the boronic acid−catechol interactions for the selective oxidation to heterodimers. On the basis of the HPLC investigation, which showed conversion rates of approximately 25% for $\mathbf{1}_{Ox}$ and up to 70% for $\mathbf{2}_{Ox}$, peptide complex $\mathbf{2}_{Ox}$ was selected for upscaling and used for all subsequent studies, including NMR studies to assess the structural parameters of the hybridization reaction and the obtained product.

Structural Analysis of Hybridized Tags by NMR, DFT Calculations, and Circular Dichroism. The structure and coordination of the hybridized peptide tags, in comparison to the single stranded peptide sequences, as well as oxidized form $\mathbf{2}_{Ox}$ were investigated by a combination of 1- and 2-dimensional NMR spectroscopy (Figure 3). 1D-^{1}H NMR shows changes in the entire chemical environment upon boronic acid−catechol (B−O) conjugation in both $\mathbf{2}_{Red}$ and $\mathbf{2}_{Ox}$ (Figure 3b, Figure S24). We observed minor impurities in both spectra (Figure 3b), presumably due to homodimers and overoxidized species, which were also observed in HPLC (Figure 2a). The most affected regions are the H_α and the H_β protons of the respective cysteines, phenyl boronic acids and catechol (Figure 3c), as well as the aromatic side chain regions, which is clearly shown in the homonuclear total correlation spectroscopy (TOCSY) derived spectra for $\mathbf{2}_{Red}$ (Figure 3d). Upon conjugation, there is a change in the electron density around the protons of both peptides BSCSB and OSCSO, as mirrored in the chemical shift difference in the spectra. With the conformational change upon binding, protons of the amino acids in the proximity of boronic acid and catechol are brought to a position with a deshielding or shielding effect of the "shielding cones", resulting in a downfield or upfield shift, respectively. The aromatic signals as well as the H_α and H_β signals of the cysteines show an upfield shift, indicating shielding effects (black arrows, Figure 3c and Figure 3d). On the other hand, a region with an inverse effect, i.e., a downfield shift, was also observed (red arrow, Figure 3c) corresponding to the H_α and H_β protons of the terminal amino acids in the sequence of each peptide bearing the boronic acid or catechol moieties. Complexation of the complementary peptides (2 mM) was further substantiated by diffusion ordered NMR (DOSY), where slower diffusion of the complex (3.4×10^{-10} m^2 s^{-1}) was observed in comparison to the single peptide (3.6×10^{-10} m^2 s^{-1}), suggesting an increase of the hydrodynamic radius (SI, Figure S25). The formation of the disulfide was proven by HPLC analysis and discussed in the subsequent section (see Figure 5d).

To gain further structural information on the peptide sequences and the oxidized conjugate $\mathbf{2}_{Ox}$, density functional theory (DFT) calculations were performed at M06-2X/def2-TZVPP/PCM(SMD,water)//B3LYP/6-31G(d) level of theory (Figure 4). The low-lying energy structures of the single peptides (BSCSB and OSCSO) are found to be relatively compact and stabilized by multiple intramolecular hydrogen bonds (SI, Figures S28−S29). Binding entails a linearization of the sequences through formation of the boronate esters, a disulfide bond and intramolecular hydrogen bonds between BSCSB and OSCSO (SI, Figure S30−S31), which heavily influence the chemical environment of the nearby protons, consistent with both the results from ^{1}H and multidimensional NMR. The linearization upon binding of the two sequences is further corroborated by CD spectrum, which shows a higher number of distinct bands and higher magnitudes of the bands. These results indicate a higher order structure than that of the single sequences alone (Figure 4d).

Furthermore, calculations suggest that the antiparallel binding (Figure 4b, N-termini on the opposite sides of the conjugate) is favored over the parallel binding (Figure 4b, N-termini on the same side), with a Gibbs free energy difference of 3.5 kcal mol^{-1}. To further understand the preference for the antiparallel topology, a distortion/interaction analysis was performed (SI, Figures S38, S40). This analysis reveals stronger overall noncovalent interactions between BSCSB and OSCSO for the antiparallel binding that overpowers the higher degree of distortion of the single peptides in this binding mode.

We further investigated the influence of chirality of different amino acids on the structure. Additional DFT calculations were performed with two additional structures: one where L-Cys in the BSCSB sequence is changed to D-Cys (BScSB) and the other where L-4-borono-phenylalanine is changed to the corresponding D-amino acid (SI, Figures S32−S37). From the DFT calculations, there was only a slight difference in electronic energy (Figure S39), no significant change in the S−S bond length (2.10 versus 2.08 Å) (Figure 4c), and the antiparallel confirmation was preferred in both cases, compared to $\mathbf{2}_{Ox}$ (SI, Table S3). To confirm these findings, the BScSB sequence was synthesized and the hybridized species, BScSB ≃ OSCSO, was detected in LC-MS after oxidation with Oxone (SI, Figure S14).

Finally, to study the influence of bulky substituents at the N-termini of the peptides on the formed hybridized structures, calculations were performed with an additional simplified model analogue comprising of a positively charged RGD sequence on OSCSO and a negatively charged fluorescein dye coupled to the N-termini of the BSCSB sequence (SI, Figures S41−S42). Similarly, the antiparallel binding was determined to be the most favored with a Gibbs free energy difference of 7.5 kcal mol^{-1}. This greater difference is attributed to further electrostatic interactions from the positively charged guanidine RGD and the negatively charged dye (SI, Figures S41−S42), suggesting that electronic factors play a role in the arrangement of the peptide sequences.

https://doi.org/10.1021/jacs.1c06559
J. Am. Chem. Soc. 2021, 143, 17047−17058

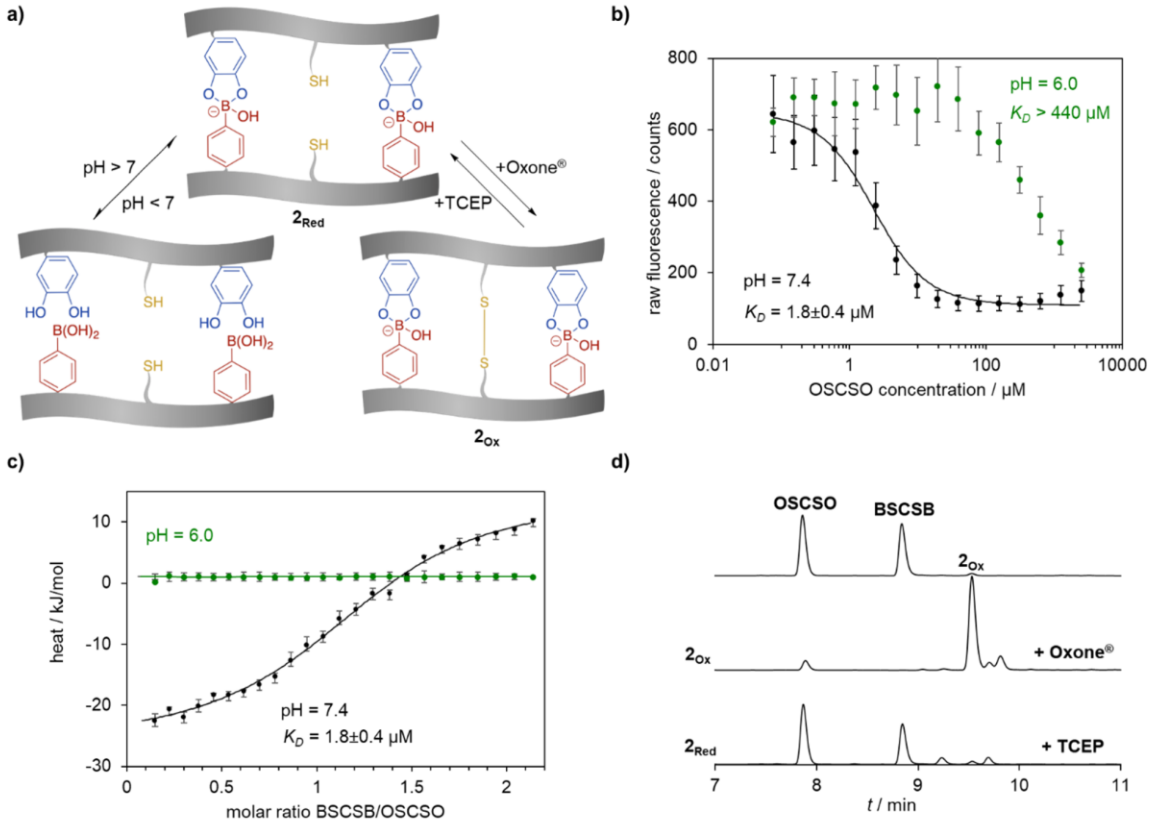

Figure 5. (a) pH- or redox-dependent formation of $\mathbf{2}_{Ox}$ and $\mathbf{2}_{Red}$. (b) Fluorescence quenching assay conducted in 100 mM phosphate buffer both at pH 7.4 and 6.0 in the presence of TCEP. (c) ITC binding curves showing integrated heats together with an independent binding model fit of $\mathbf{2}_{Red}$ in 100 mM phosphate buffer at pH 7.4 and pH 6.0. (d) HPLC analysis (using mobile phase with 0.1% trifluoroacetic acid) of formation and dissociation of disulfide bond formation under oxidizing or reducing conditions.

NMR Analysis of the Dynamics of Hybridized Tags. Next, the effects of both pH and redox conditions on the hybridized sequences were studied using $\mathbf{2}_{Ox}$ and $\mathbf{2}_{Red}$ utilizing ^{1}H NMR spectroscopy. ^{1}H NMR spectra of $\mathbf{2}_{Ox}$ are essentially the same in all cases, regardless of the pH range from 6.0 to 7.4 (Figure 3e). The only difference is the appearance of signals between 8.0 and 8.5 ppm, which belong to the amide backbone and is based on the acidity change and thus on the decreased proton exchange rate with the bulk water (Figure 3e). In contrast, under reductive conditions, in the presence of tris(2-carboxyethyl)phosphine (TCEP), the thiol groups are free, and the conjugate is bound only through pH sensitive boronate esters. Decreasing the pH affects the signals originating both from side chains and the backbones (Figure 3e) that split to eventually result in a spectrum resembling simple overlap of single peptides spectra (SI, Figure S24). Nevertheless because of the high concentration, which was about 3 orders of magnitude above the dissociation constant, complete dissociation into the monomers at pH 6 did not occur. Therefore, additional studies were performed under different pH or redox conditions using different methods.

Dual-Responsiveness of the Dynamic Covalent Tags to pH or Redox Conditions. The pH-reversible interactions of boronic acid and catechol groups, the formation of disulfides, as well as the responsiveness of the bis-peptide system were further investigated under different conditions (Figure 5). First, the boronic acid condensation with the complementary catechol and the thermodynamic properties were assessed under pH conditions that are relevant to physiological conditions, i.e., pH = 7.4 typical for extracellular environment of normal tissues and pH 6 for acidic intracellular compartments such as endosomes.[28] Equimolar concentrations of the reacting tags were applied to investigate the thermodynamic parameters associated with the formation of the heterodimer. DyLight488 labeled peptide (DL488-BSCSB) was synthesized by connecting the commercially available NHS-ester of this dye to the N-terminus of the BSCSB sequence to enable a microscale thermophoresis (MST) experiment, in which the dissociation constant could be determined. MST measurements were performed by titrating DL488-BSCSB (2 μM) against the complementary OSCSO peptide binding partner (76 nM to 5 mM). A dissociation constant in the low micromolar range (K_D = 1.8 ± 0.4 μM, Figure 5b) was obtained for DL488-BSCSB ~ OSCSO at pH = 7.4, which was 1 order of magnitude lower than the previously reported divalent analogue KOKOK ~ KBKBK (K_D = 80.0 ± 7.0 μM)[14] and 3 orders of magnitude lower than the single phenylboronic acid−catechol interaction (K_D = 1.2 mM).[14] Such an improvement could be explained by the lack of electrostatic repulsion due to the presence of the electroneutral serine (at physiological pH) in the sequence. To demonstrate pH responsiveness of the bioconjugate, the pH was adjusted to pH 6, which drastically increased the K_D to over 440 μM. To

https://doi.org/10.1021/jacs.1c06559
J. Am. Chem. Soc. 2021, 143, 17047−17058

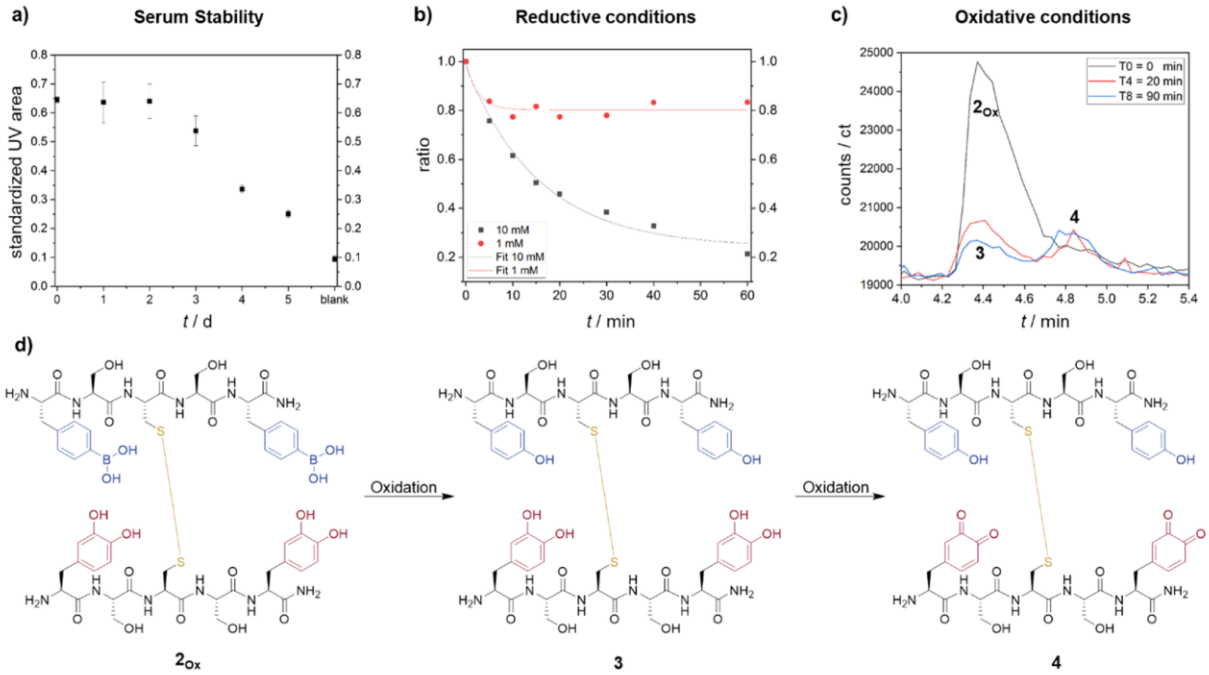

Figure 6. Stability of $\mathbf{2}_{Ox}$ under different conditions. Solutions of $\mathbf{2}_{Ox}$ were incubated in various conditions (a–c) and quantified with selective ion monitoring in LC-MS. (a) 10% fetal calf serum at 37 °C. (b) Reductive conditions with GSH/GSSG in liver cytosol. (c) Oxidative condition with 0.1% hydrogen peroxide. (d) Reaction scheme upon incubation with hydrogen peroxide.

assess the binding constant at physiological pH and to understand the type of complex formed, isothermal titration calorimetry (ITC) measurements were performed. The raw data were plotted as heat rate versus time at pH = 6 and 7.4. (SI, Figure S16). The reaction stoichiometry $n = 1.2 \pm 0.1$ indicates that primarily 1:1 complexes were formed at pH 7.4. From the independent binding model fit resulting of the integrated heat (Figure 5c), the thermodynamic parameters of interaction were obtained. At pH = 6 the heat of dilution (BSCSB to buffer) was similar to the reaction titration (BSCSB to OSCSO) indicating lack of binding. At pH = 7.4, significant exothermic signals were obtained, yielding a binding constant $K_D = 1.8 \pm 0.4\ \mu M$, similar to the one previously determined by MST. As a control, BSCSB was titrated to a sequence YSCSY, where L-DOPA was replaced with tyrosine. No binding could be observed, which further strengthens the importance of the L-DOPA/4-borono-phenylalanine motif for binding (SI, Figure S17). It is noteworthy that we are able to maximize reaction mass efficiency by using equimolar concentrations of reagents in these studies, in contrast to literature, where a large excess of one of the reagents is usually applied to improve the conversion.[14] Importantly, both ITC and MST experiments revealed that about 96% of hybridized species were observed at physiological pH at a concentration of 1 mM. Moreover, these experiments showed that even when the pH is lower than the corresponding pK_a of the 4-borono-phenylalanine (~8.9 for 4-methylphenylboronic acid[29]) the binding is sufficient for subsequent investigation in biological media. This observation is consistent with previous findings that the pK_a is not the sole parameter that affects binding.[14,30]

After precoordination based on the boronic acid–catechol interaction, $\mathbf{2}_{Red}$ can be selectively oxidized to $\mathbf{2}_{Ox}$ by forming a disulfide bridge (Figure 5a). We expect that this secondary S–S dynamic covalent bond locks the conjugate as a heterodimer introducing a reductive environment as a new stimulus for dissociation. Therefore, the formation followed by dissociation of the disulfide was also confirmed by RP-HPLC by subjecting 1 mM solutions of $\mathbf{2}_{Ox}$ and $\mathbf{2}_{Red}$, using the known oxidizing and reducing reagents, Oxone and TCEP respectively, and the peptide monomers were used as standards (Figure 5d). Directly after the addition of Oxone to the $\mathbf{2}_{Red}$ sample solution in PB, we "locked" the bis-peptide to form $\mathbf{2}_{Ox}$ with a retention time higher than any of the single components (Figure 5d). A solution of $\mathbf{2}_{Ox}$ formed by oxidizing $\mathbf{2}_{Red}$ could be reduced subsequently in situ without prior purification by addition of the reducing agent TCEP in slight excess (2.7 equiv), resulting in nearly quantitative hydrolysis of the bis-peptide into the monomeric peptide sequences (BSCSB and OSCSO) under acidic conditions (Figure 5d). This is because conjugate $\mathbf{2}_{Red}$ was formed in the presence of the reducing agent TCEP and further dissociated under acidic conditions of the measurement where the eluent contains additive of 0.1% trifluoroacetic acid (TFA), to afford BSCSB and OSCSO. The two sequences could be further oxidized in situ to form $\mathbf{2}_{Ox}$, albeit with higher amount of side products, due to the excess TCEP used in the previous step (SI, Figure S18). Taken together, our results have shown that the combination of two DCvCs in a single tag has cooperative effects and that the tags react in a pH- or redox-dependent fashion, but full reversibility of the entire system is not achievable under the conditions applied.

Application of Cooperative Dynamic Covalent Tags under Conditions Mimicking the Tumor Microenvironment. Peptides often reveal low stability in cell media. Moreover, noncovalent interactions provide responsiveness but often cannot allow for sufficient binding affinity and stability in complex cellular environments and under high dilution.[31,32]

https://doi.org/10.1021/jacs.1c06559
J. Am. Chem. Soc. 2021, 143, 17047–17058

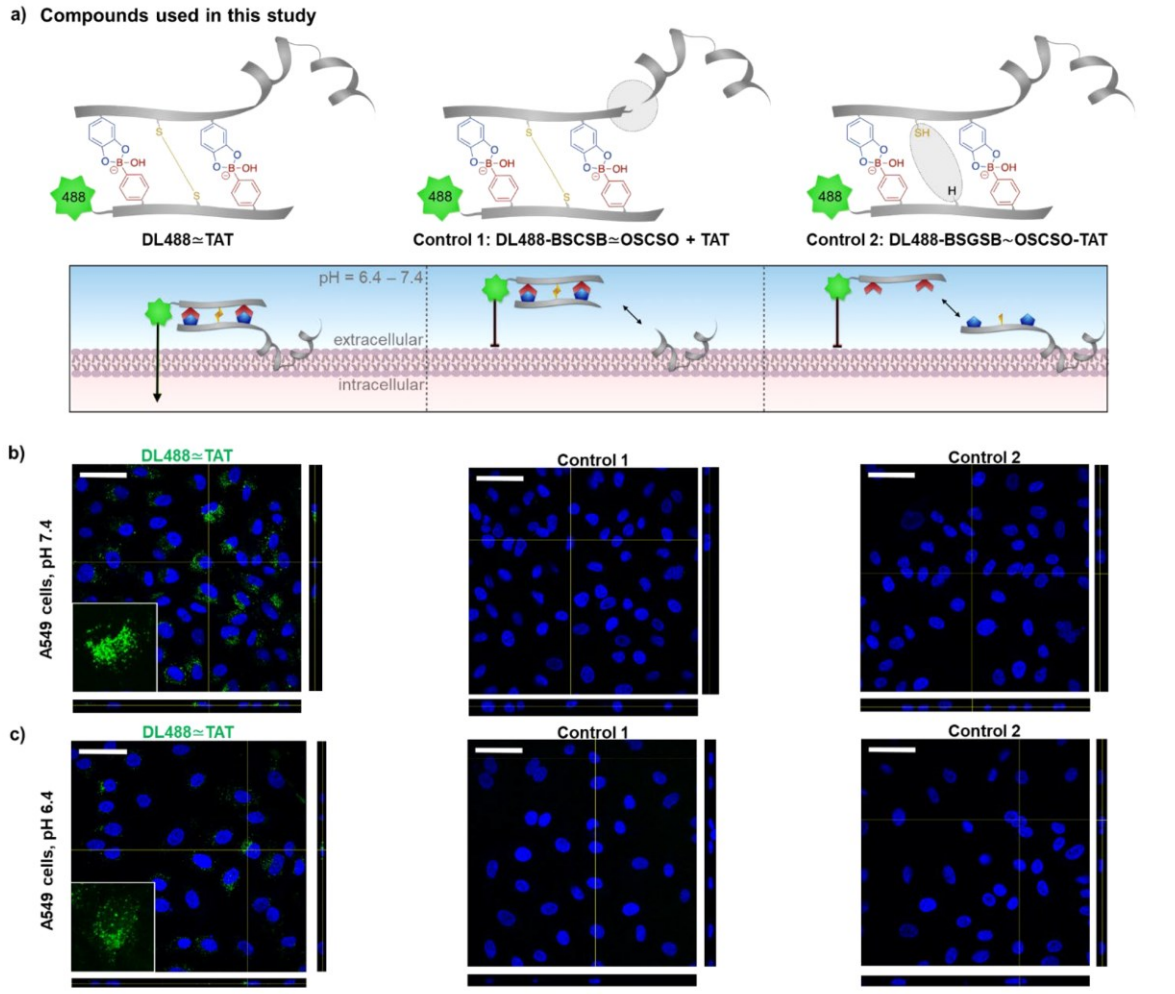

Figure 7. (a) Compounds used in this study and schematic overview. (b,c) Representative confocal orthogonal views of DL488 ≃ TAT (green) uptake in A549 cells both at (b) physiological and (c) acidic pH. Internalization is shown for modified DL488 ≃ TAT and negative controls (1: DL488-BSCSB ≃ OSCSO incubated with free TAT; 2: a conjugate without disulfide bridge (DL488-BSGSB) ~ (TAT-OSCSO)). All compounds are applied at a concentration of 10 μM. Cell nuclei are shown in blue by DAPI staining. Scale bar = 50 μm.

Therefore, we investigated the stability of $\mathbf{2}_{Ox}$ in biologically relevant environment. First, serum stability of $\mathbf{2}_{Ox}$ (1 mg mL^{-1}, 0.75 mM) was assessed by incubation in 1× phosphate buffer saline (PBS) with 10% fetal calf serum (FCS) at 37 °C and thereafter analyzed using RP-HPLC-MS with Fmoc-Phe-OH as an internal standard (SI, Figure S19). The eluent was acidified with formic acid to exclude the influence of B−O binding. Under these conditions, the conjugate remained stable for up to 2 days and started to decay over the course of 3−5 days (Figure 6a), most likely due to disulfide exchange with cysteine-rich FCS.

Next, the stability of $\mathbf{2}_{Ox}$ in glucose containing solutions were tested since it is known that phenyl boronic acids interact with sugars.[11] $\mathbf{2}_{Ox}$ was incubated in glucose solution (1 g/mL) or glucose depleted DMEM cell media (1 g/mL), which was used in the subsequent cell studies. The analysis was performed for up to 3 days and quantitative analysis was obtained using single ion monitoring (SIM) of m/z of $\mathbf{2}_{Ox}$ (m/z = 664, 388) in LC-ESI-MS to improve sensitivity in detection (SI, Figure S20). Fmoc-Phe-OH was used as an internal standard. The results show that $\mathbf{2}_{Ox}$ was determined to be nearly stable in glucose solution for 3 days (SI, Figure S20), suggesting that $\mathbf{2}_{Ox}$ is stable to competitive binding from diols due to stabilization from the disulfide. The amount of $\mathbf{2}_{Ox}$ decreased by around 20% in low glucose DMEM cell culture media after a day of incubation (SI, Figure S20). The decrease is presumably due to the disulfide exchange with free thiols inside the media (10% FCS and cysteine according to manufacturer's specifications). Nevertheless, $\mathbf{2}_{Ox}$ is sufficiently stable to potential thiol exchange for subsequent biological studies.

Thereafter, we tested the stability under conditions mimicking the tumor microenvironment, where it has been reported that cancer cells possess higher intracellular concentrations of glutathione (GSH/GSSG) in the cytosol, e.g., up to 10:0.25 mM in A549 lung carcinoma cells, compared to concentrations in healthy cells (1:0.025 mM).[4,33] Such differences in the physiological concentration of GSH have been exploited for controlled release. Thus, the GSH-induced cleavage of 1 mM of $\mathbf{2}_{Ox}$ was probed by incubation in commercially available liver cytosols spiked with physiologically relevant concentrations of GSH:GSSG (1:0.025 and 10:0.25

https://doi.org/10.1021/jacs.1c06559
J. Am. Chem. Soc. 2021, 143, 17047−17058

mM). The analysis was performed for up to 60 min and quantitative analysis was obtained using SIM in LC-MS ($\mathbf{2}_{Ox}$, m/z = 1328, 664) with Fmoc-Phe-OH as an internal standard (SI, Figure S22). As shown in Figure 6b, the complex was partially reduced when incubated with 1 mM GSH and an equilibrium state was established after approximately 10 min, with 80% of $\mathbf{2}_{Ox}$ unreacted. On the other hand, at a concentration of 10 mM (molar ratio 10:1) the reaction was slightly slower due to longer equilibration time. However, it is apparent that after 60 min, nearly all $\mathbf{2}_{Ox}$ was cleaved to the peptide monomers, BSCSB and OSCSO. Therefore, although the oxidized complex is stable over a longer period in serum (Figure 6a), GSH release could be induced in cytosolic conditions in cancer cells (Figure 6b), which would be important for controlled release as a drug delivery system.

We further determined the stability of the hybridized sequences under oxidative conditions. The oxidized complex, $\mathbf{2}_{Ox}$ was incubated with 0.1% hydrogen peroxide (30 μM). Aliquots were analyzed via LC-MS over different time intervals up to 60 min (SI, Figure S23) using SIM detection. Besides monitoring the decrease in the m/z of $\mathbf{2}_{Ox}$, SIM also offers the possibility to identify degradation products and allowed us to map the chemical processes involved in the oxidative condition implemented. The SIM profile indicates that no starting material is left after 10 min. We observed complete conversion to compound **3** (Figure 6c,d). After 10 min, the tyrosine compound is further oxidized to the tyrosine and *o*-quinone substance forming compound **4**, which elutes later due to higher hydrophobicity. This result is not surprising, since protected catechols are rather stable against oxidation considering that they are less likely to form oxygen radicals which are crucial in the oxidation process of catechols.[34] Notably, both sequences remained bound by the disulfide bridge and did not dissociate into the respective single peptide sequences, clearly underlining the stability of the hybridization under tumor-mimicking oxidative condition.

Dynamic covalent tags offer many attractive features for bioconjugate formation as their binding and release could be very useful for the delivery and stimulus-controlled release of drugs. The OSCSO tag was extended with the TAT peptide sequence (YGRKRRQRRR), which is a cell penetrating peptide derived from the human immunodeficiency virus. The TAT sequence has been widely employed for the delivery of cargoes into cells, such as small molecule drugs or proteins. TAT-OSCSO (YGRKRRQRRRS-OSCSO) was synthesized using SPPS and purified by HPLC and identified by MALDI-TOF-MS (m/z = 2281.1929 $[M + H]^+$, calc. 2281.1955 $[M + H]^+$), SI, Figure S8). A Dylight488 fluorescence dye (DL488) was conjugated to a BSCSB sequence on the N-terminus as a molecular cargo for transportation by TAT-OSCSO. DL488-BSCSB was purified by RP-HPLC and identified by ESI-MS (SI, Figure S9). The assembly of the dual responsive DL488 ≃ TAT conjugate was performed simply by mixing equal volumes of 2 mM solutions (100 mM phosphate buffer pH 7.4 with 10% DMSO) of targeting unit (TAT-OSCSO) and the cargo (DL488-BSCSB) and addition of Oxone.

For cell uptake studies, A549 cell line was selected, which is a model of alveolar Type II pulmonary epithelium.[35] The uptake was performed under two conditions to test the robustness of the resultant conjugate, which represents the extracellular conditions found in different stages of cancer progression.[36] Internalization of the conjugate was first studied in standard cell culture media (~ neutral pH). A solution of DL488 ≃ TAT was applied directly to A549 cells to a final concentration of 10 μM, without any further workup or further purification. As additional controls, (1) a conjugate DL488-BSCSB ≃ OSCSO incubated with free TAT sequence and (2) a conjugate without the disulfide bridge (DL488-BSGSB) ~ (TAT-OSCSO) where cysteine was replaced by glycine in one of the sequences were both applied at 10 μM (Figure 7a). After 24 h, no uptake was observed in the respective controls while DL488 ≃ TAT showed a significant uptake (Figure 7b). Taken together, the results indicate the immediate assembly of the conjugate and stability both to dilution and incubation in cell medium, as well as TAT-mediated uptake. Next, we proceeded to verify that the peptide tags are robust even under metastatic tumor-like microenvironment, where acidosis is a hallmark. Consequently, the low extracellular pH can result in a more invasive phenotype (Figure 7c), which is more challenging to treat.[28] First, A549 cancer cells were subjected to acute acidification to derive cells cultured at pH 6.4.[37−39] Thereafter DL488 ≃ TAT and controls 1 and 2 were applied at 10 μM for 24 h. Notably, the uptake of DL488 ≃ TAT was observed while the negative control 2, with no disulfide formation, was not internalized (Figure 7c). These results suggest that the linkers are stable due to the cooperative effect of two DCv interactions when applied to the acidic extracellular environment. Therefore, the linker chemistry can potentially be adopted for more invasive cancer phenotypes.

■ CONCLUSION

By exploiting the cooperative effect of a multivalent, fast dynamic covalent reaction of boronate esters with that of a slower and more stable dynamic disulfide formation, we have overcome the limitation of each chemistry and showed that a robust system which is dual responsive with tunable binding affinity can be achieved through rational chemical sequence programming. The pH responsive boronic acid−catechol interaction allows precoordination to convert intermolecular to intramolecular thiols of cysteine residues, allowing oxidation to form selectively the heterodimer with significantly reduced reaction time, which offers significant advantage over a single disulfide tag with slower reaction rate and the possibility of disulfide scrambling. The resultant disulfide bond stabilized the conjugate while remaining responsive to a second stimuli-redox environment. Notably, the complementary sequence consisting of two boronate esters is characterized by excellent dissociation constant, outperforming even the binding of single boronic acid with a strong coordinating ligand, i.e., salicylhydroxamate reported previously.[12] The resultant conjugate is stable under physiological conditions for up to 2 days, to glucose for 3 days, and to intracellular oxidative condition, as well as exhibiting responsive behavior in tumor-like microenvironment (low pH or high GSH concentration). This is important for, e.g., in vivo application where stability in the bloodstream is a major concern, as well as for targeted therapy to avoid unwanted release in normal tissues. Furthermore, very fast conjugation and inertness of the reaction components allows preparation of the conjugate directly before application and use in vitro directly without purification. Remarkably, the construct remains stable in acidic extracellular environment of cancer cells due to the presence of the disulfide bridge, enabling internalization of the cargo. One possible limitation is that the hybridization has to be carried out first at higher concentration (1 mM) and cannot be directly applied for biological applications where low dosage (μM) is required. But this can be resolved by incorporating more B/O in the sequence to increase the binding affinity, as shown in

https://doi.org/10.1021/jacs.1c06559
J. Am. Chem. Soc. 2021, 143, 17047−17058

our previous work.[14] We envisage that the amino acids used in these tags can also be expressed in a protein, thus holding immense promise to become a valuable tool in chemistry and biology to grant intelligent systems through the dynamic and stimuli responsive control over protein assembly or peptide/protein-cargo bioconjugates.

■ ASSOCIATED CONTENT

Supporting Information

The Supporting Information is available free of charge at https://pubs.acs.org/doi/10.1021/jacs.1c06559.

Structure data (ZIP)

Full experimental procedures and characterization data for new compounds as well as DFT coordinates (PDF)

■ AUTHOR INFORMATION

Corresponding Authors

Seah Ling Kuan − *Max Planck Institute for Polymer Research, 55128 Mainz, Germany; Institute of Inorganic Chemistry I, Ulm University, 89081 Ulm, Germany;* orcid.org/0000-0003-3945-4491; Email: kuan@mpip-mainz.mpg.de

Tanja Weil − *Max Planck Institute for Polymer Research, 55128 Mainz, Germany; Institute of Inorganic Chemistry I, Ulm University, 89081 Ulm, Germany;* orcid.org/0000-0002-5906-7205; Email: weil@mpip-mainz.mpg.de

Authors

Maksymilian Marek Zegota − *Max Planck Institute for Polymer Research, 55128 Mainz, Germany; Institute of Inorganic Chemistry I, Ulm University, 89081 Ulm, Germany*

Michael Andreas Müller − *Max Planck Institute for Polymer Research, 55128 Mainz, Germany*

Bellinda Lantzberg − *Max Planck Institute for Polymer Research, 55128 Mainz, Germany*

Gönül Kizilsavas − *Max Planck Institute for Polymer Research, 55128 Mainz, Germany*

Jaime A. S. Coelho − *Centro de Química Estrutural, Faculty of Sciences, University of Lisbon, 1749-016 Lisbon, Portugal;* orcid.org/0000-0002-7459-0993

Pierpaolo Moscariello − *Max Planck Institute for Polymer Research, 55128 Mainz, Germany*

María Martínez-Negro − *Max Planck Institute for Polymer Research, 55128 Mainz, Germany*

Svenja Morsbach − *Max Planck Institute for Polymer Research, 55128 Mainz, Germany;* orcid.org/0000-0001-9662-8190

Pedro M. P. Gois − *Research Institute for Medicines (iMed.ULisboa), Faculty of Pharmacy, University of Lisbon, 1649-003 Lisbon, Portugal;* orcid.org/0000-0002-7698-630X

Manfred Wagner − *Max Planck Institute for Polymer Research, 55128 Mainz, Germany*

David Y. W. Ng − *Max Planck Institute for Polymer Research, 55128 Mainz, Germany;* orcid.org/0000-0002-0302-0678

Complete contact information is available at: https://pubs.acs.org/10.1021/jacs.1c06559

Author Contributions

⊥M.M.Z. and M.A.M. contributed equally in this manuscript.

Funding

This project has received funding from the European Union's Horizon 2020 research and innovation program under the Marie Skłodowska-Curie Grant Agreement No. 675007, and Deutsche Forschungsgemeinschaft (DFG, German Research Foundation) Projektnummer 213555243, SFB 1066 and Projektnummer 316249678, SFB 1279. Open access funded by Max Planck Society.

Notes

The authors declare no competing financial interest.

■ ACKNOWLEDGMENTS

M. M. Zegota thanks the Marie Curie International Training Network Protein Conjugates under Grant Agreement No. 675007 for a research scholarship. The authors are grateful to the Max Planck Society and the German Research Foundation (SFB 1066 (project Q5 and B16), SFB 1279 (project C1)) for financial support. J. A. S. Coelho thanks the Fundação para a Ciência e a Tecnologia (FCT) for Scientific Employment Stimulus 2020/02383/CEECIND.

■ REFERENCES

(1) He, Q.; Chen, J.; Yan, J.; Cai, S.; Xiong, H.; Liu, Y.; Peng, D.; Mo, M.; Liu, Z. Tumor Microenvironment Responsive Drug Delivery Systems. *Asian J. Pharm. Sci.* **2020**, *15* (4), 416−448.

(2) Wang, S.; Yu, G.; Wang, Z.; Jacobson, O.; Tian, R.; Lin, L.-S.; Zhang, F.; Wang, J.; Chen, X. Hierarchical Tumor Microenvironment-Responsive Nanomedicine for Programmed Delivery of Chemotherapeutics. *Adv. Mater.* **2018**, *30* (40), 1803926.

(3) Kuan, S. L.; Fischer, S.; Hafner, S.; Wang, T.; Syrovets, T.; Liu, W.; Tokura, Y.; Ng, D. Y. W.; Riegger, A.; Förtsch, C.; Jäger, D.; Barth, T. F. E.; Simmet, T.; Barth, H.; Weil, T. Boosting Antitumor Drug Efficacy with Chemically Engineered Multidomain Proteins. *Adv. Sci.* **2018**, *5*, 1701036.

(4) Wang, T.; Ng, D. Y. W.; Wu, Y.; Thomas, J.; TamTran, T.; Weil, T. Bis-Sulfide Bioconjugates for Glutathione Triggered Tumor Responsive Drug Release. *Chem. Commun.* **2014**, *50* (9), 1116−1118.

(5) Jin, Y.; Yu, C.; Denman, R. J.; Zhang, W. Recent Advances in Dynamic Covalent Chemistry. *Chem. Soc. Rev.* **2013**, *42* (16), 6634−6654.

(6) Ulrich, S. Growing Prospects of Dynamic Covalent Chemistry in Delivery Applications. *Acc. Chem. Res.* **2019**, *52* (2), 510−519.

(7) Akgun, B.; Hall, D. G. Boronic Acids as Bioorthogonal Probes for Site-Selective Labeling of Proteins. *Angew. Chem., Int. Ed.* **2018**, *57* (40), 13028−13044.

(8) António, J. P. M.; Russo, R.; Carvalho, C. P.; Cal, P. M. S. D.; Gois, P. M. P. Boronic Acids as Building Blocks for the Construction of Therapeutically Useful Bioconjugates. *Chem. Soc. Rev.* **2019**, *48* (13), 3513−3536.

(9) Darko, A.; Wallace, S.; Dmitrenko, O.; Machovina, M. M.; Mehl, R. A.; Chin, J. W.; Fox, J. M. Conformationally Strained Trans-Cyclooctene with Improved Stability and Excellent Reactivity in Tetrazine Ligation. *Chem. Sci.* **2014**, *5* (10), 3770−3776.

(10) Bandyopadhyay, A.; Cambray, S.; Gao, J. Fast and Selective Labeling of N-Terminal Cysteines at Neutral PH via Thiazolidino Boronate Formation. *Chem. Sci.* **2016**, *7* (7), 4589−4593.

(11) Ramsay, W. J.; Bayley, H. Single-Molecule Determination of the Isomers of d-Glucose and d-Fructose That Bind to Boronic Acids. *Angew. Chem., Int. Ed.* **2018**, *57* (11), 2841−2845.

(12) Zegota, M. M.; Wang, T.; Seidler, C.; Wah Ng, D. Y.; Kuan, S. L.; Weil, T. Tag and Modify" Protein Conjugation with Dynamic Covalent Chemistry. *Bioconjugate Chem.* **2018**, *29* (8), 2665−2670.

(13) Ng, D. Y. W.; Arzt, M.; Wu, Y.; Kuan, S. L.; Lamla, M.; Weil, T. Constructing Hybrid Protein Zymogens through Protective Dendritic Assembly. *Angew. Chem., Int. Ed.* **2014**, *53* (1), 324−328.

(14) Hebel, M.; Riegger, A.; Zegota, M. M.; Kizilsavas, G.; Gačanin, J.; Pieszka, M.; Lückerath, T.; Coelho, J. A. S.; Wagner, M.; Gois, P. M. P.; Ng, D. Y. W.; Weil, T. Sequence Programming with Dynamic Boronic Acid/Catechol Binary Codes. *J. Am. Chem. Soc.* **2019**, *141* (36), 14026−14031.
(15) Lu, J.; Jiang, F.; Lu, A.; Zhang, G. Linkers Having a Crucial Role in Antibody−Drug Conjugates. *Int. J. Mol. Sci.* **2016**, *17* (4), 561.
(16) Kölmel, D. K.; Kool, E. T. Oximes and Hydrazones in Bioconjugation: Mechanism and Catalysis. *Chem. Rev.* **2017**, *117* (15), 10358−10376.
(17) Bargh, J. D.; Isidro-Llobet, A.; Parker, J. S.; Spring, D. R. Cleavable Linkers in Antibody-Drug Conjugates. *Chem. Soc. Rev.* **2019**, *48* (16), 4361−4374.
(18) Dirksen, A.; Dirksen, S.; Hackeng, T. M.; Dawson, P. E. Nucleophilic Catalysis of Hydrazone Formation and Transimination: Implications for Dynamic Covalent Chemistry. *J. Am. Chem. Soc.* **2006**, *128* (49), 15602−15603.
(19) Dirksen, A.; Hackeng, T. M.; Dawson, P. E. Nucleophilic Catalysis of Oxime Ligation. *Angew. Chem., Int. Ed.* **2006**, *45* (45), 7581−7584.
(20) Hioki, H.; Still, W. C. Chemical Evolution: A Model System That Selects and Amplifies a Receptor for the Tripeptide (D)Pro(L)Val-(D)Val. *J. Org. Chem.* **1998**, *63* (4), 904−905.
(21) Schäfer, O.; Barz, M. Of Thiols and Disulfides: Methods for Chemoselective Formation of Asymmetric Disulfides in Synthetic Peptides and Polymers. *Chem. - Eur. J.* **2018**, *24* (47), 12131−12142.
(22) Shishkan, O.; Zamfir, M.; Gauthier, M. A.; Börner, H. G.; Lutz, J. F. Complex Single-Chain Polymer Topologies Locked by Positionable Twin Disulfide Cyclic Bridges. *Chem. Commun.* **2014**, *50* (13), 1570−1572.
(23) Wu, C.; Leroux, J. C.; Gauthier, M. A. Twin Disulfides for Orthogonal Disulfide Pairing and the Directed Folding of Multicyclic Peptides. *Nat. Chem.* **2012**, *4* (12), 1044−1049.
(24) Lopes, R. M. R. M.; Ventura, A. E.; Silva, L. C.; Faustino, H.; Gois, P. M. P. N,O-Iminoboronates: Reversible Iminoboronates with Improved Stability for Cancer Cells Targeted Delivery. *Chem. - Eur. J.* **2018**, *24* (48), 12495−12499.
(25) Lu, F.; Zhang, H.; Pan, W.; Li, N.; Tang, B. Delivery Nanoplatforms Based on Dynamic Covalent Chemistry. *Chem. Commun.* **2021**, *57* (58), 7067−7082.
(26) Han, G. S.; Domaille, D. W. Tuning the Exchange Dynamics of Boronic Acid Hydrazones and Oximes with pH and Redox Control. *Org. Biomol. Chem.* **2021**, *19* (11), 4986−4991.
(27) Leguizamon, S. C.; Dunn, M.; Scott, T. F. Sequence-Directed Dynamic Covalent Assembly of Base-4-Encoded Oligomers. *Chem. Commun.* **2020**, *56* (56), 7817−7820.
(28) Ko, M.; Quiñones-Hinojosa, A.; Rao, R. Emerging Links between Endosomal PH and Cancer. *Cancer Metastasis Rev.* **2020**, *39* (2), 519−534.
(29) Kurnia, K. A.; Setyaningsih, W.; Darmawan, N.; Yuliarto, B. A Comprehensive Study on the Impact of the Substituent on PKa of Phenylboronic Acid in Aqueous and Non-Aqueous Solutions: A Computational Approach. *J. Mol. Liq.* **2021**, *326*, 115321.
(30) Yan, J.; Springsteen, G.; Deeter, S.; Wang, B. The Relationship among pKa, pH, and Binding Constants in the Interactions between Boronic Acids and Diols—It Is Not as Simple as It Appears. *Tetrahedron* **2004**, *60* (49), 11205−11209.
(31) Webber, M. J.; Langer, R. Drug Delivery by Supramolecular Design. *Chem. Soc. Rev.* **2017**, *46* (21), 6600−6620.
(32) Li, Y.; Chen, Y.; Dong, H.; Dong, C. Supramolecular, Prodrug-Based Micelles with Enzyme-Regulated Release Behavior for Controlled Drug Delivery. *MedChemComm* **2015**, *6* (10), 1874−1881.
(33) Wang, X.; Cai, X.; Hu, J.; Shao, N.; Wang, F.; Zhang, Q.; Xiao, J.; Cheng, Y. Glutathione-Triggered "off-On" Release of Anticancer Drugs from Dendrimer-Encapsulated Gold Nanoparticles. *J. Am. Chem. Soc.* **2013**, *135* (26), 9805−9810.
(34) Pillar-Little, E. A.; Guzman, M. I. Oxidation of Substituted Catechols at the Air−Water Interface: Production of Carboxylic Acids, Quinones, and Polyphenols. *Environ. Sci. Technol.* **2017**, *51* (9), 4951−4959.
(35) Foster, K. A.; Oster, C. G.; Mayer, M. M.; Avery, M. L.; Audus, K. L. Characterization of the A549 Cell Line as a Type II Pulmonary Epithelial Cell Model for Drug Metabolism. *Exp. Cell Res.* **1998**, *243* (2), 359−366.
(36) Kato, Y.; Ozawa, S.; Miyamoto, C.; Maehata, Y.; Suzuki, A.; Maeda, T.; Baba, Y. Acidic Extracellular Microenvironment and Cancer. *Cancer Cell Int.* **2013**, *13*, 89.
(37) Wojtkowiak, J. W.; Rothberg, J. M.; Kumar, V.; Schramm, K. J.; Haller, E.; Proemsey, J. B.; Lloyd, M. C.; Sloane, B. F.; Gillies, R. J. Chronic Autophagy Is a Cellular Adaptation to Tumor Acidic pH Microenvironments. *Cancer Res.* **2012**, *72* (16), 3938−3947.
(38) Mendoza, E. E.; Pocceschi, M. G.; Kong, X.; Leeper, D. B.; Caro, J.; Limesand, K. H.; Burd, R. Control of Glycolytic Flux by AMP-Activated Protein Kinase in Tumor Cells Adapted to Low Ph1. *Transl. Oncol.* **2012**, *5* (3), 208−216.
(39) Sutoo, S.; Maeda, T.; Suzuki, A.; Kato, Y. Adaptation to Chronic Acidic Extracellular pH Elicits a Sustained Increase in Lung Cancer Cell Invasion and Metastasis. *Clin. Exp. Metastasis* **2020**, *37* (1), 133−144.

https://doi.org/10.1021/jacs.1c06559
J. Am. Chem. Soc. 2021, 143, 17047−17058

Supplementary Information

Dual stimuli-responsive dynamic covalent peptide tags: Towards sequence-controlled release in tumor-like microenvironments

Maksymilian Marek Zegota,[▽1,2] Michael Andreas Müller,[▽1] Bellinda Lantzberg,[1] Gönül Kizilsavas,[1] Jaime A. S. Coelho,[3] Pierpaolo Moscariello,[1] María Martínez-Negro,[1] Svenja Morsbach,[1] Pedro M. P. Gois,[4] Manfred Wagner,[1] David Y. W. Ng,[1] Seah Ling Kuan,[*1,2] Tanja Weil[*1,2]

[1]Max Planck Institute for Polymer Research, Ackermannweg 10, 55128 Mainz, Germany

[2]Institute of Inorganic Chemistry I, Ulm University, Albert-Einstein-Allee 11, 89081 Ulm, Germany

[3]Centro de Química Estrutural, Faculty of Sciences, University of Lisbon, Campo Grande, 1749-016 Lisbon, Portugal

[4]Research Institute for Medicines (iMed.ULisboa), Faculty of Pharmacy, University of Lisbon, 1649-003 Lisbon, Portugal

Table of Contents

1. General experimental

Unless otherwise stated, all syntheses were performed without taking precautions to exclude air and moisture. All organic solvents (CH_3CN, CH_2Cl_2, DMF) were obtained from Fisher Scientific and used without further purification (HPLC or peptide grades). H_2O used for the reactions was obtained from the Millipore purification system. Reagents were obtained from Fisher Scientific, Sigma Aldrich and ChemPep Inc. Fmoc-4-boronophenylalanine(pinanediol) was synthesized according to the literature.[12] Reaction progress was monitored by thin layer chromatography (TLC) using Merck 60 F_{254} pre-coated silica gel plates and visualized under ultraviolet lamp (254 nm). Flash column chromatography was carried out using Merck silica gel 60 mesh. Solid-phase peptide synthesis (SPPS) was performed using CEM Liberty Blue peptide synthesizer. High performance liquid chromatography (HPLC) was carried out using Shimadzu HPLC system. NMR spectra were measured on Bruker Avance 850 NMR spectrometer and the chemical shifts (δ) were reported as parts per million (ppm) referenced with respect to the residual solvent peaks. The following abbreviations were used to label the multiplicities: s = singlet, d = doublet, t = triplet, q = quartet, p = pentet, dd = doublet of doublets, dt = doublet of triplets, m = multiplet. MALDI-TOF-MS spectra were acquired on a Bruker Time-of-flight MS rapifleX. HR-ESI-MS was recorded using WATERS SYNAPT G2-Si mass spectrometer. HPLC-ESI-MS analysis was performed on a Shimadzu LC-MS 2020 equipped with an electrospray ionization source and a SPD-20A UV-Vis detector. The absorbance was measured on microplate reader (Tecan Spark 20M). Fluorescence quenching assay was performed using Monolith NT.115.

2. Solid-phase peptide synthesis

Synthesis scale: 0.25 mmol

Deprotection: 20% piperidine in DMF

Activator: 0.25 M DIC (*N,N'*-diisopropylcarbodiimide) in DMF

Activator base: 0.5 M Oxyma Pure® (ethyl cyano(hydroxyimino)acetate)

Amino acids: 0.2 M in DMF

Resin: Rink-amide Resin (100-200 mesh), swelled in DMF for 2 h at room temperature

Coupling cycle:

- Standard deprotection (3 mL deprotection solution)

  75 °C (150 W) for 15s

  90 °C (30 W) for 50s
- Wash 3x (2 mL DMF)
- Standard coupling (1.25 mL amino acid, 1 mL activator, 0.5 mL activator base)

  75 °C (150 W) for 15s

90 °C (30 W) for 50s

Final deprotection cycle:

- Standard deprotection (3 mL deprotection solution)

  75 °C (150 W) for 15s

  90 °C (30 W) for 50s

- Wash 3x (2 mL DMF)

Cleavage solution: 4 mL of 95% TFA, 2.5% water, 2.5% TIPS. For deprotection of boronic acid 5 eq. of methylboronic acid was added to the cleavage solution.[13] Cleavage solution was added to the dry resin and stirred overnight at room temperature. Pentapeptides were precipitated by addition of the solution to the cold diethyl ether (-20 °C, 7.5mL per 1mL of cleavage solution) and purified by RP-HPLC. Tripeptides were purified after evaporation of TFA.

HPLC purification

Solvent A: 0.1% TFA in water, solvent B: 0.1% TFA in ACN in a binary gradient

Column 1: Gemini 5 µm, NX-C18, 110 Å (flow rate: 25 mL/min), 150 × 30 mm, column 2: Atlantis T3, 100 Å, 5 µm, 19 mm × 150 mm (flow rate: 10 mL/min)

H-CAT-Ser-Cys-CONH$_2$ (OSC)

HPLC gradient (column 1): 0% B for 1 min, 35% B in 9 min, 100% B in 2 min, 100% B for 1 min. R_t = 8.1 min.

32 mg (62.5 µmol, 25% yield) was obtained from lyophilisation as a TFA salt.

HR-ESI-MS: m/z = 267.0817 $[M\text{-}Cys+H]^+$, 387.1126 $[M+H]^+$, 409.0933 $[M+Na]^+$ (calc. 267.0975 $[M\text{-}Cys+H]^+$, 387.1333 $[M+H]^+$, 409.1152 $[M+Na]^+$, formula: $C_{15}H_{22}N_4O_6S$)

MALDI-TOF-MS: m/z= 387.1135 $[M+H]^+$ (calc. 387.1333 $[M+H]^+$)

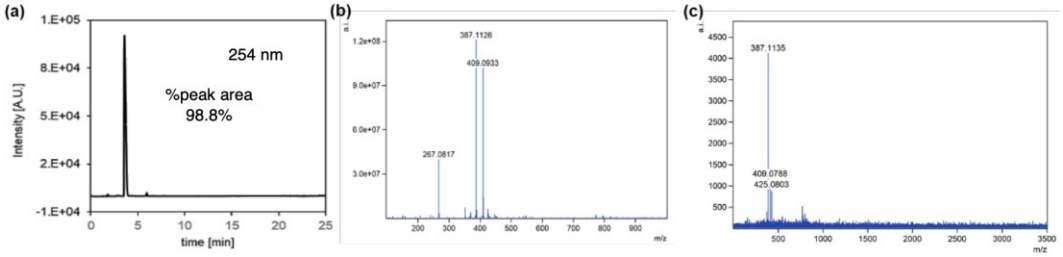

Figure S 1: (a) LC chromatogram and (b) HR-ESI-MS and (c) MALDI-TOF-MS of OSC

H-BPA-Ser-Cys-CONH$_2$ (BSC)

HPLC gradient (column 1): 0% B for 1 min, 35% B in 9 min, 100% B in 2 min, 100% B for 1 min. R_t = 10.0 min.

36 mg (72.5 µmol, 29% yield) was obtained from lyophilisation as a TFA salt.

HR-ESI-MS: m/z = 279.1620 $[M\text{-}Cys+H]^+$, 399.2092 $[M+H]^+$, 421.1940 $[M+Na]^+$ (calc. 279.1147 $[M\text{-}Cys+H]^+$, 399.1504 $[M+H]^+$, 421.1324 $[M+Na]^+$, formula: $C_{15}H_{23}BN_4O_6S$)

MALDI-TOF-MS: m/z= 517.0516 $[M+DHB\text{-}2H_2O+H]^+$ (calc. 517.1559 $[M+DHB\text{-}2H_2O+H]^+$)

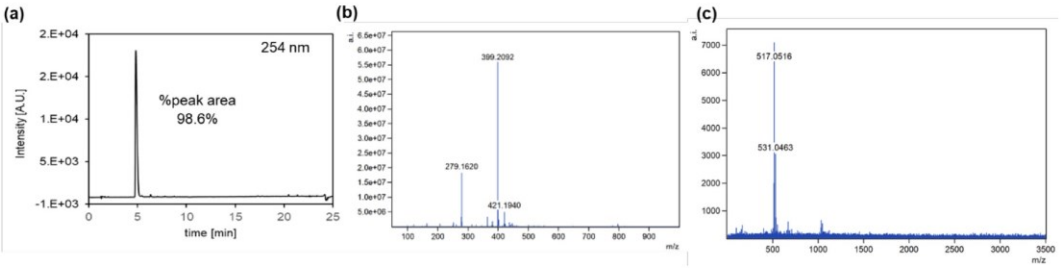

Figure S 2: (a) LC chromatogram and (b) HR-ESI-MS and (c) MALDI-TOF-MS of BSC

H-CAT-Ser-Cys-Ser-CAT-CONH$_2$ (OSCSO)

HPLC gradient (column 1): 0% B for 1 min, 20% B in 9 min, 100% B in 2 min, 100% B for 1 min. R_t = 8.9 min.

100 mg (130.0 µmol, 52% yield) was obtained from lyophilisation as a TFA salt.

HR-ESI-MS: m/z = 346.0846 $[M+H+K]^{2+}$, 653.2164 $[M+H]^+$, 675.21924 $[M+Na]^+$ (calc. 346.0934 $[M+H+K]^{2+}$, 653.2236 $[M+H]^+$, 675.2055 $[M+Na]^+$, formula: $C_{27}H_{36}N_6O_{11}S$)

MALDI-TOF-MS: m/z= 652.9538 $[M+H]^+$, 674.9305 $[M+Na]^+$, 690,9052 $[M+K]^+$ (calc. 653.2236 $[M+H]^+$, 675.2055 $[M+Na]^+$, 691.1794 $[M+K]^+$)

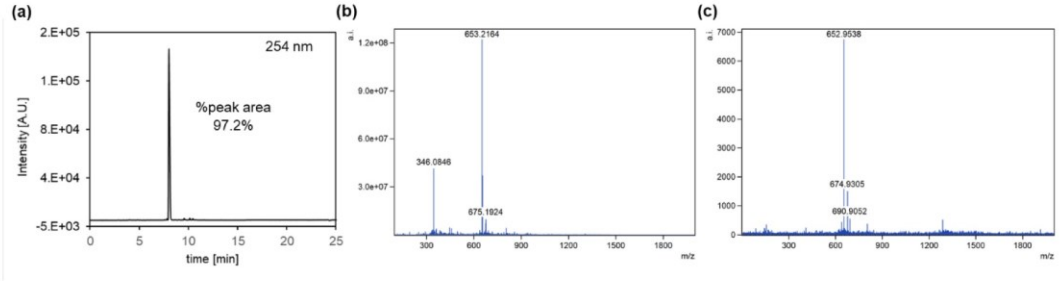

Figure S 3: (a) LC chromatogram and (b) HR-ESI-MS and (c) MALDI-TOF-MS of OSCSO

H-BPA-Ser-Cys-Ser-BPA-CONH$_2$ (BSCSB)

HPLC gradient (column 1): 0% B for 1 min, 20% B in 9 min, 100% B in 2 min, 100% B for 1 min. R_t = 9.1 min.

81 mg (102.5 µmol, 41% yield) was obtained from lyophilisation as a TFA salt.

HR-ESI-MS: m/z = 677.2578 $[M+H]^+$, 699.2272 $[M+Na]^+$ (calc. 677.2578 $[M+H]^+$, 699.2398 $[M+Na]^+$, formula: $C_{27}H_{38}B_2N_6O_{11}S$)

MALDI-TOF-MS: m/z= 913.2117 $[M+2DHB\text{-}4H_2O+H]^+$ (calc. 913.2688 $[M+2DHB\text{-}4H_2O+H]^+$)

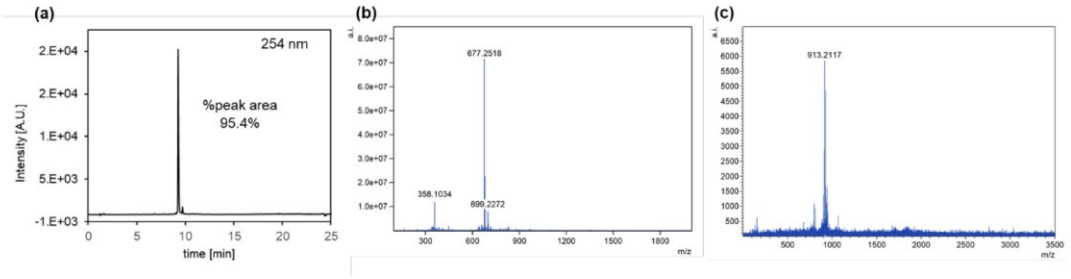

Figure S 4: (a) LC chromatogram and (b) HR-ESI-MS and (c) MALDI-TOF-MS of BSCSB

H-BPA-Ser-Gly-Ser-BPA-CONH$_2$ (BSGSB)

HPLC gradient (column 1): 0% B for 1 min, 20% B in 9 min, 100% B in 2 min, 100% B for 1 min. R_t = 9.1 min.

9.2 mg (16.9 µmol, 34% yield) was obtained from lyophilisation as a TFA salt.

HR-ESI-MS: m/z = 677.2578 $[M+H]^+$, 699.2272 $[M+Na]^+$ (calc. 677.2578 $[M+H]^+$, 699.2398 $[M+Na]^+$, formula: $C_{26}H_{36}B_2N_6O_9S$)

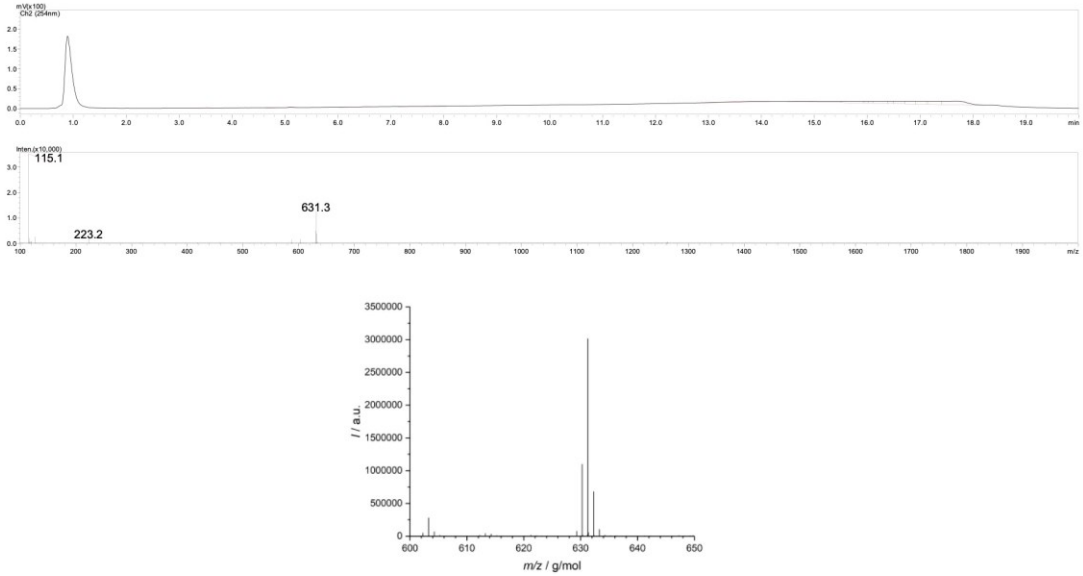

Figure S 5: LC, ESI-MS, HR-ESI of BSGSB.

H-Tyr-Ser-Cys-Ser-Tyr-CONH$_2$ (YSCSY)

HPLC gradient (column 1): 0% B for 1 min, 20% B in 9 min, 100% B in 2 min, 100% B for 1 min. R_t = 9.1 min.

13.6 mg (21.9 µmol, 44% yield) was obtained from lyophilisation as a TFA salt.

HR-ESI-MS: m/z = 677.2578 $[M+H]^+$, 699.2272 $[M+Na]^+$ (calc. 677.2578 $[M+H]^+$, 699.2398 $[M+Na]^+$, formula: $C_{27}H_{36}N_6O_{11}S$)

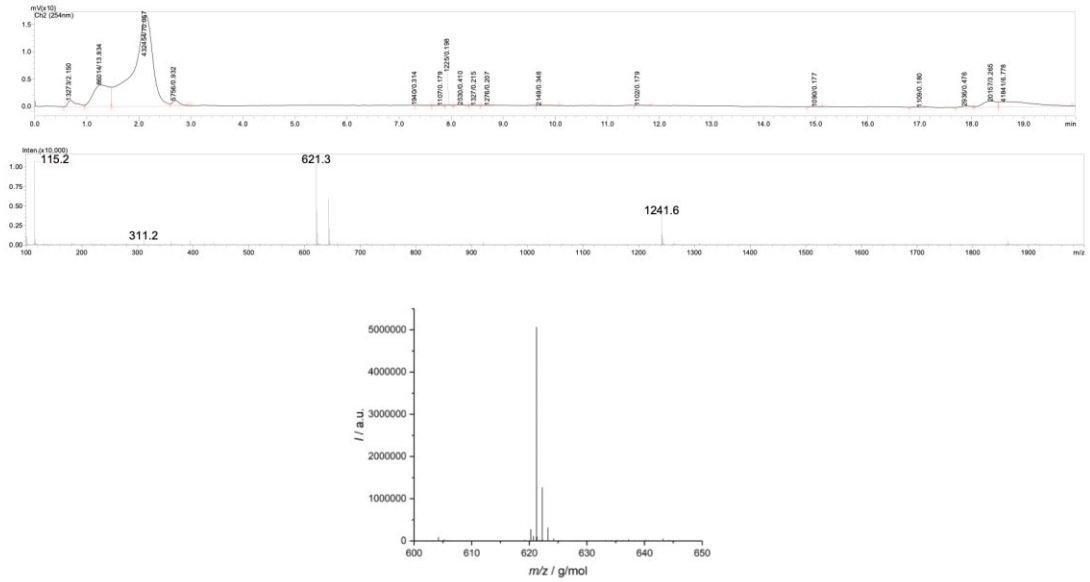

Figure S 6: LC, ESI-MS, HR-ESI of YSCSY.

H-BPA-Ser-D-Cys-Ser-BPA-CONH$_2$ (BScSB)

HPLC gradient (column 1): 0% B for 1 min, 20% B in 9 min, 100% B in 2 min, 100% B for 1 min. R_t = 9.1 min.

4,2 mg (6.2 µmol, 12% yield) was obtained from lyophilisation as a TFA salt. (low yield due to fraction spilling)

ESI-MS: m/z = 677.4 $[M+H]^+$, 699.8 $[M+Na]^+$ (calc. 677.2578 $[M+H]^+$, 699.2398 $[M+Na]^+$, formula: $C_{27}H_{38}B_2N_6O_{11}S$)

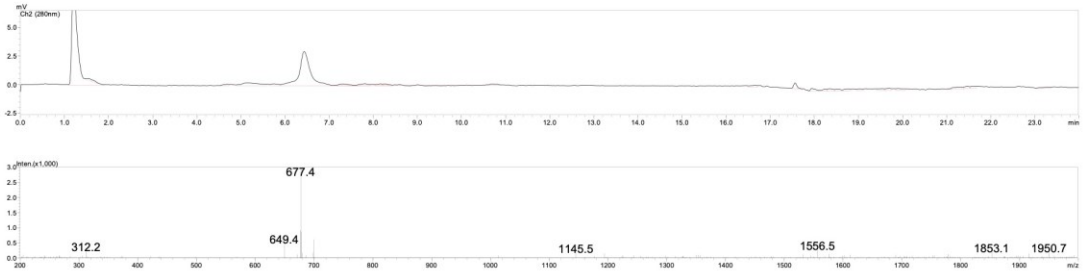

Figure S 7: LC and ESI-MS for BScSB.

H-Tyr-Gly-Arg-Lys-Lys-Arg-Arg-Gln-Arg-Arg-Arg-Ser-Cat-Ser-Cys-Ser-Cat-CONH$_2$ (TAT-OSCSO)

HPLC gradient (column 1): 0%B for 1 min, 40% B in 19 min, 100% B in 2 min, 100% B for 1 min. R_t = 11.9 min.

65 mg (15 µmol, 15% yield) was obtained from lyophilisation as a TFA salt.

ESI-MS: m/z = 457.2256 $[M+5H]^{5+}$, 571.3410 $[M+4H]^{4+}$, 761,3560 $[M+3H]^{3+}$, 1141,7422 $[M+2H]^{2+}$ (calc. 457.0449 $[M+5H]^{5+}$, 571.0543 $[M+4H]^{4+}$, 761,0700 $[M+3H]^{3+}$, 1141,1014 $[M+2H]^{2+}$, formula: $C_{94}H_{157}N_{39}O_{26}S$)

MALDI-TOF-MS: m/z = 2281.1929 $[M+H]^+$ (calc. 2281.1955 $[M+H]^+$)

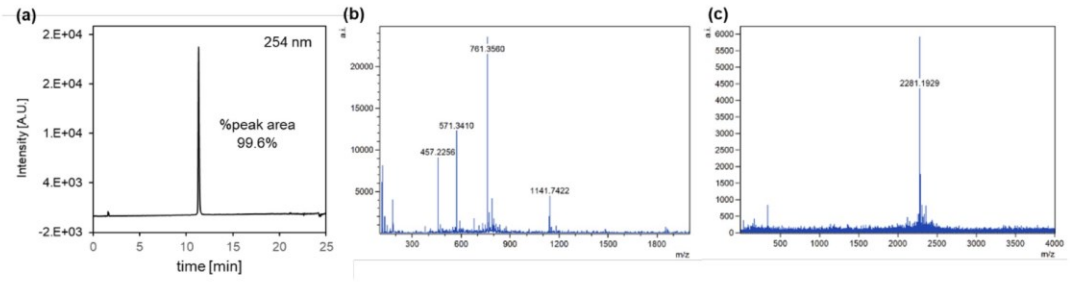

Figure S 8: (a) LC chromatogram and (b) ESI-MS and (c) MALDI-TOF-MS of TAT-OSCSO

3. Peptide modification

Dylight488-BPA-Ser-Cys-Ser-BPA-CONH$_2$ (DL488-BSCSB)

3.2 mg (4.0 µmol, 3 eq.) of BSCSB peptide was dissolved in 1.5 mL of DMF followed by addition of 1 µL (6.0 µmol, 4.5 eq). of triethylamine. Solution was added to 1 mg (1.3 µmol, 1 eq). of the dye NHS ester. Reaction was shaken overnight, DMF was evaporated, residue redissolved in water and purified by RP-HPLC (column 2) using following gradient: 0% B to 35% B in 18 min, 100% B in 1 min, 100% B for 1 min, R_t = 16.1 min. 1.5 mg (1.1 µmol, 85%) of DL488-BSCSB was obtained from lyophilisation as an orange solid.

ESI-MS: m/z = 1314.4 $[M+H]^+$; 655.9 $[M-2H]^{2-}$, 1312.6 $[M-H]^-$ (formula of DyLight488 is not disclosed by the manufacturer)

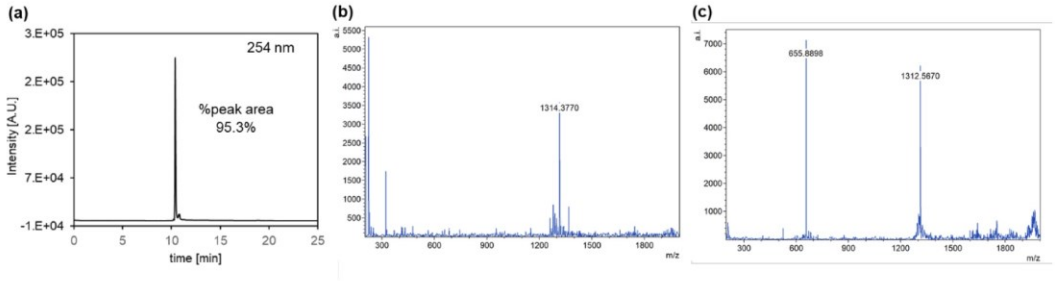

Figure S 9: (a) LC chromatogram and ESI-MS spectra in both b) positive and c) negative ion modes for DL488-BSCSB

Dylight488-BPA-Ser-Gly-Ser-BPA-CONH$_2$ (DL488-BSGSB)

2.5 mg (4.0 µmol, 3 eq.) of BSGSB peptide was dissolved in 1.5 mL of DMF followed by addition of 1 µL (6.0 µmol, 4.5 eq). of triethylamine. Solution was added to 1 mg (1.3 µmol, 1 eq). of the dye NHS ester. Reaction was shaken overnight, DMF was evaporated, residue redissolved in water and purified by RP-HPLC (column 2) using following gradient: 0% B to 35% B in 18 min, 100% B in 1 min, 100% B for 1 min, R_t = 16.1 min. 0.4 mg (0.31 µmol, 24%) of DL488-BSGSB was obtained from lyophilisation as an orange solid.

ESI-MS: m/z = 1311.4 $[M+H]^+$; 654.2 $[M-2H]^{2-}$, 1309.6 $[M-H]^-$ (formula of DyLight488 is not disclosed by the manufacturer)

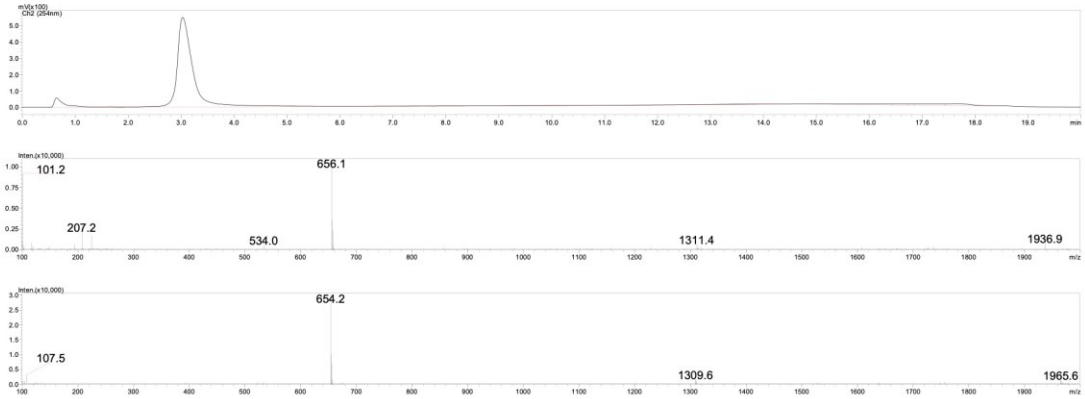

Figure S 10: LC, ESI(+)-MS and ESI(-)-MS for DL488-BSGSB.

4. Oxidation protocol

BSC≃CSO/ BSCSB≃OSCSO /TAT-DL488

50 uL of 2 mM solution of OSC/OSCSO or Tat-OSCSO in 100 mM PB, pH = 7.4 was mixed with 50 uL of 2 mM solution of BSC/BSCSB or DL488-BSCSB in 100 mM PB, pH = 7.4. The mixture was subsequently added rapidly to 2 uL of 90 mM Oxone® solution in 100 mM PB, pH = 7.4 to obtain final Oxone® concentration of 1.8 mM (1.8 eq) and pipetted up and down several times.

BSC≃OSC

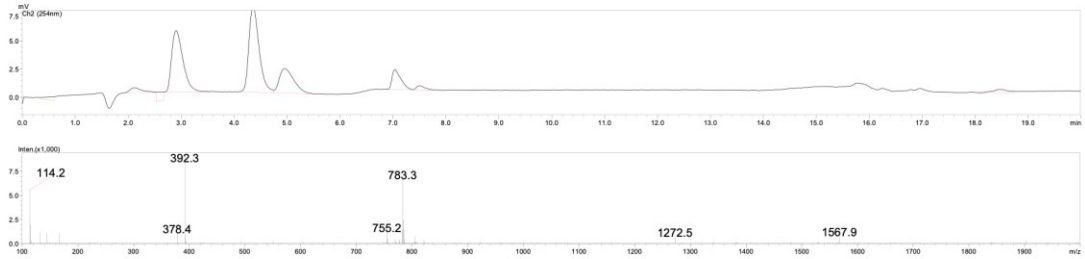

Figure S 11: LC and ESI(+)-MS of the oxidation of BSC≃OSC.

BSCSB≃OSCSO

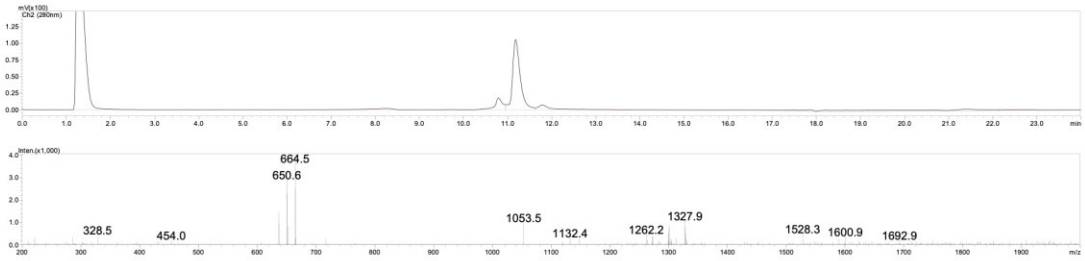

Figure S 12: LC and ESI(+)-MS of the oxidation of BSCSB≃OSCSO.

BSCSB~YSCSY

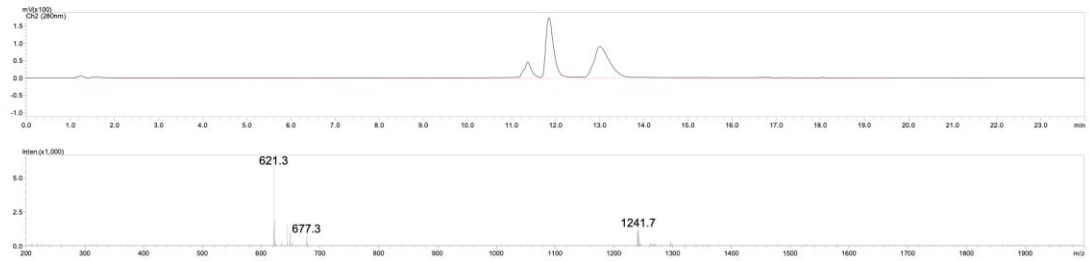

Figure S 13: LC and ESI(+)-MS for the oxidation of BSCSB~YSCSY.

BScSB≃OSCSO

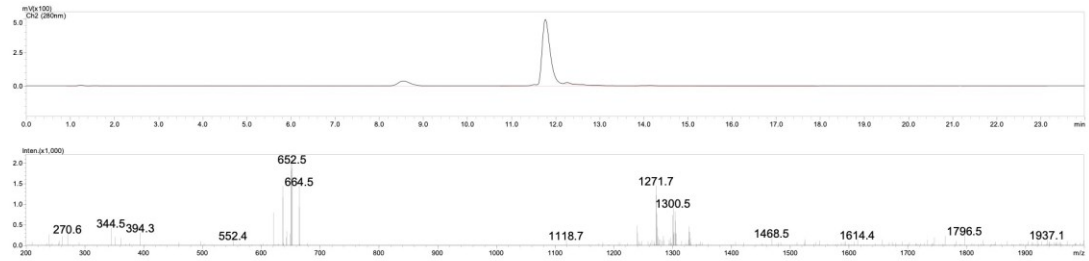

Figure S 14: LC and ESI(+)-MS for the oxidation of BScSB≃OSCSO.

5. Oxidation optimization

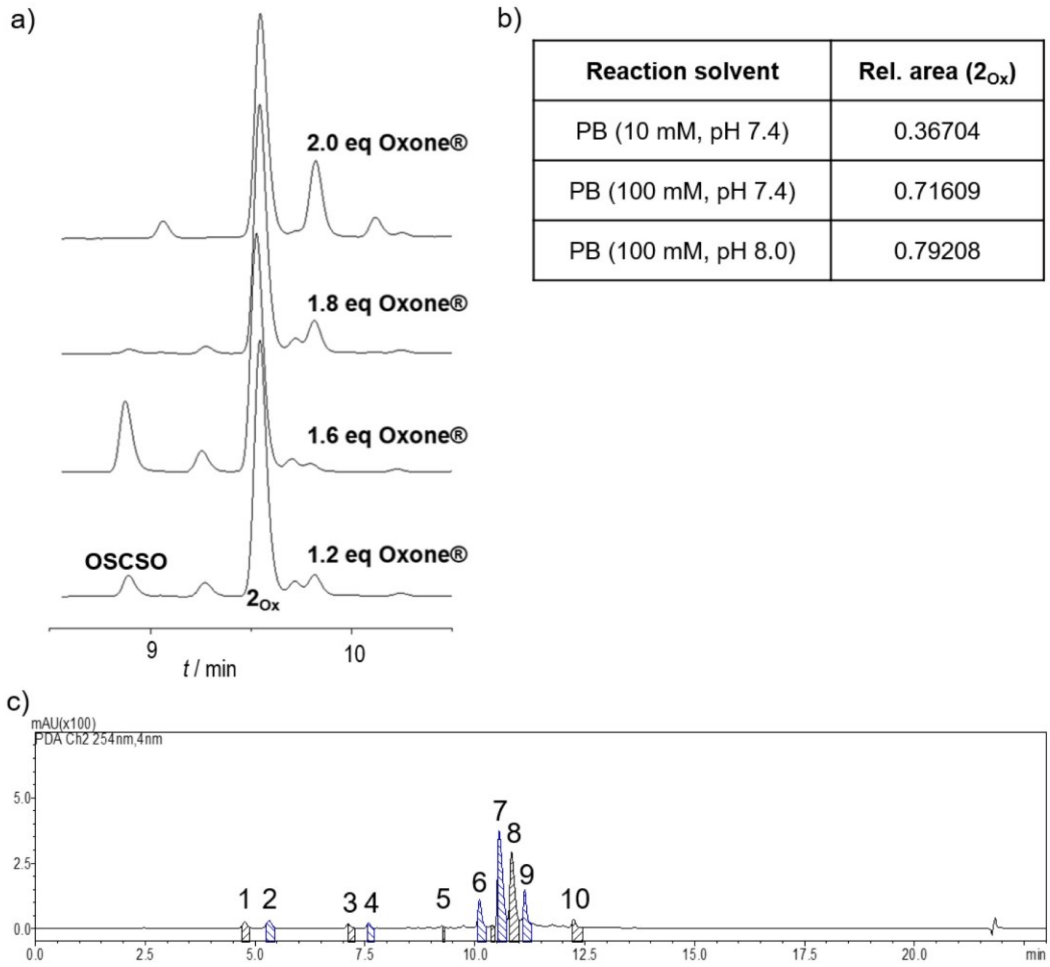

Reaction solvent	Rel. area (2_{Ox})
PB (10 mM, pH 7.4)	0.36704
PB (100 mM, pH 7.4)	0.71609
PB (100 mM, pH 8.0)	0.79208

Figure S 15: Oxidation reaction screening of OCSCO~BSCSB to 2Ox. (a) HPLC chromatograms of oxidation reaction using varying equivalents of potassium peroxymonosulfate (Oxone®). (b) Relative peak areas of 2Ox after 30 min reaction time in varying reaction solvents. Peak areas were normalized to the internal standard. c) Full HPLC-chromatogram of upscaled oxidation protocol with collected fractions (SI, Table S1).

(a) 50 µL of 2 mM solution of OSCSO in 100 mM PB, pH = 7.4 were mixed with 50 µL of 2 mM solution of BSCSB in 100 mM PB, pH = 7.4. The pH of the solution was checked and – if necessary – adjusted to 7.4 using 1M NaOH. The solution was added to 2 µL of Oxone® solution (60, 80, 90 and 100 mM, respectively) in 100 mM PB, pH = 7.4 to obtain a final Oxone® concentration of 1.2, 1.6, 1.8 and 2.0 mM (1.2, 1.6, 1.8 and 2.0 eq). Reaction solutions were diluted (10×, MeOH) and directly injected onto RP-HPLC. Addition of 1.8 eq of Oxone® led to the highest conversion while minimizing side products (Fig. S15).

(b) 47.7 µL of 2.16 mM solution of OSCSO in PB (10 mM, 100 mM pH = 7.4 or 100 mM, pH = 8.0) were mixed with 47.7 µL of 2.16 mM solution of BSCSB in PB (10 mM, 100 mM pH = 7.4 or 100 mM, pH = 8.0) and 1 µL of 50 mM Fmoc-Gly solution in DMSO was added as internal standard. The solution was stirred for 15 min and added to 3.6 µL of 50 mM Oxone® solution in PB (10 mM, 100 mM pH = 7.4 or 100 mM, pH = 8.0) to obtain a final Oxone® concentration of 1.8 mM. 10 µL aliquots of reaction solutions were injected onto RP-HPLC after 5, 30, 60 and 180 min. Higher buffer strength and pH of the reaction solutions led to the highest conversion (Fig. S15).

6. High performance liquid chromatography (HPLC) experiments and side product identification

Column: Agilent ZORBAX Eclipse XDB-C18 (4.6 × 250 mm, 5 µm, 100 Å) thermostated at 40° C

Flow rate: 2 mL/min

Solvents: 0.1% TFA in water (solvent A), 0.1% TFA in acetonitrile (solvent B) in a binary gradient

Gradient for tripeptides: 5% B for 1 min, 100% B in 10 min, 5% B in 1 min, 5% B for 6 min

Gradient for pentapeptides: 5% B for 1 min, 20% B in 9 min, 100% B in 6 min, 100% B for 1.5 min, 5% B in 0.5 min, 5% B for 4 min

All samples were prepared according to oxidation protocol described in point 4, except that vigorous vortexing was applied to the upscaled reaction mixture to induce more side product formation for their identification. All side products visible in the 254 nm UV-trace were collected. Isolated fractions from peaks 5-10 were analyzed using HR-ESI on WATERS SYNAPT G2-Si mass spectrometer. Peaks 1-4 were not analyzed due to the low quantity. Expected masses were calculated as doubly charged species unless otherwise noted based on their chemical formula with MassLynx V4.2.

Table S 1: HR-ESI(+)-MS of isolated side products.

Peak	Identification	Chemical formula	Calc. Mass	Obs. Mass
5	OSCSO	$C_{27}H_{36}N_6O_{11}S$	653.2241 $[M+H]^+$	653.2252
6	OSCSO≃OSCSO	$C_{54}H_{70}N_{12}O_{22}S_2$	652.2162 $[M+2H]^{2+}$	652.2174
7	BSCSB≃OSCSO (2Ox)	$C_{54}H_{72}B_2N_{12}O_{21}S_2$	664.2343 $[M+2H]^{2+}$	664.2361
8	YSCSB≃OSCSO	$C_{54}H_{71}BN_{12}O_{21}S_2$	650.2278 $[M+2H]^{2+}$	650.2302
9	YSCSY≃OSCSO	$C_{54}H_{70}N_{12}O_{20}S_2$	636.2214 $[M+2H]^{2+}$	636.2243
10	YSCSY≃YSCSY	$C_{54}H_{70}N_{12}O_{18}S_2$	620.2264 $[M+2H]^{2+}$	620.2277

7. Isothermal titration calorimetry

The calorimetric measurements were performed using a NanoITC Low Volume (TA Instruments, Eschborn, Germany) with an effective cell volume of 170 µL. In an experiment 50 µL of a BSCSB solution (0.1 mM in a 100 mM phosphate buffer, pH = 7.4 or 6.0) was titrated into a solution of OSCSO (0.016 mM in a 100 mM phosphate buffer, pH = 7.4 or 6.0). The experimental temperature was kept constant at 25 °C. Additionally the same amount of BSCSB solution was titrated into pure water to determine the heat of dilution for reference. As a control another sequence was checked for binding with L-tyrosines instead of L-DOPA and measured as before mentioned. The number and injected volume of the titration steps were the same for all measurements (25 × 2 µL). The spacing between injections was set to 300 s. The integrated reference heats were subtracted from the integrated heats of the adsorption experiments. An independent binding model was employed to fit the adsorption isotherms and obtain the association constant, (K_a), the reaction enthalpy (ΔH), the entropy (ΔS), the Gibbs free energy (ΔG) and reaction stoichiometry (n) (Freire, Mayorga, Straume, 1990; Lewis, Murphy, 2005). The measurements were carried out by triplicate, showing the mean value together the standard deviation for each parameter. Nano Analyze Data Analysis software from TA Instruments was used for the data evaluation of the ITC measurements (Software version 2.5.0) form TA Instruments.

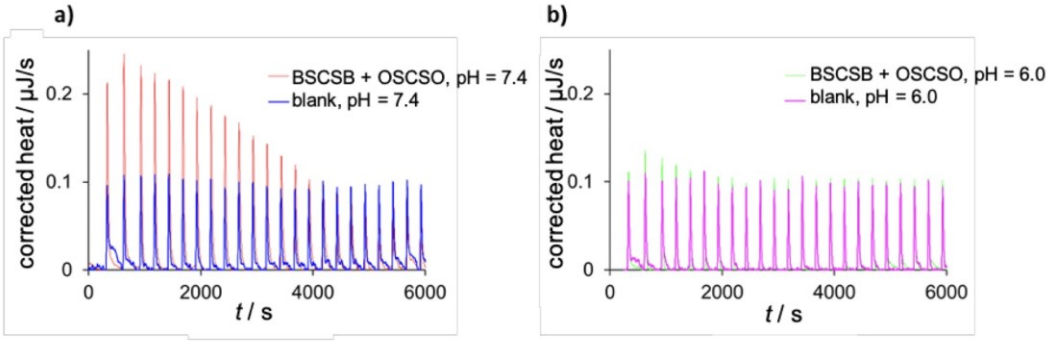

Figure S 16: ITC titrations performed at a) pH = 7.4 and b) 6.0, showing the heat rate signals after base line correction. No heat change different from the dilution (blank) was detected for pH = 6.0.

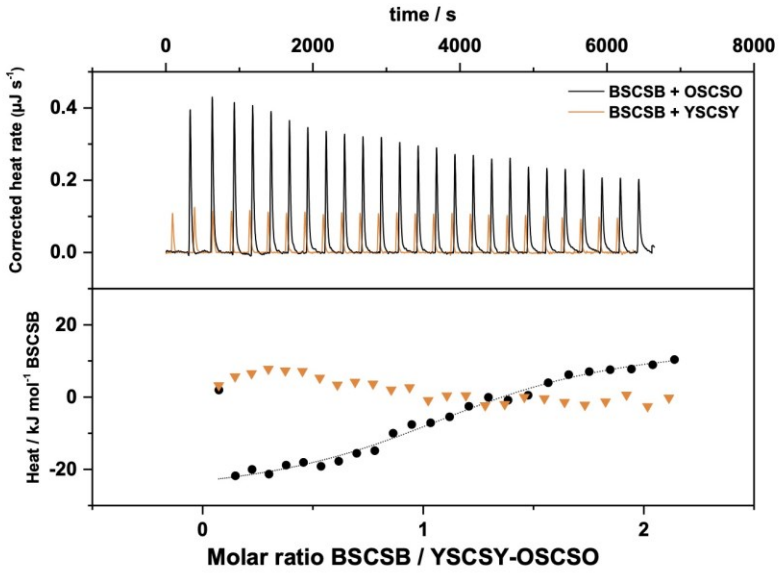

Figure S 17: ITC titrations performed at pH 7.4 with YSCSY and OSCSO as ligands in comparison. Only for OSCSO a significant heat change resulting in a sigmoidal binding curve was detected..

8. Redox cycling experiment

To determine the responsiveness to redox triggers $\mathbf{2_{Red}}$ was subjected to one full redox cycle. First, 75 µL of a 4 mM solution of BSCSB and OSCSO were prepared in 200 mM PB at pH 7.44. The higher buffer strength is to compensate the acidity of Oxone and TCEP. These two solutions were mixed and 10 µL were taken out and diluted with 10 µL MilliQ water and injected into RP-HPLC (Agilent ZORBAX Eclipse XDB-C18 (9.4 × 250 mm, 5 µm, 100 Å) thermostated at 40° C)(Cycle 0). Then 1.8 eq. Oxone were added and gently mixed. Another aliquot was taken out and treated as before (Cycle 1). After that the mixture was treated with 1.7 eq. TCEP and another chromatogram was taken. The reduction was not completed so the batch was split into two and one half was treated with another equivalent of TCEP (Cycle 2). Thereafter, the other half was treated with 2.5 eq. of Oxone and treated as before mentioned (Cycle 3). Furthermore, each cycle was also injected into LCMS to confirm fractions with ESI-MS.

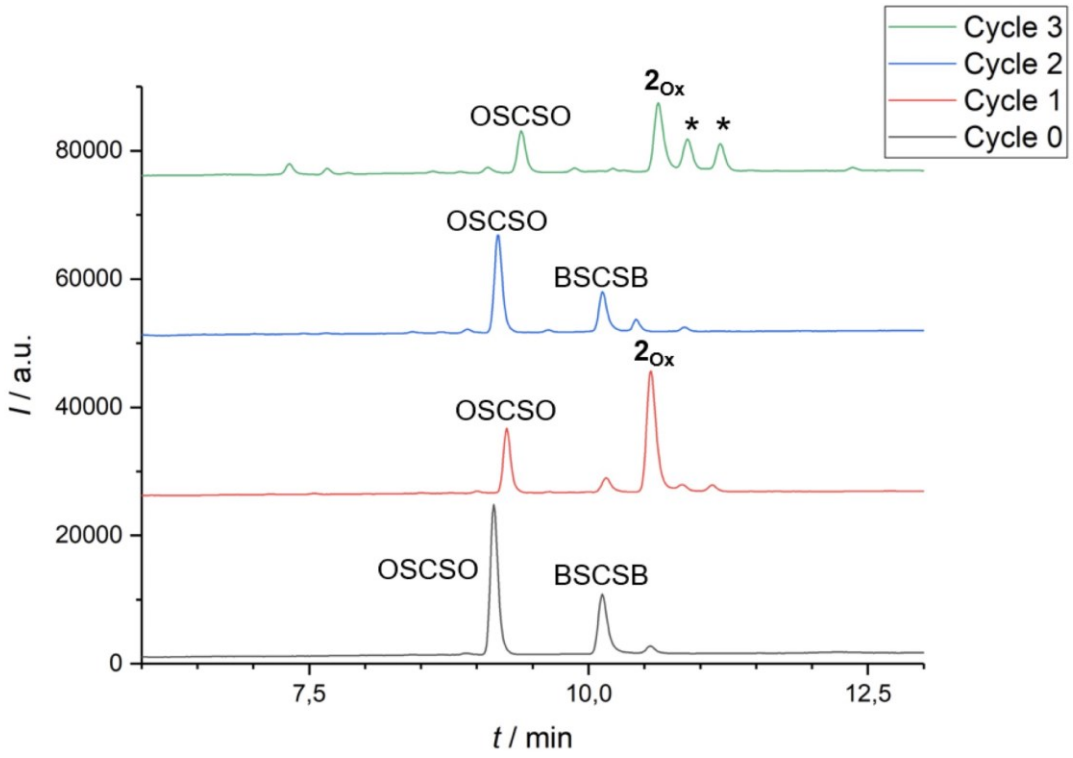

*Figure S 18: Chromatograms of the redox cycling experiment. * denotes side product.*

The first oxidation proceeds with nearly no side products as well as the reduction with 2.7 eq. TCEP to recover starting materials, OSCSO and BSCSB. The second oxidation shows considerable side product formation but we observed formation of $\mathbf{2_{Ox}}$ again.

9. Stability studies in serum mimicking media

BSCSB≃OSCSO was dissolved in 1 × PBS buffer with 10 % fetal calf serum (FCS) at a concentration of 1 mg/mL and incubated at 37 °C. 10 µL aliquots were taken at intervals of 1 day. Thereafter 90 µL of MeOH containing 20 ppm of Fmoc-Phe as an internal standard (Int. std.) was added to remove large proteins and the solution was centrifuged at 13.0 rpm for 30 min at 0°C. 10 µL of the supernatant was used for HPLC-MS analysis. Experiments were performed in triplicates. Blank consisting of 10 µL 1 × PBS buffer with 10 % fetal calf serum (FCS) treated the same way as the sample was used as a negative control. HPLC-MS analysis was performed on a Shimadzu LC-MS 2020 equipped with an electrospray ionization source and a SPD-20A UV-Vis detector (Shimadzu, Duisburg, Germany).

Column: Kinetex EVO C18 (50 × 2.1 mm, 2.6 µm, 100 Å) thermostated at 40° C

Flow rate: 0.4 mL/min

Solvents: 0.1% FA in water (solvent A), 0.1% FA in acetonitrile (solvent B) in a binary gradient

Gradient: 5%B for 1 min, 70% B in 11 min, 95% B in 1 min, 95% B for 1 min, 5% B in 0.01 min, 5% B for 4 min

Decay of BSCSB≃OSCSO was observed simultaneously by UV detection at 214 nm and MS. The amount of BSCSB≃OSCSO in each sample was determined as a ratio of the integration of the UV peak of BSCSB≃OSCSO to the internal standard. The data were plotted as mean ± SEM.

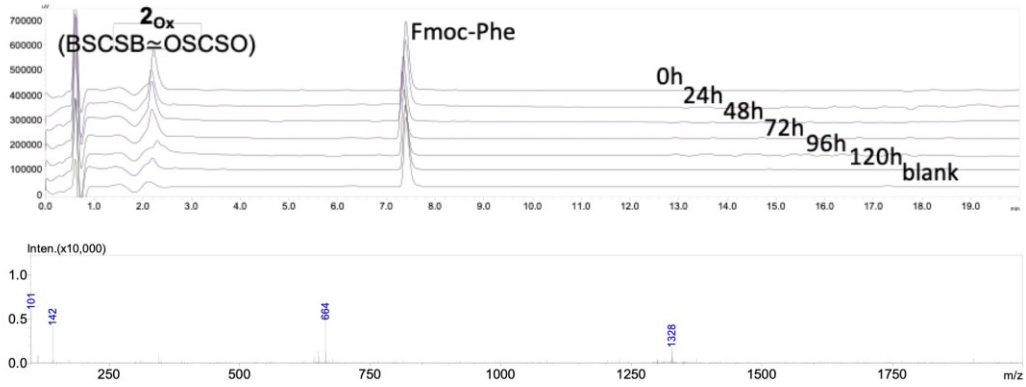

Figure S 19: Chromatograms for BSCSB≃OSCSO aliquoted daily for 5 days and a negative control together with internal standard (Fmoc-Phe). LC-ESI-MS: m/z = 664 $[M+2H]^{2+}$, 1328 $[M+H]^{+}$ (calc. 664.23 $[M+2H]^{2+}$, 1327.46 $[M+H]^{+}$, chemical formula: $C_{54}H_{72}B_2N_{12}O_{22}S_2$).

10. Stability in glucose solution and low glucose cell media

2_{ox} (1 mM) was incubated at 20 °C in glucose solution (GS, 1 g/ml) and DMEM low glucose cell media (LGM) with 10% FCS. 20 µL Aliquots were taken out and diluted with 80 µL MeOH with 20 ppm Fmoc-Phe and 0.1% FA, then spinned down and 80 µL of the clear supernatant solution was taken out and half was injected into HPLC-MS. The time points were taken each day.

HPLC-MS analysis was performed on a Shimadzu LC-MS 2020 equipped with an electrospray ionization source and a SPD-20A UV-Vis detector (Shimadzu, Duisburg, Germany).

Column: Kinetex EVO C18 (200 × 2.1 mm, 2.6 µm, 100 Å) thermostated at 40 °C

Flow rate: 0.4 mL/min

Solvents: 0.1% FA in water (solvent A), 0.1% FA in acetonitrile (solvent B) in a binary gradient

Gradient: 5% B for 1 min, 20% B in 11 min, 95% B in 1 min, 95% B for 1 min, 5% B in 0.01 min, 5% B for 4 min

SIM (m/z): 1328, 664, 388

The UV (280 nm) signals were integrated and normalized against the Fmoc-Phe standard as well as the SIM for 664 against the SIM of 388. The relative area was then plotted against the incubation time.

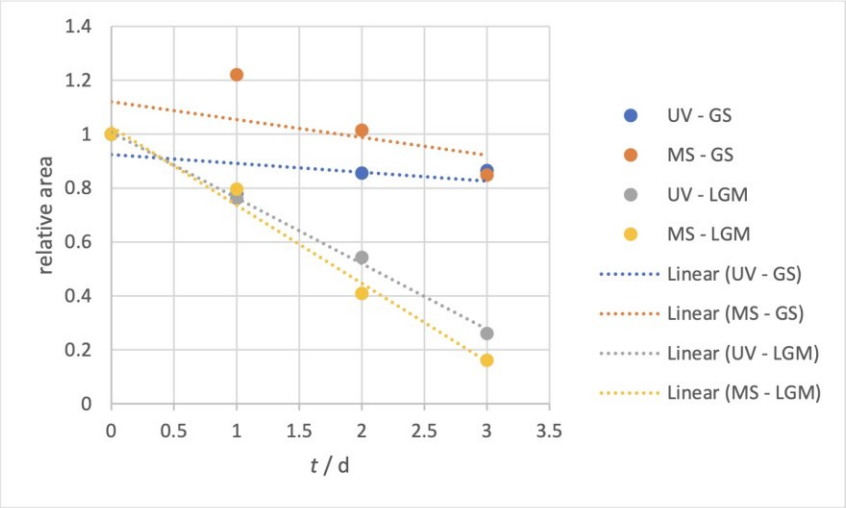

Figure S 20: Stability of $\mathbf{2_{ox}}$ in glucose solution (GS) and low glucose cell media (LGM) detected by UV-Vis and ESI-MS.

$\mathbf{2_{Ox}}$ remains nearly stable in glucose solution whereas it dissociates gradually in cell media, which was expected due to free thiols in the media (FCS and cysteine).

11. Stability in cytosol under oxidative/reductive conditions

Stability in liver cytosol

A solution of BSCSB≃OSCSO of 1 mg ml^{-1} was prepared in 150 µL liver cytosol in an Eppendorf TM tube. The solution was incubated at 37 °C while gentle shaking was applied. In well defined time intervals 10 µL sample was taken out and precipitated 90 µL ice cold methanol with 20 ppm Fmoc-Phe as an internal standard. Then the sample was centrifuged with a tabletop microcentrifuge at maximum speed (4000 rpm). 80 µL of the clear supernatant was transferred into an LC-MS vial and 25 µL were injected into the LC-MS. To deal with the delay caused by the measuring time of 20 min, the samples were stored in liquid nitrogen and directly thawed before injection.

HPLC-MS analysis was performed on a Shimadzu LC-MS 2020 equipped with an electrospray ionization source and a SPD-20A UV-Vis detector (Shimadzu, Duisburg, Germany).

Column: Kinetex EVO C18 (50 × 2.1 mm, 2.6 µm, 100 Å) thermostated at 40 °C

Flow rate: 0.4 mL/min

Solvents: 0.1% FA in water (solvent A), 0.1% FA in acetonitrile (solvent B) in a binary gradient

Gradient: 5% B for 1 min, 70% B in 11 min, 95% B in 1 min, 95% B for 1 min, 5% B in 0.01 min, 5% B for 4 min

SIM (m/z): 1328, 664

Time points	Time [min]
T_0	0
T_1	20
T_2	40
T_3	60
T_4	120
T_5	240
T_6	480

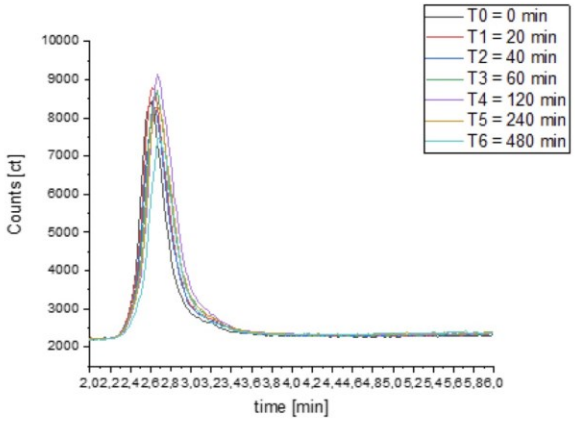

Figure S 21: Time points and SIM(664)-trace for the stability in liver cytosol.

Stability under reductive conditions

The liver cytosol was spiked with glutathione and the corresponding disulfide in a ratio of 40:1. Two different concentrations were used to mimic cancer cell and healthy cell conditions with 10 mM and 1 mM respectively. With this medium a 1 mM solution of BSCSB≃OSCSO was prepared and treated as mentioned above with different time points shown in Fig S10.

Time points	Time [min]
T_0	0
T_1	5
T_2	10
T_3	15
T_4	20
T_5	30
T_6	40
T_7	60

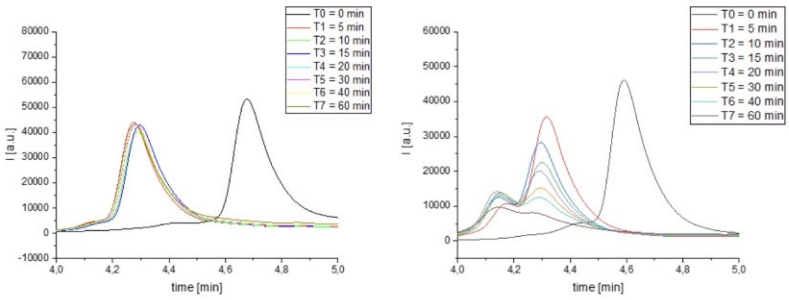

Figure S 22: Time points and SIM(664)-traces for the stability in liver cytosol under reductive conditions for 1 mM and 10mM GSH concentrations respectively.

Stability under oxidative conditions

A 1 mM solution of BSCSB≃OSCSO in ammonium bicarbonate containing 0.1% hydrogen peroxide (30 μM) was prepared and treated as before mentioned.

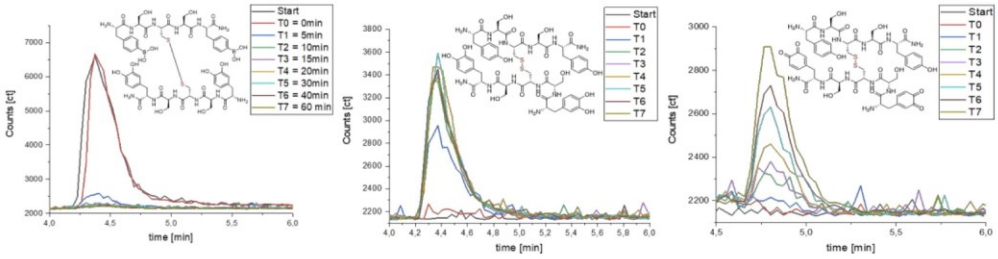

Figure S 23: SIM(664)-trace, SIM(1271)-trace, SIM(1267)-trace.

12. Fluorescence quenching assay

Four stock solutions were prepared: 5 mM OSCSO, 2 μM DL488-BSCSB in a phosphate buffer (100 mM, pH = 6.0, 2.5 mM TCEP) and 5 mM OSCSO, 2 μM DL488-BSCSB in a phosphate buffer (100 mM, pH = 7.4, 2.5 mM TCEP). OSCSO peptide was diluted in a series (1:1) 15 times to obtain concentration ranging from 5 mM down to 76 nM. Each of 16 samples from the series were mixed 1:1 with DL488-BSCSB stock solution and loaded into standard treated capillaries. FQA was measured immediately.

The procedure was repeated 3 times both for pH 6.0 and 7.4. Each point on the graph represents mean average of normalized fluorescence for one concentration from the series and error bars represent standard errors of the mean.

Binding of DL488-BSCSB by OSCSO was detected with $K_d = 1.8 \pm 0.4$ μM at pH = 7.4. Decreasing pH to 6.0 increases binding constant by over 2 orders of magnitude proving pH responsiveness of the binding.

13. ^{1}H-NMR experiments: TOCSY, DOSY

For the NMR analysis, all peptide samples used for this study were dissolved in 600μl 90% H_2O/10% D_2O yielding a typical concentration of 2 mM.

The NMR spectra were recorded on a Bruker AVANCE III 850 MHz spectrometer with a 5 mm triple resonance TXI 1H/13C/15N probe equipped with a z-gradient. All spectra were measured at 298 K. The spectra were analyzed using Bruker TopSpin 3.6.1.

For ^{1}H NMR measurements 512 scans were collected at a 17006.803 Hz (20 ppm) spectral width together with a recycling delay of 2 s and water suppression using watergate W5 pulse sequence with gradients using

double echo and an acquisition time of 1 s (Liu, Mao et al. 1998). The ^{1}H 90° pulse was calibrated for each sample individually and was used for further measurements.

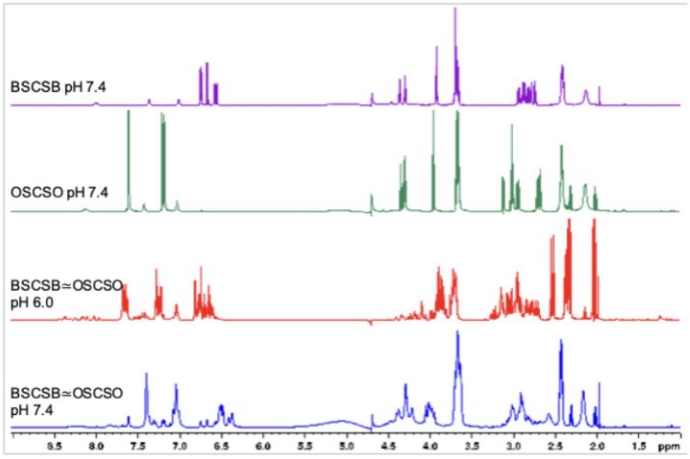

Figure S 24: Comparison of ^{1}H NMR of single tags at pH 7.4 and BSCSB≃OSCSO both at pH 6.0 and 7.4.

DOSY (Diffusion Ordered Spectroscopy) experiments were executed using stimulated echo using bipolar gradient pulses for diffusion using 1 spoil gradient water suppression using 3-9-19 pulse sequence with gradients. In these experiments we used 32 gradient steps from 2 % to 100 % with a total gradient strength of 53 G/cm. The diffusion time d20 was optimized to 80 ms and the gradient length p30 was kept at 1.6 ms.

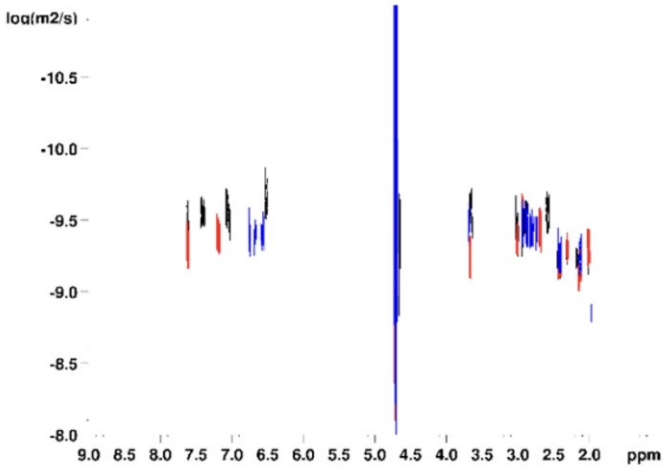

Figure S 25: DOSY for single peptides (red – BSCSB, blue – OSCSO) and BSCSB~OSCSO (black) at pH 7.4.

TOCSY (Braunschweiler and Ernst, 1983; Bax and Davis, 1985) spectra were collected using 256 t1 increments and spectral widths of 12000 Hz in both dimensions. Acquisition times were set to 1.38 s, relaxation delays were 2 s and spin-lock (MLEV-17) mixing times were 80 ms. The spin-lock pulse width (90°) was 20 µs and the trim pulses were set to 2.5 ms.

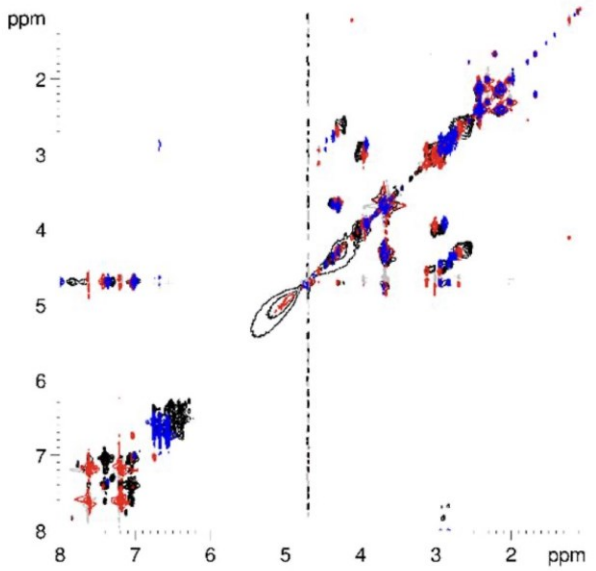

*Figure S 26: ^{1}H-^{1}H TOCSY spectra for the single peptides **BSCSB** in red, **OSCSO** in blue, and the **BSCSB≃OSCSO** conjugate in black in phosphate buffer, with 1 mM TCEP at pH 7.4.*

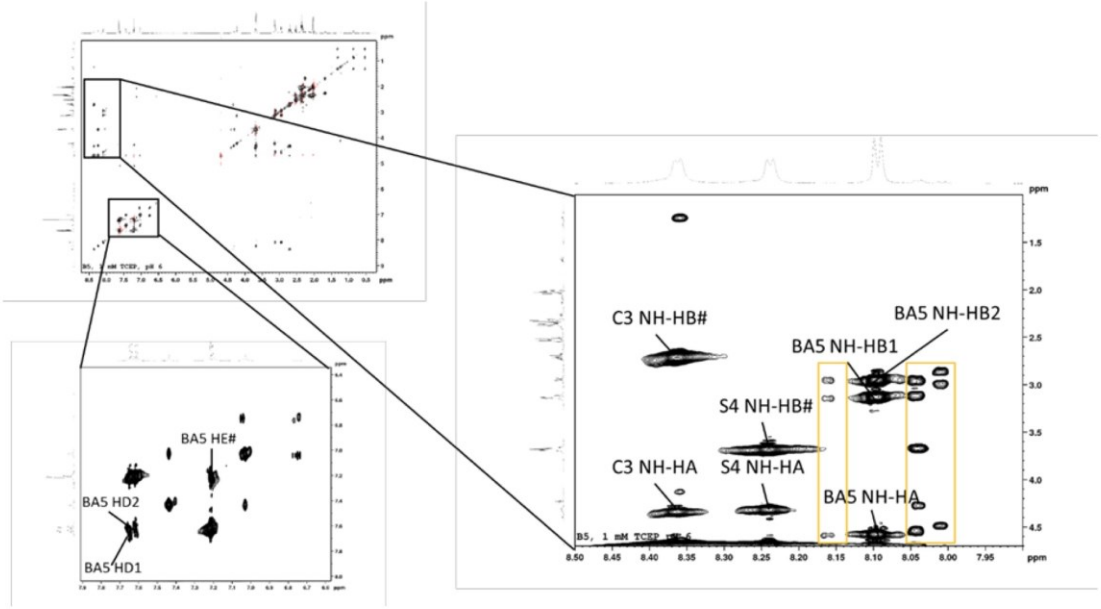

Figure S 27: ^{1}H-^{1}H TOCSY signal assignment for BSCSB

Table S 2: Proton assignments for a) BSCSB and b) OSCSO sequences.

a)

Group	Atom	Nuc	Shift
BA1	HA	1H	4.229
BA1	HB#	1H	3.144
S2	HA	1H	4.394
S2	HB#	1H	3.693
C3	HA	1H	4.335
C3	HB#	1H	2.711
C3	HN	1H	8.362
S4	HA	1H	4.314
S4	HB#	1H	3.680
S4	HN	1H	8.239
BA5	HA	1H	4.572
BA5	HB1	1H	3.129
BA5	HB2	1H	2.946
BA5	HD1	1H	7.643
BA5	HD2	1H	7.613
BA5	HE#	1H	7.214
BA5	HN	1H	8.099

b)

Group	Atom	Nuc	Shift
CAT1	HA	1H	4.162
CAT1	HB#	1H	2.99
S2	HA	1H	4.417
S2	HB#	1H	3.699
C3	HA	1H	4.4
C3	HB#	1H	2.79
C3	HN	1H	8.377
S4	HA	1H	4.328
S4	HB#	1H	3.712
S4	HN	1H	8.323
CAT5	HA	1H	4.473
CAT5	HB1	1H	2.945
CAT5	HB2	1H	2.831
CAT5	HD1	1H	6.784
CAT5	HD2	1H	6.745
CAT5	HE	1H	6.595
CAT5	HN	1H	7.954

14. Density functional theory calculations

Computational details

Conformational analysis with molecular mechanics (MM) was performed with Schrödinger Maestro 11.8[1], using the force field OPLS3e[2], solvent water, and the default method built in the program.

Density functional theory (DFT) calculations were performed using the Gaussian 09 software package[3] and structural representations were generated with *CYLview*[4]. All the geometry optimizations were carried out using the standard B3LYP functional and the valence double-zeta 6-31G(d) basis set. All of the optimized geometries were verified by frequency computations as minima (zero imaginary frequencies). Single-point energy calculations on the optimized geometries were then evaluated using the hybrid meta-GGA functional M06-2X developed by Truhlar and co-workers[5] and the valence triple-zeta Def2-TZVPP basis set, with solvent effects (water) calculated by means of the Polarizable Continuum Model (PCM) initially devised by Tomasi and co-workers,[6-9] with radii and non-electrostatic terms of the SMD solvation model, developed by Truhler and co-workers.[10] Thermal corrections were calculated from the unscaled vibrational frequencies at the B3LYP/6-31G(d) level on the optimized geometries. Entropic contributions to the reported free energies were calculated from partition functions evaluated using Truhlar's quasiharmonic (qh) approximation.[11] This method uses the same approximations as the usual harmonic one except that all vibrational frequencies lower than 100 cm^{-1} are set equal to 100 cm^{-1}.

Distortion/interaction analysis was performed by single-point energy calculations on the separated single peptides at the M06-2X/def2-TZVPP/PCM(SMD,water) level of theory. The structures of the separated peptides were obtained using the following protocol: 1) separation of the peptides of **2_{Ox} parallel** and **2_{Ox} antiparallel**, 2) addition of missing atoms (O and H) to complete the structures, 3) optimization at B3LYP/6-31G(d) level freezing all the original atoms i.e., except the atoms added in 2).

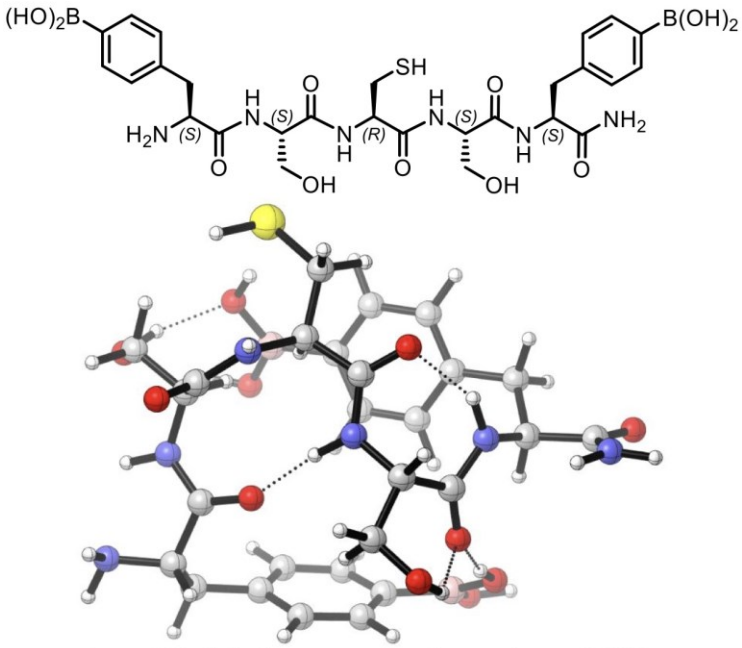

Figure S 28: Skeletal structure and low-lying conformer of BSCSB.

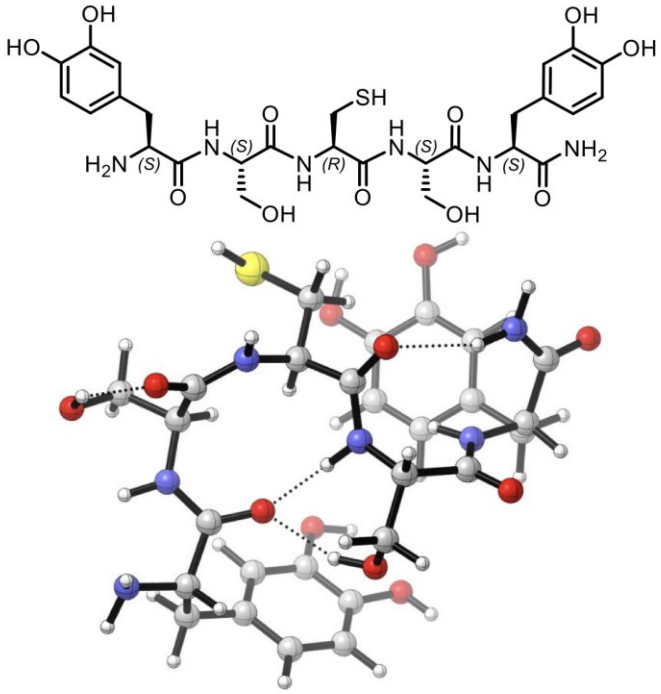

Figure S 29: Skeletal structure and low-lying conformer of OSCSO.

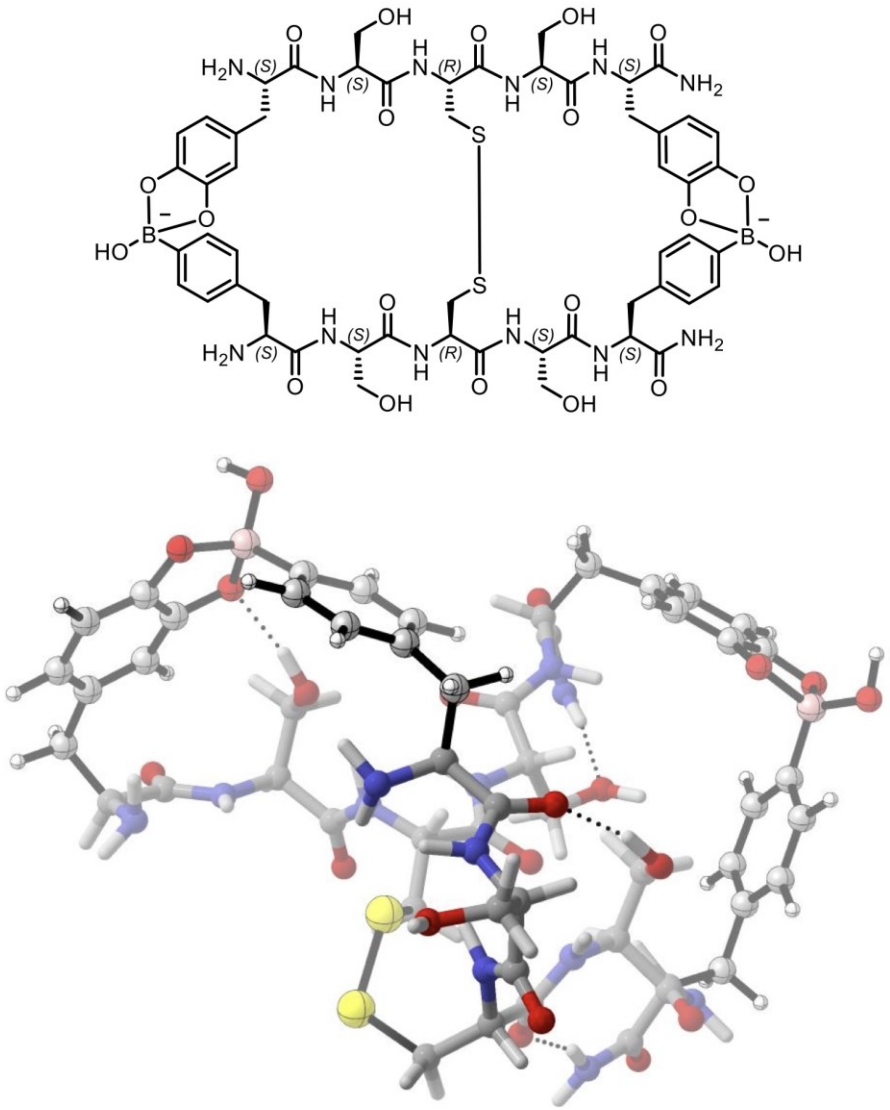

Figure S 30: Structure of the low-lying conformation of 2_{Ox} with a parallel topology (overall charge 2−).

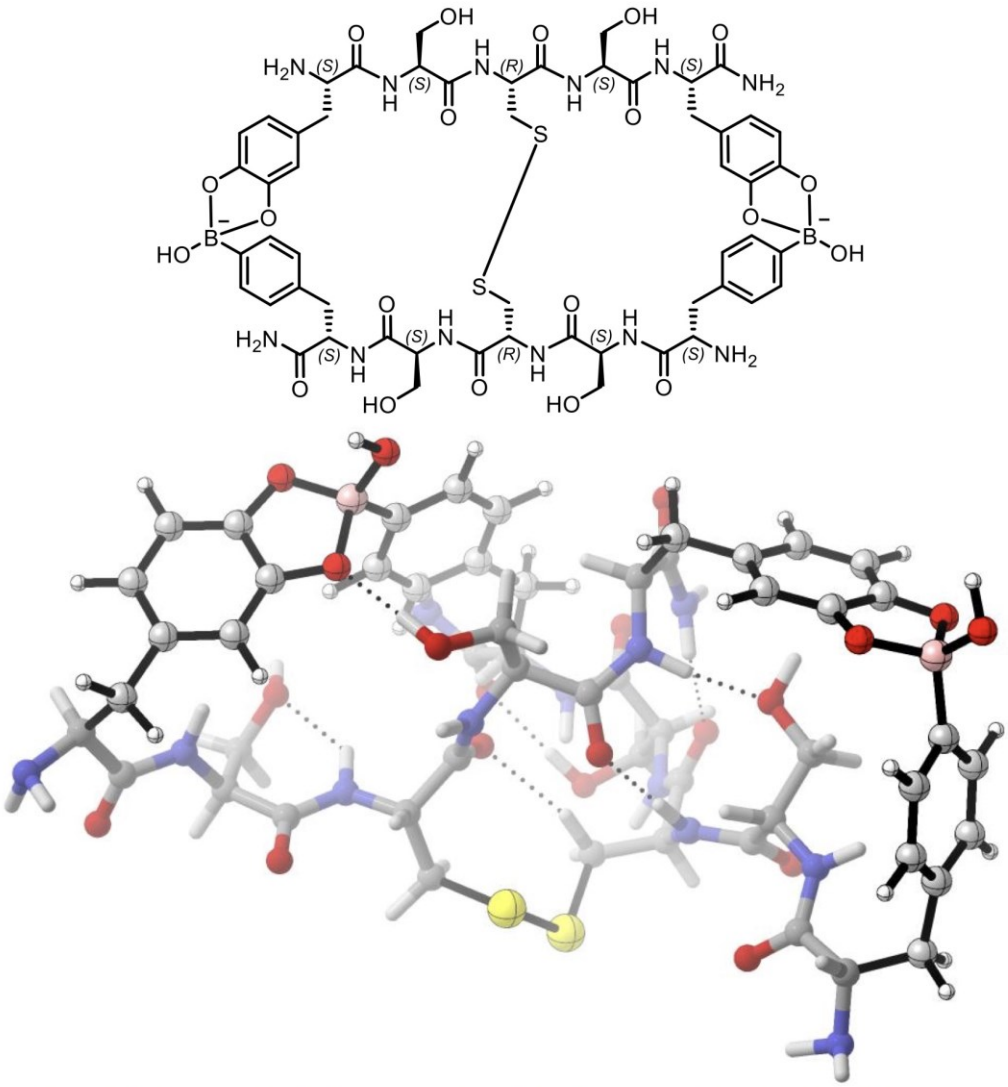

Figure S 31: Structure of the low-lying conformation of 2_{Ox} with an antiparallel topology (overall charge 2−).

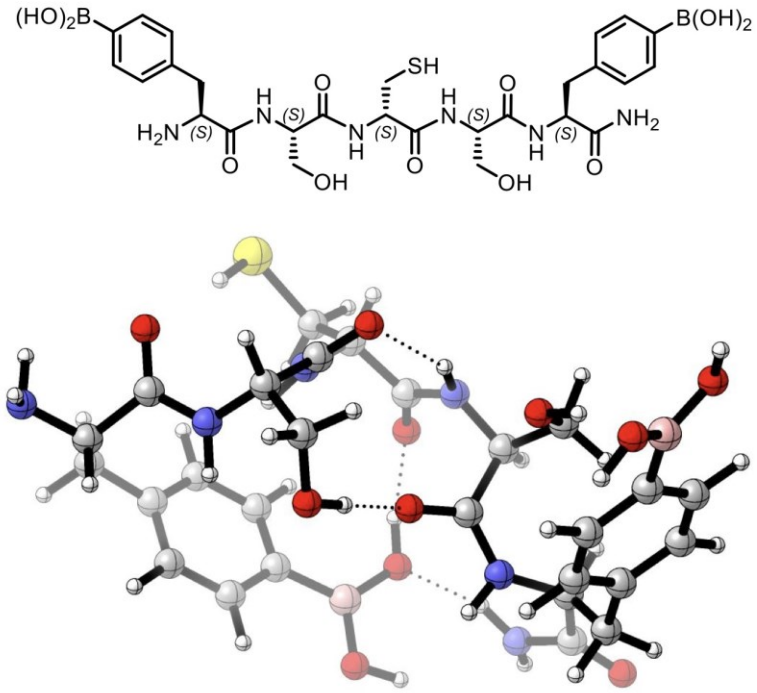

Figure S 32: Skeletal structure and low-lying conformer of BScSB.

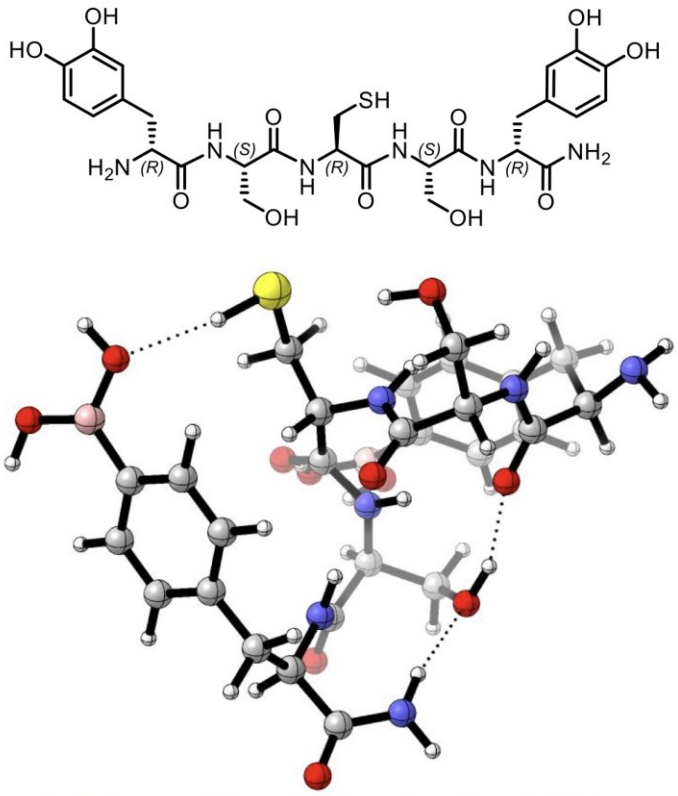

Figure S 33: Skeletal structure and low-lying conformer of bSCSb.

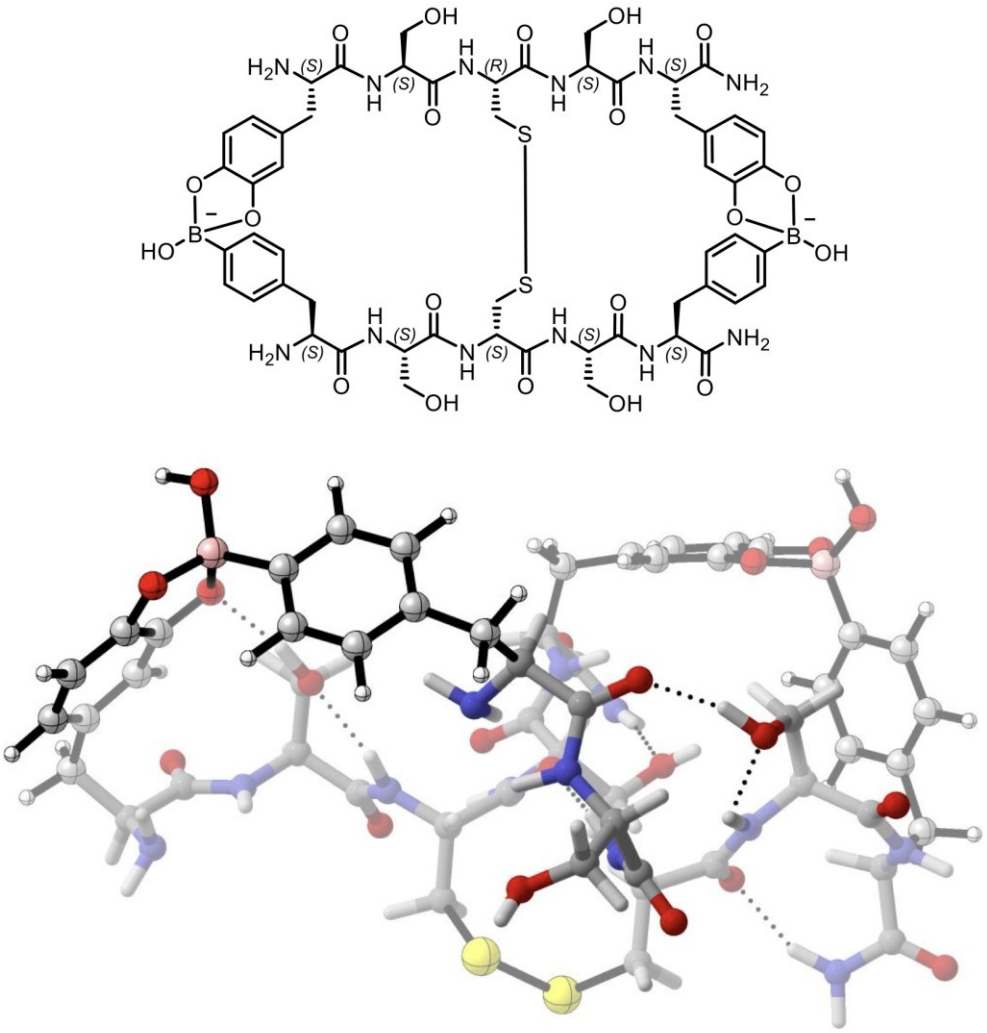

Figure S 34: Structure of BScSB≃OSCSO with a parallel topology (overall charge 2−).

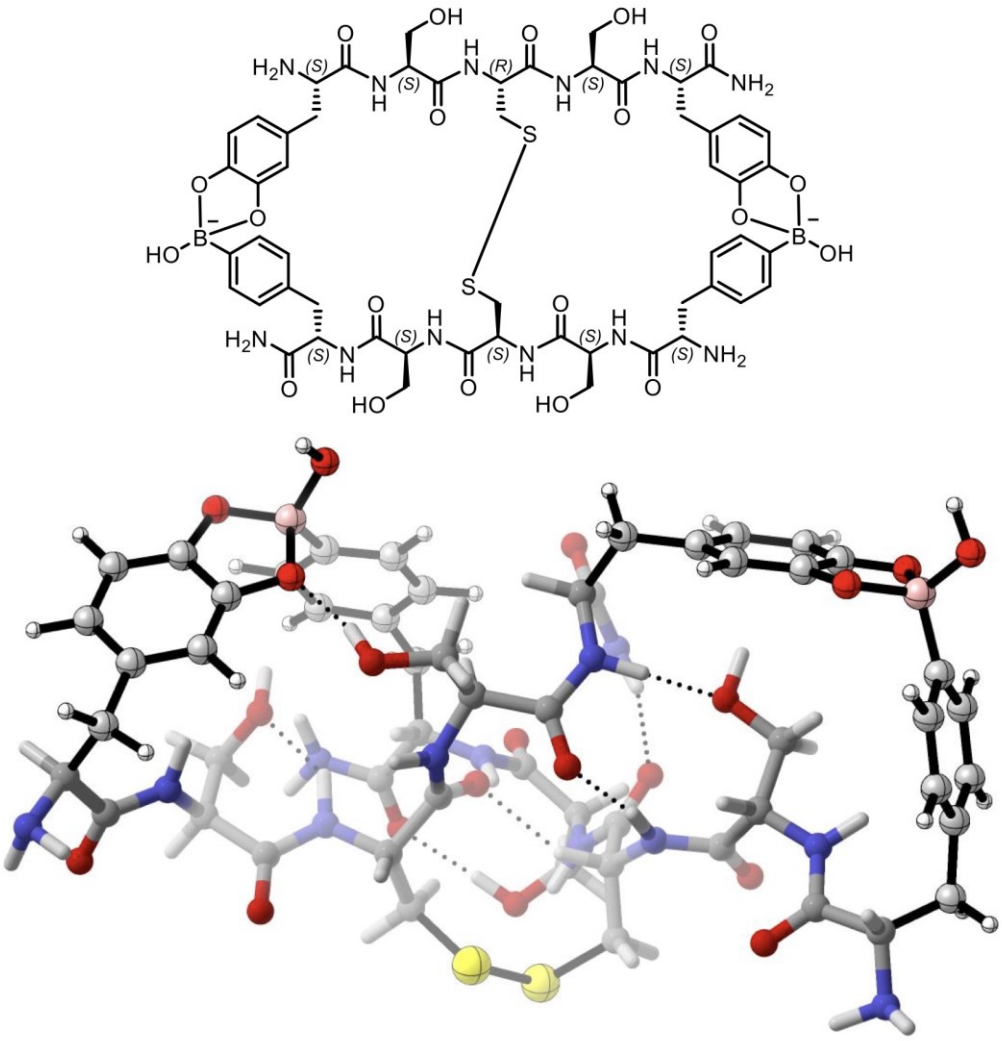

Figure S 35: Structure of BScSB≃OSCSO with an antiparallel topology (overall charge 2−).

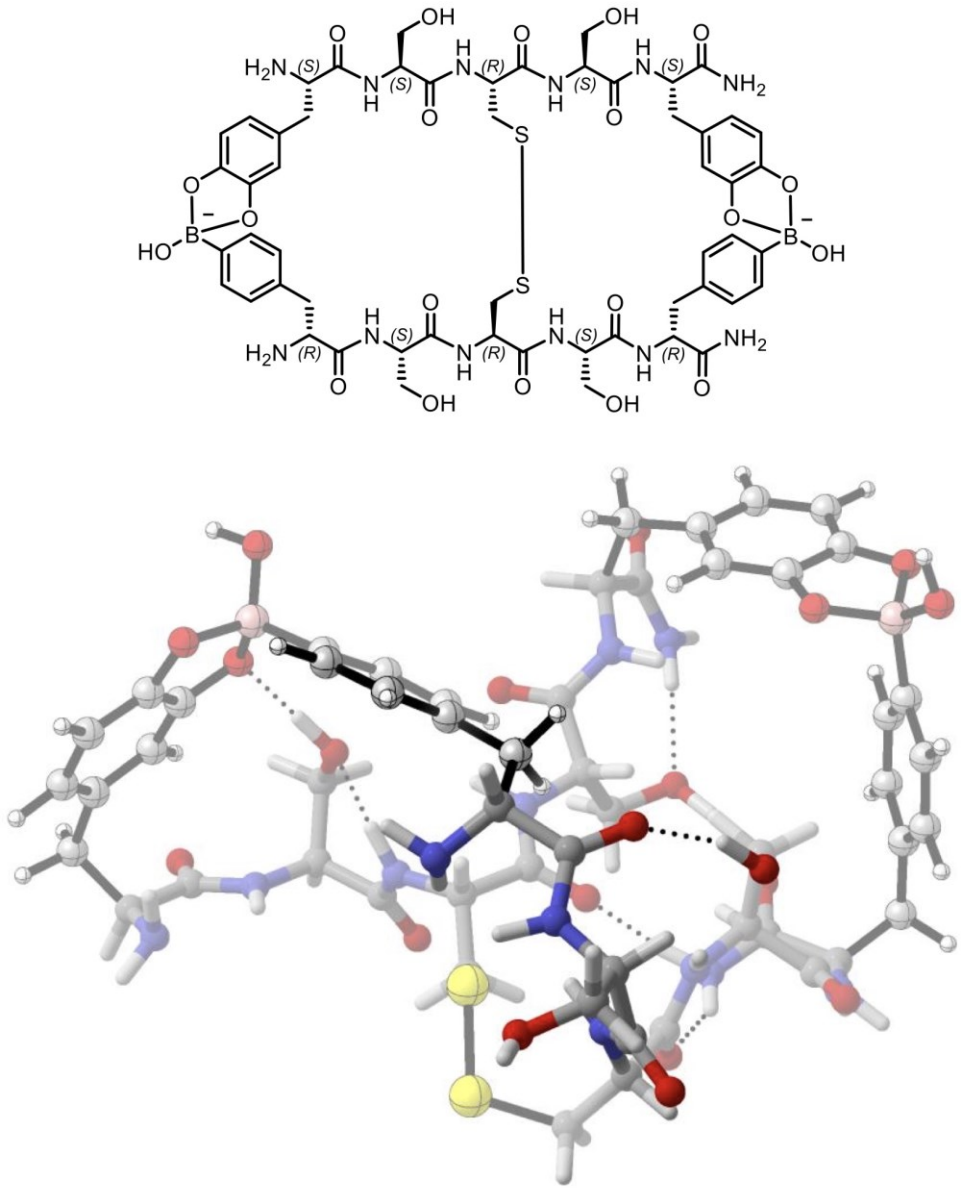

Figure S 36: Structure of bSCSb≃OSCSO with a parallel topology (overall charge 2−).

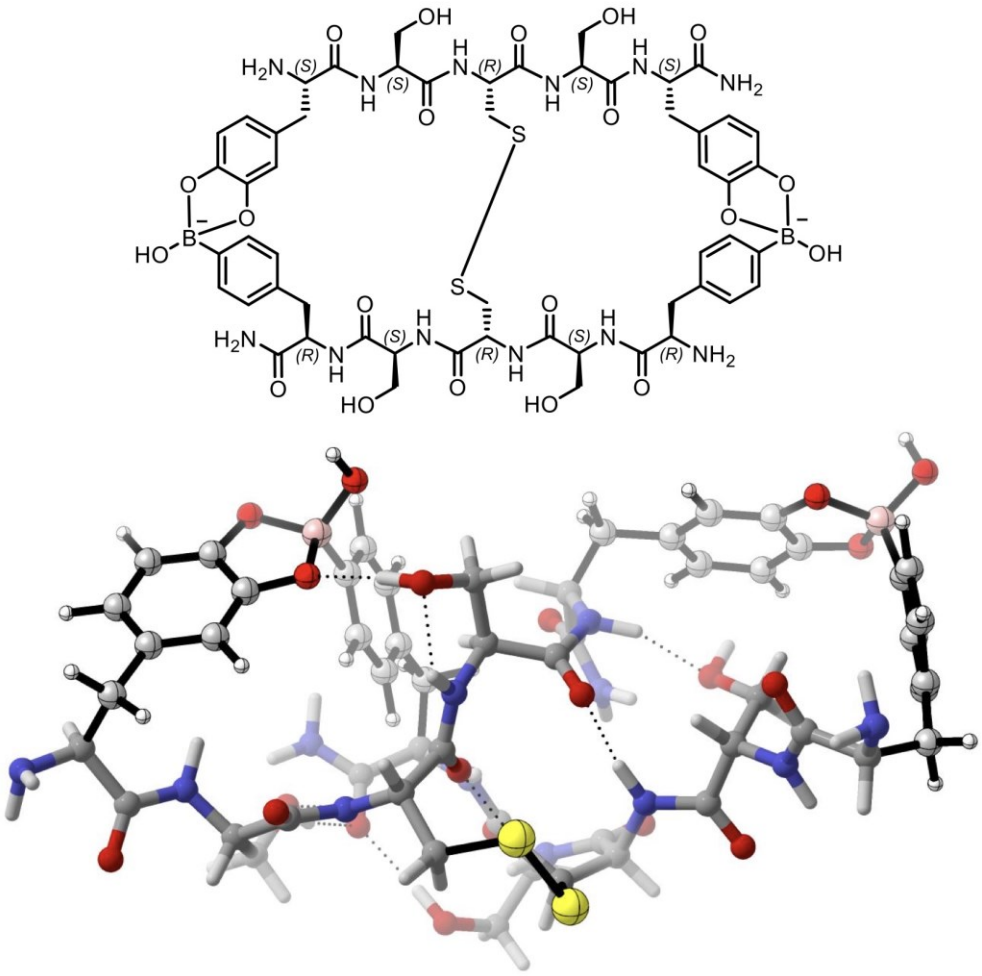

Figure S 37: Structure of bSCSb≃OSCSO with an antiparallel topology (overall charge 2−).

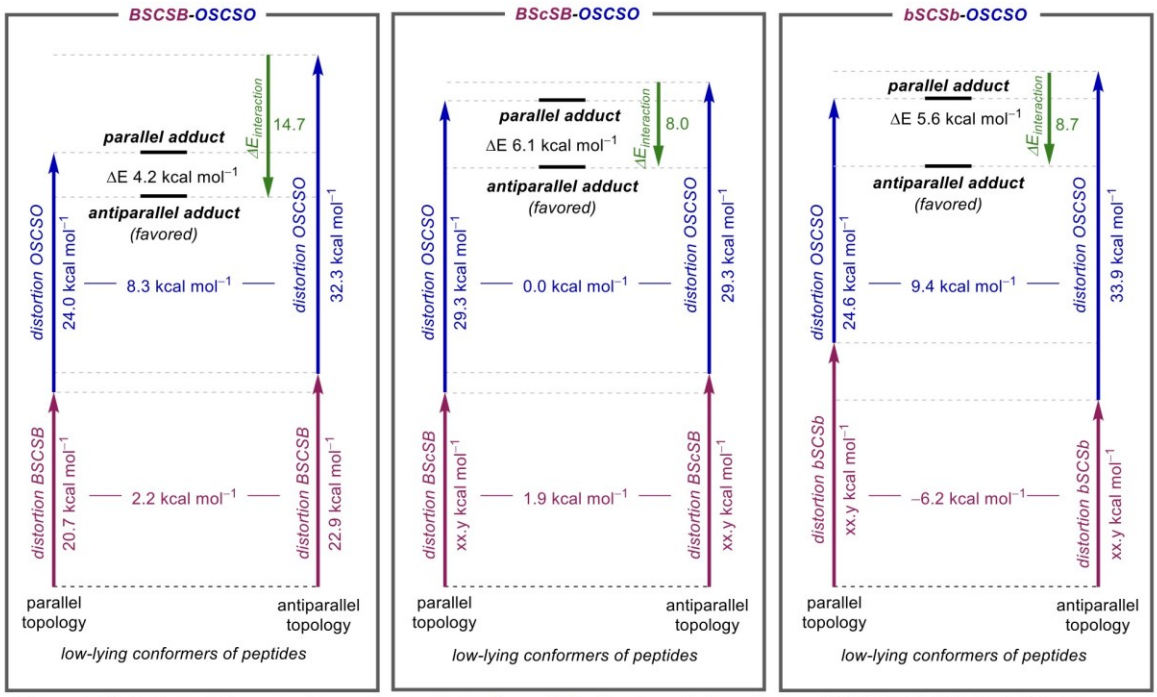

*Figure S 38: Individual distortion/interaction analysis of parallel and antiparallel topologies of BSCSB-OSCSO (**2**$_{OS}$), BScSB-OSCSO and bSCSb-OSCSO. Antiparallel topology is favored for all three cases.*

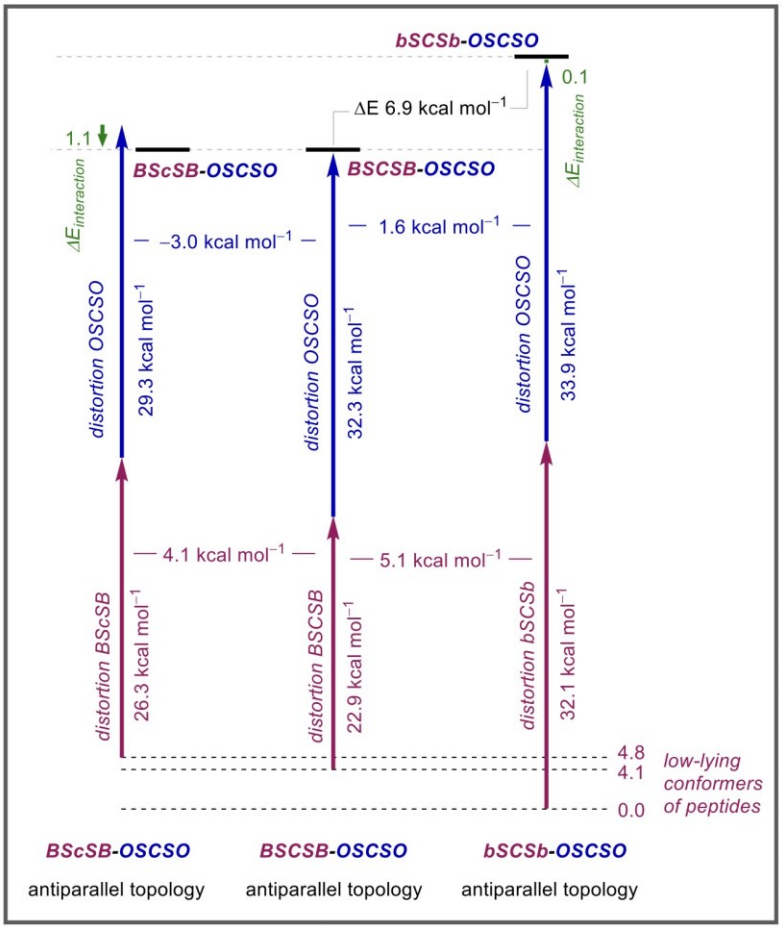

Figure S 39: Distortion/interaction analysis of antiparallel topologies of BScSB-OSCSO and bSCSb-OSCSO relative to BSCSB-OSCSO (2_{OX}). Interaction energies are similar in all three cases. Difference in the overall electronic energies arises from different distortion energies of the peptides.

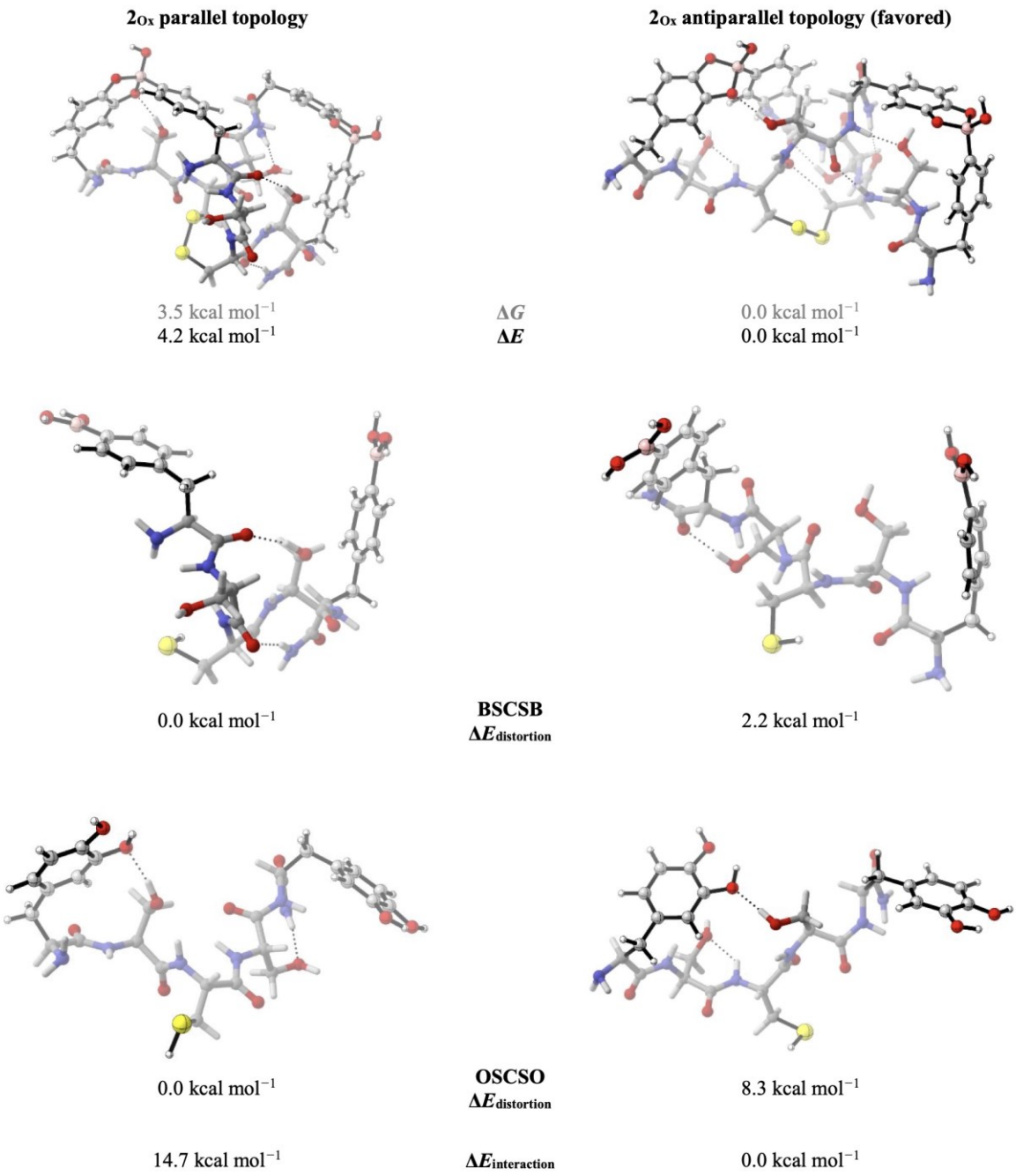

Figure S 40: Distortion/interaction analysis of the low-lying conformations of parallel and antiparallel topologies. Distortion energy of the structures of BSCSB and OSCSO is greater when adopting an antiparallel topology. However, the higher energy of interaction in this topology (as a result of several simultaneous non-covalent interactions), makes this antiparallel topology favored over the parallel topology.

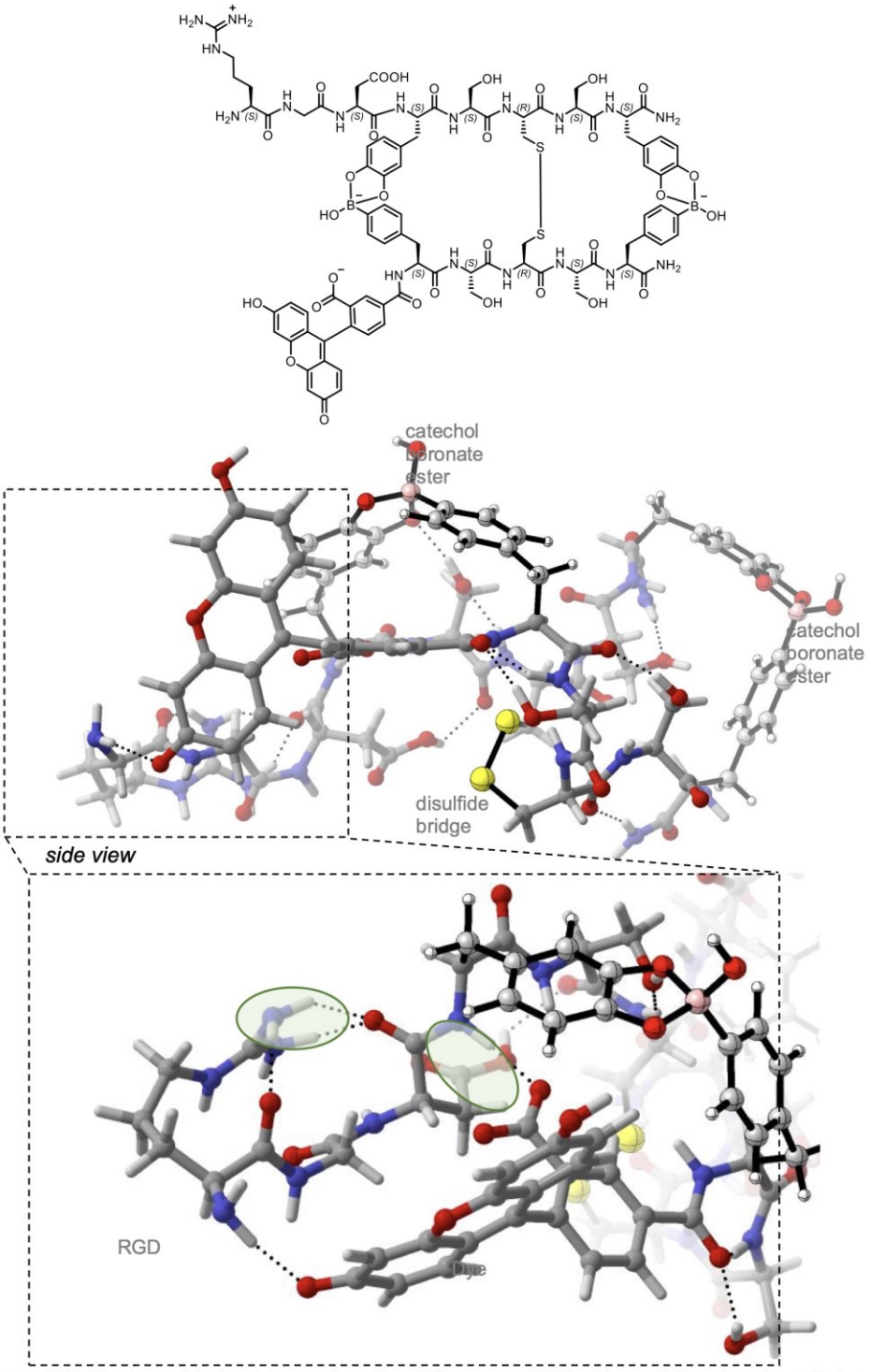

Figure S 41: Structure of the low-lying conformation of fluorescein≃RGD with parallel topology (overall charge 2−).

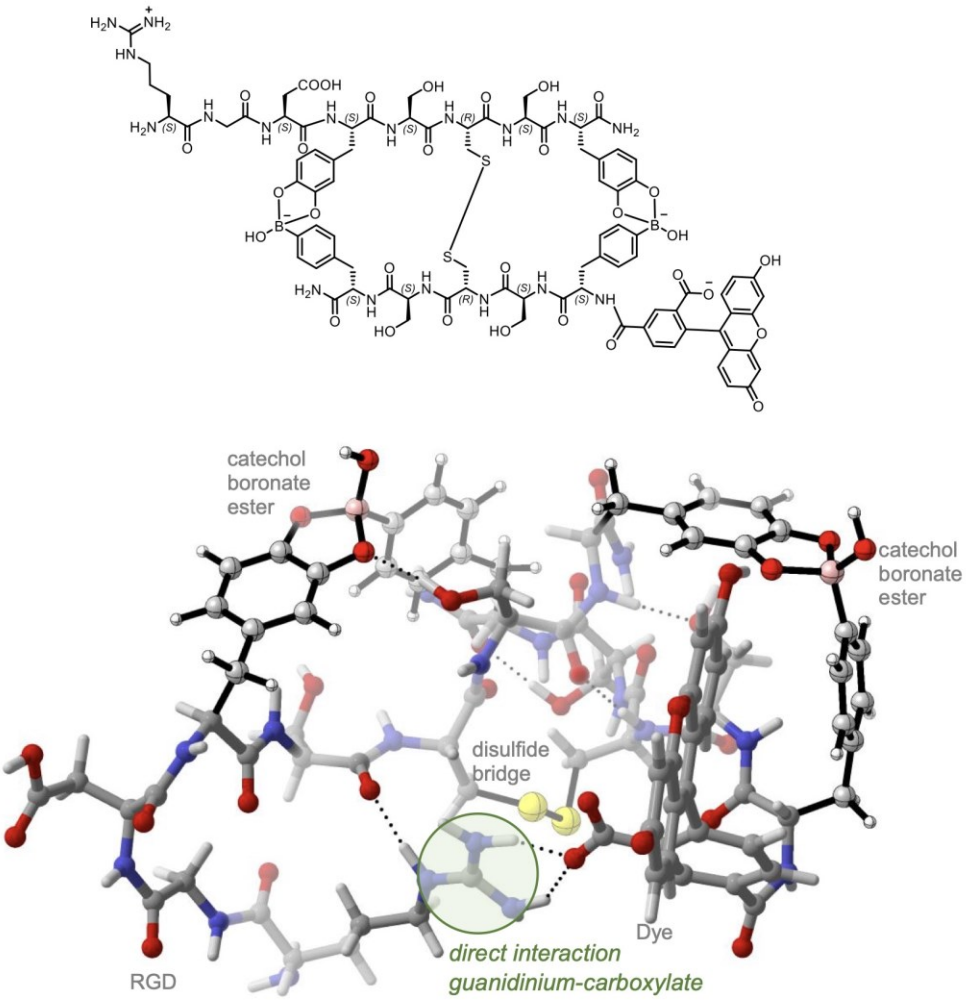

Figure S 42: Structure of fluorescein≃RGD with antiparallel topology (overall charge 2−).

Table S 3: Energies and Cartesian Coordinates.

Calculated data for the optimized structures

Structure	S-S bond distance (Å)	SCF energy (a.u.)	E_{rel} (kcal mol^{-1})		Quasiharmonic free energy correction (a.u.)	qh-G (a.u.)	qh-G_{rel} (kcal mol^{-1})	
2_{Ox} (BSCSB≃OSCSO) parallel	2.07	−5106.054384	4.2	4.2	1.132829	−5104.921555	3.5	**3.5**
2_{Ox} (BSCSB≃OSCSO) antiparallel	2.08	−5106.061017	0.0	**0.0**	1.133894	−5104.927123	0.0	**0.0**
BScSB≃OSCSO parallel	2.09	−5106.051194	6.1	6.2	1.133404	−5104.917791	4.8	**5.9**
BScSB≃OSCSO antiparallel	2.10	−5106.060946	0.0	**0.0**	1.135560	−5104.925386	0.0	**1.1**
bSCSb≃OSCSO parallel	2.07	−5106.041079	5.6	12.5	1.135425	−5104.905654	4.2	**13.5**
bSCSb≃OSCSO antiparallel	2.10	−5106.049949	0.0	**6.9**	1.137538	−5104.912411	0.0	**9.2**
fluorescein≃RGD (BSCSB≃OSCSO) parallel	2.07	−7537.884226	3.3		1.720024	−7536.164203	7.5	
fluorescein≃RGD (BSCSB≃OSCSO) antiparallel	2.08	−7537.889473	0.0		1.713384	−7536.176089	0.0	
OSCSO	N/A	−2604.946718	N/A		0.579664	−2604.367054	N/A	
BSCSB	N/A	−2656.115667	4.1		0.611686	−2655.503981	4.6	
BScSB	N/A	−2656.114543	4.8		0.609962	−2655.504581	4.2	
bSCSb	N/A	−2656.122156	0.0		0.610918	−2655.511239	0.0	

15. Cell uptake studies

Sample preparation protocol. 20 µL of 2 mM solutions of DL488-BSCSB and either OSCSO, OSCSO and TAT or TAT-OSCSO were mixed together to obtain 40 µL of 1 mM solution of preassembled conjugate (in 10 mM phosphate buffer pH = 8 with 10% DMSO). The conjugate was subsequently oxidized by addition of 1 µL 75 mM potassium peroxymonosulfate (Oxone®) solution in 100 mM PB, pH = 7.4 to obtain its final concentration as 1.8 mM. Prepared conjugate was used directly for the cell studies without any purification.

Cell culture. The human cell line A549 from adenocarcinomic lung tissue (American Type Culture Collection, Manassas, VA, US) was cultured in Dulbecco's modified Eagle medium (DMEM 4.5 g/L D-Glucose, L-Glutamine; Gibco by ThermoFisher Scientific, Germany) supplemented with 10% fetal calf serum (FCS; Sigma Aldrich, Germany) and 1% Penicillin/Streptomycin (Invitrogen, Germany) at a humified atmosphere with 37 °C and 5% CO_2. Fresh culture medium was replaced every two days and cells were subcultured after reaching 80% confluence.

Evaluation of cell uptake. A549 cells were detached by TrypLE Select (Gibco by ThermoFisher Scientific, Germany) and centrifuged 5 min at 1000 rpm. Collected cells were resuspended in DMEM-low glucose (1000 mg/L D-Glucose; Sigma-Aldrich, Germany) supplemented with 10% fetal calf serum (FCS; Sigma Aldrich, Germany) and 1% Penicillin/Streptomycin (Invitrogen, Germany) and seeded in µ-slide 8-well chambers (Ibidi GmbH, Germany) at a cell density of 10000 cells/well. 24 h after seeding, cells were treated with 10 µM of DL488-BSCSB≃OSCSO-TAT, DL488-BSCSB≃OSCSO+TAT or DL488-BSGSB~OSCSO-TAT. Untreated cells were used as control. For the uptake studies in acidic conditions, treatments were applied in DMEM low glucose (Agilent, Germany) without sodium bicarbonate supplemented with 10% fetal calf serum (FCS; Sigma Aldrich, Germany) and 1% Penicillin/Streptomycin (Invitrogen, Germany) at pH 6.4 and cells were incubated at 37 °C in absence of CO_2. After 24 h cells were washed with phosphate buffered saline (PBS) and fixed 15 min with 4% paraformaldehyde. Cell nuclei were stained with 5µg/ml of 4′,6-Diamidino-2-phenylindole dihydrochloride (DAPI; Sigma-Aldrich, Germany) diluted in PBS/0.1% Triton solution. Confocal z-stacks were taken by a TCS SP5 confocal microscope (Leica, Germany) (DAPI: Ex=405 nm, Em= 419-471 nm; DL488: Ex=488 nm, Em=503-537 nm) and orthogonal sections were obtained by image processing using Fiji (ImageJ). Experiment was carried out in triplicates from three independent cultures.

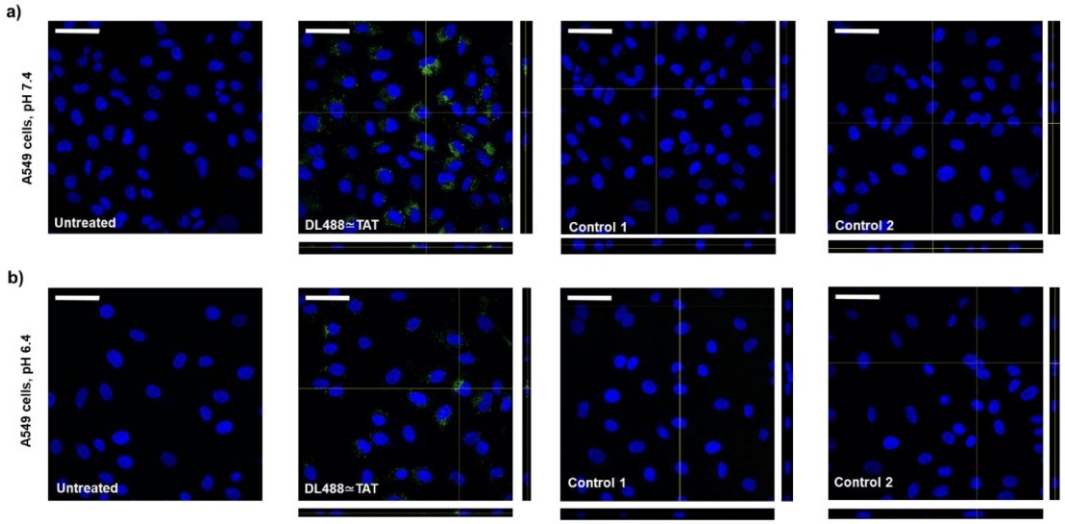

Figure S 43: Confocal images with orthogonal views to investigate cell uptake of bis-peptides, controls (10 µM) and untreated cells at a) physiological pH or b) acidic pH. Control 1: ***DL488-BSCSB≃OSCSO + TAT*** *incubated with free TAT sequence; Control 2: a conjugate without disulfide bridge* ***DL488-BSGSB~OSCSO-TAT*** *where cysteine was replaced with glycine. Scale bar = 50 µm*

References

1. Schrödinger Release 2018-4: Maestro 11.8, Schrödinger, LLC, New York, NY, 2018.
2. Roos, K.; Wu, C.; Damm, W.; Reboul, M.; Stevenson, J. M.; Lu, C.; Dahlgren, M. K.; Mondal, S.; Chen, W.; Wang, L.; Abel, R.; Friesner, R. A.; Harder, E. D., OPLS3e: Extending Force Field Coverage for Drug-Like Small Molecules. *Journal of Chemical Theory and Computation* **2019,** *15* (3), 1863-1874.
3. Frisch, M. J.; Trucks, G. W.; Schlegel, H. B.; Scuseria, G. E.; Robb, M. A.; Cheeseman, J. R.; Scalmani, G.; Barone, V.; Mennucci, B.; Petersson, G. A.; Nakatsuji, H.; Caricato, M.; Li, X.; Hratchian, H. P.; Izmaylov, A. F.; Bloino, J.; Zheng, G.; Sonnenberg, J. L.; Hada, M.; Ehara, M.; Toyota, K.; Fukuda, R.; Hasegawa, J.; Ishida, M.; Nakajima, T.; Honda, Y.; Kitao, O.; Nakai, H.; Vreven, T.; Jr., J. A. M.; Peralta, J. E.; Ogliaro, F.; Bearpark, M.; Heyd, J. J.; Brothers, E.; Kudin, K. N.; Staroverov, V. N.; Kobayashi, R.; Normand, J.; Raghavachari, K.; Rendell, A.; Burant, J. C.; Iyengar, S. S.; Tomasi, J.; Cossi, M.; Rega, N.; Millam, J. M.; Klene, M.; Knox, J. E.; Cross, J. B.; Bakken, V.; Adamo, C.; Jaramillo, J.; Gomperts, R.; Stratmann, R. E.; Yazyev, O.; Austin, A. J.; Cammi, R.; Pomelli, C.; Ochterski, J. W.; Martin, R. L.; Morokuma, K.; Zakrzewski, V. G.; Voth, G. A.; Salvador, P.; Dannenberg, J. J.; Dapprich, S.; Daniels, A. D.; Ö. Farkas; Foresman, J. B.; Ortiz, J. V.; Cioslowski, J.; Fox, D. J. GAUSSIAN 09 (Revision D.01), Gaussian, Inc.: Wallingford CT, 2009.
4. CYLview20; Legault, C. Y., Université de Sherbrooke, 2020 (http://www.cylview.org)
5. Zhao, Y.; Truhlar, D. G., The M06 suite of density functionals for main group thermochemistry, thermochemical kinetics, noncovalent interactions, excited states, and transition elements: two new functionals and systematic testing of four M06-class functionals and 12 other functionals. *Theoretical Chemistry Accounts* **2008,** *120* (1), 215-241.

6. Cances, E.; Mennucci, B.; Tomasi, J., A new integral equation formalism for the polarizable continuum model: Theoretical background and applications to isotropic and anisotropic dielectrics. *J Chem Phys* **1997,** *107* (8), 3032-3041.
7. Cossi, M.; Barone, V.; Mennucci, B.; Tomasi, J., Ab initio study of ionic solutions by a polarizable continuum dielectric model. *Chem Phys Lett* **1998,** *286* (3-4), 253-260.
8. Mennucci, B.; Tomasi, J., Continuum solvation models: A new approach to the problem of solute's charge distribution and cavity boundaries. *J Chem Phys* **1997,** *106* (12), 5151-5158.
9. Tomasi, J.; Mennucci, B.; Cammi, R., Quantum mechanical continuum solvation models. *Chem Rev* **2005,** *105* (8), 2999-3093.
10. Marenich, A. V.; Cramer, C. J.; Truhlar, D. G., Universal Solvation Model Based on Solute Electron Density and on a Continuum Model of the Solvent Defined by the Bulk Dielectric Constant and Atomic Surface Tensions. *J Phys Chem B* **2009,** *113* (18), 6378-6396.
11. Ribeiro, R. F.; Marenich, A. V.; Cramer, C. J.; Truhlar, D. G., Use of Solution-Phase Vibrational Frequencies in Continuum Models for the Free Energy of Solvation. *The Journal of Physical Chemistry B* **2011,** *115* (49), 14556-14562.
12. Marco Hebel, Andreas Riegger, Maksymilian M. Zegota, Gönül Kizilsavas, Jasmina Gačanin, Michaela Pieszka, Thorsten Lückerath, Jaime A. S. Coelho, Manfred Wagner, Pedro M. P. GoisPedro M. P. Gois, David Y. W. Ng*, and Tanja Weil*, Sequence Programming with Dynamic Boronic Acid/Catechol Binary Codes. J. Am. Chem. Soc. 2019, 141, 36, 14026–14031
13. Stefan P. A. Hinkes and Christian D. P. Klein*, Virtues of Volatility: A Facile Transesterification Approach to Boronic Acids. Org. Lett. 2019, 21, 9, 3048–3052

6. Conclusion and Outlook

The concept of nanocarriers, as understood today, was first proposed in the early 1970s, with poor targeting and premature drug release being identified shortly thereafter. By the 1990s, these problems had been widely recognized as core challenges within the field of nanomedicine – challenges that, despite incremental advances over the decades, remain unresolved to this day. Multimodal synergistic treatment strategies including the use of highly active immunomodulators have been developed within the field of immune-oncotherapy that aim to modulate immune cell function and would benefit from selective delivery to achieve tightly regulated immune activation within target tissues or cell types while reducing adverse effects, such as cytokine release syndrome (CRS), arising from systemic exposure.[400] This thesis addresses the unresolved problems of insufficient nanocarrier targeting efficiency, i.e. organ- and cell-selectivity, and drug conjugation stability, both of which contribute to the limited efficiency of current cancer therapies.

In summary, these studies introduce a TM-decorated HSA platform that enables cell-selective targeting with tunable cellular internalization and payload-protective drug loading (**Chapter 3**). They also identify epitope type and ligand density as key interdependent determinants of lectin-mediated nanocarrier uptake and selectivity demonstrating that optimal cellular targeting can be achieved at lower ligand densities than commonly assumed without compromising uptake efficiency (**Chapter 4**). In a complementary but independent approach, improved spatiotemporal control over drug release was achieved through a rationally designed, peptide-based dynamic covalent linker system incorporating two complementary linkage types (**Chapter 5**), thereby establishing linker cooperativity as the central design advance to overcome the intrinsic limitations of single dynamic covalent linkages.

These conclusions are supported by the following experimental observations obtained across the individual studies. A high-valency TM-decorated HSA loaded with TLR7/8a was comprehensively evaluated for internalization selectivity, efficiency, and efficacy *in vitro*/*ex vivo*, as well as for its biodistribution *in vivo* (**Chapter 3**). Ligand density modulation enabled tunable cellular uptake while maintaining high selectivity for cells expressing MMR (CD206) and DC-SIGN (CD209), as demonstrated in both a CD206-transduced cell line and heterogenous primary immune cell populations. An optimized denaturation-based thiol-

reactive loading strategy provided high payload capacity, with release studies revealing a traceless, two-step release necessitating initial denaturation for efficient subsequent disulfide cleavage, indicative of a payload-protective core-shell structure. Biodistribution analysis showed no protein corona formation and a complete redirection from HSA's natural systemic distribution toward rapid, homogenous accumulation of nanocarriers among hepatic target cells - LSECs, Kupffer cells and DCs - contrasting with most liver-accumulating nanocarriers, which are predominantly internalized by Kupffer cells at low carrier doses.[401]

To better understand the nanocarriers receptor interactions and to broaden the applicability of the carrier design, a comparative investigation of mannose-based targeting ligand-decorated HSAs was conducted with varying ligand type and valency (M, TM, MD, TMD) in varying ligand density (**Chapter 4**). Empirically, these studies showed that not only the epitope structure (M vs TM) but also their arrangement influenced the ligand density required for optimal uptake efficiency and shaped the overall uptake trend among increasingly ligand-modified HSA carriers *in vitro*. *Ex vivo* analysis further revealed that TM-HSA carriers exhibit a more favorable selectivity profile than M-HSA carriers across tested spleen immune cell populations, particularly at low ligand densities. Together, these results indicate that reducing the ligand density of the established TM-HSA carrier preserves its cell selectivity and a good uptake efficiency, suggesting a potential strategy to modulate pharmacokinetic behavior and biodistribution *in vivo*.

Whereas the first goal of this work focused on cell-selective nanocarrier design employing static targeting strategies, the second goal pursued a complementary avenue toward achieving precise spatiotemporally controlled delivery. A linker system was developed that enabled controlled intracellular release while exhibiting enhanced stability under (patho)physiological extracellular conditions thereby preventing premature leakage. In line with the current state-of-the-art in DDS design, this complementary strategy counteracts an unfavorable distribution by providing spatiotemporal release specificity, aiming to increase therapeutic indices. Through rational sequence design, a dynamic covalent linker system consisting of two complementary peptide tags was developed (**Chapter 5**). Fast, divalent BA-CA complex formation mediated self-sorting and heterodimer selectivity, while oxidation of preorganized cysteine thiols into a disulfide bridge stabilized the system against acid- and dilution-induced dissociation. Yet, under intracellular conditions, the system's responsiveness was preserved, thereby inducing selectivity. The peptide backbones enabled

direct bioconjugation or straightforward extension *via* solid phase peptide synthesis (SPPS) for peptide targeting sequences and non-canonical amino acids incorporating biorthogonal chemical handles. By integrating two individually established, cooperative linkage types in a multivalent manner, this approach exemplifies a complementary strategy for addressing individual limitations of DCvC. This led to an improved controlled release profile by enhancing drug conjugate stability within non-target site conditions and by preserving responsiveness within target site conditions.

While this work establishes conceptual advances in nanocarrier selectivity and dynamic covalent linker design, some limitations remain. *In vivo* evaluation of the TM-HSA nanocarrier so far focused on its biodistribution in healthy mice. The observed rapid and selective uptake by specific liver cell populations highlights its potential for further testing in immunocompetent models of hepatocellular carcinoma (HCC) or liver fibrosis, where these cells play important immune-regulatory roles.[402–405] While TLR agonists have already entered clinical evaluation for HCC,[400,406,407] the same delivery platform could also be adapted for other immunomodulators such as STAT3 inhibitors (e.g., Cucurbitacin B or Icaritin), but rationale chemical design is required for conjugation.[408,409] Ultimately, drug-loaded TM-HSA may enhance current first-line HCC treatments with ICD-like effects, together acting as a potent *in situ* cancer vaccine, and may promote more durable, patient antigen-specific immune responses compared to the typically transient activation seen in the tolerogenic liver environment.[27,410–413]

Recent studies demonstrated a shift in biodistribution tightly connected to the mannose density on albumin carriers.[308] Even though the saturated M-HSA carrier showed a higher overall uptake in direct comparison, the TM-HSA carriers exhibited slightly improved selectivity across the low- and high-valency regimes *ex vivo*. In combination, these findings suggest important design principles for future immune-selective nanocarriers that target tissues outside the liver, indicating that low-valency nanocarriers, possibly further combined with TME-responsive stealth modifications, may enable enhanced cell-selective delivery to the tumor site. In this context, the incorporation of a pH-responsive, sheddable PEG layer, as discussed in Chapter 1.2.1, represents a promising strategy to reduce hepatic sequestration and on-target, off-site receptor-mediated uptake by transiently shielding targeting ligands during systemic circulation and restoring ligand accessibility upon PEG shedding within the

TME. Yet, the potential for extra-hepatic, cell-selective delivery of the low-valency TM-HSA carriers – with or without additional modifications – requires experimental validation through quantitative pharmacokinetic data in animal models.

Using dynamic covalent peptide tags, an improved linker system was devised that dynamically targets the intracellular compartment by dual-responsiveness to the respective physicochemical environment. This system is constrained by its three-dimensional template structure during assembly and disulfide locking, as well as its overall spatial demand, rendering it not ideal as linker for small nanocarriers designed to achieve high drug loading. The self-sorting capacity is particularly well suited for surface-accessible precision peptide or protein conjugates, e.g. antibody conjugates, that benefit most from the high heterodimer selectivity and resultant high yield. Given the central role of antibodies in immunotherapy and the established use of ADCs, the developed linker system provides a promising strategy for generating ADCs, such as cancer-cell targeted conjugates or emerging immune-targeted variants, which are being explored for both cancer and non-cancer immune-related diseases.[414,415] Importantly, the non-canonical BA-containing peptide tag can be readily incorporated during recombinant protein expression, enabling a practical and scalable protein conjugation strategy. However, the improved dissociation constant in the low micromolar range during complex formation could still be a limitation, particularly for protein conjugation, which is often restricted by limited solubility at higher concentrations. To resolve this, the boronate ester valency can be increased or the CA binding partners could be replaced with higher-affinity alternatives such as salicylhydroxamic acids. Nonetheless, the system demonstrated high conceptual value through its *in chemico* and *in vitro* performance, offering tunability and modularity and, at the same time, adding another dimension towards controlling selectivity and stability.

In conclusion, this thesis demonstrates modular design principles that effectively address key limitations in nanocarrier targeting and drug linker stability, exemplified by highly selective immune-targeted nanocarriers and a cooperative dynamic covalent linker system, and lays the groundwork for their future integration into multi-layered yet translatable DDSs with precise and efficient *in vivo* performance.

References

(1) Jain, K. K. An Overview of Drug Delivery Systems. In *Drug Delivery Systems. Methods in Molecular Biology*; Jain, K. K., Ed.; Humana, New York, NY, 2020; Vol. 2059, pp 1–54. DOI: 10.1007/978-1-4939-9798-5_1.

(2) Vargason, A. M.; Anselmo, A. C.; Mitragotri, S. The evolution of commercial drug delivery technologies. *Nat. Biomed. Eng.* **2021**, *5* (9), 951–967. DOI: 10.1038/s41551-021-00698-w.

(3) de Maar, J. S.; Rousou, C.; van Elburg, B.; Vos, H. J.; Lajoinie, G. P. R.; Bos, C.; Moonen, C. T. W.; Deckers, R. Ultrasound-Mediated Drug Delivery With a Clinical Ultrasound System: In Vitro Evaluation. *Front. Pharmacol.* **2021**, *12*, 768436. DOI: 10.3389/fphar.2021.768436.

(4) Couture, O.; Foley, J.; Kassell, N. F.; Larrat, B.; Aubry, J. F. Review of ultrasound mediated drug delivery for cancer treatment: updates from pre-clinical studies. *Transl. Cancer Res.* **2014**, *3* (5), 494–511. DOI: 10.3978/j.issn.2218-676x.2014.10.01.

(5) ISO. *Nanotechnologies – Vocabulary – Part 1: Core vocabulary*, ISO 80004; Geneva, Switzerland, 2023. https://www.iso.org/obp/ui/en/#iso:std:79525:en (accessed 2025-11-13).

(6) ASTM International. *Standard terminology relating to nanotechnology*, ASTM E2456; West Conshohocken, PA, 2020. DOI: 10.1520/e2456-06r20.

(7) Murthy, S. B.; Basha, J. D.; Alagumurugan, A.; Muthukumar, S.; Vinesha, R.; Prakash, P. Nanocarriers in drug delivery. In *Futuristic Trends in Pharmacy & Nursing*; 2024; Vol. 3.

(8) Singh, R.; Lillard, J. W. Nanoparticle-based targeted drug delivery. *Exp. Mol. Pathol.* **2009**, *86* (3), 215–223. DOI: 10.1016/j.yexmp.2008.12.004.

(9) Takeishi, N.; Imai, Y. Capture of microparticles by bolus flow of red blood cells in capillaries. *Sci. Rep.* **2017**, *7* (1), 1–8. DOI: 10.1038/s41598-017-05924-7.

(10) Peer, D.; Karp, J. M.; Hong, S.; Farokhzad, O. C.; Margalit, R.; Langer, R. Nanocarriers as an emerging platform for cancer therapy. *Nat. Nanotechnol.* **2007**, *2* (12), 751–760. DOI: 10.1038/nnano.2007.387.

(11) Gressler, S.; Hipfinger, C.; Part, F.; Pavlicek, A.; Zafiu, C.; Giese, B. A systematic review of nanocarriers used in medicine and beyond – definition and categorization framework. *J. Nanobiotechnology* **2025**, *23* (1), 1–21. DOI: 10.1186/s12951-025-03113-7.

(12) EMA. *Nanotechnology-based medicinal products for human use: EU-IN horizon scanning report*; European Medicines Agency, 2025.

(13) CHMP. *Guideline on Development, Production, Characterisation and Specifications for Monoclonal Antibodies and Related Products*; European Medicines Agency, 2008.

(14) Ekladious, I.; Colson, Y. L.; Grinstaff, M. W. Polymer–drug conjugate therapeutics: advances, insights and prospects. *Nat. Rev. Drug Discov.* **2018**, *18* (4), 273–294. DOI: 10.1038/s41573-018-0005-0.

(15) Bangham, A. D.; Standish, M. M.; Watkins, J. C. Diffusion of univalent ions across the lamellae of swollen phospholipids. *J. Mol. Biol.* **1965**, *13* (1), 238–252. DOI: 10.1016/s0022-2836(65)80093-6.

(16) Oza, M.; Patel, T.; Gupta, M.; Patel, N.; Bodhe, S. A Comprehensive Review on Liposomes: As Drug Delivery System. *Int. J. Pharm. Sci.* **2025**, *3* (4), 463–475. DOI: 10.5281/zenodo.15133054.

(17) Afzal, O.; Altamimi, A. S. A.; Nadeem, M. S.; Alzarea, S. I.; Almalki, W. H.; Tariq,

A.; Mubeen, B.; Murtaza, B. N.; Iftikhar, S.; Riaz, N.; Kazmi, I. Nanoparticles in Drug Delivery: From History to Therapeutic Applications. *Nanomaterials* **2022**, *12* (24), 4494. DOI: 10.3390/nano12244494.

(18) Heap, S. B.; Gregoriadis, G. Alec Douglas Bangham. 10 November 1921 – 9 March 2010. *Biogr. Mem. Fellows R. Soc.* **2011**, *57*, 25–43. DOI: 10.1098/rsbm.2011.0004.

(19) Gregoriadis, G.; Ryman, B. E. Lysosomal localization of β-fructofuranosidase-containing liposomes injected into rats. Some implications in the treatment of genetic disorders. *Biochem. J.* **1972**, *129* (1), 123–133. DOI: 10.1042/bj1290123.

(20) Namiot, E. D.; Sokolov, A. V.; Chubarev, V. N.; Tarasov, V. V.; Schiöth, H. B. Nanoparticles in Clinical Trials: Analysis of Clinical Trials, FDA Approvals and Use for COVID-19 Vaccines. *Int. J. Mol. Sci.* **2023**, *24* (1), 787. DOI: 10.3390/ijms24010787.

(21) Ventola, C. L. Progress in Nanomedicine: Approved and Investigational Nanodrugs. *Pharm. Ther.* **2017**, *42* (12), 742–755.

(22) Rodríguez, F.; Caruana, P.; De la Fuente, N.; Español, P.; Gámez, M.; Balart, J.; Llurba, E.; Rovira, R.; Ruiz, R.; Martín-Lorente, C.; Corchero, J. L.; Céspedes, M. V. Nano-Based Approved Pharmaceuticals for Cancer Treatment: Present and Future Challenges. *Biomolecules* **2022**, *12* (6), 784. DOI: 10.3390/biom12060784.

(23) Havel, H. A. Where Are the Nanodrugs? An Industry Perspective on Development of Drug Products Containing Nanomaterials. *AAPS J.* **2016**, *18* (6), 1351–1353. DOI: 10.1208/s12248-016-9970-6.

(24) Liu, Q.; Zou, J.; Chen, Z.; He, W.; Wu, W. Current research trends of nanomedicines. *Acta Pharm. Sin. B* **2023**, *13* (11), 4391–4416. DOI: 10.1016/j.apsb.2023.05.018.

(25) Zhang, Y.; Chen, X.; Hu, B.; Zou, B.; Xu, Y. Advancements in nanomedicine delivery systems: unraveling immune regulation strategies for tumor immunotherapy. *Nanomedicine* **2024**, *19* (21–22), 1821–1840. DOI: 10.1080/17435889.2024.2374230.

(26) Hu, J.; Arvejeh, P. M.; Bone, S.; Hett, E.; Marincola, F. M.; Roh, K. H. Nanocarriers for cutting-edge cancer immunotherapies. *J. Transl. Med.* **2025**, *23* (1), 1–36. DOI: 10.1186/s12967-025-06435-0.

(27) Gong, N.; Alameh, M. G.; El-Mayta, R.; Xue, L.; Weissman, D.; Mitchell, M. J. Enhancing in situ cancer vaccines using delivery technologies. *Nat. Rev. Drug Discov.* **2024**, *23* (8), 607–625. DOI: 10.1038/s41573-024-00974-9.

(28) Sinha, A.; Ghosh, D.; Karati, D. Tumor microenvironment and immunotherapy: from bench to bedside. *Med. Oncol.* **2025**, *42* (7), 1–17. DOI: 10.1007/s12032-025-02818-x.

(29) Tang, L.; Li, J.; Pan, T.; Yin, Y.; Mei, Y.; Xiao, Q.; Wang, R.; Yan, Z.; Wang, W. Versatile carbon nanoplatforms for cancer treatment and diagnosis: strategies, applications and future perspectives. *Theranostics* **2022**, *12* (5), 2290–2321. DOI: 10.7150/thno.69628.

(30) Chandrakala, V.; Aruna, V.; Angajala, G. Review on metal nanoparticles as nanocarriers: current challenges and perspectives in drug delivery systems. *Emergent Mater.* **2022**, *5* (6), 1593–1615. DOI: 10.1007/s42247-021-00335-x.

(31) Dutta Gupta, Y.; Mackeyev, Y.; Krishnan, S.; Bhandary, S. Mesoporous silica nanotechnology: promising advances in augmenting cancer theranostics. *Cancer Nanotechnol.* **2024**, *15* (1), 1–44. DOI: 10.1186/s12645-024-00250-w.

(32) Godakhindi, V.; Tarannum, M.; Dam, S. K.; Vivero-Escoto, J. L. Mesoporous Silica Nanoparticles as an Ideal Platform for Cancer Immunotherapy: Recent Advances and Future Directions. *Adv. Healthc. Mater.* **2024**, *13* (20), 2400323. DOI:

10.1002/adhm.202400323.
(33) Tian, G.; Zhang, X.; Gu, Z.; Zhao, Y. Recent Advances in Upconversion Nanoparticles-Based Multifunctional Nanocomposites for Combined Cancer Therapy. *Adv. Mater.* **2015**, *27* (47), 7692–7712. DOI: 10.1002/adma.201503280.
(34) Jiang, Y.; Yan, C.; Li, M.; Chen, S.; Chen, Z.; Yang, L.; Luo, K. Delivery of natural products via polysaccharide-based nanocarriers for cancer therapy: A review on recent advances and future challenges. *Int. J. Biol. Macromol.* **2024**, *278*, 135072. DOI: 10.1016/j.ijbiomac.2024.135072.
(35) He, C.; Lu, J.; Lin, W. Hybrid nanoparticles for combination therapy of cancer. *J. Control. Release* **2015**, *219*, 224–236. DOI: 10.1016/j.jconrel.2015.09.029.
(36) Gajbhiye, K. R.; Salve, R.; Narwade, M.; Sheikh, A.; Kesharwani, P.; Gajbhiye, V. Lipid polymer hybrid nanoparticles: a custom-tailored next-generation approach for cancer therapeutics. *Mol. Cancer* **2023**, *22* (1), 1–44. DOI: 10.1186/s12943-023-01849-0.
(37) Nguyen, K. T.; Zhao, Y. Engineered Hybrid Nanoparticles for On-Demand Diagnostics and Therapeutics. *Acc. Chem. Res.* **2015**, *48* (12), 3016–3025. DOI: 10.1021/acs.accounts.5b00316.
(38) Lotey, N. K.; Pednekar, S.; Chaughule, R. Hybrid Nanoparticles in Biomedical Applications. In *Nanomaterials for Cancer Detection Using Imaging Techniques and Their Clinical Applications*; Chaughule, R. S., Patkar, D. P., Ramanujan, R. V., Eds.; Springer International Publishing, 2022; pp 365–400. DOI: 10.1007/978-3-031-09636-5_13.
(39) Li, J.; Lu, W.; Yang, Y.; Xiang, R.; Ling, Y.; Yu, C.; Zhou, Y. Hybrid Nanomaterials for Cancer Immunotherapy. *Adv. Sci.* **2023**, *10* (6), 2204932. DOI: 10.1002/advs.202204932.
(40) Mi, P. Stimuli-responsive nanocarriers for drug delivery, tumor imaging, therapy and theranostics. *Theranostics* **2020**, *10* (10), 4557–4588. DOI: 10.7150/thno.38069.
(41) Chen, D.; Liu, X.; Lu, X.; Tian, J. Nanoparticle drug delivery systems for synergistic delivery of tumor therapy. *Front. Pharmacol.* **2023**, *14*, 1111991. DOI: 10.3389/fphar.2023.1111991.
(42) Sun, L.; Li, Z.; Lan, J.; Wu, Y.; Zhang, T.; Ding, Y. Better together: nanoscale co-delivery systems of therapeutic agents for high-performance cancer therapy. *Front. Pharmacol.* **2024**, *15*, 1389922. DOI: 10.3389/fphar.2024.1389922.
(43) Halamoda-Kenzaoui, B.; Vandebriel, R. J.; Howarth, A.; Siccardi, M.; David, C. A. W.; Liptrott, N. J.; Santin, M.; Borgos, S. E.; Bremer-Hoffmann, S.; Caputo, F. Methodological needs in the quality and safety characterisation of nanotechnology-based health products: Priorities for method development and standardisation. *J. Control. Release* **2021**, *336*, 192–206. DOI: 10.1016/j.jconrel.2021.06.016.
(44) Bozzuto, G.; Molinari, A. Liposomes as nanomedical devices. *Int. J. Nanomedicine* **2015**, *10*, 975–999. DOI: 10.2147/ijn.s68861.
(45) Makino, K.; Shibata, A. Chapter 2: Surface Properties of Liposomes Depending on Their Composition. In *Advances in Planar Lipid Bilayers and Liposomes*; Academic Press, 2006; Vol. 4, pp 49–77. DOI: 10.1016/s1554-4516(06)04002-6.
(46) Liu, P.; Chen, G.; Zhang, J. A Review of Liposomes as a Drug Delivery System: Current Status of Approved Products, Regulatory Environments, and Future Perspectives. *Molecules* **2022**, *27* (4), 1372. DOI: 10.3390/molecules27041372.
(47) Pande, S. Liposomes for drug delivery: review of vesicular composition, factors affecting drug release and drug loading in liposomes. *Artif. Cells, Nanomedicine, Biotechnol.* **2023**, *51* (1), 428–440. DOI: 10.1080/21691401.2023.2247036.
(48) Kim, E.; Graceffa, O.; Broweleit, R.; Ladha, A.; Boies, A.; Mudakannavar, S. P.;

Rawle, R. J. Lipid loss and compositional change during preparation of simple two-component liposomes. *Biophys. Reports* **2024**, *4* (3), 100174. DOI: 10.1016/j.bpr.2024.100174.

(49) Yang, K.; Tran, K.; Salvati, A. Tuning Liposome Stability in Biological Environments and Intracellular Drug Release Kinetics. *Biomolecules* **2023**, *13* (1), 59. DOI: 10.3390/biom13010059/s1.

(50) Nikolova, M. P.; Kumar, E. M.; Chavali, M. S. Updates on Responsive Drug Delivery Based on Liposome Vehicles for Cancer Treatment. *Pharmaceutics* **2022**, *14* (10), 2195. DOI: 10.3390/pharmaceutics14102195.

(51) Xu, X.; Tian, F.; Pan, Y.; Zhang, T.; Deng, L.; Jiang, H.; Han, J.; Liu, J.; Zhao, Y.; Liu, W. Emerging mechanistic insights into liposomal stability: Full process management from production and storage to food application. *Chem. Eng. J.* **2025**, *505*, 159552. DOI: 10.1016/j.cej.2025.159552.

(52) Musakhanian, J.; Rodier, J. D.; Dave, M. Oxidative Stability in Lipid Formulations: a Review of the Mechanisms, Drivers, and Inhibitors of Oxidation. *AAPS PharmSciTech* **2022**, *23* (5), 151-. DOI: 10.1208/s12249-022-02282-0.

(53) Andra, V. V. S. N. L.; Pammi, S. V. N.; Bhatraju, L. V. K. P.; Ruddaraju, L. K. A Comprehensive Review on Novel Liposomal Methodologies, Commercial Formulations, Clinical Trials and Patents. *Bionanoscience* **2022**, *12* (1), 274–291. DOI: 10.1007/s12668-022-00941-x.

(54) Sercombe, L.; Veerati, T.; Moheimani, F.; Wu, S. Y.; Sood, A. K.; Hua, S. Advances and challenges of liposome assisted drug delivery. *Front. Pharmacol.* **2015**, *6* (DEC), 163819. DOI: 10.3389/fphar.2015.00286.

(55) Salel, S.; Iyisan, B. Polymer–lipid hybrid nanoparticles as potential lipophilic anticancer drug carriers. *Discov. Nano* **2023**, *18* (1), 114. DOI: 10.1186/s11671-023-03897-3.

(56) Mojarad-Jabali, S.; Mahdinloo, S.; Farshbaf, M.; Sarfraz, M.; Fatahi, Y.; Atyabi, F.; Valizadeh, H. Transferrin receptor-mediated liposomal drug delivery: recent trends in targeted therapy of cancer. *Expert Opin. Drug Deliv.* **2022**, *19* (6), 685–705. DOI: 10.1080/17425247.2022.2083106.

(57) Alwattar, J. K.; Mneimneh, A. T.; Abla, K. K.; Mehanna, M. M.; Allam, A. N. Smart Stimuli-Responsive Liposomal Nanohybrid Systems: A Critical Review of Theranostic Behavior in Cancer. *Pharmaceutics* **2021**, *13* (3), 355. DOI: 10.3390/pharmaceutics13030355.

(58) Seleci, M.; Seleci, D. A.; Scheper, T.; Stahl, F. Theranostic Liposome–Nanoparticle Hybrids for Drug Delivery and Bioimaging. *Int. J. Mol. Sci.* **2017**, *18* (7), 1415. DOI: 10.3390/ijms18071415.

(59) Binici, B.; Rattray, Z.; Zinger, A.; Perrie, Y. Exploring the impact of commonly used ionizable and pegylated lipids on mRNA-LNPs: A combined in vitro and preclinical perspective. *J. Control. Release* **2025**, *377*, 162–173. DOI: 10.1016/j.jconrel.2024.11.010.

(60) Sato, Y.; Note, Y.; Maeki, M.; Kaji, N.; Baba, Y.; Tokeshi, M.; Harashima, H. Elucidation of the physicochemical properties and potency of siRNA-loaded small-sized lipid nanoparticles for siRNA delivery. *J. Control. Release* **2016**, *229*, 48–57. DOI: 10.1016/j.jconrel.2016.03.019.

(61) Schlich, M.; Palomba, R.; Costabile, G.; Mizrahy, S.; Pannuzzo, M.; Peer, D.; Decuzzi, P. Cytosolic delivery of nucleic acids: The case of ionizable lipid nanoparticles. *Bioeng. Transl. Med.* **2021**, *6* (2), e10213. DOI: 10.1002/btm2.10213.

(62) Cullis, P. R.; Felgner, P. L. The 60-year evolution of lipid nanoparticles for nucleic acid delivery. *Nat. Rev. Drug Discov.* **2024**, *23* (9), 709–722. DOI: 10.1038/s41573-

024-00977-6.
(63) Tenchov, R.; Bird, R.; Curtze, A. E.; Zhou, Q. Lipid Nanoparticles from Liposomes to mRNA Vaccine Delivery, a Landscape of Research Diversity and Advancement. *ACS Nano* **2021**, *15* (11), 16982–17015. DOI: 10.1021/acsnano.1c04996.
(64) Vishweshwaraiah, Y. L.; Dokholyan, N. V. mRNA vaccines for cancer immunotherapy. *Front. Immunol.* **2022**, *13*, 1029069. DOI: 10.3389/fimmu.2022.1029069.
(65) Wang, X.; Liu, S.; Sun, Y.; Yu, X.; Lee, S. M.; Cheng, Q.; Wei, T.; Gong, J.; Robinson, J.; Zhang, D.; Lian, X.; Basak, P.; Siegwart, D. J. Preparation of selective organ-targeting (SORT) lipid nanoparticles (LNPs) using multiple technical methods for tissue-specific mRNA delivery. *Nat. Protoc.* **2022**, *18* (1), 265–291. DOI: 10.1038/s41596-022-00755-x.
(66) Guo, J.; Gu, M.; Chen, Y.; Xiong, T.; Zhang, Y.; Chen, S.; Li, M.; Chen, X.; Peng, X. Nucleic acid delivery by lipid nanoparticles for organ targeting. *Chinese Chem. Lett.* **2025**, *36* (11), 110849. DOI: 10.1016/j.cclet.2025.110849.
(67) Liao, H.; Liao, J.; Zeng, L.; Cao, X.; Fan, H.; Chen, J. Strategies for Organ-Targeted mRNA Delivery by Lipid Nanoparticles. *Wiley Interdiscip. Rev. Nanomedicine Nanobiotechnology* **2024**, *16* (5), e2004. DOI: 10.1002/wnan.2004.
(68) Hashiba, K.; Taguchi, M.; Sakamoto, S.; Otsu, A.; Maeda, Y.; Suzuki, Y.; Ebe, H.; Okazaki, A.; Harashima, H.; Sato, Y. Impact of Lipid Tail Length on the Organ Selectivity of mRNA-Lipid Nanoparticles. *Nano Lett.* **2024**. DOI: 10.1021/acs.nanolett.4c02566.
(69) Zhang, H.; Meng, C.; Yi, X.; Han, J.; Wang, J.; Liu, F.; Ling, Q.; Li, H.; Gu, Z. Fluorinated Lipid Nanoparticles for Enhancing mRNA Delivery Efficiency. *ACS Nano* **2024**, *18* (11), 7825–7836. DOI: 10.1021/acsnano.3c04507.
(70) Liu, H.; Chen, M. Z.; Payne, T.; Porter, C. J. H.; Pouton, C. W.; Johnston, A. P. R. Beyond the Endosomal Bottleneck: Understanding the Efficiency of mRNA/LNP Delivery. *Adv. Funct. Mater.* **2024**, *34* (39), 2404510. DOI: 10.1002/adfm.202404510.
(71) Cheng, L.; Zhu, Y.; Ma, J.; Aggarwal, A.; Toh, W. H.; Shin, C.; Sangpachatanaruk, W.; Weng, G.; Kumar, R.; Mao, H. Q. Machine Learning Elucidates Design Features of Plasmid Deoxyribonucleic Acid Lipid Nanoparticles for Cell Type-Preferential Transfection. *ACS Nano* **2024**, *18* (42), 28735–28747. DOI: 10.1021/acsnano.4c07615.
(72) Li, B.; Raji, I. O.; Gordon, A. G. R.; Sun, L.; Raimondo, T. M.; Oladimeji, F. A.; Jiang, A. Y.; Varley, A.; Langer, R. S.; Anderson, D. G. Accelerating ionizable lipid discovery for mRNA delivery using machine learning and combinatorial chemistry. *Nat. Mater.* **2024**, *23* (7), 1002–1008. DOI: 10.1038/s41563-024-01867-3.
(73) Lu, Y.; Zhang, E.; Yang, J.; Cao, Z. Strategies to improve micelle stability for drug delivery. *Nano Res.* **2018**, *11* (10), 4985–4998. DOI: 10.1007/s12274-018-2152-3.
(74) Lu, Y.; Yue, Z.; Xie, J.; Wang, W.; Zhu, H.; Zhang, E.; Cao, Z. Micelles with ultralow critical micelle concentration as carriers for drug delivery. *Nat. Biomed. Eng.* **2018**, *2* (5), 318–325. DOI: 10.1038/s41551-018-0234-x.
(75) Zhigaltsev, I. V.; Winters, G.; Srinivasulu, M.; Crawford, J.; Wong, M.; Amankwa, L.; Waterhouse, D.; Masin, D.; Webb, M.; Harasym, N.; Heller, L.; Bally, M. B.; Ciufolini, M. A.; Cullis, P. R.; Maurer, N. Development of a weak-base docetaxel derivative that can be loaded into lipid nanoparticles. *J. Control. Release* **2010**, *144* (3), 332–340. DOI: 10.1016/j.jconrel.2010.02.029.
(76) Pallares, R. M.; Barmin, R. A.; Wang, A.; Kiessling, F.; Lammers, T. Clinical cancer nanomedicines. *J. Control. Release* **2025**, *385*, 113991. DOI:

10.1016/j.jconrel.2025.113991.
(77) Wang, R.; Zang, J.; Zhong, H.; Zhang, Y.; Ouyang, D. Understanding the molecular insights of marketed liposomal drugs using molecular dynamics simulations of reduced scale coarse-grained models. *npj Drug Discov.* **2025**, *2*, 11. DOI: 10.1038/s44386-025-00014-5.
(78) Cazacu, A.; Ursu, E.-L.; Negut, I.; Bita, B. Polymeric Micellar Systems–A Special Emphasis on "Smart" Drug Delivery. *Pharmaceutics* **2023**, *15* (3), 976. DOI: 10.3390/pharmaceutics15030976.
(79) Banik, B. L.; Fattahi, P.; Brown, J. L. Polymeric nanoparticles: the future of nanomedicine. *Wiley Interdiscip. Rev. Nanomedicine Nanobiotechnology* **2016**, *8* (2), 271–299. DOI: 10.1002/wnan.1364.
(80) Hwang, D.; Ramsey, J. D.; Kabanov, A. V. Polymeric micelles for the delivery of poorly soluble drugs: From nanoformulation to clinical approval. *Adv. Drug Deliv. Rev.* **2020**, *156*, 80–118. DOI: 10.1016/j.addr.2020.09.009.
(81) das Neves, J.; Nunes, R.; Machado, A.; Sarmento, B. Polymer-based nanocarriers for vaginal drug delivery. *Adv. Drug Deliv. Rev.* **2015**, *92*, 53–70. DOI: 10.1016/j.addr.2014.12.004.
(82) Duncan, R.; Vicent, M. J. Do HPMA copolymer conjugates have a future as clinically useful nanomedicines? A critical overview of current status and future opportunities. *Adv. Drug Deliv. Rev.* **2010**, *62* (2), 272–282. DOI: 10.1016/j.addr.2009.12.005.
(83) Madaan, K.; Kumar, S.; Poonia, N.; Lather, V.; Pandita, D. Dendrimers in drug delivery and targeting: Drug-dendrimer interactions and toxicity issues. *J. Pharm. Bioallied Sci.* **2014**, *6* (3), 139–150. DOI: 10.4103/0975-7406.130965.
(84) European Medicines Agency. *Opaxio*. https://www.ema.europa.eu/en/medicines/human/EPAR/opaxio (accessed 2025-11-14).
(85) Chariou, P. L.; Ortega-Rivera, O. A.; Steinmetz, N. F. Nanocarriers for the Delivery of Medical, Veterinary, and Agricultural Active Ingredients. *ACS Nano* **2020**, *14* (3), 2678–2701. DOI: 10.1021/acsnano.0c00173.
(86) Fraguas-Sánchez, A. I.; Martín-Sabroso, C.; Lozza, I.; Torres-Suárez, A. I. Nanomedicine Applications in Cancer Treatment. In *Cancer Personalized Treatment. Handbook of Cancer and Immunology*; Rezaei, N., Ed.; Springer, Cham, 2025; Vol. 9, pp 205–241. DOI: 10.1007/978-3-032-00773-5_294.
(87) Jacob, J.; Haponiuk, J. T.; Thomas, S.; Gopi, S. Biopolymer based nanomaterials in drug delivery systems: A review. *Mater. Today Chem.* **2018**, *9*, 43–55. DOI: 10.1016/j.mtchem.2018.05.002.
(88) Rezvova, M. A.; Ovcharenko, E. A.; Glushkova, T. V.; Kudryavtseva, Y. A.; Barbarash, L. S. Evaluation of calcification resistance of xenopericardium treated with polyhydroxy compounds. *Vestn. Transplantologii i Iskusstv. Organov* **2021**, *23* (1), 75–83. DOI: 10.15825/1995-1191-2021-1-75-83.
(89) Lam, N. T.; McCluskey, J. B.; Glover, D. J. Harnessing the Structural and Functional Diversity of Protein Filaments as Biomaterial Scaffolds. *ACS Appl. Bio Mater.* **2022**, *5* (10), 4668–4686. DOI: 10.1021/acsabm.2c00275.
(90) Gu, C.; Mi, Y.; Zhang, T.; Wang, S. Enhancing Monodispersity and Thermal Stability of Human H-Ferritin as a Nanocarrier by Protein Design. *J. Agric. Food Chem.* **2025**, *73* (21), 12787–12798. DOI: 10.1021/acs.jafc.5c02232.
(91) Parayath, N. N.; Amiji, M. M. Therapeutic targeting strategies using endogenous cells and proteins. *J. Control. Release* **2017**, *258*, 81–94. DOI: 10.1016/j.jconrel.2017.05.004.
(92) Kang, W.; Xu, Z.; Lu, H.; Liu, S.; Li, J.; Ding, C.; Lu, Y. Advances in biomimetic

nanomaterial delivery systems: harnessing nature's inspiration for targeted drug delivery. *J. Mater. Chem. B* **2024**, *12* (29), 7001–7019. DOI: 10.1039/d4tb00565a.

(93) O'Rourke, K. F.; Gorman, S. D.; Boehr, D. D. Biophysical and computational methods to analyze amino acid interaction networks in proteins. *Comput. Struct. Biotechnol. J.* **2016**, *14*, 245–251. DOI: 10.1016/j.csbj.2016.06.002.

(94) Hartman, E. C.; Jakobson, C. M.; Favor, A. H.; Lobba, M. J.; Álvarez-Benedicto, E.; Francis, M. B.; Tullman-Ercek, D. Quantitative characterization of all single amino acid variants of a viral capsid-based drug delivery vehicle. *Nat. Commun.* **2018**, *9* (1), 1385. DOI: 10.1038/s41467-018-03783-y.

(95) Li, P.; Sun, M.; Xu, Z.; Liu, X.; Zhao, W.; Gao, W. Site-Selective in Situ Growth-Induced Self-Assembly of Protein-Polymer Conjugates into pH-Responsive Micelles for Tumor Microenvironment Triggered Fluorescence Imaging. *Biomacromolecules* **2018**, *19* (11), 4472–4479. DOI: 10.1021/acs.biomac.8b01368.

(96) Gimenez, J. A.; Schleusner, J.; Wilbers, R.; Schots, A.; Spiga, L.; Tregoning, J.; Finnern, R.; Williams, C. Le click c'est chic: a plug-and-play virus-like particle vaccination platform enabled by non-canonical amino acid incorporation and click chemistry in the tobacco BY-2 cell-free protein synthesis system. *bioRxiv*, September 16, 2025. DOI: 10.1101/2025.08.21.671528.

(97) Steinauer, A.; Steinauer, A. Protein Engineering and Directed Evolution for Nanocarrier Innovation: Medicinal Chemistry and Chemical Biology Highlights. *Chimia (Aarau).* **2024**, *78* (12), 885–888. DOI: 10.2533/chimia.2024.885.

(98) Hori, M.; Steinauer, A.; Tetter, S.; Hälg, J.; Manz, E. M.; Hilvert, D. Stimulus-responsive assembly of nonviral nucleocapsids. *Nat. Commun.* **2024**, *15* (1), 3576. DOI: 10.1038/s41467-024-47808-1.

(99) Olshefsky, A.; Richardson, C.; Pun, S. H.; King, N. P. Engineering Self-Assembling Protein Nanoparticles for Therapeutic Delivery. *Bioconjug. Chem.* **2022**, *33* (11), 2018–2034. DOI: 10.1021/acs.bioconjchem.2c00030.

(100) Rondon, A.; Mahri, S.; Morales-Yanez, F.; Dumoulin, M.; Vanbever, R. Protein Engineering Strategies for Improved Pharmacokinetics. *Adv. Funct. Mater.* **2021**, *31* (44), 2101633. DOI: 10.1002/adfm.202101633.

(101) Gou, Y.; Miao, D.; Zhou, M.; Wang, L.; Zhou, H.; Su, G. Bio-inspired protein-based nanoformulations for cancer theranostics. *Front. Pharmacol.* **2018**, *9*, 421. DOI: 10.3389/fphar.2018.00421.

(102) Ferraro, C.; Dattilo, M.; Patitucci, F.; Prete, S.; Scopelliti, G.; Parisi, O. I.; Puoci, F. Exploring Protein-Based Carriers in Drug Delivery: A Review. *Pharmaceutics* **2024**, *16* (9), 1172. DOI: 10.3390/pharmaceutics16091172.

(103) Yun, Y. H.; Lee, B. K.; Park, K. Controlled Drug Delivery: Historical perspective for the next generation. *J. Control. Release* **2015**, *219*, 2–7. DOI: 10.1016/j.jconrel.2015.10.005.

(104) Hrkach, J.; Langer, R. From micro to nano: evolution and impact of drug delivery in treating disease. *Drug Deliv. Transl. Res.* **2020**, *10* (3), 567–570. DOI: 10.1007/s13346-020-00769-6.

(105) Razmaria, A. Surgeon, Scientist, and Entrepreneur: One Man's Fight Against Cancer. *JAMA* **2016**, *316* (13), 1345–1347. DOI: 10.1001/jama.2016.9304.

(106) European Medicines Agency. *ANNEX I: Summary of product characteristics*; 2009. https://www.ema.europa.eu/en/documents/product-information/abraxane-epar-product-information_en.pdf (accessed 2025-11-17).

(107) Liggins, R. T.; Hunter, W. L.; Burt, H. M. Solid-State Characterization of Paclitaxel. *J. Pharm. Sci.* **1997**, *86* (12), 1458–1463. DOI: 10.1021/js9605226.

(108) Sato, T.; Okazaki, M.; Sano, J.; Kato, C.; Shimizu, K.; Kitagawa, M. Binding

affinities of paclitaxel and docetaxel for generic and nanoparticle albumin-bound paclitaxel-derived albumin from human serum. *Biomed. Rep.* **2021**, *14* (4), 1–5. DOI: 10.3892/br.2021.1411.

(109) Hama, M.; Ishima, Y.; Chuang, V. T. G.; Ando, H.; Shimizu, T.; Ishida, T. Evidence for Delivery of Abraxane via a Denatured-Albumin Transport System. *ACS Appl. Mater. Interfaces* **2021**, *13* (17), 19736–19744. DOI: 10.1021/acsami.1c03065.

(110) Teng, X.; Guan, Z.; Yao, Z.; Liu, D.; Zhou, N.; Luo, H.; Hawkins, M. J.; Soon-Shiong, P. A tolerability study of a cremophor free, nanoparticle albumin bound paclitaxel intravenously administered in Chinese patients with advanced solid tumor. *J. Clin. Oncol.* **2005**, *23* (16_suppl), 5571. DOI: 10.1200/jco.2005.23.16_suppl.5571.

(111) Desai, N.; Trieu, V.; Damascelli, B.; Soon-Shiong, P. SPARC Expression Correlates with Tumor Response to Albumin-Bound Paclitaxel in Head and Neck Cancer Patients. *Transl. Oncol.* **2009**, *2* (2), 59–64. DOI: 10.1593/tlo.09109.

(112) Alshawwa, S. Z.; Kassem, A. A.; Farid, R. M.; Mostafa, S. K.; Labib, G. S. Nanocarrier Drug Delivery Systems: Characterization, Limitations, Future Perspectives and Implementation of Artificial Intelligence. *Pharmaceutics* **2022**, *14* (4), 883. DOI: 10.3390/pharmaceutics14040883.

(113) Rahban, M.; Ahmad, F.; Piatyszek, M. A.; Haertlé, T.; Saso, L.; Saboury, A. A. Stabilization challenges and aggregation in protein-based therapeutics in the pharmaceutical industry. *RSC Adv.* **2023**, *13* (51), 35947–35963. DOI: 10.1039/d3ra06476j.

(114) Thalhammer-Thurner, G. C.; Debbage, P. Albumin-based nanoparticles: small, uniform and reproducible. *Nanoscale Adv.* **2023**, *5* (2), 503–512. DOI: 10.1039/d2na00413e.

(115) Natarajan, V.; Soice, N.; Mullen, J.; Bull, D. GMP implementation of a hybrid continuous manufacturing process for a recombinant non-mAb protein–A case study. *Biotechnol. Prog.* **2024**, *40* (4), e3459. DOI: 10.1002/btpr.3459.

(116) Du, J.; Shi, L. L.; Jiang, W. W.; Liu, X. A.; Wu, X. H.; Huang, X. X.; Huo, M. W.; Shi, L. Z.; Dong, J.; Jiang, X.; Huang, R.; Cao, Q. R.; Zhang, W. Crafting Docetaxel-Loaded Albumin Nanoparticles Through a Novel Thermal-Driven Self-Assembly/Microfluidic Combination Technology: Formulation, Process Optimization, Stability, and Bioavailability. *Int. J. Nanomedicine* **2024**, *19*, 5071–5094. DOI: 10.2147/ijn.s457482.

(117) Hakala, T. A.; Davies, S.; Toprakcioglu, Z.; Bernardim, B.; Bernardes, G. J. L.; Knowles, T. P. J. A Microfluidic Co-Flow Route for Human Serum Albumin-Drug–Nanoparticle Assembly. *Chem. Eur. J.* **2020**, *26* (27), 5965–5969. DOI: 10.1002/chem.202001146.

(118) Chua, A.; Tran, T. T.; Pu, S.; Park, J. W.; Hadinoto, K. Lyophilization of Curcumin–Albumin Nanoplex with Sucrose as Cryoprotectant: Aqueous Reconstitution, Dissolution, Kinetic Solubility, and Physicochemical Stability. *Int. J. Mol. Sci.* **2022**, *23* (19), 11731. DOI: 10.3390/ijms231911731.

(119) Wu, Y.; Ng, D. Y. W.; Kuan, S. L.; Weil, T. Protein–polymer therapeutics: a macromolecular perspective. *Biomater. Sci.* **2015**, *3* (2), 214–230. DOI: 10.1039/c4bm00270a.

(120) Saallah, S.; Lenggoro, I. W. Nanoparticles Carrying Biological Molecules: Recent Advances and Applications. *KONA Powder Part. J.* **2018**, *35* (35), 89–111. DOI: 10.14356/kona.2018015.

(121) Dominguez-Medina, S.; Blankenburg, J.; Olson, J.; Landes, C. F.; Link, S. Adsorption of a protein monolayer via hydrophobic interactions prevents

nanoparticle aggregation under harsh environmental conditions. *ACS Sustain. Chem. Eng.* **2013**, *1* (7), 833–842. DOI: 10.1021/sc400042h.

(122) Li, Z.; Li, D.; Zhang, W.; Zhang, P.; Kan, Q.; Sun, J. Insight into the preformed albumin corona on in vitro and in vivo performances of albumin-selective nanoparticles. *Asian J. Pharm. Sci.* **2019**, *14* (1), 52–62. DOI: 10.1016/j.ajps.2018.07.002.

(123) Li, Z.; Li, D.; Li, Q.; Luo, C.; Li, J.; Kou, L.; Zhang, D.; Zhang, H.; Zhao, S.; Kan, Q.; Liu, J.; Zhang, P.; Liu, X.; Sun, Y.; Wang, Y.; He, Z.; Sun, J. In situ low-immunogenic albumin-conjugating-corona guiding nanoparticles for tumor-targeting chemotherapy. *Biomater. Sci.* **2018**, *6* (10), 2681–2693. DOI: 10.1039/c8bm00692j.

(124) Spada, A.; Emami, J.; Tuszynski, J. A.; Lavasanifar, A. The Uniqueness of Albumin as a Carrier in Nanodrug Delivery. *Mol. Pharm.* **2021**, *18* (5), 1862–1894. DOI: 10.1021/acs.molpharmaceut.1c00046.

(125) Ji, Q.; Zhu, H.; Qin, Y.; Zhang, R.; Wang, L.; Zhang, E.; Zhou, X.; Meng, R. GP60 and SPARC as albumin receptors: key targeted sites for the delivery of antitumor drugs. *Front. Pharmacol.* **2024**, *15*, 1329636. DOI: 10.3389/fphar.2024.1329636.

(126) Fleck, A.; Hawker, F.; Wallace, P. I.; Raines, G.; Trotter, J.; Ledingham, I. M.; Calman, K. C. Increased vascular permeability: A major cause of hypoalbuminaemia in disease and injury. *Lancet* **1985**, *325* (8432), 781–784. DOI: 10.1016/s0140-6736(85)91447-3.

(127) Stukan, I.; Żuk, A.; Pukacka, K.; Mierzejewska, J.; Pawłowski, J.; Kowalski, B.; Dąbkowska, M. Wolf in Sheep's Clothing: Taming Cancer's Resistance with Human Serum Albumin? *Int. J. Nanomedicine* **2025**, *20*, 3493–3525. DOI: 10.2147/ijn.s500997.

(128) Caraceni, P.; Tufoni, M.; Bonavita, M. E. Clinical use of albumin. *Blood Transfus.* **2013**, *11* (Suppl 4), s18. DOI: 10.2450/2013.005s.

(129) Nilsen, J.; Sandlie, I.; Roopenian, D. C.; Andersen, J. T. Animal models for evaluation of albumin-based therapeutics. *Curr. Opin. Chem. Eng.* **2018**, *19*, 68–76. DOI: 10.1016/j.coche.2017.11.007.

(130) Chen, Y.; Lin, X.; Qin, Y.; Wu, D.; Gu, J.; Nie, S. Discovery of novel anti-serum albumin VHH as a building block for PK prolongation. *Antib. Ther.* **2023**, *6* (Supplement_1). DOI: 10.1093/abt/tbad014.011.

(131) Hong Toh, W.; Louber, J.; Mahmoud, I. S.; Chia, J.; Bass, G. T.; Dower, S. K.; Verhagen, A. M.; Gleeson, P. A. FcRn mediates fast recycling of endocytosed albumin and IgG from early macropinosomes in primary macrophages. *J. Cell Sci.* **2020**, *133* (5), jcs235416. DOI: 10.1242/jcs.235416.

(132) Gull, N.; Khan, J. M.; Rukhsana; Khan, R. H. Spectroscopic studies on the gemini surfactant mediated refolding of human serum albumin. *Int. J. Biol. Macromol.* **2017**, *102*, 331–335. DOI: 10.1016/j.ijbiomac.2017.03.134.

(133) Nattich-Rak, M.; Sadowska, M.; Adamczyk, Z.; Cieśla, M.; Kąkol, M. Formation mechanism of human serum albumin monolayers on positively charged polymer microparticles. *Colloids Surf B Biointerfaces* **2017**, *159*, 929–936. DOI: 10.1016/j.colsurfb.2017.08.051.

(134) Mimoto, M. S.; Karaca, A.; Scherberg, N.; Dumitrescu, A. M.; Refetoff, S. Homozygous mutation in human serum albumin and its implication on thyroid tests. *Thyroid* **2018**, *28* (6), 811–814. DOI: 10.1089/thy.2017.0564.

(135) Baker, M. E. Albumin's role in steroid hormone action and the origins of vertebrates: is albumin an essential protein? *FEBS Lett.* **1998**, *439* (1–2), 9–12. DOI: 10.1016/s0014-5793(98)01346-5.

(136) Litus, E. A.; Kazakov, A. S.; Sokolov, A. S.; Nemashkalova, E. L.; Galushko, E. I.; Dzhus, U. F.; Marchenkov, V. V.; Galzitskaya, O. V.; Permyakov, E. A.; Permyakov, S. E. The binding of monomeric amyloid β peptide to serum albumin is affected by major plasma unsaturated fatty acids. *Biochem. Biophys. Res. Commun.* **2019**, *510* (2), 248–253. DOI: 10.1016/j.bbrc.2019.01.081.

(137) Kirsipuu, T.; Zadorožnaja, A.; Smirnova, J.; Friedemann, M.; Plitz, T.; Tõugu, V.; Palumaa, P. Copper(II)-binding equilibria in human blood. *Sci. Rep.* **2020**, *10* (1), 5686. DOI: 10.1038/s41598-020-62560-4.

(138) Al-Harthi, S.; Chandra, K.; Jaremko, Ł. Lipoic Acid Restores Binding of Zinc Ions to Human Serum Albumin. *Front. Chem.* **2022**, *10*, 942585. DOI: 10.3389/fchem.2022.942585.

(139) Henning, C.; Stübner, C.; Arabi, S. H.; Reichenwallner, J.; Hinderberger, D.; Fiedler, R.; Girndt, M.; Di Sanzo, S.; Ori, A.; Glomb, M. A. Glycation Alters the Fatty Acid Binding Capacity of Human Serum Albumin. *J. Agric. Food Chem.* **2022**, *70* (9), 3033–3046. DOI: 10.1021/acs.jafc.1c07218.

(140) Zunszain, P. A.; Ghuman, J.; Komatsu, T.; Tsuchida, E.; Curry, S. Crystal structural analysis of human serum albumin complexed with hemin and fatty acid. *BMC Struct. Biol.* **2003**, *3* (1), 6. DOI: 10.1186/1472-6807-3-6.

(141) Ashraf, S.; Qaiser, H.; Tariq, S.; Khalid, A.; Makeen, H. A.; Alhazmi, H. A.; Ul-Haq, Z. Unraveling the versatility of human serum albumin – A comprehensive review of its biological significance and therapeutic potential. *Curr. Res. Struct. Biol.* **2023**, *6*, 100114. DOI: 10.1016/j.crstbi.2023.100114.

(142) Jayaraj, A.; Schwanz, H. A.; Spencer, D. J.; Bhasin, S.; Hamilton, J. A.; Jayaram, B.; Goldman, A. L.; Krishna, M.; Krishnan, M.; Shah, A.; Jin, Z.; Krenzel, E.; Nair, S. N.; Ramesh, S.; Guo, W.; Wagner, G.; Arthanari, H.; Peng, L.; Lawney, B.; Jasuja, R. Allosterically Coupled Multisite Binding of Testosterone to Human Serum Albumin. *Endocrinology* **2021**, *162* (2), 1–14. DOI: 10.1210/endocr/bqaa199.

(143) Krenzel, E. S.; Chen, Z.; Hamilton, J. A. Correspondence of fatty acid and drug binding sites on human serum albumin: A two-dimensional nuclear magnetic resonance study. *Biochemistry* **2013**, *52* (9), 1559–1567. DOI: 10.1021/bi301458b.

(144) Li, G.; Magana, D.; Dyer, R. B. Anisotropic energy flow and allosteric ligand binding in albumin. *Nat. Commun.* **2014**, *5* (1), 3100. DOI: 10.1038/ncomms4100.

(145) Yamasaki, K.; Hyodo, S.; Taguchi, K.; Nishi, K.; Yamaotsu, N.; Hirono, S.; Chuang, V. T. G.; Seo, H.; Maruyama, T.; Otagiri, M. Long chain fatty acids alter the interactive binding of ligands to the two principal drug binding sites of human serum albumin. *PLoS One* **2017**, *12* (6), e0180404. DOI: 10.1371/journal.pone.0180404.

(146) Masi, A. di; Leboffe, L.; Trezza, V.; Fanali, G.; Coletta, M.; Fasano, M.; Ascenzi, P. Drugs Modulate Allosterically Heme-Fe-Recognition by Human Serum Albumin and Heme-Fe-Mediated Reactivity. *Curr. Pharm. Des.* **2015**, *21* (14), 1837–1847. DOI: 10.2174/1381612821666150302114430.

(147) Knudsen Sand, K. M.; Bern, M.; Nilsen, J.; Noordzij, H. T.; Sandlie, I.; Andersen, J. T. Unraveling the interaction between FcRn and albumin: Opportunities for design of albumin-based therapeutics. *Front. Immunol.* **2014**, *6*, 682. DOI: 10.3389/fimmu.2014.00682.

(148) Algamal, M.; Milojevic, J.; Jafari, N.; Zhang, W.; Melacini, G. Mapping the Interactions between the Alzheimer's Aβ-Peptide and human serum albumin beyond domain resolution. *Biophys. J.* **2013**, *105* (7), 1700–1709. DOI: 10.1016/j.bpj.2013.08.025.

(149) Ishima, Y.; Maruyama, T.; Otagiri, M.; Chuang, V. T. G.; Ishida, T. The New Delivery Strategy of Albumin Carrier Utilizing the Interaction with Albumin

Receptors. *Chem. Pharm. Bull.* **2022**, *70* (5), 330–333. DOI: 10.1248/cpb.c21-01024.

(150) Schnitzer, J. E.; Bravo, J. High affinity binding, endocytosis, and degradation of conformationally modified albumins. Potential role of gp30 and gp18 as novel scavenger receptors. *J. Biol. Chem.* **1993**, *268* (10), 7562–7570. DOI: 10.1016/s0021-9258(18)53212-9.

(151) Chlenski, A.; Dobratic, M.; Salwen, H. R.; Applebaum, M.; Guerrero, L. J.; Miller, R.; DeWane, G.; Solomaha, E.; Marks, J. D.; Cohn, S. L.; Chlenski, A.; Dobratic, M.; Salwen, H. R.; Applebaum, M.; Guerrero, L. J.; Miller, R.; DeWane, G.; Solomaha, E.; Marks, J. D.; Cohn, S. L. Secreted protein acidic and rich in cysteine (SPARC) induces lipotoxicity in neuroblastoma by regulating transport of albumin complexed with fatty acids. *Oncotarget* **2016**, *7* (47), 77696–77706. DOI: 10.18632/oncotarget.12773.

(152) Zhu, A.; Yuan, P.; Du, F.; Hong, R.; Ding, X.; Shi, X.; Fan, Y.; Wang, J.; Luo, Y.; Ma, F.; Zhang, P.; Li, Q.; Xu, B. SPARC overexpression in primary tumors correlates with disease recurrence and overall survival in patients with triple negative breast cancer. *Oncotarget* **2016**, *7* (47), 76628–76634. DOI: 10.18632/oncotarget.10532.

(153) Hoogenboezem, E. N.; Duvall, C. L. Harnessing albumin as a carrier for cancer therapies. *Adv. Drug Deliv. Rev.* **2018**, *130*, 73–89. DOI: 10.1016/j.addr.2018.07.011.

(154) Nurdiansyah, R.; Rifa'I, M.; Widodo. A comparative analysis of serum albumin from different species to determine a natural source of albumin that might be useful for human therapy. *J. Taibah Univ. Med. Sci.* **2016**, *11* (3), 243–249. DOI: 10.1016/j.jtumed.2016.04.003.

(155) Jahanban-Esfahlan, A.; Dastmalchi, S.; Davaran, S. A simple improved desolvation method for the rapid preparation of albumin nanoparticles. *Int. J. Biol. Macromol.* **2016**, *91*, 703–709. DOI: 10.1016/j.ijbiomac.2016.05.032.

(156) Bartlett, B. A.; Klier, J.; Razavi, S. Preparation of bovine serum albumin nanospheres via desolvation: a study of synthesis, characterization, and aging. *Nanoscale* **2025**, *17* (10), 5715–5731. DOI: 10.1039/d4nr04682j.

(157) Dawoud, M. H. S.; Abdel-Daim, A.; Nour, M. S.; Sweed, N. M. A Quality by Design Paradigm for Albumin-Based Nanoparticles: Formulation Optimization and Enhancement of the Antitumor Activity. *J. Pharm. Innov.* **2023**, *18* (3), 1395–1414. DOI: 10.1007/s12247-022-09698-y.

(158) Tanjung, Y. P.; Dewi, M. K.; Gatera, V. A.; Barliana, M. I.; Joni, I. M.; Chaerunisaa, A. Y. Factors Affecting the Synthesis of Bovine Serum Albumin Nanoparticles Using the Desolvation Method. *Nanotechnol. Sci. Appl.* **2024**, *17*, 21–40. DOI: 10.2147/nsa.s441324.

(159) Meng, R.; Hao, S.; Sun, C.; Hou, Z.; Hou, Y.; Wang, L.; Deng, P.; Deng, J.; Yang, Y.; Xia, H.; Wang, B.; Qing, R.; Zhang, S. Reverse-QTY code design of active human serum albumin self-assembled amphiphilic nanoparticles for effective anti-tumor drug doxorubicin release in mice. *Proc. Natl. Acad. Sci. U. S. A.* **2023**, *120* (21), e2220173120. DOI: 10.1073/pnas.2220173120.

(160) Lee, S.; Lee, C.; Kim, B.; Thao, L. Q.; Lee, E. S.; Kim, J. O.; Oh, K. T.; Choi, H. G.; Youn, Y. S. A novel prototype of albumin nanoparticles fabricated by supramolecular cyclodextrin-adamantane association. *Colloids Surf B Biointerfaces* **2016**, *147*, 281–290. DOI: 10.1016/j.colsurfb.2016.08.009.

(161) Son, S.; Song, S.; Lee, S. J.; Min, S.; Kim, S. A.; Yhee, J. Y.; Huh, M. S.; Chan Kwon, I.; Jeong, S. Y.; Byun, Y.; Kim, S. H.; Kim, K. Self-crosslinked human serum

albumin nanocarriers for systemic delivery of polymerized siRNA to tumors. *Biomaterials* **2013**, *34* (37), 9475–9485. DOI: 10.1016/j.biomaterials.2013.08.085.

(162) Abolhassani, H.; Shojaosadati, S. A. A comparative and systematic approach to desolvation and self-assembly methods for synthesis of piperine-loaded human serum albumin nanoparticles. *Colloids Surf B Biointerfaces* **2019**, *184*, 110534. DOI: 10.1016/j.colsurfb.2019.110534.

(163) Li, H.; Wang, Y.; Tang, Q.; Yin, D.; Tang, C.; He, E.; Zou, L.; Peng, Q. The protein corona and its effects on nanoparticle-based drug delivery systems. *Acta Biomater.* **2021**, *129*, 57–72. DOI: 10.1016/j.actbio.2021.05.019.

(164) Kim, W.; Ly, N. K.; He, Y.; Li, Y.; Yuan, Z.; Yeo, Y. Protein corona: Friend or foe? Co-opting serum proteins for nanoparticle delivery. *Adv. Drug Deliv. Rev.* **2023**, *192*, 114635. DOI: 10.1016/j.addr.2022.114635.

(165) Wu, B.; Nan, S.; Zhang, H.; Deng, L.; Gong, T.; Zhang, Z.; Fu, Y. Effect of Albumin Corona Conformation on In Vitro and In Vivo Profiles of Intravenously Administered Nanoparticles. *Mol. Pharm.* **2023**, *20* (6), 2978–2990. DOI: 10.1021/acs.molpharmaceut.3c00021.

(166) Qu, N.; Song, K.; Ji, Y.; Liu, M.; Chen, L.; Lee, R. J.; Teng, L. Albumin Nanoparticle-Based Drug Delivery Systems. *Int. J. Nanomedicine* **2024**, *19*, 6945–6980. DOI: 10.2147/ijn.s467876.

(167) Tan, T.; Yang, Q.; Chen, D.; Zhao, J.; Xiang, L.; Feng, J.; Song, X.; Fu, Y.; Gong, T. Chondroitin sulfate-mediated albumin corona nanoparticles for the treatment of breast cancer. *Asian J. Pharm. Sci.* **2021**, *16* (4), 508–518. DOI: 10.1016/j.ajps.2021.03.004.

(168) Nicolì, E.; Syga, M. I.; Bosetti, M.; Shastri, V. P. Enhanced Gene Silencing through Human Serum Albumin-Mediated Delivery of Polyethylenimine-siRNA Polyplexes. *PLoS One* **2015**, *10* (4), e0122581. DOI: 10.1371/journal.pone.0122581.

(169) Du, C.; Deng, D.; Shan, L.; Wan, S.; Cao, J.; Tian, J.; Achilefu, S.; Gu, Y. A pH-sensitive doxorubicin prodrug based on folate-conjugated BSA for tumor-targeted drug delivery. *Biomaterials* **2013**, *34* (12), 3087–3097. DOI: 10.1016/j.biomaterials.2013.01.041.

(170) Ming, X.; Carver, K.; Wu, L. Albumin-based nanoconjugates for targeted delivery of therapeutic oligonucleotides. *Biomaterials* **2013**, *34* (32), 7939–7949. DOI: 10.1016/j.biomaterials.2013.06.066.

(171) Butzbach, K.; Rasse-Suriani, F. A. O.; Gonzalez, M. M.; Cabrerizo, F. M.; Epe, B. Albumin–Folate Conjugates for Drug-targeting in Photodynamic Therapy. *Photochem. Photobiol.* **2016**, *92* (4), 611–619. DOI: 10.1111/php.12602.

(172) Jalilinejad, N.; Rabiee, M.; Baheiraei, N.; Ghahremanzadeh, R.; Salarian, R.; Rabiee, N.; Akhavan, O.; Zarrintaj, P.; Hejna, A.; Saeb, M. R.; Zarrabi, A.; Sharifi, E.; Yousefiasl, S.; Zare, E. N. Electrically conductive carbon-based (bio)-nanomaterials for cardiac tissue engineering. *Bioeng. Transl. Med.* **2023**, *8* (1), e10347. DOI: 10.1002/btm2.10347.

(173) Fu, S.; Zheng, A.; Wang, L.; Chen, J.; Zhao, B.; Zhang, X.; McKenzie, V. A. A.; Yang, Z.; Leblanc, R. M.; Prabhakar, R.; Zhang, F. Tuneable redox-responsive albumin-hitchhiking drug delivery to tumours for cancer treatment. *J. Mater. Chem. B* **2024**, *12* (27), 6563–6569. DOI: 10.1039/d4tb00751d.

(174) Wang, W.; Yao, S. Y.; Luo, J.; Ding, C.; Huang, Q.; Yang, Y.; Shi, Z.; Lin, J.; Pan, Y. C.; Zeng, X.; Guo, D. S.; Chen, H. Engineered hypoxia-responsive albumin nanoparticles mediating mitophagy regulation for cancer therapy. *Nat. Commun.* **2025**, *16* (1), 596. DOI: 10.1038/s41467-025-55905-y.

(175) Renoux, B.; Raes, F.; Legigan, T.; Péraudeau, E.; Eddhif, B.; Poinot, P.; Tranoy-

Opalinski, I.; Alsarraf, J.; Koniev, O.; Kolodych, S.; Lerondel, S.; Le Pape, A.; Clarhaut, J.; Papot, S. Targeting the tumour microenvironment with an enzyme-responsive drug delivery system for the efficient therapy of breast and pancreatic cancers. *Chem. Sci.* **2017**, *8* (5), 3427–3433. DOI: 10.1039/c7sc00472a.

(176) Yu, Y.; Zuo, S.; Song, J.; Li, L.; Liu, T.; Guo, J.; Li, Y.; Wang, D.; Lu, Q.; Wang, H.; Zhou, D.; He, Z.; Liu, X.; Sun, B.; Sun, J. Balancing efficacy and safety of doxorubicin-loaded albumin nanoparticles utilizing pH-sensitive doxorubicin-fatty acid prodrugs. *Nano Res.* **2024**, *17* (6), 5491–5500. DOI: 10.1007/s12274-024-6533-5.

(177) ClinicalTrials.gov. *Recombinant Albumin Fusion Protein sEphB4-HSA in Treating Patients With Metastatic or Recurrent Solid Tumors*. NCT01642342. https://clinicaltrials.gov/study/NCT01642342 (accessed 2025-11-17).

(178) ClinicalTrials.gov. *Study of Recombinant Human Serum Albumin/Granulocyte Colony-Stimulating Factor Fusion Protein*. NCT02465801. https://clinicaltrials.gov/study/NCT02465801 (accessed 2025-11-17).

(179) Cini, J. K.; Kenney, R. T.; Dexter, S.; McAndrew, S. J.; Eraslan, R. N.; Brody, R.; Rezac, D. J.; Boohaker, R.; Lapi, S. E.; Mohan, P. SON-1010: an albumin-binding IL-12 fusion protein that improves cytokine half-life, targets tumors, and enhances therapeutic efficacy. *Front. Immunol.* **2024**, *15*, 1493257. DOI: 10.3389/fimmu.2024.1493257.

(180) Zhuo, S. H.; Chen, X.; Zhao, L.; Wang, T. Y.; Su, J. Y.; Yang, T.; Yang, L.; Dong, F.; Zhao, Y. F.; Li, Y. M. AlbiCDN: albumin-binding amphiphilic STING agonists augment the immune activity for cancer immunotherapy. *RSC Med. Chem.* **2025**, *16* (4), 1797–1807. DOI: 10.1039/d4md00475b.

(181) An, J. M.; Moon, H.; Verwilst, P.; Shin, J.; Kim, B. M.; Park, C. K.; Kim, J. S.; Yeo, S. G.; Kim, H. Y.; Kim, D. Human Glioblastoma Visualization: Triple Receptor-Targeting Fluorescent Complex of Dye, SIWV Tetra-Peptide, and Serum Albumin Protein. *ACS Sensors* **2021**, *6* (6), 2270–2280. DOI: 10.1021/acssensors.1c00320.

(182) Chung, S. W.; Choi, J. uk; Lee, B. S.; Byun, J.; Jeon, O. C.; Kim, S. W.; Kim, I. S.; Kim, S. Y.; Byun, Y. Albumin-binding caspase-cleavable prodrug that is selectively activated in radiation exposed local tumor. *Biomaterials* **2016**, *94*, 1–8. DOI: 10.1016/j.biomaterials.2016.03.043.

(183) Yu, C.; Hu, L.; Yu, Q.; Ren, Y.; Zhang, M.; Gao, L.; Lyu, S.; Wang, J.; Xiao, E.; Chen, Z.; Shang, Q.; Xu, P. In vivo self-assembled albumin nanoparticle elicit antitumor immunity of PD-1 inhibitor by imaging and clearing tumor-associated macrophages. *Front. Chem.* **2024**, *12*, 1469568. DOI: 10.3389/fchem.2024.1469568.

(184) Sarett, S. M.; Werfel, T. A.; Lee, L.; Jackson, M. A.; Kilchrist, K. V.; Brantley-Sieders, D.; Duvall, C. L. Lipophilic siRNA targets albumin in situ and promotes bioavailability, tumor penetration, and carrier-free gene silencing. *Proc. Natl. Acad. Sci. U. S. A.* **2017**, *114* (32), E6490–E6497. DOI: 10.1073/pnas.1621240114.

(185) Li, H.; Wang, Z.; Yu, S.; Chen, S.; Zhou, Y.; Qu, Y.; Xu, P.; Jiang, L.; Yuan, C.; Huang, M. Albumin-based drug carrier targeting urokinase receptor for cancer therapy. *Int. J. Pharm.* **2023**, *634*, 122636. DOI: 10.1016/j.ijpharm.2023.122636.

(186) Federa, A.; Schueffl, H.; Minichmayr, I. K.; Kastner, A.; Kronberger, J.; Mindt, T. L.; Heffeter, P.; Kowol, C. R. Comparative Evaluation of Thiol- and Amine-Conjugating Moieties for Endogenous Albumin Binding after Intravenous Administration. *ACS Pharmacol. Transl. Sci.* **2025**, *8* (7), 2192–2203. DOI: 10.1021/acsptsci.5c00240.

(187) Kratz, F. DOXO-EMCH (INNO-206): the first albumin-binding prodrug of

doxorubicin to enter clinical trials. *Expert Opin. Investig. Drugs* **2007**, *16* (6), 855–866. DOI: 10.1517/13543784.16.6.855.

(188) Lim, J. H.; Park, M.; Park, Y.; Park, S. J.; Lee, J.; Hwang, S.; Lee, J.; Lee, Y.; Jo, E.; Shin, Y. G. Evaluation of In Vivo Prepared Albumin-Drug Conjugate Using Immunoprecipitation Linked LC-MS Assay and Its Application to Mouse Pharmacokinetic Study. *Molecules* **2023**, *28* (7), 3223. DOI: 10.3390/molecules28073223.

(189) Kratz, F.; Müller-Driver, R.; Hofmann, I.; Drevs, J.; Unger, C. A novel macromolecular prodrug concept exploiting endogenous serum albumin as a drug carrier for cancer chemotherapy. *J. Med. Chem.* **2000**, *43* (7), 1253–1256. DOI: 10.1021/jm9905864.

(190) Chawla, S. P.; Papai, Z.; Mukhametshina, G.; Sankhala, K.; Vasylyev, L.; Fedenko, A.; Khamly, K.; Ganjoo, K.; Nagarkar, R.; Wieland, S.; Levitt, D. J. First-Line Aldoxorubicin vs Doxorubicin in Metastatic or Locally Advanced Unresectable Soft-Tissue Sarcoma: A Phase 2b Randomized Clinical Trial. *JAMA Oncol.* **2015**, *1* (9), 1272–1280. DOI: 10.1001/jamaoncol.2015.3101.

(191) Shan, L.; Zhuo, X.; Zhang, F.; Dai, Y.; Zhu, G.; Yung, B. C.; Fan, W.; Zhai, K.; Jacobson, O.; Kiesewetter, D. O.; Ma, Y.; Gao, G.; Chen, X. A paclitaxel prodrug with bifunctional folate and albumin binding moieties for both passive and active targeted cancer therapy. *Theranostics* **2018**, *8* (7), 2018–2030. DOI: 10.7150/thno.24382.

(192) Zhu, G.; Lynn, G. M.; Jacobson, O.; Chen, K.; Liu, Y.; Zhang, H.; Ma, Y.; Zhang, F.; Tian, R.; Ni, Q.; Cheng, S.; Wang, Z.; Lu, N.; Yung, B. C.; Wang, Z.; Lang, L.; Fu, X.; Jin, A.; Weiss, I. D.; Vishwasrao, H.; Niu, G.; Shroff, H.; Klinman, D. M.; Seder, R. A.; Chen, X. Albumin/vaccine nanocomplexes that assemble in vivo for combination cancer immunotherapy. *Nat. Commun.* **2017**, *8* (1), 1954-. DOI: 10.1038/s41467-017-02191-y.

(193) Taverna, M.; Marie, A. L.; Mira, J. P.; Guidet, B. Specific antioxidant properties of human serum albumin. *Ann. Intensive Care* **2013**, *3* (1), 1–7. DOI: 10.1186/2110-5820-3-4.

(194) An, F. F.; Zhang, X. H. Strategies for Preparing Albumin-based Nanoparticles for Multifunctional Bioimaging and Drug Delivery. *Theranostics* **2017**, *7* (15), 3667–3689. DOI: 10.7150/thno.19365.

(195) Liu, Y.; Li, Y.; Shen, W.; Li, M.; Wang, W.; Jin, X. Trend of albumin nanoparticles in oncology: a bibliometric analysis of research progress and prospects. *Front. Pharmacol.* **2024**, *15*, 1409163. DOI: 10.3389/fphar.2024.1409163.

(196) Berman, H. M.; Westbrook, J.; Feng, Z.; Gilliland, G.; Bhat, T. N.; Weissig, H.; Shindyalov, I. N.; Bourne, P. E. The Protein Data Bank. *Nucleic Acids Res.* **2000**, *28* (1), 235–242. DOI: 10.1093/nar/28.1.235.

(197) Sugio, S.; Kashima, A.; Mochizuki, S.; Noda, M.; Kobayashi, K. Crystal structure of human serum albumin at 2.5 Å resolution. *Protein Eng.* **1999**, *12* (6), 439–446. DOI: 10.1093/protein/12.6.439.

(198) Matsumura, Y.; Maeda, H. A New Concept for Macromolecular Therapeutics in Cancer Chemotherapy: Mechanism of Tumoritropic Accumulation of Proteins and the Antitumor Agent Smancs. *Cancer Res.* **1986**, *46* (8), 6387–6392.

(199) Köhler, G.; Milstein, C. Continuous cultures of fused cells secreting antibody of predefined specificity. *Nature* **1975**, *256* (5517), 495–497. DOI: 10.1038/256495a0.

(200) Akinc, A.; Querbes, W.; De, S.; Qin, J.; Frank-Kamenetsky, M.; Jayaprakash, K. N.; Jayaraman, M.; Rajeev, K. G.; Cantley, W. L.; Dorkin, J. R.; Butler, J. S.; Qin, L.; Racie, T.; Sprague, A.; Fava, E.; Zeigerer, A.; Hope, M. J.; Zerial, M.; Sah, D. W.;

Fitzgerald, K.; Tracy, M. A.; Manoharan, M.; Koteliansky, V.; Fougerolles, A. De; Maier, M. A. Targeted delivery of RNAi therapeutics with endogenous and exogenous ligand-based mechanisms. *Mol. Ther.* **2010**, *18* (7), 1357–1364. DOI: 10.1038/mt.2010.85.

(201) Hadjidemetriou, M.; Mahmoudi, M.; Kostarelos, K. In vivo biomolecule corona and the transformation of a foe into an ally for nanomedicine. *Nat. Rev. Mater.* **2024**, *9* (4), 219–222. DOI: 10.1038/s41578-024-00658-1.

(202) Fan, D.; Cao, Y.; Cao, M.; Wang, Y.; Cao, Y.; Gong, T. Nanomedicine in cancer therapy. *Signal Transduct. Target. Ther.* **2023**, *8* (1), 293. DOI: 10.1038/s41392-023-01536-y.

(203) Bachhav, Y.; Mannhold, R.; Buschmann, H.; Holenz, J. *Targeted Drug Delivery*; Wiley-VCH GmbH, 2023. DOI: 10.1002/9783527827855.

(204) Du, B.; Jiang, X.; Das, A.; Zhou, Q.; Yu, M.; Jin, R.; Zheng, J. Glomerular barrier behaves as an atomically precise bandpass filter in a sub-nanometre regime. *Nat. Nanotechnol.* **2017**, *12* (11), 1096–1102. DOI: 10.1038/nnano.2017.170.

(205) Wilhelm, S.; Tavares, A. J.; Dai, Q.; Ohta, S.; Audet, J.; Dvorak, H. F.; Chan, W. C. W. Analysis of nanoparticle delivery to tumours. *Nat. Rev. Mater.* **2016**, *1* (5), 16014. DOI: 10.1038/natrevmats.2016.14.

(206) Maeda, H.; Wu, J.; Sawa, T.; Matsumura, Y.; Hori, K. Tumor vascular permeability and the EPR effect in macromolecular therapeutics: a review. *J. Control. Release* **2000**, *65* (1–2), 271–284. DOI: 10.1016/s0168-3659(99)00248-5.

(207) Nguyen, L. N. M.; Lin, Z. P.; Sindhwani, S.; MacMillan, P.; Mladjenovic, S. M.; Stordy, B.; Ngo, W.; Chan, W. C. W. The exit of nanoparticles from solid tumours. *Nat. Mater.* **2023**, *22* (10), 1261–1272. DOI: 10.1038/s41563-023-01630-0.

(208) Dilliard, S. A.; Siegwart, D. J. Passive, active and endogenous organ-targeted lipid and polymer nanoparticles for delivery of genetic drugs. *Nat. Rev. Mater.* **2023**, *8* (4), 282–300. DOI: 10.1038/s41578-022-00529-7.

(209) Akinc, A.; Maier, M. A.; Manoharan, M.; Fitzgerald, K.; Jayaraman, M.; Barros, S.; Ansell, S.; Du, X.; Hope, M. J.; Madden, T. D.; Mui, B. L.; Semple, S. C.; Tam, Y. K.; Ciufolini, M.; Witzigmann, D.; Kulkarni, J. A.; van der Meel, R.; Cullis, P. R. The Onpattro story and the clinical translation of nanomedicines containing nucleic acid-based drugs. *Nat. Nanotechnol.* **2019**, *14* (12), 1084–1087. DOI: 10.1038/s41565-019-0591-y.

(210) Cirstoiu-Hapca, A.; Buchegger, F.; Lange, N.; Bossy, L.; Gurny, R.; Delie, F. Benefit of anti-HER2-coated paclitaxel-loaded immuno-nanoparticles in the treatment of disseminated ovarian cancer: Therapeutic efficacy and biodistribution in mice. *J. Control. Release* **2010**, *144* (3), 324–331. DOI: 10.1016/j.jconrel.2010.02.026.

(211) Kirpotin, D. B.; Drummond, D. C.; Shao, Y.; Shalaby, M. R.; Hong, K.; Nielsen, U. B.; Marks, J. D.; Benz, C. C.; Park, J. W. Antibody Targeting of Long-Circulating Lipidic Nanoparticles Does Not Increase Tumor Localization but Does Increase Internalization in Animal Models. *Cancer Res.* **2006**, *66* (13), 6732–6740. DOI: 10.1158/0008-5472.can-05-4199.

(212) Van Rooy, I.; Mastrobattista, E.; Storm, G.; Hennink, W. E.; Schiffelers, R. M. Comparison of five different targeting ligands to enhance accumulation of liposomes into the brain. *J. Control. Release* **2011**, *150* (1), 30–36. DOI: 10.1016/j.jconrel.2010.11.014.

(213) Kwon, I. K.; Lee, S. C.; Han, B.; Park, K. Analysis on the current status of targeted drug delivery to tumors. *J. Control. Release* **2012**, *164* (2), 108–114. DOI: 10.1016/j.jconrel.2012.07.010.

(214) Shukla, S.; DiFranco, N. A.; Wen, A. M.; Commandeur, U.; Steinmetz, N. F. To Target or Not to Target: Active vs. Passive Tumor Homing of Filamentous Nanoparticles Based on Potato virus X. *Cell. Mol. Bioeng.* **2015**, *8* (3), 433–444. DOI: 10.1007/s12195-015-0388-5.
(215) Yan, S.; Na, J.; Liu, X.; Wu, P. Different Targeting Ligands-Mediated Drug Delivery Systems for Tumor Therapy. *Pharmaceutics* **2024**, *16* (2), 248. DOI: 10.3390/pharmaceutics16020248.
(216) Kanp, T.; Dhuri, A.; Bharath, M.; Rode, K.; Aalhate, M.; Paul, P.; Nair, R.; Singh, P. K. Exploring the Potential of Nanocarriers for Cancer Immunotherapy: Insights into Mechanism, Nanocarriers, and Regulatory Perspectives. *ACS Appl. Bio Mater.* **2025**, *8* (1), 108–138. DOI: 10.1021/acsabm.4c01797.
(217) Sharma, P.; Goswami, S.; Raychaudhuri, D.; Siddiqui, B. A.; Singh, P.; Nagarajan, A.; Liu, J.; Subudhi, S. K.; Poon, C.; Gant, K. L.; Herbrich, S. M.; Anandhan, S.; Islam, S.; Amit, M.; Anandappa, G.; Allison, J. P. Immune checkpoint therapy–current perspectives and future directions. *Cell* **2023**, *186* (8), 1652–1669. DOI: 10.1016/j.cell.2023.03.006.
(218) Brown, G. D.; Willment, J. A.; Whitehead, L. C-type lectins in immunity and homeostasis. *Nat. Rev. Immunol.* **2018**, *18* (6), 374–389. DOI: 10.1038/s41577-018-0004-8.
(219) del Fresno, C.; Iborra, S.; Saz-Leal, P.; Martínez-López, M.; Sancho, D. Flexible signaling of Myeloid C-type lectin receptors in immunity and inflammation. *Front. Immunol.* **2018**, *9*, 804. DOI: 10.3389/fimmu.2018.00804.
(220) Lepenies, B.; Lang, R. Editorial: Lectins and Their Ligands in Shaping Immune Responses. *Front. Immunol.* **2019**, *10*, 2379. DOI: 10.3389/fimmu.2019.02379.
(221) Kontermann, R. E. Dual targeting strategies with bispecific antibodies. *MAbs* **2012**, *4* (2), 182–197. DOI: 10.4161/mabs.4.2.19000.
(222) Schoenfeld, K.; Harwardt, J.; Kolmar, H. Better safe than sorry: Dual targeting antibodies for cancer immunotherapy. *Biol. Chem.* **2024**, *405* (7–8), 443–459. DOI: 10.1515/hsz-2023-0329.
(223) Sun, R.; Zhang, Y.; Piao, Y.; Xiang, J.; Shao, S.; Zhou, Q.; Tang, J.; Dong, C.; Zhou, Z.; Shen, Y. Dual Enzyme-Responsive Polymer-Drug Conjugates Induce Diverse Cells Mutual Transcytosis to Achieve Deep Pancreatic Tumor Penetration. *Angew. Chem., Int. Ed.* **2025**, *64* (31), e202506038. DOI: 10.1002/anie.202506038.
(224) Liu, S.; Yuan, S.; Liu, M.; Liu, J.; Fu, S.; Gao, T.; Liang, S.; Huang, X.; Zhang, X.; Liu, Y.; Zhang, Z.; Zhang, N. In situ tumor cell engineering reverses immune escape to enhance immunotherapy effect. *Acta Pharm. Sin. B* **2025**, *15* (1), 627–641. DOI: 10.1016/j.apsb.2024.08.028.
(225) Niu, M.; Naguib, Y. W.; Aldayel, A. M.; Shi, Y. C.; Hursting, S. D.; Hersh, M. A.; Cui, Z. Biodistribution and in Vivo activities of tumor-associated macrophage-targeting nanoparticles incorporated with doxorubicin. *Mol. Pharm.* **2014**, *11* (12), 4425–4436. DOI: 10.1021/mp500565q.
(226) Schnider, B.; Rad, Y. M.; Ahmadie, J. el; de Brevern, A. G.; Imberty, A.; Lisacek, F. HumanLectome, an update of UniLectin for the annotation and prediction of human lectins. *Nucleic Acids Res.* **2024**, *52* (D1), D1683–D1693. DOI: 10.1093/nar/gkad905.
(227) Ireland, B. S.; Brockmeier, U.; Howe, C. M.; Elliott, T.; Williams, D. B. Lectin-deficient calreticulin retains full functionality as a chaperone for class I histocompatibility molecules. *Mol. Biol. Cell* **2008**, *19* (6), 2413–2423. DOI: 10.1091/mbc.e07-10-1055.
(228) Yamamoto, K.; Suzuki, K. Intracellular lectins are involved in quality control of

glycoproteins. *Proc. Japan Acad. Ser. B* **2014**, *90* (2), 67–82. DOI: 10.2183/pjab.90.67.

(229) Jung, S. Y.; Kim, S. S.; Kim, Y. Il; Chung, H. Y.; Kim, S. H.; Yeo, S. G. Expression, Distribution, and Role of C-Type Lectin Receptors in the Human and Animal Middle Ear and Eustachian Tube: A Review. *Molecules* **2018**, *23* (4), 734. DOI: 10.3390/molecules23040734.

(230) Pinho, S. S.; Alves, I.; Gaifem, J.; Rabinovich, G. A. Immune regulatory networks coordinated by glycans and glycan-binding proteins in autoimmunity and infection. *Cell. Mol. Immunol.* **2023**, *20* (10), 1101–1113. DOI: 10.1038/s41423-023-01074-1.

(231) Rabinovich, G. A.; Croci, D. O. Regulatory Circuits Mediated by Lectin-Glycan Interactions in Autoimmunity and Cancer. *Immunity* **2012**, *36* (3), 322–335. DOI: 10.1016/j.immuni.2012.03.004.

(232) Fuertes, M. B.; Molinero, L. L.; Toscano, M. A.; Ilarregui, J. M.; Rubinstein, N.; Fainboim, L.; Zwirner, N. W.; Rabinovich, G. A. Regulated expression of galectin-1 during T-cell activation involves Lck and Fyn kinases and signaling through MEK1/ERK, p38 MAP kinase and p70S6 kinase. *Mol. Cell. Biochem.* **2004**, *267* (1–2), 177–185. DOI: 10.1023/b:mcbi.0000049376.50242.7f.

(233) Seetharaman, J.; Kanigsberg, A.; Slaaby, R.; Leffler, H.; Barondes, S. H.; Rini, J. M. X-ray Crystal Structure of the Human Galectin-3 Carbohydrate Recognition Domain at 2.1-Å Resolution. *J. Biol. Chem.* **1998**, *273*, 13047–13052. DOI: 10.1074/jbc.273.21.13047.

(234) Mariño, K. V.; Cagnoni, A. J.; Croci, D. O.; Rabinovich, G. A. Targeting galectin-driven regulatory circuits in cancer and fibrosis. *Nat. Rev. Drug Discov.* **2023**, *22* (4), 295–316. DOI: 10.1038/s41573-023-00636-2.

(235) Navarro, P.; Martínez-Bosch, N.; Blidner, A. G.; Rabinovich, G. A. Impact of galectins in resistance to anticancer therapies. *Clin. Cancer Res.* **2020**, *26* (23), 6086–6101. DOI: 10.1158/1078-0432.ccr-18-3870.

(236) Wei, J.; Dai, Y.; Zhang, N.; Wang, Z.; Tian, X.; Yan, T.; Jin, X.; Jiang, S. Natural plant-derived polysaccharides targeting macrophage polarization: a promising strategy for cancer immunotherapy. *Front. Immunol.* **2024**, *15*, 1408377. DOI: 10.3389/fimmu.2024.1408377.

(237) O'Reilly, M. K.; Paulson, J. C. Multivalent Ligands for Siglecs. *Methods Enzymol.* **2010**, *478* (C), 343–363. DOI: 10.1016/s0076-6879(10)78017-4.

(238) Chang, Y. C.; Nizet, V. The interplay between Siglecs and sialylated pathogens. *Glycobiology* **2014**, *24* (9), 818–825. DOI: 10.1093/glycob/cwu067.

(239) Mantuano, N. R.; Läubli, H. Sialic acid and Siglec receptors in tumor immunity and immunotherapy. *Semin. Immunol.* **2024**, *74–75*, 101893. DOI: 10.1016/j.smim.2024.101893.

(240) Leaubli, H.; Nalle, S. C.; Maslyar, D. Targeting the Siglec–Sialic Acid Immune Axis in Cancer: Current and Future Approaches. *Cancer Immunol. Res.* **2022**, *10* (12), 1423–1432. DOI: 10.1158/2326-6066.cir-22-0366.

(241) Reis e Sousa, C.; Yamasaki, S.; Brown, G. D. Myeloid C-type lectin receptors in innate immune recognition. *Immunity* **2024**, *57* (4), 700–717. DOI: 10.1016/j.immuni.2024.03.005.

(242) Sosa Cuevas, E.; Valladeau-Guilemond, J.; Mouret, S.; Roubinet, B.; de Fraipont, F.; Landemarre, L.; Charles, J.; Bendriss-Vermare, N.; Chaperot, L.; Aspord, C. Unique CLR expression patterns on circulating and tumor-infiltrating DC subsets correlated with clinical outcome in melanoma patients. *Front. Immunol.* **2022**, *13*, 1040600. DOI: 10.3389/fimmu.2022.1040600.

(243) Li, Q. The multiple roles of C-type lectin receptors in cancer. *Front. Oncol.* **2023**, *13*, 1301473. DOI: 10.3389/fonc.2023.1301473.
(244) Yan, H.; Kamiya, T.; Suabjakyong, P.; Tsuji, N. M. Targeting C-type lectin receptors for cancer immunity. *Front. Immunol.* **2015**, *6*, 146351. DOI: 10.3389/fimmu.2015.00408.
(245) Xu, F.; Liu, J.; Liu, D.; Liu, B.; Wang, M.; Hu, Z.; Du, X.; Tang, L.; He, F. LSECtin expressed on melanoma cells promotes tumor progression by inhibiting antitumor T-cell responses. *Cancer Res.* **2014**, *74* (13), 3418–3428. DOI: 10.1158/0008-5472.can-13-2690.
(246) DeVito, N. C.; Plebanek, M. P.; Theivanthiran, B.; Hanks, B. A. Role of Tumor-Mediated Dendritic Cell Tolerization in Immune Evasion. *Front. Immunol.* **2019**, *10*, 494374. DOI: 10.3389/fimmu.2019.02876.
(247) Jain, M.; Jadhav, I. M.; Dangat, S. V.; Singuru, S. R.; Sethi, G.; Yuba, E.; Gupta, R. K. Overcoming the novel glycan–lectin checkpoints in tumor microenvironments for the success of the cross-presentation-based immunotherapy. *Biomater. Sci.* **2025**, *13* (13), 3447–3497. DOI: 10.1039/d4bm01732c.
(248) Pan, Y.; Wang, C.; Wang, S.; Wu, X.; Sheng, L.; Qi, Z. CLEC5A regulates the proliferation and migration of colon cancer via the AKT/mTOR signaling pathway. *J. Gastrointest. Oncol.* **2023**, *14* (3), 1331–1345. DOI: 10.21037/jgo-23-304.
(249) van der Zande, H. J. P.; Nitsche, D.; Schlautmann, L.; Guigas, B.; Burgdorf, S. The Mannose Receptor: From Endocytic Receptor and Biomarker to Regulator of (Meta)Inflammation. *Front. Immunol.* **2021**, *12*, 765034. DOI: 10.3389/fimmu.2021.765034.
(250) Schuette, V.; Embgenbroich, M.; Ulas, T.; Welz, M.; Schulte-Schrepping, J.; Draffehn, A. M.; Quast, T.; Koch, K.; Nehring, M.; König, J.; Zweynert, A.; Harms, F. L.; Steiner, N.; Limmer, A.; Förster, I.; Berberich-Siebelt, F.; Knolle, P. A.; Wohlleber, D.; Kolanus, W.; Beyer, M.; Schultze, J. L.; Burgdorf, S. Mannose receptor induces T-cell tolerance via inhibition of CD45 and up-regulation of CTLA-4. *Proc. Natl. Acad. Sci. U. S. A.* **2016**, *113* (38), 10649–10654. DOI: 10.1073/pnas.1605885113.
(251) Dossou, A. S.; Mantsch, M. E.; Sabnis, N.; Berg, R. E.; Fudala, R.; Lacko, A. G. Mannose-functionalization of reconstituted high-density lipoprotein nanoparticles improves payload delivery and enhances M2-to-M1 phenotype reprogramming of RAW 264.7 macrophages polarized by B16-F10 melanoma cells. *Front. Drug Deliv.* **2023**, *3*, 1281066. DOI: 10.3389/fddev.2023.1281066.
(252) Bolli, E.; Scherger, M.; Arnouk, S. M.; Pombo Antunes, A. R.; Straßburger, D.; Urschbach, M.; Stickdorn, J.; De Vlaminck, K.; Movahedi, K.; Räder, H. J.; Hernot, S.; Besenius, P.; Van Ginderachter, J. A.; Nuhn, L. Targeted Repolarization of Tumor-Associated Macrophages via Imidazoquinoline-Linked Nanobodies. *Adv. Sci.* **2021**, *8* (10), 2004574. DOI: 10.1002/advs.202004574.
(253) Dang, B. T. N.; Duwa, R.; Lee, S.; Kwon, T. K.; Chang, J. H.; Jeong, J. H.; Yook, S. Targeting tumor-associated macrophages with mannosylated nanotherapeutics delivering TLR7/8 agonist enhances cancer immunotherapy. *J. Control. Release* **2024**, *372*, 587–608. DOI: 10.1016/j.jconrel.2024.06.062.
(254) Guo, Y.; Li, Y.; Zhang, M.; Ma, R.; Wang, Y.; Weng, X.; Zhang, J.; Zhang, Z.; Chen, X.; Yang, W. Polymeric nanocarrier via metabolism regulation mediates immunogenic cell death with spatiotemporal orchestration for cancer immunotherapy. *Nat. Commun.* **2024**, *15* (1), 8586. DOI: 10.1038/s41467-024-53010-0.
(255) Zhan, X.; Jia, L.; Niu, Y.; Qi, H.; Chen, X.; Zhang, Q.; Zhang, J.; Wang, Y.; Dong,

L.; Wang, C. Targeted depletion of tumour-associated macrophages by an alendronate–glucomannan conjugate for cancer immunotherapy. *Biomaterials* **2014**, *35* (38), 10046–10057. DOI: 10.1016/j.biomaterials.2014.09.007.

(256) Lepland, A.; Malfanti, A.; Haljasorg, U.; Asciutto, E. K.; Pickholz, M.; Bringas, M.; Đorđević, S.; Salumäe, L.; Peterson, P.; Teesalu, T.; Vicent, M. J.; Scodeller, P. Depletion of Mannose Receptor–Positive Tumor-associated Macrophages via a Peptide-targeted Star-shaped Polyglutamate Inhibits Breast Cancer Progression in Mice. *Cancer Res. Commun.* **2022**, *2* (6), 533–551. DOI: 10.1158/2767-9764.crc-22-0043.

(257) Lei, J.; Qi, S.; Yu, X.; Gao, X.; Yang, K.; Zhang, X.; Cheng, M.; Bai, B.; Feng, Y.; Lu, M.; Wang, Y.; Li, H.; Yu, G. Development of Mannosylated Lipid Nanoparticles for mRNA Cancer Vaccine with High Antigen Presentation Efficiency and Immunomodulatory Capability. *Angew. Chem., Int. Ed.* **2024**, *63* (13), e202318515. DOI: 10.1002/anie.202318515.

(258) Conniot, J.; Scomparin, A.; Peres, C.; Yeini, E.; Pozzi, S.; Matos, A. I.; Kleiner, R.; Moura, L. I. F.; Zupančič, E.; Viana, A. S.; Doron, H.; Gois, P. M. P.; Erez, N.; Jung, S.; Satchi-Fainaro, R.; Florindo, H. F. Immunization with mannosylated nanovaccines and inhibition of the immune-suppressing microenvironment sensitizes melanoma to immune checkpoint modulators. *Nat. Nanotechnol.* **2019**, *14* (9), 891–901. DOI: 10.1038/s41565-019-0512-0.

(259) Freitas, R.; Peixoto, A.; Ferreira, E.; Miranda, A.; Santos, L. L.; Ferreira, J. A. Immunomodulatory glycomedicine: Introducing next generation cancer glycovaccines. *Biotechnol. Adv.* **2023**, *65*, 108144. DOI: 10.1016/j.biotechadv.2023.108144.

(260) Li, R. J. E.; Hogervorst, T. P.; Achilli, S.; Bruijns, S. C.; Arnoldus, T.; Vivès, C.; Wong, C. C.; Thépaut, M.; Meeuwenoord, N. J.; van den Elst, H.; Overkleeft, H. S.; van der Marel, G. A.; Filippov, D. V.; van Vliet, S. J.; Fieschi, F.; Codée, J. D. C.; van Kooyk, Y. Systematic Dual Targeting of Dendritic Cell C-Type Lectin Receptor DC-SIGN and TLR7 Using a Trifunctional Mannosylated Antigen. *Front. Chem.* **2019**, *7*, 479517. DOI: 10.3389/fchem.2019.00650.

(261) Geurtsen, J.; Driessen, N. N.; Appelmelk, B. J. Mannose–fucose recognition by DC-SIGN. In *Microbial Glycobiology: Structures, Relevance and Applications*; Holst, O., Brennan, P. J., Von Itzstein, M., Eds.; Academic Press, 2010; pp 673–695. DOI: 10.1016/b978-0-12-374546-0.00034-1.

(262) Ponader, D.; Wojcik, F.; Beceren-Braun, F.; Dernedde, J.; Hartmann, L. Sequence-defined glycopolymer segments presenting mannose: Synthesis and lectin binding affinity. *Biomacromolecules* **2012**, *13* (6), 1845–1852. DOI: 10.1021/bm300331z.

(263) Dimick, S. M.; Powell, S. C.; McMahon, S. A.; Moothoo, D. N.; Naismith, J. H.; Toone, E. J. On the meaning of affinity: Cluster glycoside effects and concanavalin A. *J. Am. Chem. Soc.* **1999**, *121* (44), 10286–10296. DOI: 10.1021/ja991729e.

(264) Liyanage, S. H.; Yan, M. Quantification of binding affinity of glyconanomaterials with lectins. *Chem. Commun.* **2020**, *56* (88), 13491–13505. DOI: 10.1039/d0cc05899h.

(265) Clemente, E.; Mateu, R.; Ferreira, A.; Ludtke, T.; Lopez, H.; Moya, S. E.; Lay, L.; Soliman, M. G.; Monopoli, M. P. Monosaccharide coatings on nanoparticles affect protein corona formation but not the interaction with their binding receptor. *Front. Nanotechnol.* **2024**, *6*, 1505757. DOI: 10.3389/fnano.2024.1505757.

(266) Permana, Y. S.; Jang, M.; Yeom, K.; Fagan, E.; Kim, Y. J.; Choi, J. H.; Park, J.-H. Ganglioside-incorporating lipid nanoparticles as a polyethylene glycol-free mRNA delivery platform. *Biomater. Sci.* **2025**, *13* (5), 1222–1232. DOI:

10.1039/d4bm01360c.
(267) García, I.; Sánchez-Iglesias, A.; Henriksen-Lacey, M.; Grzelczak, M.; Penadés, S.; Liz-Marzán, L. M. Glycans as Biofunctional Ligands for Gold Nanorods: Stability and Targeting in Protein-Rich Media. *J. Am. Chem. Soc.* **2015**, *137* (10), 3686–3692. DOI: 10.1021/jacs.5b01001.
(268) Pifferi, C.; Fuentes, R.; Fernández-Tejada, A. Natural and synthetic carbohydrate-based vaccine adjuvants and their mechanisms of action. *Nat. Rev. Chem.* **2021**, *5* (3), 197–216. DOI: 10.1038/s41570-020-00244-3.
(269) Apostolopoulos, V.; Thalhammer, T.; Tzakos, A. G.; Stojanovska, L. Targeting Antigens to Dendritic Cell Receptors for Vaccine Development. *J. Drug Deliv.* **2013**, *2013* (1), 869718. DOI: 10.1155/2013/869718.
(270) Wei, G.; Wang, Y.; Yang, G.; Wang, Y.; Ju, R. Recent progress in nanomedicine for enhanced cancer chemotherapy. *Theranostics* **2021**, *11* (13), 6370–6392. DOI: 10.7150/thno.57828.
(271) Bartusik-Aebisher, D.; Kotlińska, A.; Koszarska, K.; Aebisher, D. Challenges in drug delivery to the tumors–nanoparticles in medicine. *Open Explor.* **2025**, *3*, 1008126. DOI: 10.37349/eds.2025.1008126.
(272) Wang, Z.; Little, N.; Chen, J.; Lambesis, K. T.; Le, K. T.; Han, W.; Scott, A. J.; Lu, J. Immunogenic camptothesome nanovesicles comprising sphingomyelin-derived camptothecin bilayers for safe and synergistic cancer immunochemotherapy. *Nat. Nanotechnol.* **2021**, *16* (10), 1130–1140. DOI: 10.1038/s41565-021-00950-z.
(273) Dawidczyk, C. M.; Russell, L. M.; Searson, P. C. Nanomedicines for cancer therapy: State-of-the-art and limitations to pre-clinical studies that hinder future developments. *Front. Chem.* **2014**, *2*, 104975. DOI: 10.3389/fchem.2014.00069.
(274) Harrington, K. J.; Rowlinson-Busza, G.; Syrigos, K. N.; Abra, R. M.; Uster, P. S.; Peters, A. M.; Stewart, J. S. W. Influence of tumour size on uptake of111In-DTPA-labelled pegylated liposomes in a human tumour xenograft model. *Br. J. Cancer* **2000**, *83* (5), 684–688. DOI: 10.1054/bjoc.2000.1320.
(275) Colby, A. H.; Kirsch, J.; Patwa, A. N.; Liu, R.; Hollister, B.; McCulloch, W.; Burdette, J. E.; Pearce, C. J.; Oberliels, N. H.; Colson, Y. L.; Liu, K.; Grinstaff, M. W. Radiolabeled Biodistribution of Expansile Nanoparticles: Intraperitoneal Administration Results in Tumor Specific Accumulation. *ACS Nano* **2023**, *17* (3), 2212–2221. DOI: 10.1021/acsnano.2c08451.
(276) Kijanka, G.; Prokopowicz, M.; Schellekens, H.; Brinks, V. Influence of Aggregation and Route of Injection on the Biodistribution of Mouse Serum Albumin. *PLoS One* **2014**, *9* (1), e85281. DOI: 10.1371/journal.pone.0085281.
(277) Álamo, P.; Pallarès, V.; Céspedes, M. V.; Falgàs, A.; Sanchez, J. M.; Serna, N.; Sánchez-garcía, L.; Voltà-duràn, E.; Morris, G. A.; Sánchez-chardi, A.; Casanova, I.; Mangues, R.; Vazquez, E.; Villaverde, A.; Unzueta, U. Fluorescent Dye Labeling Changes the Biodistribution of Tumor-Targeted Nanoparticles. *Pharmaceutics* **2020**, *12* (11), 1004. DOI: 10.3390/pharmaceutics12111004.
(278) Schraven, S.; Rosenhain, S.; Brueck, R.; Wiechmann, T. M.; Pola, R.; Etrych, T.; Lederle, W.; Lammers, T.; Gremse, F.; Kiessling, F. Dye labeling for optical imaging biases drug carriers' biodistribution and tumor uptake. *Nanomedicine Nanotechnology, Biol. Med.* **2023**, *48*, 102650. DOI: 10.1016/j.nano.2023.102650.
(279) Cilliers, C.; Nessler, I.; Christodolu, N.; Thurber, G. M. Tracking Antibody Distribution with Near-Infrared Fluorescent Dyes: Impact of Dye Structure and Degree of Labeling on Plasma Clearance. *Mol. Pharm.* **2017**, *14* (5), 1623–1633. DOI: 10.1021/acs.molpharmaceut.6b01091.
(280) Lammers, T. Nanomedicine Tumor Targeting. *Adv. Mater.* **2024**, *36* (26), 2312169.

DOI: 10.1002/adma.202312169.

(281) Yan, Y.; Chen, B.; Yin, Q.; Wang, Z.; Yang, Y.; Wan, F.; Wang, Y.; Tang, M.; Xia, H.; Chen, M.; Liu, J.; Wang, S.; Zhang, Q.; Wang, Y. Dissecting extracellular and intracellular distribution of nanoparticles and their contribution to therapeutic response by monochromatic ratiometric imaging. *Nat. Commun.* **2022**, *13* (1), 2004. DOI: 10.1038/s41467-022-29679-6.

(282) Islam, M. R.; Patel, J.; Back, P. I.; Shmeeda, H.; Adamsky, K.; Yang, H.; Alvarez, C.; Gabizon, A. A.; La-Beck, N. M. Comparative effects of free doxorubicin, liposome encapsulated doxorubicin and liposome co-encapsulated alendronate and doxorubicin (PLAD) on the tumor immunologic milieu in a mouse fibrosarcoma model. *Nanotheranostics* **2022**, *6* (4), 451–464. DOI: 10.7150/ntno.75045.

(283) Lee, N. K.; Kim, S. N.; Park, C. G. Immune cell targeting nanoparticles: a review. *Biomater. Res.* **2021**, *25* (1). DOI: 10.1186/s40824-021-00246-2.

(284) Kzhyshkowska, J.; Shen, J.; Larionova, I. Targeting of TAMs: can we be more clever than cancer cells? *Cell. Mol. Immunol.* **2024**, *21* (12), 1376–1409. DOI: 10.1038/s41423-024-01232-z.

(285) Chen, Y.; De Koker, S.; De Geest, B. G. Engineering Strategies for Lymph Node Targeted Immune Activation. *Acc. Chem. Res.* **2020**, *53* (10), 2055–2067. DOI: 10.1021/acs.accounts.0c00260.

(286) Yao, Y.; Zhou, Y.; Liu, L.; Xu, Y.; Chen, Q.; Wang, Y.; Wu, S.; Deng, Y.; Zhang, J.; Shao, A. Nanoparticle-Based Drug Delivery in Cancer Therapy and Its Role in Overcoming Drug Resistance. *Front. Mol. Biosci.* **2020**, *7*, 558493. DOI: 10.3389/fmolb.2020.00193.

(287) Guo, X.; Sun, H.; Dong, J.; Feng, Y.; Li, H.; Zhuang, R.; Wang, P.; Cai, W.; Zhou, Y. Does nab-paclitaxel have a higher incidence of peripheral neuropathy than solvent-based paclitaxel? Evidence from a systematic review and meta-analysis. *Crit. Rev. Oncol. Hematol.* **2019**, *139*, 16–23. DOI: 10.1016/j.critrevonc.2019.04.021.

(288) Zhao, Y. C.; Li, X.; Wang, C. Q.; Jiao, Y.; Shen, Y. N.; Wang, T. J.; Zhang, C. H. Unveiling the Hidden Risks: An Update Decade-Long Analysis of Abraxane-Related Adverse Events from the FAERS Database. *Int. J. Nanomedicine* **2024**, *19*, 11847–11858. DOI: 10.2147/ijn.s490400.

(289) Man, F.; Lammers, T.; T. M. de Rosales, R. Imaging Nanomedicine-Based Drug Delivery: a Review of Clinical Studies. *Mol. Imaging Biol.* **2018**, *20* (5), 683–695. DOI: 10.1007/s11307-018-1255-2.

(290) Di Costanzo, F.; Gasperoni, S.; Rotella, V.; Di Costanzo, F. Targeted delivery of albumin bound paclitaxel in the treatment of advanced breast cancer. *Onco. Targets. Ther.* **2009**, *2*, 179–188. DOI: 10.2147/ott.s3863.

(291) Mayer, L. D.; Bally, M. B.; Cullis, P. R.; Wilson, S. L.; Emerman, J. T. Comparison of free and liposome encapsulated doxorubicin tumor drug uptake and antitumor efficacy in the SC115 murine mammary tumor. *Cancer Lett.* **1990**, *53* (2–3), 183–190. DOI: 10.1016/0304-3835(90)90212-g.

(292) Huang, B.; Abraham, W. D.; Zheng, Y.; Bustamante López, S. C.; Luo, S. S.; Irvine, D. J. Active targeting of chemotherapy to disseminated tumors using nanoparticle-carrying T cells. *Sci. Transl. Med.* **2015**, *7* (291). DOI: 10.1126/scitranslmed.aaa5447.

(293) Kanwar, M. M.; Amna Noor; Tanveer Rasool; Hafiza samin anjum; Aleena Ashraf; Aziz Ur Rahman; Maqsood ur Rehman. Meta-analysis of efficacy of nanoparticle-based chemotherapy compared to conventional chemotherapy in solid tumors. *Insights-Journal Heal. Rehabil.* **2025**, *3* (4), 257–263. DOI: 10.71000/rce00f58.

(294) Pagano, L.; Danesi, R.; Benedetti, E.; Morgagni, R.; Romani, L.; Venditti, A. The Role of CPX-351 in the Acute Myeloid Leukemia Treatment Landscape: Mechanism of Action, Efficacy, and Safety. *Drugs* **2025**, *85* (7), 855–866. DOI: 10.1007/s40265-025-02194-w.

(295) Mayer, L. D.; Harasym, T. O.; Tardi, P. G.; Harasym, N. L.; Shew, C. R.; Johnstone, S. A.; Ramsay, E. C.; Bally, M. B.; Janoff, A. S. Ratiometric dosing of anticancer drug combinations: Controlling drug ratios after systemic administration regulates therapeutic activity in tumor-bearing mice. *Mol. Cancer Ther.* **2006**, *5* (7), 1854–1863. DOI: 10.1158/1535-7163.mct-06-0118.

(296) Benderski, K.; Lammers, T.; Sofias, A. M. Analysis of multi-drug cancer nanomedicine. *Nat. Nanotechnol.* **2025**, *20* (8), 1163–1172. DOI: 10.1038/s41565-025-01932-1.

(297) Qian, J.; Olbrecht, S.; Boeckx, B.; Vos, H.; Laoui, D.; Etlioglu, E.; Wauters, E.; Pomella, V.; Verbandt, S.; Busschaert, P.; Bassez, A.; Franken, A.; Bempt, M. Vanden; Xiong, J.; Weynand, B.; van Herck, Y.; Antoranz, A.; Bosisio, F. M.; Thienpont, B.; Floris, G.; Vergote, I.; Smeets, A.; Tejpar, S.; Lambrechts, D. A pan-cancer blueprint of the heterogeneous tumor microenvironment revealed by single-cell profiling. *Cell Res.* **2020**, *30* (9), 745–762. DOI: 10.1038/s41422-020-0355-0.

(298) Cabral, H.; Matsumoto, Y.; Mizuno, K.; Chen, Q.; Murakami, M.; Kimura, M.; Terada, Y.; Kano, M. R.; Miyazono, K.; Uesaka, M.; Nishiyama, N.; Kataoka, K. Accumulation of sub-100 nm polymeric micelles in poorly permeable tumours depends on size. *Nat. Nanotechnol.* **2011**, *6* (12), 815–823. DOI: 10.1038/nnano.2011.166.

(299) Miedema, I. H. C.; Zwezerijnen, G. J. C.; Huisman, M. C.; Doeleman, E.; Mathijssen, R. H. J.; Lammers, T.; Hu, Q.; Van Dongen, G. A. M. S.; Rijcken, C. J. F.; Vugts, D. J.; Willemien Menke-Van Der Houven Van Oordt, C. PET-CT Imaging of Polymeric Nanoparticle Tumor Accumulation in Patients. *Adv. Mater.* **2022**, *34* (21), 2201043. DOI: 10.1002/adma.202201043.

(300) Ju, Y.; Li, S.; Tan, A. E. Q.; Pilkington, E. H.; Brannon, P. T.; Plebanski, M.; Cui, J.; Caruso, F.; Thurecht, K. J.; Tam, C.; Kent, S. J. Patient-Specific Nanoparticle Targeting in Human Leukemia Blood. *ACS Nano* **2024**, *18* (42), 29021–29035. DOI: 10.1021/acsnano.4c09919.

(301) Alizadeh, D.; Zhang, L.; Hwang, J.; Schluep, T.; Badie, B. Tumor-associated macrophages are predominant carriers of cyclodextrin-based nanoparticles into gliomas. *Nanomed. Nanotechnol. Biol. Med.* **2010**, *6* (2), 382–390. DOI: 10.1016/j.nano.2009.10.001.

(302) Tsvetkova, Y.; Beztsinna, N.; Baues, M.; Klein, D.; Rix, A.; Golombek, S. K.; Al Rawashdeh, W.; Gremse, F.; Barz, M.; Koynov, K.; Banala, S.; Lederle, W.; Lammers, T.; Kiessling, F. Balancing Passive and Active Targeting to Different Tumor Compartments Using Riboflavin-Functionalized Polymeric Nanocarriers. *Nano Lett.* **2017**, *17* (8), 4665–4674. DOI: 10.1021/acs.nanolett.7b01171.

(303) Lin, Z. P.; Nguyen, L. N. M.; Ouyang, B.; Macmillan, P.; Ngai, J.; Kingston, B. R.; Mladjenovic, S. M.; Chan, W. C. W. Macrophages Actively Transport Nanoparticles in Tumors after Extravasation. *ACS Nano* **2022**, *16* (4), 6080–6092. DOI: 10.1021/acsnano.1c11578.

(304) Lee, C.; Kim, G. R.; Yoon, J.; Kim, S. E.; Yoo, J. S.; Piao, Y. In vivo delineation of glioblastoma by targeting tumor-associated macrophages with near-infrared fluorescent silica coated iron oxide nanoparticles in orthotopic xenografts for surgical guidance. *Sci. Rep.* **2018**, *8* (1), 11122. DOI: 10.1038/s41598-018-29424-4.

(305) Choi, C. H. J.; Alabi, C. A.; Webster, P.; Davis, M. E. Mechanism of active targeting

in solid tumors with transferrin-containing gold nanoparticles. *Proc. Natl. Acad. Sci. U. S. A.* **2010**, *107* (3), 1235–1240. DOI: 10.1073/pnas.0914140107.

(306) Reuter, K. G.; Perry, J. L.; Kim, D.; Luft, J. C.; Liu, R.; DeSimone, J. M. Targeted PRINT Hydrogels: The Role of Nanoparticle Size and Ligand Density on Cell Association, Biodistribution, and Tumor Accumulation. *Nano Lett.* **2015**, *15* (10), 6371–6378. DOI: 10.1021/acs.nanolett.5b01362.

(307) Ota, Y.; Inagaki, R.; Takanashi, Y.; Uemachi, H.; Matsuda, K.; Matsuoka, M.; Taoda, R.; Ohe, S.; Ishitsubo, Y.; Nakamura, M.; Goto, M.; Ban, H.; Nagai, Y. Targeting Tumor-Associated Macrophages with the Immune-Activating Nanomedicine for Achieving Strong Antitumor Activity with Rapid Clearance from the Body. *ACS Nano* **2024**, *18* (34), 23757–23772. DOI: 10.1021/acsnano.4c08811.

(308) Chung, H.; Park, J. Y.; Kim, K.; Yoo, R. J.; Suh, M.; Gu, G. J.; Kim, J. S.; Choi, T. H.; Byun, J. W.; Ju, Y. W.; Han, W.; Ryu, H. S.; Chung, G.; Hwang, D. W.; Kim, Y.; Kang, H. R.; Na, Y. R.; Choi, H.; Im, H. J.; Lee, Y. S.; Seok, S. H. Circulation Time-Optimized Albumin Nanoplatform for Quantitative Visualization of Lung Metastasis via Targeting of Macrophages. *ACS Nano* **2022**, *16* (8), 12262–12275. DOI: 10.1021/acsnano.2c03075.

(309) Lee, J. H.; Sahu, A.; Jang, C.; Tae, G. The effect of ligand density on in vivo tumor targeting of nanographene oxide. *J. Control. Release* **2015**, *209*, 219–228. DOI: 10.1016/j.jconrel.2015.04.035.

(310) Zimmer, O.; Goepferich, A. On the uncertainty of the correlation between nanoparticle avidity and biodistribution. *Eur. J. Pharm. Biopharm.* **2024**, *198*, 114240. DOI: 10.1016/j.ejpb.2024.114240.

(311) Liu, Y.; Zhang, Y.; Li, H.; Hu, T. Y. Recent advances in the bench-to-bedside translation of cancer nanomedicines. *Acta Pharm. Sin. B* **2025**, *15* (1), 97–122. DOI: 10.1016/j.apsb.2024.12.007.

(312) Pimm, M. V. Drug-monoclonal antibody conjugates for cancer therapy: potentials and limitations. *Crit. Rev. Ther. Drug Carrier Syst.* **1988**, *5* (3), 189–227.

(313) Sethi, M.; Sukumar, R.; Karve, S.; Werner, M. E.; Wang, E. C.; Moore, D. T.; Kowalczyk, S. R.; Zhang, L.; Wang, A. Z. Effect of drug release kinetics on nanoparticle therapeutic efficacy and toxicity. *Nanoscale* **2014**, *6* (4), 2321–2327. DOI: 10.1039/c3nr05961h.

(314) Lee, J. H.; Yeo, Y. Controlled drug release from pharmaceutical nanocarriers. *Chem. Eng. Sci.* **2015**, *125*, 75–84. DOI: 10.1016/j.ces.2014.08.046.

(315) Enayati, M.; Mobedi, H.; Hojjati-Emami, S.; Mirzadeh, H.; Jafari-Nodoushan, M. In situ forming PLGA implant for 90 days controlled release of leuprolide acetate for treatment of prostate cancer. *Polym. Adv. Technol.* **2017**, *28* (7), 867–875. DOI: 10.1002/pat.3991.

(316) Paulides, M. M.; Dobsicek Trefna, H.; Curto, S.; Rodrigues, D. B. Recent technological advancements in radiofrequency- andmicrowave-mediated hyperthermia for enhancing drug delivery. *Adv. Drug Deliv. Rev.* **2020**, *163–164*, 3–18. DOI: 10.1016/j.addr.2020.03.004.

(317) Aslam, H.; Shukrullah, S.; Naz, M. Y.; Fatima, H.; Hussain, H.; Ullah, S.; Assiri, M. A. Current and future perspectives of multifunctional magnetic nanoparticles based controlled drug delivery systems. *J. Drug Deliv. Sci. Technol.* **2022**, *67*, 102946. DOI: 10.1016/j.jddst.2021.102946.

(318) Kolosnjaj-Tabi, J.; Gibot, L.; Fourquaux, I.; Golzio, M.; Rols, M. P. Electric field-responsive nanoparticles and electric fields: physical, chemical, biological mechanisms and therapeutic prospects. *Adv. Drug Deliv. Rev.* **2019**, *138*, 56–67. DOI: 10.1016/j.addr.2018.10.017.

(319) Jiang, R.; Fang, Q.; Liu, W.; Chen, L.; Yang, H. Recent Progress in Radiosensitive Nanomaterials for Radiotherapy-Triggered Drug Release. *ACS Appl. Mater. Interfaces* **2025**, *17* (10), 14801–14821. DOI: 10.1021/acsami.4c23023.
(320) Fan, C. H.; Ho, Y. J.; Lin, C. W.; Wu, N.; Chiang, P. H.; Yeh, C. K. State-of-the-art of ultrasound-triggered drug delivery from ultrasound-responsive drug carriers. *Expert Opin. Drug Deliv.* **2022**, *19* (8), 997–1009. DOI: 10.1080/17425247.2022.2110585.
(321) Spill, F.; Reynolds, D. S.; Kamm, R. D.; Zaman, M. H. Impact of the physical microenvironment on tumor progression and metastasis. *Curr. Opin. Biotechnol.* **2016**, *40*, 41–48. DOI: 10.1016/j.copbio.2016.02.007.
(322) Andreucci, E.; Peppicelli, S.; Ruzzolini, J.; Bianchini, F.; Calorini, L. Physicochemical aspects of the tumour microenvironment as drivers of vasculogenic mimicry. *Cancer Metastasis Rev.* **2022**, *41* (4), 935–951. DOI: 10.1007/s10555-022-10067-x.
(323) Ivey, J. W.; Bonakdar, M.; Kanitkar, A.; Davalos, R. V.; Verbridge, S. S. Improving cancer therapies by targeting the physical and chemical hallmarks of the tumor microenvironment. *Cancer Lett.* **2016**, *380* (1), 330–339. DOI: 10.1016/j.canlet.2015.12.019.
(324) Hosonuma, M.; Yoshimura, K. Association between pH regulation of the tumor microenvironment and immunological state. *Front. Oncol.* **2023**, *13*, 1175563. DOI: 10.3389/fonc.2023.1175563.
(325) Romero-Aristizabal, C.; Marks, D. S.; Fontana, W.; Apfeld, J. Regulated spatial organization and sensitivity of cytosolic protein oxidation in Caenorhabditis elegans. *Nat. Commun. 2014 51* **2014**, *5* (1), 5020-. DOI: 10.1038/ncomms6020.
(326) Yin, J.; Huang, L.; Wu, L.; Li, J.; James, T. D.; Lin, W. Small molecule based fluorescent chemosensors for imaging the microenvironment within specific cellular regions. *Chem. Soc. Rev.* **2021**, *50* (21), 12098–12150. DOI: 10.1039/d1cs00645b.
(327) Rowan, S. J.; Cantrill, S. J.; Cousins, G. R. L.; Sanders, J. K. M.; Stoddart, J. F. Dynamic Covalent Chemistry. *Angew. Chem., Int. Ed.* **2002**, *41* (6), 898–952. DOI: 10.1002/1521-3773(20020315)41:6<898::aid-anie898>3.0.co;2-e.
(328) Liu, Y.; Wu, Y.; Luo, Z.; Li, M. Designing supramolecular self-assembly nanomaterials as stimuli-responsive drug delivery platforms for cancer therapy. *iScience* **2023**, *26* (3), 106279. DOI: 10.1016/j.isci.2023.106279.
(329) Liu, Z. S.; Wen, J.; Huang, C. Y.; Zhang, P. W.; Miao, Y. L.; Cheng, H.; Li, S. Y. Nanomedicines Based on Responsive Nanocarriers for Cancer Therapy. *Adv. Ther.* **2024**, *7* (2), 2300223. DOI: 10.1002/adtp.202300223.
(330) Bhagchandani, S. H.; Vohidov, F.; Milling, L. E.; Tong, E. Y.; Brown, C. M.; Ramseier, M. L.; Liu, B.; Fessenden, T. B.; Nguyen, H. V. T.; Kiel, G. R.; Won, L.; Langer, R. S.; Spranger, S.; Shalek, A. K.; Irvine, D. J.; Johnson, J. A. Engineering kinetics of TLR7/8 agonist release from bottlebrush prodrugs enables tumor-focused immune stimulation. *Sci. Adv.* **2023**, *9* (16). DOI: 10.1126/sciadv.adg2239.
(331) Wang, B.; Van Herck, S.; Chen, Y.; Bai, X.; Zhong, Z.; Deswarte, K.; Lambrecht, B. N.; Sanders, N. N.; Lienenklaus, S.; Scheeren, H. W.; David, S. A.; Kiessling, F.; Lammers, T.; De Geest, B. G.; Shi, Y. Potent and Prolonged Innate Immune Activation by Enzyme-Responsive Imidazoquinoline TLR7/8 Agonist Prodrug Vesicles. *J. Am. Chem. Soc.* **2020**, *142* (28), 12133–12139. DOI: 10.1021/jacs.0c01928.
(332) Wang, H.; Su, H.; Xu, T.; Cui, H. Utilizing the Hofmeister Effect to Induce Hydrogelation of Nonionic Supramolecular Polymers into a Therapeutic Depot. *Angew. Chem., Int. Ed.* **2023**, *62* (43). DOI: 10.1002/anie.202306652.

(333) Pan, W.; Zhang, L.; Li, L.; Cen, J.; Song, R.; Song, C.; Zhang, G.; Hu, J.; Liu, S. Engineering Semicarbazide-Bearing Polypeptide Conjugates for Efficient Tumor Chemotherapy and Imaging of Tumor Metastasis. *Adv. Mater.* **2024**, *36* (9). DOI: 10.1002/adma.202309315.

(334) Yang, K.; Yang, Z.; Yu, G.; Nie, Z.; Wang, R.; Chen, X. Polyprodrug Nanomedicines: An Emerging Paradigm for Cancer Therapy. *Adv. Mater.* **2022**, *34* (6). DOI: 10.1002/adma.202107434.

(335) Bordat, A.; Boissenot, T.; Ibrahim, N.; Ferrere, M.; Levêque, M.; Potiron, L.; Denis, S.; Garcia-Argote, S.; Carvalho, O.; Abadie, J.; Cailleau, C.; Pieters, G.; Tsapis, N.; Nicolas, J. A Polymer Prodrug Strategy to Switch from Intravenous to Subcutaneous Cancer Therapy for Irritant/Vesicant Drugs. *J. Am. Chem. Soc.* **2022**, *144* (41), 18844–18860. DOI: 10.1021/jacs.2c04944.

(336) Xin, X.; Zhang, Z.; Zhang, X.; Chen, J.; Lin, X.; Sun, P.; Liu, X. Bioresponsive nanomedicines based on dynamic covalent bonds. *Nanoscale* **2021**, *13* (27), 11712–11733. DOI: 10.1039/d1nr02836g.

(337) Ulrich, S. Growing Prospects of Dynamic Covalent Chemistry in Delivery Applications. *Acc. Chem. Res.* **2019**, *52* (2), 510–519. DOI: 10.1021/acs.accounts.8b00591.

(338) Xu, J.; Liu, Y.; Hsu, S. hui. Hydrogels Based on Schiff Base Linkages for Biomedical Applications. *Molecules* **2019**, *24* (16), 3005. DOI: 10.3390/molecules24163005.

(339) Kulchat, S.; Chaur, M. N.; Lehn, J. M. Kinetic Selectivity and Thermodynamic Features of Competitive Imine Formation in Dynamic Covalent Chemistry. *Chem. Eur. J.* **2017**, *23* (46), 11108–11118. DOI: 10.1002/chem.201702088.

(340) Dirksen, A.; Dirksen, S.; Hackeng, T. M.; Dawson, P. E. Nucleophilic catalysis of hydrazone formation and transimination: Implications for dynamic covalent chemistry. *J. Am. Chem. Soc.* **2006**, *128* (49), 15602–15603. DOI: 10.1021/ja067189k.

(341) Dirksen, A.; Hackeng, T. M.; Dawson, P. E. Nucleophilic Catalysis of Oxime Ligation. *Angew. Chem., Int. Ed.* **2006**, *45* (45), 7581–7584. DOI: 10.1002/anie.200602877.

(342) Kalia, J.; Raines, R. T.; Kalia, J.; Raines, R. T. Hydrolytic Stability of Hydrazones and Oximes. *Angew. Chem., Int. Ed.* **2008**, *47* (39), 7523–7526. DOI: 10.1002/anie.200802651.

(343) Yang, X.; Pan, Z.; Choudhury, M. R.; Yuan, Z.; Anifowose, A.; Yu, B.; Wang, W.; Wang, B. Making smart drugs smarter: The importance of linker chemistry in targeted drug delivery. *Med. Res. Rev.* **2020**, *40* (6), 2682–2713. DOI: 10.1002/med.21720.

(344) Dowell, J. A.; Korth-Bradley, J.; Liu, H.; King, S. P.; Berger, M. S. Pharmacokinetics of Gemtuzumab Ozogamicin, an Antibody-Targeted Chemotherapy Agent for the Treatment of Patients with Acute Myeloid Leukemia in First Relapse. *J. Clin. Pharmacol.* **2001**, *41* (11), 1206–1214. DOI: 10.1177/00912700122012751.

(345) Ross, H. J.; Rudin, C. M.; Hart, L. L.; Swanson, P. M.; Rarick, M. U.; Figlin, R. A.; Jacobs, A. D.; Miller, D. M. Randomized phase II study of SGN-15 (CBR96-doxorubicin immunoconjugate) with docetaxel in patients with advanced or metastatic non-small cell lung cancer (NSCLC). *J. Clin. Oncol.* **2004**, *22* (14_suppl), 7039–7039. DOI: 10.1200/jco.2004.22.90140.7039.

(346) Ding, Y.; Sun, D.; Wang, G. L.; Yang, H. G.; Xu, H. F.; Chen, J. H.; Xie, Y.; Wang, Z. Q. An efficient PEGylated liposomal nanocarrier containing cell-penetrating

peptide and pH-sensitive hydrazone bond for enhancing tumor-targeted drug delivery. *Int. J. Nanomedicine* **2015**, *10*, 6199–6214. DOI: 10.2147/ijn.s92519.

(347) Zhang, Y.; Yang, C.; Wang, W.; Liu, J.; Liu, Q.; Huang, F.; Chu, L.; Gao, H.; Li, C.; Kong, D.; Liu, Q.; Liu, J. Co-delivery of doxorubicin and curcumin by pH-sensitive prodrug nanoparticle for combination therapy of cancer. *Sci. Rep.* **2016**, *6* (1), 21225. DOI: 10.1038/srep21225.

(348) Fan, X.; Wang, K.; Lu, Q.; Lu, Y.; Liu, F.; Li, L.; Li, S.; Ye, H.; Zhao, J.; Cao, L.; Zhang, H.; He, Z.; Sun, J. Surface-anchored tumor microenvironment-responsive protein nanogel-platelet system for cytosolic delivery of therapeutic protein in the post-surgical cancer treatment. *Acta Biomater.* **2022**, *154*, 412–423. DOI: 10.1016/j.actbio.2022.10.031.

(349) Mao, F.; Ni, W.; Xu, X.; Wang, H.; Wang, J.; Ji, M.; Li, J. Chemical Structure-Related Drug-Like Criteria of Global Approved Drugs. *Molecules* **2016**, *21* (1), 75. DOI: 10.3390/molecules21010075.

(350) Zhang, Y.; Gao, M.; Chen, C.; Wang, Z.; Zhao, Y. Residue cytotoxicity of a hydrazone-linked polymer–drug conjugate: implication for acid-responsive micellar drug delivery. *RSC Adv.* **2015**, *5* (44), 34800–34802. DOI: 10.1039/c5ra02097b.

(351) Ito, H.; Kono, Y.; Machida, A.; Mitsumoto, Y.; Omori, K.; Nakamura, N.; Kondo, Y.; Ishihara, K. Kinetic study of the complex formation of boric and boronic acids with mono- and diprotonated ligands. *Inorganica Chim. Acta* **2003**, *344*, 28–36. DOI: 10.1016/s0020-1693(02)01268-9.

(352) Ni, N.; Laughlin, S.; Wang, Y.; Feng, Y.; Zheng, Y.; Wang, B. Probing the general time scale question of boronic acid binding with sugars in aqueous solution at physiological pH. *Bioorg. Med. Chem.* **2012**, *20* (9), 2957–2961. DOI: 10.1016/j.bmc.2012.03.014.

(353) Springsteen, G.; Wang, B. A detailed examination of boronic acid–diol complexation. *Tetrahedron* **2002**, *58* (26), 5291–5300. DOI: 10.1016/s0040-4020(02)00489-1.

(354) Williams, G. T.; Kedge, J. L.; Fossey, J. S. Molecular Boronic Acid-Based Saccharide Sensors. *ACS Sensors* **2021**, *6* (4), 1508–1528. DOI: 10.1021/acssensors.1c00462.

(355) Czarnik, A. W.; James, T. D. Fluorescent Chemosensors in the Creation of a Commercially Available Continuous Glucose Monitor. *ACS Sensors* **2024**, *9* (12), 6320–6326. DOI: 10.1021/acssensors.4c02403.

(356) Brooks, W. L. A.; Deng, C. C.; Sumerlin, B. S. Structure-Reactivity Relationships in Boronic Acid-Diol Complexation. *ACS Omega* **2018**, *3* (12), 17863–17870. DOI: 10.1021/acsomega.8b02999.

(357) Terriac, L.; Helesbeux, J. J.; Maugars, Y.; Guicheux, J.; Tibbitt, M. W.; Delplace, V. Boronate Ester Hydrogels for Biomedical Applications: Challenges and Opportunities. *Chem. Mater.* **2024**, *36* (14), 6674–6695. DOI: 10.1021/acs.chemmater.4c00507.

(358) Heard, D. M.; Lessard, M. C.; Hall, D. G. Xanthopinacol Boronate: A Robust, Photochemically Assembled and Cleavable Boronic Ester for Orthogonal Chemistry. *Angew. Chemie Int. Ed.* **2025**, *64* (28), e202507571. DOI: 10.1002/anie.202507571.

(359) Wulff, G. Selective binding to polymers via covalent bonds. the construction of chiral cavities as specific receptor sites. *Pure Appl. Chem.* **1982**, *54* (11), 2093–2102. DOI: 10.1351/pac198254112093.

(360) António, J. P. M.; Russo, R.; Carvalho, C. P.; Cal, P. M. S. D.; Gois, P. M. P. Boronic acids as building blocks for the construction of therapeutically useful bioconjugates.

Chem. Soc. Rev. **2019**, *48* (13), 3513–3536. DOI: 10.1039/c9cs00184k.

(361) Banach, Ł.; Williams, G. T.; Fossey, J. S. Insulin Delivery Using Dynamic Covalent Boronic Acid/Ester-Controlled Release. *Adv. Ther.* **2021**, *4* (11), 2100118. DOI: 10.1002/adtp.202100118.

(362) Norrild, J. C. An illusive chiral aminoalkylferroceneboronic acid. Structural assignment of a strong 1 : 1 sorbitol complex and new insight into boronate–polyol interactions. *J. Chem. Soc. Perkin Trans. 2* **2001**, No. 5, 719–726. DOI: 10.1039/b100436k.

(363) Martínez-Aguirre, M. A.; Flores-Alamo, M.; Yatsimirsky, A. K. Thermodynamic and structural study of complexation of phenylboronic acid with salicylhydroxamic acid and related ligands. *Appl. Organomet. Chem.* **2018**, *32* (8), e4405. DOI: 10.1002/aoc.4405.

(364) Seidler, C.; Zegota, M. M.; Raabe, M.; Kuan, S. L.; Ng, D. Y. W.; Weil, T. Dynamic Core–Shell Bioconjugates for Targeted Protein Delivery and Release. *Chem. Asian J.* **2018**, *13* (22), 3474–3479. DOI: 10.1002/asia.201800843.

(365) Shin, S. B. Y.; Almeida, R. D.; Gerona-Navarro, G.; Bracken, C.; Jaffrey, S. R. Assembling Ligands In Situ Using Bioorthogonal Boronate Ester Synthesis. *Chem. Biol.* **2010**, *17* (11), 1171–1176. DOI: 10.1016/j.chembiol.2010.09.008.

(366) Zegota, M. M.; Wang, T.; Seidler, C.; Wah Ng, D. Y.; Kuan, S. L.; Weil, T. "tag and Modify" Protein Conjugation with Dynamic Covalent Chemistry. *Bioconjug. Chem.* **2018**, *29* (8), 2665–2670. DOI: 10.1021/acs.bioconjchem.8b00358/asset/images/large/bc-2018-00358b_0004.jpeg.

(367) Barthelmes, K.; Yaginuma, K.; Matsumoto, A. Tuning the Stability and Kinetics of Dioxazaborocanes. *Chem. Eur. J.* **2025**, *31* (5), e202402625. DOI: 10.1002/chem.202402625.

(368) Hebel, M.; Riegger, A.; Zegota, M. M.; Kizilsavas, G.; Gačanin, J.; Pieszka, M.; Lückerath, T.; Coelho, J. A. S.; Wagner, M.; Gois, P. M. P.; Ng, D. Y. W.; Weil, T. Sequence Programming with Dynamic Boronic Acid/Catechol Binary Codes. *J. Am. Chem. Soc.* **2019**, *141* (36), 14026–14031. DOI: 10.1021/jacs.9b03107/asset/images/large/ja9b03107_0003.jpeg.

(369) Ma, Y.; He, P.; Tian, X.; Liu, G.; Zeng, X.; Pan, G. Mussel-Derived, Cancer-Targeting Peptide as pH-Sensitive Prodrug Nanocarrier. *ACS Appl. Mater. Interfaces* **2019**, *11* (27), 23948–23956. DOI: 10.1021/acsami.9b09031.

(370) Xiao, W.; Sun, S.; Geng, R.; Bi, D.; Liu, Y.; Zhu, J. A General "Two-Lock" Strategy to Enhance Drug Loading and Lysosomal Escape in Intelligent Boronate Ester Polymer Nanoparticles for Improved Chemotherapy. *ACS Appl. Mater. Interfaces* **2024**, *16* (50), 68890–68904. DOI: 10.1021/acsami.4c15172.

(371) Van De Bittner, G. C.; Dubikovskaya, E. A.; Bertozzi, C. R.; Chang, C. J. In vivo imaging of hydrogen peroxide production in a murine tumor model with a chemoselective bioluminescent reporter. *Proc. Natl. Acad. Sci. U. S. A.* **2010**, *107* (50), 21316–21321. DOI: 10.1073/pnas.1012864107.

(372) Bulaj, G. Formation of disulfide bonds in proteins and peptides. *Biotechnol. Adv.* **2005**, *23* (1), 87–92. DOI: 10.1016/j.biotechadv.2004.09.002.

(373) Mallick, P.; Boutz, D. R.; Eisenberg, D.; Yeates, T. O. Genomic evidence that the intracellular proteins of archaeal microbes contain disulfide bonds. *Proc. Natl. Acad. Sci. U. S. A.* **2002**, *99* (15), 9679–9684. DOI: 10.1073/pnas.142310499.

(374) Parshad, B.; Arora, S.; Singh, B.; Pan, Y.; Tang, J.; Hu, Z.; Patra, H. K. Towards precision medicine using biochemically triggered cleavable conjugation. *Commun. Chem.* **2025**, *8* (1), 100. DOI: 10.1038/s42004-025-01491-5.

(375) Schafer, F. Q.; Buettner, G. R. Redox environment of the cell as viewed through the

redox state of the glutathione disulfide/glutathione couple. *Free Radic. Biol. Med.* **2001**, *30* (11), 1191–1212. DOI: 10.1016/s0891-5849(01)00480-4.

(376) Kalinina, E. V.; Gavriliuk, L. A. Glutathione Synthesis in Cancer Cells. *Biochem. Moscow* **2020**, *85* (8), 895–907. DOI: 10.1134/s0006297920080052.

(377) Ortega, A. L.; Mena, S.; Estrela, J. M. Glutathione in Cancer Cell Death. *Cancers (Basel).* **2011**, *3* (1), 1285–1310. DOI: 10.3390/cancers3011285.

(378) Roederer, M.; Staal, F. J. T.; Osada, H.; Herzenberg, L. A.; Herzenberg, L. A. CD4 and CD8 T cells with high intracellular glutathione levels are selectively lost as the HIV infection progresses. *Int. Immunol.* **1991**, *3* (9), 933–937. DOI: 10.1093/intimm/3.9.933.

(379) Miró-Vinyals, C.; Emmert, S.; Grammbitter, G.; Jud, A.; Kockmann, T.; Rivera-Fuentes, P. Characterization of the glutathione redox state in the Golgi apparatus. *Redox Biol.* **2025**, *81*, 103560. DOI: 10.1016/j.redox.2025.103560.

(380) Nagy, P. Kinetics and mechanisms of thiol-disulfide exchange covering direct substitution and thiol oxidation-mediated pathways. *Antioxidants Redox Signal.* **2013**, *18* (13), 1623–1641. DOI: 10.1089/ars.2012.4973.

(381) Sadowsky, J. D.; Pillow, T. H.; Chen, J.; Fan, F.; He, C.; Wang, Y.; Yan, G.; Yao, H.; Xu, Z.; Martin, S.; Zhang, D.; Chu, P.; Dela Cruz-Chuh, J.; O'Donohue, A.; Li, G.; Del Rosario, G.; He, J.; Liu, L.; Ng, C.; Su, D.; Lewis Phillips, G. D.; Kozak, K. R.; Yu, S. F.; Xu, K.; Leipold, D.; Wai, J. Development of Efficient Chemistry to Generate Site-Specific Disulfide-Linked Protein- and Peptide-Payload Conjugates: Application to THIOMAB Antibody-Drug Conjugates. *Bioconjug. Chem.* **2017**, *28* (8), 2086–2098. DOI: 10.1021/acs.bioconjchem.7b00258.

(382) Zheng, Y.; Shen, Y.; Meng, X.; Wu, Y.; Zhao, Y.; Wu, C. Stabilizing p-Dithiobenzyl Urethane Linkers without Rate-Limiting Self-Immolation for Traceless Drug Release. *ChemMedChem* **2019**, *14* (12), 1196–1203. DOI: 10.1002/cmdc.201900248.

(383) Đorđević, S.; Medel, M.; Hillaert, J.; Masiá, E.; Conejos-Sánchez, I.; Vicent, M. J. Critical Design Strategies Supporting Optimized Drug Release from Polymer–Drug Conjugates. *Small* **2024**, *20* (4), 2303157. DOI: 10.1002/smll.202303157.

(384) Jia, R.; Teng, L.; Gao, L.; Su, T.; Fu, L.; Qiu, Z.; Bi, Y. Advances in Multiple Stimuli-Responsive Drug-Delivery Systems for Cancer Therapy. *Int. J. Nanomedicine* **2021**, *16*, 1525–1551. DOI: 10.2147/ijn.s293427.

(385) Yin, W.; Ke, W.; Lu, N.; Wang, Y.; Japir, A. A. W. M. M.; Mohammed, F.; Wang, Y.; Pan, Y.; Ge, Z. Glutathione and Reactive Oxygen Species Dual-Responsive Block Copolymer Prodrugs for Boosting Tumor Site-Specific Drug Release and Enhanced Antitumor Efficacy. *Biomacromolecules* **2020**, *21* (2), 921–929. DOI: 10.1021/acs.biomac.9b01578.

(386) Liu, T.; Li, L.; Wang, S.; Dong, F.; Zuo, S.; Song, J.; Wang, X.; Lu, Q.; Wang, H.; Zhang, H.; Cheng, M.; Liu, X.; He, Z.; Sun, B.; Sun, J. Hybrid chalcogen bonds in prodrug nanoassemblies provides dual redox-responsivity in the tumor microenvironment. *Nat. Commun.* **2022**, *13* (1), 7228. DOI: 10.1038/s41467-022-35033-7.

(387) Ruiz, A. L.; Ramirez, A.; McEnnis, K. Single and Multiple Stimuli-Responsive Polymer Particles for Controlled Drug Delivery. *Pharmaceutics* **2022**, *14* (2), 421. DOI: 10.3390/pharmaceutics14020421.

(388) Schauenburg, D.; Gao, B.; Rochet, L. N. C.; Schüler, D.; Coelho, J. A. S.; Ng, D. Y. W.; Chudasama, V.; Kuan, L.; Weil, T. Macrocyclic Dual-Locked "Turn-On" Drug for Selective and Traceless Release in Cancer Cells. **2024**. DOI: 10.1002/anie.202314143.

(389) Yuan, J.; Chen, Q.; Zuo, M.; Li, X.; Ou, C. Y.; Chen, Q.; Yu, D.; Li, H.; Hao, C.; Yang, J.; Liu, S.; Cheng, D. Enhanced combination therapy through tumor microenvironment-activated cellular uptake and ROS-sensitive drug release using a dual-sensitive nanogel. *Biomater. Sci.* **2025**, *13* (6), 1554–1567. DOI: 10.1039/d4bm01377h.
(390) Aloss, K.; Hamar, P. Recent Preclinical and Clinical Progress in Liposomal Doxorubicin. *Pharmaceutics* **2023**, *15* (3), 893. DOI: 10.3390/pharmaceutics15030893.
(391) Kratz, F. A clinical update of using albumin as a drug vehicle – A commentary. *J. Control. Release* **2014**, *190*, 331–336. DOI: 10.1016/j.jconrel.2014.03.013.
(392) Xiao, Q.; Zoulikha, M.; Qiu, M.; Teng, C.; Lin, C.; Li, X.; Sallam, M. A.; Xu, Q.; He, W. The effects of protein corona on in vivo fate of nanocarriers. *Adv. Drug Deliv. Rev.* **2022**, *186*, 114356. DOI: 10.1016/j.addr.2022.114356.
(393) Sanità, G.; Carrese, B.; Lamberti, A. Nanoparticle Surface Functionalization: How to Improve Biocompatibility and Cellular Internalization. *Front. Mol. Biosci.* **2020**, *7*, 587012. DOI: 10.3389/fmolb.2020.587012.
(394) Ly, P. D.; Ly, K. N.; Phan, H. L.; Nguyen, H. H. T.; Duong, V. A.; Nguyen, H. V. Recent advances in surface decoration of nanoparticles in drug delivery. *Front. Nanotechnol.* **2024**, *6*, 1456939. DOI: 10.3389/fnano.2024.1456939.
(395) Shetty, S.; Lalor, P. F.; Adams, D. H. Liver sinusoidal endothelial cells – gatekeepers of hepatic immunity. *Nat. Rev. Gastroenterol. Hepatol.* **2018**, *15* (9), 555–567. DOI: 10.1038/s41575-018-0020-y.
(396) Alkilany, A. M.; Zhu, L.; Weller, H.; Mews, A.; Parak, W. J.; Barz, M.; Feliu, N. Ligand density on nanoparticles: A parameter with critical impact on nanomedicine. *Adv. Drug Deliv. Rev.* **2019**, *143*, 22–36. DOI: 10.1016/j.addr.2019.05.010.
(397) Feinberg, H.; Castelli, R.; Drickamer, K.; Seeberger, P. H.; Weis, W. I. Multiple Modes of Binding Enhance the Affinity of DC-SIGN for High Mannose N-Linked Glycans Found on Viral Glycoproteins. *J. Biol. Chem.* **2007**, *282* (6), 4202–4209. DOI: 10.1074/jbc.m609689200.
(398) Cummings, R. D. The mannose receptor ligands and the macrophage glycome. *Curr. Opin. Struct. Biol.* **2022**, *75*, 102394. DOI: 10.1016/j.sbi.2022.102394.
(399) Pan, C.; Kumar, C.; Bohl, S.; Klingmueller, U.; Mann, M. Comparative Proteomic Phenotyping of Cell Lines and Primary Cells to Assess Preservation of Cell Type-specific Functions. *Mol. Cell. Proteomics* **2009**, *8* (3), 443–450. DOI: 10.1074/mcp.m800258-mcp200.
(400) Rolfo, C.; Giovannetti, E.; Martinez, P.; McCue, S.; Naing, A. Applications and clinical trial landscape using Toll-like receptor agonists to reduce the toll of cancer. *npj Precis. Oncol.* **2023**, *7* (1), 26-. DOI: 10.1038/s41698-023-00364-1.
(401) Li, J.; Chen, C.; Xia, T. Understanding Nanomaterial-Liver Interactions to Facilitate the Development of Safer Nanoapplications. *Adv. Mater.* **2022**, *34* (11), e2106456. DOI: 10.1002/adma.202106456.
(402) Gan, C.; Yuan, Y.; Shen, H.; Gao, J.; Kong, X.; Che, Z.; Guo, Y.; Wang, H.; Dong, E.; Xiao, J. Liver diseases: epidemiology, causes, trends and predictions. *Signal Transduct. Target. Ther.* **2025**, *10* (1), 33. DOI: 10.1038/s41392-024-02072-z.
(403) Gracia-Sancho, J.; Caparrós, E.; Fernández-Iglesias, A.; Francés, R. Role of liver sinusoidal endothelial cells in liver diseases. *Nat. Rev. Gastroenterol. Hepatol.* **2021**, *18* (6), 411–431. DOI: 10.1038/s41575-020-00411-3.
(404) Donne, R.; Lujambio, A. The liver cancer immune microenvironment: Therapeutic implications for hepatocellular carcinoma. *Hepatology* **2023**, *77* (5), 1773–1796. DOI: 10.1002/hep.32740.

(405) van der Heide, D.; Weiskirchen, R.; Bansal, R. Therapeutic Targeting of Hepatic Macrophages for the Treatment of Liver Diseases. *Front. Immunol.* **2019**, *10*, 494110. DOI: 10.3389/fimmu.2019.02852.

(406) Yoo, C.; Verdaguer, H.; Lin, C.-C.; Qvortrup, C.; Yau, T.; Oh, D.-Y.; Lichtenegger, F.; Franjkovic, I.; Kratochwil, N.; Bessa, J.; Rossmann, E.; Hall, E.; Dai, C.; Krieter, O.; Te-Ying, A. Y.; Cannarile, M.; Schiff, C.; Sangro, B. Abstract CT096: Phase 1 study of RO7119929 (TLR7 agonist prodrug) in patients (pts) with advanced primary or metastatic liver cancers. *Cancer Res.* **2023**, *83* (8_Supplement), CT096–CT096. DOI: 10.1158/1538-7445.am2023-ct096.

(407) ClinicalTrials.gov. *A Study of TransCon TLR7/8 Agonist With or Without Pembrolizumab in Patients With Advanced or Metastatic Solid Tumors*. NCT04799054. https://clinicaltrials.gov/study/NCT04799054 (accessed 2025-11-27).

(408) Li, K.; Xiao, K.; Zhu, S.; Wang, Y.; Wang, W. Chinese Herbal Medicine for Primary Liver Cancer Therapy: Perspectives and Challenges. *Front. Pharmacol.* **2022**, *13*, 889799. DOI: 10.3389/fphar.2022.889799.

(409) Li, Q. Z.; Chen, Y. Y.; Liu, Q. P.; Feng, Z. H.; Zhang, L.; Zhang, H. Cucurbitacin B suppresses hepatocellular carcinoma progression through inducing DNA damage-dependent cell cycle arrest. *Phytomedicine* **2024**, *126*, 155177. DOI: 10.1016/j.phymed.2023.155177.

(410) Tian, Z.; Hu, Q.; Sun, Z.; Wang, N.; He, H.; Tang, Z.; Chen, W. A Booster for Radiofrequency Ablation: Advanced Adjuvant Therapy via In Situ Nanovaccine Synergized with Anti-programmed Death Ligand 1 Immunotherapy for Systemically Constraining Hepatocellular Carcinoma. *ACS Nano* **2023**, *17* (19), 19441–19458. DOI: 10.1021/acsnano.3c08064.

(411) Kim, N. J.; Yoon, J. H.; Tuomi, A. C.; Lee, J.; Kim, D. In-situ tumor vaccination by percutaneous ablative therapy and its synergy with immunotherapeutics: An update on combination therapy. *Front. Immunol.* **2023**, *14*, 1118845. DOI: 10.3389/fimmu.2023.1118845.

(412) Den Brok, M. H. M. G. M.; Sutmuller, R. P. M.; Van Der Voort, R.; Bennink, E. J.; Figdor, C. G.; Ruers, T. J. M.; Adema, G. J. In Situ Tumor Ablation Creates an Antigen Source for the Generation of Antitumor Immunity. *Cancer Res.* **2004**, *64* (11), 4024–4029. DOI: 10.1158/0008-5472.can-03-3949.

(413) Slovak, R.; Ludwig, J. M.; Gettinger, S. N.; Herbst, R. S.; Kim, H. S. Immuno-thermal ablations - boosting the anticancer immune response. *J. Immunother. Cancer* **2017**, *5* (1), 78. DOI: 10.1186/s40425-017-0284-8.

(414) Rothstein, J.; Carriere, C.; Bell, K.; Day, M.; Huang, X.; Kuta-Howe, A.; Schwertner, N.; Koroleva, I.; Kuesters, G.; Weaver, M.; Nichols, D.; McClure, M. POS0666 Immune-targeted glucocorticoid ADC for the treatment of autoimmune and inflammatory diseases. *Ann. Rheum. Dis.* **2025**, *84*, 850–851. DOI: 10.1016/j.ard.2025.06.027.

(415) He, L.; Wang, L.; Wang, Z.; Li, T.; Chen, H.; Zhang, Y.; Hu, Z.; Dimitrov, D. S.; Du, J.; Liao, X. Immune Modulating Antibody-Drug Conjugate (IM-ADC) for Cancer Immunotherapy. *J. Med. Chem.* **2021**, *64* (21), 15716–15726. DOI: 10.1021/acs.jmedchem.1c00961.

Appendix

PubMed search strategy

A comprehensive literature search, presented in Figure 2, was performed in PubMed (via NCBI, accessed September 28, 2025) to identify studies on nanocarriers used in oncology, covering publications from 2000 to date. Multiple nanocarrier material classes were considered, including protein-based, inorganic, polymeric, lipid-based, carbon-based. To compare the overall publication trends, a combined query encompassing all nanocarriers, including hybrid systems, was also conducted.

For each material class, specific search terms were used to capture relevant nanocarrier types, including common synonyms, abbreviations, and established technologies. Both MeSH terms and free-text terms were used where applicable. All queries were restricted to original research articles, excluding reviews, meta-analyses, editorials, letters, and comments.

Two separate sets of searches were performed:

1. **Preclinical studies:** To identify research articles describing nanocarrier design, synthesis, and evaluation, clinical trials and randomized controlled trials were excluded.
2. **Clinical trials:** To capture clinical evaluations of nanocarriers, separate searches were conducted for each material class, including all clinical trial phases (I–IV) and randomized controlled trials.

All searches included the keyword “cancer” or the corresponding MeSH term. The search terms used for each material class and the combined nanocarrier search are detailed below.

Research article query:	**Clinical trial query:**
“ ("search term 1"[tiab] OR "search term 2"[tiab] OR …)	“ ("search term 1"[tiab] OR "search term 2"[tiab] OR …)
AND	AND
(cancer[tiab] OR "cancer"[Mesh])	(cancer[tiab] OR "cancer"[Mesh])
AND journal article[pt]	AND
NOT review[pt]	(clinical trial[pt]
NOT systematic review[pt]	OR clinical trial, phase I[pt]

NOT meta-analysis[pt] NOT editorial[pt] NOT comment[pt] NOT letter[pt] NOT clinical trial[pt] NOT clinical trial, phase I[pt] NOT clinical trial, phase II[pt] NOT clinical trial, phase III[pt] NOT clinical trial, phase IV[pt] NOT randomized controlled trial[pt]”	OR clinical trial, phase II[pt] OR clinical trial, phase III[pt] OR clinical trial, phase IV[pt] OR randomized controlled trial[pt])”

Search terms:

Protein-based nanocarriers: protein nanoparticle, protein nanoparticles, protein nanocarrier, protein nanocarriers, protein-based nanoparticle, protein-based nanocarriers, peptide nanoparticle, peptide nanoparticles, peptide nanocarrier, peptide nanocarriers, polypeptide nanoparticle, polypeptide nanocarriers, virus-like particle, virus like particle, VLP, protein cage, ferritin nanoparticle, ferritin nanocarrier, apoferritin nanoparticle, apoferritin nanocarrier, albumin nanoparticle, albumin nanoparticles, albumin nanocarrier, albumin nanocarriers, albumin-bound, albumin-stabilized, HSA nanoparticle, HSA nanoparticles, BSA nanoparticle, BSA nanoparticles, casein nanoparticle, casein nanocarrier, nab-paclitaxel, nab technology

Inorganic nanocarriers: gold nanoparticle, gold nanoparticles, gold nanocarrier, gold nanocarriers, silver nanoparticle, silver nanoparticles, silver nanocarrier, silver nanocarriers, silica nanoparticle, silica nanoparticles, silica nanocarrier, silica nanocarriers, iron oxide nanoparticle, iron oxide nanoparticles, iron oxide nanocarrier, iron oxide nanocarriers, quantum dot, quantum dots, inorganic nanoparticle, inorganic nanoparticles, inorganic nanocarrier, inorganic nanocarriers

Polymeric nanocarriers: polymeric nanoparticle, polymeric nanoparticles, polymeric nanocarrier, polymeric nanocarriers, polymer nanoparticle, polymer nanoparticles, polymer nanocarrier, polymer nanocarriers, PLGA, PLA, PCL, polycaprolactone, polylactic, polylactic-co-glycolic, polymeric micelle, polymeric micelles, nanogel, nanogels, nanogel

nanocarrier, nanogel nanocarriers, dendrimer, dendrimers, dendrimer nanoparticle, dendrimer nanoparticles, dendrimer nanocarrier, dendrimer nanocarriers

Lipid-based nanocarriers: liposome, liposomes, liposomal, lipid nanoparticle, lipid nanoparticles, lipid nanocarrier, lipid nanocarriers, solid lipid nanoparticle, solid lipid nanoparticles, solid lipid nanocarrier, solid lipid nanocarriers, SLN, lipid micelle, lipid micelles

Carbon-based nanocarriers: carbon nanotube, carbon nanotubes, fullerene, fullerenes, carbon-based nanocarrier, carbon-based nanocarriers, carbon-based nanoparticle, carbon-based nanoparticles, carbon-based nanomaterial, carbon-based nanomaterials, carbon nanomaterial, carbon nanomaterials, carbon nanoparticle, carbon nanoparticles, carbon nanocarrier, carbon nanocarriers

All nanocarriers: liposome, liposomes, liposomal, lipid nanoparticle, lipid nanoparticles, lipid nanocarrier, lipid nanocarriers, solid lipid nanoparticle, solid lipid nanoparticles, solid lipid nanocarrier, solid lipid nanocarriers, SLN, lipid micelle, lipid micelles, polymeric nanoparticle, polymeric nanoparticles, polymeric nanocarrier, polymeric nanocarriers, polymer nanoparticle, polymer nanoparticles, polymer nanocarrier, polymer nanocarriers, PLGA, PLA, PCL, polycaprolactone, polylactic, polylactic-co-glycolic, polymeric micelle, polymeric micelles, nanogel, nanogels, nanogel nanocarrier, nanogel nanocarriers, protein nanoparticle, protein nanoparticles, protein nanocarrier, protein nanocarriers, protein-based nanoparticle, protein-based nanocarriers, peptide nanoparticle, peptide nanoparticles, peptide nanocarrier, peptide nanocarriers, polypeptide nanoparticle, polypeptide nanocarriers, virus-like particle, virus like particle, VLP, protein cage, ferritin nanoparticle, ferritin nanocarrier, apoferritin nanoparticle, apoferritin nanocarrier, albumin nanoparticle, albumin nanoparticles, albumin nanocarrier, albumin nanocarriers, albumin-bound, albumin-stabilized, HSA nanoparticle, HSA nanoparticles, BSA nanoparticle, BSA nanoparticles, casein nanoparticle, casein nanocarrier, nab-paclitaxel, nab technology, hybrid nanoparticle, hybrid nanoparticles, hybrid nanocarrier, hybrid nanocarriers, lipid-polymer hybrid, polymer-lipid hybrid, lipid-inorganic hybrid, polymer-inorganic hybrid, hybrid nanomedicine, gold nanoparticle, gold nanoparticles, gold nanocarrier, gold nanocarriers, silica nanoparticle, silica nanoparticles, silica nanocarrier, silica nanocarriers, quantum dot, quantum dots, iron oxide nanoparticle, iron oxide nanoparticles, iron oxide nanocarrier, iron oxide nanocarriers, silver nanoparticle, silver nanoparticles, silver nanocarrier, silver nanocarriers, carbon

nanotube, carbon nanotubes, fullerene, fullerenes, carbon nanoparticle, carbon nanoparticles, carbon nanocarrier, carbon nanocarriers, dendrimer, dendrimers, dendrimer nanoparticle, dendrimer nanoparticles, dendrimer nanocarrier, dendrimer nanocarriers, exosome, exosomes, extracellular vesicle, extracellular vesicles, biomimetic nanoparticle, biomimetic nanoparticles, biomimetic nanocarrier, biomimetic nanocarriers

List of peer-reviewed publications and patents

Zegota, M. M.‡; Müller, M. A.‡; **Lantzberg, B.**; Kizilsavas, G.; Coelho, J. A. S.; Moscariello, P.; Martínez-Negro, M.; Morsbach, S.; Gois, P. M. P.; Wagner, M.; Ng, D. Y. W.; Kuan, S. L.; Weil, T. Dual Stimuli-Responsive Dynamic Covalent Peptide Tags: Toward Sequence-Controlled Release in Tumor-like Microenvironments. *J. Am. Chem. Soc.* **2021**, *143* (41), 17047–17058. DOI: 10.1021/jacs.1c06559

Fuchs, N.‡; Meta, M.‡; **Lantzberg, B.**; Bros, M.; Kuan, S. L.; Weil, T.; Schirmeister, T. Subnanomolar Cathepsin S Inhibitors with High Selectivity: Optimizing Covalent Reversible α-Fluorovinylsulfones and α-Sulfonates as Potential Immunomodulators in Cancer. *ChemMedChem* **2023**, *18* (15), e202300160. DOI: 10.1002/cmdc.202300160.

Heck, A. G.; Schwiertz, D.; **Lantzberg, B.**; Nguyen, H. C.; Forster, R.; Scherger, M.; Opatz, T.; Van Ginderachter, J. A.; Nuhn, L. Introducing Targeting Units or pH-Releasable Immunodrugs into Core-Clickable Nanogels. *Eur. Polym. J.* **2024**, *214*, 113150. DOI: 10.1016/j.eurpolymj.2024.113150.

Lantzberg, B.; Weil, T.; Kuan, S. L.; Opatz, T.; Forster, R.; Bros, M.; Zeyn, Y.; Schuppan, D.; El Mard, H. *Human Serum Albumin Based Nanocarriers for Immunotherapy.* Patent publication number WO 2025/176738, 2025.

Lantzberg, B.‡; Zeyn, Y.‡; Forster, R.‡; Jian, L.; Schauenburg, D.; Hieber, C.; Nuhn, L.; Zhou, T.; Silva, M. J. S. A.; Koynov, K.; Jiang, H. L.; Kuan, S. L.; Bros, M.; Opatz, T.; Weil, T. Glycogen-inspired trimannosylated serum albumin nanocarriers for targeted delivery of toll-like receptor 7/8 agonists to immune cells and liver. *J. Control. Release* **2025**, *382*, 113705. DOI: 10.1016/j.jconrel.2025.113705.

Forster, R.‡; **Lantzberg, B.**‡; Weldert, A.‡; Rosenberger, L.; Zeyn, Y.; Kowalczyk, D.; Kuan, S. L.; Kersten, C.; Bros, M.; Weil, T.; Schirmeister, T.; Opatz, T. Surface Density of Mono- and Trivalent High-Mannan-Derived Targeting Structures with Different Affinities Impacts Cellular Uptake of Human Serum Albumin-Derived Nanocarriers. *Biomacromolecules* **2025**, *26* (11), 8087–8102. DOI: 10.1021/acs.biomac.5c01510.

‡ Authors contributed equally to this work.

Curriculum Vitae

[redacted]